PHYS

VOLUME

THE PHYSICAL REVIEW

A journal devoted to research in physics, established by E. L. Nichols in 1893

BOARD OF EDITORS

Editor

A. Goldhaber

Associate Editors

Harvey Brooks
R. E. Carter
C. L. Cottrell
M. Deutsch
T. H. Johnson
Bruno Rossi

Manuscripts for publication should be submitted to S. A. Goudsmit, Brookhaven National Laboratory, Upton, Long Island, New York. Authors' institutions are requested to pay a publication charge of $10 per printed page; if honored, entitles them to 100 free reprints. Instructions to agree with galley proofs.

Proof and all correspondence concerning papers in the process of publication should be addressed to the Publication Manager, American Institute of Physics, 57 East 55 Street, New York 22, New York.

Subscription Price

Domestic Subscription and Canada $15.00
Foreign $17.50

Back Numbers

Yearly bound volume rate when complete year is available:
Prior to 1940: $20.00
Thereafter: $25.00

Single copies: $2.00 each, prior to July, 1939.
$1.00 each, July, 1939–December, 1941.
$2.00 each, January, 1942–December, 1946.
$1.00 each, January, 1947–December, 1948.
$1.25 each, thereafter.

General index, 1893–1920: $4.00.

Subscriptions, renewals, and orders for back numbers should be addressed to the American Institute of Physics, 57 East 55 Street, New York 22, New York.

Change of address in the case of members of the American Physical Society should be addressed to the Treasurer; in the case of other subscribers, to the American Institute of Physics.

[For Publication Office of Physics Department, Cornell University, Ithaca, New York]

Published semi-monthly by the American Physical Society at the Printing Plant of the Science Press, Prince and Lemon Streets, Lancaster, Pennsylvania.

Entered as second class matter June 29, 1938, at the Post Office at Lancaster, Pennsylvania, under the Act of March 3, 1879.

Acceptance for mailing at special rate of postage provided for in Section 1103, Act of October 3, 1917, authorized on July 31, 1918.

THE
PHYSICAL REVIEW

A journal of experimental and theoretical physics established by E. L. Nichols in 1893

SECOND SERIES, VOL. 81, NO. 5 MARCH 1, 1951

A Cloud-Chamber Study of Nuclear Interactions in Lead and Aluminum. Part I*

B. P. GREGORY AND J. H. TINLOT†
Department of Physics and Laboratory for Nuclear Science and Engineering, Massachusetts Institute of Technology, Cambridge, Massachusetts

(Received October 9, 1950)

The nuclear interactions of cosmic-ray particles in lead and aluminum have been studied in two cloud-chamber experiments. The results of the first experiment, which yields an unbiased sample of interactions of protons, are used to discuss the relative and absolute cross sections in the two materials and the absolute intensity and energy spectrum of the incident protons. The second experiment was designed to select interactions of neutrons in which at least one penetrating ionizing particle was produced.

The types of interactions observed are in this case intimately related to the probability of triggering the cloud chamber. This problem is discussed in some detail, preparatory to more detailed analysis of this experiment in Part II of this paper.

I. INTRODUCTION

MANY experimenters[1–6] have used counter controlled cloud chambers to study the nuclear interactions of cosmic-ray particles. The greatest difficulty in the interpretion of data so obtained has arisen from the complicated and usually unknown effects of the method used for selecting events of interest. The present investigation was intended to minimize this difficulty by use of simple counter selection systems. The two systems used required (a) the detection of a single incident ionizing primary particle and (b) the detection of a single secondary ionizing penetrating particle.

Alternate thin lead and aluminum plates were mounted in the chamber. This particular arrangement was found useful for two reasons: (1) to compare the characteristics of nuclear interactions in two materials of widely different atomic number, and (2) to simplify the identification of particles and the definition of nuclear interactions.

The cloud chamber was operated under a wooden roof of thickness 3 g/cm² at Echo Lake, Colorado, elevation 10,600 ft (700 g/cm²). The discussion of results has been divided into two papers, which we shall denote as Part I and Part II. In Secs. II and III of Part I, we are concerned with the characteristics of the primary particles. A sample of nuclear interactions of cosmic-ray protons (Sec. II) yields information as to the relative and absolute cross sections for particular interactions and as to the flux and energy distribution of these protons. We shall consider in Sec. III the nuclear interactions of neutrons in the two materials resulting in the production of penetrating particles, and discuss some consequences of our choice of triggering arrangement.

II. EXPERIMENTS A AND A'

(1) Experimental Arrangement

The cloud chamber contained seven lead plates ¼ inch thick and six aluminum plates $\frac{3}{16}$ inch thick, alternately arranged as shown in Fig. 1. The depth of the illuminated region was six inches. Stereoscopic photographs were taken with cameras whose axes were separated by 12 inches, at a distance of 55 inches from the front of the cloud chamber.

In Experiment A, the cloud chamber was expanded by a signal from a counter telescope placed above the chamber and shielded by a one-inch lead brick, as shown in Fig. 1. The volume defined by the intersection of the cone of acceptance of the telescope and the top

* This work was supported in part by the joint program of the ONR and AEC.

† Now at The University of Rochester, Rochester, New York.

[1] W. B. Fretter, Phys. Rev. 73, 41 (1948). (Reference on previous work may be found in this article.)

[2] H. S. Bridge and W. E. Hazen, Phys. Rev. 74, 579 (1948).

[3] C. Y. Chao, Phys. Rev. 75, 581 (1948).

[4] W. B. Fretter, Phys. Rev. 76, 511 (1949).

[5] Lovati, Mura, Salvini, and Tagliaferri, Phys. Rev. 77, 284 (1950).

[6] W. W. Brown and A. S. McKay, Phys. Rev. 77, 342 (1950).

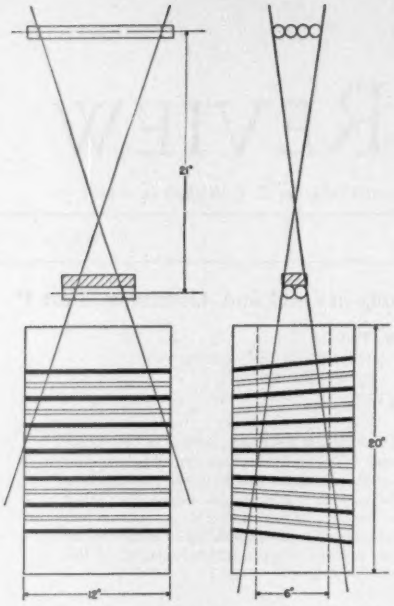

FIG. 1. Plate assembly and triggering arrangement of Experiment A.

and bottom plates in the chamber was included in the illuminated region within two percent. The primary purpose of the experiment was to obtain an unbiased sample of interactions of these particles with the material in the chamber.

In Experiment A′, a tray of eighteen counters was placed below the chamber, and the chamber was expanded whenever the telescope recorded a signal in anticoincidence with this tray, or in coincidence with the discharge of more than one counter in this tray. The resulting pictures were found to be useful only in improving the statistics on the relative numbers of protons and mesons stopping in the chamber.

(2) Triggering Events. Experiment A

One could usually identify, from the appearance of the counter age tracks in the pictures, the method by which the counter telescope had been triggered. One observed in a number of pictures only an electronic component, and considered that in this case the telescope had been triggered by an air shower. In most cases, however, a single particle entered the chamber after traversing the counter telescope. By studying the behavior of these particles, we obtain statistical information on the relative abundance of the ionizing components of cosmic radiation. For this purpose, the analysis was restricted to pictures which belonged to a series of pictures of uniformly good quality. The events observed in this set of pictures (a total number of 3827) are listed in Table I, and are discussed in detail in the following paragraphs.

(a) *Single Penetrating Particles*

Single particles (minimum range 104 g/cm² of lead) were observed to traverse the chamber without interaction in 2397 pictures of the set. The corresponding number of particles defined as belonging to the hard component (particles of range greater than 167 g/cm² of lead) is five percent less, or 2262. Since the flux of the hard component at the altitude in question is a well-known quantity, this number is one to which the number of all other events may be compared.

(b) *Particles Stopped*

The particles which stopped in the chamber were a mixture of μ-mesons, protons at the end of their range, and protons stopped by nuclear collision. The protons, whether or not at the end of their ranges, show much smaller Coulomb scattering than did the mesons, as is illustrated in Table II. One can make use of this fact to estimate the proportion of mesons and protons stopping in the chamber. One computes, from measurements on all the particles stopped, the root mean square scattering angles at the second lead plate above the plate in which the particles stopped. This value is then compared to the expected root mean square projected angle of scattering for mesons ($\alpha_\mu = 12.5°$) and protons (α_p). The upper and lower limits on the number of mesons are obtained by assuming that all protons stop by nuclear collision ($\alpha_p \simeq 0$) or stop at the end of their range ($\alpha_p = 4.8°$). From the combined pictures of Experiments A and A′, one finds in this way that, of 81 particles stopped in the fourth through twelfth plates, between 32 and 39 were mesons. The behavior of the protons is seen to have a small effect on the computation.

Of the 46 stopped particles observed in Experiment A, only 30 stopped in the fourth through twelfth plates. From the above, it is estimated that 13 of these were mesons, and 17 were protons. The correlation of the number of stopped mesons with the flux of slow mesons incident on the telescope is difficult because of the great loss through scattering in the lead block in the telescope. One computes, for example, a loss of 75 percent of all mesons of ranges such as to stop in the middle plate of the chamber. The corresponding loss of protons, however, is only 9 percent, so that the results

TABLE I. Frequency of occurrence of various types of events based on 3827 frames of the A-experiment.

Single particle emerging from telescope				Elcetronic showers		
Through	Stopping	Interacting	Nuclear scattering	High energy electron	Air shower	Blank pictures
2397	46	35	9	5	273	1062

concerning stopped protons are significant (see Sec. II-5 and Table III).

(c) *Nuclear Interactions*

In 44 cases, an ionizing particle emerging from the counter telescope produced a nuclear interaction in the illuminated region of the chamber. It is assumed that all such particles were protons. We shall discuss these interactions in detail in Sec. II-3. In particular, it will be shown that the corrected number of interactions occurring in the second through twelfth plates is 42.

(d) *Electronic Component*

We consider first the evidence for identification of single incident electrons. An electron of 1-Bev energy passing through the counter telescope would undergo multiplication in the one-inch lead block, and would appear in the chamber as a shower with about ten particles at the maximum.[7] Only five such showers were observed. This number corresponds to a directional intensity of high energy electrons of about 3×10^{-5} sec^{-1} ster^{-1} cm^{-2}. Hazen[8] has computed a directional intensity seven times as large for both electron- and photon-initiated showers in the same energy range and at the same altitude. We may explain the difference in the two figures by noting that most of the showers may well be photon-initiated, and that we detect only electron-initiated showers.

It is seen from Table I that over a quarter of the set of pictures of Experiment A showed either a purely electronic component, or were blank. The first type were easily identified as caused by ordinary extensive air showers. The blank pictures are attributable neither to accidental telescope coincidences nor to instrumental failures. It is most likely that, in these cases, the counter telescope responded to air showers of very low density, which were not visible in the cloud chamber.

(3) Description of Nuclear Interactions

Since, in this section and in Sec. II-4, we shall be concerned only with relative numbers of nuclear interactions, we shall consider a more extensive set of pictures, thus improving our statistical results. We consider in addition to the interactions of Table I others that were not of counter age, or that were observed in groups of pictures whose quality was not considered good enough for inclusion in the set of Table I. All of these interactions were produced by ionizing primaries.

TABLE II. Energy, scattering, and ionization of particles stopping in a lead plate. In this computation only losses by ionization are taken into account.

Interval	Plate	Proton Energy (Mev)	Proton rms scatt. (in)	Proton I/I_{min}	Meson (214mμ) Energy (Mev)	Meson rms scatt. (in)	Meson I/I_{min}
	Pb			-4.8	0-24		-2.2
1	Al	0-60					
2		42-76		6.6-4.0	16-30		2.8-1.9
3	Pb	78-103		4.0-3.3	31-42		1.6
4	Al	95-115		3.5-3.1	36-48		1.5
5	Pb	117-135	4.3	2.9	48-60	11	1.4
6	Al	128-145	1.0	2.8	52-62	2.6	1.3
7	Pb	148-153	3.5	2.5	62-72	9	
8	Al	157-172		2.4	65-75	2.2	
9	Pb	175-189	2.9	2.3	73-83	7.7	
10	Al	183-197		2.2	78-86	1.8	
11	Pb	199-213	2.5	2.2	87-95	6.8	
12	Al	207-220		2.1	92-100	1.6	
13	Pb	222-235	2.3		97-105	5.9	
Range in g/cm² Pb							
100		300	1.7	1.8	140	4.6	
170		400	1.3	1.5	220	3.2	
240		500	1.1	...	300	2.5	
310		600	0.9	...	385	2.0	
410		720	...		500	1.5	

(a) *Identification of Nuclear Interactions*

The various types of nuclear interactions are best illustrated by the pictures of Fig. 2. Interactions of types (1) and (2) are called "nuclear scattering." In these cases, one required that a particle of minimum ionization traverse two lead plates with no appreciable scattering (less than 1°) and then be deflected through an angle of more than 10°. When the deflection occurred

TABLE III. Absolute numbers of protons of various energies incident on the telescope. These numbers are normalized to 2262 particles of the "hard component."

	Protons stopping 4th-12th	Protons interacting (2nd-12th plates) Types 1-2	Types 3-4	Types 5-6	Type 7	
Corrected number of events	17	13	11	13	2	3
Number of protons incident on telescope	23	56	47	56	8	12
Approximate energy of the protons (Bev)	0.2 to 0.3		0.3 to 1		1 to 2	>2
Intensities relative to the hard component	10^{-2}	2.5×10^{-2}	2.1×10^{-2}	2.5×10^{-2}	0.3×10^{-2}	0.5×10^{-2}

[7] I. G. Tamm and S. Belenky, J. Phys. U.S.S.R. 1, No. 2 (1939).
[8] W. E. Hazen, Phys. Rev. 65, 67 (1944).

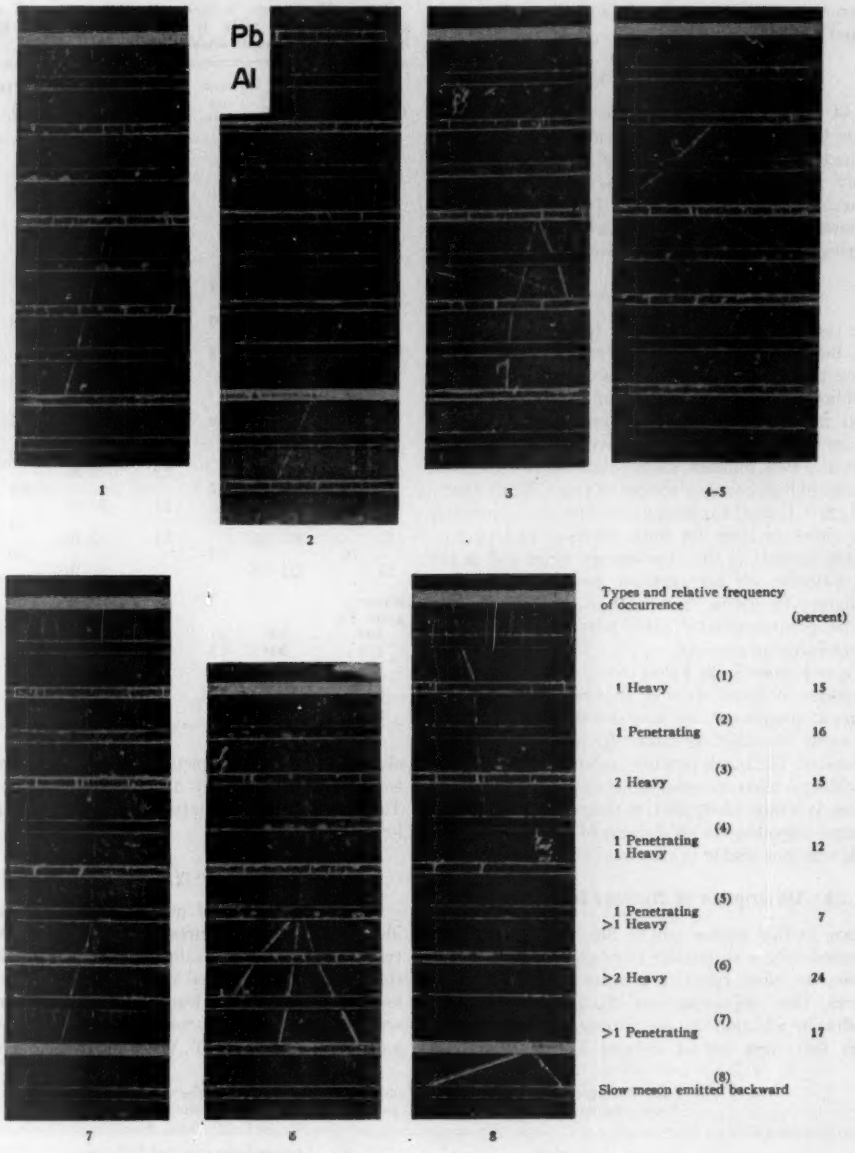

FIG. 2. A sample of nuclear interactions (Experiment A).

after traversal of more lead plates, scattering angles of 2° were accepted. All angles were measured in projection. The expected number of μ-mesons abnormally scattered through Coulomb interaction (and thus mistaken as protons suffering nuclear scattering) can then be calculated. We consider only the effect of multiple scattering. (For $\frac{1}{4}$-inch lead plates, the effect of single Coulomb scattering is negligible, if one assumes that the maximum angle of single scattering is equal to $\hbar/Rp$, in which R is the radius of the nucleus, and p is the momentum of the meson.) The probability of observing scatterings in the specified sequence

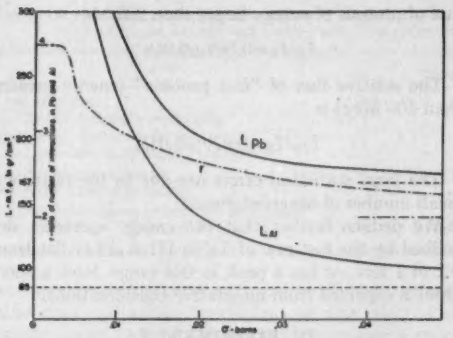

FIG. 3. Mean free path in lead and aluminum under the theory of transparency. These mean free paths are plotted as functions of the cross sections ($\bar{\sigma}$) for the interaction of the individual nucleons with the incident particle for $R=1.37A^{\frac{1}{3}}10^{-13}$ cm. The value of r is the expected ratio of the numbers of nuclear interactions occurring in 7 lead plates (49.7 g/cm²) and 6 aluminum plates (12.8 g/cm²).

is found to have an average value of 0.2 percent for mesons of range between 15 and 170 g/cm² of lead, and to be negligible for mesons of greater range. Since the intensity of "slow" mesons is 10 percent of that of the hard component, one finds that for the set of pictures of Table I, the expected number of mesons thus scattered is $0.002\times0.10\times2262\approx0.4$, as compared with the 9 cases of "nuclear scattering." Moreover, these events occurred about as frequently in lead and aluminum, and the observed deflection was larger than 20° in 9/10 of the cases. These are further indications of the nuclear origin of these interactions.

The minimum requirement for identification of interactions of types (3) to (7) was the observation of one heavily ionizing particle, or of one penetrating particle emitted at an angle of more than 10° (in projection) with the direction of the incident particle. These conditions were found to be sufficient to reject all knock-on showers of mesons.

Nuclear scatterings could not be observed in the first three plates in the chamber because of the criterion used in their selection. Moreover, the identification of all interactions occurring in the top and bottom plates was not considered reliable, and the corresponding pictures were rejected. We shall therefore consider in the following discussions only interactions observed in the second through twelfth plates, and correct the number of nuclear scatterings for the loss in plates 2 and 3. The relative frequencies of occurrence of the interactions of various types (Fig. 2) are obtained from this corrected number of 70 interactions.

(b) *Estimate of the Energy of the Primary Protons*

The following observations indicate that the energy of the protons producing the great majority of the observed interactions is below 1 Bev. If we consider the group of interactions of types (1), (2), (3), and (4), we find that in no case can a secondary meson or electronic component be detected. Furthermore, the incident protons in one quarter of these cases was visibly scattered. The protons producing interactions of types (5) and (6) were of somewhat higher energy than those of the first group, since none were visibly scattered. However, the estimated energy of the ionizing secondary particles was less than 450 Mev, and in only 4 cases out of 22 did one identify a secondary meson or electronic component.

The example of type (7) is one of the small group (11 percent of the total) of interactions of high energy protons. These were characterized by the production of two or more penetrating particles. In one-half of these cases, the energy of the ionizing secondary particles was estimated to be greater than 1 Bev.

(c) *The Possibility of Single Proton-Nucleon Collision*

We have investigated the possibility that some of the interactions of types (3) and (4) were due to a single collision between the incident proton and a proton of the nucleus.[9] We determined the directions in space of the particles, and set limits to their energies. We could then compare these values with those predicted by the energy-angle relation for collisions between free nucleons, corrected for the motion of the nucleons in the nucleus. In 22 out of 26 cases we could not interpret the event as a simple proton-proton collision, even by assuming the most favorable velocity for the struck proton. One may therefore conclude that in the collision of a proton of average energy 500 Mev with a nucleus of lead or aluminum, the secondary nucleons are a result of multiple collisions within the nucleus.

(d) *Proton-Neutron Charge Exchange*

On the basis of the results obtained in Berkeley[10] with 350-Mev protons, we expected to observe a considerable proportion of events of the type "charge exchange," in which a proton would turn into a neutron of almost the same energy. A number of interactions of types (1), (3), and (6) were interpreted as possible examples of charge exchange, in which cases an average of 100 Mev was transferred to secondary protons; this corresponded to a probable total energy loss of 200 Mev. Only one case was found in which no visible secondary particle was produced. We shall derive similar conclusions in Sec. III concerning the inverse process of neutron-proton charge exchange.

(4) Numbers of Nuclear Interactions in Lead and Aluminum. Transparency

The choice of lead and aluminum for the plates was made for the purpose of obtaining relative cross

[9] J. G. Wilson, Proc. Roy. Soc. (London) **A174**, 72 (1940). (This has been found to be the case in one picture.)

[10] University of California Radiation Laboratory Report UCRL 637, unpublished.

sections for the production of nuclear interactions in a light and heavy element. The results of this section and of Sec. III-4 will be compared with the expected relative number of interactions under the assumption of geometric cross sections (nuclear radius proportional to $A^{\frac{1}{3}}$). This ratio, for the seven lead plates (49.7 g/cm²), and the six aluminum plates (12.8 g/cm²), is found to be

$$r_0=2.0.$$

Of the 70 nuclear interactions considered in Sec. II-3, 41 occurred in five lead plates, and 29 in six aluminum plates. The ratio of the interactions in lead and in aluminum normalized to the total amount of material of the chamber is, therefore,

$$r_A=2.0\pm0.5.$$

The result is compatible with geometric cross sections. The ratio r can be related to the absolute cross sections in the two materials by application of the theory of transparency of the nucleus.[11,12] The curves of Fig. 3 illustrate the variation of this ratio and of the collision mean free paths of particles in the two materials as a function of the assumed particle-nucleon cross sections. One sees from these curves that the value $r=2.5$ (still consistent with the experimental result) corresponds to mean free paths of 200 g/cm² of lead and 140 g/cm² of aluminum.

(5) Spectrum and Absolute Intensity of Protons at 10,600 Feet

In this section we shall estimate the absolute directional intensity of protons and obtain a qualitative description of their energy spectrum. For this purpose, we shall now consider only the set of pictures of Table I.

The first row of Table III gives the number of protons stopped in the fourth through twelfth plates of the chamber [as obtained in Sec. II-2(b)], and the corrected numbers of nuclear interactions observed in the chamber from the second through twelfth plates [from Sec. II-2(c)]. We list in the third row the estimated energies of the incident protons responsible for these various types of interactions.

We obtain the absolute numbers of protons entering the telescope (listed in the second row of Table II) in the following two steps: (1) We compute the numbers of protons entering the chamber by assuming that all protons of the first column stop at the end of their ranges, and that all the other protons interact in the chamber with geometric cross sections; and (2) we increase these numbers for the loss by interaction (also with assumed geometric cross section) in the material above the chamber.

We can now compare these numbers with the corresponding flux (2262 particles) of the hard component. These relative intensities are listed in the last row of Table III. The sum of the numbers yields the relative flux of protons of energy larger than 200 Mev:

$$I_p/I_h=0.089\pm0.018.$$

The relative flux of "fast protons" (energy greater than 400 Mev) is

$$I_{fp}/I_h=0.079\pm0.015.$$

The large statistical errors are due to the relatively small number of observed events.

We deduce further that the energy spectrum described by the last row of Table III is either flat from 0.2 to 1 Bev, or has a peak in this range. Such a spectrum is expected from qualitative considerations.

III. EXPERIMENT B

(1) Experimental Arrangement

In this experiment the cloud chamber was triggered by a signal from a shielded counter telescope placed below the chamber when not accompanied by a signal from a large tray of counters placed above the chamber (Fig. 4).

This arrangement favored the recording of events in which a neutral primary particle produced secondary ionizing particles. The plate assembly was identical with that used in Experiment A. We had intended to study the effect of varying the thickness of the lead shields S_1, S_2, and S_3. Thus, the thickness of S_1 was 0, 1 in., or 7 in., while the thicknesses of S_2 and S_3 were either 1 in. and 1 in., 0 and 4 in., or 1 in. and 9 in., respectively. However, the number of pictures taken in

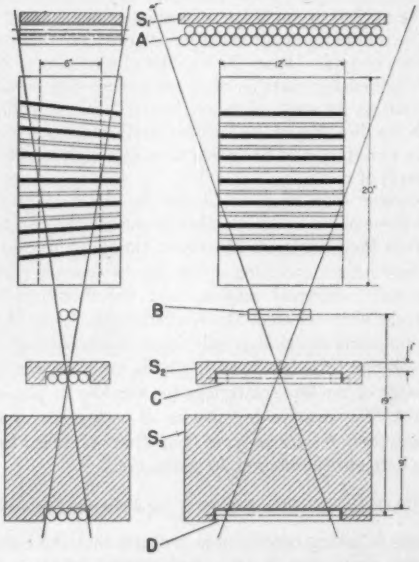

FIG. 4. Plate assembly and triggering arrangement of Experiment B.

[11] Fernbach, Serber, and Taylor, Phys. Rev. 75, 1352 (1949).
[12] R. Serber, Phys. Rev. 72, 1114 (1947).

TABLE IV. Summary of nuclear interactions of Experiment B. The 136 nuclear interactions were due to non-ionizing primaries and occurred in the first through tenth plates. The corrected relative frequency is obtained as described in Section III-3.

	Group I						Group II		
Type of picture	(1)	(1)′	(2)	(2)′	(3)	(3)′	(4)	(4)′	(5)
Number of penetrating particles	1	1	2	2	>2	>2	>2	>2	>2
Number of electronic showers	0	⩾1	0	⩾1	0	⩾1	0	⩾1	⩾1 of high energy
Total number—showers and particles					⩽6		>6		
Number of interactions	36	5	20	7	9	25	2	12	20
Corrected relative frequency	0.69		0.22		0.06		0.01		0.02
Ratio of interactions in lead and aluminum normalized to 7 Pb and 6 Al (Fig. 3)	2.3±0.6				5.0±1.4				

each arrangement was not sufficient to allow us to draw more than qualitative conclusions on this effect. For instance, with no lead above the anticoincidence tray, we observed a few purely electronic showers which apparently were due to materialization of incident photons. This was confirmed by the fact that these events were eliminated when the thickness of S_1 was 1 in. or 7 in.

From a total of about 5000 pictures obtained in this experiment, we selected for study 322 pictures of nuclear interactions. Of these interactions 237 occurred in the illuminated region, and were clearly responsible for the triggering of the counter telescope.

(2) Effect of the Triggering Requirement

In this section we shall examine in some detail the effect of the triggering arrangement of the choice of the particular events photographed. In order to be photographed, a nuclear interaction originating within the illuminated region must produce at least one particle which penetrates the shielded counter telescope. The probability that a particular interaction will accomplish this depends primarily on the multiplicity of the penetrating particles produced, and on the location of the point of origin.

One can compute, for any point of origin, the solid angle Ω_s within which a penetrating particle must be emitted in order to traverse the telescope. The value of this angle (averaged over the surface of each plate) varies from 0.007 to 0.014 steradian from the first to the tenth plate. We shall use also the solid angle Ω_D subtended by tray D at various points within the illumination (varying from 0.03 to 0.05 steradian) and the solid angle Ω_B subtended by tray B (varying from 0.03 to 0.14 steradian). The values of these average solid angles for the middle plate of the chamber are:

$$\Omega_s=0.01, \quad \Omega_D=0.04, \quad \Omega_B=0.05.$$

Note that a particle aimed at tray D from almost any point in the illuminated region traverses tray C, and therefore that the effect of tray C can be neglected.

From the above numbers, one could, in principle, compute the absolute probability of triggering for any event of given multiplicity of penetrating particles and electronic showers, originating anywhere in the chamber. It seems useless to attempt this calculation rigorously, because of the necessity of making detailed assumptions as to the energy and angular distributions of the secondary particles and showers. We shall make instead the approximation that the penetrating particles are emitted uniformly within a cone of solid angle Ω. For the present we neglect the absorption or scattering of these particles in the lead shielding of the telescope, and take a value of Ω (0.55 steradian) which corresponds to an average angle of emission of 16° (Sec. II, Part II).

We can now calculate the probability that any interaction producing N penetrating particles triggers the telescope singly (one particle traversing trays A, B, and C):

$$P_s=1-(1-\Omega_s/\Omega)^N\simeq N\Omega_s/\Omega.$$

This probability is not very sensitive to the particular plate in which the interaction occurs, and is nearly proportional to N even for high multiplicities, because of the small values of Ω_s/Ω. P_s is of the order of 2 percent for an interaction producing one penetrating particle.

The probability P_m of multiple triggering (by separate particles traversing tray B and trays C and D) is easily shown to be much smaller than P_s for low multiplicity interactions occurring in the top plates and to increase sharply with the plate number and the multiplicity N. One may use the formula:

$$P_m=\Omega_B\Omega_D N(N-1)/\Omega^2$$

for interactions occurring in the upper plates of the cloud chamber and having a multiplicity less than five. The total probability of triggering is the sum of P_s and P_m. An important result is that multiple triggering is the dominant process for interactions occurring in the bottom half of the chamber and having multiplicity larger than three. For example, P_m is equal to P_s for $N=4$ in the seventh plate, and for $N=3$ in the ninth plate.

The probability of triggering tray B approaches one when a number of electronic showers are produced, particularly if the interaction occurs in the lower plates. In this case, the triggering process is complete if one penetrating particle is emitted in the solid angle Ω_D so as to discharge tray D. The probability of this modified single triggering is, therefore,

$$P_s'\simeq\Omega_D N/\Omega\simeq 4P_s.$$

It is evident that the triggering probability varies over a wide range, depending upon the characteristics of the nuclear interaction. For example, the value P_s' for $N=5$ is 20 times the value of P_s for $N=1$.

The considerations of the preceding paragraphs are involved in the interpretation of practically all of the data obtained in Experiment B. They will be found particularly useful in discussing the following:

(i) The true frequencies of occurrence of various interactions.

(ii) The relative cross sections for nuclear interactions in different materials (since the character of the interactions, and consequently the triggering probabilities, may depend upon the material).

(iii) The relative numbers of penetrating particles and electronic showers (Part II).

(iv) The nuclear interactions of secondary penetrating particles (Part II).

(3) Description of Interactions and Results

Results relating to 136 selected nuclear interactions are given in Table IV. These interactions were caused

by a non-ionizing primary, and occurred in the illuminated region of the first ten plates in the chamber. We divided them into two groups (low and high multiplicity) and subdivided them according to the multiplicity of penetrating particles and numbers of electronic showers. The distinction of penetrating particles is often difficult in the cases of interactions of type (5), because of the production of high energy electronic showers (energy greater than 1 Bev).

The remainder of the total number (237) of interactions occurring in the illuminated region, although not included in Table IV, are considered in later discussions. These include a small number caused by ionizing primaries incident at a large inclination and a large group (76) of interactions occurring in the three lowest plates. Analysis of this last group is difficult, since one cannot identify penetrating particles or, in most cases, recognize electronic showers. These pictures will be useful only for statistical considerations for which the type of event is not of great importance. The relation frequency of occurrence of different events has been corrected for the effect of the triggering requirement according to the estimates made in the next paragraphs.

(a) *Corrected Frequencies of Occurrence of Various Interactions*

By applying the results of the discussion on the probability of triggering, one can estimate the true relative rates of occurrence of the events of the various types. In the four types of interactions of group I the electronic showers were nearly always of low energy, and did not contribute appreciably to the triggering process. Since a single particle was in nearly all cases responsible for the discharge of the counter telescope, the probabilities of triggering are given by the equation for P_s. These interactions were, as expected, fairly evenly distributed among the plates. The events of higher multiplicity (group II) occur most frequently in the lower plates, e.g., 13 in the first four plates, compared with 48 in plates 7 through 10. This is expected if the triggering process was predominantly of the multiple type. For the interactions of type (3), we estimate the triggering probability by taking an intermediate figure between the values of P_s and P_s' for a multiplicity $N=4$. When tray B was discharged with a probability of almost one (types (4) and (5)), the triggering probability was assumed to be given by P_s' for $N=5$. From the observed numbers of events of each type and with the knowledge of the appropriate triggering probabilities, one readily obtains the corrected relative frequencies of occurrence as listed in the fourth line of Table IV.

(b) *Estimate of the Energy of the Primary Neutrons*

From the amount of penetration required of the triggering particles one can estimate the minimum energy (about 400 Mev) of the neutrons producing them. The average energy of the neutrons is believed to be in the range where meson production is fairly common (i.e., about 1 Bev). For example, one observed in one-quarter of the cases of types (1) and (2) either electronic component or scattering of the penetrating particles greater than that expected for a proton.

Interactions of types (3), (4), and (5) produced ionizing secondary particles and electronic showers whose combined energy appeared to be 4 Bev, on the average. This is a crude lower limit, since one neglects the production of secondary neutrons, and arbitrarily assigns a minimum energy to each relativistic unscattered particle.

(c) *Neutron-Proton Charge Exchange*

The interactions of type (1) can be interpreted as examples of neutron-proton charge exchange. One assumes then that a neutron of energy greater than 400 Mev turned into a proton, and that a part of the original energy was dissipated in exciting a nucleus. The average energy delivered to slow protons was found to be on the average, about 200 Mev. Although this type of interaction is quite frequent (see Table IV), we are unable to compare its probability of occurrence with the probability of interactions which produce only low energy nucleons, since the latter event would not be recorded.

On the other hand, we may obtain the relative probability of charge exchange at the higher energies (above 4 Bev). If a neutron of this energy turns into a proton of nearly equal energy, one should observe in the chamber interactions of type (1) followed by an interaction of the resulting proton types (3), (4), or (5). This succession of events was never observed. From this fact, one computes a lower limit on the mean free path for neutron-proton charge exchange at high energies by the following arguments:

Let us consider all the interactions of high multiplicity occurring in the lower half of the chamber. The number of these due to neutrons incident at a large inclination can be assumed equal to the number produced by ionizing primaries which missed the anticoincidence tray. The neutrons producing the remaining interactions are assumed to have traversed the upper half of the chamber. The total amount of material thus traversed was 1900 g/cm² of lead and 600 g/cm² of aluminum.

One therefore concludes that the simple process of charge exchange is an extremely rare one at very high energies. If the process occurs at lower energies, the resultant excitation of the nucleus is of the order of 400 Mev (deduced from the observed energy of slow secondary protons).

(4) Ratio of Numbers of Interactions in Lead and Aluminum

As has been indicated, it is not possible in the case of Experiment B to obtain relative cross sections for interactions in the two materials simply by comparing the number of interactions observed in lead and alumi-

num. One can, however, obtain other information from a study of these numbers. As is shown in Table IV, the ratio of numbers of interactions having multiplicity $\geqslant 2$ is 2.3 ± 0.6, which is well in agreement with the ratio 2 expected for geometric cross sections. In the case of higher multiplicity interactions, however, the ratio[13] is 4.9 ± 1.1. (Note that, from Fig. 3, a ratio 4 corresponds to vanishingly small cross sections, assuming the ratio to be unbiased by the selection of events.)

One concludes that the measured ratio 4.9 reflects the effect of different detection probabilities for interactions of different multiplicities. The change in ratio with multiplicity is, in consequence, proof that nuclear interactions of high energy neutrons produce, on the average, a higher multiplicity of penetrating particles in lead than in aluminum. The same result has been obtained by Lovati and his co-workers.[5]

[13] This number differs from the one in Table IV because it includes the interactions of high multiplicity occurring in the lowest three plates.

PHYSICAL REVIEW VOLUME 81, NUMBER 5 MARCH 1, 1951

A Cloud-Chamber Study of Nuclear Interactions in Lead and Aluminum. Part II*

B. P. GREGORY AND J. H. TINLOT†
Department of Physics and Laboratory for Nuclear Science and Engineering, Massachusetts Institute of Technology, Cambridge, Massachusetts

(Received October 9, 1950)

The results of the cloud-chamber Experiment B described in Part I are used to discuss some properties of the particles produced in nuclear interactions. Evidence is presented showing that the electronic showers produced in nuclear interactions are all photon-initiated. Upper limits on the proportion of directly produced electrons are found to be 20 percent in interactions in aluminum and 41 percent in lead. The possibility that the photons are decay products of neutral π-mesons is strongly indicated, although no definite proof can be given. It is shown that the mean free paths for nuclear interaction of secondary penetrating particles are 172 ± 30 g/cm^2 in lead and 164 ± 50 g/cm^2 in aluminum. Assuming that the penetrating particles consist of equal numbers of π-mesons and protons, one obtains an upper limit of 250 g/cm^2 for the mean free path for interaction of π-mesons in lead.

I. INTRODUCTION

WE shall be concerned in this paper (Part II) with the study of the secondary particles produced in interactions observed in Experiment B (see Part I). In Sec. II, we shall discuss the production of the electronic component, stressing the likelihood that all of the electronic showers originate as photons. In view of recent evidence[1,2] on the existence of the neutral π-meson, it will be of interest to investigate this hypothesis in relation to the evidence obtained in this experiment.

In Sec. III, we shall show that the secondary penepenetrating particles produce nuclear interactions in lead and aluminum with cross sections near the geometric values. It will be seen that the bias introduced by the counter selection system is important even in the case of the simple selection system used in this experiment, and therefore that the difficulty of computing corrections for this effect may account for the fact that our results are at variance with those obtained in similar cloud-chamber experiments.[3–5]

We present in Figs. 1–4 some examples of nuclear interactions which are thought to be of unusual interest.

II. SOME GENERAL PROPERTIES OF SECONDARY PARTICLES

Let us first note some general properties of the secondary particles produced in the nuclear interactions of Experiment B. We are concerned here only with the penetrating particles (particles of minimum ionization traversing two lead plates without multiplication) and the electronic showers (of two or more electrons). The discussion in this paragraph and in Sec. III will be limited to a group of 82 nuclear interactions resulting in the production of more than two penetrating particles. The numbers of penetrating particles and showers observed in these cases are given in Table I. The average multiplicity of the penetrating particles is seen to be 4.5. The angle of emission of a penetrating particle is defined as the angle of its track with the average direction of the group. The average value of these angles was found to be 16°. The electronic showers are grouped

TABLE I. Production of penetrating particles and electronic showers in nuclear interactions of types 3, 3′, 4, 4′, and 5.

Number of interactions	Penetrating particles	Average angle of production	Electronic showers (number of electrons) >10	5 to 10	3 to 5	no penetration <3
82	355	16°	22	58	43	25

* This work was supported in part by the joint program of the ONR and AEC.

† Now at the University of Rochester, Rochester, New York.

[1] Steinberger, Panofsky, and Steller, Phys. Rev. 78, 802 (1950).

[2] Carlsen, Hopper, and King, Phil. Mag. 41, 701 (1950).

[3] W. B. Fretter, Phys. Rev. 76, 511 (1949).

[4] Lovati, Mura, Salvini, and Tagliaferri, Phys. Rev. 77, 285 (1950).

[5] W. W. Brown and A. S. McKay, Phys. Rev. 77, 347 (1950).

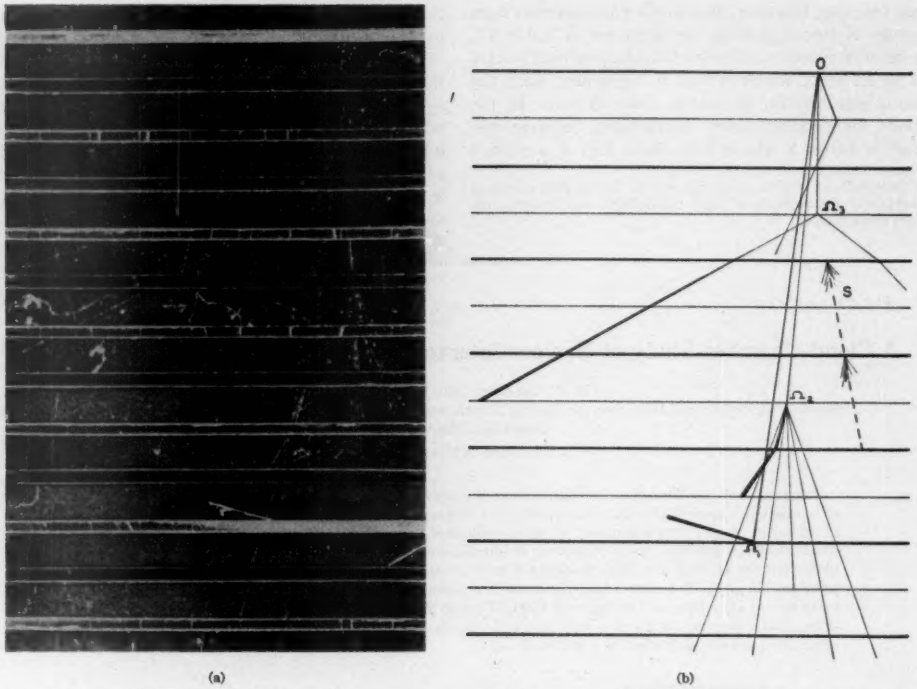

FIG. 1. In this picture, one finds an exceptionally clear example of the production of a photon in a nuclear interaction. It is also one of several pictures which indicate rather convincingly that π-mesons interact with nuclei. Three penetrating particles were produced in the first plate (lead) by an incident neutron, and were emitted within a cone of 13°. They all suffered nuclear collisions in other plates (Ω_1, Ω_2, Ω_3). The interaction at Ω_1 produced only one visible secondary particle, a low energy nucleon emerging upward from the plate. The particle which is thought to have triggered the cloud chamber was one of five penetrating particles produced at Ω_2. The third interaction (Ω_3) occurred in an aluminum plate; one observes, besides the two minimum ionization particles emitted at large angles, an electronic shower S which begins in the lead plate immediately below Ω_3, and whose axis reprojects exactly to Ω_1. This is taken as evidence of the production of a photon.

It is hardly possible that all three penetrating particles produced in the primary interaction were protons. If we choose this interpretation, we should have to assume either that the incident neutron had an extremely high energy (and therefore that relativistic contraction explains the small angular divergence of the particles), or that the protons resulted from a minimum of four elastic collisions within one nucleus (in which case the small divergence is very improbable). We believe, therefore, that at least one of these particles was a π-meson.

in Table I according to the number of electrons observed in a region near the maximum of the shower. This number is significant only if the development of the shower is observed in the well-illuminated part of the chamber. In this case the maximum may extend over a region of five or six intervals, and the average number of electrons in these intervals can be related to the energy of the shower. We have used the Tamm and Belenky[6] formula to deduce the energy of the showers; this amounts to multiplying the average number of electrons by 100 Mev. In most cases, the energies of the showers could not be estimated with any certainty; the figures tabulated in Table I give, therefore, only a crude estimate of the energy spectrum of the showers. The average number of showers per primary interaction was 1.9. It may be noted that both the angle of emission of penetrating particles and the multiplicities of particles and showers are probably underestimates, since particles emitted at wide angles could not be identified.

[6] I. H. Tamm and S. Belenky, J. Phys. U.S.S.R. 1, No. 2 (1939).

(A) The Origin of the Electronic Showers

The following analysis will show that all of the showers observed may be considered to be photon-initiated.[7] This conclusion extends to higher energies the results obtained by York, Moyer, and Bjorklund[8] at 350 Mev and confirms the observation of Kaplon, Bradt, and Peters.[9] We shall also present evidence on the possible production of the photons by a neutral meson and give an estimate of the relative number of

[7] B. P. Gregory and J. H. Tinlot, Phys. Rev. 77, 299 (1950).
[8] York, Moyer, and Bjorklund, Phys. Rev. 76, 187 (1949).
[9] Kaplon, Peters, and Bradt, Phys. Rev. 76, 1735 (1949).

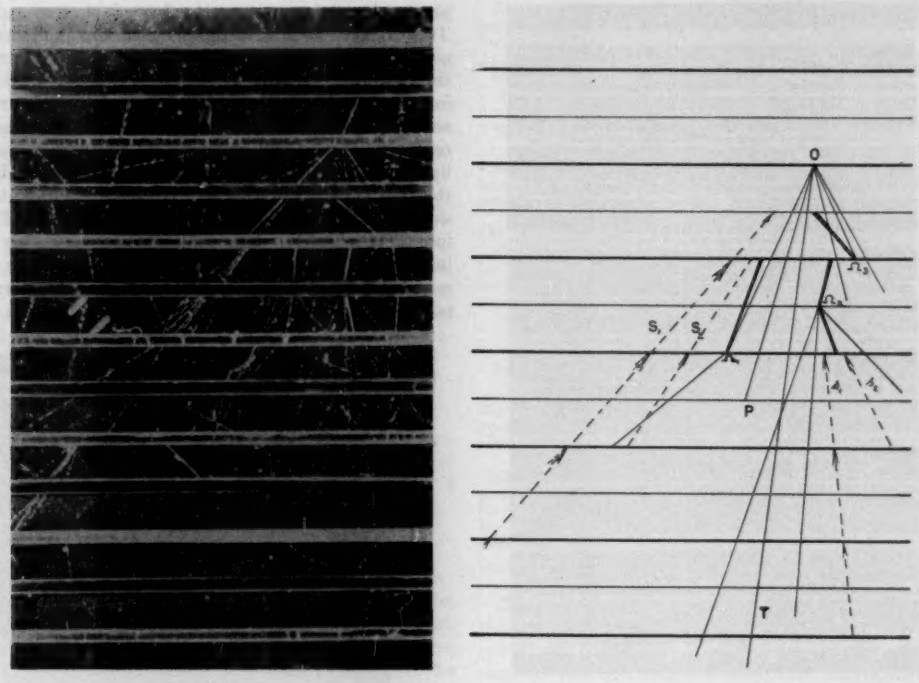

FIG. 2. This picture is a fairly representative example of the high multiplicity interactions of Experiment B. Proceeding from left to right, we find:

(a) Two electron showers S_1 and S_2 beginning in the fourth (aluminum) and fifth (lead) plates. These showers presumably were produced by two photons originating in the primary interaction, 0, in the third plate. It is therefore possible to look for correlation of the photons according to the neutral meson hypothesis, as described in Sec. II. The difficulty of estimating the energies of the photons is evident. For instance, one counts the number of electrons in S_1 in the intervals below the third plate, and obtains the following sequence: 0, 2, 5, 7, 2, 2, 5, 4. Qualitatively, the shower seems about to end near the seventh plate, but begins again at the ninth plate. Similar fluctuations in the development of showers were often observed. It is seen that large errors may be made in estimating the energy of a shower when one cannot follow its development through a number of lead plates. In this case, we estimate the number of electrons at the maximum of S_1 to be 4 to 7, and the energy of the photon to be between 400 and 700 Mev. In the case of S_2, no good measure of energy could be made, since the shower left the illuminated region after traversing only four intervals. We may, however, compute the expected energy of the second photon from the knowledge of the energy of the first photon and the angle in space between the two showers ($19°\pm2°$), under the assumption that the two photons are decay products of a neutral π-meson. The energy of the second photon should then be between 230 and 550 Mev, a result which is consistent with the appearance of S_2. The neutral meson relation cannot, however, be proved in this case.

(b) Three penetrating particles produced at 0. The first interacts at Ω_1, the second leaves the illuminated region at P, and the third particle, OT (not clearly visible on the photograph), appears to have triggered the cloud chamber.

(c) A nuclear interaction at Ω_2 (presumably caused by a neutron produced at 0) which produces two penetrating particles and two photons, which materialize in the lead plate below Ω_2. As in the previous case, it is possible to define the energy of one photon (400 to 600 Mev) and the angle between the two showers ($28°\pm2°$), but not the energy of the second photon. On the neutral meson hypothesis, the expected energy of the second photon is 150 to 250 Mev.

(d) A particle which traverses one aluminum plate and then interacts (Ω_3). This particular interaction was rejected for the analysis of Sec. III, since the particle which produced it would have left the illuminated region before traversing two lead plates, and therefore would not have been recorded as a penetrating particle.

penetrating particles and neutral mesons produced in this set of nuclear interactions.

(a) *Production of Photons in Nuclear Interactions*

We consider now a set of 80 electronic showers which penetrated at least one lead plate, had five or more electrons, and whose axes reprojected to the origins of nuclear interactions; these showers were produced in nuclear interactions occurring in the illuminated region (see Table IV, Part I). The requirement on penetration assured that the axis and direction of each shower could be defined. It was found that the axes of these showers reprojected exactly to the origin in all but a few obvious cases of atmospheric showers not directly related to the nuclear interactions. One may thus conclude that the shower-initiating particle (whether

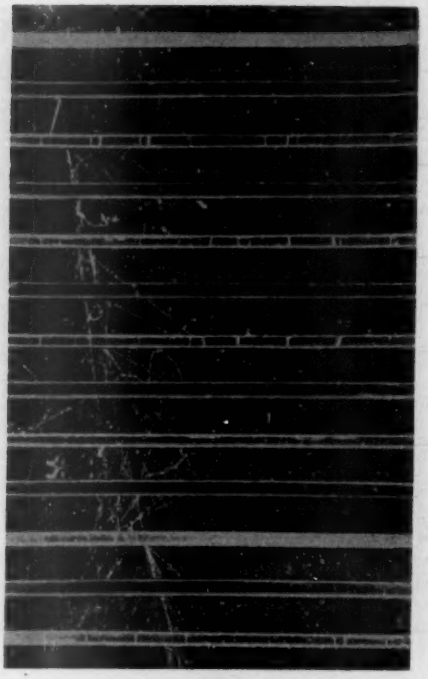

FIG. 3. This picture is representative of the large group showing low multiplicity interactions. A penetrating particle, whose track is somewhat obscured by electronic showers, penetrates five lead plates without scattering. The development of the showers is exceptionally clear. These showers are evidence of the production of two photons in the second (aluminum) plate. The energies of the photons are accurately defined (400 Mev and 900 Mev), but the angle between the showers is difficult to measure. On the neutral meson hypothesis, the angle should be 14°. The measured value is between 8° and 13°, and thus not in contradiction with the predicted value. The picture can be interpreted as showing the production by a high energy neutron of a single neutral meson of about 1300-Mev energy, and one charged meson, or possibly a recoil proton. In either case, the energy of the incident neutron must be at least 2 Bev.

photon or electron) was produced at a distance from the origin of the nuclear interaction small compared with the thickness of the plates. Examples of the appearance of such showers are given in Figs. 1, 2, and 3.

The "beginning" of each shower (the plate at which electrons first appear) was located whenever possible. When the complexity of the event obscured the development of the shower, the "beginning" of the shower could be located only to within a group of plates. The resulting data are given in Table II. For comparison, the average probabilities of materialization of a photon produced at a random depth in the plate of origin (plate No. 1) are listed in the second row of Table II.

One first notes that, within the statistical uncertainties, the experimental numbers fit well with the predicted numbers for production of photons only. The evidence is most striking when the interaction occurred in aluminum. In 22 of these cases, electron showers began in plates below the one of origin, while in no case could we identify an energetic electron emerging from the aluminum plate. The upper limit on the number of directly produced electrons is given by the number of uncertain cases (6) of column 7. We therefore set a limit of 20 percent for electron-initiated showers produced in interactions in aluminum. The interpretation of the data on interactions occurring in lead is more difficult, because of the larger number of uncertain cases[10] (columns 7 and 8). Let us assume purely photon-initiated showers. Then the 18 cases of

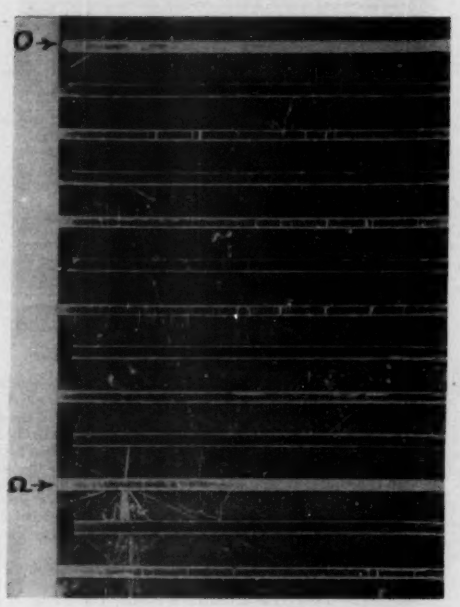

FIG. 4. In this unusual example, we observe two nuclear interactions (at O and Ω), the first of which is very simple, and the second very complex. The average direction of the particles produced at Ω lies along the line OΩ, and the tracks are of the same "age." The interactions are therefore almost certainly associated. The penetrating particle produced in the interaction at O is emitted at an angle of 10° from the direction OΩ. It is thus probably a meson, although it could be a knock-on proton resulting from two elastic collisions within one nucleus. The most likely interpretation of this picture is the following.

A neutron interacts in the first plate to produce one meson (energy unknown, but greater than 300 Mev), and a neutron of several Bev energy. The meson undergoes nuclear scattering in the sixth (aluminum) plate, but is not visibly scattered in five lead plates. The neutron interacts in the eleventh plate with great loss of energy. This picture is thus another example of low multiplicity meson production at very high energy.

[10] The increase in uncertainty was due to the greater complexity, on the average, of the interactions in lead; for example, one found (Sec. III, Part I) that the average number of penetrating particles produced in lead is greater than that produced in aluminum.

showers beginning below the plate of origin (certainly photon-initiated) correspond to a total of 33 photons, 11 of which should have produced showers beginning in plate No. 1. Instead, one finds a possible maximum of 34 such showers, if one adds the 15 uncertain cases (column 7) to the 19 showers definitely observed to begin in plate No. 1. Thus, the proportion of electrons directly produced in lead is, at the most,

$$(34-11)/(34-11+33)=41 \text{ percent.}$$

It is certainly more probable that some of the uncertain cases correspond to photon-initiated showers. In fact, one may in a reasonable way apportion among the other columns the number of uncertain cases of column 7, and so explain all of the showers as photon-initiated.

(b) *Production of Neutral Mesons*

If a neutral meson decays into two photons of energies E_1 and E_2, the angle ψ between the directions of emission of the two photons is determined, and is given by the relation,

$$(2\sin\tfrac{1}{2}\psi)^2=[\mu c^2]^2/E_1E_2.$$

As was indicated previously, we observed in a considerable number of cases two or more electron showers produced in one nuclear interaction. In these instances, one could estimate the energies and the angle ψ between pairs of showers and see if the above relation could be satisfied, assuming a neutral meson mass equal to that of the charged π-meson. Agreement was indeed possible in a number of examples, one of which has been published previously.[7] However, the probable errors on the estimated energies of the showers and, in some cases, on the angle ψ were found to be quite large. (Examples of the probable errors are given in Figs. 2 and 3.) We were brought to the conclusion that the examples in which the relation was satisfied could not be considered as proof of the existence of the neutral meson. Nevertheless, we believe that the following results give considerable support to the neutral meson hypothesis:[11]

(1) In the 13 cases in which the two showers penetrated at least one lead plate, 11 were found to satisfy the energy-angle relation for production by a neutral π-meson.

(2) In the 12 cases in which only one shower was observed, these showers had energies of less than 500 Mev. This is not surprising, since low energy mesons would produce photons at wide angles, and thus the probability of observing both of the resulting showers would be small.

If we assume hereafter that the neutral meson is responsible for the production of pairs of photons, we can compute estimates of the energy spectrum, the lifetime, and the absolute number of the mesons produced in the group of interactions under consideration.

[11] We wish to emphasize that the findings of Steinberger, *et al.* (reference 1), seem to be conclusive, but that the process investigated here is one of considerably higher energy.

TABLE II. Starting point of showers produced in nuclear interactions. Plate No. 1 is the plate in which the nuclear interaction occurred, Plate No. 2 is one immediately below, and so on.

Interactions in lead								
Beginning of shower	Plate No. 1 Pb	Plate No. 2 Al	Plate No. 3 Pb	Plate No. 4 Al	Plate No. 5 Pb	Other plates (below No. 5)	No. (1 or 2 or 3	No. (3 or 4 or 5
Observed number of showers	19	1	10	0	4	0	15	3
Calculated probability for materialization of a photon (%)	35	4	36	1	14	10	...	...

Interactions in aluminum								
Beginning of shower	Plate No. 1 Al	Plate No. 2 Pb	Plate No. 3 Al	Plate No. 4 Pb	Plate No. 5 Al	Other plates (below No. 5)	No. (1 or 2	No. (2 or 3 or 4
Observed number of showers	0	13	0	5	0	0	6	4
Calculated probability for materialization of a photon (%)	3	58	2	21	1	15	...	...

The data of Table I give a rough energy spectrum of the electronic showers; from this, one can deduce the general form of the energy spectrum of the neutral mesons. This spectrum was needed for developing the following arguments, but is otherwise of no interest, since the selection of nuclear interactions is strongly dependent on the triggering requirements.[12] If a neutral meson is produced by a nuclear interaction in a lead plate, the probability that one of the decay photons will materialize in this same plate will depend on the lifetime and the energy of the meson. We may refer to the observed number of such cases (Table II), and make use of the computed energy spectrum. The largest value of the mean life compatible with the observations was found to be

$$\tau=10^{-12} \text{ sec.}$$

The average energy of the mesons considered in this computation was about 1 Bev. This lifetime is consistent with the estimate of Kaplan, Bradt, and Peters.[9] The total number of neutral mesons produced, corresponding to the numbers of showers listed in Table I, follows immediately from the knowledge of the spectrum, if one assumes a reasonable lower limit on the observable energy. It is probable that electronic showers of energy less than 150 Mev were not detected. The number of neutral mesons corresponding to the 148 electronic showers is then 110. This gives a ratio of neutral mesons to penetrating particles of 1:3.

[12] For example, the spectrum is found to have a much smaller number of low energy mesons than is predicted by Sands [Phys. Rev. 77, 180 (1950)], and does not agree with the spectrum measured recently by Carlsen, *et al.* (reference 2).

TABLE III. Mean free path for interaction of secondary particles.

Type of primary interaction: (Part I, Table IV)	Lead				Aluminum			
	Traversals g/cm²	Nuclear interactions (ionizing particle)	Nuclear scattering	Nuclear interactions (non-ionizing particle)	Traversals g/cm²	Nuclear interactions (ionizing particle)	Nuclear scattering	Nuclear interactions (non-ionizing particle)
One penetrating particle (Types 1 and 1')	710	0	0	2	265	1	0	0
Two penetrating particles (Types 2 and 2')	730	0	0	1	278	1	0	1
Interactions of high multiplicity (Types 3, 3', 4, 4', 5)	2634	12	4	2	931	5	1	3
Origin of primary interaction outside illumination	3383	13	6	4	1211	5	2	1
Sum of 3rd and 4th row	6017	25	10	6	2142	10	3	4

III. NUCLEAR INTERACTIONS OF SECONDARY PENETRATING PARTICLES

Several authors[3–5], have measured the collision mean free path for the secondary particles comprising the penetrating showers by observing the behavior of these particles while traversing the plates in a cloud chamber. The same technique is used to obtain the results presented in this section. It is found, in common with these observers, that the main problems in interpreting the data involve corrections for possible errors of two types: (1) the effect of the finite thickness of the plates in the chamber in obscuring secondary interactions, and (2) the bias on the events observed caused by the requirements of the counter control triggering system.

Considerations of the first type usually arise in defining criteria for identifying secondary interactions. We shall show that the thickness of the plates used for this experiment was sufficiently small to cause little difficulty in identifying secondary interactions. The problem of analyzing the effects of the triggering system is much more involved. The necessary corrections will be shown to be small, but only for the cases of primary interactions of high multiplicity.

(A) Selection and Grouping of Primary Interactions

For reasons to be made evident in the succeeding paragraphs, the primary nuclear interactions were grouped according to the number of secondary penetrating particles. The pictures considered in the analyses to follow include those of primary interactions occurring in the illuminated region (listed in Table IV of Part I), and also those showing secondaries of interactions occurring outside the illuminated region. The minimum requirements for identifying an interaction of the latter type was a combination of penetrating particles and electronic showers totaling three or more, clearly diverging from a point in the material of the cloud chamber. We believe that the selection and grouping of pictures was independent of the secondary interactions.

(B) Definition of Traversals and Identification of Secondary Interactions

As a first step in determining the amount of lead and aluminum traversed by the penetrating particles (hereafter called the traversal of the particles), the track of each particle was located in space. We counted the traversal and interactions of such a particle only if its track (or its extension, if it interacted) traversed two lead plates within the illuminated region. In some cases, portions of the track of a particle were not used for computing traversal if the track was obscured by the superposition of tracks of other particles or electronic showers; nuclear interactions of particles in such regions were likewise ignored. The angle of incidence of the track with the plates was taken into account in measuring the actual amount of material traversed.

We identified secondary nuclear interactions other than scattering or nuclear stopping according to the criteria used in Experiment A (Part I). The cases of nuclear scattering were also identified whenever possible by the use of the criterion given in Part I, but extended to accept cases of large scattering associated with small scattering angles before and after. We selected in this way four interactions of type (1) and five interactions of type (2) as described in Fig. 2, Part I. Four other interactions could not be identified by this rule. A description of each case may best explain our choice:

In two cases the particle was deflected by an angle of more than 50° but was not scattered in one adjacent lead plate. (In one of these cases, the ionization changed abruptly after the scattering.)

In one case a proton was clearly identified through three lead plates after suffering a scattering of 27° in an aluminum plate.

In one case a particle stopped in a lead plate with the emission of a low energy particle in the backward direction.

It is felt that the number of these cases incorrectly identified, or of other cases missed, is small, since very few examples of large scattering were found which are not included in the above list.

The problem of defining nuclear "stopping" did not arise, because in no case was it found that a particle of minimum ionization which had traversed one lead plate without scattering was stopped in a succeeding plate without the emission of a nuclear secondary particle. The number of particles which stopped through nuclear interaction before traversing one lead plate (and which therefore could not have been identified) is thus believed to be very small. This result is similar to that found in Part I in the case of primary protons. The results of the survey of secondary interactions (uncorrected) are tabulated in Table III. The number of interactions of secondary neutrons was also recorded. Although the identification of neutron interactions is more difficult than that of interactions of ionizing particles, the data will be useful for estimating the ratio of secondary protons and π-mesons.

(C) Correction for the Effect of the Triggering Requirement

If we ignore the effect of the triggering process on the selection of events, we obtain the mean free path for interaction of the secondaries simply by dividing the total traversal by the number of interactions. This mean free path differs from the true collision mean free path principally because of two opposing effects: (1) a particle capable of triggering the counter telescope may interact without producing other particles which can trigger (absorption), and (2) a penetrating particle may produce by nuclear interaction a particle which can trigger (creation).

Since the probability of expanding the chamber is an increasing function of the number of triggering particles, absorption will increase the measured mean free path, while creation will decrease it.

We can estimate the magnitudes of these two effects and the resulting corrections to be made on the measured mean free path by assuming the effects to be independent. Let us consider how the probability of "single" triggering is altered by absorption. (Since, as shown in Sec. III-3, Part I, "single" triggering is dominant for both low and high multiplicity events, the discussion will be valid for the majority of the primary interactions.) We define a triggering particle as a penetrating particle emerging from the primary nuclear interaction and aimed at the bottom tray of the telescope. Let x be the equivalent lead thickness which a particle traverses in the chamber, y be the thickness of lead shielding in the telescope, and N be the number of triggering particles produced in a primary nuclear interaction. To correct for absorption with a mean free path λ, one must reduce the total traversal of the N particles by multiplying by the factor,

$$F(N)=\frac{1-[1-e^{-(x+y)/\lambda}]^{N-1}}{1-[1-e^{-(x+y)/\lambda}]^{N}}.$$

To calculate the values of F we may assume λ to be the geometric mean free path (167 g/cm² Pb, 82 g/cm² Al); averaging over the quantities x and y, we obtain

$$N=1, \quad F_1=0$$
$$N=2, \quad F_1=2/3$$
$$N=3, \quad F_1=6/7.$$

Other causes of triggering (electronic showers or neutron produced secondary interactions) will tend to decrease the necessary correction.

To correct for the effect of creation of triggering particles by secondary interactions one must reject a certain number of such interactions. The upper limit on this correction is obtained by rejecting all of them.

We can now proceed to apply these corrections to the different groups of primary interactions listed in Table III. Let us consider first the interactions of total multiplicity one or two. In these cases the biggest contribution to the total traversal is due to the triggering particles and the correction for absorption as calculated above is so large that the validity of the method is questionable. Moreover, of the two observed secondary interactions (for 1440 g/cm² Pb and 543 g/cm² Al), one "creates" a triggering particle. The correction for creation is also difficult.

Let us now group together the two sets of nuclear interactions listed in lines 3 and 4 of Table III. For each picture we can count the number N of triggering particles and apply a correction $F(N)$ on the corresponding traversal. For interactions originating outside of the illuminated region, the triggering particles were not visible in most cases and the correction was considered negligible.

The total correction for absorption was found to be 380 g/cm² of lead and 140 g/cm² of aluminum compared to a total traversal of all particles of 6015 g/cm² of lead and 2140 g/cm² of aluminum. One must reject in addition one interaction of a triggering particle in which case another secondary interaction created a triggering particle. The resulting correction on the mean free path is -5 percent.

Only two secondary interactions out of a total of 50 produced a triggering particle. The upper limit to the correction due to creation is therefore $+4$ percent.

The following conclusions were therefore drawn:

For all pictures of group I (low multiplicities) the corrections are extremely large and no useful result may be drawn from the data. The entire set of pictures was therefore discarded.

All other interactions were considered. The preceding analysis shows that the two errors due to absorption and creation cancel each other. Moreover, their magnitudes are small compared to the statistical error. We believe, therefore, that no appreciable error in the mean free path is introduced by the triggering requirements, if consideration is restricted to primary interactions producing more than two penetrating particles.

The figures of the last line of Table III give, therefore, the correct mean free path for interaction:

$$\lambda_{Pb}=172\pm30 \text{ g/cm}^2$$
$$\lambda_{Al}=164\pm50 \text{ g/cm}^2.$$

(D) Ratio of Mean Free Paths in Lead and Aluminum

It is seen that the mean free path in lead corresponds to the geometric cross section, while the one obtained for aluminum corresponds to one-half the geometric cross section. Although this result has a rather large statistical uncertainty, it seems to indicate some transparency of the aluminum nucleus. From the curves of

Fig. 3 (Part I) one finds that the mean free paths corresponding to a nucleon-nucleon cross section of 0.02 barn are

$$\lambda_{Pb} = 200 \text{ g/cm}^2$$
$$\lambda_{Al} = 140 \text{ g/cm}^2.$$

These numbers are quite consistent with the experimental values obtained above. It should therefore be emphasized that a mean free path in lead of more than 200 g/cm² is neither consistent with the experimental result, nor necessary to conform to the requirements of the theory of transparency.

(E) Mean Free Path for Nuclear Interaction of π-Mesons

It is not possible to establish the proportion of mesons and protons for the group of particles whose interactions were considered in this experiment. There is abundant evidence, however, that π-mesons are produced in nuclear interactions of primary particles whose energy is greater than a few hundred Mev.[13,14] Evidence of three types obtained in this experiment indicates that the group of penetrating particles considered includes considerable numbers of mesons:

(1) Relative numbers of electronic showers and penetrating particles.

As shown in Sec II-1, there is no contradiction in assuming the photons producing electronic showers to be the disintegration products of neutral π-mesons. The ratio of the computed numbers of neutral π-mesons to ionizing penetrating particles is about 1:3.

(2) Coulomb scattering of the penetrating particles.

Fifty of the 200 penetrating particles considered for study of secondary interactions suffered appreciable Coulomb scattering. Since consideration was restricted to particles of minimum ionization, it is believed that the majority of the scattered particles were mesons.

[13] O. Piccioni, Phys. Rev. 77, 1, 6 (1950).
[14] Camerini, Fowler, Lock, and Muirhead, Phil. Mag. 41, 413 (1950).

(3) Relative numbers of interactions of ionizing and non-ionizing secondary particles.

The ratio of these numbers is 35:10 (Table III). The ratio of secondary protons to secondary neutrons produced in nuclear interactions of the energies involved in Experiment B is expected to be of the order of one.

From the above it seems reasonable to assume a value of one for the ratio of mesons to protons. The mean free path for interaction for mesons is then found to be between 160 g/cm² and 250 g/cm² of lead. The upper limit is not very sensitive to the assumed ratio of mesons to protons.

(F) Summary of Evidence Relating to Secondary Interactions

The following conclusions can be drawn on the basis of the discussion in the above sections (A) through (E):

(1) The most reasonable values of the mean free path for interaction of the penetrating particles produced in the nuclear interactions of Experiment B are 200 g/cm² of lead, and 140 g/cm² of aluminum.

(2) A reasonable upper limit on the mean free path for interaction of π-mesons in lead is 250 g/cm².

(3) The characteristics of the secondary interactions observed are very similar to those observed for primary cosmic-ray protons. In particular, one notices a similar scarcity of nuclear "stopping"; the number of nuclear scatterings is likewise small (about ¼ of all the secondary interactions).

We wish to thank Professor Bruno Rossi for his continual and generous help and encouragement throughout the course of the experiments discussed in the foregoing two papers. Operation at Echo Lake, Colorado, was made possible by the facilities of the Inter-University High Altitude Laboratory, and through the friendly cooperation of Professor Byron Cohn, and Professor Mario Iona. We especially wish to acknowledge the aid of Professor Matthew Sands and Mr. W. B. Smith during portions of the experimental period.

Angular Distribution of the Pions Produced in High Energy Nuclear Collisions

ENRICO FERMI
Institute for Nuclear Studies, University of Chicago, Chicago, Illinois
(Received November 6, 1950)

The angular distribution of pions produced in a high energy collision of two nucleons is discussed in terms of the statistical theory of multiple meson production. The results are compared with experimental findings.

I. INTRODUCTION

IN a recent paper[1] a procedure for the calculation of the production of pions (π-mesons) in high energy nuclear collisions has been discussed. The basic assumption is made that the interaction between pions and nucleons is so strong that a statistical equilibrium is attained among all states that are compatible with the conservation theorems of energy, charge, angular momentum, etc. More precisely, it is assumed that when two high energy nucleons collide, the energy available in their center-of-mass system is released in a small volume having dimensions of the order of magnitude of the pion cloud surrounding the nucleons. By a succession of Yukawa processes this energy can give rise to states representing a certain number of pions in addition to the original two nucleons. The states into which the original two-nucleon state can be so converted are restricted by several conservation theorems. The basic assumption is made that the probability that the collision may result in the formation of one of the possible final states is proportional to the probability that the state in question will have all of its particles contained at the same time inside the small volume into which the energy has been concentrated.

At relatively low energies when the Lorentz contraction is negligible this volume, V_0, may be taken equal to that of a sphere of radius R, and volume

$$V_0=4\pi R^3/3. \tag{1}$$

R will be of the order of magnitude of $\hbar/\mu c$. Actually, the choice

$$R=\hbar/\mu c=1.4\times10^{-13}\text{ cm} \tag{2}$$

seems to give results in fair agreement with the experimental data and has been adopted in the numerical computations.

The effect of the Lorentz contraction should be taken into account in the discussion of collisions at a higher energy. This has been done in A by reducing the volume from the uncontracted value, V_0, to

$$V=(2Mc^2/W)V_0, \tag{3}$$

Where W is the total energy (including rest energy) of the two colliding nucleons in the center-of-mass system, so that $2Mc^2/W$ is the Lorentz contraction factor. This point may be justified as follows.

One should bear in mind that at all the energies under consideration the de Broglie wavelength of the nucleons is very small compared with R. One might therefore think of the two nucleons that approach each other as of two nonquantized objects. Their surrounding pion fields will be Lorentz contracted. When the collision takes place, therefore, all the energy will be first deposited inside the contracted volume (3). Soon afterward a number of reactions take place while the volume in which the energy is concentrated begins to expand and the density of energy decreases. The assumption (3) is justified if one takes the point of view that the relevant time for the reaction is the one when the energy concentration is highest and that the equilibrium reached at that stage is frozen before the expansion has progressed appreciably.

On this assumption the expression (3) of the volume was used in A in order to calculate the probable number of charged particles formed in a very high energy nuclear collision. Two different formulas were found for this number, namely:

$$1.2(W'/Mc^2)^{\frac{1}{4}} \tag{4}$$

or

$$1.06(W'/Mc^2)^{\frac{1}{4}}, \tag{5}$$

depending upon whether one assumes that nucleon-antinucleon pairs are or are not possible. W' is the energy of the impinging nucleon in the laboratory frame of reference.

There is not much experimental material available for testing the formulas. Most of the cosmic-ray stars produced by the collision of a high energy proton involve the break-up of a large nucleus under conditions in which plural production phenomena are obviously very important. Cases in which one might assume that the collision has effectively taken place between the cosmic-ray proton and a single nucleon are very rare. Recently Schein[2] and his collaborators have obtained a very spectacular example of this kind in which the collision is apparently due to a proton of about 30,000-Bev energy. Fifteen minimum ionization tracks are observed, several of them emerging within a core of about 0.003 radian aperture. The presence of only two lower energy tracks indicates that this collision must have taken place at the fringe of a nucleus, so that only

[1] E. Fermi, Prog. Theor. Phys. 5, 570 (1950), quoted as A.

[2] Lord, Fainberg, and Schein, Phys. Rev. 80, 970 (1950). I am indebted to the authors for informing me of their results before publication.

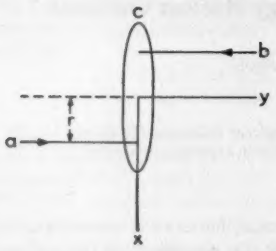

FIG. 1. Trajectories of nucleons in the center-of-mass system.

one nucleon appears to have been seriously involved. Another photograph with similar characteristics, although apparently corresponding to a collision with a proton of much lower energy, has been published by the Bristol group[3] and may have been produced by a proton of about 3000 Bev. Formulas (4) and (5) for $W'=30{,}000$ Bev give the for expected number of charged particles, respectively, 16 and 14 (observed 15). For the second star, assuming $W'=3000$ Bev, one finds from the two formulas, respectively, 9 or 8 particles (observed 7). This agreement seems to indicate that the assumption that the volume V should be Lorentz contracted is not greatly in error. One should keep in mind, however, that the number of particles emitted in a collision of this type depends only on the fourth root of the volume V. A change by a factor of 2 or 3, therefore, would produce only a relatively minor variation in the expected number of particles.

II. THE ANGULAR DISTRIBUTION

The main purpose of the present paper is to discuss the angular distribution expected according to the statistical model. The angular distribution of the particles formed in high energy nuclear collisions when observed in the laboratory frame of reference seems to show a striking tendency to divide into a very narrow distribution containing about 50 percent of the particles and a second distribution containing the remaining particles spread over a cone of considerably wider aperture. Schein and his collaborators[2] have stressed this point strongly and have concluded that when the angular distribution is transformed to the center-of-mass system, one obtains a distribution with two concentrations of particles in the two polar directions. Although this concentration is very striking, it does not correspond in the center-of-mass system to extremely small angles, since particles are found in appreciable numbers up to angles of 40 or 50 degrees from the polar axis. In the Schein star the total energy available in the center-of-mass system is about $250\,Mc^2$. Including unobservable neutral particles one can assume that perhaps a total of 25 particles has been produced, each carrying an average energy of about 10 Bev, an estimate, incidentally, which is quite compatible with the direct measurement of the energies observed in the laboratory frame of reference. Particles of 10 Bev have a de Broglie wavelength $\lambda\approx 2\times 10^{-15}$. Since the range of the nuclear interactions is about $R=1.4\times 10^{-13}$ cm, one might perhaps guess that the allowable angular deviations from the polar axis are of the order of magnitude $\lambda/R\approx 0.015\approx 1°$. This assumption is evidently in gross disagreement with the observations which give a much wider angular distribution.

We proceed now to discuss the angular distribution to be expected according to the statistical theory. At first sight one might expect that this theory should give an isotropic distribution in the center-of-mass system because one might argue that the evaporation of particles from the volume, V, will obey some analog of the Maxwell distribution law and therefore be spherically symmetric. On closer analysis, however, it is recognized that this conclusion is incorrect and that actually one might expect an angular distribution rather similar to that observed experimentally. Qualitatively, this is explained by the following reason.

It is very improbable that the collision of the two original nucleons should be exactly centered. Far more probable are collisions in which the two particles collide somewhat on one side of each other, so that the system is left with a considerable amount of angular momentum. This angular momentum could easily amount in the case of the Schein star to several hundred or a thousand $\hbar$ units. Since the angular momentum must be conserved between initial and final state, the outgoing particles will have to carry away the initial amount of angular momentum. As a consequence of this fact, the angular distribution of the outgoing particles is not spherically symmetric even if one takes literally the statistical and thermodynamic procedures of calculation adopted in A. The statistical distribution law is usually written on the assumption that the energy is the only conserved quantity, and should be changed when the system is such that other quantities, like the angular momentum, for example, also are conserved. The changes are of a nature to destroy, in general, the isotropy of the velocity distribution of the particles.

Before we proceed to a quantitative discussion of the case, the role of the Lorentz contraction flattening of the volume V should be discussed qualitatively. In Fig. 1, a and b are the trajectories of the two nucleons in the center-of-mass system, and the line c represents the section of the flattened volume V in which the energy initially is deposited. Figure 1 is drawn for the case in which the angular momentum is directed perpendicular to the drawing and upward.

We introduce a system of axes, x, y, z, centered on the center of the volume V. The y axis is drawn parallel to the trajectories a and b of the two nucleons. The z axis (not drawn in the Fig. 1) is perpendicular to the plane of a and b and is therefore the direction of the angular-momentum vector. After the collision the newly formed particles will emerge out of the volume V. Since

[3] Camerini, Fowler, Lock, and Muirhead, Phil. Mag. 41, 413 (1950).

this volume is very much flattened and the y-dimension can be neglected, the z-component of the angular momentum of a particle emerging at the point of coordinates x and z (y very small) will be

$$Z=xp\cos\vartheta, \tag{6}$$

where p is the momentum of the particle and ϑ is the angle between p and the y axis. Since the escaping particles must carry away a large amount of angular momentum, it is clear that particles emitted at places with positive x should have the $\cos\vartheta$ positive and as large as possible. That is, for them the angle ϑ should be small. Particles emerging from places with x negative will carry away a large positive angular momentum when $\cos\vartheta$ is negative and as large as possible in absolute value; that is, when ϑ is close to 180°. In this way one understands qualitatively that the angular distribution of the particles will not be isotropic, but rather will favor the two polar directions $\vartheta=0°$ and $\vartheta=180°$. In order to estimate this effect quantitatively it would be necessary to know the actual shape of the volume V. The assumption that this is a very much flattened ellipsoid obtained by Lorentz contraction of the sphere (1) is evidently an oversimplification especially in the case represented in Fig. 1, in which the two nucleons a and b collide with a relatively large value of the impact parameter. On the other hand, it would not be possible to specify the actual shape of the volume V without considerable arbitrariness. For this reason, in the calculations to follow, the assumption of a flattened ellipsoid of transverse axis R and very short symmetry axis has been adopted, with full realization of its crudeness.

The computation will be carried through in the thermodynamic approximation allowable when the energy involved is very large. If the energy W were the only quantity conserved during the collision process, one would expect that the average number of particles in a quantum state of energy w within the volume V should be

$$1/(e^{\beta w}-1), \tag{7}$$

where $\beta=1/kT$. The formula has been written for the case that the particles obey the Bose-Einstein statistics. Otherwise $+1$ should appear in its denominator instead of -1. It is found that the angular distribution in this approximation is independent of the type of statistics of the particles and therefore only the case of the Bose-Einstein statistics will be discussed in detail. Formula (7) is no longer applicable when the z-component of the angular momentum also is conserved. Instead of Eq. (7) one should use in this case the following formula for the average number of particles in a given state:

$$1/(e^{\beta w-\lambda Z}-1). \tag{8}$$

The constants β and λ appearing in this formula should be adjusted in such a way that total energy and total z-component of the angular momentum have the correct values.[4]

We restrict the discussion to the case in which all particles in the center-of-mass system are extreme relativistic. We write, therefore, w and Z in the form

$$w=cp, \quad Z=xp\eta, \tag{9}$$

where $\eta=\cos\vartheta$. Introducing further the notations

$$\gamma=c\beta, \quad \rho=\lambda R/c\beta, \tag{10}$$

the distribution law (8) can be written

$$1/\{\exp[\gamma p(1-\rho\eta x/R)]-1\}. \tag{11}$$

The actual number of particles in a volume element of phase space is obtained by multiplying Eq. (11) by the volume element of phase space divided by $(2\pi\hbar)^3$. We consider an element of phase space corresponding to a volume element

$$(2Mc^2/W)\pi(R^2-x^2)dx \tag{12}$$

comprised between the abscissas x and $x+dx$, and a volume element in momentum space

$$2\pi p^2dpd\eta \tag{13}$$

corresponding to particles having momenta with magnitudes between p and $p+dp$, for which, in addition, $\cos\vartheta$ has value between η and $\eta+d\eta$. The number of particles in this volume element is

$$dn=\frac{Mc^2}{2\pi\hbar^3W}\frac{(R^2-x^2)dxp^2dpd\eta}{\exp[\gamma p(1-\rho\eta x/R)]-1}. \tag{14}$$

Integration of this expression from zero to infinity for p, from $-R$ to $+R$ for x, and from -1 to $+1$ for η yields the total number N of particles of the given type. The result of the integration is

$$N=\frac{a}{2\pi}\frac{Mc^3R^3}{W\hbar^3\gamma^3}\left(\frac{1+\rho^2}{\rho^3}\ln\frac{1+\rho}{1-\rho}-\frac{2}{\rho^2}\right), \tag{15}$$

where

$$a=2\textstyle\sum_1^\infty 1/n^3=2.413 \tag{16}$$

is the numerical constant that comes from the integration over p. Multiplication of Eq. (14) by the energy, cp, of a particle and performance of a similar integration yields the total energy W of the particles, which is given by the following formula:

$$W=\frac{b}{3\pi}\frac{Mc^3R^3}{W\hbar^3\gamma^4}\left(\frac{1}{\rho}\ln\frac{1+\rho}{1-\rho}+\frac{2}{1-\rho^2}\right), \tag{17}$$

[4] Notice that not only the z-component of the angular momentum but also the x- and y-components are conserved. In spite of this, only the z-component appears in the formula, because the coefficients similar to λ for the other two components turn out to be zero when the components of the total angular momentum in these two directions vanish. For the same reason no terms corresponding to the momentum of the particles created appear in the exponent of Eq. (8), in spite of the fact that the momentum is also conserved. This arises from the fact that the total momentum vanishes in the center-of-mass system.

TABLE I. Numerical data for Eqs. (20) and (22).

ρ	$3f_1(\rho)/2f_2(\rho)$	$f_4(\rho)$
0	0.000	1.33
0.1	0.022	1.35
0.2	0.048	1.40
0.3	0.088	1.53
0.4	0.123	1.63
0.5	0.160	1.88
0.6	0.204	2.26
0.7	0.270	2.95
0.8	0.368	4.39
0.9	0.528	8.96
0.92	0.574	11.3
0.94	0.634	15.3
0.96	0.710	23.3
0.98	0.814	47.7
0.99	0.876	97.0
1.0	1.000	∞

where

$$b=6\sum_1^\infty 1/n^4=\pi^4/15=6.494. \tag{18}$$

One obtains finally the total z-component of the angular momentum of the particles by multiplication of Eq. (14) by the angular momentum $xp\eta$ of a particle and integration, with the result

$$M_z=\frac{b}{2\pi}\frac{Mc^2R^4}{Wh^3\gamma^4}\left(\frac{2}{\rho^3}+\frac{(4/3\rho)}{1-\rho^2}-\frac{1+\frac{1}{3}\rho^2}{\rho^4}\ln\frac{1+\rho}{1-\rho}\right). \tag{19}$$

Formulas (17) and (19) give the energy and angular momentum due to a single type of particle, for example, the neutral pions. When several types of particles are involved, such as neutral and charged pions or various types of nucleons and antinucleons, one obtains similar formulas, the only difference being in the value of the numerical constant, b. Formulas (17) and (19) can be used to determine the values of the parameters γ and ρ. In the collision represented in Fig. 1 each of the two original nucleons a and b carry the energy $W/2$ and the momentum $W/2c$. Consequently, the total angular momentum will be $M_z=Wr/c$, where r is the distance from the center of the volume V at which the nucleons collide. Using this expression of M_z and dividing Eq. (19) by Eq. (17) one finds

$$r/R=3f_1(\rho)/2f_2(\rho), \tag{20}$$

where $f_1(\rho)$ is the function of ρ appearing in parenthesis in Eq. (19) and $f_2(\rho)$ is the function appearing in parenthesis in Eq. (17). The right-hand side of Eq. (20) is given in Table I, second column. The relationship (20) can be used for the compution of the parameter ρ appearing in the distribution law (11). This parameter vanishes for $r=0$; that is, for a perfectly centered collision. In this case there is no angular dependence of the distribution law and η disappears from Eq. (11). For large values of r, ρ is close to unity and expression (11) becomes strongly dependent on the angle ϑ. In order to obtain the angular dependence explicitly we integrate Eq. (14) with respect to the variables p and x only. The result is the number of particles for which $\cos\vartheta$ lies between η and $\eta+d\eta$. One finds

$$dn/d\eta=aMc^2R^3f_4(\rho\eta)/2\pi Wh^3\gamma^3, \tag{21}$$

where f_4 is the following function:

$$f_4(\alpha)=[2/\alpha^2(1-\alpha^2)]-(1/\alpha^3)\ln(1+\alpha/1-\alpha). \tag{22}$$

Its numerical values are given in Table I.

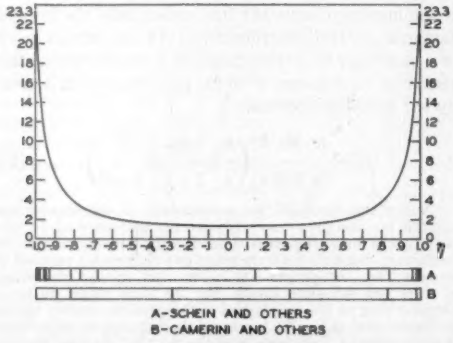

FIG. 2. Functional dependence $f_4(0.959\eta)$ *vs* η.

III. DISCUSSION

Formula (21) gives the angular distribution. Since $d\eta=-\sin\vartheta d\vartheta$ is proportional to the element of solid angle, $dn/d\eta$ would be constant for an isotropic angular distribution. This would be the case, for example, when the collision impact parameter is zero because then ρ would also vanish. When r, and consequently ρ also, are different from zero, $f_4(\rho\eta)$ is not constant but has its maximum values for $\eta=\pm1$. These maxima are most pronounced for values of ρ approaching unity.

It is to be expected that the impact parameter will be different from collision to collision and that r will range in value from zero to R. The median value of r will be $R/\sqrt{2}$. Collisions in which r is smaller or greater than this value will differ from the average because they give, respectively, a less or more strongly peaked angular distribution.

In Fig. 2 the function $f_4(\rho\eta)$ is plotted *versus* η for a value of ρ of 0.959, corresponding to the median value of the impact parameter. This gives the plot of the angular distribution to be expected in an average collision. The plot is such that a straight line would correspond to an isotropic distribution. One can see that there is a very pronounced concentration at the two poles $\eta=\pm1$. The concentration is still appreciable for the values ±0.8 of η which correspond to ϑ values of 37° or 143°. For comparison an attempt has been made to plot under the graph of Fig. 2 a guess as to the angular distribution in the two stars already quoted.[2,3] This involves some arbitrariness in the conversion from

the laboratory system to the center-of-mass system, so that the points indicated should not be taken to be more than a mere indication of the general type of experimental results. One can see, however, that the theoretical angular distribution is not at all incompatible with the results of the observation.

As pointed out, it is possible that in various collisions of the general type discussed here one might find a variety of different angular distributions. Centered collisions should give angular distributions more isotropic than Fig. 2. Very eccentric collisions should give more peaked distributions.

The angular distribution calculated above is independent of the energy of the collision. The simple form of theory discussed here breaks down, however, at low energies for two reasons: The first is that the flattening of the volume V is no longer very pronounced, while the other is that it is no longer permissible to assume that all of the particles are extreme relativistic in the center-of-mass system.

PHYSICAL REVIEW VOLUME 81, NUMBER 5 MARCH 1, 1951

Relative High Energy Neutron Yields from Targets Bombarded with Protons and Deuterons*

WILLIAM J. KNOX
Radiation Laboratory, Department of Physics, University of California, Berkeley, California
(Received November 21, 1950)

Relative neutron yields in the forward direction from various target elements bombarded with 340-Mev protons and 190-Mev deuterons have been measured. Bismuth fission chambers with a threshold of about 50 Mev were used to detect the high energy neutrons. When a deuteron beam is used, the neutron yields for light elements agree with the values predicted by the deuteron stripping theory. For the heavy elements, the observed values are fitted best by adding a function proportional to Z^2 to the stripping theory values. This can be interpreted as evidence for the production of high energy neutrons by the electric field disintegration of the deuteron. The neutron yields from the proton beam vary approximately as $(A-Z)^{\frac{1}{2}}$ for target elements from carbon to uranium. This indicates that the heavy elements are not completely transparent to 340-Mev protons. Beryllium has an anomalous neutron yield 50 percent higher than that for carbon.

I. INTRODUCTION

THE production of a beam of high energy neutrons when 190-Mev deuterons were allowed to impinge upon a target was observed in the first stages of operation of the 184-inch cyclotron.[1] A similar beam of neutrons of higher energy was produced later by the action of 340-Mev protons on a target in the cyclotron. These beams have been investigated experimentally and theoretically by various observers. A mechanism has been proposed for the production of neutrons from deuterons in which the proton is stripped from the deuteron in a collision with a nucleus while the neutron continues on in its original direction.[2] Several features of this mechanism have been verified experimentally.[3–5] The production of high energy neutrons by the proton beam presumably takes place as a result of various types of collisions between the incident proton and the particles within the nuclei of the target material.

It is the purpose of this paper to present and discuss data on the variation of neutron yield with atomic number for various targets bombarded by both the deuteron and proton beams.

II. APPARATUS AND EXPERIMENTAL TECHNIQUE

The deuterons produced by the 184-inch cyclotron have a maximum energy of 190 Mev, and a beam of about 10^{-6}-amp average current can be obtained. The protons have a maximum energy of 340 Mev and can be produced with an average beam current of the order of 5×10^{-7} amp. A target of any desired material can be inserted into the path of these particles, through a vacuum lock in the cyclotron tank, by means of the target probe. The targets can be set at different radii to obtain different energies if desired. The maximum energies mentioned above are obtained at a radius of 81 inches from the center of the cyclotron. These experiments were performed with the targets at radii from 80½ to 81 inches.

When the particles impinge on a target, neutrons are given off in the general forward direction. These neutrons can be intercepted in a wide beam just outside the cyclotron tank wall, or they can be obtained in a highly collimated beam, about 50 feet from the target, emerging from a two-inch diameter hole in the concrete shielding surrounding the cyclotron. In the present

* This work was performed under the auspices of the AEC.
[1] Brobeck, Lawrence, MacKenzie, McMillan, Serber, Sewell, Simpson, and Thornton, Phys. Rev. 71, 449 (1947).
[2] R. Serber, Phys. Rev. 72, 1008 (1947).
[3] Helmholz, McMillan, and Sewell, Phys. Rev. 72, 1003 (1947).
[4] Chupp, Gardner, and Taylor, Phys. Rev. 73, 742 (1948).
[5] Hadley, Kelly, Leith, Segrè, Weigand, and York, Phys. Rev. 75, 351 (1949).

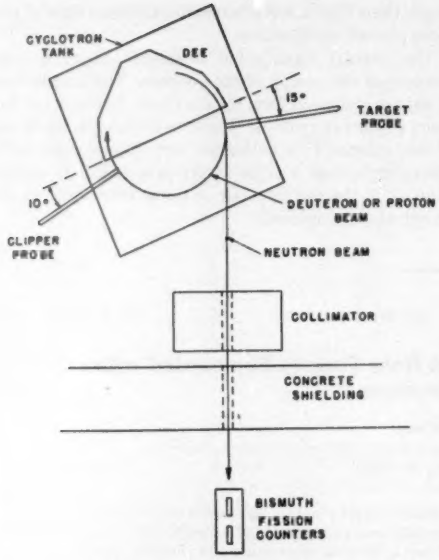

FIG. 1. Arrangement of apparatus.

experiments bismuth fission counters were placed in this collimated beam outside the shielding. The plates of the fission counters subtended a solid angle of about 10^{-6} steradian from the target, and the targets were placed in the beam so that the counters were located within one degree or less of the direction in which the beam was traveling when it struck the target.

The neutrons from the deuteron beam have a most probable energy of about 90 Mev and an energy distribution with a width at half-maximum[2,5] of about 27 Mev. The energy maximum and distribution vary slightly with different materials and thicknesses of targets. The energy distribution of neutrons from the proton beam appears to be a very broad distribution with a maximum at about 270 Mev and a width at half-maximum[6] of about 140 Mev.

Ideally, the particles in the proton or deuteron beam travel approximately midway between the top and bottom of the dee. Actually, the particles acquire vertical oscillations, varying in amplitude from 0 to 2.4 inches, which is the maximum allowed by the dee aperture. If a beam of smaller vertical dimension is desired, a beam clipper may be inserted on a special probe about 155° around the cyclotron from the target probe. This clipper is made of copper about 1 inch thick and 5 inches high with a horizontal slot cut in it to allow only the center of the beam to pass through without obstruction. The clipper cuts out all particles which acquire vertical oscillations greater than some prescribed amplitude. The clippers used in the present experiments had vertical apertures of 1 or $1\frac{1}{2}$ inches. They restricted the beam particles to amplitudes of less than $\frac{1}{2}$ or $\frac{3}{4}$ inch from the beam plane and extended from about 60-inch radius to about $81\frac{1}{2}$-inch radius in the cyclotron. The back of the clipper at about $81\frac{1}{2}$-inch radius also cuts off particles which have outward radial oscillations or deflections from the target of greater than $\frac{1}{2}$ or $\frac{3}{4}$ inch from the 81-inch orbit. The average beam current is reduced by a factor of about 3 when a 1-inch clipper is used. Figure 1 shows the arrangements described above diagrammatically.

In order to be able to change targets quickly in the cyclotron without going into the tank through the vacuum lock, a device was built which would rotate four different targets successively into the beam, and which could be controlled from the outside. This device is described in the following paper. Using the target rotator, targets could be changed without stopping the cyclotron beam and without altering any of its conditions of operation for more than a fraction of a second. Thus, one could assume a constant beam on the four targets in a single run.

Bismuth fission chambers were used to detect the high energy neutrons. The construction and operation of these chambers have been described in detail elsewhere.[7,8] They have a threshold of about 50 Mev, since this is the energy necessary to initiate fission in bismuth with neutrons. They are used in connection with linear amplifiers, and standard scaling and recording circuits. A collection voltage of about 500 to 700 v is used. The linear amplifiers have bias controls so that pulses below any specified height may be discriminated against. When a counting rate *versus* bias curve is taken, initially it shows a very steep slope because of pile-ups, or coincidences of protons or other ionizing particles passing through the chamber. Then the curve flattens out to a slope of about one or two percent per bias volt and then eventually drops off again when even the fission pulses are discriminated out. One operates in the flattest part of the curve at a bias high enough to insure that the counting rate of coincidences of the ionizing particles other than fission recoils is not appreciable. A sample counting rate *versus* discriminator voltage curve is shown in Fig. 2.

The elements used as targets were beryllium, carbon (graphite), aluminum, copper, silver, lead, and uranium. Pieces of these elements were machined into blocks 1 inch by 1 inch square, and varying in thickness from $\frac{1}{8}$ to 1 inch. The densities of the targets were determined by weighing and measuring the blocks, and with the exception of the graphite, all the densities agreed closely with the accepted values. The densities of the graphite targets used varied from 1.45 to 1.49.

Graphite monitors were used to determine the fluxes of protons or deuterons traversing the targets. The monitors were attached to the target so that the beam

[6] Cladis, Crandall, and Hadley (to be published).

[7] C. Wiegand, Rev. Sci. Instr. **19**, 790 (1948).

[8] J. DeJuren and N. Knable, Phys. Rev. **77**, 606 (1950).

passed, simultaneously, through both target and monitor. At the end of the bombardment the monitor was removed and the counting rate of the C^{11} activity in it was determined on a Geiger-Mueller counter at a suitable later time. These monitors were milled from C-18 graphite down to about 0.010 inch thick and cut into 1 inch × 1 inch squares. A chemical analysis of a specimen of this graphite showed that it contained a total of about 0.15 percent of impurities.

It was necessary to take precautions against the contamination of the monitors by recoils or fission fragments from the targets. Beryllium and carbon targets did not contaminate the monitors, but aluminum, copper, silver, lead, and uranium targets did. In order to avoid this contamination it was necessary to place additional graphite foils both between a target and its monitor, and on the outside of the monitor.

Monitors were placed on the front and back of each target. The activities in the front and back monitors on thin targets ($\frac{1}{4}$ inch or less) agreed to within 10 percent. When thicker targets were used, alignment of the target with respect to the beam became quite critical. Thin targets were used in most of the measurements.

In making a set of measurements, the following procedure was generally used. The clipper was inserted into the cyclotron and a current reading target was put on the target probe. The beam was turned on and maximized, and the cyclotron field was adjusted to give the maximum amount of beam current through the aperture of the clipper. Then a beryllium target was put on and the bias voltage *versus* counting rate curves were taken on the bismuth fission chambers in the neutron beam. Finally, a target rotating device with its four aligned targets and monitors was put on the target probe and its rotating action was tested by watching it rotate, through a window in the cyclotron tank wall. At a given recorded instant the beam was turned on and held, at a steady level, on the first target, while the bismuth fission chambers and their related circuits recorded the counting rate in the neutron beam. After the beam had run for a prescribed length of time on the first target, the second target was rotated into place without stopping or altering the cyclotron beam, and the counting rate in its neutron beam was recorded. The same procedure was followed for the third and fourth targets, and then the beam was turned off. The time at the beginning and end of bombardment of each target was recorded. A decay curve was taken on the C^{11} activity in each monitor after it had decayed to a level suitable for counting on a Geiger-Mueller counter.

III. CALCULATIONS

The neutron counts registered by the one or more bismuth fission chambers in the neutron beam were converted to counts per second for each target that was bombarded in a given run. The counting rates were always quite low, ranging from 1 to 10 counts/sec, so there was no necessity to make coincidence corrections. The resolving time of the counters and circuits is of the order of 5 μsec. The cyclotron beam is pulsed for about 100 μsec 60 times per second, so that for a counting rate of 10 counts/sec there is very seldom more than one count per beam pulse.

Decay curves were taken of the C^{11} activity produced in the monitors attached to each target. The C^{11} activity was then extrapolated back to the time at the end of bombardment of the target, and a correction was made for the length of bombardment to give the activity, which would have been produced in a bombardment of infinite length. Usually, the decay curve showed almost pure C^{11} activity and the extrapolation could be made directly. However, sometimes it was necessary to wait for 12 to 15 half-lives of the C^{11} before the level was low enough to count and a small amount of long-lived impurity would appear. In this case the long-lived activity was subtracted out of the curve before extrapolating back to the end of bombardment. Sometimes decay curves were taken through an aluminum absorber so that the positron annihilation radiation of the C^{11} was counted instead of the positrons themselves. The relative fluxes through the targets calculated

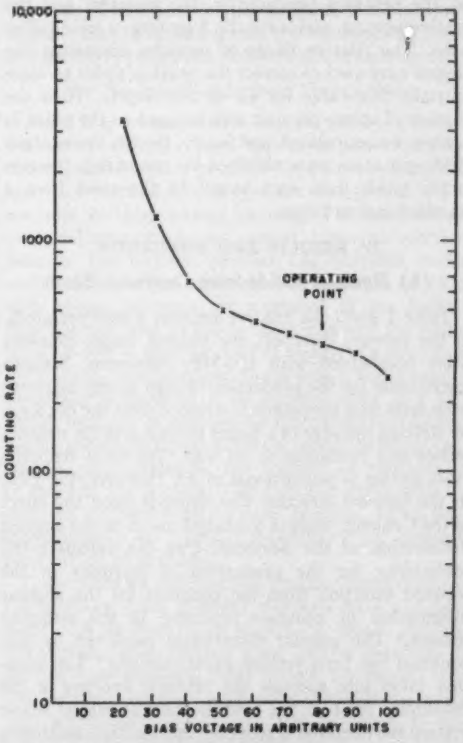

FIG. 2. Sample counting rate *versus* bias voltage curve for a bismuth fission counter.

TABLE I. Relative neutron yields per atom for targets bombarded with 190-Mev deuterons.

Target	Thickness	Yield in forward direction	Forward direction probability	Relative total yield
Be	0.25″	0.93	0.995	0.93
C	0.25″	1.00	0.99	1.00
Al	0.25″	1.34	0.97	1.37
Cu	0.25″, 0.20″	1.44	0.90	1.58
Ag	0.184″	1.88	0.85	2.19
Pb	0.25″, 0.21″	2.69	0.73	3.65
U	0.121″	2.77	0.71	3.86

from the annihilation radiation decay curves, or from the positron decay curves, agreed within the error of the measurements. Since the relative fluxes through the targets were all that were desired, and since all the monitors were of the same shape and thickness, there was no necessity to make absorption corrections. The fluxes through the targets were considered to be proportional to the activities induced in the monitors after the extrapolation to the end of bombardment and the correction for length of bombardment were made.

For each of the four targets used in a given run, the neutron counting rate was determined and corrected for the neutrons produced in the monitors and the relative neutron yields for the four targets were calculated. The relative fluxes of particles traversing the targets were used to correct the neutron yields to some constant flux value for all of the targets. Then the number of atoms per unit area exposed to the beam in a target was calculated, and finally, the relative neutron yields per atom were obtained by comparing the corrected yields from each target to the yield from a standard carbon target.

IV. RESULTS AND DISCUSSION

(A) Neutron Yields from Deuteron Beam

Table I gives the relative neutron yields per atom, in the forward direction, for various target elements when bombarded with 190-Mev deuterons. Serber's mechanism[2] for the production of high energy neutrons postulates that the proton is stripped from the deuteron by striking the edge of a target nucleus and the neutron misses and continues on its way. The total stripping cross section is proportional to $A^{\frac{1}{3}}$. However, the yield in the forward direction also depends upon the effect of the Coulomb fields of the target nuclei on the angular distribution of the neutrons. One can calculate the probability for the production of neutrons in the forward direction from the equation for the angular distribution of neutrons produced in the stripping process.[9] The angular distribution predicted by this equation has been verified experimentally.[2] The equation takes into account the intrinsic bending of the deuteron's orbit in the field of the nucleus, at whose surface the deuteron is stripped, and multiple scattering of the deuteron beam in the target. Also, in order to take into account energy losses, the kinetic energy of the deuteron at the time of stripping is taken as the bombarding energy, minus the Coulomb energy lost in approaching the stripping nucleus, minus one-half the energy loss of the deuteron in one traversal of the target. The forward direction probabilities calculated from the formula mentioned above are given in Table I. The relative total yields are then obtained by dividing the experimental yields by the forward direction probabilities. No attempt was made to take into account additional energy losses or scattering arising from more than one traversal of the target. This effect is relatively small for the neutrons from stripping of 190-Mev deuterons. If it were taken into account, the forward direction probabilities would be slightly lower than given in the table for the heavy elements.

The observed values for the light nuclei fit the shape of the calculated curve fairly well but the values for the heavy nuclei lie above the curve. An explanation for this deviation may lie in another mechanism for the production of high energy neutrons by deuterons, the disintegration of the deuteron in the Coulomb field of the nucleus.[10] This effect has been predicted and calculated[11] for 200-Mev deuterons but has not been verified by the experimental measurements on the angular distributions of the neutrons. The angular distribution

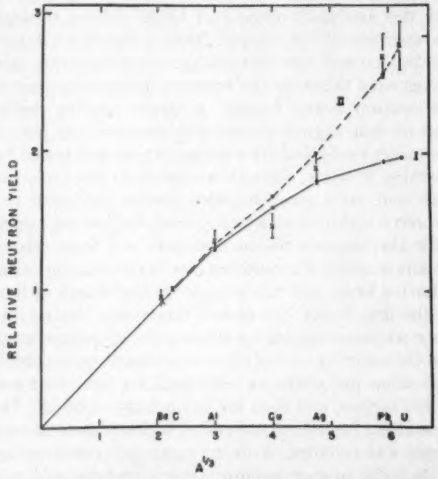

FIG. 3. Relative neutron yields in the forward direction from targets bombarded with 190-Mev deuterons. The crosses are the observed neutron yields in the forward direction in arbitrary units. Curve I (solid) shows the values predicted by stripping theory relative to the value for carbon. Curve II (dotted) shows the values obtained by adding a function proportional to Z^2 to the stripping theory values. A probable error of ±6 percent is shown on each point, except the value for carbon to which the other values are relative.

[9] Reference 2, Eq. (25).

[10] J. R. Oppenheimer, Phys. Rev. 47, 845 (1935).

[11] S. M. Dancoff, Phys. Rev. 72, 1017 (1947).

calculated for neutrons coming from the electric disintegration of the deuteron was narrower than the distribution from the stripping process. The experimental points for heavy elements fitted the distribution predicted by stripping but not the distribution predicted by the combined processes of stripping and electric disintegration. However, it is possible that the distribution of neutrons from the electric disintegration process could be widened by Coulomb effects of the target nuclei enough, so that the width of the distribution would be about the same as that for the stripping process. In this case the angular distribution measurements would fit either the stripping process, or the combined stripping and electric disintegration processes.

The cross section for the electric disintegration process is proportional to Z^2, and if a function proportional to Z^3 is added to the values predicted by the stripping theory, a good fit can be obtained for all the points. Figure 3 shows the observed relative neutron yields with their estimated probable errors plotted *versus* $A^{\frac{1}{3}}$. Also shown are the values for the yields in the forward direction calculated from stripping theory, and a curve for which the stripping theory predictions have been combined with a function proportional to Z^3. The points calculated from stripping theory do not give a smooth curve because the densities and thicknesses of the targets enter into the corrections. The proportionality factor for the Z^3 function which gives the best fit for the observed points indicates an electric field disintegration cross section for uranium equal to about one-half of the stripping cross section in the forward direction, which is the correct order of magnitude according to theory.[11] The total stripping cross section is theoretically equal to $5A^{\frac{1}{3}}\times10^{-26}$ cm², while the electric disintegration cross section is about $1.35Z^2$ $\times10^{-29}$ cm² for heavy elements. These values give a ratio of about $\frac{1}{3}$ for uranium.

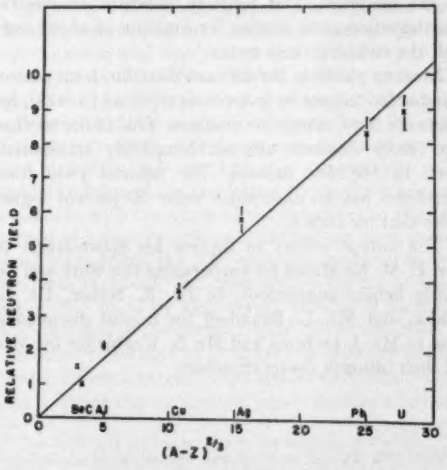

FIG. 4. Relative neutron yields in the forward direction from targets bombarded with 340-Mev protons.

TABLE II. Relative neutron yields per atom in the forward direction from targets bombarded with 340-Mev protons.

Target	Thickness	Relative neutron yield
Be	0.25″, 0.50″	1.5
C	0.25″, 0.50″	1.0
Al	0.25″, 0.50″	2.1
Cu	0.20″, 0.25″	3.7
Ag	0.184″	5.8
Pb	0.21″, 0.25″	8.3
U	0.12″, 0.25″	8.9″

The energy distribution of neutrons from heavy elements is lower than that from light elements because of the barrier energy loss before the stripping of the deuteron. This energy loss is regained by a stripped proton, but not by a neutron. Since the Bi fission cross section increases with energy, neutrons from uranium or lead should be detected with lower efficiency than those from beryllium or carbon. Consequently, the experimental values for uranium and lead are lower limits with respect to this source of error. Ionization energy loss in the target is a further effect in the same direction. Corrections for these effects, if made, would increase the difference between the experimental values and the curve predicted, without electric disintegration.

(B) Neutron Yields from Proton Beam

Table II gives the relative neutron yields per atom in the forward direction from various targets when bombarded with 340-Mev protons. No detailed mechanism has been worked out as yet for the production of neutrons by high energy protons. The neutrons are produced presumably in various types of collisions between the incident protons and particles in the nuclei of the target material. The collisions in which high energy neutrons are produced in the forward direction are most probably those in which the proton gives up only a small amount of energy to a neutron in the nucleus, but exchanges charge with it and continues essentially undeviated in its forward flight as a high energy neutron. In this case for the transparent nucleus model, one might expect the cross section to be approximately proportional to the number of neutrons or particles in the nucleus. This does not agree with the observed values for the forward direction, which have approximately an $(A-Z)^{\frac{1}{3}}$ dependency for elements from carbon to uranium.

Corrections for differences in angular distributions of the neutrons from different elements have not been made. These corrections should be small. Angular distribution measurements using carbon detectors on the neutrons produced from targets bombarded with 340-Mev protons show very wide distributions which vary only slightly for targets from beryllium to uranium.[12] Hence, the present measurements indicate that

[12] Miller, Sewell, and Wright, Phys. Rev. 81, 374 (1951).

the heavy nuclei are not completely transparent, even to 340-Mev protons. Beryllium has an anomalous value with respect to the dependency on $A-Z$ which is 50 percent higher than the value for carbon. Figure 4 shows the observed relative neutron yields per atom in the forward direction for targets bombarded with 340-Mev protons plotted *versus* $(A-Z)^{\frac{1}{3}}$. The values lie fairly close to a straight line passing through the origin.

A qualitative explanation for the anomalous behavior of beryllium may lie in its peculiar nuclear structure. If the odd neutron in the beryllium nucleus is bound much more loosely than the remaining neutrons, the cross section for this neutron will be higher than that for the rest of the neutrons, and also the energy distribution may be higher.[13] The cross section for bismuth fission by neutrons increases rapidly with respect to the energy of the neutrons[14] in the range 60 to 90 Mev. The cross section is still rising at the energy of neutrons produced by 340-Mev protons.[15] This would make the present detection method somewhat dependent on the differences in energy distributions of the neutrons from the various targets. No correction has been made for this effect. Because of the very high energy of the incident protons, it is thought that the differences in the energy distributions of neutrons from the various target elements are not very great, with the possible exception of the distribution from beryllium. The group of neutrons produced by exchange collisions with the loosely bound neutron in the beryllium nucleus might have a significantly higher energy distribution than the rest of the neutrons. In this case, the detection efficiency for these neutrons would be higher and the apparent yield from beryllium would be increased.

It is intended to make absolute measurements on the neutron yields from both proton and deuteron bombarded targets. These values will be published at a later date.

It is estimated from the present work that 190-Mev deuterons yield about 40 times more neutrons per unit solid angle in the forward direction than 340-Mev protons when a carbon target is bombarded with a given particle flux. The total high energy neutron production by deuterons is of the order of three times greater than that by protons. This estimate includes an increase by a factor of three in the bismuth fission cross section in going from 90- to 270-Mev neutrons[15] and uses values of 65 mb for the $C^{12}(d,dn)C^{11}$ cross section[16] and 38 mb for the $C^{12}(p,pn)C^{11}$ cross section.[17]

[13] G. Chew (private communication).
[14] E. Kelley and C. Wiegand, Phys. Rev. **73**, 1135 (1948).
[15] J. DeJuren, Phys. Rev. **80**, 27 (1950).
[16] V. Peterson (unpublished data).
[17] Aamodt, Peterson, and Phillips (to be published).

V. ERRORS

The relative neutron yield from a given element was obtained by comparison of its corrected neutron yield to the yield from a standard carbon target. The estimated probable error of a single determination of such a ratio is about 10 percent. This error arises mainly in the determination of the flux of deuterons or protons traversing a target, but also has contributions from the neutron counting statistics and from the correction made for the production of neutrons in the carbon monitors. The errors in measurements of the thicknesses and densities of the targets are negligible. The results given in Tables I and II are the averages of from 2 to 4 individual determinations. Preliminary results which were obtained before the final technique was developed are not included, but they were in agreement with the final values. The probable error calculated from the mean square deviation of all of the individual results from the average values given in Tables I and II is about 3 percent. This gives a measure of the reproducibility of the results. A combination of the reproducibility of the individual results with an estimate of the possible errors involved in the technique leads to a probable error of about 6 percent for the final values. This is the error shown on all values in Figs. 3 and 4, except the arbitrary value for carbon, which was the standard.

VI. SUMMARY

Relative high energy neutron yields in the forward direction from deuteron bombarded targets agree with stripping theory for the light elements. A better fit is obtained for both light and heavy elements if a function proportional to Z^2 is added. This may be interpreted as evidence for the process of electric field disintegration of the deuteron. This function indicates an electric disintegration cross section for uranium of about one-half the stripping cross section.

Neutron yields in the forward direction from proton bombarded targets vary approximately as $(A-Z)^{\frac{1}{3}}$, for elements from carbon to uranium. This indicates that the heavy elements are not completely transparent even to 340-Mev protons. The neutron yield from beryllium has an anomalous value 50 percent higher than that for carbon.

The author wishes to express his appreciation to Dr. E. M. McMillan for encouraging this work and for many helpful suggestions, to Dr. R. Serber, Dr. G. Chew, and Mr. L. Baumhoff for helpful discussions, and to Mr. J. DeJuren and Mr. N. Knable for the loan of their bismuth fission chambers.

Multiple Traversals of High Energy Particles in a Cyclotron Beam through Thin Targets*

W. J. KNOX
Radiation Laboratory, Department of Physics, University of California, Berkeley, California
(Received November 21, 1950)

An experimental determination has been made of the average number of times that 340-Mev protons traverse various targets in the Berkeley 184-inch cyclotron. The numbers range from slightly above 1 for a 1-inch thick copper target to about 15 for an aluminum target 0.0015 inch thick. The results are compared with calculated values based on multiple scattering in the target and oscillations of the particles in the cyclotron. It is believed that the results can be adapted to apply to various particles of different energies in the cyclotron. Calculations are made on the energy distribution of beam particles which cause reactions in a target, and distributions are shown for several targets. The selection of targets for the production of high energy neutron beams is discussed. Histograms are presented showing the depth of radial penetration of the 340-Mev proton beam into various targets.

I. INTRODUCTION

IT has been known for some time that some of the high energy particles in a cyclotron beam pass through a thin target more than once. It has also been pointed out that the magnitude of this effect is probably dependent upon the amount of multiple scattering of the particles in the target.[1] In the work described in the preceding paper,[2] it became evident that the effective flux of particles through targets of different thicknesses might vary by an order of magnitude even when the targets were bombarded under identical cyclotron conditions. This has an obvious bearing on certain problems, such as the energy distributions of neutrons or other particles produced in a target, and the relative yields of particles or isotopes produced in different targets. Consequently, it was thought that some further investigation of the effect was called for.

II. EXPERIMENTAL PROCEDURE

Targets of different thicknesses and materials were placed in the path of the circulating beam of the 184-inch cyclotron and bombarded with 340-Mev protons at a radius of 80.5 inches. These targets were one inch high, from a few mils to one inch thick, and were held in place by a clamp one-half inch back from the edge of the target. With each target was mounted one or more aluminum foil monitors one and one-half mils thick. The edges of the monitors were carefully aligned to coincide with the edges of the targets. The relative amount of beam through each target was then determined by counting the Na^{24} activities produced in the aluminum monitors. The cross section for the production of Na^{24} in Al by high energy protons is constant (± 15 percent) in the energy region[3] 100 to 340 Mev.

In order to be able to compare the effective beams through different targets under similar cyclotron conditions, a device was constructed which would rotate four different targets successively into the beam, and which could be controlled from outside of the cyclotron shielding. This device is actuated by a coil which hangs with its axis perpendicular to the magnetic field of the cyclotron. When a current is passed through the coil, it rotates through 90° so that its axis is parallel to the magnetic field, and when the current is stopped, the coil falls back to its original position by gravitational action. This rotating action is transmitted mechanically to a windmill which has targets clamped on the ends of its arms. A mechanical positioner is added so that the windmill can end up only in one of four discrete positions, 90° apart. A single rotation through 90° can be accomplished in a time of the order of one second.

With the targets and monitors mounted on the target rotator, the assembly was inserted into the cyclotron and bombarded with protons. The constancy of the cyclotron beam during the five minutes or so that a given target was bombarded was observed with ionization chambers inside the cyclotron shielding which measured the general level of radiation from the cyclotron and target. It was found by comparison of the ionization chamber readings with the counting rates of neutrons produced in the targets that the ion chamber readings could be used to determine the constancy of the beam through the target to about 10 percent. The transition from one target to another was accomplished in a time of the order of one second, and it is necessary to assume only that the cyclotron operating conditions do not change rapidly during this period. Actually, it was quite easy to hold operating conditions steady within 10 percent for twenty minutes or more during which a set of four targets could be bombarded. Thus, in each run four targets were bombarded with all cyclotron conditions the same except the nature of the target itself. At the end of the run the monitors were allowed to decay for about 24 hours to allow the 2-hr F^{18} and shorter lived activities to die out, and then the 15-hr Na^{24} was counted with a chlorine quenched Geiger-Mueller tube and related circuits. When targets of atomic number greater than aluminum were bom-

* This work was carried out under the auspices of the AEC.
[1] Helmholz, McMillan, and Sewell, Phys. Rev. 72, 1003 (1947).
[2] W. Knox, Phys. Rev. 81, 687 (1951).
[3] R. L. Folger and P. C. Stevenson (to be published).

TABLE I. Data obtained by direct comparison of activities produced by 340-Mev proton beam in monitors attached to different targets. In each run the four targets were bombarded under identical cyclotron operating conditions.

Run	Target	Thickness in inches	Multiple scattering angle in milliradians	Relative flux through target
I	Al	0.0015	0.48	9.3
	Al	0.0115	1.33	5.3
	Al	0.126	4.4	2.0
	Al	0.758	10.8	1.00
II	Be	0.750	5.0	0.92
	Al	0.160	5.0	1.08
	Cu	0.024	4.9	1.02
	Pb	0.009	5.0	0.97
III	Be	0.25	2.9	4.5
	Al	0.25	6.2	1.9
	Cu	0.25	16.0	1.4
	Pb	0.25	26.6	1.00

barded, the monitors were shielded from the targets with other aluminum foils to prevent recoils or fission fragments from contaminating the monitors.

Monitors were placed on both the front and back of all thick targets ($>1/2$ in.) and some thin targets ($\leqslant 1/2$ in.). In four of the thick target cases the back monitor read from 10 to 25 percent less than the front monitor after correction for attenuation. In all other cases the two monitors agreed within 10 percent. The average value of the activities in the two monitors was used. This effect probably depends on the alignment of the edge of the target with the beam direction. From the distribution of activity in the monitors it can be estimated that a one degree misalignment of a one-inch target would cause about 15 percent of the beam to miss one of the monitors. Scattering also tends to cause some of the beam to miss the back monitor.

III. CALCULATIONS AND RESULTS

Using the above procedure data were obtained in the form of groups of four values for the Na^{24} activity observed in the monitors attached to four different targets bombarded under the same cyclotron conditions. This activity was interpreted as being proportional to the actual flux of particles traversing the target under consideration. It was found that the flux varied by as much as a factor of 10 in comparing a thick target to a thin target.

It was assumed that the proper variable to use as a basis for comparison of targets of different thicknesses and different atomic numbers was the root mean square multiple scattering angle of the target to 340-Mev protons. The formula used for the plane projected mean square scattering angle was

$$\langle\theta^2\rangle_{\text{Av}} = 8\pi Z^2 e^4 N t \frac{E^2}{(E^2-E_0^2)^2} \ln(183Z^{-\frac{1}{3}}),$$

where E and E_0 are the total and rest energies of the bombarding proton and the other symbols refer to the target. This is taken from Williams' scattering formula[4] using the nuclear radius and Bohr radius for cut-off parameters, with some refinements for shielding. In order to verify this assumption, targets of Be, Al, Cu, and Pb, of thicknesses calculated to give the same multiple scattering angle, were compared in one run and; it was found that the fluxes through these targets were the same within 10 percent (see Table I, Run II). The 10 percent variation is probably about the reproducibility of the technique for individual results; the variations did not show any trend with respect to atomic number or thickness.

Table I shows the results of several individual runs. Each of these groups of four values can be plotted in arbitrary units as relative beam through a target *versus* the multiple scattering angle of the target. The actual number of times that the beam circulated through the target, or the beam which would be observed with a target thick enough to stop the beam completely, is still unknown. However, since it is known that the multiple scattering angle is the proper variable with which to compare targets, the different groups can be plotted on the same graph and the vertical scale for each group can be adjusted arbitrarily until all of the values lie on a smooth curve. Furthermore, it can be assumed that if the data were carried out to targets thick enough to stop the beam, the activity in the

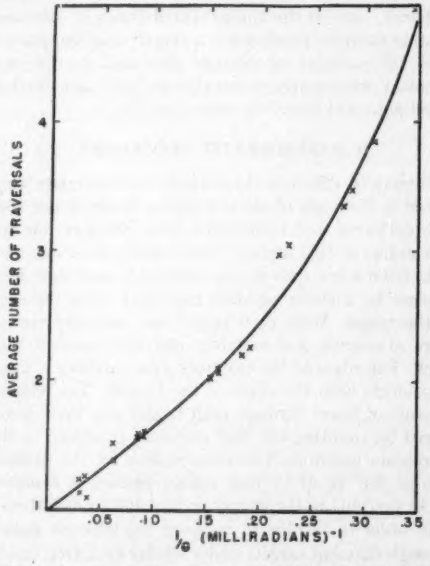

FIG. 1. Average number of traversals of 340-Mev proton beam through various targets. Abscissa is the inverse of the root mean square multiple scattering angle of the target to the beam. The vertical scale has been adjusted so that the curve extrapolates to a value of one.

[4] E. J. Williams, Proc. Roy. Soc. (London) **169**, 531 (1939).

monitor would represent the actual current accelerated by the cyclotron. The particles would be accelerated, would strike the target, and none of the particles would circulate in the cyclotron and strike the target a second time. If one now considers the average number of traversals of the particles in the beam through targets, it is seen that the data extrapolated to very thick targets should approach a value of one. Figure 1 shows the thick target data plotted *versus* the inverse of the multiple scattering angle adjusted to approach a value of unity. The extrapolation to zero is short and not very critical. In this way an absolute scale is determined empirically for the average number of traversals of particles in the beam through various targets. The uncertainty in this scale, because of the extrapolation to thick targets, is of the order of 5 percent. The final data are presented in Fig. 2.

Some of the monitors were cut up into thin strips parallel to the edge of the target, and these strips were counted separately in order to determine the extent of radial penetration of the beam into targets. Histograms showing the specific activity of the monitor *versus* the distance from the edge of the target are presented in Fig. 3. The total area in each histogram has been made proportional to the average number of traversals of the beam particles through the target. The distributions are only valid out to 1.25 cm for the target thickness indicated. Between 1.25 and 2.5 cm from the edge of the target, the beam passed through the target clamps ($\frac{1}{4}$ inch of brass) as well as the target and monitors.

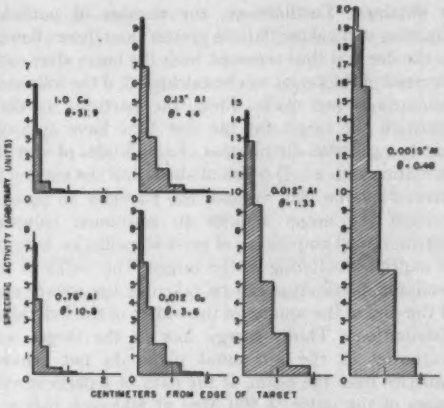

FIG. 3. Distribution of activity in monitors attached to various targets as a function of distance from edge of target. The distributions are only valid up to 1.25 cm for the target thickness indicated (see text). The multiple scattering angle of each target to 340 Mev protons is indicated near each histogram. The total area of each histogram is proportional to the average number of traversals of the beam through the corresponding target. (On the figure read 1.0" Cu, 0.012" Cu, and $\theta=4.4$.)

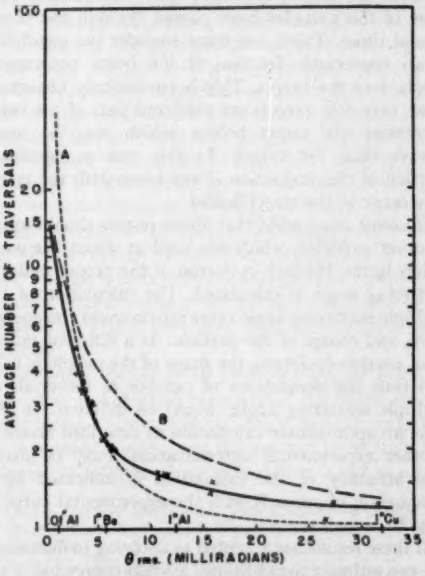

FIG. 2. Average number of traversals of 340-Mev proton beam through targets as a function of multiple scattering angle of target. Solid line is a smooth curve drawn through the experimental points. Dotted line (A) is a theoretical curve based on removal of particles from beam by gas scattering. Dashed line (B) is an approximate calculation for removal of particles from beam after scattering in target.

IV. DISCUSSION

Two calculated curves can be compared to the data. Theoretical calculations have been made on the removal of particles from the bevatron beam by gas scattering.[5] The type of function for gas scattering in the bevatron, which is comparable to the present data, is $(1+k/\theta^2)$, where θ is the multiple scattering angle of the particles by the gas in one traversal of the bevatron.[6] A function of this type (Fig. 2, curve A) falls off more rapidly with increasing θ than does the experimental curve. This is to be expected, since the mean free path of high energy particles in the bevatron is long with respect to the wave length of vertical oscillations. In the cyclotron, all of the scattering in the target occurs in such a short distance that only the resultant multiple scattering distribution is important in determining the number of particles lost from the beam. Thus, one would expect particles to be lost faster in the bevatron gas scattering case than in the cyclotron target scattering case.

An absolute multiple traversal curve based on certain simplifying physical assumptions can be calculated. From the radial variation of the magnetic field in the cyclotron, the wavelength of vertical oscillations of particles in the beam, and thus a relationship between the projected vertical scattering angle and the maximum amplitude of oscillation allowed by the dee, can

[5] N. M. Blachman and E. D. Courant, Phys. Rev. 74, 140 (1948); Phys. Rev. 75, 315 (1949).
[6] A. Garren (private communication).

be obtained. Furthermore, the number of particles acquiring vertical oscillations greater than those allowed by the dee and thus removed from the beam after each traversal of the target can be calculated, if the following assumptions are made. First, the particles as they approach the target for the first time have approximately a gaussian distribution of amplitudes of vertical oscillation with a half-width of about half the maximum allowed by the dee. Second, the particles on passing through the target acquire an additional gaussian distribution of amplitudes of vertical oscillation because of multiple scattering in the target. The width of the resultant distribution can be taken as the square root of the sum of the squares of the widths of the individual distributions. Third, energy loss in the target and scattering in the horizontal plane do not remove particles from the beam. If the path of a particle with losses of the order of 100 Mev at 80.5-inch radius is plotted, it is seen that the particle will describe an approximate circle of much smaller radius but with its center displaced so that the particle comes back to within a few tenths of an inch of where it struck the target. This can be regarded as an enormous radial oscillation of the particle about a smaller equilibrium orbit which is centered in the cyclotron. The maximum of this oscillation will precess until the particle strikes the target again. In most cases the effect of scattering in the horizontal plane is small compared with the effect of energy loss in the target on the resultant orbit of the particle. Fourth, the root mean square amplitude of oscillation of the particles can never exceed a value obtained by compounding the maximum amplitude passed by the dee and the amplitude acquired in one passage through the target. Using these assumptions and taking into account absorption in thick targets, one can calculate the rate of removal of particles from the beam and the average number of traversals expected through a given target. For thick targets in which the root mean square scattering angle in one traversal of the target is comparable to the maximum allowable scattering angle, approximately a constant fraction of the beam survives after each traversal of the target. For thin targets the survival fraction is not constant but gradually decreases to a constant value as the number of traversals increases.

The result of these calculations is shown in Fig. 2, curve B. The calculated curve agrees with the data fairly well for thin targets and for thick targets, but it is high in the intermediate region by a factor of up to 1.7. The agreement for thin targets is fortuitous since in this region the calculated curve is strongly dependent upon the first assumption. However, the general shape of the curve and the approximate magnitude of the absolute calculated values is in agreement with the observed values. Evidently, particles are lost from the beam slightly faster than can be accounted for with the above assumptions. This type of calculation could be considered as giving a maximum value for multiple traversals.

In Fig. 3 the distribution of the monitor activity as a function of the distance from the edge of the target is shown for several targets. It can be seen that the beam penetrates more deeply into thin targets than into thick targets. For the one-inch copper target, about 80 percent of the beam is concentrated in the first two millimeters from the edge of the target. For the thinnest target, 0.0015-inch aluminum, about 30 percent of the activity is in the first 2 millimeters. It should be noted that even though only a few percent of the total effective beam is passing through the target clamps in the case of the thin aluminum target, this is almost equal to the total beam passing through the one-inch copper target.

V. CONCLUSIONS

These results have several obvious implications. First, if a large effective beam or high specific activity in the target is desired, a thin target should be used. However, if the largest total production of particles or activity is desired, a thick target should be used. The decrease in yield as a result of less target atoms in the path of the beam is only partially compensated for by the increase caused by multiple traversals. Second, in calculating the energy distribution of particles which react in the target, one must take into account that some of the particles have passed through the target several times. Third, one must consider the possibility of an appreciable fraction of the beam penetrating deeply into the target. This is particularly important when very thin targets are used and part of the beam penetrates the target holder, which may be much thicker than the target. In this case a significant fraction of the interaction of the beam with the target may occur in the target holder.

It seems reasonable that these results should apply to other particles, which are used at about the same radius in the 184-inch cyclotron, if the proper multiple scattering angle is calculated. The calculation of the multiple scattering angle takes into account the energy, mass, and charge of the particle. At a different radius, or in another cyclotron, the shape of the magnetic field, and thus the dependence of number of traversals on multiple scattering angle, would be different. In this case, an approximate calculation as described above or another experimental determination must be made. The accuracy of the calculation is indicated by a comparison of curve B with the experimental curve in Fig. 2.

If these results are accepted as applying to deuterons, one can estimate the additional average energy loss of the deuterons in the target because of multiple traversals. This results in a lowering of the peak of the predicted energy distribution of the neutrons or protons from stripping. If this correction is made, the predictions come into slightly better agreement with the experimental results

on the energy distributions of protons[7] and neutrons[8] from the stripping of 190-Mev deuterons. The low energy tail on the neutron distribution also can be explained in this manner. The correction amounts to a lowering of the peak energy by 2.5 Mev in the proton experiments in which a $\frac{1}{16}$-inch copper target was used, and by about 4 Mev in the neutron experiments in which a $\frac{1}{2}$-inch beryllium target was used.

An estimate of the actual energy distribution of the particles interacting with the target can be made. Using the calculation described above plus a form factor which makes the calculated curve fit the experimental results, the fraction of the beam which passes through the target n times can be estimated. For thick targets this amounts to about the same as taking the experimental value from Fig. 2 for the average number of traversals and using the terms of a geometric series which sums to this value to represent the survival fraction of the beam. The distribution is shown for several targets in Fig. 4a. This procedure assumes a monochromatic incident beam. It is known that radial oscillations occur in the cyclotron which must have some effect on the energy of particles which strike the target.[1] Although there is little direct experimental evidence to fix the magnitude of this effect, it is thought that the amplitude of radial oscillations is of the order of 2 inches at a radius of 80 or 81 inches in the 184-inch cyclotron. Since a particle should strike the target near the maximum of its oscillation, the effective radius of curvature of the particle when it strikes the target is of the order of from 0 to 2 inches less than the nominal radius of curvature. If the assumption is made that the radii of curvature of the particles are uniformly distributed through this range, then there is a width of about 15 Mev in the incident 340-Mev proton beam, and about 10 Mev in the 190-Mev deuteron beam. The effect of superimposing this width on that of ionization energy loss, including multiple traversals, is shown in Fig. 4b. The tails of the distributions in Fig. 4 for very large energy degradation should not be taken too seriously. The changes in scattering, rate of ionization energy loss, and attenuation with energy have been neglected.

Combining the factors of neutron yield per atom[2] as a function of Z, barrier energy loss,[9] ionization energy loss in target and multiple traversals, one can make the following predictions about the neutron beam from the stripping of 190 Mev deuterons. A thin target of low Z should give the highest peak energy but low yield. A very thin target of high Z should give the least spread in energy because of ionization loss in the target but very low yield. A thick target of low Z should give the highest yield but wide energy distribution. For optimum performance combining low barrier energy loss, narrow distribution, and high yield, a beryllium target about $\frac{1}{4}$ or $\frac{1}{2}$ inch thick should be used. In this particular case one must consider that the stripping process itself gives a broad neutron energy distribution, so that little is gained by going to a thin target of high Z, which gives the sharpest incident beam. Similar considerations may be applied to the selection of targets for other purposes.

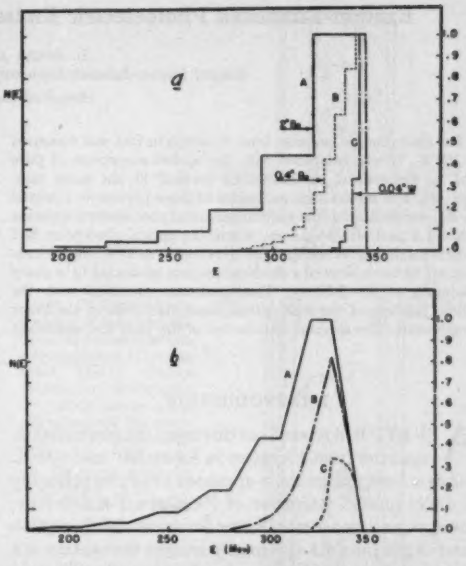

FIG. 4. Spread in energy of proton beam from ionization energy loss and multiple traversals. $N(E)$ is proportional to the number of particles which have an energy E as they pass through the target. (a) The incident beam is assumed to be monochromatic at 345 Mev. (b) The incident beam is assumed to be square in energy distribution with a maximum of 345 Mev and a width of 15 Mev from radial oscillations. Curve A is for a 2-in. beryllium target, curve B for a 0.4-in. beryllium target, curve C for a 0.040-in. wolfram target.

The author wishes to express appreciation to Professor E. M. McMillan for his support and encouragement of this work. Helpful suggestions and discussions have been contributed by K. Brueckner, A. Garren, and H. York. The cooperation of the operating staff of the 184-inch cyclotron is gratefully acknowledged.

[7] Chupp, Gardner, and Taylor, Phys. Rev. **73**, 742 (1948).
[8] Hadley, Kelly, Leith, Segrè, Wiegand, and York, Phys. Rev. **75**, 351 (1949).
[9] R. Serber, Phys. Rev. **72**, 1008 (1947)

Exciton-Enhanced Photoelectric Emission from *F*-Centers in RbI near 85°K

L. Apker and E. Taft
General Electric Research Laboratory, Schenectady, New York
(Received August 1, 1950)

The photoelectric emission from *F*-centers in RbI was measured at 300°K. It was compared with the optical absorption of pure RbI as determined by Fesefeldt's method at the same temperature. The results were analogous to those previously reported for KI, and indicated that exciton-enhanced photoelectric emission reached a peak at $h\nu \sim 5.6$ ev, where the optical absorption had its first maximum. When the films were cooled to 85°K, the exciton-induced emission showed a *double* maximum separated by a sharp minimum at $h\nu = 5.72$ ev. This minimum coincided with the shifted position of the first optical absorption peak at the lower temperature. The spectral distribution of the yield had somewhat the appearance of a self-reversed spectral line. An attractive explanation is that the photoelectric emission at first increases with the optical absorption, reaches a maximum for an absorption constant near 10^6 cm^{-1}, and then decreases as the absorption constant becomes still larger. The decrease is attributed to a sparsity of *F*-centers near the surface, and to a growing destruction of excitons at the surface as the layer in which they are formed becomes thinner. Yields near the photoelectric threshold were compared qualitatively with Herring's theory of photoemission from impurities in a polar crystal. An upper limit of 1.9 ev was placed on the electron affinity of these RbI films.

I. INTRODUCTION

A PREVIOUS report[1] has discussed the photoelectric emission from *F*-centers in KI at 300° and 400°K. For $h\nu < 5$ ev, the emission appeared to be due primarily to direct photon ionization of *F*-centers. For $h\nu > 5$ ev, however, excitons formed in the fundamental absorption band of the pure KI apparently ionized the centers in a secondary process. As a result, the photoelectric yield was enhanced by more than an order of magnitude. It showed an extremely sharp maximum at $h\nu = 5.66$ ev, a point essentially coincident with the first fundamental optical absorption peak as determined by Fesefeldt.[2]

This paper reports subsequent experiments on RbI. The measurements were carried out both at 300°K (where the results were like those for KI) and at 85°K. At the lower temperature, a new phenomenon became evident. The spectral distribution of the yield showed two maxima instead of one. These two peaks were separated by a sharp minimum which was practically coincident with the very sharp optical absorption peak of RbI at 85°K. The results are attributed to a non-uniform distribution of *F*-centers, and to an increasingly important destruction of excitons at the surface when the optical absorption constant increases beyond 10^6 cm^{-1}.

II. EXPERIMENTAL DETAILS OF PHOTOELECTRIC MEASUREMENTS

The general technique used here in measuring photoelectric yields has been described in previous papers[3] and will not be repeated at this point. The photo-tubes were designed to permit measurements near the temperature of liquid nitrogen or air. A typical example is shown in Fig. 1. The thin films of RbI were formed by evaporating the salt from the platinum spiral (7) in Fig. 1 onto the platinized glass face (2) of the emitter structure in the photo-tube. The evaporations were completed in a few minutes at the most. The layers ranged from $<10^{-5}$ cm to 5×10^{-5} cm in thickness, as indicated by interference fringes visible against the platinum substrate. A magnet held the glass shield (5) in Fig. 1 over the hole in the collector during the evaporation to prevent possible contamination of the glass envelope (4) with RbI. As in the previous work on KI, photo-currents showed no evidence of being limited by the electrical conductivity of the salt film. Results were obtained on six separately evaporated samples in three tubes.

F-centers were made in three ways: (1) by irradiating the samples at 300°K with a narrow band of ultraviolet (of width ~0.02 ev) at $h\nu \sim 5.6$ ev; (2) by irradiating at 300°K with the entire output of a 10-atmos Hg arc (*AH4*) in a fused quartz envelope; (3) by bombarding the sample, of area ~1 cm², for roughly 1 sec with 1 ma of electron current at 100 v. The results were like those found previously for KI under similar treatment,[1] except that variations were somewhat larger. In different tubes, the absolute values of the photoelectric yields differed by as much as a factor of 5, and the thresholds varied by a few tenths of 1 ev. Variations for different activations of any single surface were several times less. In all cases, the features of interest in this paper were clearly reproducible.

Attempts at forming *F*-centers at 85°K by method (2) above gave spectral distributions different from those obtained when the centers were formed at 300°K. The photoelectric thresholds were roughly 0.5 ev higher, and the yields due to direct ionization rose more slowly with increasing $h\nu$. In such cases, an irreversible change occurred when the film was first warmed to 300°K. Thereafter, the behavior was quite like that for centers formed at the higher temperature. A more extensive investigation of this effect has not yet been carried out. It was assumed that the phenomenon was traceable to the diffusion processes which, according to the work of Seitz,[4] accompany *F*-center formation. All results for 85°K discussed in this paper were obtained by forming

[1] L. Apker and E. Taft, Phys. Rev. **79**, 964 (1950).
[2] H. Fesefeldt, Z. Physik **64**, 623 (1930).
[3] See papers cited in footnote 5 of reference 1.
[4] F. Seitz, Revs. Modern Phys. **18**, 384 (1946).

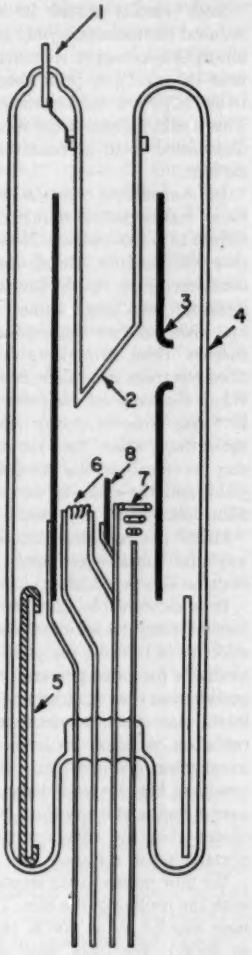

FIG. 1. Cross-section sketch of typical photocell. (1) Lead-in to platinized glass emitter (2), which can be filled with liquid nitrogen or air. (3) Stainless steel collector. (4) Corning 9741 glass envelope. (5) 9741 glass shield with nickel armature. (6) Tungsten filament electron source. (7) Platinum spiral for evaporation of RbI. (8) Shield between (6) and (7) to prevent contamination.

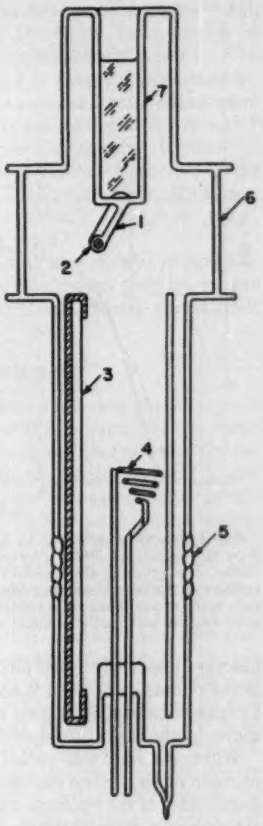

FIG. 2. Cross-section diagram of tube used for optical transmission measurements. (1) 1-mm fused quartz window attached to toroidal tube (2), which carries liquid nitrogen from the reservoir (7). (3) Glass shield with nickel armature. (4) Platinum spiral for evaporating RbI. (5) Graded seal. (6) Fused quartz window.

the centers at 300°K and subsequently cooling the film to the lower temperature.

III. EXPERIMENTAL DETAILS OF OPTICAL MEASUREMENTS

Figure 2 shows the type of tube used for optical transmission measurements. It is similar to one used by Fesefeldt[3] except that it was constructed almost entirely of fused quartz. At 85°K the thermal conductivity of this material is very low. Hence, the quartz substrate (1) for the thin RbI film was fused to a surrounding toroidal tube (2) carrying liquid nitrogen or air from the reservoir (7). The increased cross section thus available for thermal conduction prevented appreciable temperature gradients from appearing in the quartz plate when it absorbed thermal radiation from its surroundings.

The optical transmission of the system was first determined by sending a beam from a Gaertner quartz monochromator through a 0.1-cm² area of the quartz window (1). The transmitted radiation was detected with an Sb—Cs alloy photo-tube. RbI was then evaporated from the platinum spiral (4) onto the quartz window while the shield (3) was held in place with a magnet. After the shield was removed, the transmission measurement was repeated. No corrections were made for reflection losses. Tests on KI showed absorption peaking at 5.63 and 5.80 ev for film temperatures of 300° and 85°K, respectively, in excellent agreement with Fesefeldt's results.[3]

IV. DISCUSSION OF RESULTS

Figure 3 shows the frequency variation of the photoelectric yield from *F*-centers in a typical RbI sample. The concentration of centers was near the limiting value attainable by irradiation with 4×10^{11} quanta sec^{-1} cm^{-2} at $h\nu\sim5.6$ ev (temperature, 300°K). The result is quite

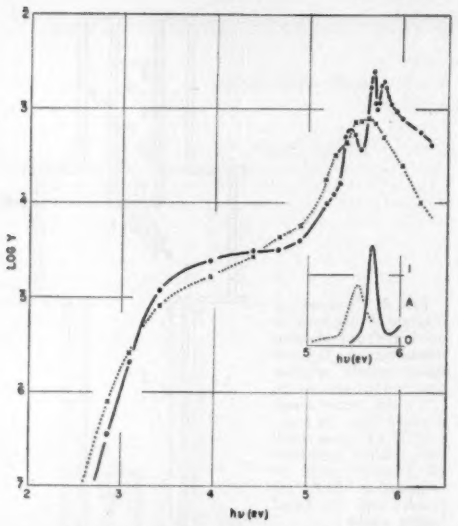

FIG. 3. Spectral distribution of the photoelectric yield Y from F-centers in RbI at 300°K (dotted curve) and at 85°K (solid curve). Y is given in electrons/quantum (note that the characteristics of the logarithms are negative). Below the photoelectric data is the optical absorption coefficient in arbitrary units on the same abscissa scale and on a linear ordinate scale.

like that previously given for KI at 300°K.[1] The peak in the photoelectric yield is not as sharp as for KI. Its location, however, is in good agreement with the peak shown by the optical absorption constant at $h\nu = 5.53$ ev.

When the film was cooled to ~85°K with liquid nitrogen or air, several changes occurred in the spectral distribution of the photoelectric yield. First, the threshold energy increased slightly, and the yield rose more rapidly with increasing $h\nu$ in this vicinity. Second, the small inflection at $h\nu \sim 5.3$ ev on the curve for 300°K shifted toward higher energies by roughly 0.15 ev and formed a separated peak. Third, the peak in the exciton-enhanced emission shifted toward higher energies and split into two clearly resolved maxima separated by a minimum near $h\nu = 5.72$ ev.

We shall consider the last of these effects first. When the temperature decreases from 300° to 85°K, the optical absorption peak shifts by about 0.15 ev, from 5.53 ev to about 5.68 ev. The exciton-induced peaks in the photoelectric yield show a like displacement. However, the peak for 300°K is flattened, and it is in the flattened region that the maximum optical absorption occurs. At 85°K, the yield curve has a contour somewhat like that of a self-reversed spectral line, and the central minimum corresponds to the optical absorption peak.[5] The flattened peak at 300°K appears to be an incipient form of this phenomenon.

Such results would be expected if the exciton-induced photoelectric yield at first rose with increasing absorption constant A, reached a maximum for an A near 10^6 cm^{-1} (the peak absorption at 300°K is known to be 7×10^5 cm^{-1}),[6] and then fell as A increased further. This would happen if the F-centers were non-uniformly distributed with a relatively low density near the surface.

In considering certain luminescence phenomena, Fano[7] has suggested that excitons are destroyed if they diffuse to a free surface. Now such a process may compete with exciton stimulation of F-centers in the RbI considered here. As the fundamental optical absorption increases from small values, the photoelectric yield at first rises because the excitons are created nearer the surface. Thus, in ionizing F-centers, they produce excited electrons in a more favorable position for escape. When the excitons are formed in a layer thinner than 10^{-6} cm, however, many may be lost by diffusion to the surface, where they are destroyed. This destruction may overshadow the tendency toward an increasing yield, and the emission accordingly may show a maximum followed by a decrease.

Hebb[8] has considered these effects in a quantitative way and has also estimated their influence on photoelectron energy distributions.

It is conceivable that the high density of excitons formed when the optical absorption is large may also be effective in limiting the yield. The number of F-centers available for ionization may be depleted. Seitz has suggested to us that excitons might be destroyed by mutual interaction. Such processes would depend on incident radiation intensity or would lead to hysteresis and irreversible changes. Explicit tests showed that the results of Fig. 3 were independent of radiation intensity over a factor of more than 10. We have therefore concluded that the effects mentioned here were not important in our samples.

We now return to the second change associated above with the cooling of the film. This concerns the inflection near $h\nu = 5.3$ ev at 300°K (and the peak near 5.45 ev at 85°K). We have seen similar effects, in varying degrees of intensity, in all of our data on the iodides of K, Rb, and Cs. The inflection, for example, is visible in the result for KI given in reference 1. Remembering that the peak absorption constants are near 10^6, one notices that the phenomenon occurs when the absorption constant reaches values of the order of 10^5. We have therefore concluded that it may be an optical effect that sets in when the transparency of the film ($\sim10^{-5}$ cm thick) becomes small. Thus, radiation

[5] There is some indication that these features in the photoelectric curves occur at $h\nu$-values a few hundredths of 1 ev higher than the optical absorption peaks. The experiments, however, may not be accurate enough to render such an observation significant.

[6] R. W. Pohl, Proc. Phys. Soc. (London) (extra part) **49**, 3 (1937).

[7] U. Fano, Phys. Rev. **58**, 544 (1940). We wish to thank F. E. Williams and Malcolm Hebb for bringing Fano's work to our attention and for helpful suggestions regarding this mechanism.

[8] Malcolm Hebb, Phys. Rev. **81**, 702 (1951).

reflected from the platinum substrate is no longer important, and the effective radiation intensity at the surface decreases by 30 percent, say, if interference effects are ignored. The photoelectric yield decreases accordingly, and an inflection or peak may result.[9] Thus, in Fig. 3, if the yields in the transparent region were lowered by an appropriate factor, this section of the curve should join smoothly to that for the opaque region. Within the experimental error in Fig. 3, a factor of two removes most of the structure even at 85°K. This factor is rather high, but it is possible that interference effects are present. While it is difficult to obtain sufficiently accurate data to be conclusive, there are indications that these inflections shift slightly, as expected, toward lower $h\nu$ when the films are made thicker.

Until more exhaustive tests are made, however, it is probably unsound to exclude the possibility that the structure arises in other ways. It is conceivable, for example, that surface impurities could produce such results in the photoelectric emission without affecting the optical absorption as measured here.

Finally, we consider the changes which occur in the low energy part of the spectral distribution when the film is cooled. The threshold increases slightly, the slope near 3 ev becomes steeper, the curvature at the "knee" increases, and the yield rises in the range from 3.3 to 4.4 ev. The relative positions of the curves in Fig. 3 are qualitatively correct, although the F-center density may have been slightly different in the two cases. Thus, in explicit tests at 3.39 ev, the yield rose and fell by 10 to 20 percent when the temperature was alternately lowered and raised five times in a total time so short that the F-center density did not change appreciably.

The increased yield at the lower temperature may be due in part to an increased free path for emerging photo-electrons, and the threshold may be affected by a temperature dependence of the electron affinity. However, an increased threshold, slope, and curvature as described above are consistent with a theory worked out by Herring[10] for photo-emission from impurities in a polar crystal. According to this viewpoint, the electrons in F-centers may be considered to occupy a band of energy states having roughly a gaussian form. The width B of this band is determined by the interaction between the F-center electron and the lattice (the Franck-Condon principle being kept in mind). In order of magnitude, B should be comparable with the width of the F-center optical absorption band, which in evaporated films is an appreciable fraction of 1 ev. The center of the gaussian band of energy states lies below the conduction band by an amount D somewhat greater than the photon energy at the middle of the optical F band. In crude fashion, the photoelectric threshold T may then be set equal to $A+D-B/2$, where A is the electron affinity. Taking $T=3$ ev, $B=1$ ev, $D>1.6$ ev, one finds that the electron affinity A is 1.9 ev or less, a theoretically reasonable value.[11]

Since the surface discussed here showed evidence of electrical non-uniformity,[12] the writers feel that a more quantitative application of Herring's work should await more extensive data.

V. SUMMARY

The results presented here show that photo-emission from F-centers in RbI at 300°K is quite like that found previously for KI. The work thus furnishes additional evidence for exciton-induced photo-emission. A new effect found near 85°K shows that the efficiency of this process at first increases with increasing optical absorption, reaches a maximum of more than 10^{-3} electron/quantum for an absorption constant near 10^6 cm^{-1}, and then decreases. This result may be explained qualitatively by a non-uniform distribution of F-centers, and by Fano's hypothesis that excitons are destroyed when they diffuse to a free surface. Hebb has derived interesting information in a quantitative analysis of the effect. A minor variation on the low energy side of the exciton-induced peak in the photoelectric yield is attributed to the onset of opacity in the thin salt film. The temperature variation of the yield due to direct ionization is described. Satisfactory qualitative agreement was obtained with Herring's analysis of photo-emission from impurities in polar crystals.

The effects treated above are, of course, not restricted to RbI. Attention was confined to this substance here because data on it were most complete. The same type of phenomena appeared with KI, KI doped with Tl, and CsI.

We are indebted by Frederick Seitz, Harvey Brooks, and Malcolm Hebb for valuable discussions of theoretical questions. Jean Dickey has given us her generous help throughout the experiments.

[9] For a related effect, see E. A. Taft and J. E. Dickey, Phys. Rev. 79, 625 (1950). H. B. DeVore has informed us that he has observed a similar phenomenon in BaO. Thick layers of KI heavily doped with Tl show a like decrease in yield at the edge of the Tl absorption band.

[10] C. Herring, Phys. Rev. 73, 1238 (1948).

[11] F. Seitz, *The Modern Theory of Solids* (McGraw-Hill Book Company, Inc., New York, 1940), Chapter 11; N. F. Mott and R. W. Gurney, *Electronic Processes in Ionic Crystals* (Clarendon Press, Oxford, England, 1940), p. 97.

[12] As a function of applied voltage, the photo-current increased five to eight times more rapidly than that from a uniform metal. See also reference 1.

Mechanism of Exciton-Enhanced Photoelectric Emission in Alkali Halides

MALCOLM H. HEBB
General Electric Research Laboratory, Schenectady, New York
(Received November 15, 1950)

A theoretical interpretation is made of the photoelectric yield from RbI as observed by Apker and Taft. The mechanism used is the following: (1) In the neighborhood of the first peak in the optical absorption, excitons produced in the crystal diffuse to *F*-centers and eject electrons from them. (2) The electrons diffuse to the surface and appear as external photo-electrons. Competing with (1) are other processes of destruction of excitons. It is found necessary to suppose that these are localized near the surface to form a dead layer either because of preferential destruction there or a sparsity of *F*-centers needed for (1). In (2) electrons gradually lose energy to the lattice so that probability of escape through the surface decreases with increasing depth of origin. Combination of these two effects gives photoelectric yield first rising then falling with increasing absorption coefficient in agreement with observation. Energy distribution of emitted electrons is calculated and compared with experiment.

I. INTRODUCTION

THE photoelectric yield from films of RbI containing *F*-centers both at 300°K and 85°K has been measured by Apker and Taft.[1] In the region of the first maximum in the optical absorption, they find a remarkable difference in the form of the photoelectric emission at the two temperatures. At the higher temperature, the emission has a single peak corresponding closely to the optical peak. At the lower temperature, the emission shows a double peak, the valley between coinciding with the peak in the optical absorption. Apker and Taft explain this phenomenon in the following way. The peak optical absorption is some 70 percent greater at 85°K than at 300°K. Suppose now that the photoelectric yield first rises with increasing absorption coefficient, reaches a maximum, and then falls. The observed behavior will follow if the absorption at which the yield is a maximum lies between the peak absorptions at 300°K and 85°K. It is the purpose of the present paper to give a more quantitative account of this effect.

II. FORMATION AND DESTRUCTION OF EXCITONS

Following Apker and Taft,[2] we suppose that electrons ejected by absorption in the first optical absorption peak are the result of a secondary process. An exciton produced by the primary absorption diffuses to an *F*-center in the crystal, where it ejects the electron from the center and is simultaneously destroyed.[3] The photoelectric yield consists of those electrons that are able to escape through the surface from their point of origin in the crystal.

One can represent the yield in electrons per quantum as the integral of a product

$$Y=\int_0^\infty S(z)P(z)dz, \tag{1}$$

in which S is the number of electrons per unit depth produced at depth z by a single incident quantum and P is the probability of escape from this depth. It is presumed that $P(z)$ is a decreasing function of z. A simple assumption would be to let

$$S(z)=\alpha\epsilon^{-\alpha z}, \tag{2}$$

where α is the optical absorption coefficient; i.e., to suppose that the generation of electrons is proportional to the destruction of light quanta at each point. However, this immediately gives a yield Y which, contrary to the experimental result, always increases with α. In order to get a maximum in Y with respect to α, it is necessary to reduce S compared to (2) at small z; in other words, to reduce the production of electrons near the surface. The following mechanisms might be expected to contribute to this result.

(A) Excitons may be preferentially destroyed at the crystal surface. Fano[4] has used this hypothesis to explain the low efficiency of phosphors under bombardment by electrons of low energy.

(B) Excitons may experience a force urging them toward the surface. This would make (A) more effective than with diffusion alone. In principle, one should expect a dipole image force and a force due to distortion of the crystal near the surface.

(C) The density of *F*-centers at the surface may be considerably lower than it is in the interior.

(D) Surface irregularities and cracks may extend to some depth so that mechanism (A) may make ineffective a layer of appreciable thickness.

By assuming free diffusion of excitons and destruction at an ideal surface according to (A), we have been unable to account for the experimental results in a satisfactory way. It is possible to get a maximum in the curve of yield *vs* absorption constant, but the maximum is too flat to give as deep a minimum in yield *vs* frequency as is observed.

We have therefore made the more drastic assumption that there is a dead layer of thickness h at the surface

[1] L. Apker and E. Taft, Phys. Rev. **81**, 698 (1951).
[2] L. Apker and E. Taft, Phys. Rev. **79**, 964 (1950).
[3] At lower energies photons eject electrons from *F*-centers directly, but this process is unimportant here.
[4] U. Fano, Phys. Rev. **58**, 544 (1940).

of the crystal and that there is no production of electrons by excitons in this layer. At greater depths, the production will be supposed to follow Eq. (2). We thereby neglect the effect of diffusion of the excitons which in any case is completely overshadowed by the effect of the dead layer.

III. ELECTRON ESCAPE

As a simple preliminary to the application of age theory to the diffusion and escape of the electrons, we shall calculate the yield using an exponential escape probability[5]

$$P(z)=e^{-\gamma z}. \tag{3}$$

We have then to integrate Eq. (1), replacing the lower limit 0 by h, and using Eqs. (2) and (3). The result is

$$Y=\alpha e^{-(\alpha+\gamma)h}/(\alpha+\gamma). \tag{4}$$

According to Apker and Taft,[1] the maximum yield is about 2.2×10^{-3}, and it occurs at $\alpha=0.6\times10^{6}$ cm^{-1}. These data suffice to fix both γ and h. One finds $1/\gamma=38$A, $h=136$A. The solid curve in Fig. 1 shows the yield Y as function of α, for these values of the parameters.

We now consider more precisely the escape of electrons from the crystal. Let us suppose that electrons are being produced at a depth $z=z_0$ with an initial energy ϵ_0 relative to the bottom of the conduction band.[6] As they diffuse from their origin at z_0, they will gradually lose energy and an electron reaching the surface will have an energy $\epsilon\leqq\epsilon_0$. If ϵ is greater than the electron affinity A, which is the height of the surface barrier above the bottom of the conduction band, then it may surmount the barrier and escape into the vacuum. If $\epsilon<A$, the electron cannot leave the crystal. Actually, an electron with $\epsilon>A$ will not be able to escape unless the energy associated with its motion perpendicular to the barrier exceeds A. In the diffusion problem, this means that a fraction A/ϵ of the electrons impinging on the surface are turned back. However, if the energy loss per collision is small, an electron once reaching the surface will have a large number of opportunities to escape before there is any appreciable change in its energy. Then, if $\epsilon>A$, it will be almost certain to escape. We shall assume that this treatment is sufficiently accurate for our purpose.

The simultaneous diffusion and slowing down of electrons is conveniently treated by the "age theory" of Fermi.[7] Let λ and $\Delta\epsilon$ be the mean free path and mean energy loss per collision. Both may be functions of the energy ϵ. Then the "age," which is actually the square of a length, is defined by

$$\tau=\int_{\epsilon}^{\epsilon_0}\lambda^2 d\epsilon/3\Delta\epsilon. \tag{5}$$

The slowing down density q is defined as the number of electrons per cm^3 which reach energy ϵ or age τ per sec. It satisfies

$$\partial^2 q/\partial z^2=\partial q/\partial\tau.$$

The boundary conditions suitable to our problem are

$$q=0 \text{ at } z=0 \text{ and } z=\infty,\ q=\delta(z-z_0) \text{ at } \tau=0.$$

The last condition specifies a source of one electron per cm^2 per second with energy ϵ_0 (age zero) at depth $z=z_0$. The requirement $q=0$ at $z=0$ implies escape of all electrons reaching the surface. As discussed above, this will be closely true for $\epsilon>A$, which is the only range of interest. It is easily verified that the solution for q is

$$q=\{\exp[-(z-z_0)^2/4\tau]-\exp[-(z+z_0)^2/4\tau]\}/(4\pi\tau)^{\frac{1}{2}}.$$

The flux of electrons of age τ escaping through the surface $z=0$, per cm^2 per sec per unit age is

$$\Gamma(z_0,\tau)=(\partial q/\partial z)_{z=0}=z_0\exp(-z_0^2/4\tau)/(4\pi\tau^3)^{\frac{1}{2}}. \tag{6}$$

To find the escape probability for electrons produced at depth z_0, we have to integrate Γ over the range of

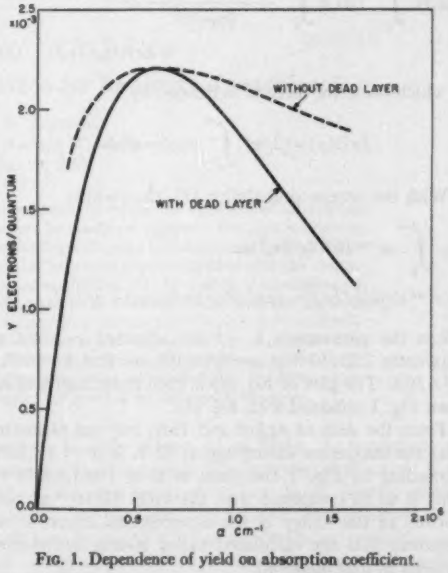

FIG. 1. Dependence of yield on absorption coefficient.

[5] An exponential escape probability has been used by J. A. Burton, Phys. Rev. **72**, 531 (A) (1947) and by N. D. Morgulis, Compt. rend. acad. sci. U.R.S.S. **52**, 675 (1946) for Cs_3Sb surfaces. There it is generally assumed that the electron affinity is zero so that electrons encounter no barrier at the surface. Then the exponential law follows from the assumption of free diffusion together with a uniform bulk absorption of electrons. In the alkali halides, there is no immediate justification for the exponential law.

[6] We have taken the initial energy ϵ_0 the same for all electrons. It would be more realistic to assume a distribution of values corresponding to a spread in energy of the excitons. Such a spread will exist if the excitons are produced with a range of energies or if they are produced with an energy higher than the minimum allowable in the crystal and subsequently lose energy.

[7] E. Fermi, *Nuclear Physics* (Chicago University Press, Chicago, 1950); R. E. Marshak, Revs. Modern Phys. **19**, 185 (1947).

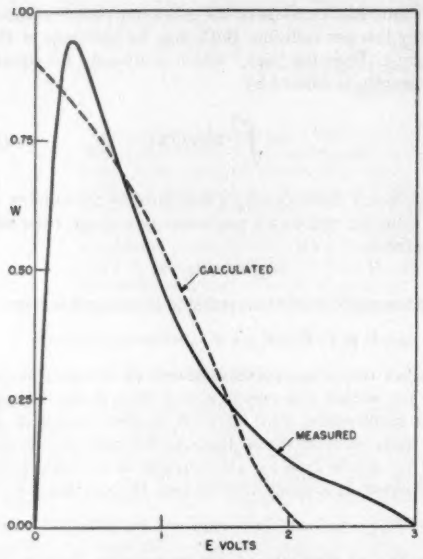

FIG. 2. Energy distribution of photo-electrons from RbI $h\nu = 5.56$ volts, $T = 300°K$.

ages corresponding to $A < \epsilon < \epsilon_0$. Let the age at which $\epsilon = A$ be τ_a; then the escape probability is

$$P(z_0) = \int_0^{\tau_a} \Gamma d\tau = \int_0^{\tau_a} \frac{z_0 \exp(-z_0^2/4\tau)}{(4\pi\tau^3)^{\frac{1}{2}}} d\tau$$

$$= Erfc(z_0/2\tau_a^{\frac{1}{2}}), \quad (7)$$

in which the error integral is defined by

$$Erfc(x) = (2/\pi^{\frac{1}{2}}) \int_x^\infty \exp(-x^2) dx.$$

With the escape probability (7), the yield is

$$Y = \int_h^\infty \alpha\epsilon^{-\alpha z} Erfc(z/2\tau_a^{\frac{1}{2}}) dz$$

$$= \epsilon^{-\alpha h} Erfc(h/2\tau_a^{\frac{1}{2}}) - \exp(\alpha^2\tau_a) Erfc(\alpha\tau_a^{\frac{1}{2}} + h/2\tau_a^{\frac{1}{2}}). \quad (8)$$

When the parameters h, $\tau_a^{\frac{1}{2}}$ are adjusted to yield a maximum 2.2×10^{-3} at $\alpha = 0.6 \times 10^6$, we find $h = 146$A, $\tau_a^{\frac{1}{2}} = 50$A. The plot of Eq. (8) is then indistinguishable from Fig. 1 obtained with Eq. (4).

From the data of Apker and Taft, one can estimate that the maximum absorption at 85°K is $\alpha = 1.4 \times 10^6$. According to Fig. 1 the yield is then $Y \simeq 1.4 \times 10^{-3}$. This is to be compared with the yield 1×10^{-3} at the bottom of the valley in the experimental curve. It is apparent that the calculated valley is only two-thirds as deep as that observed.

It was stated earlier that destruction of excitons at an ideal surface in accordance with mechanism (A) could not account for the observations. The broken line in Fig. 1 is obtained with this hypothesis. The parameters used were $\tau_a^{\frac{1}{2}} = 47$A and $L = 800$A, where L is the diffusion length for the excitons. The curve is so flat that the reduction at $\alpha = 1.4 \times 10^6$ is only a fifth of that required.

The mean free path λ is connected with the age τ by Eq. (5). In order to estimate λ we suppose that the integrand is constant and find

$$\lambda = [3\tau_a \Delta\epsilon/(\epsilon_0 - A)]^{\frac{1}{2}}.$$

We have already found $\tau_a^{\frac{1}{2}} = 50$A. The difference $\epsilon_0 - A$ is just the difference in $h\nu$ at the peak and threshold, *viz.*, $5.7 - 3.0 = 2.7$ volts. Estimating $\Delta\epsilon = 0.05$ volt, we get $\lambda \cong 10$A in order of magnitude.

IV. ENERGY DISTRIBUTION OF PHOTO-ELECTRONS

Further evidence in support of the mechanism proposed here and of the existence of a dead layer on the surface comes from a study of energy distribution of the photo-electrons. Preliminary results at room temperature have shown that the exciton-enhanced emission consists predominantly of slow electrons.[8] This fits nicely with the hypothesis of a dead layer, since electrons originating at a depth in the crystal will become degraded in energy on diffusing to the surface. The distribution in age of electrons reaching the surface is

$$W(\tau) = \int_0^\infty S(z)\Gamma(z, \tau) dz$$

$$= (4\pi\tau^3)^{-\frac{1}{2}} \int_h^\infty \alpha\epsilon^{-\alpha z} z \exp(-z^2/4\tau) dz$$

$$= \alpha^2 \{[1/\alpha(\pi\tau)^{\frac{1}{2}}] \exp(-\alpha h - h^2/4\tau)$$

$$- \exp(\alpha^2\tau) Erfc(\alpha\tau^{\frac{1}{2}} + h/2\tau^{\frac{1}{2}})\},$$

with the help of Eq. (6). The age τ and energy ϵ of the electrons are related by Eq. (5). If we suppose λ and $\Delta\epsilon$ independent of ϵ then

$$\tau/\tau_a = 1 - E/E_0, \quad (9)$$

where $E = \epsilon - A$ is the kinetic energy of the emitted electron and $E_m = \epsilon_0 - A$ is its maximum value.

Figure 2 shows a comparison between the distribution according to Eq. (8) and that measured at $h\nu = 5.56$ volts by Apker and Taft.[8] The parameters used in constructing the theoretical curve were $\alpha = 0.72 \times 10^6$, $h = 115$A, $\tau_a^{\frac{1}{2}} = 50$A, $E_m = 2.6$ volts. These were obtained by assuming that the observed yield of 8×10^{-3} electron/quantum at the maximum with respect to $h\nu$ was also the maximum with respect to α. Then h and α are determined if $\tau_a^{\frac{1}{2}}$ is fixed at the value found previously. This procedure is admittedly rough but is probably adequate in view of the preliminary nature of the data. It should be emphasized that the measurements showing self-reversal in the yield, the measurements of optical

[8] L. Apker and E. Taft (to be published).

absorption and the measurements of energy distribution were taken each on a different surface in a different tube. Further, there is good evidence that the parameters, particularly h, vary with the preparation of the surface.[8] One does not seem to be justified, therefore, in attempting a more accurate determination of the constants.

The principal feature of the experimental curve, namely, the steep rise at low energies, is well represented by the theoretical curve. It is not at all surprising that in other respects there are some differences between them. It should be remarked that the comparison of the energy distributions is a more severe test of the theory than comparison of yields, since the latter is a comparison of the integral of the former. Further, to determine the energy distribution, it is necessary to assume an explicit form for the connection between age and energy which is not required for the yield.

The differences between the curves of Fig. 2 can be explained in a reasonable way in terms of the model which we have used. There are two considerations that have been left out of account that will raise the calculated distribution at the high end where it is too low. First, one should expect a gradual transition from the surface dead layer to the active material in the crystal. Thus, some electrons will be able to originate at depths less than h, and these will lose less energy in reaching the surface. Second, one can expect the electrons to be produced with an initial spread in energy of several tenths of a volt.[6] Those that are abnormally energetic at birth will be likely to reach the surface with an excess of energy. Neither of these effects can make any noticeable change in the course of the yield.

At $E=0$ the theoretical curve drops discontinuously to zero. This is to be attributed to our assumption that an electron reaching the surface with $\epsilon > A$ will surely surmount the surface barrier and escape. Actually, when $\epsilon - A$ is small, the chance of escape in a single encounter $(\epsilon - A)/\epsilon$ becomes so small that a large fraction of electrons will lose their extra energy without getting over the barrier. The resulting distribution would decrease continuously to zero in better agreement with observation.

The distribution to be expected when there is no dead layer but destruction of excitons at the surface (mechanism A) has also been calculated. In this case, diffusion of the excitons is taken into account. It turns out then that the distribution in age decreases with increasing age. With the linear connection (9) between age and energy, this means that the energy distribution rises with energy in violent contradiction with experiment. We conclude that a dead layer is essential to the explanation of both the energy distribution and the yield.

It is a pleasure to acknowledge indebtedness to LeRoy Apker and to Harvey Brooks for many stimulating discussions and suggestions and to the latter for the introduction to age theory.

PHYSICAL REVIEW VOLUME 81, NUMBER 5 MARCH 1, 1951

Consequences of Gauge Invariance for Radiative Transitions*

R. G. Sachs and N. Austern†
University of Wisconsin, Madison, Wisconsin
(Received September 28, 1950)

Consideration is given to any system of particles whose behavior under the influence of an external electromagnetic field can be described by a gauge invariant Schroedinger equation. Detailed restrictions on the form of the hamiltonian which are imposed by the condition of gauge invariance are derived. These provide a simple means to the solution of many problems of the interaction of a system with the electromagnetic field. In particular the following consequences are established: (1) In multipole expansions for single photon processes the electric multipole operators have the usual form but the form of the magnetic multipole operators may depend in a detailed way on the interactions between particles and electromagnetic field. (2) The f-sum rule can be expressed in closed form in terms of the interactions. (3) A generalization of the f-sum rule to all electric multipole orders is given. (4) The cross section for scattering of a low energy photon can be expressed in terms of the electrostatic polarizability quite independently of the interactions. Applications of these methods to problems in nuclear physics are given in an accompanying paper.

I. INTRODUCTION

IT is generally assumed for any molecular, atomic, or nuclear system that, to the approximation in which it can be described by a Schroedinger equation, the electromagnetic interactions of the system must appear in such a way as to leave the equations of motion gauge invariant. The purpose of this note is to show that this assumption has many general consequences for radiative transitions. For example, the well known f-sum rule for the oscillator strengths can be obtained directly from the gauge property as can similar sum rules for the other electric multipole orders.

Since nuclear processes involve charge-bearing quanta

* Supported in part by the U.S. AEC and in part by the Wisconsin Alumni Research Foundation.
† AEC Predoctoral Fellow.

(mesons) in a manner which has not yet been adequately described, little is known about the electromagnetic interactions of nuclei. To the extent that these properties can be incorporated into a Schroedinger equation (phenomenological theory) tentative theoretical discussions[1,2] usually assume that the system must be gauge invariant. The radiative properties of nuclei are thereby affected in a manner which can be discovered by application of the general results given here. That application is made in the following paper.

For molecular and atomic systems, the electromagnetic interactions are well known so that no information of a fundamental nature can be expected to ensue from this study. However a somewhat deeper understanding of well-known relationships is provided. Furthermore, for the treatment of certain molecular problems it is convenient to replace the interactions by approximate interactions which involve exchange or velocity dependence.[3] To this approximation, results obtained here serve as a convenient device for the study of electromagnetic properties.[4]

II. GENERAL PROPERTIES OF THE HAMILTONIAN

It will be found convenient to make an explicit separation of the center of mass variables and the relative coordinates. The coordinate and momentum of the center of mass are denoted by $\mathbf{R}$ and $\mathbf{P}$ respectively. The internal variables will be denoted symbolically by a set of operators φ_λ which, for different values of λ, may include relative coordinates, relative momenta, spin variables, exchange operators, and so on. The essential property of φ_λ is that it commutes with $\mathbf{R}$ and $\mathbf{P}$.

In the absence of an electromagnetic field the hamiltonian of the system is

$$T_0(\mathbf{P})+H_0(\varphi_\lambda).$$

We now assume that in the presence of an external electromagnetic field described by a vector potential $\mathbf{A}(\mathbf{r})$, the Hamiltonian is written as[5]

$$T\{\mathbf{P}, \mathbf{A}(\mathbf{r})\}+H\{\varphi_\lambda, \mathbf{A}(\mathbf{r})\},$$

with

$$T\{\mathbf{P}, \mathbf{A}(\mathbf{r})\}=T_0(\mathbf{P}-\textstyle\sum_\alpha (e_\alpha/c)\mathbf{A}_\alpha), \qquad (1)$$

where e_α is the charge on the αth particle, and $\mathbf{A}_\alpha=\mathbf{A}(\mathbf{r}_\alpha)$, $\mathbf{r}_\alpha$ being the position of that particle. The operator H includes the internal kinetic energy and terms involving the interactions between the particles. However, the latter terms need not be obtainable by a simple prescription from the field free interactions in H_0.

In most problems concerning the interaction of the field with atomic systems, the field is weakly coupled to the system and $H\{\varphi_\lambda, \mathbf{A}\}$ can be expanded in powers of the coupling coefficient. This expansion into terms of successively higher order is then taken to be

$$H\{\varphi_\lambda, \mathbf{A}\}=H_0(\varphi_\lambda)+H_1\{\varphi_\lambda, \mathbf{A}(\mathbf{r})\} +(1/2!)H_2\{\varphi_\lambda, \mathbf{A}(\mathbf{r})\}+\cdots, \qquad (2)$$

where the H_n are hermitian operators.

Particular properties of the operator H_1 are of interest since this term represents the interaction responsible for emission or absorption of a single photon. It can be seen easily that H_1 is linearly dependent on $\mathbf{A}(\mathbf{r})$:

$$H_1\{\varphi_\lambda, \epsilon\mathbf{A}+\epsilon'\mathbf{A}'\}=\epsilon H_1\{\varphi_\lambda, \mathbf{A}\}+\epsilon' H_1\{\varphi_\lambda, \mathbf{A}'\}. \qquad (3)$$

Furthermore, the magnetic moment of the system about its center of mass may be defined in terms of H_1. For a weak uniform magnetic field $\mathbf{H}$, we set

$$\mathbf{A}=-\tfrac{1}{2}[(\mathbf{r}-\mathbf{R})\times\mathbf{H}]$$

and the first-order interaction energy is

$$-(\mathbf{M}\cdot\mathbf{H})=-\tfrac{1}{2}H_1\{\varphi_\lambda, (\mathbf{r}-\mathbf{R})\times\mathbf{H}\}, \qquad (4)$$

where $\mathbf{M}$ is the magnetic moment operator. Note that the introduction of $\mathbf{R}$ in this way is possible because $\mathbf{R}$ can be treated as a number in H_1 by virtue of its commutation with all the φ_λ. Since H_1 is linear, we can divide by the magnitude of the magnetic field and obtain

$$(\mathbf{M}\cdot\mathbf{n})=\tfrac{1}{2}H_1\{\varphi_\lambda, \boldsymbol{\varrho}\times\mathbf{n}\} \qquad (5)$$

for the definition of an arbitrary component of the magnetic moment in terms of the unit vector $\mathbf{n}$. The definition of $\boldsymbol{\varrho}$ is

$$\boldsymbol{\varrho}=\mathbf{r}-\mathbf{R}, \qquad (6)$$

the coordinate relative to the center of mass.

III. GENERAL CONSEQUENCES OF GAUGE INVARIANCE

The requirement of gauge invariance can be presented in terms of an arbitrary gauge function $G(\mathbf{r})$ and the associated expression

$$g=(i/\hbar c)\textstyle\sum_\alpha e_\alpha G(\mathbf{r}_\alpha). \qquad (7)$$

The hamiltonian is gauge invariant if[6]

$$T\{\mathbf{P}, \mathbf{A}+\text{grad}G\}+H\{\varphi_\lambda, \mathbf{A}+\text{grad}G\} =e^g[T\{\mathbf{P}, \mathbf{A}\}+H\{\varphi_\lambda, \mathbf{A}\}]e^{-g}. \qquad (8)$$

By the definition, Eq. (1), the operator T is independently gauge invariant so the terms in T may be dropped from Eq. (8) to give

$$H\{\varphi_\lambda, \mathbf{A}+\text{grad}G\}=e^g H\{\varphi_\lambda, \mathbf{A}\}e^{-g}. \qquad (9)$$

With $\mathbf{A}=0$ the left side of Eq. (9) can be expanded in

[1] R. G. Sachs, Phys. Rev. **74**, 433 (1948).
[2] R. K. Osborne and L. L. Foldy, Phys. Rev. **79**, 795 (1950).
[3] The introduction of a velocity dependent interaction to facilitate the treatment of electrons in a periodic lattice serves as an example. See J. C. Slater, Phys. Rev. **76**, 1592 (1949).
[4] In this connection see the discussion of the modification of sum rules in atomic systems given by V. Fock, Z. Physik **89**, 744 (1934).
[5] The braces are used to indicate that H and T are *functionals* of the vector field $\mathbf{A}(\mathbf{r})$.
[6] H. Weyl, *Theory of Groups and Quantum Mechanics* (Dover Publications Inc., New York), p. 100.

accordance with Eq. (2) while the right side can be expanded in terms of commutators of g with H_0:

$$H_0(\varphi_\lambda)+H_1\{\varphi_\lambda, \text{grad}G\}+(1/2!)H_2\{\varphi_\lambda, \text{grad}G\}+\cdots = H_0(\varphi_\lambda)+[g, H_0]+(1/2!)[g, [g, H_0]]+\cdots. \quad (10)$$

By equating terms of equal order from Eq. (10) gauge invariance is seen to imply the conditions

$$H_1\{\varphi_\lambda, \text{grad}G\}=[g, H_0], \quad (11)$$

$$H_2\{\varphi_\lambda, \text{grad}G\}=[g, [g, H_0]], \quad (12)$$

and, in general,

$$H_n\{\varphi_\lambda, \text{grad}G\}=c^n H_0/cg^n, \quad (13)$$

where the expression on the right denotes the commutator of H_0 taken n times with respect to g.

All of the consequences of gauge invariance relevant to problems discussed here are expressed by Eqs. (13). These equations are conditions on the form of the hamiltonian and can henceforth be used freely without regarding G as a gauge function.

Note that, subsequent to writing down a hamiltonian of a given form, the electromagnetic field can be quantized without modification of the equations. This is correct if the hamiltonian involves only variables that commute with $\mathbf{A}$.

IV. SINGLE PHOTON PROCESSES

For the sake of definiteness we consider the emission of a single photon. The vector potential for the radiation field is taken to be

$$\mathbf{A}=c(2\pi\hbar/V)^{\frac{1}{2}}\sum_{\mathbf{k},\mathbf{u}} q_{\mathbf{k},\mathbf{u}}\omega^{-\frac{1}{2}}\mathbf{u}\exp(i\mathbf{k}\cdot\mathbf{r}), \quad (14)$$

with $q_{\mathbf{k},\mathbf{u}}=a_{\mathbf{k},\mathbf{u}}+a_{-\mathbf{k},\mathbf{u}}^*$ where $a_{-\mathbf{k},\mathbf{u}}^*$, $a_{\mathbf{k},\mathbf{u}}$ are the creation and annihilation operators for a photon of propagation vector $\mathbf{k}$ and polarization $\mathbf{u}$ with $(\mathbf{u}\cdot\mathbf{k})=0$; $\omega=ck$ is the angular frequency of the photon, and V is the volume of the enclosure introduced for purposes of normalization. For single photon processes, $\mathbf{A}$ is to be treated only in first order. Then, by Eq. (2), the interaction of the radiation field with the internal motion of the system is

$$I=\sum_{\mathbf{k},\mathbf{u}} c(2\pi\hbar/V\omega)^{\frac{1}{2}}q_{\mathbf{k},\mathbf{u}}H_1\{\varphi_\lambda, \mathbf{u}\exp(i\mathbf{k}\cdot\mathbf{r})\}. \quad (15)$$

Denoting by I', the matrix element of I with respect to the radiation field for emission of the photon $(\mathbf{k}, \mathbf{u})$,

$$I'=c(2\pi\hbar/V\omega)^{\frac{1}{2}}H_1\{\varphi_\lambda, \mathbf{u}\exp(-i\mathbf{k}\cdot\mathbf{r})\}. \quad (16)$$

The radiative transition probabilities may then be obtained in terms of the matrix element of I' with respect to wave functions of the system of particles. Since $\mathbf{R}$ commutes with the φ_λ, it may be treated as a constant with the result

$$I'=c(2\pi\hbar/V\omega)^{\frac{1}{2}} \times\exp(-i\mathbf{k}\cdot\mathbf{R})H_1\{\varphi_\lambda, \mathbf{u}\exp(-i\mathbf{k}\cdot\boldsymbol{\rho})\}, \quad (17)$$

where $\boldsymbol{\rho}=\mathbf{r}-\mathbf{R}$. This form is convenient since the external factor merely establishes the conservation of total momentum while the argument appearing in H_1 depends only on the internal variables of the system.

The wave functions of the system can be written as the product of $\exp(i\mathbf{K}\cdot\mathbf{R})$ with a function describing the state of the internal motion. The matrix element of I' will vanish unless $\mathbf{K}$ decreases by the amount $\mathbf{k}$ in the emission process. Taking this change of momentum into account, the transition probability is determined by the matrix element of

$$I''=c(2\pi\hbar/V\omega)^{\frac{1}{2}}H_1\{\varphi_\lambda, \mathbf{u}\exp(-i\mathbf{k}\cdot\boldsymbol{\rho})\} \quad (18)$$

with respect to the internal wave functions only. The operator I'' will be called the *effective* interaction.

A multipole expansion of the effective interaction about the center of mass can now be made. Introducing the definitions

$$G_l(\mathbf{r})=(\mathbf{u}\cdot\boldsymbol{\rho})(\mathbf{k}\cdot\boldsymbol{\rho})^{l-1}/l!k^{l-1}, \quad (19)$$

and

$$\mathbf{W}_l(\mathbf{r})=l\boldsymbol{\rho}(\mathbf{k}\cdot\boldsymbol{\rho})^{l-1}/(l+1)!k^{l-1}, \quad (20)$$

then

$$\mathbf{u}\exp(-i\mathbf{k}\cdot\boldsymbol{\rho}) =\sum_{l=1}^{\infty}(-ik)^{l-1}\{\text{grad}G_l+i[\mathbf{u}\times\mathbf{k}]\times\mathbf{W}_l\}. \quad (21)$$

The gradient is taken with respect to $\mathbf{r}$. Substitution into Eq. (18) and use of the linear property of H_1, gives the effective interaction as

$$I''=c(2\pi\hbar/V\omega)^{\frac{1}{2}}\sum_{l=1}^{\infty}(-ik)^{l-1}[H_1\{\varphi_\lambda, \text{grad}G_l\} +iH_1\{\varphi_\lambda, [\mathbf{u}\times\mathbf{k}]\times\mathbf{W}_l\}]. \quad (22)$$

Introducing

$$D_l=\textstyle\sum_a e_a G_l(\mathbf{r}_a) \quad (23)$$

the gauge condition, Eq. (11), with $g=(i/\hbar c)\sum_l D_l$, yields

$$I''=-(2\pi\hbar/V\omega)^{\frac{1}{2}}\sum_{l=1}^{\infty}(-ik)^{l-1}[(i/k)[H_0, D_l] -icH_1\{\varphi_\lambda, [\mathbf{u}\times\mathbf{k}]\times\mathbf{W}_l\}]. \quad (24)$$

From the definitions Eq. (23) and Eq. (19), we see that

$$D_l=\textstyle\sum_a e_a(\mathbf{u}\cdot\boldsymbol{\rho}_a)(\mathbf{k}\cdot\boldsymbol{\rho}_a)^{l-1}/l!k^{l-1} \quad (25)$$

is just the electric 2^l-pole moment[7] and the corresponding terms in Eq. (24) are the time derivatives of the electric multipole moments. It is of some conse-

[7] Actually the multipole moments are usually defined in terms of surface harmonics (see Dancoff and Morrison, Phys. Rev. 55, 122 (1939)), which are irreducible representations of the rotation group, rather than these reducible tensors. However, since the multipole expansion is always used in the sense that only the lowest term with nonvanishing matrix element is to be considered, the extra terms which are included here would vanish as a consequence of the selection rules.

quence[8] that the electric multipole terms appear this way whatever the interaction. The other terms, which are magnetic in character, may depend very strongly on the interactions between particles, as shown in the following paper.

Defining a vector $\mathbf{M}_l$ by

$$(\mathbf{u}\times\mathbf{k}\cdot\mathbf{M}_l)=-H_1\{\varphi_\lambda,[\mathbf{u}\times\mathbf{k}]\times\mathbf{W}_l\}, \tag{26}$$

the effective interaction becomes

$$I''=-(2\pi\hbar/V\omega)^{\frac{1}{2}}\sum_{l=1}^{\infty}(-i\mathbf{k})^{l-1}[\dot{D}_l+ic(\mathbf{u}\times\mathbf{k}\cdot\mathbf{M}_l)]. \tag{27}$$

Equation (20), defining $\mathbf{W}_l$, and Eq. (26) show on comparison with Eq. (5) that $\mathbf{M}_1$ is just the magnetic moment of the system. In general, the $\mathbf{M}_l$ provide the magnetic multipole moments of order 2^l. To demonstrate this it must be shown that $\mathbf{M}_l$ transforms under rotation and inversion of the particle variables like a component of a tensor of rank l with parity $(-)^{l-1}$. First consider transformations of *all* vectors, including $\mathbf{u}$ and $\mathbf{k}$. Then

$$(\mathbf{u}\times\mathbf{k}\cdot\mathbf{M}_l)\rightarrow(\mathbf{u}\times\mathbf{k}\cdot\mathbf{M}_l) \tag{28}$$

since H_1 (and each H_n) is a scalar operator for transformations of all variables. Now under transformations of $\mathbf{u}$ and $\mathbf{k}$ *alone* $[(\mathbf{u}\times\mathbf{k})\times\mathbf{W}_l]$ transforms, according to Eq. (20), like a tensor of rank l with parity $(-)^{l-1}$. Since H_1 is linear, the defining Eq. (26) shows that under this transformation $(\mathbf{u}\times\mathbf{k}\cdot\mathbf{M}_l)$ transforms similarly. If the transformation of $\mathbf{u}$ and $\mathbf{k}$ is supplemented by the same transformation of particle variables, Eq. (28) shows that $(\mathbf{u}\times\mathbf{k}\cdot\mathbf{M}_l)$ must undergo the inverse transformation, which establishes the required property.

The important result is the multipole expansion Eq. (27) of the effective interaction which was obtained only for the internal part, H of the hamiltonian. It is still to be shown that the interaction terms in $T\{\mathbf{P},\mathbf{A}\}$, given by Eq. (1), have a negligible influence on transitions. Since

$$T_0(\mathbf{P})=\mathbf{P}^2/2M_0, \tag{29}$$

M_0 the total mass of the system, the terms in T which contribute to single photon processes are

$$T_1=(-1/M_0)(2\pi\hbar/V\omega)^{\frac{1}{2}}\times\exp(-i\mathbf{k}\cdot\mathbf{R})\textstyle\sum_a e_a\exp(-i\mathbf{k}\cdot\boldsymbol{\varrho}_a)(\mathbf{u}\cdot\mathbf{P}). \tag{30}$$

Now the multipole expansion is an expansion of $\exp(-i\mathbf{k}\cdot\boldsymbol{\varrho}_a)$ in powers of $(\mathbf{k}\cdot\boldsymbol{\varrho}_a)$, and we note that the matrix element of the zero-order term vanishes because the internal wave functions are orthogonal. The first-order term in $(\mathbf{k}\cdot\boldsymbol{\varrho}_a)$ (quadrupole order) makes a contribution only if the dipole selection rules are satisfied; but then there is a contribution of dipole order from I'' so terms of quadrupole order should be neglected. In general we see that T_1 contributes in one higher order than I'' so it may always be neglected for the single photon process.

[8] See following paper. Also C. Møller and L. Rosenfeld, Kgl. Danske Videnskab Selskab Mat.-fys. Medd. 20, No. 12 (1943).

V. SUM RULES FOR ELECTRIC MULTIPOLE RADIATION

The transition probability for the emission of electric 2^l-pole radiation in the direction $d\Omega$ when the system goes from a state n to a state j is found by Eq. (27) to be

$$w_{jn}{}^l=\frac{2\pi}{\hbar}\rho_E|I_{jn}''|^2=\frac{e^2}{Mc^{2l+1}}\frac{\omega^{2l}}{}\left(\frac{\omega_{nj}}{\omega}\right)f_{jn}{}^l\frac{d\Omega}{4\pi}, \tag{31}$$

where M is some appropriate particle mass and $\hbar\omega_{nj}$ is the change in *internal* energy of the system. This energy change differs from $\hbar\omega$ by the very small recoil energy of the center of mass. The generalized oscillator strength $f_{jn}{}^l$ is defined by

$$f_{jn}{}^l=(2M/\hbar e^2)\omega_{nj}|(D_l)_{jn}|^2, \tag{32}$$

but, for present purposes, it is more conveniently written in the form

$$f_{jn}{}^l=(-M/\hbar^2e^2)\{[[H_0,D_l]_{jn}(D_l)_{nj}-(D_l)_{jn}[H_0,D_l]_{nj}\}. \tag{33}$$

Then the sum of the oscillator strength over all initial states n is

$$\textstyle\sum_n f_{jn}{}^l=-(M/\hbar^2e^2)[[H_0,D_l],D_l]_{jj}, \tag{34}$$

i.e., the expectation value of the double commutator in state j. However, according to Eq. (12) and the definition, Eq. (23), of D_l, the double commutator can be expressed directly in terms of H_2:

$$\textstyle\sum_n f_{jn}{}^l=(Mc^2/e^2)\langle H_2\{\varphi_\lambda,\operatorname{grad}G_l\}\rangle_{jj} \tag{35}$$

where G_l is given explicitly in Eq. (19) and the gradient is taken with respect to $\mathbf{r}$. Equation (35) is the *generalized f-sum rule.*

That Eq. (35) leads to the usual f-sum rule for dipole radiation can easily be established by noting that

$$\operatorname{grad}G_1=\mathbf{u}. \tag{36}$$

Consider, as a particular example, particles of mass m_a whose mutual interaction can be described by an ordinary potential $U(\rho_1,\rho_2,\cdots)$.

Then the internal hamiltonian may be written as

$$H\{\varphi_\lambda,\mathbf{A}\}=\frac{1}{4M_0c^2}\sum_{\alpha,\beta}m_\alpha m_\beta\left(\frac{c}{m_\alpha}\mathbf{p}_\alpha-\frac{c}{m_\beta}\mathbf{p}_\beta-\frac{e_\alpha}{m_\alpha}\mathbf{A}_\alpha+\frac{e_\beta}{m_\beta}\mathbf{A}_\beta\right)^2+U \tag{37}$$

where M_0 is the total mass of the system. The operator H_2 is

$$H_2\{\varphi_\lambda,\mathbf{A}\}=\frac{1}{2M_0c^2}\sum_{\alpha,\beta}m_\alpha m_\beta\left(\frac{e_\alpha}{m_\alpha}\mathbf{A}_\alpha-\frac{e_\beta}{m_\beta}\mathbf{A}_\beta\right)^2. \tag{38}$$

Therefore

$$H_2\{\varphi_\lambda, \mathbf{u}\}=\frac{1}{2M_0c^2}\sum_{\alpha,\beta} m_\alpha m_\beta\left(\frac{e_\alpha}{m_\alpha}-\frac{e_\beta}{m_\beta}\right)^2, \quad (39)$$

and the sum rule for dipole radiation becomes

$$\sum_n f_{jn}{}^1=\frac{M}{2M_0c^2}\sum_{\alpha,\beta} m_\alpha m_\beta\left(\frac{e_\alpha}{m_\alpha}-\frac{e_\beta}{m_\beta}\right)^2. \quad (40)$$

For a system of Z electrons of mass m in the field of a nucleus of charge Ze, we choose M to be m/M_0 times the nuclear mass and find

$$\sum_n f_{jn}{}^1=Z \quad (41)$$

in agreement with the usual result. Again note that the mass appearing in the definition of this oscillator strength differs slightly from the electron mass.

VI. THE SCATTERING OF LIGHT

As a further example of the consequences of gauge invariance, consider the elastic scattering by the system of a photon of propagation vector $\mathbf{k}$ and polarization vector $\mathbf{u}$ into the state $\mathbf{k}'$, $\mathbf{u}'$. It will be shown that gauge invariance just leads to the cancellation of diamagnetic terms which is required to establish the usual relationship between the static electric polarizability and the cross section for the scattering of a low energy photon.

The second-order terms must be carried for this two-quantum process so the interaction is

$$I=H_1\{\varphi_\lambda, \mathbf{A}\}+\tfrac{1}{2}H_2\{\varphi_\lambda, \mathbf{A}\}+T\{\mathbf{P}, \mathbf{A}\}. \quad (42)$$

Application of the vector potential, Eq. (14), to the center of mass interaction $T\{\mathbf{P}, \mathbf{A}\}$ leads directly to the Thomson cross section for the scattering of light by a charged mass point. Consideration is now restricted to the internal part of the hamiltonian. In this case only the terms of electric dipole order are carried in the vector potential, which is then written as

$$\mathbf{A}=c(2\pi\hbar/V)^{\frac{1}{2}}\sum_{k,u}\omega^{-\frac{1}{2}}q_{k,u}\mathbf{u}\exp(i\mathbf{k}\cdot\mathbf{R}). \quad (43)$$

If a function $G(\mathbf{r})$ is defined by

$$G=c(2\pi\hbar/V)^{\frac{1}{2}}\sum_{k,u}\omega^{-\frac{1}{2}}q_{k,u}[\mathbf{u}\cdot(\mathbf{r}-\mathbf{R})]\exp(i\mathbf{k}\cdot\mathbf{R}) \quad (44)$$

then

$$\mathbf{A}=\text{grad}G. \quad (45)$$

The gauge conditions, Eqs. (11) and (12), may therefore be used to transform Eq. (42) to

$$I=(i/\hbar)(2\pi\hbar/V)^{\frac{1}{2}}\sum_{k,u}\omega^{-\frac{1}{2}}q_{k,u}[D, H_0]\exp(i\mathbf{k}\cdot\mathbf{R})$$
$$-(\pi/V\hbar)\sum_{k,u}\sum_{k',u'}(\omega\omega')^{-\frac{1}{2}}q_{k,u}q_{k',u'}[D,[D', H_0]] \quad (46)$$

with

$$D=\textstyle\sum_\alpha e_\alpha(\mathbf{u}\cdot\varrho_\alpha), \quad D'=\sum_\alpha e_\alpha(\mathbf{u}'\cdot\varrho_\alpha). \quad (47)$$

Now the transition amplitude[9] for the absorption of $(\mathbf{k}, \mathbf{u})$ and the emission of $(\mathbf{k}', \mathbf{u}')$ is found from Eq. (46) to be

$$T=-\frac{2\pi}{V\hbar}(\omega\omega')^{-\frac{1}{2}}\Big\{\sum_j\Big(\frac{[D, H_0]_{0j}[D', H_0]_{j0}}{\hbar\omega_{0j}+\hbar\omega}$$
$$+\frac{[D', H_0]_{0j}[D, H_0]_{j0}}{\hbar\omega_{0j}-\hbar\omega'}\Big)$$
$$+\tfrac{1}{2}[D,[D', H_0]]_{00}+\tfrac{1}{2}[D',[D, H_0]]_{00}\Big\}, \quad (48)$$

if the initial and final internal state of the particle system is denoted by the subscript "0." On using the relationship

$$[D, H_0]_{0j}=-\hbar\omega_{0j}D_{0j}, \quad (49)$$

T becomes

$$T=\frac{\pi}{V\hbar}(\omega\omega')^{-\frac{1}{2}}\Big\{\sum_j\Big(\frac{D_{0j}[D', H_0]_{j0}-[D, H_0]_{0j}D_{j0}'}{1+\omega/\omega_{0j}}$$
$$+\frac{D_{0j}'[D, H_0]_{j0}-[D', H_0]_{0j}D_{j0}}{1-\omega'/\omega_{0j}}\Big)$$
$$-[D,[D', H_0]]_{00}-[D',[D, H_0]]_{00}\Big\}. \quad (50)$$

Now if an expansion of the energy denominators in powers of ω/ω_{0j} and ω'/ω_{0j} is carried out, the zero-order term in the summation is just cancelled by the diamagnetic terms represented by the double commutators. The first-order term is proportional to the very small difference between ω and ω' so, neglecting this difference, T is to second order

$$T=(2\pi/V\hbar)\textstyle\sum_j(\omega/\omega_{0j})(D_{0j}D_{j0}'+D_{0j}'D_{j0}). \quad (51)$$

Thus

$$T=-(2\pi/V)\omega\alpha_{u,u'}, \quad (52)$$

where $\alpha_{u,u'}$ is the $(\mathbf{u}, \mathbf{u}')$ component of the electrostatic polarizability tensor. Note that this result is quite independent of the detailed interactions between the particles except through the influence of the interactions on the wave functions which determine the matrix elements.

---

[9] The term transition amplitude is used here for the quantity T which appears in the expression for the transition probability, $w=(2\pi/\hbar)\rho_E|T|^2$. Sometimes it is referred to as the "matrix element."

Interaction Effects on Radiative Transitions in Nuclei*

N. AUSTERN† AND R. G. SACHS
University of Wisconsin, Madison, Wisconsin
(Received September 28, 1950)

Electromagnetic transition processes in nuclei are considered on the assumption that the influence of an external electromagnetic field on a nucleus can be incorporated into a gauge invariant Schroedinger equation for the nucleons (phenomenological theory). From the results of the preceding paper it is concluded that equations for electric multipole transition probabilities have the usual form but that the *f*-sum rule is modified in a manner depending on the nuclear interactions. Explicit expressions for the generalization of the *f*-sum rule to all electric multipole orders are given for exchange and velocity dependent interactions. The magnetic multipole moments, and therefore the corresponding transition probabilities, depend markedly on the form of the interaction with the electromagnetic field. General formulas are given for all magnetic multipole moments of nuclei in which exchange forces and velocity dependent interactions play a role. In addition it is possible to incorporate into the theory the spin-antisymmetric addition to the magnetic dipole moment implied by the static moments of H^3 and He^3.

Detailed application is limited in this paper to magnetic dipole transitions. The theoretical cross section for the capture of thermal neutrons by protons is found to have about a 4 percent addition, due entirely to the spin-antisymmetric term. In heavier nuclei this spin term, exchange interactions, and the velocity interaction proposed to account for high energy nucleon-nucleon scattering contribute to the magnetic dipole transitions. The ratio of magnetic dipole to electric quadrupole transition probabilities is of the order of $(25/\hbar\omega)^2A^{-4/3}$, where A is the nuclear mass number and $\hbar\omega$ is the photon energy in Mev. Similar emphasis of the magnetic over electric transitions at low energies is anticipated for higher multipole orders, so interpretations of isomeric transitions on the basis of lifetime require re-examination.

I. INTRODUCTION

THE structure of nucleons and the mechanism of interaction between nucleons seem to involve charge bearing quanta in some way. It should therefore be possible to investigate questions of either structure or interaction mechanism by utilizing the influence of an external electromagnetic field on a nuclear system. For example, Pais[1] and Villars[2] have shown that in meson theory nuclear radiative transition probabilities and nuclear magnetic moments may depend on the detailed nature of the meson field. Relationships of this type were first emphasized by Siegert.[3]

At present the theoretical investigation of such problems by means of meson theories has all the disadvantages of the tenuous nature of current theories. This, combined with the difficulty of carrying through the required calculations, discourages the study of electromagnetic effects in terms of a detailed meson theory. As a matter of fact, certain general properties of the electromagnetic effects are obscured by the complicated character of each meson calculation. To the extent that the description of a nucleus may be given by a gauge invariant Schroedinger equation involving only nucleon variables and electromagnetic field variables, such properties of electromagnetic effects can be associated with the interaction appearing in the Schroedinger equation.[4] While a theory of this type may not have a domain of validity much beyond that of the adiabatic approximation in meson theory, it does provide a simple phenomenological approach which yields quantitative results. It is the purpose of this paper to derive some of the results which such an approach yields for radiative transitions in nuclei.

Specific examples of the relationships to be considered here have already been discussed. Feenberg has shown[5] that space exchange forces cause a modification of the *f*-sum rule for electric dipole transition probabilities, and this fact has been applied[6–8] many times. Furthermore, certain phenomenological magnetic moments,[9] which are a direct consequence of the assumption of exchange forces, indicate a modification of magnetic dipole transition probabilities.

It has been customary to call all effects associated with the nuclear interactions *exchange effects*. In view of the fact that they are not necessarily related to an exchange process the term seems to be inappropriate. In this paper they will instead be termed *interaction effects*. For example, *interaction moment* designates any contribution to the magnetic moment which is associated with the nucleon-nucleon interaction mechanism. The term *exchange effect* will be reserved for the particular interaction effects which arise directly from the introduction of a space exchange operator in the nucleon-nucleon coupling. Since even this does not yield a unique definition,[9,10] because free choice of a divergenceless term in the current is possible, we choose to include only those effects which arise in the "natural"

* Supported in part by the U. S. AEC and in part by the Wisconsin Alumni Research Foundation.
† AEC Predoctoral Fellow.
[1] A. Pais, Kgl. Danske Videnskab. Selskab Mat.-fys. Medd. **20**, No. 17 (1943).
[2] F. Villars, Phys. Rev. **72**, 257 (1947); Helv. Phys. Acta **20**, 476 (1947).
[3] A. J. F. Siegert, Phys. Rev. **52**, 787 (1937); C. Møller and L. Rosenfeld, Kgl. Danske Videnskab. Selskab Mat.-fys. Medd. **20**, No. 12 (1943).
[4] See the preceding paper, hereinafter referred to as **I**. Numbered equations in **I** will be referred to as Eq. (**I**-1), etc.
[5] E. Feenberg, Phys. Rev. **49**, 328 (1936).
[6] K. Way, Phys. Rev. **51**, 552 (1937).
[7] J. S. Levinger and H. A. Bethe, Phys. Rev. **78**, 115 (1950).
[8] J. F. Marshall and E. Guth, Phys. Rev. **78**, 738 (1950).
[9] R. G. Sachs, Phys. Rev. **74**, 433 (1948); Erratum, Phys. Rev. **75**, 1605 (1949).
[10] R. K. Osborne and L. L. Foldy, Phys. Rev. **79**, 795 (1950).

way (i.e., according to a conventional prescription) demonstrated in reference 9.

II. NATURE OF THE RADIATIVE EFFECTS

The most convenient expression of the interaction with the electromagnetic field is for present purposes given by Eq. (36-27), which exhibits all first-order radiative interactions of a system. The equation gives the effective interaction for the emission of a photon in a nuclear transition. It is apparent that, as has often been conjectured for the dipole term, the electric multipole terms do not depend explicitly on the nuclear interaction.[11] That this result is plausible may be seen by an extension of the argument of Siegert. Although a modification of the definition of current density may be forced[9, 9] by the forms of the nuclear interactions, the definition of charge density need not be changed. Thus, one would expect the electric moment operators to be unchanged, but the magnetic moment operators to reflect the change in the current density.

The change in the magnetic moment operators is contained implicitly in the form of the $\mathbf{M}_l$ given by Eq. (36-26). There are two distinctly different reasons for believing that the $\mathbf{M}_l$ contain terms in addition to the ordinary 2^l-pole magnetic moments. One is the evidecne that the nuclear interactions involve a space exchange factor, which is already known to lead to additional terms. The other is the relationship between the nuclear interaction mechanism and static magnetic moments which is so strongly suggested by the apparent[12] non-additivity of the spin and orbital moments in H^3 and He^3. Theories which have been devised to account for the phenomenon would appear to fit into the gauge invariant Schroedinger formalism treated in 36. They involve the introduction into the nuclear hamiltonian of an interaction between the electromagnetic field and pairs of nucleons which is antisymmetric in the nucleon spins.[2, 10, 13]

Both contributions may lead to observable modifications of magnetic multipole transitions in nuclei.

For the particular case $l=1$, the operator $\mathbf{M}_1$, which provides magnetic dipole transitions, is identical with the static magnetic moment operator. This exhibits the close correspondence between static and dynamic effects and has the consequence that *any interaction effect on the magnetic moment should show up as an equivalent effect on the magnetic dipole transition probability*. Thus, the aforementioned interpretation of the H^3 and He^3 moments must have immediate consequences for magnetic dipole transition probabilities in all other nuclei as well as for their magnetic moments.

There appear to be several possibilities for the experimental investigation of the effects discussed here. One would be the interaction effect on the cross section for photo-disintegration of the deuteron or on the inverse process of neutron-proton capture. Another possibility concerns the interpretation of isomeric transitions. It would seem that those parity and angular momentum assignments made on the basis of lifetime may be in error wherever a magnetic multipole transition is a possibility. The probabilities for magnetic transitions may be sufficiently increased by interaction effects that they would be confused with electric transitions of the same multipole order.

Conclusions concerning the absorption of high energy gamma radiation by nuclei are also affected. Thus an extension of the calculation of Levinger and Bethe,[7] taking into account the magnetic dipole effects, would seem to be in order.

It is of interest that the treatment of electric dipole absorption by Levinger and Bethe offers a good example of an interaction effect on electric multipole transitions. They make use of the modification of the *f*-sum rule due to exchange forces. A similar modification for the quadrupole and higher multipole transitions is provided by Eq. (36-35). From this equation it is seen that although interaction effects on electric multipole transitions are not immediately apparent, they do appear for the sum rules. However, here the *second-order* term, H_2, in the hamiltonian is involved, rather than the first-order term, H_1, which contains all the magnetic interaction effects.

Formulas are given in the Appendix for the magnetic multipole moment operators of nuclei and the generalized *f*-sum rules for ordinary interactions, exchange interactions, and the velocity dependent interactions linear in the momentum.

III. MAGNETIC DIPOLE EFFECTS

Applications of the phenomenological method will be limited in this paper to interaction effects on magnetic dipole transitions, and three cases are considered. These include the two effects whose existence was emphasized in the preceding section, and a third but much more tentative effect associated with a velocity dependent nuclear interaction. This interaction was introduced recently to account for high energy nucleon-nucleon scattering as well as spin-orbit coupling in heavy nuclei.[13, 14]

The transition probability due to exchange effects can be computed from the exchange moment operator whose form, already known, is given by Eq. (A-16). However, as the exchange moment does not account[15] for the static moment anomaly of H^3 and He^3 the need for some other moment operator is seen. Fortunately, rather general statements can be made concerning the form of the required operator.

[11] This fact is convenient for calculation and has been used in the dipole case by several authors. Since the forms of the operators are not affected by the nuclear interactions, it is necessary only to guess at wave functions in order to estimate nuclear electric multipole transition probabilities.

[12] R. Avery and R. G. Sachs, Phys. Rev. 74, 1320 (1948).

[13] Blanchard, Avery, and Sachs, Phys. Rev. 78, 292 (1950).

[14] K. M. Case and A. Pais, Phys. Rev. 80, 203 (1950).

[15] R. Avery and E. N. Adams, Phys. Rev. 75, 1106 (1949). There is a misprint in the expression given for the three-body wave function. A factor ½ should be inserted in the exponent.

The interaction moment is presumed to arise in conjunction with two-body interactions. Then it must have an operational form satisfying the following conditions.[15a] (a) It is a sum of operators, each depending on one pair of particles. (b) It is symmetric for interchange of any pair of nucleons (in isotopic spin notation). (c) It can be written in terms of the internal variables, ϱ_α, and other internal operators such as the spins and relative momenta. (d) It is a pseudovector which changes sign on time reversal.

The operator making up the sum in (a) will contain as a factor a symmetric scalar function, $\Phi(|\varrho_{\alpha\beta}|)$, which gives the intensity of the interaction effect as a function of the distance between the pair.

All proposals extant concerning interaction moments lead to a magnetic moment operator satisfying these conditions.[2, 10, 13] Of the operators satisfying (a), (b), (c), and (d), there is one particularly simple form which is capable of accounting for the H^3 and He^3 moments if the ground states of these nuclei are assumed to be predominantly S state. This is

$$\Delta\mathbf{M}_1=(e\hbar/2Mc)\tfrac{1}{2}\sum_{\alpha,\beta}(\boldsymbol{\sigma}_\alpha-\boldsymbol{\sigma}_\beta)(\tau_{\alpha\beta}/2)\Phi_{\alpha\beta}. \quad (1)$$

For the sake of definiteness Eq. (1) will be used as the basis for the discussion of radiative transitions.[16] Analysis of the three-body problem assuming that the form of Φ is

$$\Phi(\rho)=(MJ_0/\hbar^2\mu^2)(e^{-\mu\rho}/\mu\rho), \quad (2)$$

with $\mu^{-1}=1.18\times10^{-13}$ cm, leads to

$$J_0=-13 \text{ Mev}, \quad (3)$$

as the value required to account for the moment anomaly.

Turning to the velocity-dependent interaction of Case and Pais,[14] we note that they finally settled on the linear combination[15a] $\frac{1}{2}$(II+III′+IV), which is just (3) of reference 13. The additional interaction moment operator thereby produced is given by the same linear combination of the corresponding magnetic moments, given in the Appendix:

$$\Delta_v\mathbf{M}_1=(e/4\hbar c)\sum_{\alpha,\beta}\left\{[\varrho_\alpha\times(\mathbf{S}_{\alpha\beta}\times\varrho_{\alpha\beta})]\frac{1-\tau_\alpha}{2}\frac{3+\boldsymbol{\tau}_\alpha\cdot\boldsymbol{\tau}_\beta}{2}\right.$$
$$\left.-\frac{i}{2\hbar}(\varrho_{\alpha\beta}\times\mathbf{p}_{\alpha\beta}\cdot\mathbf{S}_{\alpha\beta})[\varrho_\alpha\times\varrho_\beta]\frac{\tau_{\alpha\beta}}{2}\frac{1+\boldsymbol{\tau}_\alpha\cdot\boldsymbol{\tau}_\beta}{2}\right\}J_{\alpha\beta}{}^{(v)}. \quad (4)$$

The factor $J_{\alpha\beta}{}^{(v)}$ is taken to be[14]

$$J^{(v)}(\rho)=(J_v/\lambda\rho)\frac{d}{d(\lambda\rho)}(e^{-\lambda\rho}/\lambda\rho), \quad (5)$$

with

$$J_v=3 \text{ Mev}. \quad (6)$$

IV. NEUTRON-PROTON CAPTURE; PHOTO-EFFECT ON THE DEUTERON

The capture of slow neutrons by protons provides the clearest nuclear example of a magnetic dipole transition. Theoretical determinations of the capture cross section have not taken into account the interaction effects; yet they are in quite good agreement with the experimental value.[17] A large interaction effect, and therefore any interaction which leads to such an effect, is to be excluded. However, it turns out that none of the interactions set forth in Sec. III is excluded in this way.

The velocity-dependent term, Eq. (4), makes no contribution to the deuteron problem, since it vanishes for all even states of the two-body system. Similarly, the exchange moment operator, Eq. (A-16), vanishes for the two-body system, since it is proportional to $\varrho\times\varrho$. Thus, the only interaction effect on the capture cross section arises from the operator, Eq. (1), whose introduction is an immediate consequence of the interpretation of the H^3 and He^3 moments. This suggests that the neutron-proton capture might provide a direct test of that interpretation.

The interaction moment acts only within a region comparable with the range of the forces, while the spin-orbital moment acts over the entire volume of the deuteron. Thus, for this $^1S\rightarrow{}^3S$ transition the ratio of the matrix element of the moment Eq. (1) to that of the ordinary moment can be estimated as

$$\langle\Delta\mathbf{M}\rangle/\langle\mathbf{M}\rangle\approx-(MJ_0/\hbar^2\mu^2)(2\gamma/\mu)^2/(\mu_P-\mu_N), \quad (7)$$

where μ_P and μ_N are neutron and proton moments in nuclear magnetons. The quantity γ is related to the deuteron binding energy by

$$E_B=\hbar^2\gamma^2/M, \quad (8)$$

so $1/2\ \gamma$ is the "radius" of the deuteron. For $\mu^{-1}=1.18\times10^{-13}$ cm we have $\gamma=0.28\mu$, and the value of (7) is

$$\langle\Delta\mathbf{M}\rangle/\langle\mathbf{M}\rangle\approx0.03. \quad (9)$$

The transition probability is proportional to the square of the matrix element of the total moment, so the change in the cross section introduced by Eq. (9) amounts to about 6 percent.

An accurate determination of this interaction effect requires a detailed knowledge of the distribution function $\Phi(\rho)$ in Eq. (1). A convenient way to avoid too detailed assumptions is to treat the auxiliary problem of the effect produced by a thin shell distribution,

$$\Phi(\rho)=\Phi_0\delta(\rho-b), \quad (10)$$

as a function of the radius, b, of the shell. From the results, it is possible to draw rather general conclusions

[15a] See Appendix for notation.

[16] All static terms which are capable of yielding the three-body moments are incorporated in Eq. (1) if the definition of $\Phi_{\alpha\beta}$ is extended to include terms linear in $\varrho_\alpha+\varrho_\beta$ as well as functions of $\varrho_{\alpha\beta}$. The only information concerning $\Phi_{\alpha\beta}$ is to be obtained from the three-body moments, and this one datum would not appear to justify taking too general a form for the function.

[17] For a detailed discussion of the comparison with experiment see H. A. Bethe and C. Longmire, Phys. Rev. 77, 647 (1950).

concerning the form of the distribution. This calculation was carried out as follows. The interaction moment of the triton was determined from Eqs. (1) and (10) by using the space-symmetric ^2S wave function given in reference 15, normalized to 100 percent. The value of $\Phi_0(b)$ was fixed by setting this moment equal to 0.27 nuclear magnetons, the presumed experimental value. Then the matrix element of the operator Eq. (1), for the same function Φ, was calculated for the $^3S \rightarrow {}^1S$ transition in the deuteron, using wave functions given by Bethe and Longmire.[17] The resulting relative contribution to this matrix element is shown in Fig. 1.

The exponential rise of the curve for large values of b is a direct consequence of the small size of the triton relative to the deuteron; since the triton function is small at large distances, a very large Φ_0 is required when b is large compared with the triton radius. It follows that if the actual distribution function Φ has appreciable magnitude beyond distances comparable to the triton radius, a large interaction effect would result. On the other hand, if the distribution of magnetization is limited to a small radius, the effect is very nearly independent of the shape of Φ and the change, ϵ_i, in the cross section has the minimum value, 3.5 percent. Thus,[18]

$$\epsilon_i \gtrsim 0.035. \tag{11}$$

The influence of variations in the triton wave function may be estimated by noting that in the region of interest ϵ_i is roughly proportional to the damping length of that function.

Since the interaction effects are expected to occur only within the range of the nuclear forces and since the triton wave function extends somewhat beyond this range, the value of ϵ_i is not likely to exceed greatly the lower limit given in Eq. (11). However, any excess may be of some use in determining the shape of Φ. A numerical example may serve to illustrate the point. For $\Phi \sim e^{-\mu\rho}/\mu\rho$, with $\mu^{-1}=1.18\times10^{-13}$ cm one finds $\epsilon_i = 0.036$. On the other hand, for $\Phi \sim \rho^2 e^{-\mu\rho}/\mu\rho$ the distribution is moved out far enough to yield $\epsilon_i = 0.052$.

The conditions which must be met in order to obtain an experimental value of ϵ_i are best expressed in terms of the ratio of theoretical to experimental cross section. Referring to the paper by Bethe and Longmire,[17] modification of their expression to include the interaction effect yields

$$\sigma_{th}/\sigma_{exp} = 1.10[1-0.116(r_{os}-r_{ot})+2.8\epsilon_1+1.5\epsilon_2 -0.15\epsilon_3-\epsilon_4+\epsilon_i]. \tag{12}$$

Here r_{os} and r_{ot} are the singlet and triplet effective ranges, expressed in units of 10^{-13} cm; ϵ_1, ϵ_2, ϵ_3, ϵ_4 are, in order, the experimental uncertainties in deuteron binding energy, slow neutron-proton total scattering cross section, slow neutron-proton coherent scattering cross section, and slow neutron-proton capture cross section. The values used by Bethe and Longmire are: H^3 binding energy, 2.235 Mev; thermal NP total scattering cross section, 20.36×10^{-24} cm^2; thermal NP coherent scattering cross section, 0.624×10^{-24} cm^2; thermal NP capture cross section, 0.310×10^{-24} cm^2 at 2200 m per sec neutron velocity.

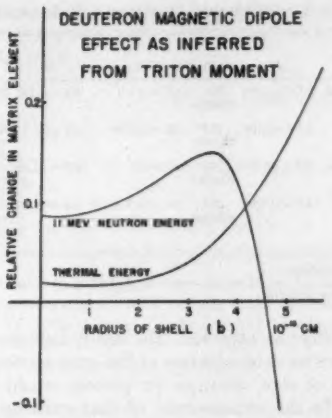

FIG. 1. Relative contribution of thin shell (δ-function) interaction moment operator to the matrix element for a radiative transition in the deuteron. The corresponding contribution for any other distribution of magnetization, $\Phi(\rho)$, is the harmonic mean of this curve with respect to a weight function given by multiplying $\Phi(\rho)$ by the product of the initial and final state radial wave functions of the deuteron.

We take the ϵ_2 and ϵ_4 values of Bethe and Longmire

$$\epsilon_2 = \pm 0.005, \quad \epsilon_4 = \pm 0.04. \tag{13}$$

The best value[19] of ϵ_1 appears to be

$$\epsilon_1 = -0.004 \pm 0.001. \tag{14}$$

The best value[20] of ϵ_3 is taken from the liquid mirror experiments:

$$\epsilon_3 = -0.08 \pm 0.02. \tag{15}$$

The value chosen for r_{ot} is[17,21]

$$r_{ot} = (1.59+2.7\epsilon_1+5.0\epsilon_2-1.5\epsilon_3). \tag{16}$$

For r_{os} we take the value[21] from the proton-proton system

$$r_{os} = 2.71 \pm 0.13. \tag{17}$$

The introduction of these into Eq. (12) gives

$$\sigma_{th}/\sigma_{exp} = 1.02 \pm 0.05 + \epsilon_i, \tag{18}$$

if the uncertainties are all treated as random.

Comparison of Eqs. (11) and (18) leads to no contradiction. It does suggest that ϵ_i has nearly its mini-

[18] Note that the term linear in $\rho_a+\rho_s$, mentioned in reference 16, would contribute neither in the deuteron nor in the triton ^2S state.

[19] R. C. Mobley and R. A. Laubenstein, Phys. Rev. **80**, 309 (1950).

[20] Hughes, Burgy, and Ringo, Phys. Rev. **77**, 291(L) (1950).

[21] H. A. Bethe, Phys. Rev. **76**, 38 (1949).

TABLE I. Selection rules for magnetic dipole transitions.

Magnetic moment	J	Parity	L	S	Configuration
Spin orbital	$\Delta J=\pm1,0^a$	No change	$\Delta L=\pm1,0$	$\Delta S=\pm1,0$	No change.
Exchange	$\Delta J=\pm1,0^a$	No change	$\Delta L=\pm1,0^b$	$\Delta S=0$	At most two particles change state.
Interaction, Eq. (1)	$\Delta J=\pm1,0^a$	No change	$\Delta L=0^b$	$\Delta S=\pm1,0$	At most two particles change state.
Velocity, Eq. (4)	$\Delta J=\pm1,0^a$	No change	$\Delta L=\pm2,\pm1,0$	$\Delta S=\pm1,0$	At most two particles change state.

[a] 0→0 forbidden.
[b] $\Delta L=\pm2,\pm1$ would be allowed if a slightly more general form than Eq. (1) were assumed.

mum value, as expected. The result indicates that a more precise determination of the cross section for the capture of slow neutrons by protons would be very useful. In the measurement of that quantity lies the principal source of the uncertainty in Eq. (18).

Examination of the behavior of the interaction effect at somewhat higher energies shows that it should be of greater relative importance than at thermal energy. This occurs because the range of the interaction moment operator is small compared with the size of the deuteron. Therefore, the contribution to the matrix element by the interaction moment arises from a region in which energy changes of the free neutron state have very little influence on the ^1S wave function, at least until the neutron wave length is comparable to the range of the forces. On the other hand, the matrix element for the usual magnetic effect involves principally the outer region and decreases rapidly with energy.

Such behavior immediately suggests that a measurement at higher energy should yield more definite information concerning the interaction effect. Unfortunately, with increasing energy the electric dipole moment rapidly becomes the main contributor to photo-disintegration, so that a separation of magnetic and electric effects is required as a preliminary to the resolution of the interaction effect. The separation can be accomplished in principle by a measurement of the angular distribution of the photo-disintegration products, but this difficult experiment has not yet been carried out with an accuracy at all sufficient for our purposes. The relative contribution of the interaction moment to the photo-magnetic effect nevertheless is given in Fig. 1 for a photon energy of 13 Mev. Note that for small b this contribution is much larger than at low energies, but not yet so strikingly large as to be separable, for the photo-magnetic cross section at this energy is only about 2 percent of the photoelectric cross section.

V. MAGNETIC DIPOLE TRANSITIONS IN HEAVIER NUCLEI

The interaction effects on heavier nuclei might be expected to influence lifetimes in isomeric transitions as well as level widths in nuclear reactions. The former usually correspond to transitions of higher order than magnetic dipole. However, in order to obtain an early judgment concerning the order of magnitude of the effects, estimates will be made here only for magnetic dipole transitions.

Each of the three interaction moments described in Sec. III can be expected to play a role in the emission of quanta in magnetic dipole transitions. The selection rules for their contributions to the magnetic moment are given in Table I. J is the total angular momentum, L the orbital, and S the spin angular momentum.

The column labeled "configuration" refers to one nucleon wave functions and is useful if these functions provide a reasonable approximation. It is very often assumed that the configuration can be specified. Then the selection rules show that interconfigurational magnetic dipole transitions can take place only if interaction effects are present. The limitation on the number of particles that can change state is a consequence of the assumption of two-body forces.

In order to obtain an estimate of the order of magnitude of the magnetic dipole transition probability it will be assumed that the configuration can be specified and that S is given for each of the states involved. All the interaction effects have the property that a transition in which only one nucleon changes state is much more probable than a two-nucleon transition. The reason is that only the term in the moment involving both particles contributes to the two-particle transition, while the number of terms involved in the single particle transition is equal to the number of particles with which the particle interacts. The matrix element for the one-nucleon transition is about A times that for the two-nucleon transition, so the latter will be neglected.

The interactions act only over a range μ^{-1}, so a contribution to the matrix element arises only within the fraction $(\mu R)^{-3}$ of the total nuclear volume, $4\pi R^3/3$. Since

$$(\mu R)^3 \approx A, \tag{19}$$

this factor very nearly compensates for the large number of terms that contribute to the one-particle transition. Thus, the order of magnitude of the matrix element for the one-particle transition would be $(e/\hbar c)(\bar{J}/\mu^2)$, where $\bar{J}$ is the average strength of those interaction moments which contribute to the particular transition. A convenient standard for comparison is provided by the quadrupole transitions, with which the magnetic dipole transitions can often compete. The order of magnitude of the matrix element of the quadrupole moment may be taken to be $e\omega R^2/c$. Then the ratio of the magnetic dipole transition probability to the quadrupole transition probability is roughly

$$w_m/w_q \approx (\bar{J}/\hbar\omega)^2(\mu R)^{-4}. \tag{20}$$

According to Eq. (19),

$$w_m/w_q \approx (\bar{J}/\hbar\omega)A^{-4/3}. \tag{21}$$

A reasonable estimate of J is

$$J \approx 25 \text{ Mev}. \tag{22}$$

Then for light nuclei ($A \approx 27$), the magnetic transitions predominate for $\hbar\omega$ less than 2.5 Mev. For the heaviest nuclei ($A \approx 238$) the corresponding energy is 1 Mev. Thus, it seems to be very probable that magnetic dipole transitions due to interaction effects are of much greater importance than quadrupole transitions for the very low lying levels of nuclei. Of course, the intraconfigurational transitions should be included in the consideration of the very low levels so that the magnetic transition probability will be increased further by the spin-orbital moment, which is then also effective.

VI. CONCLUSION

On the basis of prevailing ideas about nuclear forces, all magnetic multipole transitions will show interaction effects, and it is possible to make reasonable estimates of their influence on magnetic dipole transition probabilities. These estimates show that for transitions between low lying nuclear levels, magnetic dipole radiation is strongly favored over electric quadrupole when the selection rules allow both. Similar results are to be expected for the higher multipole orders, so that previous identifications of isomeric transitions on the basis of lifetime may be in error.

The most compelling test of the theory is suggested by the 4 percent contribution to the neutron-proton capture cross section. More accurate measurement of this cross section would be very helpful. However, information by this means is limited to the spin-antisymmetric interaction presumed to be responsible for the anomaly in the H^3, He^3 magnetic moments. Information concerning exchange effects or the velocity dependent interaction of Case and Pais can only be obtained from nuclei heavier than the deuteron. No simple method of discrimination of the various effects in the heavier nuclei is suggested in view of the lack of knowledge concerning nuclear wave functions.

APPENDIX. SOME FORMULAS FOR SPECIFIC INTERACTIONS

For a given hamiltonian the interaction effects may be obtained directly from the equations given in Ⓑ. Several important examples will be considered to illustrate the effects in question. Ignoring, for the sake of simplicity, the contributions of the spin magnetic moments, the internal hamiltonian takes the form

$$H=(\tfrac{1}{2}AM)\sum_{\alpha,\beta}[\mathbf{p}_{\alpha\beta}-(e_\alpha\mathbf{A}_\alpha/c)+(e_\beta\mathbf{A}_\beta/c)]^2+U, \tag{A-1}$$

where U is the gauge invariant nuclear interaction potential. $\mathbf{p}_{\alpha\beta}=\mathbf{p}_\alpha-\mathbf{p}_\beta$ is the relative momentum of the α and β nucleons. $\mathbf{A}_\alpha=\mathbf{A}(\mathbf{r}_\alpha)$ is the vector potential at the position of the designated particle. The integer A is the nuclear mass number, and M is the mass of a nucleon.

Ordinary Forces

For this case,

$$U=\tfrac{1}{2}\sum_{\alpha,\beta}{}'J_{\alpha\beta}{}^{(0)}, \tag{A-2}$$

which is the sum over nucleon pairs of ordinary, two-body potentials. The only nonvanishing H_n are H_1 and H_2. These are

$$H_1=-(1/4AMc)\sum_{\alpha,\beta}\{[\mathbf{p}_{\alpha\beta}\cdot(e_\alpha\mathbf{A}_\alpha-e_\beta\mathbf{A}_\beta)] + [(e_\alpha\mathbf{A}_\alpha-e_\beta\mathbf{A}_\beta)\cdot\mathbf{p}_{\alpha\beta}]\} \tag{A-3}$$

$$H_2=(1/2AMc^2)\sum_{\alpha,\beta}(e_\alpha\mathbf{A}_\alpha-e_\beta\mathbf{A}_\beta)^2. \tag{A-4}$$

Equations (Ⓑ-20) and (Ⓑ-26) provide the magnetic multipole moment operators

$$\mathbf{M}_l{}^{(0)}=\frac{el}{2Mc(l+1)!}\sum_\tau\{[\boldsymbol{\rho}_\tau\times(\mathbf{p}_\tau-\mathbf{P}/A)](\boldsymbol{\kappa}\cdot\boldsymbol{\rho}_\tau)^{l-1} + (\boldsymbol{\kappa}\cdot\boldsymbol{\rho}_\tau)^{l-1}[\boldsymbol{\rho}_\tau\times(\mathbf{p}_\tau-\mathbf{P}/A)]\}, \tag{A-5}$$

where $\boldsymbol{\kappa}$ is the unit propagation vector; the subscript τ denotes a proton variable; $\boldsymbol{\rho}_\alpha=\mathbf{r}_\alpha-\mathbf{R}$ is the position of the αth particle relative to the center of mass; $\mathbf{P}$ is the center-of-mass momentum.

Defining the electric 2^l-pole moment by Eq. (Ⓑ-25),

$$D_l=(e/l!)\sum_\tau(\mathbf{u}\cdot\boldsymbol{\rho}_\tau)(\boldsymbol{\kappa}\cdot\boldsymbol{\rho}_\tau)^{l-1}, \tag{A-6}$$

where $\mathbf{u}$ is the unit polarization vector, satisfying $(\mathbf{u}\cdot\boldsymbol{\kappa})=0$. Then the generalized oscillator strength for electric 2^l-pole radiation is Eq. (Ⓑ-32),

$$f_{ja}{}^l=(2M\omega_{aj}/\hbar e^2)|(D_l)_{aj}|^2, \tag{A-7}$$

for a transition from state a to state j of the nucleus. The sum rule may now be obtained from Eq. (Ⓑ-35) and Eq. (Ⓑ-19) by use of Eq. (A-4):

$$\Sigma_a f_{ja}{}^l=(1/2Ae^2(l!)^2)\sum_{\alpha,\beta}\langle[e_\alpha(\boldsymbol{\kappa}\cdot\boldsymbol{\rho}_\alpha)^{l-1}-e_\beta(\boldsymbol{\kappa}\cdot\boldsymbol{\rho}_\beta)^{l-1}]^2 + (l-1)^2[e_\alpha(\mathbf{u}\cdot\boldsymbol{\rho}_\alpha)(\boldsymbol{\kappa}\cdot\boldsymbol{\rho}_\alpha)^{l-2}-e_\beta(\mathbf{u}\cdot\boldsymbol{\rho}_\beta)(\boldsymbol{\kappa}\cdot\boldsymbol{\rho}_\beta)^{l-2}]^2\rangle_{jj}, \tag{A-8}$$

where the angular brackets indicate the expectation value for state j of the nucleus. In particular, for dipole transitions ($l=1$) one obtains the usual result in terms of Z, the number of protons, and N, the number of neutrons:

$$\Sigma_a f_{ja}{}^1=ZN/A. \tag{A-9}$$

Similarly, for quadrupole radiation:

$$\Sigma_a f_{ja}{}^2=(1/8Ae^2)\sum_{\alpha,\beta}\langle[\boldsymbol{\kappa}\cdot(e_\alpha\boldsymbol{\rho}_\alpha-e_\beta\boldsymbol{\rho}_\beta)]^2 + [\mathbf{u}\cdot(e_\alpha\boldsymbol{\rho}_\alpha-e_\beta\boldsymbol{\rho}_\beta)]^2\rangle_{jj}. \tag{A-10}$$

Exchange Interaction

In Eq. (A-1) U is taken to be[9]

$$U=\tfrac{1}{2}\sum_{\alpha,\beta}{}'\exp\left\{\frac{i}{\hbar c}(e_\alpha-e_\beta)\int_{\rho_\beta}^{\rho_\alpha}A_s\,ds\right\}J_{\alpha\beta}{}^{(s)}P_{\alpha\beta}. \tag{A-11}$$

$P_{\alpha\beta}$ is a space exchange operator, A_s is the component of $\mathbf{A}$ along the line joining $\boldsymbol{\rho}_\alpha$ and $\boldsymbol{\rho}_\beta$, and the line integral is taken along that straight line. Only the interaction, U, need be considered, as the kinetic energy terms are the same as for ordinary forces. Expansion of U in successive orders in $\mathbf{A}$, corresponding to the expansion Eq. (Ⓑ-2), gives terms of all orders, with

$$U_1=\frac{ie}{\hbar c}\sum_{\tau,\nu}\left(\int_{\rho_\nu}^{\rho_\tau}A_s\,ds\right)J_{\tau\nu}{}^{(s)}P_{\tau\nu}, \tag{A-12}$$

$$U_2=-\frac{e^2}{\hbar^2c^2}\sum_{\tau,\nu}\left(\int_{\rho_\nu}^{\rho_\tau}A_s\,ds\right)^2J_{\tau\nu}{}^{(s)}P_{\tau\nu}, \tag{A-13}$$

where τ, ν label proton and neutron variables.

As can be seen from Eq. (Ⓑ-26) the magnetic multipole moment is made up additively of a contribution from the kinetic energy, given by Eq. (A-5), and a contribution from U_1:

$$\mathbf{M}_l{}^{(s)}=\mathbf{M}_l{}^{(0)}+\Delta_s\mathbf{M}_l, \tag{A-14}$$

with the exchange multipole moment given by

$$\Delta_s\mathbf{M}_l=\frac{ie}{\hbar c(l+1)!}\sum_{\tau,\nu}\frac{(\boldsymbol{\rho}_\tau\times\boldsymbol{\rho}_\nu)}{(\boldsymbol{\kappa}\cdot\boldsymbol{\rho}_{\tau\nu})}\{(\boldsymbol{\kappa}\cdot\boldsymbol{\rho}_\tau)^l-(\boldsymbol{\kappa}\cdot\boldsymbol{\rho}_\nu)^l\}J_{\tau\nu}{}^{(s)}P_{\tau\nu}. \tag{A-15}$$

For $l=1$ we obtain the expression for the exchange moment operator:[22]

$$\Delta_x \mathbf{M}_1=(ie/2\hbar c)\sum_{\tau,\nu}(\boldsymbol{\rho}_\tau\times\boldsymbol{\rho}_\nu)J_{\tau\nu}{}^{(x)}P_{\tau\nu}. \quad \text{(A-16)}$$

The sum rules are also changed from Eq. (A-8) by the addition of a term introduced by U_2 into Eq. (8-35). Since Eq. (8-35) is linear in H_2, the change is simply additive and can easily be shown to be

$$\Delta_x \Sigma_\alpha f_{jm}{}^l=\frac{-M}{\hbar^2(l!)^2}\Big\langle\sum_{\tau,\nu}[(\mathbf{u}\cdot\boldsymbol{\rho}_\tau)(\boldsymbol{\kappa}\cdot\boldsymbol{\rho}_\tau)^{l-1} -(\mathbf{u}\cdot\boldsymbol{\rho}_\nu)(\boldsymbol{\kappa}\cdot\boldsymbol{\rho}_\nu)^{l-1}]P_{\tau\nu}P_{\tau\nu}\Big\rangle_{jj}. \quad \text{(A-17)}$$

For $l=1$ this result is identical with that obtained by Feenberg[6] and recently applied in some detail by Levinger and Bethe.[7] The result has not been given before[23] for higher l.

Velocity-Dependent Interactions

Velocity-dependent interactions[13,14] provide a useful example of interaction effects other than those due to exchange. The two-body interactions, linear in the momentum, which are tabulated by Wigner and Eisenbud,[24] are considered here. Although one of the six interactions (IV) can be eliminated on the basis of experience,[13] it will be considered for the sake of completeness.

In Eq. (A-1) U is taken to be

$$U=\frac{1}{4\hbar}\sum_{\alpha,\beta}\Big\{\Big(\boldsymbol{\rho}_{\alpha\beta}\times\Big[\mathbf{p}_{\alpha\beta}-\frac{e_\alpha}{c}\mathbf{A}_\alpha+\frac{e_\beta}{c}\mathbf{A}_\beta\Big]\cdot\mathbf{S}_{\alpha\beta}\Big)T_{\alpha\beta} +\text{hermitian conjugate}\Big\}J_{\alpha\beta}{}^{(x)}. \quad \text{(A-18)}$$

The operators appearing in U are most easily described in terms of the isotopic spin vector $\boldsymbol{\tau}_\alpha$ of the αth particle, with components $\tau_{\alpha 1}$, $\tau_{\alpha 2}$, $\tau_{\alpha 3}$; $\tau_{\alpha 3}=1$ for a neutron, $\tau_{\alpha 3}=-1$ for a proton. For the sake of simplicity $\tau_{\alpha 3}$ will be replaced by τ_α wherever possible and $(\tau_\alpha-\tau_\beta)$ by $\tau_{\alpha\beta}$. Then the e_α are the operators,

$$e_\alpha=\tfrac{1}{2}(1-\tau_\alpha)e, \quad \text{(A-19)}$$

and the operators $\mathbf{S}_{\alpha\beta}$ and $T_{\alpha\beta}$ are defined as follows for each of the six interactions:[25]

$$\mathbf{S}_{\alpha\beta}=(\boldsymbol{\sigma}_\alpha+\boldsymbol{\sigma}_\beta),\quad \begin{cases} T_{\alpha\beta}=\tfrac{1}{2}(\tau_\alpha+\tau_\beta) & \text{(I)}\\ T_{\alpha\beta}=\tfrac{1}{2}(1+\tau_\alpha\tau_\beta) & \text{(II)}\\ T_{\alpha\beta}=\tfrac{1}{2}(1+\boldsymbol{\tau}_\alpha\cdot\boldsymbol{\tau}_\beta)\times\exp\Big\{\dfrac{-ie}{\hbar c}\dfrac{\tau_{\alpha\beta}}{2}\displaystyle\int_{\rho_\alpha}^{\rho_\beta}A_s ds\Big\} & \text{(III')}\\ T_{\alpha\beta}=\tfrac{1}{2}(\tau_\alpha-\tau_\beta) & \text{(IV)}\end{cases}$$

$$\mathbf{S}_{\alpha\beta}=(\boldsymbol{\sigma}_\alpha-\boldsymbol{\sigma}_\beta),\quad T_{\alpha\beta}=\tfrac{1}{2}(\tau_\alpha-\tau_\beta) \quad \text{(V)}$$

$$\mathbf{S}_{\alpha\beta}=[\boldsymbol{\sigma}_\alpha\times\boldsymbol{\sigma}_\beta],\quad T_{\alpha\beta}=\tfrac{1}{2}[\boldsymbol{\tau}_\alpha\times\boldsymbol{\tau}_\beta]_3\exp\Big\{\frac{-ie}{\hbar c}\frac{\tau_{\alpha\beta}}{2}\int_{\rho_\alpha}^{\rho_\beta}A_s ds\Big\}. \quad \text{(VI)}$$

Gauge invariance, as expressed by Eq. (8-9), can easily be established for these interactions by making use of the well-known commutation relations for the components of $\boldsymbol{\tau}_\alpha$. The first- and second-order contributions of A to U are

$$U_1=-(1/2\hbar c)\sum_{\alpha,\beta}(\boldsymbol{\rho}_{\alpha\beta}\times[e_\alpha\mathbf{A}_\alpha-e_\beta\mathbf{A}_\beta]\cdot\mathbf{S}_{\alpha\beta})T_{\alpha\beta}J_{\alpha\beta}{}^{(v)}, \quad \text{(A-20)}$$

$$U_2=0, \quad \text{(A-21)}$$

for the non-exchange interactions (I), (II), (IV), and (V). For the exchange interactions (III') and (VI)

$$U_1=\frac{-1}{4\hbar c}\sum_{\alpha,\beta}\Big\{(\boldsymbol{\rho}_{\alpha\beta}\times[e_\alpha\mathbf{A}_\alpha-e_\beta\mathbf{A}_\beta]\cdot\mathbf{S}_{\alpha\beta})T_{\alpha\beta}{}^{(0)} +\frac{ie}{\hbar}(\boldsymbol{\rho}_{\alpha\beta}\times\mathbf{p}_{\alpha\beta}\cdot\mathbf{S}_{\alpha\beta})T_{\alpha\beta}{}^{(0)}\Big(\frac{\tau_{\alpha\beta}}{2}\Big) \times\int_{\rho_\alpha}^{\rho_\beta}A_s ds+\text{H.c.}\Big\}J_{\alpha\beta}{}^{(v)} \quad \text{(A-22)}$$

$$U_2=\frac{e}{2\hbar^2c^2}\sum_{\alpha,\beta}\Big\{i(\boldsymbol{\rho}_{\alpha\beta}\times[e_\alpha\mathbf{A}_\alpha-e_\beta\mathbf{A}_\beta]\cdot\mathbf{S}_{\alpha\beta})T_{\alpha\beta}{}^{(0)}\Big(\frac{\tau_{\alpha\beta}}{2}\Big)\int_{\rho_\alpha}^{\rho_\beta}A_s ds -\frac{e}{2\hbar}(\boldsymbol{\rho}_{\alpha\beta}\times\mathbf{p}_{\alpha\beta}\cdot\mathbf{S}_{\alpha\beta})T_{\alpha\beta}{}^{(0)}\Big(\frac{\tau_{\alpha\beta}}{2}\Big)^2 \times\Big(\int_{\rho_\alpha}^{\rho_\beta}A_s ds\Big)^2+\text{H.c.}\Big\}J_{\alpha\beta}{}^{(v)}, \quad \text{(A-23)}$$

where $T_{\alpha\beta}{}^{(0)}$ is obtained from $T_{\alpha\beta}$ by setting $\mathbf{A}=0$.

The 2^l-pole interaction magnetic moments are obtained in the usual way from Eq. (8-26). For the non-exchange interactions

$$\Delta_v\mathbf{M}_l=\frac{el}{\hbar c(l+1)!}\sum_{\alpha,\beta}(\boldsymbol{\kappa}\cdot\boldsymbol{\rho}_\alpha)^{l-1}[\boldsymbol{\rho}_\alpha\times(\mathbf{S}_{\alpha\beta} \times\boldsymbol{\rho}_{\alpha\beta})]\frac{1-\tau_\alpha}{2}T_{\alpha\beta}J_{\alpha\beta}{}^{(v)}. \quad \text{(A-24)}$$

For the exchange interactions

$$\Delta_{ex}\mathbf{M}_l=\frac{el}{2\hbar c(l+1)!}\sum_{\alpha,\beta}\Big\{[\boldsymbol{\rho}_\alpha\times(\mathbf{S}_{\alpha\beta}\times\boldsymbol{\rho}_{\alpha\beta})]\frac{1-\tau_\alpha}{2} -\frac{i}{l\hbar}(\boldsymbol{\rho}_{\alpha\beta}\times\mathbf{p}_{\alpha\beta}\cdot\mathbf{S}_{\alpha\beta})\frac{(\boldsymbol{\rho}_\alpha\times\boldsymbol{\rho}_\beta)}{(\boldsymbol{\kappa}\cdot\boldsymbol{\rho}_\alpha)}(\boldsymbol{\kappa}\cdot\boldsymbol{\rho}_\alpha)^l\frac{\tau_{\alpha\beta}}{2}\Big\} \times(\boldsymbol{\kappa}\cdot\boldsymbol{\rho}_\alpha)^{l-1}T_{\alpha\beta}{}^{(0)}J_{\alpha\beta}{}^{(v)}+\text{hermitian conjugate}. \quad \text{(A-25)}$$

The change in the sum rule is again to be obtained from Eq. (8-35), with U_2 given by Eq. (A-21) or Eq. (A-23). For the non-exchange interactions:

$$\Delta_x\Sigma_\alpha f_{jm}{}^l=0. \quad \text{(A-26)}$$

For the exchange interaction

$$\Delta_{ex}\Sigma_\alpha f_{jm}{}^l=\frac{M}{\hbar^2(l!)^2}\Big\langle\sum_{\alpha,\beta}\Big\{i(\boldsymbol{\rho}_{\alpha\beta}\times[\mathbf{u}(\boldsymbol{\kappa}\cdot\boldsymbol{\rho}_\alpha)^{l-1} +(l-1)\boldsymbol{\kappa}(\mathbf{u}\cdot\boldsymbol{\rho}_\alpha)(\boldsymbol{\kappa}\cdot\boldsymbol{\rho}_\alpha)^{l-2}]\cdot\mathbf{S}_{\alpha\beta})\frac{1-\tau_\alpha}{2} -\frac{1}{2\hbar}(\boldsymbol{\rho}_{\alpha\beta}\times\mathbf{p}_{\alpha\beta}\cdot\mathbf{S}_{\alpha\beta})(\mathbf{u}\cdot\boldsymbol{\rho}_\alpha)(\boldsymbol{\kappa}\cdot\boldsymbol{\rho}_\alpha)^{l-1}\frac{\tau_{\alpha\beta}}{2}\Big\}\times\{(\mathbf{u}\cdot\boldsymbol{\rho}_\alpha)(\boldsymbol{\kappa}\cdot\boldsymbol{\rho}_\alpha)^{l-1} -(\mathbf{u}\cdot\boldsymbol{\rho}_\beta)(\boldsymbol{\kappa}\cdot\boldsymbol{\rho}_\beta)^{l-1}\}\frac{\tau_{\alpha\beta}}{2}T_{\alpha\beta}{}^{(0)}J_{\alpha\beta}{}^{(v)}+\text{H.c.}\Big\rangle_{jj}. \quad \text{(A-27)}$$

The determination of the hermitian conjugate operator, indicated in the foregoing equations, is greatly facilitated by the relationships

$$T_{\alpha\beta}{}^{(0)}\tau_\alpha=\tau_\beta T_{\alpha\beta}{}^{(0)}$$

and

$$\tau_{\alpha\beta}T_{\alpha\beta}{}^{(0)}=-T_{\alpha\beta}{}^{(0)}\tau_{\alpha\beta}.$$

---

[22] Note that Eq. (A-16) differs from the expression given in reference 9 in that the vector $\boldsymbol{\rho}_\tau\times\boldsymbol{\rho}_\nu$ has replaced $\mathbf{r}_\tau\times\mathbf{r}_\nu$. However, reference 9 is concerned only with the expectation value of the magnetic moment operator and the expectation value of the difference of the two operators can easily be seen to vanish.

[23] The statement by Marshall and Guth (reference 8) that the correction vanishes for $l=2$ appears to be inconsistent with Eq. (A-17).

[24] L. Eisenbud and E. P. Wigner, Proc. Nat. Acad. Sci. **27**, 281 (1941).

[25] These expressions are, with one exception, ordered in the same manner as in reference 13 and numbered accordingly. (III') differs from (3) of that reference by the elimination of the non-exchange part.

The Time Average Magnetic Field at the Nucleus in Nuclear Magnetic Resonance Experiments*†

W. C. DICKINSON‡
Research Laboratory of Electronics, Massachusetts Institute of Technology, Cambridge, Massachusetts
(Received September 13, 1950)

For the high precision measurement of a nuclear gyromagnetic ratio by the Purcell or Bloch resonance methods, accurate knowledge of the time average magnetic field H_{hr} at the positions of the nuclei is necessary. The various component fields contributing to H_{hr} are listed. An experimental study is made of two of these fields: the magnetic shielding field in molecules and the magnetization field of paramagnetic ions added to a sample. In an earlier paper accurate computed values were given of the magnetic shielding field for free atoms and monatomic ions. The effect of these fields on the attainable precision in the measurement of nuclear moments is discussed.

I. INTRODUCTION

IN a nuclear magnetic resonance experiment, using the Purcell technique of resonance absorption[1,2] or the Bloch technique of nuclear induction,[3–5] the nuclei are not isolated but are contained in atoms, ions, or molecules. These in turn contribute to the composition of a macroscopic sample of matter which is used in the experiment. It should be expected, therefore, that the effective (i.e., time average), magnetic field to which the resonating nuclei are exposed will not be exactly the same as the externally applied field, since the latter field will induce certain small internal fields in the sample. The purpose of the present paper is to investigate the magnitude and characteristics of these internal fields under various experimental conditions.

For nuclei with gyromagnetic ratio $\gamma=\mu/I\hbar$, the resonance condition may be written

$$\omega_{res}=\gamma H_{hr}, \tag{1}$$

where H_{hr} is the time average value of the magnetic field at the position of one of the nuclei, the average to be taken over a long time interval,[6] and ω_{res} is the corresponding angular Larmor frequency and hence the radiofrequency which must be applied to induce the maximum resonance absorption in the sample. Since magnetic fields are difficult to measure with high precision, it is customary to measure the ratio of two nuclear magnetic moments (we assume the spins are known), by comparison of their Larmor frequencies in the "same" magnetic field. If this condition could actually be satisfied, we would have, for two nuclear species A and B,

$$\mu_A/\mu_B=(I_A/I_B)(\omega_{resA}/\omega_{resB}). \tag{2}$$

It is, presently, possible to measure a frequency ratio in the radiofrequency region with a precision of 1 part in 10^6 or better, and resonance line widths in liquids have been reported as small as 1 part in 10^5 of the applied magnetic field. Estimating conservatively that the center of a resonance line can be determined to within 10 percent of the line width, we see that the present attainable precision inherent in the measurement of a nuclear moment ratio by the Purcell or Bloch techniques is of the order of 1 part in 10^6. However, evidence is presented in this paper to show that even though both nuclear species are exposed to the same external field H_0, the field H_{hr} at the two may be significantly different. Hence, to utilize this high precision, accurate knowledge of the internal fields contributing to H_{hr} is of prime necessity.

It will be assumed that the electronic state of the atom, ion, or molecule which contains the resonating nucleus is characterized by zero permanent magnetic moment. If this were not the case, the field acting at the nucleus due to such a moment would generally be considerably stronger than the applied field, so that the above nuclear resonance phenomenon would be obliterated completely. Also, we will not be concerned with fluctuating fields at the nucleus having a time average, of zero, since such fields do not affect the resonance condition, Eq. (1). For example, there is the so-called local field H_{loc} defined by Bloembergen, Purcell, and Pound[2] (hereafter referred to as BPP), as being the instantaneous sum of the dipole fields at one nucleus due to all its neighbors. Although the local field can have a magnitude of several gauss, it generally fluctuates in a random manner with almost zero average, since nuclear magnetization is small. It is further found

* From a thesis submitted in partial fulfillment of the requirements for the degree of Ph.D. in Physics at the Massachusetts Institute of Technology. A preliminary report of these findings was presented at the meeting of the American Physical Society, New York, February 2, 1950; [Phys. Rev. 78, 339 (1950)].

† This work has been supported in part by the Signal Corps, Air Materiel Command, and ONR.

‡ Now at the Los Alamos Scientific Laboratory, Los Alamos, New Mexico.

[1] Purcell, Torrey, and Pound, Phys. Rev. 69, 37 (1946).

[2] Bloembergen, Purcell, and Pound, Phys. Rev. 73, 679 (1948). This reference is referred to in the text as BPP.

[3] Bloch, Hansen, and Packard, Phys. Rev. 69, 127 (1946).

[4] F. Bloch, Phys. Rev. 70, 460 (1946).

[5] Bloch, Hansen, and Packard, Phys. Rev. 70, 474 (1946).

[6] By a long time interval is meant a time longer than molecular configuration times in the sample. The definition of H_{hr} as the time average field at one nucleus is valid only if the applied magnetic field is perfectly homogeneous over the sample volume and all nuclei experience the same structural surroundings. If either of these conditions is not met, H_{hr} would be defined as the weighted mean of the time average fields for all the nuclei.

that in most liquids it fluctuates at a rate much higher than the nuclear Larmor frequency. It is for this reason that the natural line width of a resonance in a liquid is so extremely small, the observed width being usually determined solely by the inhomogeneity of the applied magnetic field over the sample volume.[7] On the other hand, in the case of solid substances where the structures are rigid in the sense that molecular configuration times are considerably longer than the nuclear precession time, the local field will result in a broadening of the resonance line by, perhaps, several orders of magnitude. Indeed, in some cases a statistical analysis shows that the local field may give rise to a fine structure in the broad resonance line. Such a fine structure has been observed in certain single crystals and crystalline powders[8,9] and, surprisingly, it has recently been observed in a liquid.[10] It should be stressed, however, that the center of symmetry of a resonance line possessing this type of fine structure will be at the same position at which a single resonance line would occur for the same nucleus.[11] The analysis indicates that there is a higher statistical weighting around certain values of H_{loc}; the average of H_{loc} over all the nuclei in the sample is zero.

II. THE FIELDS CONTRIBUTING TO H_N

For a liquid, the time average field at the nucleus may be divided into three significant components

$$H_N = H_0 + H' + H''. \tag{3}$$

(1). H_0 is the external or magnet field and is, of course, the chief component of the field H_N. In the majority of past nuclear moment ratio measurements, separate samples have been used, placed side by side in the magnet field. Often elaborate precautions have been taken to insure that the field H_0 is the same at both samples, but, in any event, this method is undesirable in that an additional source of error is introduced. To insure that both nuclear species see the same space average field H_0, it is desirable to use a single sample containing both types of nuclei. Also, in this way, any asymmetry in resonance line shape due to nonuniformity in H_0 over the sample volume will be duplicated; hence, in determining line centers no error is introduced by this factor. Descriptions of the single-sample technique as applied to the Bloch and Purcell type of experiments have been given in the literature.[12,13]

(2). H' is the magnetic shielding field at the nucleus due to the induced motions of the electrons of the atom or molecule containing the nucleus.

For an atom or monatomic ion, in which case Larmor's theorem is valid, this field is given by[14]

$$H' = \frac{eH_0}{3mc^2}\int_0^\infty \frac{\rho(r)dr}{r} = \frac{eH_0}{3mc^2}v(0), \tag{4}$$

where $\rho(r)$ is the radial charge density of the electrons at a distance r from the nucleus, and $v(0)$ is the electrostatic potential produced at the nucleus by the atomic electrons. In a previous paper[15] the author has given computed values of $v(0)$ for all atoms and singly-charged ions which have been treated by the Hartree or Hartree-Fock self-consistent field method. By interpolation and the use of Eq. (4), H'/H_0 values for all neutral atoms are given. It is estimated from experimental evidence as to the accuracy of the self-consistent field method that these values can be trusted to within 5 percent except for the heaviest atoms, where the relativity effect becomes important.

In diatomic and polyatomic molecules and ions there is an additional component of the magnetic shielding field which is attributed to a second-order paramagnetism. The existence of this component was only recently reported by various observers,[16–18] although some months before the experimental discovery it was suggested to the author by Professor F. Bitter that a second-order paramagnetic field should exist at the nucleus of normally diamagnetic atoms and molecules owing to a Paschen-Back type of uncoupling of the paired electron spins characteristic of diamagnetism. That, for atoms, the energy required for uncoupling is great is seen by the fact that the Paschen-Back effect becomes important only for magnetic fields of the order of 10^5 gauss or greater. Bitter pointed out, however, that for molecules, where the excited states are closer together, the uncoupling would be expected to begin at much lower field strengths and, hence, might be observed experimentally.

It is well known from the theory of molecular diamagnetism[19] that the molar susceptibility of $^1\Sigma$ molecules consists of two terms, *viz.*,

$$\chi_{mol} = -\frac{Ne^2}{6mc^2}\sum\langle r^2\rangle_N + \frac{2}{3}N\sum_{n\neq 0}\frac{|(0|m^0|n)|^2}{E_n - E_0}, \tag{5}$$

where N is here the Avogadro number. The first term is the ordinary Pauli expression for the diamagnetism of atoms (the summation now to be extended over all the electrons in the molecule), while the second gives

[7] If the nuclei possess an electric quadrupole moment, the resonance line may be considerably broadened because of the interaction of the quadrupole moment with the fluctuating inhomogeneous electric fields in a liquid.

[8] G. E. Pake, J. Chem. Phys. **16**, 327 (1948).

[9] Gutowsky, Kistiakowsky, Pake, and Purcell, J. Chem. Phys. **17**, 972 (1949).

[10] W. G. Proctor and F. C. Yu, Phys. Rev. **78**, 471 (1950).

[11] Another source of resonance fine structure is the nuclear electric quadrupole interaction in crystalline substances having lower than cubic symmetry. R. V. Pound, Phys. Rev. **79**, 685 (1950).

[12] Bloch, Levinthal, and Packard, Phys. Rev. **72**, 1125 (1947).

[13] W. C. Dickinson and T. F. Wimett, Phys. Rev. **75**, 1769 (1949). The technique described in this paper was introduced by F. Bitter.

[14] W. E. Lamb, Jr., Phys. Rev. **60**, 817 (1941).

[15] W. C. Dickinson, Phys. Rev. **80**, 563 (1950).

[16] W. D. Knight, Phys. Rev. **76**, 1259 (1949).

[17] W. C. Dickinson, Phys. Rev. **77**, 736 (1950).

[18] W. G. Proctor and F. C. Yu, Phys. Rev. **77**, 717 (1950).

[19] J. H. Van Vleck, *Electric and Magnetic Susceptibilities* (Oxford University Press, London, 1932), Chapter X.

the contribution of the high frequency matrix elements of the orbital paramagnetic moment of the molecule, the summation to be extended over all the n-excited states of the molecule. According to Van Vleck,[19] the existence of this second term is based physically on the fact that the nuclei in a diatomic or polyatomic molecule act at different attracting centers and so exert a torque on the electrons. This torque causes a continual transfer of angular momentum back and forth between the electrons and nuclei of the molecule, with the result that although the mean orbital angular momentum of a $^1\Sigma$ molecule is zero, the mean square value is not zero. It is found experimentally that the large majority of molecular compounds are diamagnetic, showing that the first term in Eq. (5) is usually larger than the second. There are a few instances where the second term predominates, with the substance showing a feeble, temperature-independent paramagnetism.

From the two terms of Eq. (5) can in principle be found the net additional fields at the nuclei of a molecule due respectively to the diamagnetism and second-order paramagnetism of all the other molecules in the sample. As will be shown below, the field due to the diamagnetic term almost always can be neglected, hence, also the field due to the second term. It cannot be concluded from this, however, that the *internal* diamagnetic and second-order paramagnetic fields (i.e., the fields at the nuclei of a molecule due to the extra-nuclear electrons of the molecule itself) are negligible. Indeed, since the internal diamagnetic shielding field H' for atoms constitutes an important correction in nuclear resonance experiments, the existence in some cases of a significant internal second-order paramagnetic component in molecules might well be expected.

In a theoretical treatment of the problem, Ramsey[20] obtains an expression for the total molecular shielding field consisting of a diamagnetic and a second-order paramagnetic term. Owing to the choice of the coordinate origin at the nucleus at which the field is desired, his expression for the diamagnetic term becomes identical with Eq. (4) except that the integration is extended over all the electrons in the molecule rather than only the one atom containing the resonating nucleus. Because of the $1/r$ dependence of $v(0)$, perturbations of the valence electrons of an atom by molecular binding have little effect on the atomic value of $v(0)$.[15] Also, except possibly for the lightest atoms, contributions to $v(0)$ from electrons belonging to other atoms of a molecule would be relatively small. (Examples: for an F_2 molecule the contribution of the electrons of one F atom to the value of $v(0)$ at the nucleus of the other atom would be about 7 percent of the $v(0)$ value for a free F atom. For a $GaCl_3$ molecule the contribution of the electrons of the three chlorine atoms to the value of $v(0)$ at the nucleus of the Ga atom would be only about 3 percent of the $v(0)$ value for a free Ga atom.) Hence, to a first approximation, except for the lightest atoms, values of the internal diamagnetic correction H'/H_0 for free atoms can also be used for the diamagnetic term in Ramsey's expression.

The second term of Ramsey's expression for the molecular shielding H'/H_0 is of the same general form as the second term in Eq. (5), although more complicated. Unfortunately, the numerical evaluation of this term would be difficult for most molecules, since knowledge of wave functions of the excited states of the molecule would be needed. However, for the important case of molecular hydrogen, Ramsey[20] has been able to calculate the second-order paramagnetic term utilizing the experimentally measured value of the spin-rotational interaction constant for the H_2 molecule.[21] The diamagnetic term Eq. (4) for molecular hydrogen has been calculated by Anderson[22] using Nordsieck's wave functions. Thus, the total shielding field is found to be[23]

$$H'/H_0=(-3.24+0.56)\times10^{-5}=-2.68\times10^{-5}.$$

Although for H_2 the second-order paramagnetic term is only about 17 percent of the diamagnetic term, no similar prediction can be made concerning more complex molecules. Van Vleck[19] points out that for molecules in which the nuclear field is less nearly centro-symmetric than is the case for H_2 the second term in the expression for the molecular susceptibility Eq. (5) would be expected to become more important. He also points out that this term would be expected to be particularly large for molecules formed out of atoms whose ground states were not ^1S. Similar predictions can, hence, be made about the importance of the internal second-order paramagnetism. It is, indeed, conceivable that in some cases the second-order paramagnetic term could be larger than the diamagnetic term in Ramsey's expression so that the shielding field H'/H_0 would have a positive value.

(3). H'' is the magnetization field due to any paramagnetic ions that might be added to the sample for the purpose of shortening the spin-lattice relaxation time T_1 of the nuclear spin system. The inverse time T_1^{-1} is a measure of the rate at which energy absorbed by the nuclear spin system can be transferred to the atomic lattice. If T_1 is excessively long, the population of the $2I+1$ nuclear energy levels, originally governed by the Boltzmann factor $\exp(\mu H_0 m/IkT)$, becomes equalized as resonance is approached with a resulting decrease in the rate of absorption. This "heating up" of the nuclear spins is referred to as saturation and causes distortion of the resonance line shape as well as decrease of the signal-to-noise ratio. The large fluctuating magnetic fields associated with paramagnetic ions create better

[20] N. F. Ramsey, Phys. Rev. **78**, 699 (1950).

[21] Kellogg, Rabi, Ramsey, and Zacharias, Phys. Rev. **57**, 677 (1940).

[22] H. L. Anderson, Phys. Rev. **76**, 1460 (1949).

[23] E. Hylleraas and S. Skavlem, Phys. Rev. **79**, 117 (1950), obtain by an essentially different method a value for this shielding constant between 2.66×10^{-5} and 2.95×10^{-5}.

TABLE I. Bulk diamagnetic susceptibility χ_{vol} for some common liquids.

Liquid		$-\chi_{vol}\times10^6$
HNO_3		0.700
H_2O		0.721
$(C_2H_5)_2O$	Ethyl ether	0.546
$C_2H_4O_2$	Acetic acid	0.552
C_6H_6	Benzene	0.636
C_2H_6O	Ethyl alcohol	0.587
CCl_4	Carbon tetrachloride	0.685
Cl_2	(Liquid)	0.887

spin-lattice coupling,[24] thus shortening T_1. The line broadening associated with a shortening of T_1 will not be observed for small enough ionic concentrations, since, as previously mentioned, the natural line width in liquids is usually much less than the observed line width which is due to inhomogeneities in H_0. Since any observable line broadening lowers precision, there is usually an optimum ionic concentration in any particular case.

In past nuclear moment ratio measurements, where paramagnetic ions have been used, one of the following three assumptions has generally been made as to the effect of the magnetization field (our H''), on the precision of the experiment:

(a) On adding paramagnetic ions to one of two samples used in a moment comparison, the concentration is small enough so that any field shift would be negligible.

(b) On adding the same concentration of paramagnetic ions to both samples, both nuclear species would experience the same magnetization field. This assumption also is made when paramagnetic ions are added to a single sample containing both nuclear species.

(c) When only one nuclear resonance is needed in an experiment (e.g., comparison of proton and neutron moments), by using a spherically shaped sample, the field H'' would be exactly zero.

The validity of these assumptions may be tested by means of experimental data presented in Sec. V.

In addition to the three significant field components in liquids discussed above, the following fields should be listed as also contributing to H_N:

(4). The bulk diamagnetic field. From random values of χ_{vol} for liquids given in Table I it is seen that diamagnetic volume susceptibilities are quite small and do not vary considerably from liquid to liquid. Referring to Table I, we might expect the maximum difference in χ_{vol} for liquids to be about 5×10^{-7}. The corresponding fractional field difference $\Delta H/H_0$ would vary from zero for spherical samples to about 1 part in 10^6 for transverse cylindrical samples. (Sec. V.) In the experiments reported below the smallest fractional field difference that could be detected between two samples was about 5 parts in 10^6 so that differences in bulk diamagnetic field could be neglected. Of course, when both nuclear species are contained in a single sample, they both will experience the same diminution of field strength due to bulk diamagnetism.

In the case of solids, χ_{vol} may be somewhat larger than for liquids, but due to the broad resonance lines characteristic of solids, the bulk diamagnetic field can always be neglected.

(5). The static nuclear paramagnetic field. The volume susceptibility of a sample due to nuclear dipole alignment is given by the Curie law, *viz.*,

$$\chi_0=[(I+1)/I](N\mu^2/3kT), \tag{6}$$

where N is the number of nuclei per cc with moment μ and spin I, and T is the absolute temperature. As an example of the magnitude of χ_0, we might take water with its high density of protons. Thus,

$$(\chi_0)_{H_2O}\approx3.2\times10^{-10}. \tag{7}$$

Since the contribution to H_N would be of the order of χ_0H_0, it is seen that nuclear dipole orientation is a perfectly negligible factor. The contribution to H_N of the field due to orientation of molecular rotation moments will likewise be negligible, since these moments are known to be of the same order as nuclear moments.

(6). It is shown by Bloch and Siegert[25] for the special case of nuclei with spin $\frac{1}{2}$ that the use of a linear oscillating rather than a rotating r-f field necessitates replacing the resonance field value H_0 by an effective value $H_0^*=H_0(1-H_1^2/16H_0^2)$, where H_1 is the amplitude of the r-f field.[26] In resonance absorption experiments and modern nuclear induction experiments $H_1/H_0\approx10^{-4}$ to 10^{-6}. Hence, not only would this result in a negligible shift in the resonance curve, but in a moment ratio measurement the resonances from both nuclear species would be shifted in the same direction and by about the same amount.

(7). The field due to electronic paramagnetism in metals.[27] Knight[16] found that the nuclear resonance frequency for an atom in the metallic state is usually appreciably greater than the resonance frequency when the atom is in a nonmetallic compound. These frequency shifts are of the order of a few tenths of one percent and have been attributed[28] to the large probability density near the nuclei of the conduction electrons in a metal, resulting in an enormous concentration of the local magnetic susceptibility in the vicinity of the nuclei. The obvious precaution is to use only nonmetallic compounds in a moment comparison.

[24] The reader is referred to BPP for a detailed theoretical treatment of the effect of paramagnetic ions on spin-lattice relaxation.

[25] F. Bloch and A. Siegert, Phys. Rev. **57**, 522 (1940).

[26] Professor Ramsey has pointed out to the author that this same result can be derived classically, independent of the nuclear spin value, by using a simple rotating coordinate system method.

[27] Powdered metallic samples can be used in resonance experiments provided the metal particles are sufficiently insulated from one another so that the sample is a nonconductor. In some cases (e.g., Al, Cu) F. Bitter has found that a pure metal powder can be used; the surface oxidation of the metal particles provides adequate insulation.

[28] Townes, Herring, and Knight, Phys. Rev. **77**, 852 (1950).

III. EXPERIMENTAL TECHNIQUE FOR MEASUREMENT OF RESONANCE LINE SHIFTS

The theoretical and physical principles of nuclear magnetic resonance absorption have been given in detail by BPP. The radiofrequency bridge technique and modulation method described there is, in all essentials, that used for the work reported in this paper. Figure 1 is a block diagram of the circuit and equipment employed. The magnet is an iron-core, water-cooled electromagnet designed by F. Bitter. The gap width is 2½ in. and the pole faces are 8 in. in diameter with rims adjustable for maximum field homogeneity. The current is supplied by a bank of submarine batteries. For a field of 7000 gauss, with the magnet windings connected in series, 50 volts and about 45 amp are required; this current can be maintained for 8 hours or more with no observable steady drift due to the batteries. The current is monitored by a galvanometer and a Rubicon potentiometer which measure the voltage drop across a low resistance shunt placed in series with the magnet circuit. The exact resistance of the shunt is unimportant, since it is never necessary to measure the absolute value of the current. For the slow variation of the magnet field through resonance, a motor-driven rheostat is used. Small fluctuations in battery current limit the slowness with which the field may be varied. For the work reported here, a sweep rate of approximately 1 gauss/min was used although a considerably slower rate can be attained easily.

The experimental problem is the detection and measurement of shifts in resonance position which are usually small compared with the resonance line width. By a shift in resonance position is meant that on varying some parameter in the sample (e.g., the concentration of paramagnetic ions), the nuclear resonance under investigation occurs at a slightly different value of applied field H_0, holding the radiofrequency at a constant value. Such a shift is interpreted as arising from a small change in the time average field H_n experienced by the nuclei, necessitating an equal and opposite change in the applied field H_0 in order that the resonance condition Eq. (1) be satisfied.

The method developed for the measurement of these small shifts consisted in the use of two identical r-f bridge circuits, each with separate receiver, 30-cps narrow-band, lock-in amplifier, and recording milliammeter, but both coupled to the same G. R. 605-B signal generator. A nuclear species in the "standard" sample of the one bridge gives a resonance at a constant field position with which to compare the resonance position of the same nuclear species in the "variable" sample of the other bridge. Any frequency drift of the generator will shift both resonances the same fractional amount and, hence, will have no effect on the measurement of a shift. The sample coils for the two bridges consisted of No. 30 copper wire wound on 10-mm o.d. cylindrical glass sample holders placed side by side in a single brass box. The liquid sample materials were

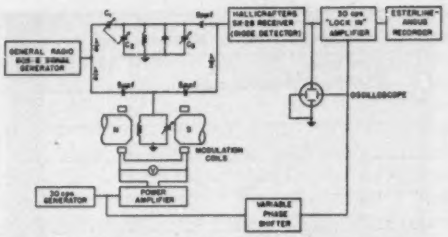

FIG. 1. Block diagram of nuclear resonance absorption bridge circuit. Two such r-f bridges, both fed by a single frequency generator, were used for the experiments.

contained in either 8-mm o.d. spherical bulbs blown at the end of 3-mm glass tubing or in 8-mm o.d. long cylindrical test tubes; in either case a snug fit was made with the inside of the sample holders. Since both the sample coils were driven at the same frequency, they had to be well shielded from each other to prevent any coupling between the two bridges. Although it is desirable that the samples be placed very close together so that they will experience as small a magnetic field gradient as possible, a limit is set by the lowering of the Q of the coils when they are placed too close to the brass shield between them. It was found that the coil Q's were only slightly lowered for the center-to-center distance between sample holders of 16.5 mm.

In order that the nuclear resonances from identical samples in the two bridges will occur simultaneously as the magnet field is varied slowly through resonance, the sample box must be so adjusted in the magnet that the position of zero-field gradient (maximum field), is just halfway between the two sample coils. A rough adjustment is made easily by means of oscilloscope observation of the proton resonance, using only one bridge. Then, with identical samples in both sample holders and using both bridges, final adjustment is made, by means of a positioning mechanism on the magnet, until the resonance curves from the two samples occur simultaneously on the respective Esterline-Angus recorder tapes. After adjustment of the sample box in this manner, the proton derivative of absorption curve[39] (qualitatively similar to a dispersion curve), had a peak-to-peak width of about 0.3 gauss in a field of 7000 gauss. This can be compared with a peak-to-peak width of about 0.1 gauss, when the sample is in the position of zero field gradient. The width between the two small minima for a derivative of dispersion curve was found, in general, to be closely twice the peak-to-peak width for a derivative of absorption curve.

A resonance shift is measured as follows. Identical samples are placed in the two sample holders. The two resonances are traversed, first, with the magnet

[39] With the modulation method used in these experiments the output of the lock-in amplifier reproduces the derivative of the original absorption or dispersion resonance curves (see reference 2 for details).

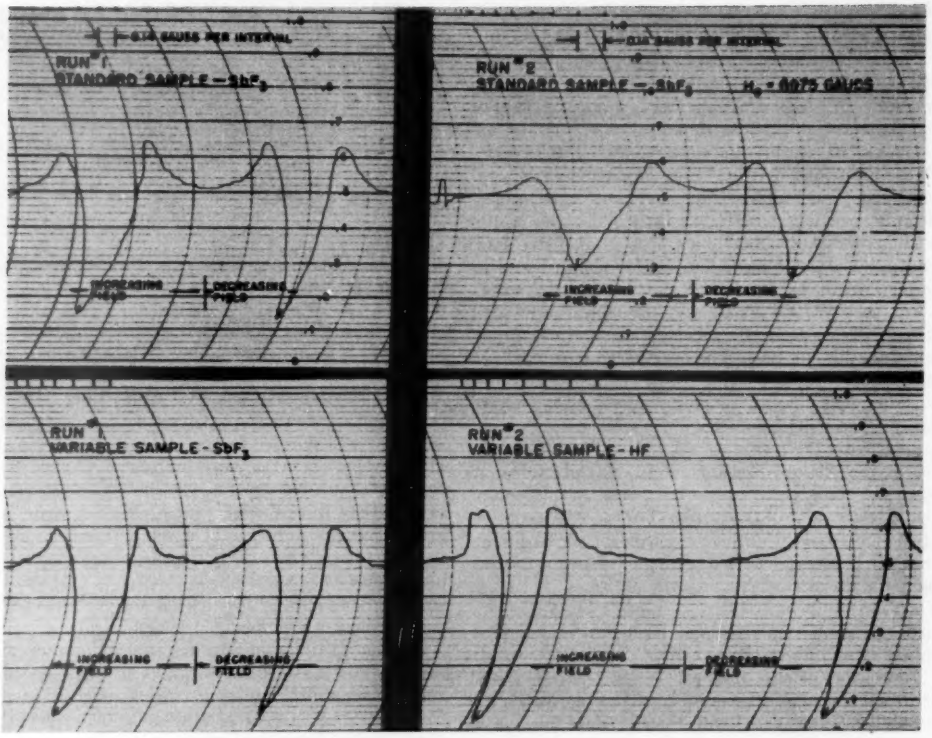

FIG. 2. Record of two runs. In Run No. 1 the F^{19} resonance in SbF_3 was simultaneously observed in both bridges. In Run No. 2 the variable sample was changed to HF, the standard sample remaining SbF_3. Note the large resonance shift. The SbF_3 resonance curves are wider in Run No. 2 than in Run No. 1 due to the nonlinearity in sweep rate of the motor-driven rheostat. In Run No. 2, due to the wider separation of the two HF resonances, a larger section of the rheostat had to be traversed. The SbF_3 resonances were traversed at the end of the rheostat where the rate was slowest, hence, the broadness.

current increasing, then with the magnet current decreasing, and, then, once more with the magnet current increasing. We will call such a series of three resonance pairs a run. On traversing the second pair of resonances in a run the recorder tapes are simultaneously marked by means of a relay switch for equal intervals of current as read from the galvanometer scale. A second run is now made, the outer pairs of resonances being for decreasing rather than increasing magnet current as for the first run. This procedure eliminates error due to the effect of hysteresis, to be mentioned below. The variable sample is now removed and, for example, a definite concentration of paramagnetic ions added. Replacing the sample, two more runs are made in the same manner. It was usual practice after a series of runs were made, changing the variable sample several times, to end the experiment by once more making the variable sample identical to the standard sample. Thus, if the sample box had been moved accidentally or if the relative field at the two samples had changed for any other reason, this would have been detected.

An illustration of two runs (F^{19} resonances), is given in Fig. 2. For lack of space only two of the three pairs of resonances are shown in each run. The sections of tape in the upper and lower left hand corner constitute the first run in which the two samples were identical—both containing an aqueous solution of SbF_3. It is seen that the resonances occur practically simultaneously. The sections of tape in the upper and lower right-hand corner constitute the second run in which the variable sample is now HF. The standard sample, of course, is left unchanged. The current calibration is seen in the upper left-hand corner of each section of tape. The large shift observed here is attributed to a difference in the molecular shielding field between SbF_3 and HF. It is a much larger shift than is usually observed on addition of paramagnetic ions.

The current calibration is changed to a magnetic field calibration as follows. The magnet field is centered

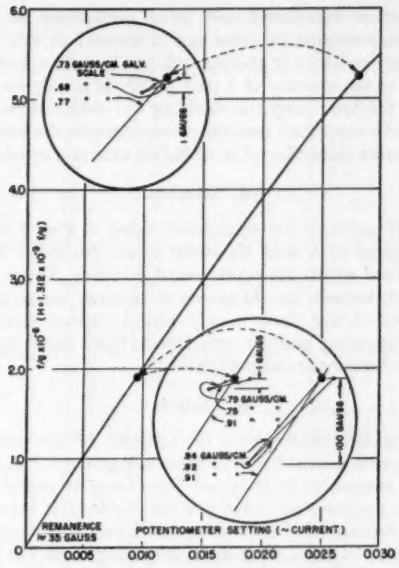

FIG. 3. Effect of hysteresis in magnetic field calibration.

on a resonance and the radiofrequency measured with a Zenith BC-221-T frequency meter. Then, the signal generator is slightly changed in frequency and the magnet current changed until the resonance is once more centered. The corresponding galvanometer deflection is read; and from the relation $dH=d\omega/\gamma$, the galvanometer scale is calibrated in gauss/cm. It is important to warn that even when there is no saturation of the magnet field, it is incorrect to write $di/i=dH/H$ and, hence, determine dH with the potentiometer alone. This ignores the phenomenon of reversible magnetization, which means only that at any point on the i *vs* H curve for an iron-core electromagnet a small hysteresis curve is traced out. For this reason, as seen in Fig. 3, the field calibration is slightly dependent on whether the magnet current is increasing or decreasing. By making the calibration several times in each direction, an average calibration is obtained which can be trusted to 10 percent in accuracy. Also, as seen in Fig. 3, the calibration depends on the magnitude of the field change dH. Care was taken to calibrate the field over about the same field increment as was actually traversed for the resonances.

The determination of a resonance shift from a run consists in the measurement and comparison of distances *between* the three resonance centers on each tape. This eliminates any systematic errors which might arise from time lags in the apparatus. The importance of estimating accurately the centers of the resonance lines is obvious, particularly in the case of shifts much smaller than the line width. It was rarely possible experimentally to traverse in succession the three pairs of resonance curves in a run without one or both bridges drifting slightly from the desired balance. This causes a slight dissymmetry in the resulting resonance curves due to a mixing of dispersion and absorption. In order to be able to determine the true line center when such dissymmetries occur, an analysis was made of "mixed" resonance line shapes[30] using Gaussian shape functions given by Pake and Purcell.[31] (According to the criteria given by these authors the gaussian derivative curves fit our experimental curves much better than the corresponding Lorentz curves.) On the basis of this analysis, Fig. 4 illustrates an "impure" derivative of dispersion-type curve, where the difference between the true and observed line center is 5 percent of the line width, measured between the two minima. In some cases the actual resonance field shift which is to be measured is not much larger than this.

It was found over a large range of experiments that the smallest resonance shift of the variable sample with respect to the standard sample that could be detected was about 0.03 gauss in a field of 7000 gauss. This corresponds to a shift equal to about 1/20th of the line width of a derivative of dispersion-type curve; or stated differently, to a shift of 4 to 5 parts in 10^6 with respect to the applied field. The accuracy to which this shift could be measured was also found to be about 5 parts in 10^6 of the applied field. Hence, a shift of 0.03 gauss could only be measured to an accuracy of the order of the shift itself, while a shift of 0.3 gauss could be measured to an accuracy of about 10 percent. Because of the uncertainty attached to the magnetic field calibration, it is felt that an accuracy of 10 percent is the best that can be quoted—even for shifts larger than 0.3 gauss.

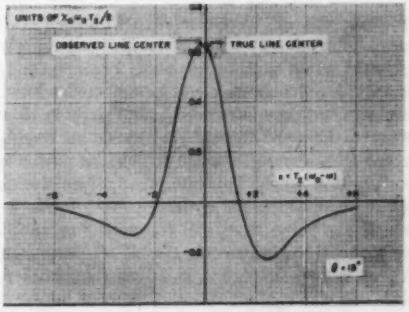

FIG. 4. Line shape (gaussian), of an "impure" nuclear magnetic resonance. If $d\chi''/dx$ represents the derivative of an absorption curve and $d\chi'/dx$ the derivative of a dispersion curve, the equation of the above curve is $(d\chi'/dx)\cos\theta+d\chi''/dx\sin\theta$, where θ is the circuit "balance factor." Any experimental curve more distorted than the one shown above was rejected.

[30] On request, the author will gladly furnish the results of this analysis to other workers in this field.

[31] G. E. Pake and E. M. Purcell, Phys. Rev. 74, 1184 (1948).

IV. THE MAGNETIC SHIELDING FIELD FOR MOLECULES

Knight[16] was the first to observe a dependence of nuclear resonance position on chemical compound. In a letter reporting shifts of the nuclear resonance in several metals, he briefly mentioned observing shifts of the P^{31} resonance of about 0.01 percent among some phosphorous compounds. Independently, the author[17] reported a dependence of the F^{19} resonance on the chemical compound, and Proctor and Yu[18] reported an even more pronounced effect for the N^{14} resonance. With this indication that such a dependence was not uncommon, a survey was made of the nuclear resonance positions in different chemical compounds of several light elements. In the data given below for each element, the shielding field in different molecules is compared with the shielding field in the molecule for which the nuclear resonance is found to come at the *highest* value of applied magnetic field (i.e., zero or lowest non-zero contribution of second-order paramagnetism, assuming that the diamagnetic contribution is closely the same in all cases). This is rather an arbitrary procedure, since there may be other molecular compounds, not observed here, in which the resonance comes at a still higher applied field. Thus, it is impossible to determine the absolute value of the second-order paramagnetic field for any molecule, unless for the standard compound it is known that the resonating nucleus is contained in a simple diamagnetic ion or atom rather than a molecule. The second-order paramagnetism would be zero in this case, and a comparison with other molecular compounds would determine the absolute value of the second-order paramagnetic contribution for those molecules.

(A) Hydrogen

Proton resonances were compared with each other in acetone, mineral oil (Nujol), distilled water, glacial acetic acid, ethyl alcohol, glycerin, benzene, and anhydrous ether. No shifts could be detected within the accuracy of the experiment of about 5 parts in 10^6 with respect to the applied field. It would, no doubt, be expected that any shifts occurring in the proton resonance position would be quite small, since the single covalent bond which the hydrogen atom forms would be about the same from one compound to another.[32] Since the total shielding correction H'/H_0 for molecular hydrogen is only 2.7×10^{-5}, it is seen that a difference in shielding of less than about 20 percent between the above molecules would not have been detected. An important experiment will be a comparison of the proton resonance in water and in mineral oil with the proton resonance in gaseous or liquid hydrogen, preferably to an accuracy of 1 part in 10^6. It is only for H_2 that the total magnetic shielding has been computed, while in most high precision measurements the proton resonance from mineral oil or H_2O is used as a standard.

(B) Lithium

The series of Li^7 compounds listed in Fig. 5 were compared in a field $H_0=6950$ gauss. No shifts were observed within the experimental accuracy. This is, no doubt, because the Li atoms in solution are entirely ionized—losing their loosely bound valence electron and becoming positive ions. Hence, there would be no second-order paramagnetism.

(C) Boron

The data obtained for the different B^{11} compounds compared in a field $H_0=7100$ gauss is given in Table II. The resonances in BCl_3 and BBr_3 come at nearly the same position, but there is a noticeable shift between the resonances in these compounds and the resonance in $BF_3{:}O(C_2H_5)_2$. This is not surprising, since the BF_3 forms a bond with the ether molecule. Also, Pauling[33] points out that BF_3 differs from BCl_3 and BBr_3 in that the B—F bond has a greater ionic character (63 percent for B—F; 22 percent for B—Cl).

(D) Fluorine

The data for the different F^{19} compounds compared in a field $H_0=6975$ gauss are given in Table III. It would be expected that NaF and KF in aqueous solution would be entirely ionized. Therefore, it is surprising to find that the resonances in BeF_2, BF_3, and HF occur at a higher applied field than those in NaF and KF. Since the second-order paramagnetic field must always be an aiding field, resonances in compounds that are not totally ionized would be expected to occur at a lower applied field than those in NaF and KF. The only plausible explanation for this is that the diamagnetic contribution may be slightly greater for BeF_2, BF_3, and HF than for the F^- ions in the NaF and KF solutions. Indeed, when the observed resonance shifts in a light element such as fluorine are much smaller than the magnitude of the internal diamagnetic field for the atom ($H'=3.2$ gauss for F^{19} at $H_0=7000$ gauss), this might well be the case.

According to the analysis made by Ramsey,[20] the molecular shielding field should be linearly proportional to the applied field. Thus, the difference of this field between different molecules also should be proportional to the applied field. This was checked experimentally by also observing the F^{19} shifts at a field $H_0=2500$ gauss. From Table IV it is seen that the average ratio

[32] G. Lindstrom, Phys. Rev. **78**, 817 (1950), finds that the deuteron-proton moment ratio differs by $4(\pm3)$ parts in 10^6 depending on whether the proton sample was paraffin oil or H_2O. Such a small difference might well be due to a difference in the bulk diamagnetic field between the two substances. Also H. S. Gutowsky and C. J. Hoffman, Phys. Rev. **80**, 110 (1950), report that the magnetic shielding in mineral oil is (3 ± 1.5) parts in 10^6 to (8 ± 1.5) parts in 10^6 higher than in benzene, CF_3CO_2H, HBF_4, $CHCl_3$, concentrated HCl, and HNO_3.

[33] L. Pauling, *The Nature of the Chemical Bond* (Cornell University Press, 1940), Chapter VII.

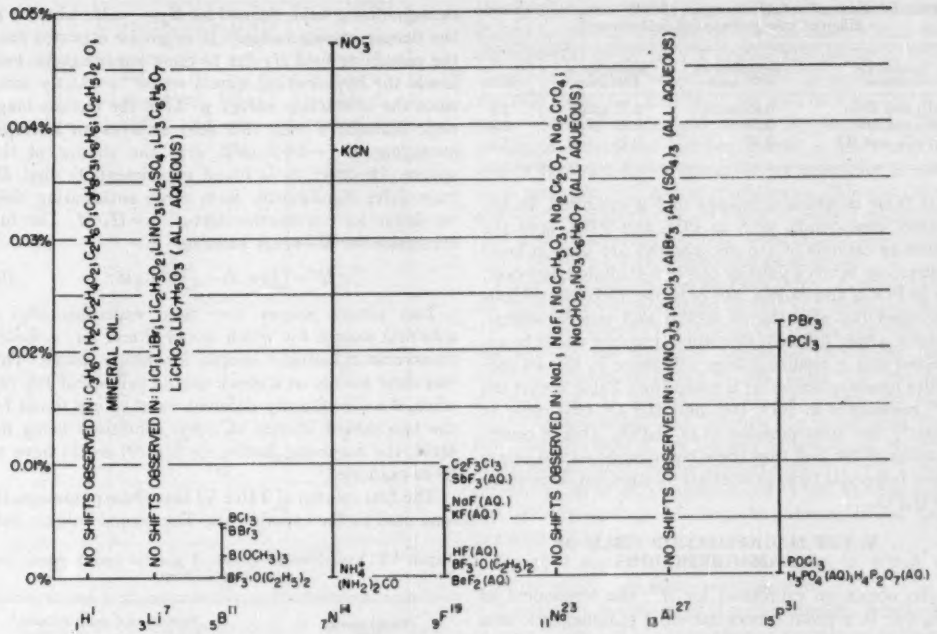

FIG. 5. Percentage differences in the magnetic shielding H'/H_0 for molecules of several light elements.

of the shifts at the two field strengths is 2.5. Since the ratio of the applied fields is 2.8, it can be stated that within the experimental error the molecular shielding field is, indeed, linearly proportional to H_0. In the work of Proctor and Yu[18] on shifts in N^{14}, linearity in the field dependence was also observed.

(E) Sodium

The series of Na^{23} compounds listed in Fig. 5 were compared in a field $H_0=6950$ gauss. As for Li^7, the observance of no shifts can be attributed to the ionic form of the Na compounds in aqueous solution. It would be interesting to obtain some metal-organic compounds containing Li and Na to compare with the aqueous solutions of the salts. A shift should be observed due to the bonding of the Li and Na atoms into the organic molecule.

TABLE II. Differences in the magnetic shielding field for some B^{11} compounds. $H_0=7100$ gauss. The resonance in $BF_3{:}O(C_2H_5)_2$ was observed at the highest value of applied magnetic field.

Compound	$\Delta H'$ (gauss)	$\Delta H'/H_0$ (%)
$BF_3{:}O(C_2H_5)_2$	0.00	0.00
$B(OCH_3)_3$	0.13	0.0018
BBr_3	0.31	0.0044
BCl_3	0.33	0.0046

(F) Aluminum

In the series of Al compounds listed in Fig. 5 no shifts were observed within the experimental error. Again, this can be attributed to complete ionization in the aqueous solution, since it would be extremely unlikely that the second-order paramagnetism would be exactly the same for all the molecules compared.

(G) Phosphorus

A comparison of several P^{31} compounds was made at a field $H_0=5800$ gauss. The results are given in Table V. It is seen that a large shift occurs between those compounds where the phosphorous exhibits a valency of 3

TABLE III. Differences in the magnetic shielding field for some F^{19} compounds. $H_0=6975$ gauss. The resonance in BeF_2 (aq) was observed at the highest value of applied magnetic field.[a]

Compound	$\Delta H'$ (gauss)	$\Delta H'/H_0$ (%)
BeF_2 (aq)	0.00	0.00
HF (aq) and $BF_3{:}O(C_2H_5)_2$	0.10	0.0014
KF (aq)	0.40	0.0057
NaF (aq)	0.42	0.0060
SbF_3 (aq)	0.63	0.0090
$C_2F_3Cl_3$	0.67	0.0096

[a] These values are 36 percent smaller than those previously listed by the author (reference 17), owing to an unfortunate error in magnetic field calibration. H. S. Gutowsky and C. J. Hoffman, Phys. Rev. 80, 110 (1950), have checked the F^{19} shifts reported here and their values are in essential agreement with those given above. They also give the magnetic shielding for several other F^{19} compounds.

TABLE IV. Resonance field separations for F^{19} compounds at two different values of applied field strength.

Compounds compared	Separation at 6975 gauss	Separation at 2500 gauss	Ratio
SbF_3 and BeF_2	0.63 gauss	0.23 gauss	2.8
SbF_3 and HF	0.53	0.22	2.4
$C_2F_3Cl_3$ and HF	0.57	0.26	2.2

and those in which a valency of 5 is exhibited. In the former compounds, such as PCl_3 and PBr_3, only the three $3p$ orbitals of the phosphorous are used in bond formation. When a valency of five is exhibited, however, as in $POCl_3$ and H_3PO_4, not only the three $3p$ orbitals are used but also the $3s$ orbital and one $3d$ orbital. Hence, a very different electronic structure would be expected and a resulting large difference in the second-order paramagnetism. It is noted from Table V that the P^{31} resonances in P_2O_5 (aq) and $H_4P_2O_7$ (aq) come at exactly the same position as in H_3PO_4. This is confirmation of the fact that these compounds do not retain their molecular form in aqueous solution but decompose to H_3PO_4.

V. THE MAGNETIZATION FIELD OF PARAMAGNETIC IONS

To obtain an expression for H'', the component of H_N due to a given concentration of paramagnetic ions added to the sample, we follow the method introduced by Debye[34] for electric dipoles. It is assumed that the applied field H_0 is homogeneous over the sample volume and that the sample container is in the shape of an ellipsoid so that the magnetization[35] $M=\chi H_0$, created by the paramagnetic ions, will be homogeneous. The field H'' may be thought of as consisting of three components

$$H''=H_1+H_2+H_3. \tag{8}$$

The field H_1 (not to be confused with the r-f field H_1), is ascribed to the induced magnetic poles on the surface of a small hypothetical sphere[36] with its center at the nucleus. This is the so-called Lorentz or cavity field and has the value $(4\pi/3)M$. The field H_2 is the familiar demagnetizing field, defined by $H_2=-\alpha M$, where α is the demagnetizing factor.[37] It might be expected that the remaining field H_3 due to those paramagnetic ions inside the hypothetical sphere would be exactly zero, since the interaction energy $\boldsymbol{\mu}\cdot\mathbf{H}_3$ of the nuclear magnetic moment μ with this field involves an isotropic averaging of $(-1+3\cos^2\theta)$ over the volume of the sphere. However, it is found experimentally that H_3 may differ significantly from zero; anticipating this, we define an "interaction factor" $q=H_3/M$. The full expression for H'' hence becomes

$$H''=[(4\pi/3)-\alpha]M+qM. \tag{9}$$

Two sample shapes were used experimentally: a spherical sample for which $\alpha=4\pi/3$ and an "infinite" transverse cylindrical sample for which $\alpha=2\pi$. This was done mainly as a check on the validity of Eq. (9), since, if a significantly different value of q is found for the two sample shapes, all other conditions being the same, the reasoning leading to Eq. (9) would have to be re-examined.

The first column of Table VI lists those paramagnetic ions used in the experiments. The second column lists

TABLE V. Differences in the magnetic shielding field for some P^{31} compounds. $H_0=5800$ gauss. The resonance in H_3PO_4 (aq) was observed at the highest value of applied magnetic field.

Compound	$\Delta H'$ (gauss)	$\Delta H'/H_0$ (%)
H_3PO_4 (aq); $H_4P_2O_7$ (aq); and P_2O_5 (aq)	0.00	0.00
$POCl_3$	0.05	0.0009
PCl_3	1.18	0.020
PBr_3	1.30	0.022

TABLE VI. Experimental values of μ_{eff} for paramagnetic ions used in experiments.

Paramagnetic ion	Experimental μ_{eff} (solutions) M.I.T.	Van Vleck
Ni^{++}	3.26	3.23
Co^{++}	5.00	4.6–5.0
Cu^{++}	1.82	1.8–2.0
Fe^{++}	5.45	5.33
Mn^{++}		5.2–5.96
Cr^{+++}		3.68–3.86
Er^{+++}		9.4–9.6

$\mu_{eff}=(3\chi kT/N\beta^2)^{\frac{1}{2}}$ (T is the absolute temperature, N the number of paramagnetic ions per cc, and β the Bohr magneton), calculated from susceptibilities measured at M.I.T. for several of the saturated paramagnetic solutions used.[38] In the third column are listed experimental values of μ_{eff} as given by Van Vleck.[39] The agreement between the M.I.T. values and those given by Van Vleck is so satisfactory that confidence was felt in using the average values of Van Vleck for the remaining solutions in Table VI where the susceptibility was not measured at M.I.T. From μ_{eff} the magnetization M required in Eq. (9) is obtained. It should be mentioned that the field H'' differs from the experi-

[34] P. Debye, Physik. Z. **13**, 97 (1912).

[35] The rigorous definition of M is $M=\chi H_i$, where H_i is the field inside the sample. However, the difference between H_i and H_0 is negligible, since paramagnetic permeabilities are so nearly unity.

[36] The radius of this sphere should be small on a macroscopic scale but large enough so that the nucleus at its center will experience negligible fluctuations in field owing to thermal movement of the ions outside of the sphere.

[37] Actually, the magnetization is not quite homogeneous, since the sample to which paramagnetic ions were added was necessarily in a position where a gradient of the magnet field existed. Thus, there would be a "magnetization charge" per unit volume as well as the magnetic poles on the surface which we have considered. It was determined experimentally, however, that this effect was negligible, the resonance shifts being the same whether the sample was in its normal position or shifted to a position of zero-field gradient.

[38] The author is greatly indebted to Mr. O. J. VanSant, Jr. for the measurement of these susceptibilities.

[39] J. H. Van Vleck, reference 19, pp. 243 and 285.

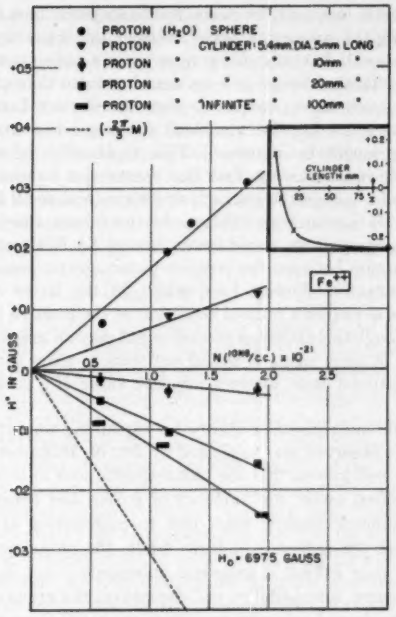

FIG. 6. Illustration of the dependence of H'' on sample shape. $FeCl_2$ added to H_2O. Proton resonance.

mentally measured resonance shift by the small amount which the external magnetization field from the paramagnetic ions in the variable sample contributes to the total field at the standard sample. Thus, for the dimensions used, it was calculated that there was an opposing field of $0.04M$ at the standard sample when the variable sample was spherical and $0.14M$ when the variable sample was cylindrical.

To determine the length of the transverse cylinder needed to approximate an infinite cylinder, H'' was measured *vs* concentration of Fe^{++} ions for a series of cylinders of increasing length. The results are shown in Fig. 6. From the insert which is a plot of H'' *vs* cylinder length for a concentration $N=2\times10^{21}$ ions/cc, it is seen that the 100-mm cylinder closely approximates the infinite case. This length was, subsequently, used, care being taken that the cylinder was placed in the sample holder so that the r-f coil was at the center of the cylinder length. The dotted line in Fig. 6 (also in Figs. 7, 8, and 9), represents the field H'' for an infinite cylinder if the interaction factor q were zero. For a spherical sample H'' would be always zero if q were zero. Hence, it is seen that for Fe^{++} ions in H_2O the proton q value is positive—the measured q being $+1.1$ for both the spherical and "infinite" transverse cylindrical samples.

Figure 7 illustrates what was found in general; that for a given paramagnetic ion, the field H'' depends strongly on the resonating nucleus. Another finding illustrated in Fig. 7 is that H'' is the same, within the experimental error, for the proton and deuteron resonances in water. It would, of course, be expected that the magnetization field shift for two isotopes in the same chemical compound would be identical. The proton and deuteron isotopes furnish a good test of this in that the radiofrequencies for resonance in the same magnetic field H_0 are considerably different (29.5 and 4.5 Mc, respectively, in a field $H_0=6975$ gauss), so that if the magnetization field were in any way influenced by the r-f field, this should be observed.

Figure 8 illustrates two findings. First, as shown by the fluorine resonance shifts in HF and SbF_3, we see that H'' may depend not only on the resonating nucleus but also on the chemical compound containing the nucleus. (The shift shown in Fig. 8 for the fluorine resonance in HF on addition of Co^{++} ions was the largest of any observed.) Second, Fig. 8 confirms the fact that the field H'' is linearly proportional, within experimental error, to the applied field H_0 for a given concentration of paramagnetic ions. Thus, the ratio of the field strengths is 3.0, and the ratio of H'' at the two fields is 2.7.

Figure 9 shows one of the few cases in which a negative interaction factor was measured.

A complete summary of the experimental results is given in Table VII as a tabulation of interaction factors.

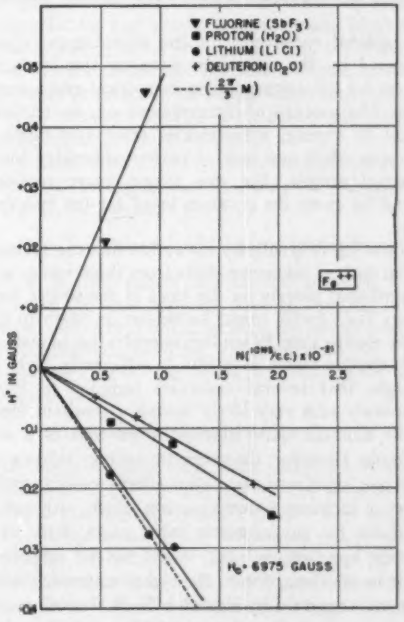

FIG. 7. Illustration of the dependence of H'' on resonating nucleus. $FeCl_2$. "Infinite" cylinder.

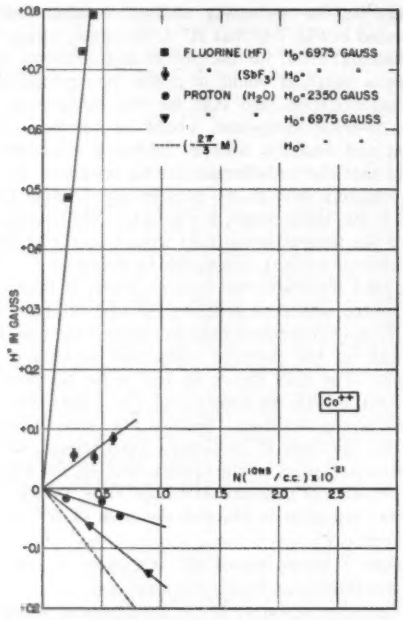

FIG. 8. Illustration of the dependence of H'' on chemical compound containing resonating nucleus and of the linear dependence of H'' on applied field H_0. $CoCl_2$. "Infinite" cylinder.

The general consistency of the experimental data is indicated by the agreement between the interaction factors for the corresponding cylindrical and spherical cases. The amount of disagreement can be attributed partly to general experimental error and partly to meniscus effect and lack of perfect sphericity for the spherical sample. For this reason, more confidence should be given the q values listed for the cylindrical case.

It was felt originally by the author that the deviations in the nuclear resonance shifts from those which would be predicted naively on the basis of the simple Debye theory (i.e., $q=0$), might be similar in origin to those in the electric case. When the concentration of molecules with electric dipole moments is sufficiently high, it is thought that several molecules combine to form a temporary unit very likely having a resultant electric dipole moment quite different from that of a single molecule. However, the magnetic analogy is not a very good one, since such association effects would constitute a sort of incipient ferromagnetism which, although not unknown for paramagnetic salts, particularly at extremely low temperatures, would not be expected to occur in solutions, due to the higher magnetic dilution.

It was suggested by Professor E. M. Purcell (private communication), that there might be a spin-dependent, electron exchange process occurring between the paramagnetic ions and the normally diamagnetic ions containing the resonating nuclei, whence the latter would for a small fraction of the time be in a paramagnetic state. This exchange process would have to take place at a much higher frequency than the nuclear Larmor frequency, otherwise abnormal resonance line broadening would be observed. This explanation gives a simple reason for the fact that interaction factors are large for a negative ion such as fluorine and small for a positive ion such as lithium. In the former case, the exchange process would be facilitated by electrostatic attraction between the positive paramagnetic ions and the negative fluorine ions, while, in the latter case, there would be a mutual repulsion of the positive ions. Although this exchange process might play an important part in some cases, it would not seem to allow for the exceptional cases where a negative value of q is measured.

The most plausible theory for explaining the type of shifts observed was suggested by Dr. N. Bloembergen. It is well known that the paramagnetic ions in crystals are often under the influence of strong and generally asymmetric electric fields due to neighboring atoms. Under the influence of these fields, the paramagnetic ions may exhibit a magnetic anisotropy; that is, the measured susceptibility will depend on the orientation of the crystal axis with respect to the applied magnetic field. Bloembergen suggested that there might be a

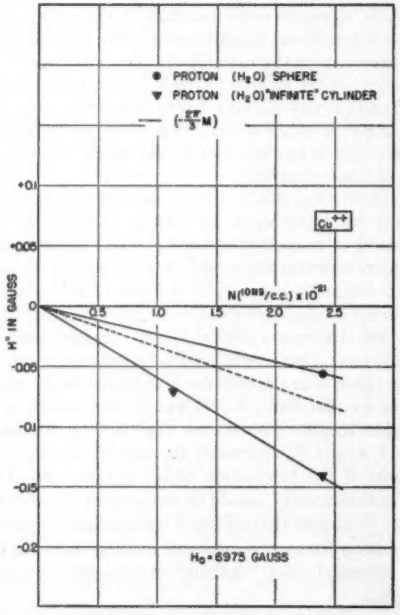

FIG. 9. Example of a negative interaction factor. $CuCl_2$ added to H_2O. Proton resonance.

similar directional effect on the g-factors of paramagnetic ions in liquids. A paramagnetic ion in a liquid is subjected to strong varying electric fields. These are responsible for the quenching of the orbital momentum, so that the effective magnetic moment of the ion is close to the "spin only" value. Although the average electric field in the liquid will have spherical symmetry, the field at any instant will deviate from the average. From an analysis made on this basis,[40] defining g as the value obtained from susceptibility measurements, i.e., $g=\mu_{\text{eff}}/[S(S+1)]^{\frac{1}{2}}$, the following expression for q is obtained:

$$q=(16\pi b^3/45a^3)(g_{\parallel}^2-g_{\perp}^2)/g^2, \qquad (10)$$

where $g_{\parallel}$ and $g_{\perp}$ are effective g values of the paramagnetic ion depending on whether the instantaneous angle between the axis of the internal electric field acting at the paramagnetic ion and the magnetic field H_0 is 0° or 90°, and b^3/a^3 is a rather crudely introduced geometrical factor, the magnitude of which depends on the closeness of approach between the ions of the liquid which contain the resonating nuclei and the added paramagnetic ions. Although Eq. (10) would clearly not offer any type of quantitative check of the experimental q values, it would seem that $g_{\parallel}^2-g_{\perp}^2$ for a liquid would have a value comparable to those observed in crystals. Also from Eq. (10), one would expect that the q value for a positive ion would be smaller than the value for a negative ion because of the difference in the average distance of approach in the two cases. Lastly, this theory would account for negative as well as positive q values, depending only on the relative magnitudes of $g_{\parallel}$ and $g_{\perp}$.

A confirmation of this theory is provided by the following experimental finding of Proctor and Yu.[18] For a solution of NH_4NO_3, without paramagnetic ions, the N^{14} resonance from the NH_4^+ complex was found to come at a higher magnetic field than the N^{14} resonance from the NO_3^- complex (for a fixed frequency). On addition of Mn^{++} ions the difference in field between the two resonances is found to increase. This is best explained by assuming that the q value for the NO_3^- complex is greater than that for the NH_4^+ complex as would be expected from the results given above.

VI. DISCUSSION: ATTAINABLE PRECISION IN NUCLEAR MOMENT MEASUREMENTS

Now that the various factors influencing the positions of nuclear resonances have been considered, an attempt will be made to analyze each factor as to its effect on the attainable precision in the measurement of nuclear moments by the resonance absorption and nuclear induction methods. Since the first successful application of these two methods in 1945, many nuclear moment ratio measurements have been published; the quoted precision ranges from about 1 part in 10^2 to 1 part in 10^6.

[40] N. Bloembergen and W. C. Dickinson, Phys. Rev. 79, 179 (1950).

TABLE VII. Experimental values of the interaction factor q for "infinite" transverse cylindrical and spherical sample shapes.

Paramagnetic ion	Resonating nucleus	Chemical compound	q value cylinder	q value sphere
Ni^{++} (Cl_2)	H^1	H_2O	−1.0	−0.1
	F^{19}	SbF_3 (aq)	2.3	2.2
	Li^7	LiCl (aq)	0.9	
Ni^{++} (SO_4)	H^1	H_2O	0.0	0.0
	F^{19}	SbF_3 (aq)	3.5	2.5
	Li^7	LiCl (aq)	0.3	
Co^{++} (Cl_2)	H^1	H_2O	0.7	0.9
	F^{19}	SbF_3 (aq)	3.1	2.3
	F^{19}	HF (aq)	19.0	
Cu^{++} (Cl_2)	H^1	H_2O	−1.8	−1.5
Fe^{++} (Cl_2)	H^1	H_2O	1.1	1.1
	D^2	D_2O	1.2	
	F^{19}	SbF_3 (aq)	5.1	4.0
	Li^7	LiCl (aq)	0.0	
Mn^{++} (Cl_2)	Li^7	LiCl (aq)	0.5	
Cr^{+++} (Cl_3)	H^1	H_2O	−3.0	
	F^{19}	HF (aq)	6.0	
Er^{+++} (Cl_3)	H^1	H_2O	1.1	

Considering the evidence accumulated in the present paper, it would appear that the precision indices quoted in some of these measurements have been unjustifiably high. There is little doubt, however, that the resonance absorption and nuclear induction methods will replace all others for the high precision measurement of nuclear moments, and it is for this reason that the different factors which influence the precision of these measurements must be carefully noted and taken into account.

We first consider the effect of the atomic diamagnetic shielding correction on the precision to which the ratio of the nuclear moment μ_x to the proton moment μ_p can be measured. Setting $\mu_x/\mu_p=M$, $\omega_x/\omega_p=\Omega$, $H_x'/H_0=X$, and $H_p'/H_0=P$, we have

$$M=(I_x/I_p)\Omega_0=(I_x/I_p)\Omega_m(1-P)/(1-X), \qquad (11)$$

where Ω_0 is the ratio of the Larmor precession frequencies in the same magnetic field H_0, and Ω_m is the measured ratio which will differ from the former because of the diamagnetic shielding. Differentiating Eq. (11), remembering that X and P are small compared with unity, gives closely

$$\Delta M/M=(\Delta\Omega_m/\Omega_m)+\Delta(X-P). \qquad (12)$$

By employing a simple heterodyne technique in which a small beat frequency and one of the original frequencies are measured, rather than the two original frequencies, Ω_m can always be determined to a precision of 1 part in 10^5 or better. This assumes that the frequency-measuring meter is limited in precision to about 1 part in 10^4 as is usually the case. With more elaborate technique, it is possible to measure a frequency ratio to a precision of 1 part in 10^6 to 1 part in 10^7. Hence, we

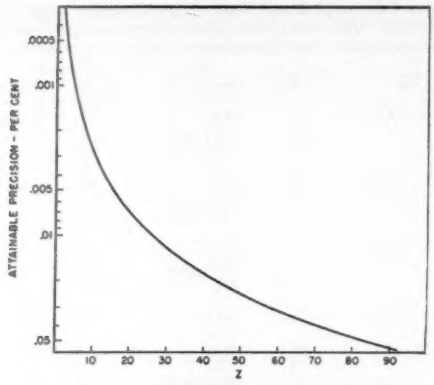

FIG. 10. Attainable precision in a nuclear moment ratio measurement as limited by the accuracy to which the atomic diamagnetic correction is known.

assume that the first term on the right side of Eq. (12) can always be neglected as compared with the second term. From an analysis of the accuracy of Hartree wave functions, it was estimated that values of H'/H_0 computed from these functions can be trusted to 5 percent.[15] Considering the agreement between the computation of Ramsey and that of Hylleraas and Skavlem for the shielding constant H_p'/H_0 of molecular hydrogen, it can also probably be given a maximum uncertainty of 5 percent.[41] Since $P \ll X$ for all but the lightest elements (e.g., $X/P=11$ for ${}_5B$), Eq. (12) reduces to

$$\Delta(\mu_z/\mu_p)/(\mu_z/\mu_p) \cong 0.05 H_z'/H_0. \qquad (13)$$

Figure 10 is a plot of Eq. (13) and gives the *limiting* precision attainable in a measurement of μ_z/μ_p considering the present accuracy to which the atomic diamagnetic correction can be quoted.[42]

An estimate will next be made of the largest concentration of paramagnetic ions that can be used in a ratio measurement if the resulting shift of resonances is to be neglected. For this purpose, we may assume conservatively that no resonance shifts will exceed the extraordinarily large shift found for the F^{19} resonance in HF on addition of Co^{++} ions (Fig. 8). This shift was 1 gauss in an applied field $H_0=7000$ gauss for a concentration $N(Co^{++})=0.5\times10^{21}$ ions/cc. Doubling this, to take into account the possibility that the shift occurring in the one nuclear species is of opposite sign to that in the other, gives a total shift of 0.028 percent for a 0.83-molar paramagnetic solution. Hence, for a measurement with precision 0.01 percent, a molarity of 0.3 would allow a shift equal to the precision limit. We might place as an upper limit a shift equal to $\frac{1}{3}$ the precision limit. Hence,

precision = 0.01 percent: maximum allowable paramagnetic molarity of sample = 0.1 molar.

This allows a large safety factor, since most of the observed shifts were only of the order of $\frac{1}{10}$ to $\frac{1}{3}$ of the shift assumed in the above calculation.

Unfortunately, the effect of second-order paramagnetism on the precision of a nuclear moment measurement cannot be predicted in advance. It is necessary to compare the nuclear resonance position in several different molecular compounds containing the nucleus being measured. Even if no shifts are observed, it cannot be concluded with certainty that the second-order paramagnetism is zero for those compounds. However, it is improbable that this field would be the same in several different molecules—particularly if the atom containing the resonating nucleus did not exhibit the same valency in all the molecules examined. For atoms such as Li, Na, and Al, where no second-order paramagnetic shifts were observed for a series of compounds, it is safe to assume that the nuclei are contained in simple ions, so that the atomic diamagnetic correction may be directly applied. Of course, this is also the case when the resonating nucleus is contained in a free atom (e.g., He^3, $Xe^{129, 131}$).

For current theoretical considerations regarding nuclear structure it is important that very precise values of the nuclear moment ratios of isotopic pairs be available. Fortunately, it is these ratios which can be measured most precisely by the resonance method. When both isotopes are contained in the same chemical compound, the magnetic shielding field will be the same for both nuclei.[43] It has been shown in the present paper that the shift of nuclear resonance due to added paramagnetic ions is closely the same for an isotopic pair (Fig. 7). Hence, it would seem that the nuclear moment ratio of an isotopic pair can be measured to a precision limited only by the resonance line widths and by the attainable precision in the measurement of the frequency ratio.[44]

An individual nuclear moment, of course, cannot be

[41] If H_2O or mineral oil is used for the proton standard, we must assume that the comparison with the proton resonance in molecular hydrogen has been made.

[42] For the heavy elements ($Z \gtrsim 70$), the relativity effect makes it impossible to attach a 5 percent accuracy to the diamagnetic correction. The numerical coefficient in Eq. (13) would, hence, be slightly higher in this region. (See reference 15.)

[43] W. G. Proctor and F. C. Yu (private communication), have confirmed the validity of this statement for the isotopic pairs $N^{14,15}$ and $Cl^{35,37}$.

[44] Small discrepancies exist between some recent high precision measurements of the deuteron-proton moment ratio. Whether they have physical significance or are due to experimental causes has not yet been ascertained. A further investigation is now in process by T. Wimett at M.I.T.

quoted to a higher precision than that to which the standard moment used in the experiment is known. Recent measurements of the proton moment, involving different physical principles, give:

$$\mu_p = (1.4100 \pm 0.0002) \times 10^{-23} \text{ ergs/gauss}^{45}$$
$$\mu_p = (15.2106 \pm 0.0007) \times 10^{-4} (e\hbar/2mc)^{46}$$
$$\mu_p = (15.2100 \pm 0.0002) \times 10^{-4} (e\hbar/2mc)^{47}$$
$$\mu_p = 2.79273 \pm 0.00006 (e\hbar/2M_p c).^{48}$$

All of these values include the diamagnetic correction for atomic hydrogen ($H'/H_0 = 1.8 \times 10^{-5}$), although the proton was contained in a molecule (H_2O, NaOH, mineral oil, and H_2O, respectively). This is probably of no importance considering the precision of the first value of μ_p, but the last three values will be improved when the actual molecular shielding correction is determined by a comparison with H_2. §

I wish to express my appreciation to Professor F. Bitter for the encouragement and guidance he has given during this investigation. Thanks are given to Professor N. F. Ramsey and Dr. J. Benedict for the privilege of several valuable discussions.

[45] Thomas, Driscoll, and Hipple, Phys. Rev. **78**, 787 (1950).
[46] H. Taub and P. Kusch, Phys. Rev. **75**, 1481 (1949).
[47] J. H. Gardner and E. M. Purcell, Phys. Rev. **76**, 1262 (1949).
[48] Sommer, Thomas, and Hipple, Phys. Rev. **80**, 487 (1950).

§ *Note added in proof:* This comparison has been made recently by H. A. Thomas, Phys. Rev. **80**, 901 (1950). On the basis of Ramsey's calculated magnetic shielding value of 2.68×10^{-5} for H_2, he obtains 2.62×10^{-5} for H_2O and 2.84×10^{-5} for mineral oil (Petrolatum U.S.P.—Light). Also, H. S. Gutowsky and R. E. McClure, Phys. Rev. (to be published), have measured these shifts. Again based on Ramsey's value for H_2, they obtain 2.71×10^{-5} for H_2O and 3.05×10^{-5} for mineral oil (Nujol). The discrepancy between the H_2O values is not appreciably greater than the probable errors involved in the two measurements. However, Gutowsky (private communication) finds that the greater part of the difference between the mineral oil values is real and due to the different types of mineral oil used. Using an average value for the H_2O and mineral oil corrections the last two values of μ_p given above become, respectively, 15.2101×10^{-4} and 2.79275.

PHYSICAL REVIEW VOLUME 81, NUMBER 5 MARCH 1, 1951

An Increase of the Primary Cosmic-Ray Intensity Following a Solar Flare*

MARTIN A. POMERANTZ
Bartol Research Foundation of the Franklin Institute, Swarthmore, Pennsylvania

(Received October 24, 1950)

An increase of 15.4±4.3 percent has been detected in the intensity of cosmic rays at altitudes between 95,000 and 100,000 feet, occurring approximately 19 hours after the commencement of the outstanding solar flare of May 10, 1949. The observations were conducted with a quadruple-coincidence counter train inclined at a zenith angle of 60°, and containing an interposed absorber of 1 cm of Pb. Complications introduced by atmospheric absorption, possible directional asymmetry, and multiplicative effects preclude a precise evaluation of the increase in terms of absolute primary particle intensity. The effect of the particles emitted by the sun during the chromospheric eruption does not manifest itself at altitudes below approximately 55,000 feet.

I. INTRODUCTION

SUDDEN increases in the cosmic ray intensity coincident with the occurrence of a solar flare have been registered on four occasions by instruments operating near sea level or at relatively low altitudes.[1-6] From the variation in the effect with altitude and latitude, as recorded by Compton-Bennett ionization chambers, which were completely shielded by 12 cm Pb, it was concluded[6] that the largest of these increases was attributable to the nucleonic component produced by relatively low energy charged primary particles accelerated by some solar mechanism.

It has been reported[7] recently that the rate of production in photographic emulsions of stars having 3 to 8 prongs exceeded the normal value at an altitude of 95,000 feet by 50±13 percent during the period 18:48–22:30 GMT on May 11, 1949, about 23 hours following the occurrence of the outstanding solar flare[8] of May 10, 1949. This bright chromospheric eruption, of importance 3+, the greatest possible on the scale of the International Astronomical Union, commenced at 20:00–20:03 GMT. Solar noise radiometer, ionospheric, and magnetic field measurements had all returned to normal before 22:20 GMT May 10, 1949, at which time the flare had subsided, but not disappeared, on

* Assisted by the joint program of the ONR and AEC.
Extract from a dissertation submitted to the Graduate Council of Temple University in partial fulfillment of the requirements for the degree of Doctor of Philosophy.
[1] S. E. Forbush, Phys. Rev. **70**, 771 (1946).
[2] A. Duperier, Proc. Phys. Soc. (London) **57**, 473 (1945).
[3] D. W. N. Dolbear and H. Elliott, Nature **159**, 58 (1947).
[4] H. V. Neher and W. C. Roesch, Revs. Modern Phys. **20**, 350 (1948).
[5] D. C. Rose, Phys. Rev. **78**, 181 (1950).
[6] Forbush, Stinchcomb and Schein, Phys. Rev. **79**, 501 (1950).
[7] Lord, Elston, and Schein, Phys. Rev. **79**, 540 (1950).
[8] A. H. Shapley and R. M. Davis, Science **110**, 159 (1949).

TABLE I. Flight summary. Interposed absorber 1.0 cm of Pb. Geomagnetic latitude 52°N.

Date	Ceiling altitude (feet)	Time of arrival at ceiling (GMT)
April 12, 1949	117,000	15:04
May 11, 1949	110,000	15:14
January 5, 1950	110,000	15:54

H_α spectroheliograms.[9] An intense magnetic storm began at 06:24 GMT on May 12.

During an extensive program of investigation of the directional distribution of cosmic-ray intensity at very high altitudes,[10] a balloon flight was conducted in the interval between the occurrence of the solar flare and the launching of the aforementioned[7] flight which indicated the increased nuclear disintegration intensity.

II. EXPERIMENTAL ARRANGEMENT

The instrument was a standard quadruple-coincidence counter train of the type described previously[11] (designated apparatus *A* in reference 11) inclined at a zenith angle of 60°, and containing an interposed absorber of 1 cm Pb. The flight reached a maximum altitude of 110,000 feet at 15:14 GMT, 19½ hours after the onset of the solar flare. A similar instrument had been released one month earlier, and a third check flight was subsequently conducted in accordance with the observation that the counting rate, near the "top of the atmosphere," of the instrument released on May 11 was higher than that of the previous ascent.

The tape records of the three flights summarized in Table I have just been analyzed, and the distinct increase in the primary cosmic-ray intensity during the period following the solar flare is apparent in Fig. 1. The solid circles represent averages of all data obtained during both ascent and descent of two flights on normal days, whereas the square points represent data based on the flight conducted during the post-flare period. In each case, points obtained during the ascent and descent are in good agreement. Furthermore, the data from the flights of April 12, 1949, and January 5, 1950, were in agreement within the expected statistical uncertainties. No corrections or normalizations have been applied to the data. The instruments were identical within a statistical uncertainty of less than 1 percent, as may be seen in the ground-run summary of Table II. A statistical analysis of the counts obtained at one-minute intervals in each of the flights revealed that in each case the distribution was normal.

The magnitude of the effect near the top of the atmosphere may best be determined from a comparison of the quadruple-coincidence rates based upon all counts

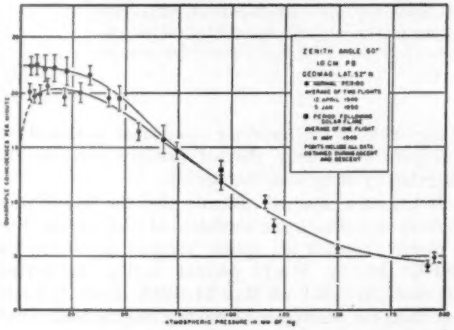
ZENITH ANGLE 60°
1.0 CM Pb
GEOMAG. LAT. 52° N
AVERAGE OF TWO FLIGHTS
10 APRIL 1949
5 JAN 1950
PERIOD FOLLOWING SOLAR FLARE
AVERAGE OF ONE FLIGHT
11 MAY 1949
FLIGHTS INCLUDE ALL DATA OBTAINED DURING ASCENT AND DESCENT
QUADRUPLE COINCIDENCES PER MINUTE
ATMOSPHERIC PRESSURE IN MM OF Hg

FIG. 1. *Intensity vs altitude* curves for cosmic radiation capable of penetrating 1 cm of Pb, and passing through the counter train at a zenith angle of 60°, at geomagnetic latitude 52°N, during normal and disturbed periods, respectively. The indicated uncertainties represent statistical standard deviations.

TABLE II. Ground run summary. No interposed absorber. Swarthmore, Pennsylvania, altitude 296 feet.

Flight date	Ground counting rate (counts/min)
April 12, 1949	0.913±0.010
May 11, 1949	0.918±0.013
January 5, 1950	0.925±0.012
Average	0.918±0.007

TABLE III. Average counting rates based upon all data obtained during three flights in the pressure interval 4.8 to 10.0 mm of Hg.

Date	Counting rate (counts/min)
April 12, 1949	18.5±0.7
January 5, 1950	20.4±0.7
Average of above	19.5±0.5
May 11, 1949	22.5±0.7

recorded in a particular pressure interval during the disturbed and normal periods respectively. Table III lists the average value for each flight in the region between 95,000 feet and 110,000 feet. The uncertainties indicated are statistical standard deviations. The increase during the disturbed period amounts to 15.4 ±4.3 percent. From the *statistical* point of view, the odds against the fortuitous observation of such an increase are roughly 6000 to 1. Furthermore, the value of the difference is reduced only slightly, if the interval over which the averages are taken is increased by an extension of the lower altitude limit.

The aforementioned magnitude of the effect is regarded as a conservative lower limit. As may be seen in Table III, the flight on January 5, 1950 yielded slightly higher counting rates (near the top of the atmosphere only) than that of April 12, 1949, although the difference is not inconsistent with expected statistical fluctuations. If only the latter flight, which chro-

[9] H. W. Dodson, Astrophys. J. 110, 382 (1949).

[10] M. A. Pomerantz, unpublished. A preliminary account of some of these experiments was given in abstract form—Phys. Rev. 75, 1335 (1949).

[11] M. A. Pomerantz, Phys. Rev. 75, 1721 (1949); see also 75, 69 (1949); 77, 830 (1950).

nologically is much closer to the flight released during the disturbed period, is considered, the increase is, in fact, enhanced.

III. DISCUSSION

It is not possible to express the increase in terms of absolute primary particle intensity for several reasons. In the first place, the counter trains were inclined at an angle of 60° with the vertical, as a consequence of which particles propagating their original direction traverse an air path corresponding to twice the pressure at the point of observation. Thus, the effective atmospheric absorber thickness for such a primary is about 10 g/cm². In addition, the interposed lead and counter walls amount to 16 g/cm². This effectively attenuates the enhanced incident beam to an extent contingent upon the energy distribution upon arrival at the earth's atmosphere of the additional group of particles emitted by the sun during the flare. On the other hand, multiplicative effects in the atmospheric layer above the detecting instrument would amplify the intensity.

If the directional distribution of the particles emitted during the solar eruption is not isotropic at the top of the atmosphere (a possibility which seems quite reasonable), then the actual effect is much greater than is indicated by the measurement. The counter train rotates freely about a vertical axis, and the results actually represent an average over-all azimuths, at a specific zenith angle. Hence, a very great increase in a favored direction would be smeared out.

No measurable change was observed with ionization chambers or counters at ground stations[12] while any of these balloon flights were aloft. Statistical considerations preclude an accurate determination of the atmospheric depth to which the disturbance was propagated. At altitudes lower than 55,000 feet, however, the points representing the normal and post-flare periods ostensibly overlap.

The counting rate of a single G-M counter was observed by Johnson and Korff[13] to remain constant within 2 percent at the 20-km level (about 42 mm of Hg), on July 27, 1938, for a period of 7 hours, during which a solar flare of intensity 2 occurred. Even if every flare were effective in increasing the primary cosmic-ray intensity, (a matter which remains to be investigated), the presence of particles having the requisite energy for penetration even to this depth, and with sufficient intensity to be detectable above the extremely high soft component background rate characteristic of a single counter, may be a relatively infrequent phenomenon.

Comparison of the data of Lord, Elston, and Schein[7] with the present results, (on the questionable assumption of an isotropic distribution and constancy during the period between 15:30 GMT and 18:50 GMT on May 11, 1950), reveals that the increase in the rate of production of nuclear disintegrations is 3 ± 1 times as great as that of the charged-particle intensity. Of course, it must be remembered that a substantial fraction of the stars are produced by neutral particles.

The time lag which ensues between the solar eruption and the arrival at the earth of charged particles emitted by the sun suggests a slowly acting mechanism of acceleration, rather than the direct action of Menzel-Salisbury[14] low frequency electromagnetic waves originating in the extreme outer edge of the solar corona, as postulated by McMillan.[15]

Grateful acknowledgment is made for the continued sponsorship by the National Geographic Society of certain phases of the program of cosmic-ray investigations during the course of which these experiments were performed.

Note added in proof: Previously available information (Table I, reference 8) had indicated a return to normalcy before 22:20 GMT on May 10, 1949, of all the observed solar characteristics. In a search for relationships between cosmic-ray and solar phenomena, we have just examined the records of measurements of solar noise characteristics at 205 Mc obtained by the Cornell University Radio Astronomy project.† Midday observations on May 11, 1949, averaged over a period of two hours and centered about local noon (1700 GMT, and very close to the time of the balloon flight reported here) revealed the following characteristics:

(1) Base level = 10. (Ratio of average minimum power radiated by the sun during averaging period to the average power radiated by the sun when it is very quiet).

(2) Relative number of bursts = *C*, the highest rating, denoting large number of bursts per hour (momentary increases in solar radiation, the time between significant increase and significant decrease being less than three seconds).

(3) Burst distribution in time = *X*, indicating moderate tendency toward burst grouping.

(4) Amplitude of bursts = 1–2 times average base-level (average amplitude of large bursts during averaging period).

Intensities of this magnitude are relatively rare. For example, of 264 observations tabulated during 1949 only four exceeded the aforementioned base level (three being on successive days), four more were higher than 8.0, whereas 230 were less than 3.0. On April 12, 1949, the base level value was 1.3 and there were no bursts (code notation 1.3*Q*). No solar noise observations were made on January 5, 1950, the date of the other normal flight, but protracted periods before and after were characterized by minimum activity (1.0*Q*).

This is the first instance of a simultaneous correlation between a solar phenomenon and the cosmic-ray intensity near the top of the atmosphere. Although any generalization based upon a single observation would obviously be premature, the relationship is extremely suggestive, and cooperative efforts now in progress to obtain additional evidence of this nature should be very fruitful.

[12] J. W. Broxon and H. W. Boehner, Phys. Rev. 78, 411 (1950); J. Clay and H. F. Jongen, Phys. Rev. 79, 908 (1950); S. E. Forbush (private communication); D. C. Rose (private communication).

[13] T. H. Johnson and S. A. Korff, Terr. Mag. 44, 23 (1939).

[14] D. H. Menzel and W. W. Salisbury, Nucleonics 2, 67 (1948).

[15] E. M. McMillan, Phys. Rev. 79, 498 (1950).

† C. R. Burrows, private communication (November, 1950).

Radioactivity of Ag^{111}, Cd^{111}, In^{111}, and Sn^{111}

C. L. McGinnis
Department of Physics, University of California, Berkeley, California
(Received November 7, 1950)

By considering the 111-isobars as a unit it has been possible to specify the spin and parity of the ground states of Ag^{111}, Cd^{111}, In^{111}, and Sn^{111}, and of four excited states of Cd^{111}. The characteristics of the transitions between these levels are given. The electron spectra associated with a 5-hr In^{110}, 4.2-hr In^{109}, and 50-min In^{108} are also given.

I. INTRODUCTION

THE 111 isobars have been separately studied by many investigators.[1] Here, they are considered as a unit with the result that it has been possible to characterize their disintegration scheme uniquely and, in particular to make a definite assignment of spin and parity to the several states.

II. THE ISOBARS OF MASS NUMBER 111

Ag^{111}

This activity was first observed[2] in the silver fraction from palladium bombarded with deuterons. It was assigned to Ag^{111} and characterized by a 7.5-day half-life with 0.8 Mev β^-. Subsequently, the maximum beta-energy of 1.06±0.03 Mev was spectrographically measured.[3] By absorbing $\beta\gamma$-coincidences Storruste[4] detected a 0.33-Mev γ-ray occurring in 6.5 percent of the disintegrations. More recently the photoelectric spectrum[5] has shown the presence of 340±2- and 243±2-kev π-rays in the ratio 8:1 and a complex β^- spectrum. Johansson gives 7.50±0.12 days as the half-life. We have produced Ag^{111} by the reaction $Ag(\alpha,p\rho)Ag^{111}$.

Cd^{111}

A 50±5-min activity chemically identified as belonging to cadmium was first produced by neutron bombardment of cadmium.[6] X-rays of 1.5 Mev on cadmium excited this activity[7,8] showing that it is an isomer. The capture of thermal neutrons by enriched Cd^{110} assigned the activity[9] to Cd^{111m}. We have also produced it[10] by fast neutron bombardment of enriched Cd^{111} and Cd^{112}, from $Ag(\alpha,pn)$ and $Pd(\alpha,n)$. Our half-life measurement of 48.6±0.3 min agrees with the previously reported value.[8] Spectrographically we found internal conversion electrons from 149- and 247-kev γ-rays, the former highly converted and the latter the same as observed[10] in the decay of In^{111}. By means of delayed coincidences with[11] Cd^{111m} and[12] In^{111} Deutsch and his co-workers measured $8\pm1\times10^{-8}$ sec for the half-life of this latter γ-ray. Hole[13] has also observed the electron spectrum using a rather thick source (10 mg/cm²), and found internal conversion electrons from 146±4- and 235±5-kev γ-rays with K/L ratios of 1.8±0.2 and >10, respectively. From the photoelectric spectrum he estimates that the intensity of the 146 quanta is <10 percent of that of the 235-kev ray, and from this he computes that the former is >92 percent converted and the latter 16±3 percent. Hole found the ratio of the 146 to 235 electrons to be 5.7 and concluded that the former is responsible for the isomeric state.

Slow neutron bombardment of cadmium has failed to reveal the presence of an isomer with a half-life[14] between 10^{-3} and 1 sec.

In^{111}

A 2.7-day indium activity was first produced[15] by bombardment of cadmium with deuterons. Lawson and Cork[16] found this activity to be characterized by two internally converted 172.8±1- and 246.7±1-kev γ-rays with K/L and K/M ratios of 6.6±0.5, 35±10 and 5.6±0.5, 30±10, respectively. From the high intensity of the Cd K x-rays, observed by critical absorption, they concluded that it decays by K-capture. They also set an upper limit to the occurrence of positrons at <0.005 of the electrons. This activity was assigned to mass number 111 by Ag+α excitation functions,[17,18] the threshold being 15±0.5-Mev $\gamma\gamma$-coincidence measurements showed that these two γ-rays are in cascade.[19] By measuring ee, $e\gamma$, and $\gamma\gamma$-coincidences Boehm *et al.*,[20] find α_k and α_L for the 172 and

[1] For a list of references see G. T. Seaborg and I. Perlman, Revs. Modern Phys. **20**, 611 (1948).
[2] J. D. Kraus and J. M. Cork, Phys. Rev. **52**, 763 (1937).
[3] Helmholz, Hayward, and McGinnis, Phys. Rev. **75**, 1469 (1949).
[4] A. Storruste, Phys. Rev. **79**, 193 (1950).
[5] S. Johansson, Phys. Rev. **79**, 896 (1950).
[6] M. Dode and B. Pontecorvo, Compt. rend. **207**, 287 (1938).
[7] J. R. Feldmeier and G. B. Collins, Phys. Rev. **59**, 937 (1941).
[8] M. L. Wiedenbeck, Phys. Rev. **67**, 92 (1945).
[9] M. Goldhaber and C. O. Muehlhause, Phys. Rev. **74**, 1248 (1948).
[10] A. C. Helmholz and C. L. McGinnis, Phys. Rev. **74**, 1559 (1948).
[11] M. Deutsch and W. E. Wright, Phys. Rev. **77**, 139 (1950).
[12] M. Deutsch and D. T. Stevenson, Phys. Rev. **76**, 184 (1949).
[13] N. Hole, Arkiv Mat. Astron. Fysik **36A**, No. 9 (1948).
[14] Holmes, Mei, and Turgel, Phys. Rev. **75**, 889 (1949).
[15] J. M. Cork and J. L. Lawson, Phys. Rev. **56**, 291 (1939).
[16] J. L. Lawson and J. M. Cork, Phys. Rev. **57**, 982 (1940).
[17] D. J. Tendam and H. L. Bradt, Phys. Rev. **72**, 527 (1947).
[18] S. N. Ghoshal, Phys. Rev. **73**, 417 (1948).
[19] Bradt, Gugelot, Huber, Medicus, Preiswerk, and Scherrer, Helv. Phys. Acta **19**, 77 (1945).
[20] Boehm, Huber, Marmier, Preiswerk, and Steffen, Helv. Phys. Acta **22**, 69 (1949).

TABLE I. Experimental results.

Activity	Half-life	γ-ray (kev)	K/L	conv. ϵ^- / 247 ϵ^-	Percent conv.
Cd^{111m}	48.6±0.3 min	149.6±0.3 246±2	1.99±0.3 5.12±0.22	14.5±1.0 <0.014 for any others >100 kev	87±13
In^{111}	2.84±0.03 d	172.1±0.5 246.6±0.7 330±10 93±10	6.6±0.4 5.19±0.01	1.73±0.03 $2.5\pm0.1\times10^{-4}$ $1.3\pm0.5\times10^{-4}$ $<2.5\times10^{-4}$ for any others >100 kev	10.4±0.9 6.0±0.5
		$\beta^+<4\times10^{-4}$ of the electrons ratio transitions 172/247 = 0.97±0.10			
Sn^{111}	35±1 min	1.51±0.03 Mev β^+		$K/\beta^+=2.50\pm0.25$	

247 γ-rays to be 0.081±0.008, 0.009±0.001 and 0.036 ±0.005, 0.006±0.001, respectively, and the ratio of the conversion electrons to be 2.1±0.1. We have observed 2.84±0.03 days for the half-life[3] of In^{111} and have produced this activity from the bombardment of cadmium as well as of silver with alphas. Mallary and Pool[21] report a measurable number of positrons associated with the 2.84-day activity of In^{111}.

Sn^{111}

By the bombardment of enriched cadmium isotopes with α-particles Hinshaw and Pool[22] produced a 35.0±0.5-min positron activity (1.45 Mev by absorption), in the tin fraction and assigned it to Sn^{111}.

III. EXPERIMENTAL RESULTS

The experimental results are summarized in Table I. The electron spectra were investigated with a magnetic lens spectrometer similar to one described by Siegbahn.[23] In computing the K/L ratios and the ratios of the conversion electrons the areas under the lines were used.

Using a 0.16- and a 0.48-mg/cm² Ag radiator, the ratio of the photo-electrons of the two In^{111} γ-rays was measured to be 2.32±0.24. According to the experimental data of Jones[24] for a silver radiator and these energies the 172 γ-ray is 2.51 times more efficient than the 247. Thus, the γ-ray ratio is 0.93. With the percent the two γ's are converted, the ratio of the transitions is, thus, 0.97±0.10.

The percent by which each In^{111} γ-ray is converted was measured by absorbing in aluminum the electron-electron coincidences at 180°. After subtracting the background coincidences (εγ, ε-x-ray, etc.), Fig. 1, curve B, presents N_{ee}, the number of $\epsilon^-\epsilon^-$ coincidences, divided by the total number of electrons, $N_{\epsilon 172}+N_{\epsilon 247}$, counted in the G-M tube with zero absorber as a function of the mg/cm² of Al over the other counter. Curve A represents N_{ee} divided by the electrons counted in the tube covered with absorber. Thus, between the range of the 172-kev γ-ray conversion electrons (35 mg/cm²), and that of the 247 γ-ray electrons (60 mg/cm²), we have

$$N_{ee}/N_{\epsilon 247}=\Omega\times(1-e^{-\lambda t})=(3.88\pm0.20)\times10^{-3} \quad (1)$$

and at zero absorber

$$N_{ee}/(N_{\epsilon 172}+N_{\epsilon 247})=\Omega xy(1-e^{-\lambda t}) =(2.35\pm0.10)\times10^{-3}. \quad (2)$$

x and y are the percentages by which the 172 and 247 γ-rays are converted. t is the resolving time of the coincidence counter $=2.5\times10^{-7}$ sec. λ is the decay constant for the 247-kev γ-ray. Ω is the percentage of the total solid angle subtended by the source equal to 3.8±0.2. Ω was measured by aluminum absorption of the βγ coincidences of Co^{60}. Thus,

from (1), $x=11.5\pm1.7$ $y=6.64\pm1.0$,
from (2), $x=9.5\pm1.4$ $y=5.48\pm0.8$.

Therefore, $x=10.4\pm0.9$ and $y=6.0\pm0.5$.

As the Co^{60} β-spectrum has the allowed shape[25] the angular correlation is isotropic.[26] The theoretical treatment of the directional correlation of successive internal conversion electrons only includes the case of electric multipole radiation.[27] According to this theory, if the 172-kev γ-ray were pure electric quadrupole, the measured x and y would then be increased by a factor of 5.5. However, no correction of this type has been made.

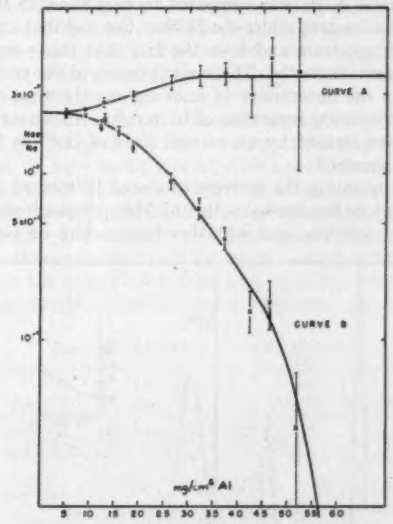

FIG. 1. Aluminum absorption of the In^{111} electron-electron coincidences.

[21] E. C. Mallary and M. C. Pool, Phys. Rev. **76**, 186 (1949).
[22] R. A. Hinshaw and M. L. Pool, Phys. Rev. **76**, 358 (1949).
[23] K. Siegbahn, Phil. Mag. **37**, 181 (1946).
[24] M. T. Jones, Phys. Rev. **50**, 110 (1936).
[25] Deutsch, Elliot, and Roberts, Phys. Rev. **68**, 193 (1945).
[26] D. L. Falkoff and G. E. Uhlenbeck, Phys. Rev. **79**, 334 (1950).
[27] J. W. Gardner, Proc. Phys. Soc. (London) **62A**, 763 (1949).

Comparison between our measurements and the theoretical internal conversion coefficients (see below) show that the 172-kev γ-ray is probably pure magnetic dipole, and the 247-kev γ is pure electric quadrupole.

N_{ee} as a function of the mg/cm² of Al placed over both counters was also measured, which showed that <1 percent of the 247-kev conversion electrons are in coincidence with those of any γ-ray more energetic than 172 kev.

The ratio of the 172/247 conversion electrons was measured to be 1.70±0.03 through a 0.4 mg/cm² Nylon window in the magnetic spectrograph (Fig. 2). Using a Nylon window 0.8 mg/cm² the ratio was decreased 2 percent. Hence, the absorption is estimated to have been 2 percent, making the ratio 1.73±0.03. For Cd^{111m} the measured ratio of 149/247 electrons was 13.8±1.0. The absorption correction is estimated as 5 percent, and so this ratio is 14.5±1.0.

A search was made for the conversion electrons from a possible excited state of In^{111} by observing spectrographically the indium fractions obtained from Ag bombarded with alphas of several different energies. It is not possible to ascribe any of the observed lines (see below), to an excited level of In^{111}, and, thus, between 50 and 700 kev there are no conversion electrons due to an isomeric state of In^{111} with a half-life >20 min or <100 days.

The Sn^{111} was obtained from Cd bombarded with 39.6-Mev alphas. The β^+ spectrum produced a straight-line FK plot with an upper energy of 1.51±0.03 Mev. The ratio K/β^+ was computed to be 2.50±0.25 from the relative area under the 247-kev line and that under the β^+ spectrum and from the fact that this γ-ray is 6 percent converted. The major portion of the error is due to the uncertainty in knowing exactly when $t=0$ in the chemical separation of In from Sn. No conversion electrons caused by an excited state of Sn^{111} or In^{111} were observed.

By counting the activity produced in stacked cadmium foils bombarded with 9.67-Mev protons from the 60-in. cyclotron and 3.75-Mev from a Van de Graaff

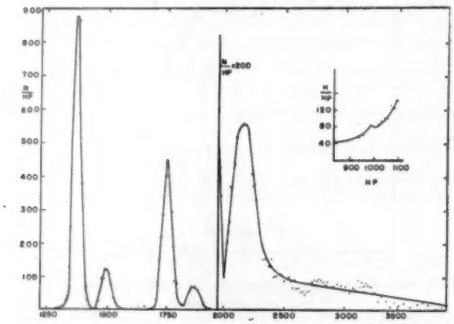

FIG. 2. Composite electron spectrum of the In^{111} activity showing conversion electrons from 172-, 247-, 340-, and (insert) 93-kev γ-rays.

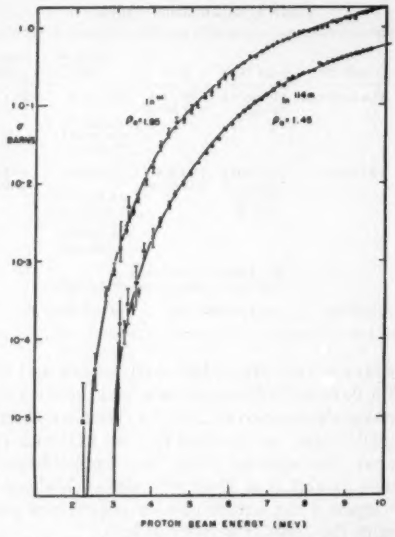

FIG. 3. $Cd^{111}(p,n)In^{111}$ and $Cd^{114}(p,n)In^{114}$ excitation functions. The solid curves are the theoretical shapes for the indicated radii.

generator we find the threshold for the production of In^{111} occurs at a proton energy of 2.35±0.20 Mev (Fig. 3). With the n-p difference[28] as 0.79 Mev the 2.84-day In^{111} is, thus, 1.56±0.20 Mev above the ground level of Cd^{111}. The 48-day In^{114m} was also produced in the same foils, and we find this level is 2.26±0.20 Mev above the ground state of Cd^{114}. As discussed below this is a reasonable value for the In^{114} threshold indicating that the In^{111} threshold is probably correct. In absolute magnitude the cross sections shown in Fig. 3 are believed to be accurate within a factor of two.

According to Stephens, Spruch, and Schiff,[29] near the threshold the yield of the (p,n) reaction varies as $(E_p-E_t)^{\frac{1}{2}}$, where E_p and E_t are the proton beam and threshold energies, respectively. Below 3×10^{-4} barns the curves of Fig. 3 have been drawn in this shape.

Applying statistical methods to the theory of the compound nucleus Weisskopf and Ewing[30] have computed the cross section for (p,n) reactions. The shape of the excitation curves can be fitted best by assuming $r_0=1.85$ for Cd^{111} and 1.45 for Cd^{114}, the nuclear radius being $r_0A^{\frac{1}{3}}\times10^{-13}$ cm. With these radii the theoretical cross sections for the production of In^{111} and In^{114m} are 1/6 and 1/18, respectively, of those observed. Although the absolute magnitude of the nuclear radius is not too accurate, their relative magnitude, probably, is substantially correct.

[28] Franzen, Halpern, and Stephens, Phys. Rev. **76**, 317 (1947).
[29] Quoted by Shoupp, Jennings, and Sun, Phys. Rev. **75**, 2 (1940).
[30] V. F. Weisskopf and P. H. Ewing, Phys. Rev. **57**, 472 (1940).

TABLE II. $100N_e/(N_e+N_\gamma)$ computed from Rose's value of $(N_e/N_\gamma)_K$ and the measured K/L ratio.

γ-ray	Expt.	Elect. 1	Elect. 2	Elect. 3	Mag. 1	Mag. 2	Mag. 3
172.1	10.4±0.9	3.50	16.95	48.8	9.85	41.0	79.2
246.6	6.0±0.5	1.36	5.88	19.8	4.18	17.2	51.1

TABLE III. Theoretical ratio 172/247 conversion electrons.

172-kev γ-ray	Elect. 1	Elect. 2	Mag. 1	Experiment
172/(247 elect. 2)	0.60	2.88	1.67	1.73±0.03
172/(247 mag. 1)	0.84	4.05	2.35	

In light of the single-particle model of the nucleus it is interesting to note that the even-odd nucleus has a radius about 25 percent greater than the even-even nucleus.

IV. CALCULATIONS

In evaluating the "Fermi Coulomb correction factor," F_e, we used the approximation of Bethe and Bacher as given by Feister.[31] The latter has shown that for β^- emission this approximation deviates from the accurate computation by less than 0.4 percent for $Z=50$.

In computing f_+ for positrons the "screening correction factor" as given by Reitz[32] has been applied to F_e. For capture, Marshak's formulas[33] for the Fermi function, f_c, were used. The f values tabulated below have been multiplied by the factor $(2I_f+1)/(2I_i+1)$ for those cases in which it was found that the spin of the parent I_i is less than that of the final nucleus I_f.

The γ-ray half-lives were computed from the formula given by Axel and Dancoff[34] and the K internal conversion coefficients, $(N_e/N_\gamma)_k$, from the table privately distributed by Rose *et al.*[35]

V. DISCUSSION

From hyperfine structure the ground-state spin of Cd^{111} has been found[36] to be 1/2. According to the shell structure model of the nucleus[37] this is a $3s_{1/2}$ state, i.e., even parity.

As only the 247-kev γ-ray is common[3] to the activity of In^{111} and Cd^{111m}, the first excited state of the latter is thus at 247 kev. Comparison between theory and experiment (Tables II and III), clearly indicates that this γ-ray is electric quadrupole. On this basis the possibility of a small admixture of magnetic dipole cannot be eliminated. Thus, the spin of this level can be either 5/2 or 3/2 with even parity. The 172-kev γ-ray is likewise clearly magnetic dipole with the possibility of a slight admixture of electric quadrupole. Hence, this latter transition involves a spin change of one unit.

If the 247-kev level has a spin of 3/2, then the 419-kev level would have a spin of 5/2 making the theoretical ratio of 419/172 transitions 8×10^2, whereas it is observed to be $<10^{-4}$. Hence, the 247-kev level must have spin 5/2, i.e., this γ-ray is pure electric quadrupole, and the 419-kev level has spin 7/2 and even parity. The computed ratio of 419/172 transitions is, then, 3×10^{-7} in agreement with the measurements (Table VII).

The screening correction factor increases Rose's value of $(N_e/N_\gamma)_k$ by 3.6 percent for the 172-kev magnetic dipole and by 3.9 percent for the 247-kev electric quadrupole γ-rays. The observed $(N_e/N_\gamma)_k$ and the theoretical values with the screening correction applied are given below.

γ-ray	experiment	theory
172.1	0.10 ±0.010	0.0982±0.0013
246.6	0.054±0.005	0.0544±0.0008.

The error listed for the theoretical value arises from an uncertainty of 1 kev in the γ-ray energy.

The theoretical half-lives of the 172- and 247-kev γ-rays are 4×10^{-8} and 7×10^{-10} sec, respectively. The latter has been measured[12] to be $8\pm1\times10^{-9}$ sec.

This assignment, spins 7/2, 5/2 both even parity, agrees with the γγ angular correlation experiment of Boehm and Walter,[38] who found the distribution given by $1-(0.07\pm0.04)\cos^2\theta$. Theoretically,[39] the coefficient for the first-transition dipole and the second quadrupole is -0.103 for spins 7/2 and 5/2; and -0.074 for spins 5/2 and 3/2.

The recent work of Johansson[5] on Ag^{111} also agrees with this assignment. The ft values (Table IV) for the decay of Ag^{111} to the ground state and to the 340-kev level of Cd^{111} are empirically[40] classified as first forbidden. $ft=2.59\times10^9$ for the decay to the 247-kev level is usually characteristic of a second-forbidden transition. However, Shull and Feenberg[41] have pointed out that in the case of a first-forbidden transition involving a spin change of 2 with a change of parity, and, conse-

TABLE IV. Values of ft for Ag^{111} and Sn^{111}.

Activity	Transition	W_0	%	$T_{\frac{1}{2}}\times10^{-4}$ sec	f	$ft\times10^{-4}$	$(W_0^2-1)ft\times10^{-10}$
Ag^{111}	to ground	3.08	91[a]	73.6	34.5	254	0.0216
	to 247 level	2.59	1[a]	6690	37.5	25,900	1.43
	to 340 level	2.41	8[a]	589	15.9	936	0.045
Sn^{111}	capture	3.95	72	0.294	38.9	1.14	$\frac{f_c}{f_+}=2.89\pm0.12$
	positrons	3.95	28	0.732	13.5	0.99	

[a] The percentage (%) values for the Ag^{111} transitions are taken from Johansson (reference 5).

[31] I. Feister, Phys. Rev. **78**, 375 (1950).
[32] J. R. Reitz, Phys. Rev. **77**, 10 (1950).
[33] R. E. Marshak, Phys. Rev. **61**, 446 (1942).
[34] P. Axel and S. M. Dancoff, Phys. Rev. **76**, 892 (1949).
[35] See also Rose, Goertzel, Spinrad, Harr, and Strong, Phys. Rev. **76**, 1883 (1949).
[36] Schüler and Brück, Z. Physik **56**, 291 (1929).
[37] M. Mayer, Phys. Rev. **78**, 16 (1950).
[38] F. Boehm and M. Walter, Helv. Phys. Acta **22**, 379 (1949).
[39] D. R. Hamilton, Phys. Rev. **58**, 122 (1940).
[40] E. J. Konopinski, Revs. Modern Phys. **15**, 209 (1943).
[41] F. P. Shull and E. Feenberg, Phys. Rev. **75**, 1768 (1949).

TABLE V. In^{111} f values.

Transition	W_0	f^0	$f^1\times10^3$	$f^2\times10^7$	Ratio of transitions from In^{111} to Cd^{111} levels Theory $\frac{f^0}{565}$	$\frac{f^1\times10^4}{5.65}$	$\frac{f^2\times10^8}{5.65}$	Experiment
to 419 level	1.23	5.65	1.09		1.00			0.97±0.10
to 396 level	1.28	8.34	1.61	1.09	1.48	2.85	1.93	$<10^{-4}$
to 340 level	1.39	6.55	1.34	1.04	1.16	2.37	1.84	0.0082
to 247 level	1.57	7.55	1.83	1.57	1.33	3.24	2.78	0.03±0.10
β^+ to 419 level	1.23	7.3×10^{-8}			1.3×10^{-6}			$<6\times10^{-4}$

quently, having a β-spectrum of forbidden shape, the product $(W_0^2-1)ft$ is about 10^{10}. For the transition to the 247-kev level this product is 1.43×10^{10} indicating that it is of this type. These results combined with the known spin and parity, 1/2 and 5/2 both even, of the ground and 247-kev level of Cd^{111} serve to fix the spin of Ag^{111} as 1/2 with odd parity.

From the relative intensity in the Ag^{111} decay of the 247- and 340-kev γ-rays (1:8), it is seen that the latter goes directly to the ground state of Cd^{111}. Thus, the 340-kev level may have a spin of 3/2 or 1/2 with even parity. The value of $(W_0^2-1)ft$ is more than a factor of ten too low for this transition to involve a spin change of two.

Although the ft of In^{111} for an allowed transition, 1.38×10^6 (Table V) is about a factor of 10 higher than the empirical classification, that for first forbidden, 2.67×10^5, is too low by a factor of 10^5. Hence, it is concluded that this is an allowed transition. The results on the photoelectric spectrum show that no measurable number of decays go directly to the 247-kev level. This fixes the ground state of In^{111} with spin 9/2 and even parity, which is in agreement with the shell model.[37] Also in agreement is the fact that both stable isotopes of indium, 113 and 115, have measured ground state spins of 9/2.

We have observed the internal conversion electrons of a 330±10 kev γ-ray in the decay of In^{111} (Fig. 2). This is undoubtedly the same as the 340-kev γ-ray that is reported by Johansson[5] in the decay of Ag^{111}. This 330±10-kev γ-ray can, thus, originate either by a direct capture decay of the In^{111} ground state or from the dual decay of the Cd^{111} 419-kev level. If the former is the case, the ft value for an allowed transition is 1.6×10^5, a factor of 10^9 higher than the empirical classification. It it originates from a first-forbidden transition the ft, 3.3×10^4, is a factor of 10^2 lower than the empirical classification. Moreover, with the spin and parity assignments possible under these circumstances the observed number of 330-kev transitions is 10^7 less than that permitted by the theoretical γ-ray half-lives. Therefore, the assumption that it originates by a direct transition from the ground level of In^{111} is not justified by the experimental evidence.

TABLE VI. Theoretical ratio of 149/247-kev conversion electrons and the percentage by which the 149-kev γ-ray is converted.

149.6-kev γ-ray	Elec. 3	Elec. 4	Elec. 5	Mag. 2	Mag. 3	Mag. 4	Expt.
Ratio	11.4	15.7	16.6	10.2	15.3	16.7	14.5±1.0
% converted	66.8	92.0	98.3	59.8	89.7	98.2	87±13

We, thus, conclude that a 340-kev γ-ray arises from the dual decay of the 419-kev level of Cd^{111}. Our work limits the spin of this level to either 3/2 or 5/2 with even parity. For example, with spin 1/2 and even parity there are 10^5 more of these transitions observed than are permitted by the theoretical γ-ray half-lives. Combining this result with Johansson's work uniquely fixes the spin of the 340-kev level at 3/2 with even parity.

In addition to decaying to the ground state this 340-kev level can also decay to the 247-kev level. The expected 93-kev γ-ray conversion electrons were observed (Fig. 2). Theoretically the ratio of 93/340 transitions is 0.005, which is consistent with the observed value of 0.085, since other assumptions of spin and parity give ratios differing by factors of 10^6.

Although we have been unable to observe spectrographically any positrons associated with the 2.84-day In^{111}, it can only be stated that they must occur by a factor of 4×10^{-3} smaller than the electrons, i.e., in less than 6×10^{-4} of the disintegrations. The theoretical value of f_+/f_e is 1.3×10^{-5} in agreement with the measurement.

According to Axel and Dancoff's classification[34] the 149-kev transition is characterized by $\Lambda=4$. The half-lives given below for the indicated Λ are to be compared to the experimental half-life of 2916 sec.

Λ	3	4	5
half-life	8×10^{-4}	117	2×10^7.

By comparison of the measured percentage by which this π-ray is converted and the ratio of the 149/247 conversion electrons with the theoretical values (Table VI), it is also seen that the best agreement is obtained by assigning $\Lambda=4$ to this transition.

Thus, the 396-kev level has even parity and may have a spin of either 11/2 or 13/2. We have been unable to extract chemically any 48-min Cd from the 2.84-day In and can, thus, state that transitions to this level must occur in less than 10^{-4} of the total. Hence, the In^{111} decay to this level is second forbidden, which fixes the spin of the 396-kev level at 13/2 with even

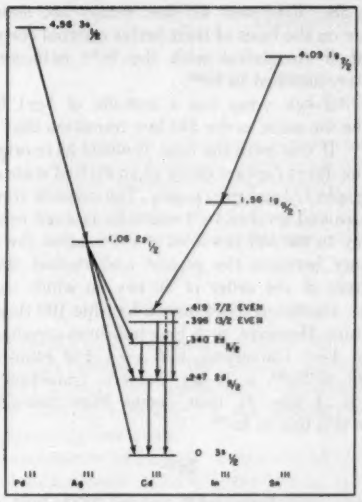

FIG. 4. Decay scheme of the 111-isobars.

parity; i.e., the 149-kev γ-ray is pure electric 2^4 pole (Table VI).

The ft values for Sn^{111} (Table IV) show that this decay is allowed. The screening correction increased the f_+ by 4 percent. As no conversion electrons from an excited state of either the parent or daughter were observed, it is concluded that the transition takes place between the ground states. Thus, Sn^{111} may have a spin of either 7/2, 9/2, or 11/2 with even parity. According to the shell structure model of the nucleus the 61st neutron is expected to be in either the $1g_{7/2}$ or $2d_{5/2}$ state. On this basis the spin of Sn^{111} is taken as 7/2 with even parity.

The 26-min Pd^{111} activity[42] has a value $ft=7.9\times10^6$, which is characteristic of a first-forbidden transition. The spin can thus be 1/2 with even parity. The resulting disintegration scheme of the 111 isobars is shown in Fig. 4.

The spin and parity assignments are all in agreement with Mayer's spin-orbit coupling model of the nucleus with the exception of the 396-kev metastable level of Cd^{111m}. The single-particle model would only permit a level with spin 11/2 and odd parity; i.e., the 149-kev transition would have to have $\Delta=3$. As discussed above such an assignment is not in agreement with the experimental evidence. This suggests that the single-particle model is not valid for the higher excited states (Table VII).

TABLE VII. Theoretical and experimental transition ratios for Cd^{111}.

Transition ratio	22.5/172	79/172	419/172	56/149	396/149	93/340
Theory	10^{-14}	9×10^{-3}	3×10^{-7}	10^{-18}	7×10^{-9}	5×10^{-3}
Experiment	$<10^{-4}$	8.2×10^{-3}	$<10^{-4}$	$<8\times10^{-4}$	$<10^{-4}$	8.5×10^{-3}

[42] E. Segrè and G. T. Seaborg, Phys. Rev. 59, 212 (1941).

TABLE VIII. γ-rays associated with the 5.0±0.2-hr In^{110}.

γ-ray energy in kev	119	590?	651	885	935
Relative intensity of conversion electrons	1.0±0.2	0.02±0.01	1	0.13±0.03	0.11±0.01

VI. OTHER RESULTS

Incidental to the main investigation the following results were also obtained.

Cd^{107}, Cd^{109}

In the Cd fraction from Ag bombarded with 39.6-Mev alphas the conversion electrons of a long-lived 88-kev γ-ray and those from a 6.7-hr 93-kev γ-ray were spectrographically observed. These well-known lines[1] are associated with the activity of Cd^{109} and Cd^{107}, respectively. It is suggested that the former was produced for the main part by $Ag^{107}(\alpha,pn)Cd^{109}$ and the latter from the decay[43] of the 33-min In^{107} produced by $Ag^{107}(\alpha,4n)In^{107}$. The relative yield Cd^{107}/Cd^{109} is estimated to have been 1 percent.

TABLE IX. γ-rays associated with the 4.2±0.2 hr In^{109}.

γ-ray energy in kev	58	205	347	427
Relative intensity of conversion electrons	0.6±0.1	1	0.080±0.003	0.016±0.005
K/L ratio	0.9±0.1	3±1		

Sn^{108}, In^{108}

In the tin fraction obtained by bombarding Cd with 39.6-Mev alphas we found, in addition to the Sn^{111} activity, both the K and L conversion electrons from a long-lived 159-kev γ-ray which has already been assigned to an isomeric transition[44] in Sn^{117} and those from the well-known[1] 390-kev γ-ray of In^{113m} belonging to the 105-day K-capture activity of Sn^{113}.

We also observed a 50±5-min build-up and a 4.0±0.3-hr decay of positrons which from the FK plot have an upper energy of 2.31±0.02 Mev. Conversion electrons of a 285-kev γ-ray, which has not been previously reported, decayed with a 4.0±0.3 hr half-life. The K/L ratio is estimated to be 3 or greater. The ratio, positrons to conversion electrons, is 20:1. As none of the lines associated with the decay of In^{107}, In^{109}, or In^{110} were detected (see below), comparable with that expected from the observed number of positrons, the activity is limited to mass number 106 or 108. Identifying this activity with Sn^{108}, 4-hr K-capture, In^{108}, 50-min positrons, agrees with the assignment of Mallary and Pool,[45] who obtained a similar activity from the bombardment of enriched Cd isotopes with alphas and deu-

[43] E. C. Mallary and M. L. Pool, Phys. Rev. 76, 1454 (1949).
[44] E. C. Mallary and M. L. Pool, Phys. Rev. 77, 75 (1950); J. W. Mihelich and R. D. Hill, Phys. Rev. 79, 781 (1950).

terons. If the 285 γ-ray belongs to Cd^{108}, it is 6.4 percent converted with theory giving 1.1, 8.7, and 3.3 percent for electric dipole, quadrupole, and magnetic dipole respectively. From the linearity of the FK plot[46] the positron branching between the 285-kev level and ground state is smaller than 5 percent.

In^{110}

In the indium fractions from Ag bombarded with alphas of different energies we observed in addition to the conversion electrons associated with the activity of Cd^{109} and In^{111} those corresponding to the γ-rays shown in Tables VIII and IX. These have not been reported previously as belonging to the assigned activities. Owing to the similarity of the half-lives the mass assignments were made by noting the correlation of their conversion electrons with each other and with those belonging to In^{111}.

In the decay of the 270-day Ag^{110} Siegbahn[46] has observed 116-, 935-, 885-, and 656-kev γ-rays, the latter three being in cascade in that order to the ground level of Cd^{110}. He did not observe any coincidences between the 116-kev electrons and the β-spectrum and so ascribes this γ-ray to the isomeric transition, which occurs about 3 percent of the time, between the 270-day level and the 24-sec ground state of Ag^{110}. For the 116-kev line he found a K/L ratio of about 1.3 and for the 656-kev γ-ray $N_e/N_\gamma=2.5\times10^{-3}$.

The conversion electrons from 119-, 935-, 885-, and 661-kev γ-rays, having a 5.0 ± 0.2-hr half-life, are associated with the decay of In^{110}. The latter three are, thus, the same that Siegbahn observed. In^{110} is known to have a 65-min 1.6-Mev positron decay.[1] Hence, the 5-hr activity must result from the decay of an isomeric level of In^{110}. It is suggested that the 119-kev π-ray is the isomeric transition. The K/L ratio for this line is 4.5 ± 1.0 showing that it is not the same as the 116 line reported by Siegbahn. Although this ratio is more characteristic of $\Delta=4$ than $\Delta=5$, the former has a theoretical half-life of 5 min and the latter 195 days. From the experimental data this 119-kev transition occurs about 0.3 percent of the 5-hr capture decay, giving it a half-life of 75 days, i.e., $\Delta=5$ for the isomeric transition in In^{110}.

In^{109}

From the bombardment of enriched Cd isotopes with alphas and deuterons Mallary and Pool[45] find a 4.30 ± 0.15-hr indium activity which they assign to In^{109}. We find four γ-rays decaying with a 4.2 ± 0.2-hr half-life (Table IX), which are the product of $Ag(\alpha,2n)In$. They may thus be associated with either In^{109} or In^{111}. If assigned to the latter the expected growth of the ground level would be less than 10 percent, which growth it was not possible to detect.

The 58-, 205-, and 427-kev γ-rays are associated together on the basis of their better internal correlation than their correlation with the In^{111} radiation and, hence, are ascribed to In^{109}.

The 347-kev γ-ray has a half-life of 5 ± 1 hr and could be the same as the 340-kev transition that occurs in Cd^{111}. If this were the case, it would have originated from the direct capture decay of an excited state of In^{111} having spin 1/2 and even parity. The isomeric transition to the ground level of In^{111} would be favored compared to decay to the 340-kev level of Cd^{111} unless the energy difference between the ground and excited states of In^{111} were of the order of 30 kev, in which case the isomeric transition could have a half-life 100 times that of capture. However, such long half-lives are characteristic of $\Delta=5$ transitions, not $\Delta=4$. For example, the half-life of Sb^{124}, a 20-kev isomeric transition[47] with $\Delta=4$, is 21 min. It, thus, seems more reasonable to ascribe this line to In^{109}.

In^{114}

Boehm and Preiswerk[48] proved that In^{114} decays not only by β^- to Sn^{114} but also to Cd^{114} with the emission of 715- and 548-kev γ-rays. Mei *et al.*[49] have shown that they are in cascade by observing the combination 1.27-Mev γ-ray. Positrons of 650 ± 100 kev have also been detected occurring about 10^{-4} of the β^- which is of the order of magnitude to be expected from bremsstrahlung pair production.[48]

Our threshold measurements show that the 72-sec ground state of In^{114} is 2.07 ± 0.20 Mev above the ground state of Cd^{114}, which, thus, permits the emission of 1.05-Mev positrons. With this energy difference the Fermi theory yields $f_e/f_-=8\pm2$ percent compared to 3 ± 1 percent observed[48] and $f_+/f_-=3.6\pm0.6\times10^{-3}$ compared to the measured ratio of about 10^{-4}. This disagreement between theory and experiment is of the order of magnitude to be expected due to the difference in the nuclear matrix elements, e.g., for Cu^{64} $f_e/f_-=0.1$ and $f_+/f_-=8.9$ and experiment[50] gives 1.75 and 2.0, respectively. Our threshold measurement is, thus, not in disagreement with these experiments indicating that the true energy differences $In^{114}-Cd^{114}$ and $In^{111}-Cd^{111}$ probably lie within our observed limits.

It is a pleasure to express my appreciation to Professor A. C. Helmholz for his helpful guidance during the course of this work. I also express my thanks to Mr. Bernie Rossi and the 60-in. cyclotron crew for making the many bombardments and to the Radiation Laboratory for assistance throughout the work.

[45] H. Brown and V. Perez-Mendez, Phys. Rev. **78**, 812 (1950).
[46] K. Siegbahn, Phys. Rev. **77**, 233 (1950).
[47] der Mateosian, Goldhaber, Muehlhause, and McKeown, Phys. Rev. **72**, 1271 (1947).
[48] F. Boehm and P. Preiswerk, Helv. Phys. Acta **22**, 331 (1949).
[49] Mei, Mitchell, and Zaffarano, Phys. Rev. **76**, 1883 (1949).
[50] Bradt, Gugelot, Huber, Medicus, Preiswerk, Scherrer, and Steffen, Helv. Phys. Acta **19**, 219 (1946); M. Deutsch. Phys. Rev. **72**, 729 (1947).

Half-Life of the Long-Lived Tc^{99}

SHERMAN FRIED, A. H. JAFFEY, N. F. HALL,* AND L. E. GLENDENIN
Chemistry Division, Argonne National Laboratory,† Chicago, Illinois

(Received October 5, 1950)

The half-life of Tc^{99} has been determined on materials isolated both from fission products and from irradiated molybdenum. The determinations were made on aliquots of solutions prepared by dissolving weighed portions of compounds of known composition.

The counts were made absolute by comparing them with Co^{60} and RaDEF standards. These determinations resulted in a value of 2.12×10^5 years for the half-life of Tc^{99}.

A detailed description of the absolute beta-counting techniques is given.

I. INTRODUCTION

TECHNETIUM, element number 43, long a missing element in the periodic system, was discovered through its radioactivity by Perrier and Segrè in 1937 as a product of the bombardment of molybdenum by deuterons.[1]

Various other investigators[2,3] demonstrated the occurrence of this element in fission products as the radioactive isotope Tc^{99}. This isotope can also be prepared[4,5] by irradiation of natural molybdenum in a chain reacting pile, where it is formed by the reaction

$$Mo^{98}(n,\gamma)Mo^{99}\xrightarrow[67\text{ hr}]{\beta}Tc^{99}. \qquad (1)$$

Other isotopes of technetium have been prepared by various methods[6] and now the mass range from Tc^{92} to Tc^{105} is known with more or less certainty.[7]

The isotope Tc^{99} is the most suitable one for chemical investigation because of its long half-life, variously estimated as 2×10^5 to 9×10^5 years. These values were based either on yield estimates or on an assumed formula for a particular compound. Since early workers in the field had little information as to the chemical formulas of technetium compounds, these measurements were correspondingly uncertain.

Recently, some aspects of the chemistry of technetium have been elucidated and several definite compounds have been prepared and identified;[8] and it was with this new information in mind that it was proposed to re-examine the half-life determination of Tc^{99} and, if possible, to reconcile the various values given in the literature. It was decided to make the determinations on technetium isolated from pile-irradiated molybdenum as well as from material from fission products. Because of the high fission yield of Tc^{99} and the sufficiently high neutron capture cross section of Mo^{98}, enough material was available from both sources to make reasonably accurate weighings of compounds possible.

The absolute counting necessary for a specific activity determination was done relative to coincidence-counter standardized Co^{60} samples. The Co^{60} beta-radiation has almost the same energy and aluminum absorption curve as Tc^{99}, which simplifies the problem of geometry standardization.

II. PURIFICATION OF TECHNETIUM AND PREPARATION OF TECHNETIUM SAMPLES

The details of the purification of technetium from gross amounts of impurities and from radiochemical contaminants are to be described in a paper devoted to

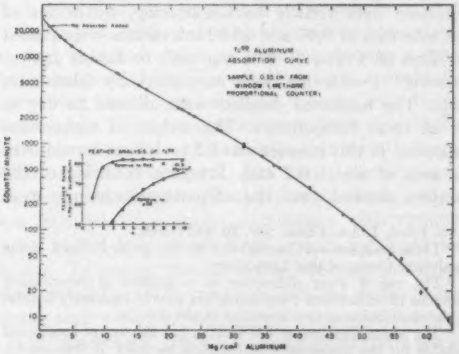
Tc^{99} ALUMINUM ABSORPTION CURVE
SAMPLE 0.35 cm FROM WINDOW 1 METHANE PROPORTIONAL COUNTER
FEATHER ANALYSIS OF Tc^{99}
COUNTS/MINUTE
mg/cm² ALUMINUM

FIG. 1. Complete aluminum absorption curve of Tc^{99}, including a Feather analysis relative to RaE.

* On leave of absence from the University of Wisconsin, Madison, Wisconsin.

† The material presented here was given in part in a paper by Sherman Fried and Norris F. Hall presented at a meeting of the American Chemical Society, April, 1950.

[1] C. Perrier and E. Segrè, J. Chem. Phys. **5**, 712 (1937).

[2] D. C. Lincoln and W. H. Sullivan, "Discovery of the 10^6y. Tc^{99} isotope. I." Paper 7.17.2, *Radiochemical Studies: The Fission Products* (McGraw-Hill Book Co., Inc., New York, to be published), National Nuclear Energy Series, Division IV, Vol. 9B; Hanford Report No. (H)CN-3449, October 25, 1945, unpublished.

[3] R. P. Schuman, "Discovery of the 10^6y. Tc^{99} isotope. II.," Paper 7.17.3, *Radiochemical Studies: The Fission Products;* Metallurgical Laboratory Report No. CC-3434, February 16, 1946, unpublished.

[4] E. E. Motta and G. E. Boyd, Oak Ridge National Laboratory Report MonC-169, September 15, 1946, unpublished.

[5] Motta, Boyd, and Larson, Phys. Rev. **72**, 1270 (1947).

[6] G. T. Seaborg and I. Perlman, Revs. Modern Phys. **20**, 585 (1948).

[7] Technetium isotopes of masses 103 and 104 have not yet been found.

[8] Paper presented at a meeting of the American Chemical Society, April, 1950, by S. Fried and N. F. Hall.

the chemistry of the element; but, in brief, the purification involved the reduction of technetium sulfide to the metal by action of hydrogen[9] at 1000–1100°C. Subsequent high temperature oxidation of the metal to the oxide by oxygen allowed it to be sublimed away from impurities, since the oxide is quite volatile.

The aluminum absorption curve shown in Fig. 1, which agrees with those found by other workers in the field,[3–5] shows the absence of radioactive contaminants. Spectrographic analysis of solutions of technetium prepared by this method indicated no gross impurities.[10]

The compound NH_4TcO_4 has been prepared[8] by action of a mixture of ammonium hydroxide and hydrogen peroxide on technetium oxide. The formula of the compound was deduced by Prof. W. H. Zachariasen using x-ray diffraction analysis.[11] It is soluble in water and is nonhygroscopic. Since it contains a known proportion of technetium, it can serve as a gravimetric standard for the preparation of solutions of known concentration of technetium for use in beta-counting.

Technetium metal itself also serves as a gravimetric standard, but more elaborate methods must be employed. The metal cannot be directly dissolved in a suitable solvent.[12] To dissolve the technetium, a weighed sample of the metal was converted quantitatively to the volatile oxide (presumably TcO_3), and was then washed out of the reaction tube into a calibrated volumetric flask. In this way the concentration of technetium in solution was determined directly from the initial weight of the metal. The equations representing the sequence of reactions probably are:

$$\mathrm{Tc} \xrightarrow[400\text{–}600^\circ\mathrm{C}]{\mathrm{O_2}} \mathrm{Tc\ oxide\ (TcO_3)} \xrightarrow{\mathrm{NH_4OH+H_2O_2}} \mathrm{NH_4TcO_4\ (in\ solution).} \quad (2)$$

Aliquots were withdrawn from the standardized solutions by means of calibrated micro-pipettes.[13] To minimize beta-particle back-scattering, quantities of the solutions of 9.97 and 25.02 microliters were placed on films of Tygon (~0.05 mg/cm²) or rubber hydrochloride[14] (~0.6 mg/cm²) supported by aluminum rings. The measured droplets were allowed to dry in air at room temperature. The weight of technetium deposited in this manner was 0.5 to 1.5 μg, spread over an area of about 0.2 cm². Precision counting of the samples showed that the aliquoting technique gave results reproducible to about 0.3 percent. From the weight of technetium in a sample and its counting rate, a relative specific activity could be determined, requiring only the determination of the counter geometry to make it an absolute value.

Sulfur in Technetium

Although spectrographic analyses showed no large amount of impurities, the first result for the relative specific activity of the molybdenum-derived technetium was 25 percent lower than that of the fission product material. A sulfate test with barium chloride on the former solution showed that this discrepancy was due to the presence of sulfur in the technetium metal. The presence of any appreciable quantity of sulfur of course introduces a gravimetric error, which tends to decrease the apparent specific activity and hence increase the measured value of the half-life. Because of the difficulty of detection, this impurity was missed in the spectrographic analyses. The preparation of the metal in a fairly pure state was found to require prolonged action of hydrogen at high temperatures.

Fortunately an independent method for the determination of technetium was developed. The absorption spectrum of Tc(VII) in perchloric acid solution showed characteristic intense bands in the ultraviolet region[15] at 2440 and 2490A. Since the absorption follows Beer's Law, it was possible to determine the concentration of technetium after having once determined the molar extinction coefficient of a known standard solution.

The molybdenum-derived technetium was made into metal again, and the specific activity redetermined. The result was still 4 percent lower than that of the fission-product technetium; but absorption spectrum analysis, standardized with fission-product technetium, showed the concentration of the solution to be 94.5 (±1.0) percent of that calculated from the weight of the metal. The relative specific activity of the molybdenum-derived technetium thus agreed within experimental error with that of the fission-product material.

Although this discrepancy was removed, it must be noted that the presence of small amounts of sulfur in the fission-product technetium cannot be entirely ruled out, although a test with barium chloride gave no precipitate. However, another aspect of the present measurements makes this possibility unlikely. Following purification, the fission-product material was twice passed through the cycle: Tc sulfide→Tc metal→Tc oxide→NH_4TcO_4 solution→specific activity determination. In the first run, the solution concentration was determined by weighing the metal; in the second run, the solution was evaporated and the NH_4TcO_4 was weighed. The two specific activities determined from these independent weighings checked closely (Table II). Since it is very unlikely that the amounts of sulfur

[9] S. Fried, J. Am. Chem. Soc. **70**, 442 (1948).

[10] These analyses were carried out by Mr. John P. Faris of the Analytical Group of this Laboratory.

[11] The use of x-ray diffraction as a method of determining formulas of technetium compounds has proved extremely fruitful in the elucidation of the chemistry of the element.

[12] The metal dissolves in 8*M* HNO_3, but this is not considered suitable for the preparation of counting samples. It was feared, at the present state of knowledge of Tc chemistry, that loss of Tc would result from drying acid solutions. All counting samples were made from neutral or alkaline solutions of Tc salts.

[13] The technique is described in P. L. Kirk, *Quantitative Ultramicro Analysis* (John Wiley & Sons, Inc., New York, 1950).

[14] Reed Laboratories, Akron, Ohio.

[15] The absorption spectrum of Tc(VII) and analyses of the Tc solutions were determined by J. C. Hindman and Philip Wehner of this Laboratory with a Cary Recording Spectrophotometer.

carried through these runs were in just the right proportions to give apparent agreement, we conclude that the fission-product material was essentially free of sulfur impurity.

III. PREPARATION AND CALIBRATION OF STANDARD SAMPLES

The Co^{60} standards, each containing less than a microgram of cobalt, were prepared from Oak Ridge material having a specific activity of 300 mc/g. To minimize back-scattering, the material was deposited on rubber hydrochloride films identical with those used for the technetium samples. The beta-activities of the first samples prepared were found to have decreased after several months, apparently due to the deposition of water on the hygroscopic cobalt nitrate. The formation of the insoluble CoS by evaporation of the deposited droplet in an atmosphere of H_2S served to eliminate the difficulty. However, since this salt tended to concentrate in a narrow ring, the cobalt was kept spread during evaporation by the addition of a small amount of glue. The final samples were spread over an area of about 0.3 cm^2, and contained approximately 4×10^5 disintegrations per minute (dis/min).

The absolute disintegration rates of these samples were determined by coincidence counting of β's and γ's in the usual manner.[16] The simplicity of the Co^{60} disintegration made possible a calibration free of many of the difficulties occurring with complex decay schemes. Co^{60} disintegrates[6] through the emission of a 310-kev beta-particle, followed by two gamma-rays in cascade (1.17 and 1.33 Mev). The disintegration rate N was calculated from the expression

$$N=N_\beta N_\gamma/C_{\beta\gamma}, \tag{3}$$

where N_β = singles counting rate due to the Co^{60} beta-particles in one detector, N_γ = singles counting rate due to Co^{60} gamma-rays in the other detector, and $C_{\beta\gamma}$ = coincidence rate. N_β was corrected for background, for gamma-ray counting rate in the beta-particle detector, and for resolution losses; N_γ was corrected for background and resolution losses; $C_{\beta\gamma}$ was corrected for accidentals, gamma-gamma-coincidences, cosmic-ray background, and resolution losses in both channels. All corrections were relatively small. Since the conversion coefficients of the Co^{60} gamma-rays have been found to be very small,[17] no correction was necessary for conversion electrons.

The flow-type atmospheric proportional counters (methane or argon-10 percent methane) used as detectors were shaped like the usual bell-shaped mica-window G-M tube, except that a loop of 1-mil wire served as center electrode. The beta-counting tube had a 0.6 mg/cm^2 window of rubber hydrochloride. A 300 mg/cm^2 aluminum absorber was used over the gamma-counting tube to cut out beta-particles and to act as a radiator for increasing the gamma-ray efficiency. Highly active sources gave sufficiently high coincidence rates without the use of more efficient gamma-counters. It was possible to use such active sources only because of the high singles counting rates attainable with the beta-counting proportional counter.

When a methane containing tube was used at about 1 mv sensitivity, the plateau for Co^{60} betas started at 2600 volts; with the argon-methane mixture, the plateau started at 1750 volts. These voltages were higher than would be the case with other tube designs and were largely necessitated by the small pulses from tracks in the corners of the tube (e.g., near the edge of the window). Since the plateau voltages were relatively high, the fact that the effective dead-time t of the tube increased with voltage for both gases, led to fairly high values for t, about 5 μsec for methane, and 8–12 μsec for argon-methane.

The effective dead-times were measured empirically[18] by the paired-sample technique and corresponded to losses of 0.8 percent at 100,000 counts/min in the methane counter. Counting rates in the argon-methane tube were relatively low, resulting in small corrections.

The proportional counters, mounted coaxially, were placed with windows as close together as possible, leaving only enough space between them for absorbers and sample. For determining the gamma-gamma-coincidence correction and the gamma-ray correction for the beta-ray singles count, an aluminum absorption curve was taken with the beta-ray tube. Because of the large variation of gamma-counting efficiency with absorber thickness, the gamma-ray absorption curve was extrapolated from beyond the beta-range to zero absorber. To minimize the number of apparent gamma-gamma-coincidences due to back-scattered Compton gamma-rays, the sample was sandwiched between two lead absorbers having holes only large enough to ensure both tube windows "seeing" the entire sample.

The signal from each proportional counter passed through a cathode-follower, and then through a cable to the main amplifier. The amplifier input contained a compressor circuit (crystal diode in series with 10,000 ohms) and a differentiating network. Each coincidence channel contained a pulse-height discriminating univibrator (cathode-coupled, first tube normally conducting), operating at a fixed $\frac{1}{2}$-volt sensitivity, which was followed by a similar univibrator with variable pulse width. A modified Rossi circuit was used for mixing. To ensure that all pulses entering the mixer were counted as single counts as well, the pulses to the singles scalers were taken from the second univibrators.

The pulses from the proportional counters were found

[16] J. V. Dunworth, Rev. Sci. Instr. 11, 167 (1940).
[17] M. Deutsch and K. Siegbahn, Phys. Rev. 77, 680 (1950) (for each gamma-ray, $\alpha=0.0002$).
[18] T. P. Kohman, "General method for determining coincidence corrections of counting instruments," paper 22.50, *The Transuranium Elements* (McGraw-Hill Book Company, Inc., New York, 1949), National Nuclear Energy Series, Division IV, Vol. 14B.

TABLE I. Co^{60} standards calibrated by coincidence counting (in units of 10^3 dis/min).

	Sample No.	dis/min as of Jan. 1, 1950	Ratio to Co-17 from gamma-count	Co-17 dis/min Jan. 1, 1950	Deviation from mean
Coincidence circuit I	Co-17	$3.83_9 \pm 0.02_9$	1.000	$3.83_9 \pm 0.02_9$	0.02_4
	Co-T-II	$2.88_6 \pm 0.04_6$	$0.753_2 \pm 0.005_9$	$3.91_7 \pm 0.06_1$	0.05_4
	Co-T-III	$2.93_1 \pm 0.05_4$	$0.740_8 \pm 0.005_3$	$3.96_1 \pm 0.08_9$	0.09_8
	Co-IV	$4.77_7 \pm 0.05_9$	$1.221_8 \pm 0.005_7$	$3.91_3 \pm 0.04_7$	0.04_0
	Co-VI	$4.85_1 \pm 0.05_1$	$1.222_1 \pm 0.005_9$	$3.96_5 \pm 0.04_4$	0.10_2
	Co-18	$3.79_8 \pm 0.03_4$	$0.998_1 \pm 0.004_8$	$3.80_8 \pm 0.03_8$	0.05_8
	Co-19	$3.85_8 \pm 0.01_9$	$0.998_4 \pm 0.004_7$	$3.86_2 \pm 0.02_8$	0.00_8
			Weighted mean	$3.86_2 \pm 0.01_3$	
Coincidence circuit II	Co-17	$3.83_4 \pm 0.04_9$	1.000	$3.83_4 \pm 0.04_9$	0.01_3
	Co-19	$3.81_3 \pm 0.01_9$	$0.998_4 \pm 0.004_7$	$3.82_1 \pm 0.02_8$	0.02_4
	Co-VI	$4.73_4 \pm 0.02_1$	$1.222_1 \pm 0.005_9$	$3.87_2 \pm 0.02_8$	0.02_8
			Weighted mean	$3.84_7 \pm 0.01_6$	

to have a relatively large range of lagging-times, probably due to a mixture of two effects: (1) detector lag-time due to variations in transit-time of the original, ionization-formed electrons through the detector gas (atmospheric pressure), and (2) variation in tripping time of the pulse-height discriminating univibrator due to wide range of pulse heights. A plateau of coincidence rate *vs* resolving time (τ) was determined, and measurements were normally taken well on the plateau, at $\tau = 1.3$ μsec. Despite the large value for τ, corrections for accidental coincidences were relatively small.

A number of samples were measured at various times. Table I includes the data on seven samples, corrected for decay to a standard time using the half-life value[6] of 5.3 years. All of the samples were compared in relative activity by gamma-counting to Sample-Co-17, and this sample was used as the primary standard.

Because of the disagreement (see below) between the geometry determined by these Co^{60} standards and that measured with a RaE standard, a number of measurements were attempted with other coincidence systems. Another type of coincidence circuit was used[19] in conjunction with detectors consisting of anthracene crystals and liquid nitrogen cooled photo-multipliers (1P21).

The disintegration rate, N [Eq. (3)] was measured as a function of the photo-multiplier voltages (using a fixed pulse-height discriminator). If the only effect of changing these voltages were to change the counter efficiencies (essentially by varying the pulse-height selection level), the value of N calculated from Eq. (3) would be expected to be independent of the photo-multiplier current gain. It was found, however, that N was a function of the multiplier voltages. Between 1250 and 1400 volts, a voltage plateau existed giving values of N about 20 percent higher than those in Table I. As the voltage dropped, N decreased until another sloping plateau was found between 750 and 800 volts giving N values checking with those in Table I. Since it is difficult to see why $C_{\beta\gamma}$ [Eq. (3)] should be too low at high photo-multiplier voltages, or too high at low voltages, it seems reasonable to assume that the high N values were due to spurious counts in the singles channels. Other evidence in this laboratory and elsewhere indicates that such spurious counts do occur.

The calibration was repeated some months later with the same proportional counters and amplifiers but with another coincidence circuit,[20] which used Schmitt trigger pairs for pulse-width setting and for mixing. The results shown in Table I may be seen to check very closely with the previous values.

Since there were available in the laboratory some beta-counting standards[21] containing RaDEF mounted on thin rubber hydrochloride films, an attempt was made to check them against the Co^{60} standards. However, because of the difference in energies, extrapolation to zero absorber was quite different in the two samples, making it impossible to correct for the relatively large absorption (air and window = 1.1 mg/cm²) of the methane proportional counter. The samples were compared in a low absorption counter[22] having a gas and window absorption of 0.1 mg/cm². At the pressure used (2 cm of argon—10 percent propane), the RaDEF standard consistently gave geometry values about 18 percent lower than those derived from the Co^{60} standards.

When checking the coincidence measurements showed no error in the Co^{60} standardization, it was suspected that at the low pressure used there might actually be differences in the effective geometries of beta-emitters, depending upon the beta-energies. Such differences might arise from the variation in specific ionization with electron velocity and the greater probability that a fast electron might not ionize in the corner of the tube bordered by window and cylindrical wall.

To check this possibility, another type of low absorption counter[23] was used. It contained a proportional counter similar to the methane counter described above. A gas of relatively high density (argon—10 percent methane) was used at atmospheric pressure to increase the probability of ionization, so that electrons of all energies would be counted. The window was a multilayer film of Tygon with surface density ranging from 0.05 to 0.15 mg/cm². To decrease the gas absorption between sample and window, helium was allowed to flow through the containing Lucite box, displacing the air. Samples and absorbers were changed through an opening in the Lucite box; helium flushing followed each such change. Since the sample to window distance was only 3 mm, gas absorption was cut down to 0.05 mg/cm². Flat voltage plateaus were measured for both Co^{60} and RaE samples and all counting was done at the

[19] This measurement was performed by D. W. Engelkemeir of this Laboratory.

[20] Kindly loaned us by D. W. Engelkemeir.

[21] T. B. Novey, Rev. Sci. Instr. 21, 280 (1950).

[22] F. T. Hagemann, "New low absorption GM counter" (report to be issued).

[23] A. H. Jaffey, "Flow-type low absorption proportional counter" (to be published).

same voltage, which lay on both the RaE and Co^{60} plateaus.

Absorption curves were measured for both the RaE and Co^{60} samples and these are shown in Fig. 2. Due to the presence of the RaD beta-particles and RaF (Po^{210}) alpha-particles, it was not possible to measure the extrapolated counting rate of Novey's beta-standards directly. A sample of RaE, separated[24] from RaD and RaF was measured and normalized by comparison with the RaDEF beta-standard at absorber thicknesses exceeding the alpha-particle range. Both absorption curves may be seen to have relatively steep slopes at low absorber thicknesses.

When the small correction for gas and window thickness was made by extrapolating along the aluminum absorption curves, the geometry value using the Co^{60} standard was found to be 42.8 percent, while that from the RaDEF standard was 42.3 percent. The close agreement is fortuitous, since the one percent difference is less than the experimental errors involved in such extrapolations.

The geometry calculated from the dimensions (i.e., from the solid angle subtended by the tube window) agreed very closely with the measured geometry values, indicating that the sensitive volume began immediately in back of the window.

As an additional check on the Co^{60} standardization, the Co^{60} samples were compared with the ampoules of Co^{60} activity issued by the Bureau of Standards and standardized three years earlier. Similar ampoules of a Co^{60} solution were prepared and compared with the Bureau of Standards samples by gamma-ray count, and known aliquots of the solution were mounted on rubber hydrochloride films and compared by gamma-count with our standard Co^{60} samples. Our standardization checked that of the Bureau of Standards within 0.5 percent, which was less than the combined errors of the comparison and the Bureau of Standards standardization.

The close agreement between the various methods of calibrating the Co^{60} standard suggests that its disintegration rate was known to better than 1 percent.

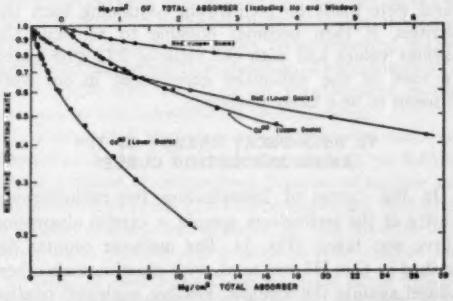

FIG. 2. Absorption curves of RaE and Co^{60} standards in flow type low absorption counter.

[24] This purification was kindly performed for us by T. B. Novey.

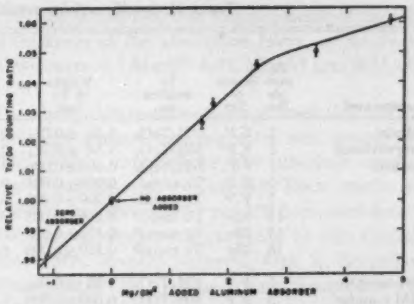

FIG. 3. Ratio of Tc and Co beta-counting rates relative to ratio with no added absorber. Measured with methane proportional counter. Extrapolation to zero absorber corrects for the effect of window and air absorption (1.13 mg/cm²), giving 0.980 for the correction factor.

IV. COMPARISON OF Tc^{99} AND Co^{60} SAMPLES: Tc^{99} HALF-LIFE

In absolute beta-counting by comparison with a standard sample, one of the most likely sources of error is the correction for air and window absorption. This is especially true when the radiation is relatively soft, since the correction is then fairly large. For many radioactivities it is not valid to assume that the aluminum absorption curve extrapolates as a straight line at very low absorber thicknesses; many activities show an upturning of the curve in this region. For example, the Co^{60} and RaE curves of Fig. 2 show this phenomenon. In addition, it is questionable, for large corrections, whether it is valid to assume that the window and air correspond to an equal weight of aluminum. For best results, the comparison between standard and unknown should be done in a low absorption counter, i.e., one in which the gas and window absorption is of the order of 0.1 mg/cm².

In the measurement described here, it was fortunate that the absorption curves for Co^{60} and Tc^{99} were almost superposable, so that an extrapolation of the activity ratios gave rise to only a small correction for air and window. This extrapolation was carried out with the methane proportional counter used for coincidence counting (air and window = 1.13 mg/cm²) and with low absorption counters.[22,23]

Because the Tc^{99} and Co^{60} absorption curves were so similar, essentially no extrapolation was necessary for the comparisons made with the low absorption counter. The correction was significant, however, for the methane proportional counter. Despite this disadvantage, the methane counter comparisons were more useful because of the greater stability of the instrument as evidenced by the reproducibility of counts. An extrapolation for the methane proportional counter is shown in Fig. 3. The resulting correction factor gives the Tc/Co counting

TABLE II. Specific activity results by comparison of Tc^{99} and Co^{60} standards.

Counter used	Tc sample No.	Source of Tc[a]	Tc weighed as	Weight of Tc (μg)	Tc/Co ratio of counts/min: No absorber added	Tc/Co ratio of counts/min: At zero absorber	Disintegration rate (dis/min) of Co^{60} std. $\times 10^{-4}$	Disintegration rate (dis/min) of $Tc^{99} \times 10^{-3}$	Tc^{99} specific activity dis/min-μg $\times 10^{-4}$
Methane proportional counter	1	F.P.	NH_4TcO_4	1.54 ±0.01$_5$	0.1593±0.0002	0.1561±0.0005	3.69 ±0.01	5.76 ±0.03	3.74±0.04
	2	F.P.	NH_4TcO_4	1.54 ±0.01$_5$	0.1605±0.0003	0.1573±0.0006	3.69 ±0.01	5.80 ±0.03	3.77±0.04
	3	F.P.	NH_4TcO_4	0.603±0.006	0.0621±0.0004	0.0609±0.0004	3.69 ±0.01	2.25 ±0.02	3.72±0.05
	6	F.P.	Tc metal	0.909±0.005	0.0948±0.0003	0.0929±0.0004	3.69 ±0.01	3.42$_5$±0.01$_5$	3.77±0.03
	7	F.P.	Tc metal	0.909±0.005	0.0952±0.0003	0.0933±0.0004	3.69 ±0.01	3.44$_0$±0.01$_5$	3.78±0.03
	14	Mo	Tc metal[b]	0.559±0.008	0.0590±0.0001	0.0578±0.0002	3.69 ±0.01	2.13$_3$±0.01$_0$	3.82±0.06
	15	Mo	Tc metal[b]	0.559±0.008	0.0591±0.0002	0.0579±0.0003	3.69 ±0.01	2.13$_4$±0.01$_2$	3.82±0.06
	16	Mo	Tc metal[b]	0.559±0.008	0.0590±0.0002	0.0578±0.0003	3.69 ±0.01	2.13$_0$±0.01$_2$	3.81±0.06
Low absorption GM counter	1	F.P.	NH_4TcO_4	1.54 ±0.01$_5$	1.076 ±0.009		0.545±0.007	5.86 ±0.09	3.80±0.07
	3	F.P.	NH_4TcO_4	0.603±0.006	0.858 ±0.010		0.269±0.001	2.31 ±0.03	3.83±0.06
	16	Mo	Tc metal[b]	0.559±0.008	0.813 ±0.010		0.267±0.001	2.16$_8$±0.02$_3$	3.88±0.07
								Weighted mean	3.78±0.02

[a] F.P. = Tc from fission products; Mo = Tc from neutron irradiated molybdenum.
[b] Specific activity values low when based on metal weight. Tc weight values actually determined by absorption spectra analysis based upon standardization with F.P. material.

ratio at zero absorber (corrected for air and window) relative to the measured ratio with no absorber added.

It was also possible to use the absorption curves taken with the low absorption counters to determine the change in Tc/Co counting rate ratio with the addition of 1.13 mg/cm² absorber. Averaging the Fig. 3 extrapolation with the low absorption counter results, the correction factor was found to be 0.980±0.003. The data for the $Tc^{99}-Co^{60}$ comparisons are given in Table II. The Co^{60} disintegration rates were corrected for decay using 5.3 years as the half-life. The average value of the specific activity of Tc was found to be 3.78×10^4 dis/min-μg, which corresponds to a half-life of 2.12×10^5 years. The error is estimated to be ±2 percent.

V. COMPARISON WITH OTHER HALF-LIFE MEASUREMENTS

The earliest half-life values of Tc^{99} were based upon beta-activity measurements of samples extracted from neutron-irradiated uranium. From estimates of the chemical yield of extraction and assuming that the fission yield was about 6 percent, Lincoln and Sullivan[3] calculated a half-life value of about 10^6 years, while Schuman[3] quoted a value of 3×10^5 years (within a factor of five).

Two measurements on weighed samples were later made at Oak Ridge. Parker, Reed, and Ruch[25] isolated milligram amounts of technetium from fission products and precipitated and weighed technetium sulfide, assuming its formula to be Tc_2S_7 (by analogy to rhenium). Counting was carried out in a low geometry, low absorption counter. The aluminum absorption curve was extrapolated to zero absorber, neglecting the observed upswing at low absorber values. Their half-life value was $5.5\pm0.4\times10^5$ years.

[25] Parker, Reed, and Ruch, Atomic Energy Commission Document AECD-2043, January 9, 1948; Oak Ridge National Laboratory Report MonN-311, June 24, 1947 (unpublished).

Motta, Boyd, and Larson[5] isolated weighable amounts of technetium from neutron irradiated molybdenum. One hundred micrograms were electroplated on a copper disk, with the assumption that the deposit was technetium metal. The sample was counted with the usual mica window GM tube, comparing them with Co^{60} standards electroplated in a similar way. Their value was 9.4×10^5 years.

The specific activity determinations of Motta, Boyd, and Larson and Parker, Reed, and Ruch depend on an assumed composition for a particular technetium sample with no opportunity for cross checks. Parker, Reed, and Ruch, using technetium sulfide, were dealing with a particularly difficult compound, since it has been our experience that such sulfides carry varying quantities of free sulfur when precipitated from solutions.

Technetium, electrodeposited from solution, was assumed to be the metal and was weighed as such. Again there was no opportunity for cross checking and it would seem possible that inert material was carried down.

If the assumption is made that previous determinations were made on technetium containing inert impurities, it then becomes possible to reconcile the various values and with our value of 2.12×10^5 years. In view of the difficulties experienced in our work it seems to be a likely possibility.

VI. BETA-DECAY ENERGY OF Tc^{99} (FROM ABSORPTION CURVE)

In the course of investigating the radiochemical purity of the technetium sample, a careful absorption curve was taken (Fig. 1). The methane counter described in Sec. III was used, with aluminum absorbers placed against the window. Feather analysis[26] relative to RaE gave a range of 81.6 mg/cm². According to the

[26] N. Feather, Proc. Camb. Phil. Soc. 34, 599 (1938).

revised Feather relationship[27]

$$E=1.92R^{0.725} \quad \begin{cases} E \text{ in Mev} \\ R<0.3 \text{ g/cm}^2 \text{ Al.} \end{cases} \qquad (4)$$

From this equation the energy of Tc^{99} is found to be 0.312 Mev, which agrees well with spectrographic values of 0.309 Mev[28] and 0.30±0.1 Mev.[29]

[27] L. E. Glendenin and C. D. Coryell, "The relationship between the range and spectrograph energy of beta particles," paper 11, *Radiochemical Studies; The Fission Products* (McGraw-Hill Book Company, Inc., New York, to be published), National Nuclear Energy Series, Division IV, Vol. 9B; Nucleonics 2, 12 (January, 1948).

[28] M. Freedman and F. Wagner (to be published).

[29] B. H. Ketelle and J. W. Ruch, Phys. Rev. 77, 565 (1950).

Previous results based on measurements of the initial half-thickness of the absorption curve, or on Feather analyses were 0.3 Mev,[2,3] 0.32 Mev,[4,5] and 0.31±0.03 Mev.[25]

The absorption measurements showed that the ratio of beta- to gamma-counting rates was greater than 20,000, which corroborates the previous measurements[3–5] indicating no gamma-ray. These results indicate less than 1 gamma-ray per 100 beta-particles.

We wish to express our gratitude to Mr. Laurence Sjoblom, Mrs. Marilyn Sietsema, Mrs. R. Hospelhorn, and particularly Mr. Jerome Lerner, who aided us at various stages of the measurements.

PHYSICAL REVIEW VOLUME 81, NUMBER 5 MARCH 1, 1951

The Reaction Energies of Light Nuclei from Magnetic Analysis*

E. N. Strait,† D. M. Van Patter, W. W. Buechner, and A. Sperduto
Physics Department and Laboratory for Nuclear Science and Engineering, Massachusetts Institute of Technology, Cambridge, Massachusetts

(Received November 28, 1950)

An extensive survey has been made of the reaction energies of ground-state transitions induced by proton and deuteron bombardment of light nuclei. A total of nineteen stable nuclei from deuterium through sulfur was investigated, and the Q-values directly measured for thirty-eight different reactions. From these Q-values, the energy releases of a number of other reactions have been computed. The reactions studied include the (p, α), (d, p), and (d, α); and the individual Q-values have been determined to precisions that are between 0.08 and 0.25 percent. The reaction products were analyzed by means of 180-degree focusing in the field of a large annular magnet.

The Q-values measured include those of a series of nuclear reactions which directly connect the mass of the alpha-particle with the deuteron mass and O^{16}. From these measurements, the mass of the alpha-particle has been determined as 4.003865±0.000007 amu.

I. INTRODUCTION

UNTIL the last few years measurements of the reaction energies of ground-state transitions involving charged particles were confined to range methods where the precision available was generally not better than 100 kev. In many cases the results of these measurements have been used to establish the masses of the nuclei involved in the reactions. However, magnetic analysis, as opposed to range measurements, makes possible an improvement in precision of approximately a factor of 10, with an attendant improvement in the accuracy to which masses can be established.

In 1947, a high resolution analyzing system was constructed at the M. I. T. High Voltage Laboratory for the specific purpose of determining Q-values of nuclear reactions to a high precision.[1] This consisted of a 90-degree deflecting magnet for analysis of the bombarding deuterons or protons and a large annular magnet for 180-degree focusing of the reaction products. During 1948 and 1949, a number of reaction energies were measured with greater accuracy than previously reported. The reactions investigated were as follows:[2–4] $Li^6(d, p)Li^7$ and $Li^7(d, p)Li^8$; $Be^9(d, \alpha)Li^7$ and $Be^9(d, p)Be^{10}$; and $C^{12}(d, p)C^{13}$ and $O^{16}(d, p)O^{17}$. During the past year, these investigations have been extended to a survey of over thirty-five reactions involving target nuclei from D^2 to S^{32}, including remeasurements of the reactions already reported. In some of these reactions, the ground-state group has not been previously observed. This paper will be confined to a report of the results on the ground-state transitions. The results on transitions to excited states of the residual nuclei will be described in other publications, some of which have already appeared in print.[5,6]

* A report of these measurements was made at the Chicago Meeting of the American Physical Society, November, 1950. Phys. Rev. 81, 315 (1951).

† Now at Northwestern University, Evanston, Illinois.

[1] Buechner, Strait, Stergiopoulos, and Sperduto, Phys. Rev. 74, 1569 (1948).

[2] E. N. Strait and W. W. Buechner, Phys. Rev. 76, 1766 (1949).

[3] W. W. Buechner and E. N. Strait, Phys. Rev. 76, 1547 (1949).

[4] Buechner, Strait, Sperduto, and Malm, Phys. Rev. 76, 1543 (1949).

[5] Buechner, Van Patter, Strait, and Sperduto, Phys. Rev. 79, 262 (1950).

[6] Van Patter, Sperduto, Strait, and Buechner, Phys. Rev. 79, 900 (1950).

II. EXPERIMENTAL PROCEDURE

While the apparatus and experimental techniques employed in these investigations were essentially similar to those described in previous papers,[1-6] a number of improvements in the methods for obtaining and analyzing the data have been incorporated, which increase the precision of the energy measurements. These changes in apparatus and techniques are described below.

In the results reported in some of the above papers,[1-4] the uncertainties in the fundamental constants used to make the conversion from observed Hr values to particle energies and the uncertainty of the Rosenblum and Dupouy[7] value for Hr of polonium alpha-particles used to calibrate our fluxmeter[4] led to uncertainties of the order of 2.5 in 10^3 in the particle energies. By adopting DuMond's value[8] of 9652.2±0.7 emu/gram for the Faraday and using exact masses for the proton, deuteron, alpha-particle, and so forth, the uncertainty in the particle energies arising from conversion from observed Hr to energy has been reduced to about 7 parts in 10^5.

Rutherford and his collaborators[9] made careful measurements of the relative velocities of alpha-particles from various radioactive sources. They found the velocity of polonium alphas to be 0.83100 that of RaC′ alphas, with an accuracy of 2 in 10^4. Briggs' value[10] for Hr of RaC′ alpha-particles is 3.99277×10^5 absolute emu to within 4 parts in 10^5. A combination of these results, together with appropriate relativity factors, gives a value of 3.3159×10^5 gauss centimeters (abs. emu), accurate to 1 part in 5000, for polonium alpha-particles. Heretofore, we have used Rosenblum's value of 3.3158×10^5 gauss centimeters, which had an uncertainty of 1 part in 1000. While no change in our previously reported energy values is required because of this change, the uncertainty in the measurements arising from the standard used for fluxmeter calibration has been reduced to 4 parts in 10^4.

A precise measurement has been made of the angle which the incident ion beam makes with the median plane of the annular magnet. Previously, this angle was known only to be within the limits imposed by the collimating system for the ion beam. These limits were necessarily rather wide for reasons of beam intensity. This is the angle with respect to the incident beam at which particle energies are observed; and, since an uncertainty δ in its value causes in the reaction energy an uncertainty $\Delta Q=2(M_1M_2E_1E_2)^{\frac{1}{2}}\delta/M_3$, it is necessary for precise results that δ be small. M_1, M_2, E_1, and E_2 are the masses and energies of the incident and emitted particles, respectively, and M_3 is the mass of the residual nucleus.[11]

To measure the angle of observation, an extension tube about 6 feet in length was placed at the ion-beam exit from the annular magnet and a proton beam was allowed to pass through the target chamber and impinge on a quartz disk at the far end of the tube. Appropriate cross hairs and narrow collimating slits made it possible to measure accurately the beam direction. Measurements were also made on the effect of the fringing field of the annular magnet at various field strengths over the range normally used for the study of reaction energies. The angle of observation was found to take on values from $(\frac{1}{2}\pi-0.0029)$ radians at zero field to $(\frac{1}{2}\pi-0.0015)$ radians at maximum field. The uncertainty, δ, varied from ±0.0007 radian at zero field to ±0.0002 radians at maximum field. The terms 0.0029 radian to 0.0015 radian represent the deviation from 90 degrees and are now applied as correction terms in the calculation of Q-values. The uncertainty, δ, is smaller by at least a factor of 10 than before and now contributes less than 1 kev to the uncertainties that must be placed on the measured reaction energies.

Calculations have been made that permit corrections for the effect of the finite acceptance angle (approximately 0.004 radian either side of the median plane) that the collector (nuclear-track plate) subtends at the target and also for the width of the portion of the target illuminated by the incident ion beam. The results of the calculations have been verified experimentally by observations of the peak shape and position as determined from counting different areas of the same plate. These corrections amount to about 1.5 kev in the cases of the more sensitive reactions, which are characterized by high Q-values and light residual nuclei. The uncertainty in such a correction, arising from the uncertainty in peak shape, is a fraction of a kilovolt.

The relative location of the alpha-particle source used for fluxmeter calibration and of the position of the beam on the target has been remeasured with improved precision. This relationship is of interest, since it is of considerably greater importance in translating fluxmeter readings into evaluations of Hr than is the full diameter of the magnet itself. To make this measurement, a nuclear-track plate was placed in a small holder in the target position and was bombarded with deuterons from the generator. In order to keep the exposure low enough to permit observation of track distribution, the emulsion was covered with an aluminum foil of appropriate thickness to stop the deuterons but to permit passage of protons from $Al^{27}(d, p)Al^{28}$. The track distribution was found to have a shape nearly identical to that obtained for thin-target reaction products focused by the analyzing magnet. This demonstrates, incidentally, the absence of any serious focusing aberrations. To relate this distribution to the location of the alpha-source, a

[7] S. Rosenblum and G. Dupouy, Compt. rend. **194**, 1919 (1932).
[8] J. W. M. DuMond, Phys. Rev. **77**, 411 (1950).
[9] W. B. Lewis and B. V. Bowden, Proc. Roy. Soc. (London) **A145**, 250 (1934).
[10] G. H. Briggs, Proc. Roy. Soc. (London) **A157**, 183 (1936).
[11] M. S. Livingston and H. A. Bethe, Revs. Modern Phys. **9**, 245 (1937), Eq. (770).

low power microscope was used with a 6× objective and a 10× ocular with scale. The source wire and a fiducial mark on the plate holder were swung in succession into the field of view, and measurements were made between the observed positions. This permitted an accuracy of at least 0.05 mm for each measurement, so that the possible error in Hr due to an uncertainty in our knowledge of this relative location is only 1 part in 10,000.

As discussed previously,[1-3] the sharpness of the high energy edge of the peak of tracks observed on the photographic plates determines the precision with which the peak can be located. In general, this sharpness is established by the statistics of the number of tracks collected in the peak and, for most of the results presented here, was such as to permit the location of the high energy edge to within 0.1 mm. The plates on which the peaks are detected are 2 inches long, and their mean distance from the target is 710 mm. Thus, the possible error in the measurement of particle energy due to this uncertainty in the location of the peak is 2 parts in 7000.

A circuit for stabilizing the current supply to the annular magnet has been used during most of the work reported here. This circuit does not supply the entire magnet current. It operates by bypassing a fraction of the current through a 6L6, the amount bypassed swinging from 0 to 0.2 amp in response to an error signal from a potentiometer and galvanometer system connected across a standard resistor in the magnet circuit. Deflection of the galvanometer from the normal balance position is detected by photo-cells in the galvanometer light beam. Except for a few minor changes, this circuit is the same as that used for maintaining constant current through the fluxmeter coil. With the stabilizing circuit in use, it is possible to employ in a routine fashion the full sensitivity, about 3 parts in 10^5, of the fluxmeter. Stability of the annular magnet is particularly important when making measurements on high energy particles where small changes in magnetic field represent large kev shifts.

The rectangular magnet, which is used to deflect the incident ion beam through 90 degrees and thus define its energy, has been operated without automatic stabilization. Fluctuations of this magnetic field contribute no more than about 5-kev uncertainty to the observations on reaction energies even in those reactions whose Q-values are most sensitive to changes in the incident energy.

The effects of surface contamination on the targets on the energies of the bombarding and emitted particles were given careful attention. They are of particular importance in low energy reactions and in those involving alpha-particle emission. We have used six different methods of estimating these effects:

1. A given reaction may be observed by means of the recoil nuclei as well as of the lighter emitted particle. The $Be^9(d, \alpha)Li^7$ reaction is a good illustration. This reaction leads to the emission from the target of energetic Li^7 particles which are singly, doubly, and triply charged. Since the doubly charged particles are focused at nearly the same field strength as the alpha-particles, they are the most convenient to study. In the absence of surface contamination, the Q-value obtained for $Be^9(d, \alpha)Li^7$ should be the same as that for $Be^9(d, Li^{7++})He^4$. However, if there is contamination present, it will affect the emitted alpha less than it does the Li^{7++}, thereby leading to a lower value for the reaction energy observed by the latter reaction. By comparing the losses of energy per unit thickness of contamination for the incident deuteron, the emitted alpha, and the Li^{7++}, it is possible to express the shift of the Q for $Be^9(d, \alpha)Li^7$ from its true value in terms of the difference between the observed Q's for $Be^9(d, \alpha)Li^7$ and $Be^9(d, Li^{7++})He^4$. Another example of this method is $Li^6(p, \alpha)He^3$ and $Li^6(p, He^{3++})He^4$.

Where suitable, this method provides a very convincing demonstration of the amount of surface contamination. Unfortunately, it is useful in only a very limited number of reactions, since in only a few do the recoil nuclei have sufficient energy to make observable tracks in the emulsion.

2. Method 1 can be extended for use where its direct application is not possible. For instance, in the $Be^9(d, p)Be^{10}$ and $Be^9(p, d)Be^8$ reactions, it is not possible to observe the recoil nuclei. However, using the example of Method 1, the air equivalence of the contamination over the Be^9 target can be calculated and then used to correct the measurements of other reaction energies using this target.

3. Where neither Method 1 nor 2 is suitable, shifting the incident energy over wide limits will achieve somewhat the same effect, since the energy losses for both the incident and the emitted particles will be different at the different voltages. However, this is not so sensitive a method as is 1.

4. In the case of targets evaporated onto thin foil backings, it is possible to examine the elastic scattering of the incident ions by both the target material and surface contamination. Any difference between the energies of the ions scattered by the target material nda of those scattered by the surface contamination, other than the difference predicted by conservation of momentum, is attributable to the thickness of the contamination and may be used to calculate this thickness. With a target evaporated onto a thin Formvar foil, the ions scattered by carbon and by oxygen show double peaks, the high energy ones being due to surface contamination on the target material, whereas, the others are due to the carbon and to the oxygen in the Formvar foil.

5. The target may be deliberately heated prior to and during bombardment in order to drive off volatile contaminants. However, the difficulty is frequently encountered of evaporating away the target material itself ,when using temperatures sufficiently high to ensure freedom from contamination.

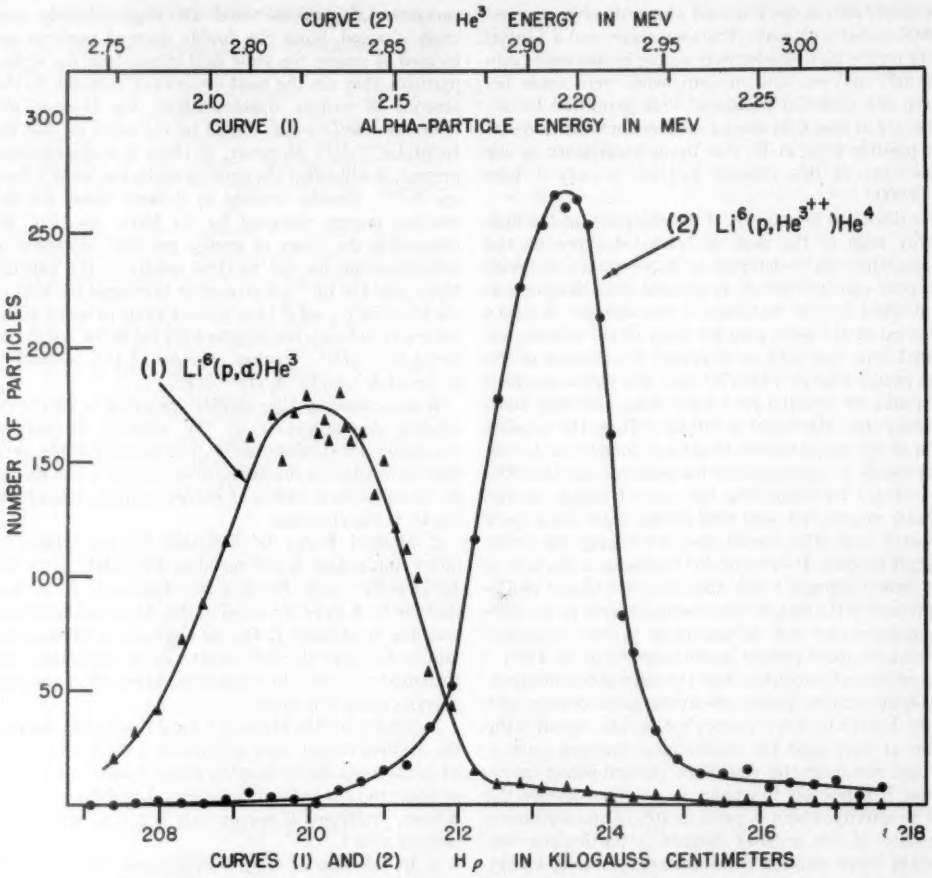

FIG. 1. Alpha-particle and He^{3++} groups from Li^6SO_4 target bombarded by 1.51-Mev protons.

6. If none of the above methods is suitable, it is necessary to rely on the use of freshly prepared targets. Experience has shown that the contamination builds up during prolonged bombardment. Therefore, if it is not possible to correct for the contamination by one of the above methods, it becomes necessary to prepare a fresh target for each bombardment. If several independently prepared targets lead to consistent values for the reaction energy, it is reasonable to assume that there is but little contamination.

III. RESULTS

A series of measurements has been made of the reaction energies of thirty-eight ground-state transitions induced by proton and deuteron bombardment of light elements from deuterium through sulfur. The bombarding energy used was usually close to 1.5 Mev; however, in a few cases, bombarding energies from 0.7 to 1.8 Mev were used. In the following sections, the reactions investigated for each nucleus are described. Each of the Q-values reported has been derived from a relativistic Q-equation, and the stated uncertainty has been arrived at from a consideration of the effect on the particular reaction of the various possible sources of error mentioned in Sec. II and in reference 4.

$D^2(d, p)T^3$

It is difficult to prepare thin deuterium targets directly, but this reaction may be observed from the deuterium deposited on targets exposed to the beam. A sharp proton group which we ascribe to this source has been found from a target of SiO_2 evaporated onto platinum sheet. Measurements on the energy of this group were made at bombarding energies of 1.60, 1.70, and 1.81 Mev. The Q-values obtained for these three energies agree to within ± 3 kev, the average being

4.030±0.006 Mev. The group was identified as arising from deuterium, since a change of 105±3 kev in the bombarding energy produced a change of 25.8±1.8 kev in the energy of the group. This is in accord with the change of 26.1±0.8 kev expected from the $D^2(d, p)T^3$ reaction and could not be correlated with the energy shift expected from any other (d, p) reaction. For example, for a target nucleus of mass 3, the shift would be 52±2 kev. This value of 4.030±0.006 Mev is in good agreement with a previous value of 4.036±0.022 Mev also obtained from magnetic analysis.[12] As will be mentioned in a later section, it is also in agreement with the value calculated from the Q-values measured for the $C^{12}(d, p)C^{13}$ and $C^{13}(d, t)C^{12}$ reactions.

$Li^6(p, \alpha)He^3$

The target used for this reaction was a thin layer of lithium sulfate, enriched in the Li^6 isotope evaporated onto a platinum backing. (The enriched lithium was obtained from the Isotopes Division, AEC, Oak Ridge.) It was found possible to observe on the same nuclear-track plate both the He^{3++} and alpha-particle groups emitted from Li^6 when bombarded by protons, as shown in Fig. 1. The ranges of the He^{3++} and He^4 particles in the nuclear-track emulsions were sufficiently different to permit the accurate resolution of the two groups. In addition, an estimate of surface contamination present could be made from the simultaneous observation of these two groups. The effect of surface contamination would be to make the Q-value determined from the He^4 group lower than that of the He^3 group because of the higher loss of energy of the alpha-particles for a given layer of contaminant. The observed Q-values for the $Li^6(p, \alpha)He^3$ and $Li^6(p, He^{3++})He^4$ reactions were 4.0202 and 4.0185 Mev, respectively. The difference between these values is −1.7±5.1 kev, indicating a correction for surface contamination of less than 3.4 kev for the $Li^6(p, \alpha)He^3$ reaction. The resulting Q-value for the $Li^6(p, \alpha)He^3$ reaction is 4.021±0.006 Mev, in agreement with the values of 4.017±0.022 Mev[13] and 3.97±0.03 Mev[14] found by other workers using magnetic analysis.

$Li^6(d, p)Li^7$

Immediately following the observation of the $Li^6(p, \alpha)He^3$ reaction, deuterons were substituted for protons as bombarding particles, and the $Li^6(d, p)Li^7$ ground-state proton group was observed. The correction for contamination was negligible for this reaction, being less than 0.1 kev. From an average of two independent observations, the Q-value of this reaction was measured as 5.019±0.007 Mev. This value is somewhat higher than the earlier value of 5.006±0.014 Mev[2] reported by this laboratory. In this earlier work, no correction was made for surface contamination. The only previous measurement of this reaction energy was Q=5.02 ±0.12 Mev[15] from range measurements.

$Li^7(p, \alpha)\alpha$

The $Li^7(p, \alpha)\alpha$ alpha-particle group was observed from the same lithium-sulfate target (enriched in Li^6) that was used for the investigation of the $Li^6(p, \alpha)He^3$ reaction described in the previous section. Since the alpha-particles from this reaction have high energy (9 Mev), the correction for surface contamination was negligible (less than 1 kev). As has been reported,[16] the Q-value measured for the $Li^7(p, \alpha)\alpha$ reaction was 17.340±0.014 Mev, which is considerably higher than the earlier range measurement of 17.28±0.03 Mev.[17] However, our value has been recently confirmed by Whaling and Li,[18] who find a value of 17.338±0.011 Mev from magnetic analysis and direct comparison with ThC′ alpha-particles.

$Li^7(d, p)Li^8$

Our earlier measurement of the $Li^7(d, p)Li^8$ reaction was made using a thin target of LiF on a silver backing, and the resulting Q-value of −0.193±0.008 Mev reported.[2] However, an observation of the $Li^7(p, \alpha)\alpha$ alpha-group was also made at that time which gave a Q-value of 17.338. Comparison with the later value of 17.340 Mev for the $Li^7(p, \alpha)\alpha$ reaction results in a correction of 5.5±5.5 kev due to surface contamination for the Q-value of the $Li^7(d, p)Li^8$ reaction. The revised Q-value of this reaction is −0.188±0.007 Mev. These results have been recently confirmed by Paul,[19] who reports a Q-value of −0.187±0.010 Mev from the measurement of the angle of recoil of the Li^8 nuclei.

$Li^7(d, \alpha)He^5$

An investigation of the $Li^7(d, \alpha)He^5$ reaction was made at 1.51-Mev bombarding energy using a thin target of LiOH evaporated onto a platinum backing. In contrast to the observations of all other ground-state transitions studied to date at this laboratory, no sharp ground-state group was found. Instead, a continuous distribution of alpha-particles was observed.

From a maximum energy of about 9 Mev, the number of alpha-particles in the distribution increased to a broad maximum at about 8.3-Mev alpha-particle energy, then decreased slowly at lower alpha-energies. The midpoint of the increasing slope occurred in a region of 8.45- to 8.63-Mev alpha-energy, corresponding to an energy release of 14.3 to 14.6 Mev. These observations are somewhat in contrast to the range measurements of

[12] Tollestrup, Jenkins, Fowler, and Lauritsen, Phys. Rev. **75**, 1947 (1949).
[13] Tollestrup, Fowler, and Lauritsen, Phys. Rev. **76**, 428 (1949).
[14] W. E. Burcham and J. M. Freeman, Phil. Mag. **41**, 921 (1940).
[15] J. D. Cockcroft and E. T. Walton, Proc. Roy. Soc. (London) A144, 704 (1934).
[16] Strait, Van Patter, Sperduto, and Buechner, Phys. Rev. **81**, 315 (1951).
[17] N. R. Smith, Phys. Rev. **56**, 548 (1939).
[18] W. Whaling and C. W. Li (private communication).
[19] E. B. Paul, Phil. Mag. **41**, 942 (1950).

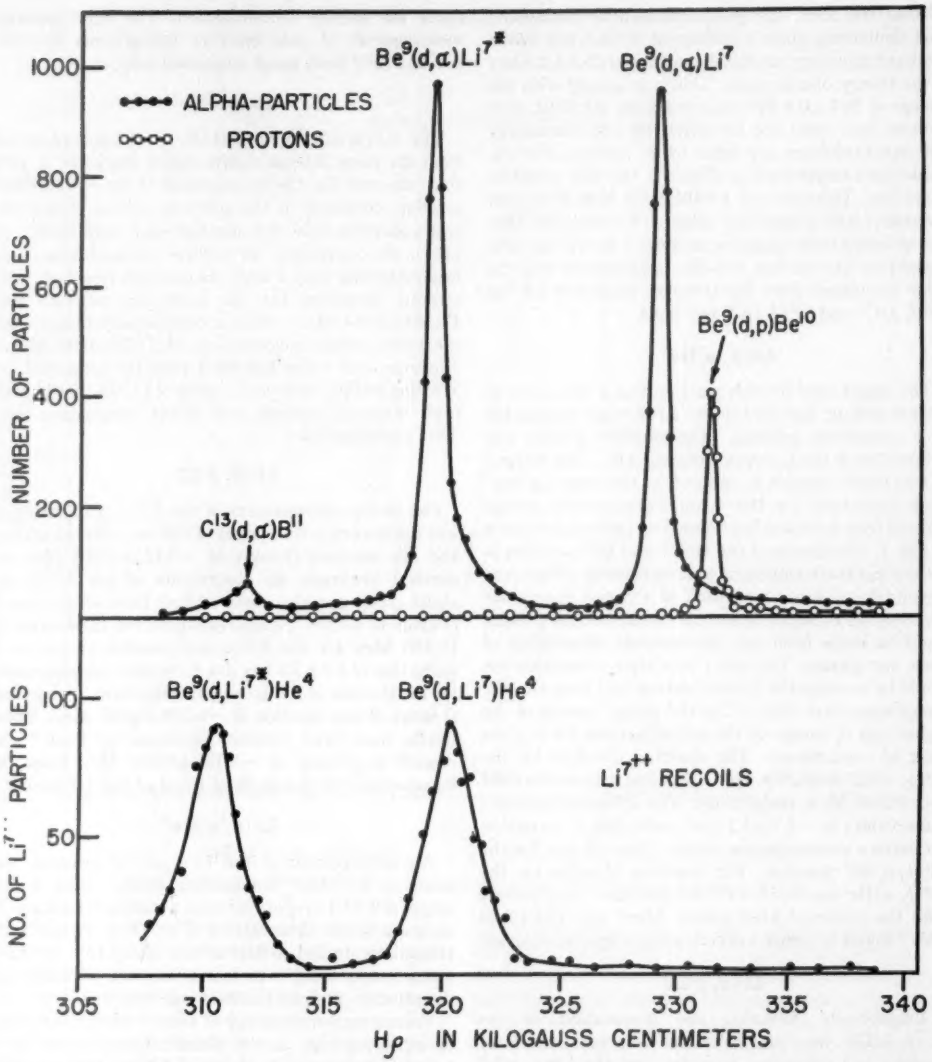

FIG. 2. Alpha-particles, Li^{7++} recoils, and protons observed from a beryllium target bombarded by 1.51-Mev deuterons.

Williams, Shepherd, and Haxby,[20] who observed a $Li^7(d, \alpha)He^6$ alpha-group with a Q of 14.3 Mev and a half-width of 0.14 Mev at 0.2-Mev bombarding energy.

Be^9

Accurate determinations have been made of the reaction energies of the (p, d), (p, α), (d, α), and (d, p) reactions of the nucleus Be^9. The targets used consisted of thin layers of beryllium evaporated onto platinum backings.

$Be^9(p, d)Be^8$

A study was made of the reaction $Be^9(p, d)Be^8$ at two bombarding energies which differed by 0.75 Mev. Because of the low Q-value of this reaction, the result of such a change in bombarding energy provides a fairly good method of estimating the amount of surface

[20] Williams, Shepherd, and Haxby, Phys. Rev. 51, 888 (1937).

contamination present, since any surface layers would cause the Q-value observed at the lower bombarding energy to be lower also. The Q-value observed at 0.75- and 1.5-Mev bombarding energies were 0.565±0.004 Mev and 0.560±0.006 Mev, indicating that the correction for contamination was negligible within the error of determination of ±4 kev. The weighted average of three measurements is $Q=0.562\pm0.004$ Mev, in good agreement with the reported value of 0.558±0.003 Mev[19] and in fair agreement with other previously reported values of 0.547±0.006 Mev[21] and 0.541±0.003 Mev.[22] The present value is also in excellent agreement with the figure of 0.560±0.004 Mev obtained from the recent precise measurements of the photo-neutron thresholds of beryllium and deuterium.[23]

$Be^9(d, \alpha)Li^7$

As described in an earlier section, the Q-value of the $Be^9(d, \alpha)Li^7$ ground-state reaction can be corrected for surface contamination by observation of both the alpha-particles and the Li^{7++} recoils. As illustrated by the data in Fig. 2, an observation was made of the Li^7 recoils corresponding to the ground-state reaction and of the alpha-particle group corresponding to the 478.5-kev[24] excited state of Li^7. The measured Q-values of these groups were 7.1399 and 6.6687 Mev. A Q-value of 7.1472 Mev was thus indicated for the $Be^9(d, \alpha)Li^7$ ground-state alpha-group. Hence, the observed difference in Q-values obtained from the alpha-particles and Li^{7++} recoils was 7.3±3.4 kev. After correction for the contribution to the half-width due to geometry, the ratio of the energy losses per unit thickness of surface layer was estimated from the observed half-widths of the Li^{7++} and alpha-particle groups. From the difference in observed Q-values, a correction for contamination of 1.5±0.7 kev was calculated for the $Be^9(d, \alpha)Li^7$ Q-value. As a result of two such measurements, an average Q-value for the $Be^9(d, \alpha)Li^7$ ground-state reaction was found to be 7.150±0.008 Mev. This is slightly higher than the earlier value of 7.145±0.024 Mev reported[3] from our laboratory. This earlier value was not corrected for surface contamination. Recently, Whaling and Li[18] have measured a Q-value of 7.151±0.010 Mev using magnetic analysis. This is in excellent agreement with the value reported here.

$Be^9(p, \alpha)Li^6$

Immediately following the measurement of the Li^{7++} and alpha-particle groups from the $Be^9(d, \alpha)Li^7$ reaction, the $Be^9(p, \alpha)Li^6$ ground-state alpha-group was observed from the same beryllium target. Assuming that the amount of surface contamination had not changed, a correction for contamination of 2.7±1.3 kev was estimated for the $Be^9(p, \alpha)Li^6$ reaction. The Q-value found is 2.142±0.006 Mev, somewhat higher than the previously reported value of 2.121±0.012 Mev, also obtained from magnetic analysis by Tollestrup, Fowler, and Lauritsen.[13]

$Be^9(d, p)Be^{10}$

An earlier measurement was made of the $Be^9(d, \alpha)Li^7$ reaction using a target with a considerably larger amount of surface contamination. On the same nuclear-track plate, the $Be^9(d, p)Be^{10}$ ground-state proton group was observed, as indicated in Fig. 2. The correction for surface contamination was estimated to be 1.9±0.2 kev for the $Be^9(d, p)Be^{10}$ reaction, resulting in a corrected Q-value of 4.585±0.008 Mev. This value is somewhat higher than our earlier reported[3] value of 4.576±0.012 Mev, which was not corrected for surface contamination. An accurate check on our value is provided by the recent measurement with a pair spectrometer of the $Be^9(n, \gamma)Be^{10}$ Q-value. This has been reported by Kinsey *et al.*[25] as 6.797±0.008 Mev. Combining their result with the latest value of 2.226±0.003 Mev[26] for the deuteron binding energy, a Q-value of 4.571±0.009 Mev is calculated for the $Be^9(d, p)Be^{10}$ reaction. Although this is somewhat lower than our value of 4.585±0.008 Mev, the difference is within the errors of the measurement.

$B^{10}(p, \alpha)Be^7$

The $B^{10}(p, \alpha)Be^7$ ground-state alpha-particles were first observed from a thin target of boron evaporated onto a thin film of Formvar. The B^{10} content of the boron used was enriched to 96 percent. (The enriched boron was obtained from the Isotopes Division, AEC, Oak Ridge.) This target had been exposed to long beam bombardments. The measured Q-value was 1.134 Mev. However, the incident proton energy calculated from the observed $B^{10}(p, p)B^{10}$ group was 3 kev lower than that calculated from the $C^{12}(p, p)C^{12}$ group, indicating a surface layer of carbon which would lower the $B^{10}(p, \alpha)Be^7$ Q-value by about 20 kev. Fresh targets of enriched B^{10} were evaporated onto platinum backings, and the $B^{10}(p, \alpha)Be^7$ ground-state group was observed at 1.30-Mev bombarding energy. The average Q-value from two measurements from targets not previously bombarded is 1.152±0.004 Mev, verifying the earlier rough estimate of surface contamination. This value for the $B^{10}(p, \alpha)Be^7$ reaction has already been reported[6] and is in agreement with the values of 1.148±0.006 Mev[26] and 1.147±0.010 Mev[27] reported by other workers.

$B^{10}(d, p)B^{11}$

The ground-state proton group from the $B^{10}(d, p)B^{11}$ reaction has been observed from targets of enriched B^{10}

[21] Allison, Skaggs, and Smith, Phys. Rev. **57**, 550 (1940).
[22] L. del Rosario, Phys. Rev. **74**, 304 (1948).
[23] R. C. Mobley and R. A. Laubenstein, Phys. Rev. **80**, 309 (1950).
[24] Ter-Pogossian, Robinson, and Goddard, Phys. Rev. **76**, 1407 (1949).
[25] Kinsey, Bartholomew, and Walker, Phys. Rev. **78**, 481 (1950).
[26] Brown, Chao, Fowler, and Lauritsen, Phys. Rev. **78**, 88 (1950)
[27] W. E. Burcham and J. M. Freeman, Phil. Mag. **41**, 337 (1950).

and natural boron on platinum and thin Formvar backings. The average of seven independent observations gave a Q-value of 9.235±0.011 Mev. A preliminary report of this result has already been given.[28]

$B^{11}(p, \alpha)Be^{8}$

Three measurements were made of the Q-value of the $B^{11}(p, \alpha)Be^{8}$ ground-state alpha-group using thin targets of natural boron which had not been previously bombarded. The three Q-values obtained agreed within ±1 kev, indicating the absence of appreciable contamination and giving an average value of 8.567±0.011 Mev. The only previous value reported is 8.60±0.10 Mev from range measurements.[29]

$B^{11}(d, p)B^{12}$

The results for the $B^{11}(d, p)B^{12}$ reaction have been previously described in detail.[5] Three observations were made of the ground-state proton group at deuteron bombarding energies of 0.7, 1.51, and 1.67 Mev. The Q-values obtained from these measurements agreed within 2 kev, indicating that no correction was necessary for surface contamination. The average Q-value obtained for the $B^{11}(d, p)B^{12}$ reaction was 1.136±0.005 Mev.

$B^{11}(d, \alpha)Be^{9}$

Three determinations of the $B^{11}(d, \alpha)Be^{9}$ ground-state Q-value were made from targets that had not been previously bombarded. As has been reported,[30] the resulting values agreed within ±3 kev, giving an average value of 8.018±0.007 Mev.

$C^{12}(d, p)C^{13}$

A careful remeasurement of the $C^{12}(d, p)C^{13}$ reaction energy has been made from several observations of the ground-state proton group originating from surface contamination containing carbon that occurs on all targets. Seven determinations of the $C^{12}(d, p)C^{13}$ reaction energy were made, all of which agreed within ±4 kev. The weighted average of these values is 2.716±0.005 Mev, somewhat lower than the earlier value of 2.729 ±0.009 Mev previously reported[4] from this laboratory. Two independent confirmations of this value can be obtained from results on other reactions. From the $C^{12}(d, n)N^{13}$ and $C^{13}(p, n)N^{13}$ Q-values of −0.281±0.003 Mev[31] and −3.003±0.003 Mev,[32] a Q-value of 2.722 ±0.004 Mev for the $C^{12}(d, p)C^{13}$ reaction may be calculated. A combination of the $C^{12}(n, \gamma)C^{13}$ Q-value of 4.947±0.008 Mev[33] and the deuteron binding energy of 2.226±0.003 gives a $C^{12}(d, p)C^{13}$ Q-value of 2.720±0.009 Mev. These values are in good agreement with the present result.

$C^{13}(d, t)C^{12}$

There have been no previous reports concerning the $C^{13}(d, t)C^{12}$ reaction. However, in these investigations, a group of particles was observed whose range in the nuclear-track plates was slightly less than the range for alpha-particles giving the same Hr value, indicating that the particles could be identified as tritons. For a change in bombarding energy of 188±3 kev, the observed energy change of this group was 126±3 kev compared with an expected change of 125±2 kev for a triton group from the $C^{13}(d, t)C^{12}$ reaction. The change in Hr was much greater than could be expected for a (d, p) or a (d, α) group reaction. This triton group was observed from four different targets, evidently originating from the 1.1 percent of C^{13} in the natural carbon contamination on the targets. The weighted average of five determinations, agreeing within ±2 kev, gave a Q-value of 1.310±0.006 Mev for the $C^{13}(d, t)C^{12}$ reaction.‡ Combining this result with our measurement of the $C^{13}(d, p)C^{13}$ reaction Q-value, a Q-value of 4.026±0.008 Mev is calculated for the $D^{2}(d, p)T^{3}$ reaction. This result agrees within the experimental errors with the directly measured value of 4.030±0.006 Mev previously mentioned.

$C^{13}(d, p)C^{14}$ and $C^{13}(d, \alpha)B^{11}$

Investigations of the $C^{13}(d, p)C^{14}$ and $C^{13}(d, \alpha)B^{11}$ ground-state reactions were made using targets of $BaCO_3$ in which the C^{13} content was enriched to 52 percent. (The enriched carbon was obtained from The Eastman Kodak Company.) In addition, both ground-state groups have been observed from the natural carbon contamination (1.1 percent C^{13}) on various targets.

The $C^{13}(d, p)C^{14}$ and $C^{13}(d, \alpha)B^{11}$ ground-state Q-values were determined to be 5.948±0.008 Mev[34] and 5.160±0.010 Mev from a weighted average of at least three measurements in both cases. The fact that the Q-values for groups arising from surface carbon contamination agreed within 5 kev with these values indicated that the correction for surface contamination could be considered as negligible.

$N^{14}(d, p)N^{15}$ and $N^{14}(d, \alpha)C^{12}$

The $N^{14}(d, p)N^{15}$ and $N^{14}(d, \alpha)C^{12}$ reactions were investigated at 1.42-Mev bombarding energy using a tantalum-nitride target on a platinum backing. This target was heated to a dull red color during exposures in order to drive off volatile contaminants. Since hot

[28] D. M. Van Patter and W. W. Buechner, Phys. Rev. **79**, 240 (1950).
[29] Oliphant, Kempton, and Rutherford, Proc. Roy. Soc. (London) **A150**, 241 (1935).
[30] Van Patter, Sperduto, Huang, Strait, and Buechner, Phys. Rev. **81**, 233 (1951).
[31] Bonner, Evans, and Hill, Phys. Rev. **75**, 1398 (1949).
[32] H. T. Richards and R. V. Smith, Phys. Rev. **77**, 752 (1950).
[33] Kinsey, Bartholomew, and Walker, Phys. Rev. **77**, 723 (1950).

‡ We are indebted to R. G. Thomas for his suggestion that this triton group might be observed in our experiments.
[34] Sperduto, Holland, Van Patter, and Buechner, Phys. Rev. **80**, 769 (1950).

tantalum combines readily with both nitrogen and oxygen, there was a possibility that nonvolatile surface contaminants remained even at high temperatures. The existence of such contaminants was investigated by a comparison of the Q-values obtained for a $N^{14}(d, \alpha)C^{12*}$ alpha-particle group from the heated tantalum-nitride target and from a freshly prepared target consisting of a thin layer of ammonium nitrate deposited on a platinum backing. It was found that a small amount of such contamination was indeed present, and the measured $N^{14}(d, p)N^{15}$ and $N^{14}(d, \alpha)C^{12}$ Q-values obtained with the tantalum-nitride target were corrected accordingly.

As has been reported,[35] the Q-value obtained for the $N^{14}(d, p)N^{15}$ ground-state reaction is 8.615 ± 0.009 Mev. The fact that the Q-values of the ground-state proton group from nitrogen contamination on other targets agreed with this value within ±5 kev indicated that the correction for contamination for this Q-value was negligible. The recent measurement of the $N^{14}(n, \gamma)N^{15}$ Q-value as 10.823 ± 0.012 Mev[33] provides an accurate comparison with our results. After subtraction of the deuteron binding energy from the $N^{14}(n, \gamma)N^{15}$ Q-value, a Q-value of 8.597 ± 0.014 Mev is predicted for the $N^{14}(d, p)N^{15}$ reaction, in agreement with our result within the stated errors.

For reasons that will be described in a succeeding section, the Q-value obtained from measurements made on the $N^{14}(d, \alpha)C^{12}$ ground-state alpha-group was not considered so reliable as the value predicted from a combination of other reaction energies determined in this work.

N^{15}

The (d, α), (p, α), and (d, p) reactions of N^{15} were investigated using tantalum-nitride targets in which the nitrogen content was enriched to 60 percent N^{15}. (The enriched nitrogen was obtained in the form of NH_4NO_3 from the Eastman Kodak Company.) Comparison with the results obtained from tantalum-nitride targets of normal nitrogen (0.4 percent N^{15}) permitted the identification of the groups arising from the N^{15} isotope.

$N^{15}(d, \alpha)C^{13}$

The $N^{15}(d, \alpha)C^{13}$ ground-state group was observed at 1.42-Mev bombarding energy from a heated tantalum-nitride target. A correction for contamination of 6 ± 2 kev was estimated from the comparison of the Q-values for a $N^{14}(d, \alpha)C^{12}$ group from this target and an ammonium-nitrate target not previously bombarded. The corrected Q-value for the $N^{15}(d, \alpha)C^{13}$ reaction was 7.681 ± 0.009 Mev, compared with the only previously reported value of 7.54 ± 0.07 Mev,[36] which was obtained from range measurements.

$N^{15}(p, \alpha)C^{12}$

The $N^{15}(p, \alpha)C^{12}$ ground-state proton group was observed at 1.20-Mev bombarding energy, corresponding to a resonance for the yield of this group.[37] The heated target used was the same as for the $N^{15}(d, \alpha)C^{13}$ reaction; assuming the same amount of surface contamination, the correction for contamination was estimated as 7 ± 3 kev. The Q-value found for the $N^{15}(p, \alpha)C^{12}$ reaction is 4.960 ± 0.007 Mev, which is in agreement with a recently reported value of 4.96 ± 0.05 Mev[38] from magnetic analysis.

$N^{15}(d, p)N^{16}$

A search was made for the ground-state group of the $N^{15}(d, p)N^{16}$ reaction at 1.42-Mev bombarding energy. Only one proton group was found that could be assigned to the N^{15} isotope; this group had a Q-value of -0.034 ± 0.005 Mev.[35] The only previous investigation of the $N^{15}(d, p)N^{16}$ reaction was recently reported by Wyly,[39] who used targets of normal and enriched ammonia (61 percent N^{15}). By subtracting the normal-target data from the enriched-target data, he obtained a proton group that was assigned to the ground-state reaction of $N^{15}(d, p)N^{16}$. This was closely accompanied by a more intense group that was assigned to an excited state in N^{16} at about 0.3-Mev excitation. The Q for the higher energy group was 0.23 ± 0.15 Mev. It is possible that our observed $N^{15}(d, p)N^{16}$ proton group corresponds to the more intense group reported by Wyly and does not correspond to the ground-state transition.

$O^{16}(d, p)O^{17}$ and $O^{16}(d, \alpha)N^{14}$

Precise determinations have been made of the $O^{16}(d, p)O^{17}$ and $O^{16}(d, \alpha)N^{14}$ reaction energies, using targets consisting of a thin layer of Formvar (containing oxygen) on platinum backings. Two measurements of the $O^{16}(d, p)O^{17}$ Q-value, agreeing within 1 kev, gave an average value of 1.917 ± 0.008 Mev, which is somewhat lower than the value of 1.925 ± 0.005 Mev[4] previously reported. From two independent determinations agreeing within 1 kev, the Q-value of the $O^{16}(d, \alpha)N^{14}$ ground-state reaction was measured as 3.112 ± 0.006 Mev, as has been reported.[16] The correction for surface contamination is considered to be negligible for both these determinations. No measurements of comparable precision have been reported in the literature for these reactions.

F^{19}

Investigations of the (p, α), (d, p), and (d, α) reactions of F^{19} have been made. The ground-state groups from these reactions were first observed from targets of CaF_2, MgF_2, and LiF evaporated onto silver backings.

[35] R. Malm and W. W. Buechner, Phys. Rev. **80**, 771 (1950).
[36] M. G. Holloway and B. L. Moore, Phys. Rev. **58**, 847 (1940).
[37] Schardt, Fowler, and Lauritsen, Phys. Rev. **80**, 136 (1950).
[38] J. M. Freeman, Proc. Roy. Soc. (London) **63A**, 668 (1950).
[39] L. D. Wyly, Phys. Rev. **76**. 316 (1949).

All of these targets had been exposed to long beam bombardments, and it was found that large surface layers of contamination were present on them. As a result, fresh targets of PbF_2 evaporated onto platinum backings were prepared, and the ground-state groups were re-examined.

$F^{19}(p, \alpha)O^{16}$

The reaction energy of the $F^{19}(p, \alpha)O^{16}$ reaction was initially reported at 8.068 Mev.[40] However, this Q-value was measured again using a PbF_2 target not previously bombarded and was found to be 8.118±0.009 Mev. This result is in agreement with the value of 8.113±0.030 Mev reported by Chao *et al.*[41] from a combination of measured Q-values for the low energy alpha-particles from $F^{19}(p, \alpha)O^{16*}$ and gamma-ray measurements on the same reaction. Freeman[38] has recently reported a somewhat lower Q-value of 8.06±0.04 Mev, using magnetic analysis.

$F^{19}(d, \alpha)O^{17}$ and $F^{19}(d, p)F^{20}$

The ground-state Q-values of the $F^{19}(d, \alpha)O^{17}$ and $F^{19}(d, p)F^{20}$ reactions have been measured as 10.050 ±0.010 and 4.373±0.007 Mev from PbF_2 targets not previously bombarded. The $F^{19}(n, \gamma)F^{20}$ reaction energy has been recently reported as 6.63±0.03 Mev,[25] corresponding to a Q-value of 4.40±0.03 Mev for the $F^{19}(d, p)F^{20}$ reaction, in agreement with the value determined in the present experiments within the stated errors.

$Na^{23}(d, p)Na^{24}$ and $Na^{23}(d, \alpha)Ne^{21}$

The $Na^{23}(d, p)Na^{24}$ and $Na^{23}(d, \alpha)Ne^{21}$ reactions have been investigated using targets of sodium hydroxide and sodium iodide evaporated onto platinum backings. Three independent measurements of the $Na^{23}(d, p)Na^{24}$ ground-state group gave Q-values which agree within ±3 kev, the weighted average being 4.731±0.009 Mev. Three measurements of the $Na^{23}(d, \alpha)Ne^{21}$ Q-value agreed within ±6 kev, the weighted average for this reaction being 6.902±0.010 Mev. The effect of surface contamination is assumed to be negligible for these determinations. In the earlier range measurements[42, 43] on the $Na^{23}(d, \alpha)Ne^{21}$ reaction the alpha-particle groups corresponding to the ground state and 0.34-Mev excited state of Ne^{21} were not resolved. Reported Q-values for the $Na^{23}(p, \alpha)Ne^{20}$ and $Ne^{20}(d, p)Ne^{21}$ reactions of 2.35±0.04 Mev[38] and 4.50±0.09 Mev[44] give a predicted Q-value of 6.85±0.10 Mev for the $Na^{23}(d, \alpha)Ne^{21}$ reaction, which is in agreement with the result reported here.

$Mg^{24}(d, p)Mg^{25}$

Two observations were made of the $Mg^{24}(d, p)Mg^{25}$ ground-state proton group from a thin target of MgF_2 evaporated onto a platinum backing. The amount of surface contamination was estimated from a comparison of the Q-values of $F^{19}(d, p)F^{20}$ proton groups observed from this target with those found from fresh PbF_2 targets. The correction to the Q-value of the $Mg^{24}(d, p)Mg^{25}$ ground-state group due to surface contamination was found to be 3±3 kev. After allowance for this contamination, the Q-value was determined to be 5.094 ±0.010 Mev, which is somewhat higher than the value of 5.03±0.05 Mev[45] found from range measurements.

Al^{27}

The (d, p) and (d, α) ground-state reactions of Al^{27} have been investigated at bombarding energies from 1.2 to 2.0 Mev. Several targets were used, including thin layers of aluminum evaporated onto thin Formvar and platinum backings. In addition, a thin self-supporting foil of aluminum was used, which was obtained by dissolving away the Formvar backing of an evaporated aluminum target.

$Al^{27}(d, p)Al^{28}$

As has been reported,[46] the ground-state proton group previously observed in range measurements was found to be a doublet, corresponding to the ground state of Al^{28} and an excited state at 31±2 kev. The weighted average of five observations on the ground state, which agreed to within ±5 kev, gave a Q-value of 5.494±0.010 Mev. From a recent measurement of the $Al^{27}(n, \gamma)Al^{28}$ ground-state Q-value of 7.72±0.02 Mev,[25] a Q-value of 5.49±0.02 Mev may be calculated for the $Al^{27}(d, p)Al^{28}$ reaction, which is in excellent agreement with the present result.

$Al^{27}(d, \alpha)Mg^{25}$

A weighted average of five determinations of the $Al^{27}(d, \alpha)Mg^{25}$ reaction-energy group, which agreed to within ±5 kev, resulted in a Q-value of 6.694±0.010 Mev, as compared with a recent measurement of 6.62 ±0.05 Mev[47] obtained by magnetic analysis. However, combining the present Q-values for the $Al^{27}(d, \alpha)Mg^{25}$ and $Mg^{24}(d, p)Mg^{25}$ reactions, the $Al^{27}(p, \alpha)Mg^{24}$ reaction energy is calculated to be 1.600±0.014 Mev, which agrees with the recent accurate measurement of 1.585±0.015 Mev.[38]

$Si^{28}(d, p)Si^{29}$

An investigation of the $Si^{28}(d, p)Si^{29}$ reaction has been made at bombarding energies from 1.5 to 1.8 Mev, using

[40] Strait, Van Patter, and Buechner, Phys. Rev. **78**, 337 (1950).
[41] Chao, Tollestrup, Fowler, and Lauritsen, Phys. Rev. **79**, 108 (1950).
[42] E. O. Lawrence, Phys. Rev. **47**, 17 (1935).
[43] E. B. M. Murrell and C. L. Smith, Proc. Roy. Soc. (London) **A173**, 410 (1939).
[44] A. Zucker and W. W. Watson, Phys. Rev. **78**, 14 (1950).
[45] H. R. Allan and C. R. Wilkinson, Proc. Roy. Soc. (London) **A194**, 131 (1948).
[46] Enge, Van Patter, Buechner, and Sperduto, Phys. Rev. **81**, 317 (1951).
[47] A. P. French and P. B. Treacy, Proc. Phys. Soc. (London) **63A**, 665 (1950).

thin targets of normal SiO_2 evaporated onto platinum. The ground-state proton group has also been observed from silicon contamination on other targets, evidently arising from the silicon in the stopcock grease used in the vacuum system. Five independent determinations, agreeing within ±4 kev, give a weighted average of the $Si^{28}(d, p)Si^{29}$ reaction energy of 6.246±0.008 Mev,[48] which is in fair agreement with the recent measurement of 6.18±0.09 Mev using range measurements.[49]

$Si^{30}(d, \alpha)Al^{28}$

There have been no previous investigations of the $Si^{30}(d, \alpha)Al^{28}$ reaction reported in the literature. From a combination of the $Al^{27}(\alpha, p)Si^{30}$ and $Al^{27}(d, p)Al^{28}$ Q-values of 5.49±0.01 and 2.38±0.2 Mev,[50] a Q-value of 3.1±0.2 Mev can be estimated for the $Si^{30}(d, \alpha)Al^{28}$ reaction. Similarly, a Q-value of 2.9±0.2 Mev is found from a combination of the $Si^{28}(d, p)Si^{29}$, $Si^{29}(d, p)Si^{30}$, and $Al^{28}(\beta^-)Si^{28}$ reaction energies.

A search was made for the $Si^{30}(d, \alpha)Al^{28}$ ground-state alpha-group from a target of $Si^{30}O_2$, in which the Si^{30} was enriched to 64 percent of the silicon content. (The enriched silicon was obtained from the Isotopes Division, AEC, Oak Ridge.) The SiO_2 was evaporated onto a platinum backing. An alpha-group of low intensity was observed which did not appear from a target of normal SiO_2. However, the alpha-group was superimposed on an appreciable background caused by scattered deuterons from the platinum backing. To eliminate this background, a target of $Si^{30}O_2$ was evaporated onto a thin film of Formvar stiffened by a layer of evaporated copper. The same alpha-group was again observed with the background considerably reduced. Seven determinations, agreeing within ±7 kev, gave an average Q-value of 3.120±0.010 Mev for this alpha-group. Since the Q-value is in agreement with the $Si^{30}(d, \alpha)Al^{28}$ reaction energy calculated from other reactions, this group has been assigned to the ground-state transition.

$Si^{30}(d, p)Si^{31}$

From a combination of the $P^{31}(n, p)Si^{31}$, $P^{31}(d, \alpha)Si^{29}$, and $Si^{29}(d, p)Si^{30}$ Q-values of −0.94±0.13 Mev,[51] 8.170 ±0.020, and 8.36±0.10 Mev,[49] a ground-state Q-value of 4.12±0.17 Mev is calculated for the $Si^{30}(d, p)Si^{31}$ reaction. Motz and Humphreys, using normal silicon and enriched Si^{30} targets, have recently reported a Q-value of 4.33±0.15 Mev[49] from range measurements.

An investigation of the $Si^{30}(d, p)Si^{31}$ reaction has been made using normal SiO_2 (3 percent Si^{30}) and enriched SiO_2 (64 percent Si^{30}) targets evaporated onto platinum backings. At 1.80-Mev bombarding energy a proton group with a Q-value of 4.364±0.010 Mev was observed from both types of targets. The ratio of the observed yields of this group was approximately equal to the ratio of the amounts of Si^{30} in the two targets. No additional $Si^{30}(d, p)Si^{31}$ proton groups with an intensity greater than 0.15 the intensity of the group with Q=4.367 Mev were observed in the energy range which would correspond to Q-values from 4.25 to 4.95 Mev. As a result, this proton group has been assigned to the ground-state $Si^{30}(d, p)Si^{31}$ transition.

$P^{31}(d, \alpha)Si^{29}$

The previously unreported $P^{31}(d, \alpha)Si^{29}$ ground-state alpha-group was observed at 1.81-Mev bombarding energy, both from a 300-kev phosphorus target and from a 20-kev zinc-phosphate target. The Q-values observed from these targets agreed within 1 kev, the average being 8.170±0.020 Mev.[48] Because several $Si^{28}(d, p)$ proton groups were observed from these targets, indicating the presence of an unknown amount of surface contamination, a probable error of 20 kev has been placed on the $P^{31}(d, \alpha)Si^{29}$ Q-value.

$P^{31}(d, p)P^{32}$

A search was made for the ground-state $P^{31}(d, p)P^{32}$ proton group at 1.81-Mev bombarding energy using a thin zinc-phosphate target evaporated onto a platinum backing. The Q-value of the ground-state group has been reported as 5.9±0.3 Mev[52] from range measurements. The highest energy proton group observed that could be assigned to the $P^{31}(d, p)P^{32}$ reaction had a Q-value of 5.704±0.009 Mev, an average of four determinations which agreed to within ±5 kev. Although this Q-value is about 0.2 Mev lower than expected from masses, the masses of nuclei in this region of the periodic table are not known to much better than 0.2 Mev.[53] In addition, a combination of the Q-values of −0.931±0.008 Mev,§ −19.15[53] (no error given), and −12.35±0.2 Mev[54] for the $S^{32}(n, p)P^{32}$, $S^{32}(\gamma, d)P^{30}$, and $P^{31}(\gamma, n)P^{30}$ reactions gives a predicted value of 5.68±0.2 Mev for the $P^{31}(d, p)P^{32}$ reaction. Finally, Allen and Rall[55] have recently investigated the $P^{31}(d, p)P^{32}$ reaction and find a Q-value of 5.42±0.10 Mev for the ground-state group. This Q-value may be too low, since we have found a $P^{31}(d, p)P^{32}$ group with Q=5.627±0.009 Mev which would not have been resolved from the ground-state group by the range measurements of Allen and Rall. In the light of the above evidence, it is concluded that the proton group with Q=5.704±0.009 Mev corresponds to the $P^{31}(d, p)P^{32}$ ground-state transition.

$S^{32}(d, p)S^{33}$

The $S^{32}(d, p)S^{33}$ ground-state proton group has been observed at 1.81-Mev bombarding energy from a thin

[48] Endt, Van Patter, and Buechner, Phys. Rev. **81**, 317 (1951).
[49] H. T. Motz and R. F. Humphreys, Phys. Rev. **80**, 595 (1950).
[50] H. H. Landon, Phys. Rev. **78**, 338 (1950).
[51] Metzger, Alder, and Huber, Helv. Phys. Acta **21**, 278 (1948).
[52] E. Pollard, Phys. Rev. **59**, 1086 (1940).
[53] A. S. Penfold, Phys. Rev. **80**, 116 (1950).
§ This value is obtained from the 1.713±0.008-Mev end point for the P^{32} beta-ray spectrum and the $(n-p)$ difference of 782±2 kev.
[54] McElhinney, Hanson, Becker, Duffield, and Diven, Phys. Rev. **75**, 542 (1949).
[55] R. C. Allen and W. Rall, Phys. Rev. **81**, 60 (1951).

TABLE I. Observed reaction energies.

Reaction	Q-value (Mev)	Reaction	Q-value (Mev)
$D^2(d, p)T^3$	4.030±0.006	$N^{14}(d, p)N^{15}$	8.615±0.009
$Li^6(p, \alpha)He^3$	4.021±0.006	$N^{15}(p, \alpha)C^{12}$	4.960±0.007
$Li^6(d, p)Li^7$	5.019±0.007	$N^{15}(d, \alpha)C^{13}$	7.681±0.009
$Li^7(p, \alpha)\alpha$	17.340±0.014	$O^{16}(d, \alpha)N^{14}$	3.112±0.006
$Li^7(d, p)Li^8$	−0.188±0.007	$O^{16}(d, p)O^{17}$	1.917±0.005
$Be^9(p, \alpha)Li^6$	2.142±0.006	$F^{19}(p, \alpha)O^{16}$	8.118±0.009
$Be^9(p, d)Be^8$	0.562±0.004	$F^{19}(d, \alpha)O^{17}$	10.050±0.010
$Be^9(d, \alpha)Li^7$	7.150±0.008	$F^{19}(d, p)F^{20}$	4.373±0.007
$Be^9(d, t)Be^8$	4.597±0.013	$Na^{23}(d, \alpha)Ne^{21}$	6.902±0.010
$Be^9(d, p)Be^{10}$	4.585±0.008	$Na^{23}(d, p)Na^{24}$	4.731±0.009
$B^{10}(p, \alpha)Be^7$	1.152±0.004	$Mg^{24}(d, p)Mg^{25}$	5.094±0.010
$B^{10}(d, p)B^{11}$	9.235±0.011	$Al^{27}(d, \alpha)Mg^{25}$	6.694±0.010
$B^{11}(p, \alpha)Be^8$	8.567±0.011	$Al^{27}(d, p)Al^{28}$	5.494±0.010
$B^{11}(d, \alpha)Be^9$	8.018±0.007	$Si^{28}(d, p)Si^{29}$	6.246±0.008
$B^{11}(d, p)B^{12}$	1.136±0.005	$Si^{30}(d, \alpha)Al^{28}$	3.120±0.010
$C^{12}(d, p)C^{13}$	2.716±0.005	$Si^{30}(d, p)Si^{31}$	4.364±0.010
$C^{13}(d, \alpha)B^{11}$	5.160±0.010	$P^{31}(d, \alpha)Si^{29}$	8.170±0.020
$C^{13}(d, t)C^{12}$	1.310±0.006	$P^{31}(d, p)P^{32}$	5.704±0.009
$C^{14}(d, p)C^{15}$	5.948±0.008	$S^{32}(d, p)S^{33}$	6.422±0.011

target of iron sulfide evaporated onto a platinum backing and also from sulfur contamination of a zinc-phosphate target. Three measurements of the ground-state Q-value agreed within ±2 kev, giving a weighted average of 6.422±0.011 Mev. The correction for surface contamination is considered to be negligible because, in the case of one measurement, the iron-sulfide target had not been previously bombarded. An accurate verification of this result is provided by the recent measurement of the $S^{32}(n, \gamma)S^{33}$ Q-value as 8.66±0.02 Mev,[25] which gives a predicted $S^{32}(d, p)S^{33}$ Q-value of 6.43±0.02 Mev.

In Table I, we have listed the reaction energies that have been measured in these experiments. We have omitted from this table the results of measurements on the $N^{15}(d, p)N^{16}$ reaction where there is an uncertainty regarding the identification of the ground-state group. We have also omitted the results on the $Li^6(d, \alpha)\alpha$, $B^{10}(d, \alpha)Be^8$, and $N^{14}(d, \alpha)C^{12}$ reactions. As will be discussed in the following section, we believe our experimental results on these three reactions are somewhat too high and that more accurate values are obtained from calculations based on the Q-values in Table I.

IV. DISCUSSION

The measurements which are outlined in the preceding paragraphs and which have led to the reaction energies listed in Table I were made over a considerable period of time. It is possible to check their internal consistency and to determine whether any systematic variation in our standards had occurred during this period by calculating certain of the Q-values from the others and by comparing the values thus obtained with those directly observed. As has been mentioned, the Q-value for $D^2(d, p)T^3$ calculated from the results on $C^{12}(d, p)C^{13}$ and $C^{13}(d, t)C^{12}$ agrees within 4 kev with the directly measured value. Four other such calculations and comparisons are:

$Be^9(p, \alpha)Li^6$	2.142±0.006	$B^{11}(d, \alpha)Be^9$	8.018±0.007
$Li^6(d, p)Li^7$	5.019±0.007	$Be^9(p, d)Be^8$	0.562±0.004
$Be^9(d, \alpha)Li^7$	7.161±0.009 (calc)	$B^{11}(p, \alpha)Be^8$	8.580±0.011 (calc)
$Be^9(d, \alpha)Li^7$	7.150±0.008 (obs)	$B^{11}(p, \alpha)Be^8$	8.567±0.011 (obs)
$N^{15}(p, \alpha)C^{12}$	4.960±0.007	$F^{19}(p, \alpha)O^{16}$	8.118±0.009
$C^{13}(d, p)C^{14}$	2.716±0.005	$O^{16}(d, p)O^{17}$	1.917±0.005
$N^{15}(d, \alpha)C^{13}$	7.676±0.009 (calc)	$F^{19}(d, \alpha)O^{17}$	10.035±0.011 (calc)
$N^{15}(d, \alpha)C^{13}$	7.681±0.009 (obs)	$F^{19}(d, \alpha)O^{17}$	10.050±0.010 (obs)

It can be seen that the four reaction cycles are consistent to within 5 to 15 kev and that, in all cases, the differences are within the stated uncertainties of the measurements. It is to be noted that in each case the observed value is compared with one calculated from two lower energy Q-values. Since in two of the cases the observed value is less than the one calculated, while in the other two cases it is higher, it is concluded that there is no systematic deviation in the measurements at the highest magnetic field strengths required to observe the reaction products from those reactions listed in Table I. This view is strengthened by the fact that for those reactions where measurements of comparable precision have been made by other workers their results are in general agreement with those in Table I.

In obtaining the results discussed above, the highest energy particles encountered were the protons from $B^{10}(d, p)B^{11}$. This group had an Hr of 448 kilogauss cm at the bombarding energy used. We have also made measurements on four reactions which emitted particles with considerably higher Hr values. These were the $N^{14}(d, \alpha)C^{12}$, $Li^6(d, \alpha)\alpha$, $B^{10}(d, \alpha)Be^8$, and $Be^9(d, t)Be^8$ reactions. The Hr values for the ground-state groups from these were approximately 480, 490, 510, and 511 kilogauss cm, respectively, corresponding to field strengths in the gap of the annular magnet in the range from 13,500 to 14,500 gauss. At these high fields the iron of the magnet is close to saturation, and it appears that under these conditions the magnetic field at the position of the fluxmeter is no longer accurately proportional to that in which the reaction products are focused. As a result, the measured fields for very large magnet currents have been found to be too high by as much as 0.2 percent. Thus, the Q-values for the four reactions observed under these conditions are too high by corresponding amounts. In the case of $Be^9(d, t)Be^8$, the error expressed in kilovolts is not so serious as in the case of the other reactions, since, for a given Hr, a triton has only one-third the energy of a proton or an alpha-particle. Hence, after a correction based on the results for the other reactions, the measured Q-value for $Be^9(d, t)Be^8$ is listed in Table I. However, for the other three reactions observed at high field strengths, more precise Q-values may be calculated from those of other reactions measured at lower fields, and these calculated values, together with those similarly calculated for certain other reactions, are listed separately in Table II.

The measured Q-value for the $N^{14}(d, \alpha)C^{12}$ reaction was 13.622 Mev after a 5-kev correction was made for surface contamination. This is 47 kev higher than the

value of 13.575±0.012 Mev predicted from our measured Q-values for the $N^{14}(d, p)N^{15}$ and $N^{15}(p, \alpha)C^{12}$ reactions and 45 kev higher than the value of 13.577 ±0.012 Mev obtained from a combination of the $N^{14}(d, p)N^{15}$, $N^{15}(d, \alpha)C^{13}$, and $C^{13}(d, p)C^{14}$ Q-values. Additional indication that this calculated Q-value is more nearly correct than the one directly measured may be obtained from the Q-value of 9.137±0.006 Mev which we have measured for the $N^{14}(d, \alpha)C^{12*}$ alpha-group corresponding to the first excited state of C^{12}. The position of this state can be estimated as 4.431±0.011 Mev from the reported Q-value of 0.529±0.008 Mev[56] for the $N^{15}(p, \alpha)C^{12*}$ alpha-group corresponding to this level and from the present measurement of 4.960±0.007 Mev for the $N^{15}(p, \alpha)C^{12}$ ground-state transition. From these values, the ground-state $N^{14}(d, \alpha)C^{12}$ Q-value is found to be 13.568±0.012 Mev. The agreement of this value with those calculated from the other reaction cycles involving $N^{14}(d, p)N^{15}$ provides additional confirmation that, at the 442 kilogauss cm setting for the $N^{14}(d, p)N^{15}$ ground-state group that had the highest Hr of the groups involved in the calculations, the field measurements were not seriously affected by the effects of saturation.

Similarly, the measured Q-value of the $Li^6(d, \alpha)\alpha$ reaction was higher than the value calculated from the $Li^7(p, \alpha)\alpha$ and $Li^6(d, p)Li^7$ reaction energies. This calculated value is 22.359±0.017 Mev. In a series of measurements made on this reaction, the alpha-particle group whose Hr was in the region of 490 kilogauss cm had an energy which was consistently 0.1 to 0.4 percent higher than that calculated from the above Q-value.

The $B^{10}(d, \alpha)Be^8$ reaction energy can be calculated from two reaction cycles. From a combination of the $B^{10}(d, p)B^{11}$ and $B^{11}(p, \alpha)Be^8$ reactions, a $B^{10}(d, \alpha)Be^8$ Q-value of 17.802±0.016 Mev is calculated; from the $B^{10}(d, p)B^{11}$, $B^{11}(d, \alpha)Be^9$, and $Be^9(p, d)Be^8$ reactions, a value of 17.815±0.015 Mev is found. A weighted average of these results gives 17.809±0.015 Mev for the $B^{10}(d, \alpha)Be^8$ Q-value. The ground-state alpha-group from this reaction, observed at an Hr of 511 kilogauss cm, had an energy which was 0.25±0.11 percent higher than expected from the calculated value.

The $Be^9(d, t)Be^8$ ground-state triton group was observed at nearly the same Hr value as was the ground-state group from $B^{10}(d, \alpha)Be^8$. Using the result obtained for the $B^{10}(d, \alpha)Be^8$ group, a correction of −0.3±0.2 percent was applied to the observed energy of the triton group. Three measurements were made of the $Be^9(d, t)Be^8$ Q-value which agreed to ±7 kev. Corrections for surface contamination of less than 10 kev, estimated from previous measurements of the Li^{7++} and He^4 particles from the $Be^9(d, \alpha)Li^7$ reaction on the same target, were made to the measured Q-values. The weighted average of these measurements was 4.597±0.013 Mev for the $Be^9(d, t)Be^8$ Q-value, in agreement with the value of 4.592±0.008 Mev calculated from the $Be^9(p, d)Be^8$ and $D^2(d, p)T^3$ Q-values of 0.562±0.004 and 4.030±0.006 Mev.

TABLE II. Reaction energies calculated from Table I.

Reaction	Q-value (Mev)
$Li^6(d, \alpha)\alpha$	22.359±0.017
$Li^7(d, t)Li^6$	−0.989±0.009
$B^{10}(\alpha, p)C^{13}$	4.075±0.015
$B^{10}(d, \alpha)Be^8$	17.809±0.015
$N^{14}(d, \alpha)C^{12}$	13.577±0.012
$O^{17}(p, \alpha)N^{14}$	1.195±0.007
$O^{17}(d, t)O^{16}$	2.113±0.008
$Al^{27}(p, \alpha)Mg^{24}$	1.600±0.014
$Al^{27}(\alpha, p)Si^{30}$	2.374±0.015
$P^{31}(p, \alpha)Si^{28}$	1.924±0.022

In addition to those cases discussed above, the Q-values from Table I may be used to calculate the energy release of a number of other reactions. We have listed in Table II the Q-values obtained in this way for certain reactions with stable target nuclei. In some cases these reactions have not been observed. In general, the Q-values thus calculated are more accurate than those available or computed from present tables of nuclear masses.

V. MASSES OF THE LIGHT NUCLEI

There have been a number of compilations of nuclear masses based on nuclear-reaction Q-values and mass-spectrographic results, the most recent being that of Tollestrup, Fowler, and Lauritsen.[56] While the mass difference between the proton and deuteron, as determined by reaction data, is in good agreement with the value obtained from mass-spectrographic doublets, there has been a discrepancy between the values found for the mass of the alpha-particle. It has been suggested by Bainbridge[57] that this discrepancy may originate in the Q-values that have previously been available for the $Li^7(p, \alpha)\alpha$ and $Li^6(d, \alpha)\alpha$ reactions.

It is possible to calculate the mass difference $(2D^2-He^4)$ directly from nuclear data and to compare the value obtained with the result of mass-spectrographic doublet measurements. Thus, by adding the Q-values of the $Be^9(p, d)Be^8$ and $Be^8(\alpha)\alpha$ reactions and subtracting the result from the sum of the Q-values for the $Be^9(d, \alpha)Li^7$ and $Li^7(p, \alpha)\alpha$ reactions, $(2D^2-He^4)$ = 0.025599±0.000020 amu is obtained. In this calculation, the value 0.093±0.005 Mev, from a weighted average of two results of 0.102±0.010 Mev[58] and 0.089±0.005 Mev,[15] was used for the $Be^8(\alpha)\alpha$ reaction. The remaining three reaction energies were taken from Table I. In the conversion from energy to mass units, the value 1 amu = 931±0.1 Mev was employed.[59] Similar results, agreeing within the experimental errors,

[56] Tollestrup, Fowler, and Lauritsen, Phys. Rev. 78, 372 (1950).
[57] K. T. Bainbridge, Phys. Rev. 81, 146 (1951). We are indebted to Professor Bainbridge for the privilege of seeing his results in advance of publication.
[58] A. Hemmendinger, Phys. Rev. 75, 1267 (1949).
[59] A. H. Wapstra, Physica 16, 611 (1950).

are obtained from other cycles of the Q-values of the lighter nuclei listed in Tables I and II.

This value of 0.025599 ± 0.000020 amu obtained for $(2D^2 - He^4)$ from the more accurate nuclear data is in good agreement with the mass-spectrographic measurement of Ewald[60] and the recent unpublished result of Nier,[57] these values being 0.025604 ± 0.000009 and 0.025612 ± 0.000008 amu, respectively. The larger error associated with the result from disintegration data arises from the circumstance that, from the addition and subtraction of the reactions involved in the calculations, the mass of a single alpha-particle is equated to a combination of four Q-values. Using 2.014723 ± 0.000005 amu for the mass of the deuteron[56] and the above value calculated for $(2D^2 - He^4)$, the mass of He^4 is computed to be 4.003847 ± 0.000022 amu.

The results obtained in the present work also make possible a more ambitious calculation for the He^4 mass, the result of which is that the mass of seven alpha-particles is expressed in terms of the deuteron mass and a sum of seven of the directly measured Q-values in Table I. Hence, it is possible to reduce considerably the probable error for the He^4 mass as compared with that calculated in the more limited cycles from which the mass of a single alpha-particle results. This calculation involves the $O^{16}(d, \alpha)N^{14}$, $N^{14}(d, p)N^{15}$, $N^{15}(d, \alpha)C^{13}$, $C^{13}(d, \alpha)B^{11}$, $B^{11}(d, \alpha)Be^{9}$, $Be^{9}(d, \alpha)Li^{7}$, and $Li^{7}(p, \alpha)\alpha$ reactions. Addition of these reactions leads to the equation:

$$He^4 = (1/7)(O^{16} + 6D^2 - \Sigma Q),$$

where ΣQ is the sum of the Q-values of the seven reactions listed above. This calculation leads to 4.003863 ± 0.000007 amu for the mass of He^4. In the estimation of the probable error, the systematic and random errors in the Q-value measurements have been considered separately. The important contributions to the probable error consisted of 4.3 kev from the uncertainty of the deuteron mass, 3.4 kev from the random errors, and 4.4 kev from systematic errors, such as those in the Hr for polonium alpha-particles and in the diameter of the magnet.

One other series of reactions has been used to calculate the mass of He^4. This series consists of $O^{16}(d, \alpha)N^{14}$, $N^{14}(d, p)N^{15}$, $N^{15}(d, \alpha)C^{13}$, $C^{13}(d, \alpha)B^{11}$, $B^{11}(p, \alpha)Be^{8}$, and $Be^{8}(\alpha)\alpha$. Addition of these reactions leads to the relation:

$$He^4 = (1/6)(O^{16} + 4D^2 - \Sigma Q),$$

where ΣQ is the sum of the Q-values involved. This yields 4.003867 ± 0.000006 amu for the mass of He^4, the estimate of the probable error containing contributions of 3.3 kev from the error in the deuteron mass and 3.2 and 2.8 kev from the random and systematic errors of the Q-value measurements.

A weighted average of these two results gives 4.003865 ± 0.000007 amu for the mass of He^4. This result agrees within the probable errors with that obtained from the shorter cycle and is significantly lower than the previous value[56] of 4.003910 based on nuclear-reaction data. It remains somewhat higher than the value of 4.003842 ± 0.000013 calculated by Bainbridge[57] from mass-spectra measurements, although the two results nearly overlap within the probable errors. While the probable error calculated for the result based on the present series of measurements may be somewhat too small in that unexpected compounding of errors may occur in the cycles used, it is to be noted that even if all the Q-values involved in the cycles based on O^{16} are increased to the limits allowed by the individual errors, the resulting He^4 mass is only reduced to 4.003854 and 4.003859 in the two cases. Also, if the discrepancy is to be attributed to an error in the determination of any single reaction energy, it is necessary to postulate an error of over 100 kev for one of the Q-values involved. Thus, the mass of He^4, as determined from nuclear data, appears to remain somewhat higher than that derived from mass spectra. The origin of this remaining discrepancy may be determined when the new Q-values reported here are also measured at other laboratories.

Together with other disintegration data, the results presented in Table I can be used to compile a table of nuclear masses based on O^{16} and the proton mass. Unfortunately, the lack of accurate Q-values for the reactions of the neon isotopes prevents the present extension of such a table beyond fluorine. It is hoped that neon targets suitable for precise experiments may become available so as to make such an extension possible.

We are indebted to our colleagues in the High Voltage Laboratory who have collaborated in various stages of this work. We wish to thank Mrs. Cecilia Bryant, Mr. W. A. Tripp, Mrs. Hester Sperduto, and Mrs. Clara Stucky for their assistance in connection with the reading of the photographic plates.

[60] H. Ewald, Z. Naturforsch. 5, 1 (1950).

Neutron-Deuteron Scattering at High Energy

R. L. GLUCKSTERN* AND H. A. BETHE
Cornell University, Ithaca, New York

(Received October 20, 1950)

The neutron-deuteron total scattering cross section at high energy has been calculated by expressing it as a sum over two-particle states over a wide range of energy. A sum rule was then applied to give the total cross section, that is, the elastic *and* inelastic cross sections. The calculations were performed with a Serber type exchange force for the neutron-proton force in agreement with present neutron-proton scattering data and a neutron-neutron force of arbitrary depth and exchange character. The neutron-neutron well depth was then determined for an ordinary, Serber type and pure exchange force between the two neutrons by making use of the experimental neutron-deuteron total cross section. The neutron-deuteron elastic scattering was then calculated for the three different types of neutron-neutron exchange and was found to agree best with the experimental value for the Serber type exchange (no force in odd states). The cross section for production of low energy protons was also calculated and confirmed the Serber type exchange force between the two neutrons when compared with the experimental value. Finally, a qualitative discussion of the angular and energy distribution of the low and high energy protons was given.

I. INTRODUCTION

AT first glance it appears likely that the neutron-deuteron scattering cross section can be given accurately as the sum of the individual neutron-proton and neutron-neutron cross sections for sufficiently high energy. However, as has been pointed out by Chew[1] and others,[2,3] the interference between the free particle collisions is appreciable at all energies, since collisions of small momentum transfer are favored. One must therefore correct the sum of the neutron-proton and neutron-neutron cross sections by the correctly evaluated interference term. It will be seen that another important correction arises from the fact that the neutron-proton cross section itself is affected when the Pauli principle is applied to the two neutrons. In the process of evaluating the total neutron-deuteron cross section, we shall determine the magnitude of both of these effects, as well as the influence of such factors as spin dependent and exchange type forces.

We shall assume that the neutron-proton interaction is a Serber force, in agreement with the interpretation of the present experimental evidence.[4] By comparison of the calculated and experimental results for neutron-deuteron scattering[5,6] we hope to derive some information concerning the magnitude and exchange character of the neutron-neutron force.

The calculations will be performed using the Born approximation; i.e., considering the interaction between the incident neutron and either particle in the deuteron as the perturbing potential. We shall express the total cross section as the sum of three terms: a neutron-proton cross section, a neutron-neutron cross section, and an interference term. If we can then identify the neutron-proton and neutron-neutron terms as those which would be obtained in the corresponding Born approximation calculations for the two-particle collisions, we can use the experimental cross sections wherever possible. In this way the calculated neutron-deuteron cross section will be more satisfactory than might be expected with the Born approximation.

In calculating the total neutron-deuteron cross section we shall need to sum over final states which are made up of two-particle states covering a wide range in energy. By rearranging the integrals we shall be able to express the cross section as a sum over the two-particle states; the use of sum rules will then give the total cross section without requiring the explicit calculation of the two-particle continuum states. However, the continuum states *will* be needed for the differential cross section.

In order to illustrate the method, we shall outline the calculation in Sec. II under the following assumptions. (a) There are no spin dependent forces. (b) There are no exchange forces. (c) The particles are all distinguishable; i.e., there is no Pauli principle. These assumptions will be removed in Sec. III. The calculations will be carried out only in the nonrelativistic case, although relativistic corrections start to be important at about 200 Mev. Tensor forces will not be included in the present paper.

II. ORDINARY SPIN-INDEPENDENT FORCES WITHOUT PAULI PRINCIPLE

Let $\mathbf{r}_1$, $\mathbf{r}_2$, and $\mathbf{r}_3$ be the coordinates of the neutron and proton in the deuteron and the incident neutron, respectively. We shall transform to the coordinates $\mathbf{R}$, $\mathbf{x}$, and $\mathbf{r}$ as shown in Fig. 1.

$$\left.\begin{aligned}\mathbf{R}&=\tfrac{1}{3}(\mathbf{r}_1+\mathbf{r}_2+\mathbf{r}_3)\\ \mathbf{x}&=\mathbf{r}_3-\tfrac{1}{2}(\mathbf{r}_1+\mathbf{r}_2)\\ \mathbf{r}&=\mathbf{r}_1-\mathbf{r}_2\end{aligned}\right\}. \quad (1) \qquad \left.\begin{aligned}\mathbf{r}_1&=\mathbf{R}-\tfrac{1}{3}\mathbf{x}+\tfrac{1}{2}\mathbf{r}\\ \mathbf{r}_2&=\mathbf{R}-\tfrac{1}{3}\mathbf{x}-\tfrac{1}{2}\mathbf{r}\\ \mathbf{r}_3&=\mathbf{R}+\tfrac{2}{3}\mathbf{x}\end{aligned}\right\}. \quad (2)$$

* Present address: Sloane Physics Laboratory, Yale University, New Haven, Connecticut.

[1] G. F. Chew, Phys. Rev. 74, 809 (1948).
[2] T. Y. Wu and J. Ashkin, Phys. Rev. 73, 986 (1948).
[3] F. de Hoffmann, Phys. Rev. 78, 216 (1950).
[4] R. S. Christian and E. W. Hart, Phys. Rev. 77, 441 (1950).
[5] Cook, McMillan, Peterson, and Sewell, Phys. Rev. 72, 1264 (1947); 75, 7 (1949).
[6] W. M. Powell, private communication.

The energy of the entire system is

$$\begin{aligned}\mathcal{E}=&\frac{(M\dot{\mathbf{r}}_1)^2}{2M}+\frac{(M\dot{\mathbf{r}}_2)^2}{2M}+\frac{(M\dot{\mathbf{r}}_3)^2}{2M}+V_{NP}(|\mathbf{r}_1-\mathbf{r}_2|)\\&+V_{NN}(|\mathbf{r}_1-\mathbf{r}_3|)+V_{NP}(|\mathbf{r}_3-\mathbf{r}_2|)\\=&\frac{(3M\dot{\mathbf{R}})^2}{2(3M)}+\frac{(\frac{2}{3}M\dot{\mathbf{x}})^2}{2(\frac{2}{3}M)}+\frac{(\frac{1}{2}M\dot{\mathbf{r}})^2}{2(\frac{1}{2}M)}+V_{NP}(r)\\&+V_{NN}(|\mathbf{x}-\tfrac{1}{2}\mathbf{r}|)+V_{NP}(|\mathbf{x}+\tfrac{1}{2}\mathbf{r}|),\end{aligned}\tag{3}$$

where the dots are time derivatives and the V's are the two-particle interaction potentials. If we now consider the last two terms in (3) as the perturbing potentials and eliminate the motion of the center of mass, we can write the initial state of the system, Ψ_i, as the product of a plane wave normalized in a box of volume L^3, and the ground state of the deuteron, $\psi_0(r)$.

$$\Psi_i=L^{-\frac{3}{2}}\exp(i\mathbf{k}\cdot\mathbf{x})\psi_0(r),\tag{4}$$

where $\hbar\mathbf{k}=\frac{2}{3}M\dot{\mathbf{x}}_i$. The total energy of the system in the laboratory system ($\dot{\mathbf{r}}_1=\dot{\mathbf{r}}_2=0$, $\dot{\mathbf{r}}_3=\dot{\mathbf{x}}_i$) is

$$E=\tfrac{1}{2}M\dot{\mathbf{r}}_3^2-\epsilon=\tfrac{1}{2}M\dot{\mathbf{x}}_i^2-\epsilon=(9\hbar^2k^2/8M)-\epsilon,\tag{5}$$

where ϵ is the binding energy of the deuteron.

We shall take for the asymptotic motion of the final state

$$\hbar\mathbf{k}'=\tfrac{2}{3}M\dot{\mathbf{x}}_f,\quad \hbar\mathbf{k}''=\tfrac{1}{2}M\dot{\mathbf{r}}_f,\tag{6}$$

but we must be careful in our choice of a wave function for the final state. Since the energy in the center-of-mass system is still quite large, there will always be at least one particle which may be taken as free after the collision, with a possible strong interaction between the other two. We shall therefore divide the momentum space for the final state into three regions:

(a) particle 3 free, interaction between 1 and 2 (near $\dot{\mathbf{r}}_1=\dot{\mathbf{r}}_2$; $\mathbf{k}''=0$),
(b) particle 1 free, interaction between 2 and 3 (near $\dot{\mathbf{r}}_2=\dot{\mathbf{r}}_3$; $\mathbf{k}'=\frac{2}{3}\mathbf{k}''$),
(c) particle 2 free, interaction between 1 and 3 (near $\dot{\mathbf{r}}_1=\dot{\mathbf{r}}_3$; $\mathbf{k}'=-\frac{2}{3}\mathbf{k}''$).

Since conservation of energy is given by[7]

$$k'^2+(4/3)k''^2=k^2,\tag{7}$$

region (a) can be taken, for example, as

$$0\leq k''/k\leq s\approx 0.6,\quad 1\geq k'/k\geq t\approx 0.7,\tag{8}$$

the exact values of s and t being unimportant. A similar choice for regions (b) and (c) is possible, but we shall show later that the boundary of the three regions has little bearing on the problem.

We can now write the final wave function in the three regions as

(a) $\Psi_f=L^{-\frac{3}{2}}\exp(i\mathbf{k}'\cdot\mathbf{x})\psi_{k''}(\mathbf{r})$ particle 3 free, (9a)

(b) $\Psi_f=L^{-\frac{3}{2}}\exp[i\mathbf{k}'''\cdot(\frac{3}{4}\mathbf{r}-\frac{1}{2}\mathbf{x})]\psi_{k^{iv}}(-\mathbf{x}-\frac{1}{2}\mathbf{r})$ particle 1 free, (9b)

(c) $\Psi_f=L^{-\frac{3}{2}}\exp[i\mathbf{k}^{v}\cdot(-\frac{3}{4}\mathbf{r}-\frac{1}{2}\mathbf{x})]\times\psi_{k^{vi}}(-\mathbf{x}+\frac{1}{2}\mathbf{r})$ particle 2 free, (9c)

where $\hbar\mathbf{k}'''$, $\hbar\mathbf{k}^{iv}$, $\hbar\mathbf{k}^{v}$, and $\hbar\mathbf{k}^{vi}$ are the momenta conjugate to the coordinates $\frac{3}{4}\mathbf{r}-\frac{1}{2}\mathbf{x}$, $-\mathbf{x}-\frac{1}{2}\mathbf{r}$, $-\frac{3}{4}\mathbf{r}-\frac{1}{2}\mathbf{x}$, and $-\mathbf{x}+\frac{1}{2}\mathbf{r}$, respectively. The wave functions, $\psi_{k'}$, are two particle wave functions corresponding to relative momenta $\hbar k'$ and may either represent the ground state (elastic collisions) or the continuum solutions of the two-particle problem. These are just the functions to which we hope to apply the sum rules.

Let us first consider a collision with values of $\mathbf{k}'$ and $\mathbf{k}''$ in region (a). The matrix element for the transition is

$$\begin{aligned}\mathfrak{M}=&\int\Psi_f^*V\Psi_i d\tau=L^{-3}\int\int\psi_{k''}^*(\mathbf{r})\psi_0(r)\\&\times\exp[-i(\mathbf{k}'-\mathbf{k})\cdot\mathbf{x}]\{V_{NN}(|\mathbf{x}-\tfrac{1}{2}\mathbf{r}|)\\&+V_{NP}(|\mathbf{x}+\tfrac{1}{2}\mathbf{r}|)\}d\mathbf{r}d\mathbf{x}.\end{aligned}\tag{10}$$

If we make the change of variables $\mathbf{r}=\mathbf{r}$, $\mathbf{x}-\frac{1}{2}\mathbf{r}=\mathbf{y}$ in the V_{NN} term and $\mathbf{r}=\mathbf{r}$, $\mathbf{x}+\frac{1}{2}\mathbf{r}=\mathbf{y}$ in the V_{NP} term, the matrix element becomes

$$\begin{aligned}\mathfrak{M}=L^{-3}\Big\{&V_{NN}(q)\int\psi_{k''}^*(\mathbf{r})\psi_0(r)\exp(-\tfrac{1}{2}i\mathbf{q}\cdot\mathbf{r})d\mathbf{r}\\&+V_{NP}(q)\int\psi_{k''}^*(\mathbf{r})\psi_0(r)\exp(\tfrac{1}{2}i\mathbf{q}\cdot\mathbf{r})d\mathbf{r}\Big\}\end{aligned}\tag{11}$$

with

$$V(q)=\int V(y)\exp(\pm i\mathbf{q}\cdot\mathbf{y})d\mathbf{y},\tag{12a}$$

$$\mathbf{q}=\mathbf{k}'-\mathbf{k}.\tag{12b}$$

The cross section is given by

$$d\sigma=L^3(2\pi/\hbar v)|\mathfrak{M}|^2\rho_E(\mathbf{k}',\mathbf{k}'')d\mathbf{k}'d\mathbf{k}'',\tag{13a}$$

where $v=|\dot{\mathbf{x}}_i|=(3\hbar k/2M)$ is the velocity of the incident particle in the laboratory system and $\rho_E(\mathbf{k}',\mathbf{k}'')d\mathbf{k}'d\mathbf{k}''$

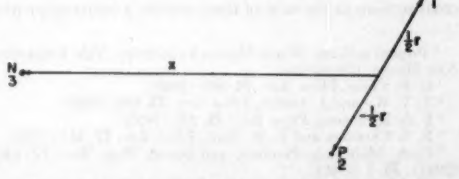

FIG. 1. Change of coordinates from $\mathbf{r}_1$, $\mathbf{r}_2$, $\mathbf{r}_3$ to $\mathbf{R}$, $\mathbf{x}$, $\mathbf{r}$.

[7] We shall later show that the binding energy can be neglected with respect to the incident energy in the conservation of energy. See Appendix D.

is the energy density of final states,

$$\rho_E(\mathbf{k}', \mathbf{k}'')d\mathbf{k}'d\mathbf{k}''=\left(\frac{L}{2\pi}\right)^3 k'^2\left(\frac{\partial k'}{\partial E}\right)_{k''} d\Omega'\left(\frac{L}{2\pi}\right)^3 d\mathbf{k}'';$$

$$\left(\frac{\partial E}{\partial k'}\right)_{k''}=\frac{3\hbar^2 k'}{2M}.$$

The cross section therefore becomes

$$\sigma=\int (M^2/9\pi^2\hbar^4)(k'/k)d\Omega'(L/2\pi)^3 d\mathbf{k}''|L^3\mathfrak{M}|^2. \quad (13b)$$

To evaluate the total cross section we must now integrate over all values of Ω', Ω'', and k'' for which energy is conserved, remembering however, that we have an upper limit sk on k'' which bounds region (a). The integrations on Ω' and Ω'' are over all solid angles. To obtain the total cross section for region (a) we shall hold k'' (and by (7), therefore k') fixed and change from the variable Ω' to q.

$$q^2=|\mathbf{k}'-\mathbf{k}|^2=k'^2+k^2-2kk'\cos\theta; \quad (14a)$$

$$-2qdq=2kk'd(\cos\theta)=kk'd\Omega'/\pi. \quad (14b)$$

The cross section for region (a) becomes, using the value of $\mathfrak{M}$ from (11),

$$\sigma_a=(2M^2/9\pi\hbar^4k^2)\int_0^{sk}(L/2\pi)^3k''^2dk''\int d\Omega''$$

$$\times\int_{k-k'}^{k+k'} qdq\left|V_{NN}(q)\int\psi_{k''}^*(\mathbf{r})\psi_0(r)\exp(-\tfrac{1}{2}i\mathbf{q}\cdot\mathbf{r})d\mathbf{r}\right.$$

$$\left.+V_{NP}(q)\int\psi_{k''}^*(\mathbf{r})\psi_0(r)\exp(\tfrac{1}{2}i\mathbf{q}\cdot\mathbf{r})d\mathbf{r}\right|^2. \quad (15)$$

The region of integration is shown in Fig. 2. It is bounded by the lines $k''=0$, $k''=sk$ and by the ellipse

$$(q-k)^2+(4/3)k''^2=k^2. \quad (16)$$

The point A represents a possible strong interaction between particle 3 and either 1 or 2, and must be avoided.

If we perform the integration first over the entire region between the two vertical lines $q=0$ and $q=2k$, and then subtract the integration over the shaded area, we obtain

$$\sigma_a=\sigma_{1a}+\sigma_{2a}+\sigma_{3a}-\sigma_a', \quad (17)$$

where

$$\sigma_{1a}=(2M^2/9\pi\hbar^4k^2)$$

$$\int_0^{2k} qdqV_{NN}^2(q)\int_0^\infty (L/2\pi)^3d\mathbf{k}''$$

$$\times\left|\int\psi_{k''}^*(\mathbf{r})\psi_0(r)\exp(-\tfrac{1}{2}i\mathbf{q}\cdot\mathbf{r})d\mathbf{r}\right|^2, \quad (18a)$$

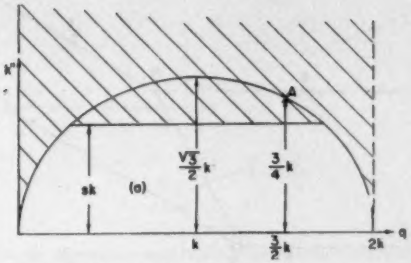

FIG. 2. Region of integration for I in the $k''q$ plane.

$$\sigma_{2a}=(2M^2/9\pi\hbar^4k^2)$$

$$\times\int_0^{2k} qdqV_{NP}^2(q)\int_0^\infty (L/2\pi)^3d\mathbf{k}''$$

$$\times\left|\int\psi_{k''}^*(\mathbf{r})\psi_0(r)\exp(\tfrac{1}{2}i\mathbf{q}\cdot\mathbf{r})d\mathbf{r}\right|^2, \quad (18b)$$

$$\sigma_{3a}=2(2M^2/9\pi\hbar^4k^2)$$

$$\times\int_0^{2k} qdqV_{NN}(q)V_{NP}(q)\int_0^\infty (L/2\pi)^3d\mathbf{k}''$$

$$\times Re\left\{\left(\int\psi_{k''}^*(\mathbf{r})\psi_0(r)\exp(-\tfrac{1}{2}i\mathbf{q}\cdot\mathbf{r})d\mathbf{r}\right)^*\right.$$

$$\left.\times\int\psi_{k''}^*(\mathbf{r})\psi_0(r)\exp(\tfrac{1}{2}i\mathbf{q}\cdot\mathbf{r})d\mathbf{r}\right\}, \quad (18c)$$

$$\sigma_a'=(2M^2/9\pi\hbar^4k^2)\int qdq\int(L/2\pi)^3d\mathbf{k}''|L^3\mathfrak{M}|^2. \quad (18d)$$

(shaded region in Fig. 2)

We have finally achieved what we set out to do: to express the total cross section in some way as the sum over final states for the *two-particle* wave functions. The $\int_0^\infty(L/2\pi)^3d\mathbf{k}''$ represents just such a sum, and we can now apply a sum rule to evaluate σ_{1a}, σ_{2a}, and σ_{3a}, which, as we shall show, represent the major portion of σ_a. We shall use

$$\sum_f(\psi_f, M\psi_0)^*(\psi_f, N\psi_0)=\sum_f {}_0M_f^*\,{}_fN_0={}_0(M^*N)_0, \quad (19)$$

where M and N are hermitian operators, and

$${}_2M_1\equiv\int\psi_2^*(\mathbf{r})M\psi_1(\mathbf{r})d\mathbf{r}\equiv(\psi_2, M\psi_1).$$

σ_{1a}, σ_{2a}, and σ_{3a} therefore become[8]

[8] We have assumed in applying the sum rule that for fixed q, M and N do not depend on the final state. However, it appears that they do, since they seem to depend on the direction as well as on the magnitude of $\mathbf{q}$. But by performing the angular integration on $\mathbf{k}''$ first, one can see that the integrals σ_{1a}, σ_{2a}, and σ_{3a} are functions only of the magnitude of $\mathbf{q}$, since there is no preferred direction possible.

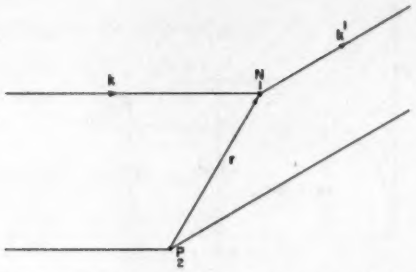

FIG. 3. Superposition of the two-particle scattered waves.

$$\sigma_{1a}=(2M^2/9\pi\hbar^4k^2)\int_0^{2k} qdqV_{NN}^2(q)\int\psi_0^2(r)d\mathbf{r}, \quad (20a)$$

$$\sigma_{2a}=(2M^2/9\pi\hbar^4k^2)\int_0^{2k} qdqV_{NP}^2(q)\int\psi_0^2(r)d\mathbf{r}, \quad (20b)$$

$$\sigma_{3a}=2(2M^2/9\pi\hbar^4k^2)\int_0^{2k} qdqV_{NN}(q)V_{NP}(q)$$

$$\times Re\left\{\int\psi_0^2(r)\exp(i\mathbf{q}\cdot\mathbf{r})d\mathbf{r}\right\}. \quad (20c)$$

The integration over the shaded region in Fig. 2 is mostly for large k''. In this region, we shall therefore replace $\psi_{k''}^{(+)}(\mathbf{r})$ by $L^{-\frac{1}{2}}\exp(-i\mathbf{k}''\cdot\mathbf{r})$, its asymptotic form for large k''. This approximation will be justified in Appendix E.

We have seen that the application of the sum rule to σ_{1a}, σ_{2a}, and σ_{3a} gives a result independent of the form of the $\psi_{k''}(\mathbf{r})$. The only requisite is that the $\psi_{k''}(\mathbf{r})$ form a *complete* set of eigenfunctions, a condition which we satisfy by extending the k'' integration up to ∞ and by including the ground state in the case of triplet interaction. Exactly the same result would have been obtained if we had used the set of plane waves $L^{-\frac{1}{2}}\exp(i\mathbf{k}''\cdot\mathbf{r})$ for the $\psi_{k''}(\mathbf{r})$. We therefore arrive at the result that we can obtain the cross section σ_a by using *plane waves* for the two-particle wave functions in the original region of integration [region (a)]. This is quite startling, since it is in just this region that the two-particle wave functions are *not* plane waves. The reason for this surprising result is that the contribution of the elastic scattering is just canceled by the corrections to the plane waves which must be applied for the low energy free two-particle states. The elastic scattering in a sense "robs" the neighboring low energy two-particle states.

It now appears that the total cross section is a more fundamental quantity than the inelastic cross section, and calculations should be directed accordingly. To be sure, the total cross section is made up of an elastic and an inelastic part, but these complement one another in such a way that the two-particle wave functions approximate a complete set only if both parts are taken together.

In a similar manner the same result can be obtained for regions (b) and (c). It now becomes clear that the total cross section can be obtained without splitting the region of integration by using plane waves throughout, that is, in the entire half-ellipse in Fig. 2.

Of course, in the calculation of the angular and energy distributions of either neutrons or protons, a better approximation to the wave function, $\psi_{k''}(\mathbf{r})$ will be necessary, since there are no sums over two particle states. This matter will be treated in Sec. VI.

We shall now evaluate the total cross section by replacing $\psi_{k''}^{(+)}(\mathbf{r})$ by the plane wave

$$\psi_{k''}(\mathbf{r})=L^{-\frac{1}{2}}\exp(i\mathbf{k}''\cdot\mathbf{r}),$$

as we have just discussed, and by extending the region of integration for (15) to the half ellipse in Fig. 2. If we define the momentum distribution (Fourier transform) of the final state as

$$\varphi(z)=\int\exp(i\mathbf{z}\cdot\mathbf{r})\psi_0(r)d\mathbf{r}, \quad (21)$$

we obtain for the total cross section

$$\sigma=(2M^2/9\pi\hbar^4k^2)\int_0^{2k} qdq\int(1/2\pi)^3d\mathbf{k}''$$

$$\times|V_{NN}(q)\varphi(|\mathbf{k}''+\tfrac{1}{2}\mathbf{q}|)+V_{NP}(q)\varphi(|\mathbf{k}''-\tfrac{1}{2}\mathbf{q}|)|^2. \quad (22)$$

If we neglect the contribution above the ellipse, we obtain the expressions in (20) combined to give

$$\sigma'=(2M^2/9\pi\hbar^4k^2)\int_0^{2k} qdq\int d\mathbf{r}$$

$$\times|V_{NN}(q)+V_{NP}(q)\exp(i\mathbf{q}\cdot\mathbf{r})|^2\psi_0^2(r). \quad (23)$$

We shall now find it possible to give a simple physical picture to both (22) and (23).

Let us consider the wave scattered by each of two particles, separated by a displacement, $\mathbf{r}$, as in Fig. 3. The amplitude for transferring a momentum $\mathbf{q}$ is proportional to $V(q)$ for each particle, and the difference in phase for the two waves is $\mathbf{k}'\cdot\mathbf{r}-\mathbf{k}\cdot\mathbf{r}=\mathbf{q}\cdot\mathbf{r}$. Since the probability of finding the deuteron with a relative separation $\mathbf{r}$ is $\psi_0^2(r)d\mathbf{r}$, the cross section for this calculation will be proportional to

$$\int d\mathbf{r}|V_{NN}(q)+V_{NP}(q)\exp(i\mathbf{q}\cdot\mathbf{r})|^2\psi_0^2(r),$$

which when integrated over angle with appropriate factors gives the expression (23) for σ'. The inaccuracy in this expression then lies in the assumption that the particle not struck remains stationary.

If instead we consider the deuteron as a superposition of plane wave states of momenta $\mathbf{z}$ with amplitude $\varphi(z)$,

the amplitude for scattering from the state given in Fig. 4(a) in the laboratory system to the state in Fig. 4(c) is proportional to $V_{NN}(q)\varphi(z)$. However, we may also obtain the final state in Fig. 4(c) by starting with the state in Fig. 4(b) with an amplitude for this transition proportional to $V_{NP}(q)\varphi(|\mathbf{z}-\mathbf{q}|)$. If we now let the momentum of the struck neutron and proton relative to their center of mass be $\mathbf{k}''$, we have $\mathbf{z}=\mathbf{k}''+\frac{1}{2}\mathbf{q}$. The cross section for this calculation will therefore be proportional to

$$|V_{NN}(q)\varphi(|\mathbf{k}''+\tfrac{1}{2}\mathbf{q}|)+V_{NP}(q)\varphi(|\mathbf{k}''-\tfrac{1}{2}\mathbf{q}|)|^2,$$

which, when integrated over all values of $\mathbf{q}$ and $\mathbf{z}$ that conserve the over-all energy, leads to the expression (22) for σ. The reason for the validity of this picture is that we have justified using plane waves to obtain the *total* cross section.

Before calculating the value of these integrals, we shall remove the simplifying assumptions used in this section.

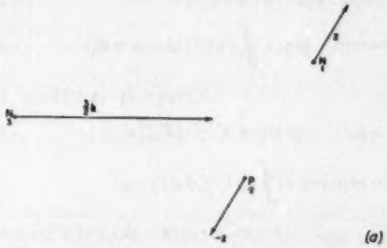

FIG. 4a. Momentum state before a neutron-neutron collision.

III. SPIN DEPENDENT, EXCHANGE FORCES WITH PAULI PRINCIPLE

Since the neutrons are indistinguishable, we must apply the operator $(1-P_{13}Q_{13})/\sqrt{2}$ to both the initial and final state wave functions, where P and Q exchange the space and spin coordinates, respectively. The matrix element will then be

$$\mathfrak{M}=\tfrac{1}{2}(\{1-P_{13}Q_{13}\}\Psi_f\chi_f,\quad V\{1-P_{13}Q_{13}\}\Psi_i\chi_i), \quad (24)$$

where χ_i and χ_f are the initial and final spin wave functions. The perturbation V must be chosen differently for the direct and antisymmetrized terms; it must be taken as the interaction between the particle described as free in the Ψ_i or $P_{13}\Psi_i$ and the other two. This gives

$$\mathfrak{M}=\tfrac{1}{2}(\{1-P_{13}Q_{13}\}\Psi_f\chi_f,\ \{1-P_{13}Q_{13}\}\{V_{NN}^{13}+V_{NP}^{23}\}\Psi_i\chi_i).$$

Since $1-P_{13}Q_{13}$ is hermitian and

$$(1-P_{13}Q_{13})^2=2(1-P_{13}Q_{13}),$$

we obtain for the matrix element

$$\mathfrak{M}=(\Psi_f\chi_f,\{1-P_{13}Q_{13}\}\{V_{NN}^{13}+V_{NP}^{23}\}\Psi_i\chi_i). \quad (25)$$

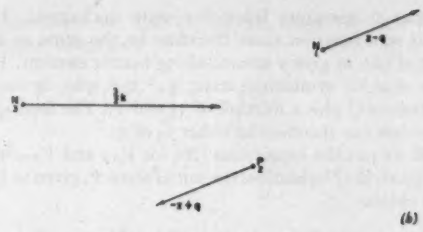

FIG. 4b. Momentum state before a neutron-proton collision.

We shall choose a linear combination of Wigner, Majorana, Bartlett, and Heisenberg forces for the neutron-proton interaction. For the neutron-neutron interaction only the Wigner and Majorana forces are necessary.

$$V_{NP}^{23}=V_{NP}(r_{23})(w_p+m_pP_{23}+b_pQ_{23}+h_pP_{23}Q_{23}), \quad (26a)$$

$$V_{NN}^{12}=V_{NN}(r_{12})(w_n+m_nP_{12}). \quad (26b)$$

There are eight linearly independent and orthogonal spin functions which may be written as

$$\chi_1=a_1a_2a_3, \quad (27a)$$

$$\chi_2=(1/\sqrt{3})(a_1a_2b_3+a_1b_2a_3+b_1a_2a_3), \quad (27b)$$

$$\chi_3=(1/\sqrt{3})(b_1b_2a_3+b_1a_2b_3+a_1b_2b_3), \quad (27c)$$

$$\chi_4=b_1b_2b_3, \quad (27d)$$

$$\chi_5=[1/(6)^{\frac{1}{2}}](2a_1a_2b_3-a_1b_2a_3-b_1a_2a_3), \quad (27e)$$

$$\chi_6=[1/(6)^{\frac{1}{2}}](2b_1b_2a_3-b_1a_2b_3-a_1b_2b_3), \quad (27f)$$

$$\chi_7=(1/\sqrt{2})(a_1b_2a_3-b_1a_2a_3), \quad (27g)$$

$$\chi_8=(1/\sqrt{2})(b_1a_2b_3-a_1b_2b_3). \quad (27h)$$

The first four are quartet spin functions corresponding to a total spin of $\frac{3}{2}$. The other four are states of total spin $\frac{1}{2}$, the first two of which are symmetric and the last two antisymmetric in the two particles 1 and 2, originally in the deuteron.

The initial state is clearly either a quartet or a doublet symmetric state with a relative frequency of occurrence of two to one. For the quartet states all the spin

FIG. 4c. Momentum state after either collision with a momentum transfer $\mathbf{q}$.

exchange operators leave the state unchanged. The final spin function must therefore be the same as the initial one to give a nonvanishing matrix element. For the doublet symmetric state, χ_6,[9] the spin exchange operators Q give a mixture of χ_6 and χ_7. The final spin function can therefore be either χ_6 or χ_7.

If we put the expressions (26) for V_{NP} and V_{NN} into $\mathfrak{M}$ given in (25), and use the initial state Ψ_i given in (4), we obtain

$$\begin{aligned}L^3\mathfrak{M}=(\Psi_f,\{&a_1V(|\mathbf{x}-\tfrac{1}{2}\mathbf{r}|)\exp(i\mathbf{k}\cdot\mathbf{x})\psi_0(r)\\&+a_2V(|\mathbf{x}-\tfrac{1}{2}\mathbf{r}|)\exp[i\mathbf{k}\cdot(\tfrac{3}{4}\mathbf{r}-\tfrac{1}{2}\mathbf{x})]\psi_0(|\mathbf{x}+\tfrac{1}{2}\mathbf{r}|)\\&+a_3V(|\mathbf{x}+\tfrac{1}{2}\mathbf{r}|)\exp(i\mathbf{k}\cdot\mathbf{x})\psi_0(r)\\&+a_4V(|\mathbf{x}+\tfrac{1}{2}\mathbf{r}|)\exp[i\mathbf{k}\cdot(-\tfrac{3}{4}\mathbf{r}-\tfrac{1}{2}\mathbf{x})]\psi_0(|\mathbf{x}-\tfrac{1}{2}\mathbf{r}|)\\&+a_5V(r)\exp[i\mathbf{k}\cdot(\tfrac{3}{4}\mathbf{r}-\tfrac{1}{2}\mathbf{x})]\psi_0(|\mathbf{x}+\tfrac{1}{2}\mathbf{r}|)\\&+a_6V(r)\exp[i\mathbf{k}\cdot(-\tfrac{3}{4}\mathbf{r}-\tfrac{1}{2}\mathbf{x})]\psi_0(|\mathbf{x}-\tfrac{1}{2}\mathbf{r}|)\}).\end{aligned}\quad(28)$$

We have used

$$\begin{aligned}&P_{12}\mathbf{x}=\mathbf{x}, && P_{12}\mathbf{r}=-\mathbf{r},\\&P_{23}\mathbf{x}=-\tfrac{3}{4}\mathbf{r}-\tfrac{1}{2}\mathbf{x}, && P_{23}\mathbf{r}=-\mathbf{x}+\tfrac{1}{2}\mathbf{r},\\&P_{13}\mathbf{x}=\tfrac{3}{4}\mathbf{r}-\tfrac{1}{2}\mathbf{x}, && P_{13}\mathbf{r}=-\mathbf{x}-\tfrac{1}{2}\mathbf{r},\end{aligned}\quad(29)$$

TABLE I. Values of the coefficients a_l for the quartet, doublet symmetric, and doublet antisymmetric matrix elements in (33) and (35).

	Quartet	Doublet χ_6	Doublet χ_7
a_1	w_n-m_n	$w_n+\frac{1}{2}m_n$	$\frac{1}{2}m_n\sqrt{3}$
a_2	$-w_n+m_n$	$\frac{1}{2}w_n+m_n$	$\frac{1}{2}w_n\sqrt{3}$
a_3	w_p+b_p	$w_p-\frac{1}{2}b_p$	$\frac{1}{2}b_p\sqrt{3}$
a_4	m_p+h_p	$m_p-\frac{1}{2}h_p$	$\frac{1}{2}h_p\sqrt{3}$
a_5	$-w_p-b_p$	$\frac{1}{2}w_p+\frac{1}{2}b_p$	$\frac{1}{2}(w_p-b_p)\sqrt{3}$
a_6	$-m_p-h_p$	$\frac{1}{2}m_p+\frac{1}{2}h_p$	$\frac{1}{2}(m_p-h_p)\sqrt{3}$

$$\begin{aligned}&Q_{12}\chi_1=\chi_1,\quad Q_{12}\chi_6=\chi_6,\quad Q_{12}\chi_7=-\chi_7,\\&Q_{23}\chi_1=\chi_1,\quad Q_{23}\chi_6=-\tfrac{1}{2}\chi_6+\tfrac{1}{2}\sqrt{3}\chi_7,\\&\qquad\qquad Q_{23}\chi_7=\tfrac{1}{2}\sqrt{3}\chi_6+\tfrac{1}{2}\chi_7,\\&Q_{13}\chi_1=\chi_1,\quad Q_{13}\chi_6=-\tfrac{1}{2}\chi_6-\tfrac{1}{2}\sqrt{3}\chi_7,\\&\qquad\qquad Q_{13}\chi_7=-\tfrac{1}{2}\sqrt{3}\chi_6+\tfrac{1}{2}\chi_7.\end{aligned}\quad(30)$$

The a's[10] are given in Table I. The total cross section can now be obtained as

$$\sigma_{TOT}=\tfrac{3}{4}\sigma_{QUAR}+\tfrac{1}{4}(\sigma_{DOUB\,SYM}+\sigma_{DOUB\,ANTISYM}),\quad(31)$$

where the σ's on the right side of (31) are given by (13b) and (14b) except for a factor $\frac{1}{2}$ due to the identity of the two neutrons in the final state;[11] for example,

$$\sigma_{QUAR}=(M^2/9\pi\hbar^4k^2)\int_0^{k\sqrt{3}}(L/2\pi)^3k''^2dk''\times\int d\Omega''\int_{k-k'}^{k+k'}qdq\,|L^3\mathfrak{M}_{QUAR}|^2,\quad(32)$$

where $\mathfrak{M}_{QUAR}$ is obtained from (28) by using the quartet values for the a's in Table I.

In considering the final state we shall, as before, divide the $\mathbf{k}'$, $\mathbf{k}''$ space into three regions. In the region in which particle 3 can be considered free the final state is given by (9a). The matrix element, after appropriate changes of variables, becomes

$$L^3\mathfrak{M}=\sum_{l=1}^{6}a_l\int\psi_{k''}{}^*(\mathbf{r})F_l(\mathbf{r})d\mathbf{r},\quad(33)$$

where

$$F_1(\mathbf{r})=\psi_0(r)\exp(-\tfrac{1}{2}i\mathbf{q}\cdot\mathbf{r})V(q),\quad(34a)$$

$$F_2(\mathbf{r})=\exp(-\tfrac{1}{2}i\mathbf{q}\cdot\mathbf{r})\int d\mathbf{y}V(y)\psi_0(|\mathbf{y}+\mathbf{r}|)\times\exp[-i\mathbf{y}\cdot(\mathbf{q}+\tfrac{3}{2}\mathbf{k})],\quad(34b)$$

$$F_3(\mathbf{r})=\psi_0(r)\exp(\tfrac{1}{2}i\mathbf{q}\cdot\mathbf{r})V(q)=F_1{}^*(\mathbf{r}),\quad(34c)$$

$$F_4(\mathbf{r})=\exp(\tfrac{1}{2}i\mathbf{q}\cdot\mathbf{r})\int d\mathbf{y}V(y)\psi_0(|\mathbf{y}-\mathbf{r}|)\times\exp[-i\mathbf{y}\cdot(\mathbf{q}+\tfrac{3}{2}\mathbf{k})]=F_2{}^*(\mathbf{r}),\quad(34d)$$

$$F_5(\mathbf{r})=V(r)\exp[\tfrac{1}{2}i\mathbf{r}\cdot(\mathbf{q}+3\mathbf{k})]\varphi(|\mathbf{q}+\tfrac{3}{2}\mathbf{k}|),\quad(34e)$$

$$F_6(\mathbf{r})=V(r)\exp[-\tfrac{1}{2}i\mathbf{r}\cdot(\mathbf{q}+3\mathbf{k})]\varphi(|\mathbf{q}+\tfrac{3}{2}\mathbf{k}|)=F_5{}^*(\mathbf{r}).\quad(34f)$$

When we now take $|L^3\mathfrak{M}|^2$ we obtain 36 terms of the type

$$\int\psi_{k''}{}^*(\mathbf{r})F_l(\mathbf{r})d\mathbf{r}\int\psi_{k''}(\mathbf{r})F_{l'}{}^*(\mathbf{r})d\mathbf{r}.$$

As before, we can apply a sum rule in evaluating the total cross section. The procedure is similar to that in the preceding section and justifies the use of plane waves for the $\psi_k''(\mathbf{r})$ throughout the elliptical region in Fig. 2.[12]

[9] χ_6 and χ_8 differ from χ_5 and χ_7 by interchanging a and b so that they need not be considered separately in obtaining the matrix element.

[10] A sample calculation for the doublet χ_6 a's is given in Appendix F.

[11] As in neutron-neutron scattering.

[12] One important difference is that the $F_l(\mathbf{r})$ are not really independent of the final state. In the preceding section we considered only the terms F_1 and F_3 and we were able to show that the variation of the direction of $\mathbf{q}$ over the final states had no effect, but the argument is not valid here since the other F's depend on $\mathbf{q}$. After the Ω'' and $\mathbf{r}$ integrations are performed the terms will still depend on the angle between $\mathbf{q}$ and $\mathbf{k}$ which depends on *both* q and k'', and can be expressed, with the use of (12b) and (7), as

$$\mathbf{k}\cdot\mathbf{q}=\tfrac{1}{2}(k'^2-k^2-q^2)=-\tfrac{1}{2}q^2-\tfrac{3}{2}k''^2.$$

However we now see that, for small k'', where the sum rules are necessary, the angle between $\mathbf{q}$ and $\mathbf{k}$ is reasonably constant and

If we now set

$$\psi_{\mathbf{k}''}^{*}(\mathbf{r}) = L^{-1}\exp(-i\mathbf{k}''\cdot\mathbf{r})$$

in the matrix element (33), we obtain

$$L^{9/2}\mathfrak{M} = \sum_{i=1}^{6} a_i G_i, \tag{35}$$

where

$$G_1 = V_{NN}^{O;\,X,\,A.S.}(q)\varphi(|\mathbf{k}''+\tfrac{1}{2}\mathbf{q}|) = V(q)\varphi(|\mathbf{k}''+\tfrac{1}{2}\mathbf{q}|), \tag{36a}$$

$$G_2 = V_{NN}^{X;\,O,\,A.S.}(|\tfrac{3}{2}\mathbf{k}+\tfrac{1}{2}\mathbf{q}-\mathbf{k}''|)\varphi(|\mathbf{k}''+\tfrac{1}{2}\mathbf{q}|) = V(q')\varphi(|\mathbf{k}^{iv}+\tfrac{1}{2}\mathbf{q}'|), \tag{36b}$$

$$G_3 = V_{NP}^{O}(q)\varphi(|\mathbf{k}''-\tfrac{1}{2}\mathbf{q}|) = V(q)\varphi(|\mathbf{k}''-\tfrac{1}{2}\mathbf{q}|), \tag{36c}$$

$$G_4 = V_{NP}^{X}(|\tfrac{3}{2}\mathbf{k}+\tfrac{1}{2}\mathbf{q}+\mathbf{k}''|)\varphi(|\mathbf{k}''-\tfrac{1}{2}\mathbf{q}|) = V(q'')\varphi(|\mathbf{k}^{vi}+\tfrac{1}{2}\mathbf{q}''|), \tag{36d}$$

$$G_5 = V_{NP}^{O,\,A.S.}(|\tfrac{3}{2}\mathbf{k}+\tfrac{1}{2}\mathbf{q}-\mathbf{k}''|)\varphi(|\tfrac{3}{2}\mathbf{k}+\mathbf{q}|) = V(q')\varphi(|\mathbf{k}^{iv}-\tfrac{1}{2}\mathbf{q}'|), \tag{36e}$$

$$G_6 = V_{NP}^{X,\,A.S.}(|\tfrac{3}{2}\mathbf{k}+\tfrac{1}{2}\mathbf{q}+\mathbf{k}''|)\varphi(|\tfrac{3}{2}\mathbf{k}+\mathbf{q}|) = V(q'')\varphi(|\mathbf{k}^{vi}-\tfrac{1}{2}\mathbf{q}''|), \tag{36f}$$

where the subscripts and superscripts on the $V_k^{c,a}$ are included for clarity, and describe (a) the type of force (O, ordinary, or exchange) between (b) the two particles interacting and (c) whether or not the term arises from the antisymmetrized part of the initial wave function. G_1 and G_2 can arise in two different ways; these are separated by semicolons. The G's have also been expressed in terms of the momentum vectors $\mathbf{k}''' = \mathbf{q}+\mathbf{k}'$, $\mathbf{k}^{iv}$, $\mathbf{k}^{v} = \mathbf{q}''+\mathbf{k}$, $\mathbf{k}^{vi}$ obtained from a cyclic permutation of the three particles. A little thought will show that the forms of the G's are necessarily the same as in the $\mathbf{k}'$, $\mathbf{k}''$ space, since the space exchange operators giving rise to the terms G_2, G_4, G_5, and G_6 do nothing more than permute (and invert the "sense" of) the three particles. In addition the density of final states can be expressed in terms of the permuted momentum vectors since

$$\frac{d\mathbf{k}'d\mathbf{k}''}{dE} = \frac{d\mathbf{k}'''d\mathbf{k}^{iv}}{dE} = \frac{d\mathbf{k}^{v}d\mathbf{k}^{vi}}{dE}.$$

If we now put the matrix element (35) into the cross section (32), we find we have $6+\frac{1}{2}(6\cdot5)=21$ integrals to evaluate. However, because of the symmetry mentioned in the previous paragraph all these integrals are not distinct. In fact, there are only five different integrals

$$I = \int G_1^2 = \int G_2^2 = \int G_3^2 = \int G_4^2 = \int G_5^2 = \int G_6^2, \tag{37a}$$

$$II = \int G_1G_3 = \int G_2G_5 = \int G_4G_6, \tag{37b}$$

$$III = \int G_1G_2 = \int G_3G_4 = \int G_5G_6, \tag{37c}$$

$$IV = \int G_1G_4 = \int G_1G_5 = \int G_2G_3 = \int G_2G_6 = \int G_3G_5 = \int G_4G_6, \tag{37d}$$

$$V = \int G_2G_4 = \int G_1G_6 = \int G_3G_5, \tag{37e}$$

$$I = \int_0^{2k} qdqV^2(q)\int_0^{Q} k''^2dk''\int d\Omega''\varphi^2(|\mathbf{k}''+\tfrac{1}{2}\mathbf{q}|), \tag{38a}$$

$$II = \int_0^{2k} qdqV^2(q)\int_0^{Q} k''^2dk''\int d\Omega'' \times\varphi(|\mathbf{k}''+\tfrac{1}{2}\mathbf{q}|)\varphi(|\mathbf{k}''-\tfrac{1}{2}\mathbf{q}|), \tag{38b}$$

$$III = \int_0^{2k} qdqV(q)\int_0^{Q} k''^2dk''\int d\Omega'' \times V(|\tfrac{3}{2}\mathbf{k}+\tfrac{1}{2}\mathbf{q}-\mathbf{k}''|)\varphi^2(|\mathbf{k}''+\tfrac{1}{2}\mathbf{q}|), \tag{38c}$$

$$IV = \int_0^{2k} qdqV(q)\int_0^{Q} k''^2dk''\int d\Omega'' \times V(|\tfrac{3}{2}\mathbf{k}+\tfrac{1}{2}\mathbf{q}-\mathbf{k}''|) \times\varphi(|\mathbf{k}''+\tfrac{1}{2}\mathbf{q}|)\varphi(|\mathbf{k}''-\tfrac{1}{2}\mathbf{q}|), \tag{38d}$$

$$V = \int_0^{2k} qdqV(q)\int_0^{Q} k''^2dk''\int d\Omega'' \times V(|\tfrac{3}{2}\mathbf{k}+\tfrac{1}{2}\mathbf{q}+\mathbf{k}''|)V(|\tfrac{3}{2}\mathbf{k}+\tfrac{1}{2}\mathbf{q}-\mathbf{k}''|) \times\varphi(|\mathbf{k}''+\tfrac{1}{2}\mathbf{q}|)\varphi(|\mathbf{k}''-\tfrac{1}{2}\mathbf{q}|), \tag{38e}$$

where

$$Q^2 = \tfrac{3}{4}q(2k-q). \tag{39}$$

Detailed evaluation of the integrals I–V is carried out in the Appendices A, B, and C. However, there are several qualitative features which may be discussed without specifying a particular potential. If we change

$\mathbf{q}$ may therefore be considered fixed. In addition it can be seen from (36) that the vicinity $k''=0$ contributes only very slightly in all but the first and third terms.

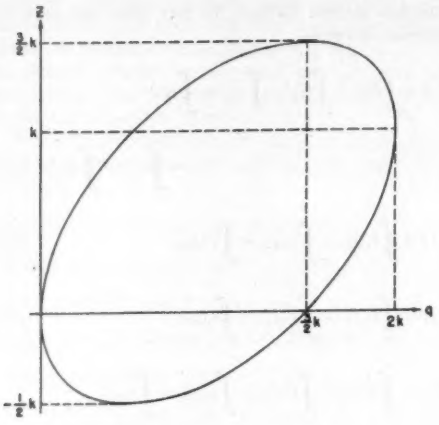

FIG. 5. Region of integration for I in the zq plane.

the variable Ω'' to $z=|\mathbf{k}''+\frac{1}{2}\mathbf{q}|$ as in the appendix, we can express I as

$$I=2\pi\int_0^{2k}dqV^2(q)\int_{|q-Q}^{|q+Q}z\varphi^2(z)dz \times\{zq-(q^2+z^2-\tfrac{1}{2}qk)\}. \quad (40)$$

The region of integration is shown in Fig. 5. Since the deuteron is large compared with the wavelength of the incident particle, $\varphi(z)$ will be important only for small z. We can obtain a rough approximation to the integral at high energy by integration from $-\infty$ to ∞ on z wherever the z integration goes through $z=0$, that is, for $0\leq q\leq\frac{3}{2}k$ and using zero for the z integral otherwise; i.e., for $q>\frac{3}{2}k$. If we do this, only the even part of the z integrand will contribute and we will obtain for this approximation to I

$$I_0=2\pi\int_0^{\frac{3}{2}k}qdqV^2(q)\int_{-\infty}^{\infty}z^2\varphi^2(z)dz. \quad (41)$$

Since

$$\int_{-\infty}^{\infty}z^2\varphi^2(z)dz=(1/2\pi)\int_{\text{all space}}\varphi^2(z)d\mathbf{z}$$

and

$$\int\varphi^2(z)d\mathbf{z}=(2\pi)^3\int\psi_0^2(r)d\mathbf{r}=(2\pi)^3$$

because of closure, I becomes

$$I_0=(2\pi)^3\int_0^{\frac{3}{2}k}qdqV^2(q). \quad (42)$$

As can be seen from (20a, b) this is just what was obtained when we neglected the contribution of the region above the ellipse in Fig. 2 and used the sum rule result exclusively. One slight change is that the upper limit on the q integration has been changed from $2k$ to the more accurate value $\frac{3}{2}k$. This agrees with the *two*-particle picture where the maximum momentum transfer $\frac{3}{2}k$ is obtained in a head-on collision between the incident particle and one of the particles in the deuteron.

We have obtained our results thus far without the use of an explicit potential. However, we must now choose a particular form for the potential and for the corresponding deuteron ground-state wave function. We shall use the Yukawa interaction[13]

$$V(r)=V_0e^{-\mu r}/\mu r \quad (43)$$

with $V_0=67.8$ Mev, $\mu^{-1}=1.18\times10^{-13}$ cm. For the ground state $\psi_0(r)$ we shall use the Hulthén wave function

$$r\psi_0(r)=N(e^{-\alpha r}-e^{-\beta r}) \quad (44)$$

with $N^2=\alpha\beta(\beta+\alpha)/2\pi(\beta-\alpha)^2$, $\alpha=(M\epsilon/\hbar^2)^{\frac{1}{2}}$, $\beta/\alpha=7$. The value of 7 for β/α differs from Chew's value of $5\frac{1}{2}$ and represents an average of the values obtained[14] by using a variational principle on the binding energy, calculating the effective range[15,16] in terms of β/α, satisfying the Schroedinger equation at $r=0$, and using a variational principle on the wave function in momentum space. These criteria give values for β/α of 6.8, 6.9, 7.3, and 7.1, respectively.

We shall consider an incident energy of 90 Mev, for which $k^{-1}=0.72\times10^{-13}$ cm. The latest value of the binding energy[17] is 2.226 Mev and leads to the deuteron radius $\alpha^{-1}=4.314\times10^{-13}$ cm, and $\beta^{-1}=\alpha^{-1}/7=0.616\times10^{-13}$ cm.

Using the Yukawa potential (43), we obtain for I_0, the sum rule approximation to I,

$$I_0=(2\pi)^3(4\pi V_0/\mu)^2(1/2\mu^2)\{1-(1+9k^2/4\mu^2)^{-1}\}. \quad (45)$$

The exact evaluation of the integral I in the appendix shows that the value obtained for I is 14 percent smaller than the value obtained for I_0 at an incident energy of 90 Mev. The main contribution to the 14 percent comes from the fact that we have extended the lower limit on the z integration to $-\infty$. If instead we use

$$\int_{-\frac{1}{2}k}^{\infty}z^2\varphi^2(z)dz$$

in (41), our result for I will be only $4\frac{1}{2}$ percent too small.

A similar phenomenon occurs in the interference term *II*. If we change variables from k'' and Ω'' to $r_1=|\mathbf{k}''+\frac{1}{2}\mathbf{q}|$ and $r_2=|\mathbf{k}''-\frac{1}{2}\mathbf{q}|$ as in Appendix B, we

[13] These are the values used by Chew (footnote 1) and represent the best fit with the Berkeley data without tensor forces.
[14] E. E. Salpeter, private communication.
[15] G. F. Chew and M. L. Goldberger, Phys. Rev. **77**, 470 (1950).
[16] H. A. Bethe and C. Longmire, Phys. Rev. **77**, 647 (1950).
[17] R. C. Mobley and R. A. Laubenstein, Phys. Rev. **80**, 309 (1950).

obtain

$$II=2\pi\int_0^{2k}dqV^2(q)\int_{|q-Q|}^{|q+Q|}r_1\varphi(r_1)dr_1 \times\int_{q-r_1}^{(3qk-r_1^2-q^2)^{\frac{1}{2}}}r_2\varphi(r_2)dr_2. \quad (46)$$

We have shown in Appendix B that at high energy II reduces to

$$II_0=(2\pi)^3\int_0^k qdqV^2(q)\int\psi_0^2(r)\exp(i\mathbf{q}\cdot\mathbf{r})d\mathbf{r}, \quad (47)$$

which is the result obtained in (23) for the interference term evaluated directly from the sum rule, independent of the explicit form of the potential.

The exact evaluation of II in the appendix shows that II is smaller than II_0 by 19 percent at 90 Mev. This is somewhat larger than the error in I_0 but is due to approximately the same cause.

The relative value of I and II at 90 Mev is

$$II=0.46I. \quad (48)$$

This implies quite a large interference term and is surprising in view of the high energy. Because of the factor $V^2(q)$ in the integrands, the most important momentum transfers are of order of magnitude $q\sim\mu$. Since the most important values of r in (47) are $r^{-1}\sim 2\alpha$, the most likely phase factor will be $\exp(i\mu/2\alpha)$. Since μ is *not* much larger than $2\alpha[(\mu/2\alpha)=1.8]$, the interference term will *not* be small. Moreover, the ratio, II/I, will not decrease appreciably with increasing energy. This can be seen from (42) and (47), since neither I_0 or II_0 are appreciably affected by raising the upper limit on q. Of course, we have omitted the constant factor, which is inversely proportional to the energy in each of these terms. However, this does not affect their ratio.

The evaluation of III is considerably more difficult and has been done only approximately in the appendix. The value obtained is

$$III=0.43I, \quad (49)$$

which is quite large. This integral represents interference between direct and exchange *two*-particle scattering (G_1G_2, G_3G_4, G_5G_6) and is similar to the corresponding term arising in either neutron-proton or neutron-neutron scattering. It need not be calculated accurately, since it can be obtained from the two-body scattering experiments. We shall later group it with terms which will represent the experimentally observed neutron-neutron and neutron-proton cross sections.

The integrals IV and V are also evaluated approximately and represent more complicated interference terms. Their values are

$$IV=0.11I, \quad (50)$$

$$V=0.03I. \quad (51)$$

We are now in a position to evaluate the total cross section. In order to do so, we must specify the exchange character and spin dependence of both the neutron-proton and neutron-neutron forces. For the neutron-proton interaction we shall use the spin-dependent Serber force

$$V(r)=V_0{}^T\frac{e^{-\mu r}}{\mu r}\left(\frac{1+P}{2}\right)\left(\frac{1+\eta}{2}+\frac{1-\eta}{2}Q\right), \quad (52)$$

where $\eta=V_0{}^S/V_0{}^T=46.5/67.8=0.686$ and for the neutron-neutron force

$$V(r)=V_0{}^T(e^{-\mu r}/\mu r)\xi[\tfrac{1}{2}(1+\delta)+\tfrac{1}{2}(1-\delta)P], \quad (53)$$

where δ describes the space exchange character of the force.[18] We therefore have

$$\left.\begin{aligned} w_p=m_p=\tfrac{1}{4}(1+\eta), \quad & b_p=h_p=\tfrac{1}{4}(1-\eta)\\ w_n=\tfrac{1}{2}(1+\delta)\xi, \quad & m_n=\tfrac{1}{2}(1-\delta)\xi \end{aligned}\right\}, \quad (54)$$

so that the a's take on the values in Table II. If we now use (31), (32), and (35–38), we obtain for the total cross section

$$\sigma_{TOT}=(\sigma_{NP}+\sigma_{INTERF}+\sigma_{NN}), \quad (55)$$

where

$$\sigma_{NP}=(M^2/9\pi\hbar^4k^2)(1/2\pi)^3\{\tfrac{1}{4}(3+\eta^2)(I+III) -\tfrac{1}{16}(5-2\eta+\eta^2)(II+2IV+V)\}, \quad (56a)$$

$$\sigma_{INTERF}=(M^2/9\pi\hbar^4k^2)(1/2\pi)^3\{\tfrac{1}{4}(1+\eta) \times(II+2IV+V)+\tfrac{1}{4}\delta(5+\eta)(II-V)\}, \quad (56b)$$

$$\sigma_{NN}=(M^2/9\pi\hbar^4k^2)(1/2\pi)^3 \times\{\tfrac{1}{2}(I+III)+\tfrac{3}{2}\delta^2(I-III)\}. \quad (56c)$$

We have used the subscripts NP, $INTERF$, and NN to correspond to the source of these terms as evidenced in the particular power of ξ in each term.

If we had made separate calculations of free neutron-proton and neutron-neutron cross sections at the same incident energy using the Born approximation, we would have obtained

$$\sigma_{NP}{}^{free}=(M^2/9\pi\hbar^4k^2)\tfrac{1}{4}(3+\eta^2)\left\{\int_0^{2k}qdqV^2(q) +\int_0^{2k}qdqV(q)V(|\tfrac{1}{2}\mathbf{k}+\mathbf{q}|)\right\}, \quad (57a)$$

TABLE II. Values of the coefficients a_i for the neutron-proton force in (52) and the neutron-neutron force in (53).

	Quartet	Doublet χ_0	Doublet χ_1
a_1	$\delta\xi$	$\xi(3+\delta)/4$	$\xi(1-\delta)\sqrt{3}/4$
a_2	$-\delta\xi$	$\xi(3-\delta)/4$	$\xi(1+\delta)\sqrt{3}/4$
a_3	$\frac{1}{4}$	$(1+3\eta)/8$	$(1-\eta)\sqrt{3}/8$
a_4	$\frac{1}{4}$	$(1+3\eta)/8$	$(1-\eta)\sqrt{3}/8$
a_5	$-\frac{1}{4}$	$\frac{1}{4}$	$\eta\sqrt{3}/4$
a_6	$-\frac{1}{4}$	$\frac{1}{4}$	$\eta\sqrt{3}/4$

[18] δ is the relative magnitude of the neutron-neutron force in odd and even l states.

$$\sigma_{NN}^{\text{free}}=(M^2/9\pi\hbar^4k^2)\xi^2\left\{\tfrac{1}{2}(1+3\delta^2)\int_0^{2k}qdqV^2(q)\right.$$
$$\left.+\tfrac{1}{2}(1-3\delta^2)\int_0^{2k}qdqV(q)V(|\tfrac{1}{2}\mathbf{k}+\mathbf{q}|)\right\}. \quad (57b)$$

Since the integrals I and III are given by (38a) and (38c) as

$$I=\int qdqV^2(q)\int\varphi^2(z)d\mathbf{z}, \quad (58a)$$

$$III=\int qdqV(q)\int V(|\tfrac{1}{2}\mathbf{k}+\mathbf{q}-\mathbf{z}|)\varphi^2(z)d\mathbf{z} \quad (58b)$$

integrated over appropriate values for $\mathbf{z}$, where $\mathbf{z}=\mathbf{k}''+\frac{1}{2}\mathbf{q}$, and since

$$\int_{\text{all }\mathbf{z}}\varphi^2(z)d\mathbf{z}=(2\pi)^3,$$

we see that σ_{TOT} contains terms which are very similar to the two-body cross sections. There are therefore three corrections to considering the total cross section as the sum of the two-body cross sections.

(a) The integrals must be performed over only those momentum states of the deuteron permitted by conservation of energy.

(b) The interference term must be taken into account.

(c) There is a correction to the neutron-proton cross section which arises from the interference between the exchange scattering of the direct and antisymmetrized neutrons by the proton. This is the second term in (56a) and is considerably smaller than the first.

Since the Born approximation for the total scattering gives a result which is a corrected sum of the two-particle cross sections calculated with the Born approximation, it seems reasonable that the *exact* total cross section would give the sum of the *exact* two-particle cross sections, corrected in a similar way. If this is so, we ought to use the measured two-particle cross sections rather than those calculated by Born approximation when evaluating the total scattering. An argument which may make this more plausible is the following.

Consider the next order Born approximation, that is, double scattering in the potential wells of the two nucleons. This may take place either twice in the neutron well, once in each well, or twice in the proton well. Since the radius of the deuteron is considerably larger than the range of the forces, the term corresponding to successive scattering by the neutron and the proton will be smaller than the term corresponding to a double scattering in either well, and will be omitted. If we also neglect successive scattering in higher orders, then, roughly speaking, the amplitude for the total scattering is just the sum of the first, second, and higher order scatterings in the neutron well and the first, second, and higher order scattering in the proton well, that is, the sum of the true neutron-neutron and neutron-proton scattering amplitudes (with appropriate phase factors). We may therefore feel justified in replacing the appropriate terms in (56) by the observed values wherever possible. Although this treatment is far from rigorous,[19] it should be a considerable improvement over using the Born approximation directly.

Let us therefore adjust the constant in (56) so that σ_{NP}^{obs} is 83 mb, the observed neutron-proton cross section[5] where $\sigma_{NP}=\sigma_{NP}^{\text{obs}}-\Delta\sigma_{NP}$. The corresponding neutron-deuteron cross section[5] is 117 mb. Since we know all the quantities in σ_{TOT} except δ and ξ, we obtain the following relation between δ and ξ:

$$[1-0.15]+\xi[0.24+0.49\delta]+\xi^2[0.58+0.69\delta^2]=117/83.$$

If we set $\delta=+1$, 0, -1 corresponding to ordinary, Serber, and pure exchange forces, respectively, for the neutron-neutron interaction, we can determine ξ and therefore the relative value of each term. The results are given in Table III.

It may be noticed from (56a, b) that the form of the interference term for $\delta=0$ is the same as the correction for the neutron-proton cross section. As we mentioned before, the reason for this is that the neutron-proton correction term is mainly an interference term between the exchange scattering of the direct and antisymmetrized neutrons by the proton, a term which has exactly the same form as the interference between the incident neutron scattered by the neutron and by the proton. The similarity of these two terms can be seen more easily if we antisymmetrize the final state instead of the initial state. A neutron-proton exchange collision will then give rise to a proton in the forward direction and two slowly moving neutrons. If we now antisymmetrize this final state in the two neutrons, we see that the two terms represent very similar states and therefore will interfere. This interference will therefore be analogous to the ordinary interference between the small momentum transfer neutron-neutron and neutron-proton collisions. The similarity of these two terms in magnitude is most likely accidental, since they depend differently on η and ξ. We evaluated the form of these two terms for a neutron-proton force of arbitrary

TABLE III. Division of σ_{ND} between σ_{NP}, σ_{INTERF}, and σ_{NN} as a function of the exchange character of the neutron-neutron force.

δ	1	0	-1
N–N force	1	$\frac{1}{2}(1+P)$	P
$\xi=V_{NN}/V_{NP}{}^T$	0.44	0.80	0.77
σ_{NP}	71 mb	71 mb	71 mb
σ_{INTERF}	26 mb	16 mb	-16 mb
σ_{NN}	20 mb	30 mb	62 mb
σ_{TOT}	117 mb	117 mb	117 mb

[19] Perhaps the most important error is due to the phase factors in the exact scattering amplitudes, which cannot easily be determined from experiment.

exchange character and found that only in the case of a Serber force for both interactions is the form of the two correction terms, σ_{INTERF} and $\Delta\sigma_{NP}$, the same.

If we are to choose between the values of $+1$, 0, and -1 for δ, we must make use of other measured values, such as the elastic scattering and the angular and energy distributions. For this reason we have repeated Chew's calculation of the elastic scattering,[1] with arbitrary δ and ξ. This work is discussed in the next section.

IV. ELASTIC SCATTERING

The elastic scattering is obtained from (31), (32), and (33) by replacing the two-particle wave function $\psi_{\mathbf{k}''}(\mathbf{r})$ by the ground state $\psi_0(r)$. In addition, the integration over $\mathbf{k}''$ reduces to the single state $\psi_0(r)$, so that $(L/2\pi)^3\int d\mathbf{k}''$ in (32) is replaced by unity. We then obtain for the elastic cross section[20]

$$\sigma_{el}=(2M^2/9\pi\hbar^4k^2)\int_0^{2k} qdq\left|\sum_{l=1}^{6}a_lH_l\right|^2, \tag{59}$$

where

$$H_1=H_3\equiv I_1=V(q)\int d\mathbf{r}\psi_0^2(r)\exp(\tfrac{1}{2}i\mathbf{q}\cdot\mathbf{r}), \tag{60a}$$

$$H_2=H_4\equiv I_2=\int d\mathbf{r}\psi_0(r)\exp(\tfrac{1}{2}i\mathbf{q}\cdot\mathbf{r})\int d\mathbf{y}V(y)\times\psi_0(|\mathbf{y}-\mathbf{r}|)\exp[-i\mathbf{y}\cdot(\mathbf{q}+\tfrac{3}{2}\mathbf{k})], \tag{60b}$$

$$H_5=H_6\equiv I_3=\varphi(|\mathbf{q}+\tfrac{3}{2}\mathbf{k}|)\int d\mathbf{r}\psi_0(r)V(r)\times\exp[\tfrac{1}{2}i(\mathbf{q}+3\mathbf{k})\cdot\mathbf{r}], \tag{60c}$$

and the a_l's are given as before in Table I. The integrals I_1, I_2, and I_3 correspond to Chew's[1] notation for the elastic cross section.

With our assumptions for $V(r)$ and $\psi_0(r)$ as stated in (43) and (44), I_1 and I_3 can be calculated explicitly, but I_2 must be evaluated numerically. The term I_1 represents a small momentum transfer to either the neutron or proton in the deuteron and is therefore the main term, giving a large forward peak for the incident neutrons. I_2 and I_3 represent the effects of antisymmetrization and exchange forces and include the possibility of "pick-up" processes, that is, collisions in which the incident neutron forms a deuteron by "picking up" the proton in the initial deuteron, giving a small backward peak for the free neutron.

In our sum over final spins, it must be remembered that the deuteron exists only in a triplet spin state. The final spin must be either a quartet or doublet symmetric spin state, and therefore the doublet antisymmetric term in (31) will be absent. The elastic cross section is then given by

$$\sigma_{el}=\tfrac{2}{3}\sigma_{el\ quar}+\tfrac{1}{3}\sigma_{el\ doub}, \tag{61}$$

where $\sigma_{el\ quar}$ and $\sigma_{el\ doub}$ are given by (59) with the appropriate a_l's.

We have calculated I_1 and I_3 explicitly and an approximate expression for I_2 assuming the range of nuclear forces much smaller than the radius of the deuteron[21] $(1/\mu\ll 1/\alpha)$. The integrations in (59) have been performed numerically and the final result for the elastic cross section can be obtained in a form similar to (56). If we use the values of δ and ξ in Table III, we obtain the values for σ_{el} of 80, 60, 30 mb for the direct, Serber, and pure exchange neutron-neutron forces, respectively. Since the measured value for the elastic cross section is[22] 48 mb, it appears a Serber type exchange force between the two neutrons is not inconsistent.

It may seem surprising that the elastic scattering is such a large fraction of the total. As we have previously pointed out, this is due to the fact that small momentum transfers ($q\sim\mu$), independent of energy, are favored at high energies. For this reason the ratio of the elastic to the total cross section should approach a constant as the energy is increased. The value of this constant is related to the probability of the deuteron remaining bound after absorbing a momentum transfer of order $q\sim\mu$.

The wide variation of the elastic cross section with the exchange character of the neutron-neutron force is due in part to the fact that an exchange may result in the wrong spin state for the proton and the exchanged neutron, thus causing them to separate. It also seems that the interference is destructive when there is a neutron-neutron exchange. This is similar to what happens in the total scattering where the interference term (Table III) is negative for a pure exchange neutron-neutron force.

V. LOW ENERGY PROTON COMPONENT

The cross section for the production of protons of low energy has recently been measured[23] in order to obtain additional information about the neutron-neutron interaction. It was thought that low energy protons result most probably from neutron-neutron collisions which break up the deuteron. We shall calculate the low energy proton cross section by first calculating the *total* cross section for low energy free and bound protons.

This cross section for the production of slow protons will necessarily include those that remain bound in elastic collisions. For this reason, we must evaluate the elastic cross section for slow deuterons and subtract it from the calculated total low energy proton cross section. This will give us what we are after, namely, the cross section for the production of low energy *free* protons.

Protons resulting from neutron-deuteron scattering

[20] The factor $\frac{1}{2}$ (footnote 11) is no longer present, since the neutron and deuteron in the final state are distinguishable.

[21] This is admittedly not too good, but we shall only be interested in the qualitative features of the results.

[22] W. Powell (private communication).

[23] W. Powell, Phys. Rev. 79, 219 (1950).

fall roughly into two groups: a high energy group which results from small momentum transfer neutron-proton exchange collisions, and a low energy group which results from all low momentum transfer collisions except the neutron-proton exchange. These groups are quite well separated, so that the total cross section for the production of protons in the low energy group will involve a sum over a wide range of final two-particle states for all terms except those due to neutron-proton exchange collisions, namely, F_4 and F_6 in (34). This can also be seen from (36) in which the final momentum of the proton in the *laboratory* system is $\mathbf{z}=\mathbf{k}''+\frac{1}{2}\mathbf{q}$. For small $\mathbf{z}$ all the terms except G_4 and G_6 can be large when integrated over $\mathbf{q}$. G_1 and G_3 are large near $\mathbf{q}=0$, and G_2 and G_5 are large near $\mathbf{q}=-\frac{3}{2}\mathbf{k}$. We shall therefore set $G_4=G_6=0$ in (35) to evaluate the low energy proton component. Using the values of δ and ξ in Table I we obtain 66, 69, 75 mb for the direct, Serber, and pure exchange neutron-neutron forces, respectively.

As we previously mentioned, the part of the elastic cross section giving rise to low energy deuterons must be subtracted. In order to do this we must confine the integrations in (59) to values of q for which the deuteron has low energy. Since the momentum of the deuteron in the laboratory system after the collision is just $\mathbf{q}$, we can restrict the range of integration in q from 0 to k. In this way, the backward peaks for I_2 and I_3 mentioned in Sec. IV are omitted. The values of the integrals in (60) change somewhat and lead to cross sections for the collisions resulting in low energy deuterons of 65, 50, 25 mb for the direct, Serber, and pure exchange neutron-neutron forces, respectively.

If we now subtract the cross sections just evaluated, we obtain 1, 19, 50 mb for the cross section for the production of low energy protons for the direct, Serber, and pure exchange neutron-neutron forces, respectively.

The experimental value reported for this cross section is 6 mb in the backward direction. For lack of more detailed information we can assume that, since the low energy protons are more or less spherically symmetric, the cross section in all directions[24] is 12 mb. This evidence is therefore once again not inconsistent with a Serber type exchange force between the two neutrons. The discrepancy may be accounted for by the fact that there are a considerable number of protons of quite small energy which may not have been counted.

It may be worthwhile pointing out that the low energy proton cross section is not directly connected with the neutron-neutron cross section. The bound states play an important part and must be included in the calculation.

[24] Since the system as a whole has forward motion, there will probably be more protons forward than backward. This will raise the 12 mb into closer agreement with the calculated value for a Serber exchange neutron-neutron force. We have investigated the approximate angular distribution of low energy protons in the next section.

VI. ENERGY DISTRIBUTION OF PROTONS AND NEUTRONS AT VARIOUS ANGLES

In order to calculate the energy distribution of protons or neutrons at various angles, we can no longer use plane waves for the $\psi_{k''}(\mathbf{r})$; there is no complete sum over final states to which we may apply a sum rule. We must instead find a more accurate expression for $\psi_{k''}(\mathbf{r})$ to use in the integrations.

Before investigating the problem in detail we shall be able to make a rough guess as to the nature of the angular and energy distribution from the qualitative features already discussed. There will be two main groups of protons: a group at low energy resulting from neutron-neutron and ordinary neutron-proton collisions (favoring small momentum transfers) which break up the deuteron, and a group of high energy protons which result from neutron-proton exchange collisions. The low energy group will be roughly isotropic, since the momentum distribution of the particles in the deuteron is isotropic; but the high energy proton group will be confined to the forward direction as in the scattering of neutrons by protons.

In order to set up the expressions for the angular distribution, we must transform the momenta $\mathbf{k}'$ and $\mathbf{k}''$ to the laboratory system. We shall outline the calculation for the more easily measurable proton distribution.

For the high energy proton group, it will be more convenient to use the description of the final state in which particle 2 is free, namely, (9c) in terms of the quantities $\mathbf{k}^{\nu}$ and $\mathbf{k}^{\nu i}$. The angular distribution of the low energy group will require a description of the final state in which either particle 1 or 3 is free.

If we now put the final state (9c) into (28), the matrix element $\mathfrak{M}$ in (33) becomes

$$L^{k}\mathfrak{M}=\sum_{l=1}^{6} a_l \int \psi_{k''}^{*}(\mathbf{r})F_l'(\mathbf{r})d\mathbf{r}, \tag{62}$$

where

$$F_1'(\mathbf{r})=V(r)\exp[\tfrac{1}{2}i\mathbf{r}\cdot(\mathbf{q}+3\mathbf{k})]\varphi(|\mathbf{q}''+\tfrac{3}{2}\mathbf{k}|), \tag{63a}$$

$$F_2'(\mathbf{r})=V(r)\exp[-\tfrac{1}{2}i\mathbf{r}\cdot(\mathbf{q}+3\mathbf{k})]\varphi(|\mathbf{q}''+\tfrac{3}{2}\mathbf{k}|), \tag{63b}$$

$$F_3'(\mathbf{r})=\exp[-\tfrac{1}{2}i\mathbf{q}''\cdot\mathbf{r}]\int d\mathbf{y}V(y)\psi_0(|\mathbf{y}+\mathbf{r}|) \times\exp[-i\mathbf{y}\cdot(\mathbf{q}''+\tfrac{3}{2}\mathbf{k})], \tag{63c}$$

$$F_4'(\mathbf{r})=\psi_0(r)\exp(-\tfrac{1}{2}i\mathbf{q}''\cdot\mathbf{r})V(q''), \tag{63d}$$

$$F_5'(\mathbf{r})=\exp[\tfrac{1}{2}i\mathbf{q}''\cdot\mathbf{r}]\int d\mathbf{y}V(y)\psi_0(|\mathbf{y}-\mathbf{r}|) \times\exp[-i\mathbf{y}\cdot(\mathbf{q}''+\tfrac{3}{2}\mathbf{k})], \tag{63e}$$

$$F_6'(\mathbf{r})=\psi_0(r)\exp(\tfrac{1}{2}i\mathbf{q}''\cdot\mathbf{r})V(q''). \tag{63f}$$

As mentioned previously, these expressions can be obtained directly by a proper cyclic transformation of

the relative coordinates. The similarity between (63) and (34) is evident.

The relative importance of the various terms in (63) can be obtained *qualitatively* by using the plane wave expression for $\psi_{k^{vi}}(\mathbf{r})$, that is by using

$$\psi_{k^{vi}}(\mathbf{r})=L^{-\frac{1}{2}}\exp(-i\mathbf{k}^{vi}\cdot\mathbf{r}).$$

The matrix element (62) can now be written as

$$L^{9/2}\mathfrak{M}=\sum_1^4 a_iG_i', \tag{64}$$

where

$$G_1'=\varphi(|\mathbf{q}''+\tfrac{2}{3}\mathbf{k}|)V_{NN}^{O;\,X,\,A.S.}(|\tfrac{2}{3}\mathbf{k}+\tfrac{1}{2}\mathbf{q}''-\mathbf{k}^{vi}|), \tag{65a}$$

$$G_2'=\varphi(|\mathbf{q}''+\tfrac{2}{3}\mathbf{k}|)V_{NN}^{X;\,A.S.}(|\tfrac{2}{3}\mathbf{k}+\tfrac{1}{2}\mathbf{q}''+\mathbf{k}^{vi}|), \tag{65b}$$

$$G_3'=\varphi(|\mathbf{k}^{vi}+\tfrac{1}{2}\mathbf{q}''|)V_{NP}^{O}(|\tfrac{2}{3}\mathbf{k}+\tfrac{1}{2}\mathbf{q}''-\mathbf{k}^{vi}|), \tag{65c}$$

$$G_4'=\varphi(|\mathbf{k}^{vi}+\tfrac{1}{2}\mathbf{q}''|)V_{NP}^{X}(q''), \tag{65d}$$

$$G_5'=\varphi(|\mathbf{k}^{vi}-\tfrac{1}{2}\mathbf{q}''|)V_{NP}^{A.S.}(|\tfrac{2}{3}\mathbf{k}+\tfrac{1}{2}\mathbf{q}''+\mathbf{k}^{vi}|), \tag{65e}$$

$$G_6'=\varphi(|\mathbf{k}^{vi}-\tfrac{1}{2}\mathbf{q}''|)V_{NP}^{X,\,A.S.}(q''). \tag{65f}$$

(65) is of course identical to (36) written in terms of $\mathbf{q}''$ and $\mathbf{k}^{vi}$

The high energy proton group is obtained in the vicinity $\mathbf{q}''\approx 0$, $\mathbf{k}^{v}\approx\mathbf{k}$, $\mathbf{k}^{vi}\approx 0$. Since both $\varphi(\frac{2}{3}k)$ and $V(\frac{2}{3}k)$ are small compared to $\varphi(0)$ and $V(0)$, respectively, most of the contribution to the cross section comes from the terms G_4' and G_6'. We shall therefore consider only F_4' and F_6' in (63) with a corrected expression for $\psi_{k^{vi}}(\mathbf{r})$ in order to obtain the high energy proton differential cross section.

If we now select a particular proton direction and energy, there still remain two degrees of freedom; these are the two variables needed to specify the direction of $\mathbf{k}^{vi}$. In order to obtain the differential cross section as a function of the proton momentum, we must square the matrix element (62), multiply by the appropriate density of final states, and integrate over Ω^{vi}, the direction associated with $\mathbf{k}^{vi}$. The differential cross section for high energy protons will therefore be given by[25]

$$d\sigma=(M/12\pi^2\hbar^2k)(L/2\pi)^3(dk^vd\mathbf{k}^{vi}/dE)\,|L^{3}\mathfrak{M}|^2. \tag{66}$$

Since the energy in the center-of-mass system is given from (3) and (6) as

$$E=(\hbar^2k^{v2}/(4/3)M)+(\hbar^2k^{vi2}/M),$$

we may use

$$(\partial E/\partial k^{vi})_{k^v}=(2\hbar^2k^{vi})/M.$$

If we transform the momentum $\mathbf{k}^v$ to the momentum of the proton in the laboratory system

$$\mathbf{k}_p=\mathbf{k}^v+\tfrac{1}{2}\mathbf{k}=\mathbf{q}''+\tfrac{3}{2}\mathbf{k};\quad d\mathbf{k}^v=d\mathbf{k}_p, \tag{67}$$

we obtain for the differential cross section

$$d\sigma=(M^2/24\pi^2\hbar^4k)(1/2\pi)^3d\mathbf{k}_pk^{vi}\int d\Omega^{vi}\,|L^{3}\mathfrak{M}|^2, \tag{68}$$

where the matrix element

$$L^{3}\mathfrak{M}=V(q'')\int d\mathbf{r}\psi_{k^{vi}}^{*}(\mathbf{r})\psi_0(r)$$

$$\times\{a_4\exp(-\tfrac{1}{2}i\mathbf{q}''\cdot\mathbf{r})+a_6\exp(\tfrac{1}{2}i\mathbf{q}''\cdot\mathbf{r})\} \tag{69}$$

is obtained from (62) and (63) by using only the terms $l=4$ and $l=6$.

As before the cross section will be the sum of the quartet and doublet cross sections. However, we must now remember that the two-particle wave functions $\psi_{k^{vi}}(\mathbf{r})$ for particles 1 and 3 will depend on the spin symmetry between these two particles (triplet or singlet). Since the spin states χ_5 and χ_7 are neither symmetric nor antisymmetric in particles 1 and 3, we shall change our complete set of spin states to χ_1, χ_2, χ_3, χ_4, χ_5', χ_6', χ_7', χ_8', where the four quartet spin states are unchanged and the doublet spins states are given by[26]

$$\chi_5'=[1/(6)^{\frac{1}{2}}](2a_1b_2a_3-a_1a_2b_3-b_1a_2a_3)$$

$$=Q_{23}\chi_5=-\tfrac{1}{2}\chi_5+\tfrac{1}{2}\sqrt{3}\chi_7, \tag{70a}$$

$$\chi_7'=(1/\sqrt{2})(a_1a_2b_3-b_1a_2a_3)$$

$$=Q_{23}\chi_7=\tfrac{1}{2}\sqrt{3}\chi_5+\tfrac{1}{2}\chi_7. \tag{70b}$$

We now obtain the cross section by summing over the spin states χ_1, χ_5', and χ_7' giving

$$d\sigma=\tfrac{3}{4}(d\sigma)_{\chi_1}+\tfrac{1}{4}(d\sigma)_{\chi_5'}+\tfrac{1}{4}(d\sigma)_{\chi_7'}, \tag{71}$$

where each $d\sigma$ is given by (68). We must use the triplet wave function $\psi_{k^{vi}}^{T}(\mathbf{r})$ in $(d\sigma)_{\chi_1}$ and $(d\sigma)_{\chi_5'}$ and the singlet wave function $\psi_{k^{vi}}^{S}(\mathbf{r})$ in $(d\sigma)_{\chi_7'}$. The corresponding values of a_4 and a_6, obtained from (70) and Table II, are

$$(a_4)_{\chi_5'}=-\tfrac{1}{2}(a_4)_{\chi_5}+\tfrac{1}{2}\sqrt{3}(a_4)_{\chi_7}=(1-3\eta)/8, \tag{72a}$$

$$(a_6)_{\chi_5'}=-\tfrac{1}{2}(a_6)_{\chi_5}+\tfrac{1}{2}\sqrt{3}(a_6)_{\chi_7}=-(1-3\eta)/8, \tag{72b}$$

$$(a_4)_{\chi_7'}=\tfrac{1}{2}\sqrt{3}(a_4)_{\chi_5}+\tfrac{1}{2}(a_4)_{\chi_7}=(1+\eta)\sqrt{3}/8, \tag{72c}$$

$$(a_6)_{\chi_7'}=\tfrac{1}{2}\sqrt{3}(a_6)_{\chi_5}+\tfrac{1}{2}(a_6)_{\chi_7}=(1+\eta)\sqrt{3}/8. \tag{72d}$$

We must now evaluate the integrals

$$J_1=\int d\Omega^{vi}\left|\int d\mathbf{r}\psi_{k^{vi}}^{*}(\mathbf{r})\psi_0(r)\exp(\tfrac{1}{2}i\mathbf{q}''\cdot\mathbf{r})\right|^2 \tag{73a}$$

[25] The factor $\frac{1}{4}$ due to the identity of the two neutrons has been included as before.

[26] χ_6' and χ_8' are obtained from χ_5' and χ_7', respectively, by interchanging a and b.

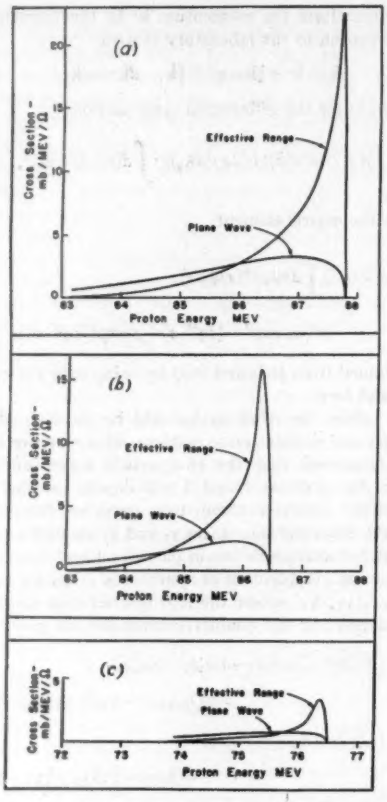

FIG. 6. Approximate energy spectrum for high energy protons in the forward direction at laboratory angles of (a) 0°, (b) 10°, and (c) 30°.

and

$$J_2=\int d\Omega^{pi}Re\left\{\int dr\psi_k{}^{pi}(r)\psi_0(r)\exp(\tfrac{1}{2}i\mathbf{q}''\cdot\mathbf{r})\times\int dr\psi_k{}^{pi*}(\mathbf{r})\psi_0(r)\exp(\tfrac{1}{2}i\mathbf{q}''\cdot\mathbf{r})\right\} \quad (73b)$$

for both the triplet and singlet $\psi_k{}^{pi}(\mathbf{r})$. Since we are interested mainly in the proton cross section in the forward direction at high energies, $\mathbf{k}^{pi}$ and $\mathbf{q}''$ will be quite small. For simplicity we shall set[27] $\mathbf{q}''=0$ in J_1 and J_2. In this rough approximation only the spherically symmetric part of $\psi_k{}^{pi}(\mathbf{r})$ enters. The resulting integrals for small k^{pi} are

$$\int_0^\infty r^2dr\psi_k{}^{pi\,T}(r)\psi_0(r) \quad \text{and} \quad \int_0^\infty r^2dr\psi_k{}^{pi\,S}(r)\psi_0(r).$$

[27] A more accurate method of calculating J_1 and J_2 is given in Appendix G, but the present method is adequate for our purposes.

The first of these vanishes because the triplet wave function $\psi_k{}^{pi\,T}(r)$ is necessarily orthogonal to the ground state $\psi_0(r)$. The remaining integral is the same as the one that occurs in the photo-magnetic disintegration of the deuteron. The integral has been evaluated by Bethe and Longmire[28] at low energy using the effective range method. The result, after proper normalization, is

$$J_s\equiv L^1\int_0^\infty r^2dr\psi_k{}^{pi\,S}(r)\psi_0(r)=\frac{N\sin\delta_s}{k^{pi}}\left\{\frac{\alpha+k^{pi}\cot\delta_s}{\alpha^2+k^{pi2}}-\tfrac{1}{4}(r_{0t}+r_{0s})\right\}, \quad (74)$$

where r_{0t} and r_{0s} are the triplet and singlet effective ranges and N is the ground-state normalization factor given by

$$N^2=\alpha/[2\pi(1-\alpha r_{0t})].$$

This value of N is equivalent to that given in (44), leading to the relation between α, β and r_{0t}

$$r_{0t}=4/(\alpha+\beta)-1/\beta.$$

The singlet phase shift δ_s is given by

$$k^{pi}\cot\delta_s=-1/a_s+\tfrac{1}{2}k^{pi2}r_{0s}, \quad (75)$$

where a_s in the singlet scattering length. The integral J_s can therefore be written as

$$J_s=\left\{\frac{\alpha}{2\pi(1-\alpha r_{0t})}\right\}^{\frac{1}{2}}\{k^{pi2}+(-1/a_s+\tfrac{1}{2}k^{pi2}r_{0s})^2\}^{-\frac{1}{2}}\times\left\{\frac{\alpha-1/a_s+\frac{1}{2}k^{pi2}r_{0s}}{\alpha^2+k^{pi2}}-\tfrac{1}{4}(r_{0t}+r_{0s})\right\}. \quad (76)$$

Since the integrals J_1 and J_2 vanish in first approximation for triplet wave functions, the cross section becomes, using (68), (69), (71), and (72)

$$d\sigma=(M^2k^{pi}/48\pi^2\hbar^4k)V^2(q'')(1+\eta)^2J_s{}^2k_p{}^2dk_pd\Omega_p. \quad (77)$$

If we had used a plane wave for $\psi_k{}^{pi}(\mathbf{r})$ in the same approximation ($\mathbf{q}''=0$), we would have obtained the same cross section (77) with a different value for J_s

$$J_s{}^{P.W.}=\varphi(k^{pi})/4\pi=\left(\frac{\alpha}{2\pi(1-\alpha r_{0t})}\right)^{\frac{1}{2}}\left\{\frac{1}{\alpha^2+k^{pi2}}-\frac{1}{\beta^2+k^{pi2}}\right\}. \quad (78)$$

In Fig. 6 we have plotted the approximate spectrum for high energy protons in the forward direction for both the effective range and plane wave values of J_s at angles of 0°, 10°, and 30°. We have used the values:

$$\left.\begin{aligned}r_{0s}=2.7\times10^{-13}\text{ cm},\quad r_{0t}=1.71\times10^{-13}\text{ cm},\\ a_s=-23.8\times10^{-13}\text{ cm}.\end{aligned}\right\} \quad (79)$$

[28] H. A. Bethe and C. Longmire, Phys. Rev. 77, 647 (1950).

From the curves we see that the high energy protons are confined to high energies and small angles. This is what we had supposed, since these high energy protons come from neutron-proton exchange collisions which favor small momentum transfers. The angular dependence of the cross section (77) comes about primarily from the factor $V^2(q'')$. For this reason the angular distribution of the high energy protons should be very similar to the angular dependence in neutron-proton scattering.

One feature of the high energy proton spectrum which is rather surprising is that the protons seem to be crowded more toward higher energies than would be expected in the plane wave approximation. This is due to the interaction between the two neutrons, and since the energy of the neutrons is small, most of the contribution to the cross sections occurs for a singlet spin state between the two neutrons. The energy width of the proton peak is proportional to $(1/a_s)^2$, whereas the energy width for the plane wave calculation is proportional to α^2. The ratio of these two widths,

$$\Delta E_p/\Delta E_p{}^{P.W.}=(1/a_s)^2/\alpha^2\approx 1/30, \tag{80}$$

is quite small and accounts for the highly peaked proton spectrum.

The sharp peak in the energy distribution could be used in practice in order to obtain very nearly monochromatic beams of neutrons. For this purpose, the inverse process is used; i.e., protons of given energy E are permitted to fall on a deuterium target. Then, in the forward direction, neutrons will be emitted whose energy is slightly below $E-\epsilon$ (ϵ=binding energy). According to Fig. 6a, the width of the energy distribution is only about 1 Mev, and is not appreciably increased if neutrons up to 10° angle with the proton beam are included. To get an appreciable neutron yield, probably liquid deuterium should be used as a target, but apart from this technical difficulty the neutron beam obtainable seems far superior to that from other methods.

We have only performed a rough calculation of the high energy proton distribution. More exact calculations can be performed along the lines mentioned in Appendix G. The work is considerably more involved and the major changes will occur where $k^{\nu i}$ and q'' are not small, that is, for proton energies away from the maximum and for large scattering angles. However, our results should remain essentially unchanged.

The total cross section for the production of high energy protons can be obtained approximately by retaining only the a_4 and a_8 terms in (35) and (36). These are the terms which represent neutron-proton exchange collisions and which therefore are mainly responsible for high energy protons. The result is that the cross section for high energy protons is approximately 20 mb.

As mentioned earlier there is also a group of low energy protons in the laboratory system resulting from neutron-neutron and ordinary neutron-proton collisions which break up the deuteron. Since small momentum transfers are most probable, the incident neutron[39] will continue in the forward direction and will be essentially free. We may therefore use the representation of the matrix element in (33) and (34) with particle 3 free.

Since we are now asking for a final state with particle 3 only "slightly" scattered, only the terms F_1 and F_2 in (34) will contribute. If we use the approximation $\mathbf{q}=0$ in F_1 and F_2, we see that we have to evaluate the same integrals as before:

$$\int_0^\infty r^2 dr \psi_{k''}{}^T(r)\psi_0(r) \quad \text{and} \quad \int_0^\infty r^2 dr \psi_{k''}{}^S(r)\psi_0(r).$$

Once again, only the singlet wave function contributes and gives a value for the integral given by (74) with $k^{\nu i}$ replaced by k''.

We must now remember that we are fixing the angle and energy of the *proton* in the final state. The remaining degree of freedom to be removed is therefore the angle of the vector $\mathbf{k}^{\nu i}$ *not* $\mathbf{k}''$. This integration will be quite complicated, but we shall make some rough approximations to allow us to carry the calculation through in order to obtain qualitative results.

As we have seen in the calculation of the high energy proton distribution, the sharp peak was due to the smallness of $|1/a_s|$ compared to α. The integral J_s can be given approximately from (74) by neglecting the terms with r_{0s} and r_{0t}. We then have

$$J_s'\approx\frac{N}{[(1/a_s)^2+k''^2]^{\frac{1}{2}}}\cdot\frac{\alpha}{\alpha^2+k''^2}. \tag{81}$$

The cross section is now given by

$$d\sigma=(M^3/72\pi^2\hbar^4 k)(1/2\pi)^3 d\mathbf{k}_p k^{\nu i}$$

$$\times\int d\Omega^{\nu i}(4\pi)^2 V^2(q)J_s'^2\frac{3}{64}[4\xi^2(1-\delta)^2+(1-\eta)^2] \tag{82}$$

obtained from (77) by replacing $4\pi k^{\nu i}$ by $k^{\nu i}\int d\Omega^{\nu i}$, q'' by q, J_s by J_s' in (76), and

$$\tfrac{3}{16}(1+\eta)^2=[(a_4)_{\chi_T'}+(a_6)_{\chi_T'}]^2$$

by

$$(3/64)[4\xi^2(1-\delta)^2+(1-\eta)^2]=[(a_1)_{\chi_T'}+(a_3)_{\chi_T'}]^2.$$

The vectors $\mathbf{q}$ and $\mathbf{k}^{\nu i}$ are given in terms of $\mathbf{q}''$ and $\mathbf{k}''^{\nu i}$ as

$$\mathbf{q}=\mathbf{k}^{\nu i}-(\tfrac{2}{3}\mathbf{k}+\tfrac{1}{2}\mathbf{q}''); \tag{83a}$$

$$\mathbf{k}''=-\tfrac{1}{2}\mathbf{k}^{\nu i}-\tfrac{3}{4}(\mathbf{k}+\mathbf{q}''). \tag{83b}$$

The vector $\mathbf{q}''$ (and therefore $\mathbf{k}_p=\frac{2}{3}\mathbf{k}+\mathbf{q}''$) and the *magnitude* of $\mathbf{k}^{\nu i}$ are fixed during the angular integration over $d\Omega^{VI}$. Both q and k'' will therefore vary over the

[39] The free neutron may also be the antisymmetrized neutron, but, since we have antisymmetrized only the initial state, we may consider only collisions in which the incident neutron (particle 3) remains free.

integration. However, the effect of the variation of q will be dwarfed by that of k'', since μ is considerably larger than both α and $|1/a_s|$; q can then be set equal to zero in $V(q)$.

If we now measure the angle of $\mathbf{k}^{vi}$ with respect to the fixed vector $\mathbf{k}+\mathbf{q}''$, we can change the angular variable Ω^{VI} to the magnitude of $\mathbf{k}''$ by using (83b). In fact,

$$\tfrac{3}{4}k^{vi}|\mathbf{k}+\mathbf{q}''|d\Omega^{vi}=2\pi dk''^3;$$
$$k^{vi}d\Omega^{vi}=(8\pi/3)(dk''^3/|\mathbf{k}+\mathbf{q}''|).$$

Since we are interested mainly in small $\mathbf{k}_p$, $\mathbf{q}''$ will be approximately $-\frac{3}{2}\mathbf{k}$, so that we have

$$k^{vi}d\Omega^{vi}\approx(16\pi/3)(dk''^3/k).$$

The cross section now becomes

$$\frac{d\sigma_p}{d\mathbf{k}_p}=K\int_{k''^3_{\min}}^{k''^3_{\max}}\frac{dk''^3}{[(1/a_s)^2+k''^2](\alpha^2+k''^2)^2}, \tag{84}$$

where K is a constant and $k''_{\min}$ and $k''_{\max}$ are given by

$$\left.\begin{aligned}k''_{\min}&=|\tfrac{1}{2}k^{vi}-\tfrac{3}{4}|\mathbf{k}+\mathbf{q}''||,\\ k''_{\max}&=\tfrac{1}{2}k^{vi}+\tfrac{3}{4}|\mathbf{k}+\mathbf{q}''|.\end{aligned}\right\} \tag{85}$$

k^{vi} is given from conservation of energy by

$$k^{vi}=\tfrac{1}{2}\sqrt{3}(k^2-|\mathbf{k}+\mathbf{q}''|^2-(4/3)M\epsilon/\hbar^2)^{\frac{1}{2}},$$

where the binding energy ϵ now becomes important. For small $\mathbf{k}_p$ we can write

$$|\mathbf{k}+\mathbf{q}''|=|\tfrac{1}{2}\mathbf{k}-\mathbf{k}_p|\approx\tfrac{1}{2}k-(\mathbf{k}\cdot\mathbf{k}_p)/k$$

and

$$k^{vi}\approx\tfrac{1}{2}\sqrt{3}[\tfrac{3}{4}k^2+\mathbf{k}\cdot\mathbf{k}_p-(4/3)M\epsilon/\hbar^2]^{\frac{1}{2}}$$
$$\approx\tfrac{3}{4}k+\tfrac{1}{2}[(\mathbf{k}\cdot\mathbf{k}_p)/k]-\tfrac{2}{3}M\epsilon/\hbar^2k.$$

We can therefore set $k''^3_{\max}=\infty$ and

$$k''^3_{\min}\approx[\tfrac{3}{8}k+(\tfrac{1}{4}\mathbf{k}\cdot\mathbf{k}_p/k)-\tfrac{1}{3}(M\epsilon/\hbar^2k)-\tfrac{3}{8}k$$
$$+\tfrac{3}{4}(\mathbf{k}\cdot\mathbf{k}_p)/k]^2\approx\{[(\mathbf{k}\cdot\mathbf{k}_p)/k]-\tfrac{1}{3}M\epsilon/\hbar^2k\}^2.$$

The integral in (84) can be evaluated, and for $\alpha^2\gg(1/a_s)^2$ is approximately

$$d\sigma_p\approx\frac{K}{2\alpha^4}\ln\left\{\frac{\alpha^2+\{[(\mathbf{k}\cdot\mathbf{k}_p)/k]-\frac{1}{3}M\epsilon/\hbar^2k\}^2}{(1/a_s)^2+\{[(\mathbf{k}\cdot\mathbf{k}_p)/k]-\frac{1}{3}M\epsilon/\hbar^2k\}^2}\right\}$$
$$\times k_p dk_p{}^2 d\Omega_p. \tag{86}$$

This represents a peaked distribution of low energy protons, but *not* isotropic. The maximum cross section at a given angle, for $(1/a_s)^2\ll\alpha^2$, occurs approximately at

$$k_p\cos\theta\approx\tfrac{1}{3}(M\epsilon/\hbar^2k)+\alpha,$$

where θ is the angle of the proton momentum with respect to the incident direction in the laboratory system.

Since $\frac{1}{3}M\epsilon/\hbar^2k^2\approx\frac{1}{4}\epsilon/E_0$, where E_0 is the incident energy, $\frac{1}{3}M\epsilon/\hbar^2k$ will be considerably smaller than α (a ratio of $\sim1/20$). The "width" of the peak will therefore vary approximately as

$$\Delta E_p\sim\alpha^2/\cos^2\theta. \tag{87a}$$

For angles near 90°, $(\mathbf{k}\cdot\mathbf{k}_p)/k$ must be replaced by k_p^2/k so that

$$\Delta E_p(90°)\sim\alpha k. \tag{87b}$$

The distribution of low energy protons is now seen to be approximately egg-shaped, with the peak in the spectrum occuring at increasing energies as the angle to the incident direction is increased up to 90°. The term containing the binding energy in (86) will favor the forward direction over the backward direction slightly, but the main feature of the low energy proton group is the large difference between the 0° and 90° scattering.

It was mentioned before that the low energy proton group may favor the forward direction rather than being isotropic, because of the over-all forward motion of the system. Although the binding energy term *is* in this direction, this situation should still exist for no binding energy. The reason for its disappearance is as follows:

(1) The reason that the forward direction should be favored is that the two-particle collisions can only result in an additional *forward* motion to the struck particle.

(2) We have found from (81) and (84), however, that only final states for which k'' is of order of magnitude α give much contribution. Since

$$\mathbf{q}+\tfrac{1}{2}\mathbf{k}''=-(\tfrac{3}{4}\mathbf{k}+\mathbf{q}'')=-\mathbf{k}_p,$$

q will necessarily be about the same size as k'', that is, $q\sim\alpha$.

(3) For this reason we have neglected q compared with μ, that is we have taken $V(q)=V(0)$. Since we have also set $q=0$ in the exponentials, we have effectively considered only *very* small momentum transfers which give practically no additional forward motion to the struck particle.

If we were to consider the case $q\neq0$, we would have to evaluate both the singlet and triplet integrals in (73) and we would obtain a low energy proton distribution which would favor the forward direction. However, because of the above discussion the effect would be rather small.

It should be mentioned that the *free* particle calculation with $q=0$ predicts an isotropic low energy proton component varying as $\varphi^2(k_p)$ and therefore having an energy width $\Delta E_p\sim\alpha^2$, agreeing qualitatively with the more correct width given by (87a) near the incident direction. As can be seen from (86), however, the spectrum predicted does not agree.

VII. CONCLUSIONS

(1) The total cross section (inelastic plus elastic) can be calculated using plane waves for the final state of

the three particles involved. No such simple method is available for the inelastic scattering alone, or for the differential cross section.

(2) The total cross section is given within about 20 percent by elementary interference theory, in which the amplitudes of the waves scattered by a neutron and a proton at rest are added, taking into account spin and symmetry. A better approximation is obtained by considering the motion of neutron and proton in the initial state of the deuteron. (See Sec. II.)

(3) From the total cross section one cannot deduce a unique value for the neutron-neutron cross section. Different assumptions on the exchange properties of the neutron-neutron force lead to values of σ_{NN} at 90 Mev from 20 mb for ordinary forces to 62 mb for pure exchange forces (Table III). The interference between the scattering from neutron and proton may give either a positive (for ordinary N–N forces) or negative (exchange forces) contribution. (See Sec. III.)

(4) The elastic scattering permits a decision between the various types of neutron-neutron forces, being greatest for an ordinary force (Table IV). The experimental value of about 50 mb is closest to the result for a Serber type N–N force (Sec. IV).

(5) The cross section for the production of low energy protons does not agree with the N–N cross section (Sec. V and Table IV) but is generally smaller. The observed cross section is again compatible with a Serber force.

(6) The energy distribution of the protons in the forward direction show a very sharp peak near the incident neutron energy (Fig. 6a, b) which is closely related to the cross section for the photo-magnetic disintegration of the deuteron. The reverse reaction, i.e., the bombardment of deuterons with high energy protons, should yield very nearly monochromatic neutrons.

(7) In Table IV, we have summarized the most important results not contained in Table III.

TABLE IV. Calculated cross sections in millibarns for different exchange character of the N–N interaction.

	1	0	−1
N–N force	1	$\frac{1}{2}(1+P)$	P
Total elastic	80	60	30
Elastic scattering giving low energy deuterons	65	50	25
Low energy protons	1	19	50
N–N cross section	20	30	62

APPENDIX A.

EVALUATION OF INTEGRAL I

The integral I given in (38a) can be evaluated completely once the radial dependence of the potential and the deuteron ground state are decided upon. We shall use the Yukawa potential and Hulthén wave function as given in (43) and (44).

The variable Ω'' in (38a) represents the angle of $\mathbf{k}''$ and can be taken with respect to $\mathbf{q}$ if k'' and q are kept constant. Let us now change from the variable Ω'' to the variable $z=|\mathbf{k}''+\frac{1}{2}\mathbf{q}|$ just as we did in (14) when setting up the integral over the final states.

$$k''d\Omega''=4\pi z dz/q.$$

The z integration must now be performed first between the limits $|\frac{1}{2}q-k''|$ and $\frac{1}{2}q+k''$, so that I is given by

$$I=2\pi\int_0^{2k}dqV^2(q)\int_0^{Q}2k''dk''\int_{\frac{1}{2}q-k''}^{\frac{1}{2}q+k''}z\varphi^2(z)dz, \qquad (A1)$$

where $Q=\frac{1}{2}q(2k-q)$ and where $\frac{1}{2}q-k''$ has been written without an absolute value sign, since the integrand is an odd function of z. We would now like to interchange the order of the k'' and z integrations and can do so with proper regard to the limits. The integral then becomes

$$I=2\pi\int_0^{2k}dqV^2(q)\int_{\frac{1}{2}q-Q}^{\frac{1}{2}q+Q}zdz\varphi^2(z)\int_{|z-\frac{1}{2}q|}^{Q}2k''dk''. \qquad (A2)$$

If the k'' integration is now performed, we obtain

$$I=2\pi\int_0^{2k}dqV^2(q)\int_{\frac{1}{2}q-Q}^{\frac{1}{2}q+Q}zdz\varphi^2(z)\{zq-(z^2+q^2-\tfrac{1}{4}kq)\}. \qquad (A3)$$

The region of integration in the qz plane is shown in Fig. 5.

We now have to determine $V(q)$ and $\varphi(z)$. Using (43) and (44) we readily obtain

$$V(q)=\left(\frac{4\pi V_0}{\mu}\right)\left(\frac{1}{\mu^2+q^2}\right), \qquad (A4)$$

$$\varphi(z)=4\pi N\left(\frac{1}{\alpha^2+z^2}-\frac{1}{\beta^2+z^2}\right). \qquad (A5)$$

If we now interchange the order of the q and z integrations, we obtain

$$I=2\pi\left(\frac{16\pi^2NV_0}{\mu}\right)^2\int_{-\frac{1}{2}k}^{\frac{1}{2}k}zdz\left(\frac{1}{\alpha^2+z^2}-\frac{1}{\beta^2+z^2}\right)^2 \times\int_{z-}^{z+}dq\left\{\frac{q(z+\frac{1}{2}k)-z^2-q^2}{(\mu^2+q^2)^2}\right\},$$

where

$$z\pm=\tfrac{1}{2}k+\tfrac{1}{2}z\pm\{(\tfrac{1}{2}k+\tfrac{1}{2}z)(\tfrac{1}{2}k-\tfrac{1}{2}z)\}^{\frac{1}{2}}.$$

If we now perform the q integration, we obtain

$$I=2\pi\left(\frac{16\pi^2NV_0}{\mu}\right)^2\frac{1}{2\mu^2}\int_{-\frac{1}{2}k}^{\frac{1}{2}k}zdz\left(\frac{1}{\alpha^2+z^2}-\frac{1}{\beta^2+z^2}\right)^2 \times(z^2+\mu^2)(w-\tan^{-1}w), \qquad (A6)$$

where

$$w=\{2\mu/(\mu^2+z^2)\}\{(\tfrac{1}{2}k+\tfrac{1}{2}z)(\tfrac{1}{2}k-\tfrac{1}{2}z)\}^{\frac{1}{2}}. \qquad (A7)$$

The remaining integration can fortunately be performed by contour integration if we notice that w is real for $-\frac{1}{2}k\leq z\leq\frac{1}{2}k$ and imaginary for other values of z along the real axis. Therefore, $\tan^{-1}w$ will be real for $-\frac{1}{2}k\leq z\leq\frac{1}{2}k$; for other real values of z, since

$$\tan^{-1}i|w|=\frac{1}{2i}\ln\left(\frac{1-|w|}{1+|w|}\right),$$

$\tan^{-1}w$ will be imaginary as long as $|w|<1$. If we write

$$w=\{2i\mu/(\mu^2+z^2)\}\{z^2-(\tfrac{1}{2}z+\tfrac{1}{4}k)^2\}^{\frac{1}{2}},$$

we see that for $z<-\frac{1}{2}k$ and for $z>\frac{1}{2}k$ we may write

$$|w|\leq 2\mu z/(\mu^2+z^2)\leq 1.$$

We can therefore extend the integral along the entire real axis and take the real part in order to obtain the integral between the limits $-\frac{1}{2}k$ and $\frac{1}{2}k$. If we now close the contour in the upper half-plane, we find that we must avoid the four branch points $z=-\frac{1}{2}k$, $z=\frac{1}{2}k$, and $z=z_1$, $z=z_2$, the two branch points for which $w=\mp i$. The contour is shown in Fig. 7. The integrals from z_1 to ∞ and z_2 to ∞ can be readily evaluated, since $\tan^{-1}w$ changes by $\pm 2\pi i$ on going around the branch points z_1 and z_2. z_1 and z_2 are given by

$$z_1=\tfrac{1}{2}i\mu+\{\tfrac{1}{4}\mu^2+\tfrac{1}{2}i\mu k\}^{\frac{1}{2}},\ w=-i, \qquad (A8a)$$

$$z_2=-\tfrac{1}{2}i\mu+\{\tfrac{1}{4}\mu^2-\tfrac{1}{2}i\mu k\}^{\frac{1}{2}},\ w=+i, \qquad (A8b)$$

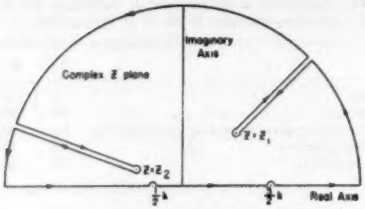

FIG. 7. Contour integration for I in the complex z plane.

where the "angle" of the square roots is taken between 0 and π. The only poles of the integrand inside the contour are at $z=i\alpha$ and $z=i\beta$, and residues must be taken at these points.

If we now evaluate the residues, subtract the integrals along the branch cuts, and take the real part we obtain

$$I=\left(\frac{16\pi^2NV_0}{\mu}\right)^2\frac{\pi^2}{\mu^3}\left[\frac{2\mu^3-\alpha^3-\beta^3}{\beta^3-\alpha^3}\mathrm{Im}\{W(i\alpha)-W(i\beta)\}\right.$$
$$+\frac{\mu^3-\alpha^3}{2\alpha}\mathrm{Re}\{W'(i\alpha)\}+\frac{\mu^3-\beta^3}{2\beta}\mathrm{Re}\{W'(i\beta)\}$$
$$+\frac{\mu^3-\alpha^3}{2}\mathrm{Re}\left\{\frac{1}{\alpha^3+z_1^3}-\frac{1}{\alpha^3+z_2^3}\right\}+\frac{\mu^3-\beta^3}{2}\mathrm{Re}\left\{\frac{1}{\beta^3+z_1^3}-\frac{1}{\beta^3+z_2^3}\right\}$$
$$\left.+\frac{2\mu^3-\alpha^3-\beta^3}{2(\beta^3-\alpha^3)}\ln\left|\frac{(\alpha^3+z_1^3)(\beta^3+z_2^3)}{(\alpha^3+z_2^3)(\beta^3+z_1^3)}\right|\right], \quad \text{(A9)}$$

where

$$W(z)=w-\tan^{-1}w; \quad W'(z)=\frac{w^3}{1+w^2}\frac{dw}{dz},$$

and w is given by (A7). Using the numerical values

$$\left.\begin{aligned}\mu^{-1}&=1.18\times10^{-13}\text{ cm}\\ \alpha^{-1}&=4.31\times10^{-13}\text{ cm}\\ \beta^{-1}&=0.616\times10^{-13}\text{ cm}\\ k^{-1}&=0.720\times10^{-13}\text{ cm}\end{aligned}\right\} \quad \text{(A10)}$$

which have previously been given, we obtain

$$I=\{(2\pi)^3/2\mu^3\}\{4\pi V_0/\mu\}^2(0.739). \quad \text{(A11)}$$

From (45) I_0 can be evaluated to give

$$I_0=\{(2\pi)^3/2\mu^3\}(4\pi V_0/\mu)^2(0.858). \quad \text{(A12)}$$

We therefore have

$$I=0.86I_0. \quad \text{(A13)}$$

The discussion of this result follows (45) in Sec. III.

APPENDIX B.

EVALUATION OF INTEGRALS II AND II_0

We shall first show that at high energy II given in (46) goes over into II_0 given in (47). In this limit we may replace the elliptical region in the r_1q plane by the strip $0\leq q\leq\frac{1}{2}k$ and $-\infty<r_1<\infty$ as before (Fig. 5). The upper limit on the r_2 integration can also be made infinite. Let us now express $\varphi(r_1)$ in terms of $\psi_0(r)$ by integrating (21) over angles

$$\varphi(r_1)=(4\pi/r_1)\int_0^\infty x dx\psi_0(x)\sin r_1x. \quad \text{(B1)}$$

The integral II then goes over into

$$II_0=32\pi^3\int_0^{\frac{1}{2}k}dqV^2(q)\int_{-\infty}^{\infty}dr_1\int_0^\infty xdx\psi_0(x)\sin r_1x$$
$$\times\int_{q-r_1}^{\infty}dr_2\int_0^\infty ydy\psi_0(y)\sin r_2y. \quad \text{(B2)}$$

If we interchange the order of integration for r_2 and y, we can perform the r_2 integration giving[30]

$$II_0=32\pi^3\int_0^{\frac{1}{2}k}dqV^2(q)\int_{-\infty}^{\infty}dr_1\int_0^\infty xdx\psi_0(x)\sin r_1x\int_0^\infty dy\psi_0(y)$$
$$\times[\cos qy\cos r_1y+\sin qy\sin r_1y]. \quad \text{(B3)}$$

Only that part of the integrand which is even in r_1 contributes, so that the cosine term vanishes. If we now perform the r_1 integration, we obtain a delta-function; in fact,

$$\int_{-\infty}^{\infty}\sin xr_1\sin yr_1dr_1=\pi\delta(x-y) \quad \begin{cases}x\geq0\\ y\geq0\end{cases}$$

so that II_0 becomes

$$II_0=(2\pi)^3\int_0^{\frac{1}{2}k}qdqV^2(q)\int_0^\infty\psi_0^2(x)4\pi(\sin qx/qx)x^2dx. \quad \text{(B4)}$$

This is clearly the same as

$$II_0=(2\pi)^3\int_0^{\frac{1}{2}k}qdqV^2(q)\int\psi_0^2(r)\exp(i\mathbf{q}\cdot\mathbf{r})d\mathbf{r} \quad \text{(B5)}$$

after performing the angular integration on $\mathbf{r}$ in (B5).

We can carry out the x integration in (B4) by using the expression (44) for $\psi_0(x)$. This gives

$$II_0=(2\pi)^24\pi N^2\int_0^{\frac{1}{2}k}dqV^2(q)\{\tan^{-1}[q/2\alpha]$$
$$+\tan^{-1}[q/2\beta]-2\tan^{-1}[q/(\alpha+\beta)]\}. \quad \text{(B6)}$$

This integral can be readily performed by numerical methods and gives

$$II_0=0.49I_0. \quad \text{(B7)}$$

In order to evaluate II in (38b) we shall change the variables of integration from k'' and Ω'' to $r_1=|\mathbf{k}''+\frac{1}{2}\mathbf{q}|$ and $r_2=|\mathbf{k}''-\frac{1}{2}\mathbf{q}|$.[31] The volume element becomes

$$k''^2dk''d\Omega''=2\pi r_1dr_1r_2dr_2/q.$$

We must now determine the limits on the r_1 and r_2 integrations to give as the region of integration the sphere of radius Q shown in Fig. 8. For a fixed value of r_1, the limits on r_2 will depend on whether Q is greater than or less than $\frac{1}{2}q$ and whether r_1 is greater or less than $|Q-\frac{1}{2}q|$. Specifically,

$$Q\geq\tfrac{1}{2}q\begin{cases}0\leq r_1\leq Q-\frac{1}{2}q, & |q-r_1|\leq r_2\leq q+r_1\\ Q-\frac{1}{2}q\leq r_1\leq Q+\frac{1}{2}q, & |q-r_1|\leq r_2\leq(3kq-r_1^2-q^2)^{\frac{1}{2}}\end{cases} \quad \text{(B8a), (B8b)}$$

$$Q\leq\tfrac{1}{2}q: \ \tfrac{1}{2}q-Q\leq r_1\leq\tfrac{1}{2}q+Q, \quad |q-r_1|\leq r_2\leq(3kq-r_1^2-q^2)^{\frac{1}{2}}. \quad \text{(B8c)}$$

Let us now consider the integral over the regions

$$Q\geq\tfrac{1}{2}q\begin{cases}\frac{1}{2}q-Q\leq r_1\leq0, & |q-r_1|\leq r_2\leq(3kq-r_1^2-q^2)^{\frac{1}{2}}\\ 0\leq r_1\leq Q-\frac{1}{2}q, & |q-r_1|\leq r_2\leq(3kq-r_1^2-q^2)^{\frac{1}{2}}\end{cases}. \quad \text{(B9)}$$

Since the integrands are odd functions of r_1 and r_2, if we change the sign of r_1 in the first of the two regions, we must then subtract the two regions of integration from one another. This means that the region

$$0\leq r_1\leq Q-\tfrac{1}{2}q, \quad q+r_1\leq r_2\leq(3kq-r_1^2-q^2)^{\frac{1}{2}}$$

must be subtracted from the region,

$$0\leq r_1\leq Q-\tfrac{1}{2}q, \quad |q-r_1|\leq r_2\leq(3kq-r_1^2-q^2)^{\frac{1}{2}},$$

leaving the region

$$Q\geq\tfrac{1}{2}q: \ 0\leq r_1\leq Q-\tfrac{1}{2}q, \quad |q-r_1|\leq r_2\leq q+r_1.$$

The region given in (B8a) is therefore equivalent to the regions in (B9). If these regions are now combined with the region in (B8b), we obtain the same region as in (B8c), so that the integral

$$II=\int_0^{\frac{1}{2}k}qdqV^2(q)\int_0^Q k''^2dk''\int d\Omega''\varphi(|\mathbf{k}''+\tfrac{1}{2}\mathbf{q}|)\varphi(|\mathbf{k}''-\tfrac{1}{2}\mathbf{q}|)$$

may finally be written as the single integral

$$II=2\pi\int_0^{\frac{1}{2}k}dqV^2(q)\int_{\frac{1}{2}q-Q}^{\frac{1}{2}q+Q}r_1dr_1\varphi(r_1)\int_{q-r_1}^{(3kq-r_1^2-q^2)^{\frac{1}{2}}}r_2dr_2\varphi(r_2).$$

[30] The upper limit gives no contribution since an exponential convergence factor must be used.

[31] r_1 and r_2 are directly related to spheroidal coordinates. See, for example, J. A. Stratton, *Electromagnetic Theory* (McGraw-Hill Book Company, Inc., New York, 1941), p. 56.

The absolute value sign has been dropped from $q-r_1$, since $r_2\varphi(r_2)$ is an odd function of r_2. If we now put in the expressions (A4) and (A5) for $\varphi(z)$ and $V(q)$, we obtain

$$II=(16\pi^2V_0N/\mu)^2 2\pi\{II_{\alpha\alpha}-II_{\alpha\beta}-II_{\beta\alpha}+II_{\beta\beta}\},$$

where

$$II_{\alpha\beta}=\int_0^{2k}\frac{dq}{(\mu^2+q^2)^2}\int_{\frac{1}{2}q-Q}^{\frac{1}{2}q+Q}\frac{r_1dr_1}{\alpha^2+r_1^2}\int_{q-r_1}^{(3kq-r_1^2-q^2)^{\frac{1}{2}}}\frac{r_2dr_2}{\beta^2+r_2^2}$$

and $II_{\alpha\alpha}$, $II_{\beta\alpha}$, and $II_{\beta\beta}$ are similarly defined. We can now perform the r_2 integration giving

$$II_{\alpha\beta}=\frac{1}{2}\int_0^{2k}\frac{dq}{(\mu^2+q^2)^2}\int_{\frac{1}{2}q-Q}^{\frac{1}{2}q+Q}\frac{r_1dr_1}{\alpha^2+r_1^2}$$
$$\times\{\ln(\beta^2+3qk-r_1^2-q^2)-\ln(\beta^2+(q-r_1)^2)\}.$$

Let us make the change of variable

$$x^2=3qk-r_1^2-q^2;\quad xdx=-r_1dr_1;\quad \alpha^2+r_1^2=\alpha^2+3qk-q^2-x^2$$

in the first term in the bracket. The limits on x become

$$x_{\min}^{\max}=\{3qk-q^2-(\tfrac{1}{2}q\pm Q)^2\}^{\frac{1}{2}}=\tfrac{1}{2}q\mp Q.$$

If we make the change of variable

$$x=q-r_1;\quad dx=-dr_1;\quad \alpha^2+r_1^2=\alpha^2+(q-x)^2$$

in the second term in the bracket, the limits on x also become

$$x_{\min}^{\max}=q-(\tfrac{1}{2}q\pm Q)=\tfrac{1}{2}q\mp Q.$$

The integral $II_{\alpha\beta}$ may therefore be written as

$$II_{\alpha\beta}=\frac{1}{2}\int_0^{2k}\frac{dq}{(\mu^2+q^2)^2}\int_{\frac{1}{2}q-Q}^{\frac{1}{2}q+Q}dx\ln(\beta^2+x^2)$$
$$\times\left\{\frac{x}{\alpha^2+3qk-q^2-x^2}-\frac{q-x}{\alpha^2+(q-x)^2}\right\}$$

with similar expressions for $II_{\alpha\alpha}$, $II_{\beta\alpha}$, and $II_{\beta\beta}$. If we now interchange the order of integration as we did for I, we can perform the q integration by partial fractions. The x integration remaining is quite complicated and can only be done numerically. The result of the numerical integration[22] is

$$II=0.81II_0;\quad II=0.46I.$$

APPENDIX C.

EVALUATION OF INTEGRALS *III*, *IV*, AND *V*

The integral

$$III=\int_0^{2k}qdqV(q)\int_0^Q k''^2dk''\int d\Omega''V(|\tfrac{1}{2}\mathbf{k}+\tfrac{1}{2}\mathbf{q}-\mathbf{k}''|)\varphi^2(|\mathbf{k}''+\tfrac{1}{2}\mathbf{q}|)$$

can be evaluated accurately but only after an extremely laborious numerical integration. We have previously mentioned that the value of this integral need not be calculated accurately, since it can be obtained indirectly from the two-particle cross sections. We shall therefore evaluate III approximately by assuming that the major contributions to the integral come near $|\mathbf{k}''+\tfrac{1}{2}\mathbf{q}|=0$. The integral then becomes

$$III\approx\int_0^{2k}qdqV(q)V(|\tfrac{1}{2}\mathbf{k}+\mathbf{q}|)\int_0^Q k''^2dk''\int d\Omega''\varphi^2(|\mathbf{k}''+\tfrac{1}{2}\mathbf{q}|).$$

The k'' integration is now the same as the one encountered in the evaluation of I in (38a). We shall therefore make use of our experience with I in Appendix A: the integral is 14 percent less than the $Q=\infty$ value (I_0), and the limit of $2k$ on q is changed to the more accurate value $\frac{3}{2}k$. We therefore have

$$III\approx(2\pi)^2(0.86)\int_0^{\frac{3}{2}k}qdqV(q)V(|\tfrac{1}{2}\mathbf{k}+\mathbf{q}|).$$

Near $\mathbf{k}''=-\frac{1}{2}\mathbf{q}$ we have

$$|\tfrac{1}{2}\mathbf{k}+\mathbf{q}|^2=(9/4)k^2+q^2+3\mathbf{k}\cdot\mathbf{q}=(9/4)k^2-\tfrac{1}{2}q^2-2k''^2\approx(9/4)k^2-q^2.$$

So that the integral becomes

$$III\approx(2\pi)^2(0.86)(4\pi V_0/\mu)^2\int_0^{\frac{3}{2}k}\frac{qdq}{(\mu^2+q^2)(\mu^2+9k^2/4-q^2)}$$
$$\approx(2\pi)^2(0.86)(4\pi V_0/\mu)^2(1/2\mu^2)$$
$$\times\{1+(9k^2/8\mu^2)\}^{-1}\ln\{1+(9k^2/4\mu^2)\}.$$

Using (43) and (A10) we therefore obtain

$$III\approx0.56I.$$

We have made a rough calculation of the error in III due to the approximations made and have found it to be quite large. This error cannot be easily calculated; but, as we have mentioned, and as we shall show, the value of III need not be known accurately. We shall include the rough estimate of the error and use the value $III\approx0.43I$.

The integral

$$IV=\int_0^{2k}qdqV(q)\int_0^Q k''^2dk''\int d\Omega''V(|\tfrac{1}{2}\mathbf{k}+\tfrac{1}{2}\mathbf{q}-\mathbf{k}''|)$$
$$\times\varphi(|\mathbf{k}''+\tfrac{1}{2}\mathbf{q}|)\varphi(|\mathbf{k}''-\tfrac{1}{2}\mathbf{q}|)$$

is quite difficult to evaluate, but can be done approximately with little difficulty. We shall again assume that the deuteron is large, so that the main contribution to the integral occurs near $|\mathbf{k}''+\tfrac{1}{2}\mathbf{q}|=0$ and $|\mathbf{k}''-\tfrac{1}{2}\mathbf{q}|=0$, that is, near $k''=0$, $q=0$. We shall therefore set $k''=q=0$ compared to $\frac{1}{2}k$ in the second V term. This then gives

$$IV\approx V(\tfrac{1}{2}k)\int_0^{2k}qdqV(q)\int_0^Q k''^2dk''\int d\Omega''$$
$$\times\varphi(|\mathbf{k}''+\tfrac{1}{2}\mathbf{q}|)\varphi(|\mathbf{k}''-\tfrac{1}{2}\mathbf{q}|).$$

The similarity between this integration and the one in (38b) for the interference term II, is now evident and we shall once again make use of our experience with II. The calculation of II in Appendix B gave the result that II is 19 percent less than the value calculated for $Q=\infty$ (II_0) and that the upper limit for the q integration changes to $\frac{1}{2}k$. We therefore have for IV

$$IV\approx(2\pi)^2(0.81)V(\tfrac{1}{2}k)\int_0^{1k}qdqV(q)\int\psi_0^2(r)\exp(iq\cdot r)dr$$
$$\approx(2\pi)^2(0.81)V(\tfrac{1}{2}k)4\pi N^2\int_0^{1k}dqV(q)$$
$$\times\{\tan^{-1}(q/2\alpha)+\tan^{-1}(q/2\beta)-2\tan^{-1}[q(\alpha+\beta)]\}$$

as in (B6). This integral can be readily performed by numerical methods and gives $IV\approx0.11I$.

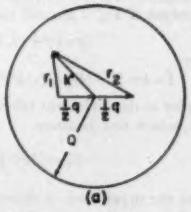

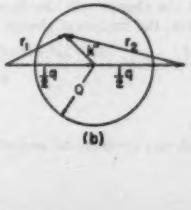

FIG. 8. Diagrams to determine limits on r_1 and r_2 after change of variables in Appendix B.

[22] All the calculations were originally performed with the incorrect value of $5\frac{1}{2}$ for β/α. The calculations for I, I_0, and II_0 were repeated for $\beta/\alpha=7$ and were found to give values that differed from the old by approximately 0 to 2 percent. Since the work involved in calculating II was quite complicated, the value of II for $\beta/\alpha=7$ was inferred from the way in which the others changed. The value given for II (and for III, IV, and V) should be good to within ±0.01 I.

The integral

$$V=\int_0^{2k} q\,dq\int_0^Q k''^2\,dk''\int d\Omega'' V(|\tfrac{1}{2}\mathbf{k}+\tfrac{1}{2}\mathbf{q}+\mathbf{k}''|) \times V(|\tfrac{1}{2}\mathbf{k}+\tfrac{1}{2}\mathbf{q}-\mathbf{k}''|)\varphi(|\mathbf{k}''+\tfrac{1}{2}\mathbf{q}|)\varphi(|\mathbf{k}''-\tfrac{1}{2}\mathbf{q}|)$$

can be treated in an analogous way and gives

$$V\approx(2\pi)^3(0.81)V^2(\tfrac{1}{2}k)4\pi N^2\int_0^{1k} dq\,\{\tan^{-1}[q/2\alpha] +\tan^{-1}[q/2\beta]-2\tan^{-1}[q/(\alpha+\beta)]\}.$$

The integral can be performed directly and gives

$$V\approx 0.03I.$$

We shall not try to estimate the errors made in the approximations used in evaluating IV and V.

We shall now demonstrate that our results do not depend critically on the numerical value of III. In order to do so, we shall repeat the calculations for Table III with the uncorrected value

$$III=0.56I.$$

The new numerical values given in Table V are quite close to those in Table III and show clearly that the exact value of the ratio III/I, is unimportant. As previously mentioned, this is because the total cross section was expressed as the sum of the three terms σ_{NP}, σ_{INTERF}, and σ_{NN}, and the experimentally observed value of σ_{NP} was used.

TABLE V. Table III recalculated with the uncorrected value of the integral $III=0.56I$ instead of the corrected value $III=0.43I$ used in Table IV.

δ	1	0	−1
N–N force	1	$\frac{1}{2}(1+P)$	P
$\xi=V_{NN}/V_{NP}{}^T$	0.46	0.79	0.83
σ_{NP}	72 mb	72 mb	72 mb
σ_{INTERF}	26 mb	15 mb	−16 mb
σ_{NN}	19 mb	30 mb	61 mb
σ_{TOT}	117 mb	117 mb	117 mb

APPENDIX D.

EFFECT OF INCLUDING THE BINDING ENERGY IN THE CONSERVATION OF ENERGY

If the binding energy had been included, the conservation of energy (7), would have been

$$k'^2+(4/3)k''^2=k^2-(4/3)(M\epsilon/\hbar^2).$$

The arguments given for replacing $\psi_{k''}(\mathbf{r})$ by a plane wave in the half-ellipse of Fig. 2 are still valid; but the ellipse is now given by

$$(q-k)^2+(4/3)k''^2=k^2(1-\delta)^2,$$

where

$$1-\delta=\{1-(4/3)M\epsilon/\hbar^2k^2\}^{\frac{1}{2}},\quad \delta\approx\tfrac{2}{3}M\epsilon/\hbar^2k^2=\tfrac{2}{3}(\alpha/k)^2.$$

In order to determine the effect of δ, we need only consider the I_0 term, which now becomes

$$I_0'=(2\pi)^3\int_{\delta k}^{(1-\delta)k} q\,dq\,V^2(q),$$

where the upper limit is determined by where the new ellipse in Fig. 5 crosses the q axis. Clearly, at the lower limit, the factor q in the integrand will make the change small; and at the upper limit the change will also be small because of the size of $V^2(\frac{1}{2}k)$. In fact, the fractional change can be given approximately as

$$\frac{I_0-I_0'}{I_0}=(0.86)\frac{(\delta k)^2/2\mu^4+(\delta k)(\frac{1}{2}k)/(\mu^2+9k^2/4)^2}{2\mu^2} =\frac{0.86\delta^2k^2}{\mu^2}+\frac{0.64\delta k^2\mu^2}{(\mu^2+9k^2/4)^2}\approx 0.002,$$

which can certainly be neglected.

APPENDIX E.

VALIDITY OF THE ASSUMPTION OF A PLANE WAVE FOR $\psi_{k''}(r)$ IN THE SHADED REGION OF FIG. 2

In the justification of the use of plane waves in the elliptical region in Fig. 2 it was assumed that $\psi_{k''}(\mathbf{r})$ could be replaced by a plane wave in the shaded region which occurs mostly for large k''. The most questionable region for this assumption is in the lower left corner of the shaded region where k'' *can* be small. The lower right corner will give a small contribution because of the factor $V^2(q)\approx V^2(2k)$.

In order to obtain a more accurate expression for $\psi_{k''}(\mathbf{r})$ in the region mentioned we shall use the first Born approximation in a deuteron potential, so that $\psi_{k''}(\mathbf{r})$ will be given by

$$\psi_{k''}(\mathbf{r})\approx L^{-\frac{1}{2}}\exp(i\mathbf{k}''\cdot\mathbf{r})+L^{-1}V_0 f(\mathbf{k}'',\mathbf{r}),\qquad (E1)$$

where $f(\mathbf{k}'',\mathbf{r})$ is a function depending on the details of the Born approximation and V_0 is either the triplet or singlet Yukawa well depth. We now wish to evaluate the integral in (18):

$$\int\psi_{k''}{}^*(\mathbf{r})\psi_0(r)\exp(\pm\tfrac{1}{2}i\mathbf{q}\cdot\mathbf{r})d\tau.\qquad (E2)$$

Since the region being considered contains only small values of q (much smaller than k'', since the boundary ellipse is given by $q\approx\frac{2}{3}k''^2/k$ near the origin), we shall set the exponential equal to unity. The remaining integral will be just the orthogonality integral and will necessarily vanish for a triplet wave function; that is,

$$\int\psi^*{}_{k''}{}^T(\mathbf{r})\psi_0(r)d\tau=0.\qquad (E3)$$

From (E1) we therefore must have

$$V_0{}^T\int f(\mathbf{k}'',\mathbf{r})\psi_0(r)d\tau\approx-\int\exp(-i\mathbf{k}''\cdot\mathbf{r})\psi_0(r)d\tau=-\varphi(k'').\qquad (E4)$$

In the case of a singlet potential we have

$$\int\psi^*{}_{k''}{}^S(\mathbf{r})\psi_0(r)d\tau\approx L^{-\frac{1}{2}}\varphi(k'')+L^{-1}V_0{}^S\int f(\mathbf{k}'',\mathbf{r})\psi_0(r)d\tau.\qquad (E5)$$

Using (E4), this becomes

$$\int\psi^*{}_{k''}(\mathbf{r})\psi_0(r)d\tau\approx L^{-\frac{1}{2}}\varphi(k'')(1-V_0{}^S/V_0{}^T).$$

We therefore reach the following conclusions.

(1) In the case of a triplet interaction we have subtracted too great an amount in the region near the origin. A calculation of the integral using a plane wave in this region shows that I should be increased by about 4 percent.

(2) In the case of the singlet interaction we have again subtracted too much in the region near the origin, but this time by an amount

$$4\text{ percent}\{1-(1-V_0{}^S/V_0{}^T)^2\},$$

since the integral (E2) appears squared in (18). Using the value of $V_0{}^S/V_0{}^T=0.686$, this becomes 3¼ percent, or approximately the same as in the triplet case.

This adjustment is also necessary in the other integrals, II–V, and will be approximately the same. For this reason the ratios (48), (49), (50), and (51) will *not* change appreciably and all the numerical results in Table III should be valid.

The use of a plane wave for the $\psi_{k''}(\mathbf{r})$ should be better at higher k''. The failure of the plane wave to be orthogonal to the ground state for the triplet case makes little difference, since the factor $\exp(\pm\frac{1}{2}i\mathbf{q}\cdot\mathbf{r})$ is now a rapidly oscillating function. The reason is that the most important values of q are large because of the factor $V(q)$.

We have investigated the validity of using the plane wave in the entire shaded region in some detail and found that the correction is quite appreciable—in fact, it is about one-half of the 14 percent discrepancy between the values of I and I_0. However, this correction must also be applied to the integrals II–V. As mentioned before, this will leave the ratios (48), (49), (50), and

(51) only slightly changed and will not appreciably affect the numerical results in Table III.

APPENDIX F.

EXAMPLE OF EVALUATION OF COEFFICIENTS a_l IN TABLE I

As an example of the manner in which the a_l's in (28) and in Table I are obtained, we shall evaluate the doublet χ_3 coefficients in (28). This means that both the initial and final spin states will be χ_3. If we then insert (26) into (25), we obtain for the matrix element

$$\mathfrak{M}=(\Psi_f\chi_3,\ \{1-P_{13}Q_{13}\}V_{NN}(r_{13})\{w_n+m_nP_{13}\}\Psi_i\chi_3)$$
$$+(\Psi_f\chi_3,\ \{1-P_{13}Q_{13}\}V_{NP}(r_{23})$$
$$\times\{w_p+m_pP_{23}+b_pQ_{23}+h_pP_{23}Q_{23}\}\Psi_i\chi_3). \quad \text{(F1)}$$

From (30) we find that

$$(\chi_3,\chi_3)=1, \qquad (\chi_3,Q_{13}\chi_3)=-\tfrac{1}{2},$$
$$(\chi_3,Q_{23}\chi_3)=-\tfrac{1}{2}, \quad (\chi_3,Q_{13}Q_{23}\chi_3)=-\tfrac{1}{2},$$

so that (F1) becomes

$$\mathfrak{M}=(\Psi_f,\ \{(w_n+\tfrac{1}{2}m_n)+(\tfrac{1}{2}w_n+m_n)P_{13}\}V_{NN}(r_{13})\Psi_i)$$
$$+(\Psi_f,\ \{(w_p-\tfrac{1}{2}b_p)+(m_p-\tfrac{1}{2}h_p)P_{23}+(\tfrac{1}{2}w_p+\tfrac{1}{2}b_p)P_{13}$$
$$+(\tfrac{1}{2}m_p+\tfrac{1}{2}h_p)P_{13}P_{23}\}V_{NP}(r_{23})\Psi_i). \quad \text{(F2)}$$

If we now use (29) and the initial state

$$\Psi_i=L^{-\frac{1}{2}}\exp(-i\mathbf{k}\cdot\mathbf{x})\psi_0(r).$$

(F2) goes directly into (28) with the a_l's as given in the doublet χ_3 row of Table I.

APPENDIX G.

A MORE ACCURATE CALCULATION OF J_1 AND J_2 IN EQ. (73)

We were faced with the evaluation of

$$J_1=\int d\Omega^{\nu i}\left|\int d\tau\psi_{k^{\nu i}}^{(-)*}(\mathbf{r})\psi_0(r)\exp(\tfrac{1}{2}i\mathbf{q}''\cdot\mathbf{r})\right|^2 \quad \text{(G1a)}$$

and

$$J_2=\int d\Omega^{\nu i}R_0\Big\{\int d\tau\psi_{k^{\nu i}}^{(-)*}(\mathbf{r})\psi_0(r)\exp(\tfrac{1}{2}i\mathbf{q}''\cdot\mathbf{r})$$
$$\times\int d\tau\psi_{k^{\nu i}}^{(-)*}(\mathbf{r})\psi_0(r)\exp(\tfrac{1}{2}i\mathbf{q}''\cdot\mathbf{r})\Big\} \quad \text{(G1b)}$$

for both the triplet and singlet $\psi_{k^{\nu i}}(\mathbf{r})$. Since we are interested in these integrals only for small values of $k^{\nu i}$, we must find an approximate expression for $\psi_{k^{\nu i}}(\mathbf{r})$ at low energies. We shall therefore expand $\psi_{k^{\nu i}}(\mathbf{r})$ into spherical harmonics with the intention of using only the lowest order terms. We shall set

$$\psi_{k^{\nu i}}(\mathbf{r})=\Sigma_l A_l(k^{\nu i}r)Y_{l0}(\mathbf{k}^{\nu i},\mathbf{r}), \quad \text{(G2)}$$

where the $Y_l^0(\mathbf{k}^{\nu i},\mathbf{r})$ are spherical harmonics in terms of the angle of $\mathbf{k}^{\nu i}$ with respect to the polar axis in the direction $\mathbf{r}$, and the $A_l(k^{\nu i}r)$ are the corresponding coefficient in the expansion. If we also expand the exponential

$$\exp(\tfrac{1}{2}i\mathbf{q}''\cdot\mathbf{r})=\Sigma_{l''}B_{l''0}(\tfrac{1}{2}q''r)Y_{l''}^0(\mathbf{r},\mathbf{q}'') \quad \text{(G3)}$$

and use the addition theorem

$$Y_l^0(\mathbf{k}^{\nu i},\mathbf{r})=[4\pi/(2l+1)]^{\frac{1}{2}}\Sigma_m\ Y_{l^m}^*(\mathbf{k}^{\nu i},\mathbf{q}'')Y_l^m(\mathbf{r},\mathbf{q}''), \quad \text{(G4)}$$

the integral J_1 in (G1a) becomes

$$J_1=\int d\Omega^{\nu i}\int d\mathbf{r}\int d\mathbf{r}'\sum_{l''l'l'''}{}'\left\{\frac{(4\pi)^2}{(2l+1)(2l'+1)}\right\}^{\frac{1}{2}}A_l^*(k^{\nu i}r)$$
$$\times A_{l'}(k^{\nu i}r')Y_{l^m}^*(\mathbf{k}^{\nu i},\mathbf{q}'')Y_l^m(\mathbf{r},\mathbf{q}'')Y_{l'}^{m'}(\mathbf{k}^{\nu i},\mathbf{q}'')$$
$$\times Y_{l'}^{m'}(\mathbf{q}'',\mathbf{r}')B_{l''0}^*(\tfrac{1}{2}q''r)B_{l'''0}(\tfrac{1}{2}q''r')$$
$$\times Y_{l'''}^{*0}(\mathbf{r},\mathbf{q}'')Y_{l'''}^0(\mathbf{r}',\mathbf{q}''). \quad \text{(G5)}$$

Since

$$\int d\Omega_{\mathbf{a}}Y_{l^m}^*(\mathbf{x},\mathbf{a})Y_{l'}^{m'}(\mathbf{x},\mathbf{a})=\delta_{mm'}\delta_{ll'},$$

the integral reduces to

$$\Sigma_l\left|\int A_l(k^{\nu i}r)B_l(\tfrac{1}{2}q''r)\psi_0(r)r^2dr\right|^2\{4\pi/(2l+1)\}. \quad \text{(G6)}$$

From this result we see that the various angular momentum states in the sum (G2) do not interfere with one another in the cross section. We can therefore evaluate the cross section for different l's and add the individual results. The same will be true for the second integral J_2 in (G1b).

The integral for $l=0$ at low energy can be treated quite satisfactorily by the effective range method, but for higher l's we shall use the corresponding components of the plane wave approximation. The result is that the integrals J_1 and J_2 can be written as

$$J=J_{l=0}+J_{PW}-J_{PW\ l=0},$$

where $J_{l=0}$ is the $l=0$ term evaluated by the effective range method, J_{PW} is the integral evaluated using a plane wave for $\psi_{k^{\nu i}}(\mathbf{r})$, and $J_{PW\ l=0}$ is just the $l=0$ term of the plane wave approximation.

Artificial Chains Collateral to the Heavy Radioactive Families*

W. W. MEINKE,† A. GHIORSO, AND G. T. SEABORG
Radiation Laboratory and Department of Chemistry, University of California, Berkeley, California

(Received November 7, 1950)

A number of heavy alpha-particle emitting nuclides, members of decay chains which are "collateral" to the heavy radioactive series, have been observed and their radioactive properties characterized. Some of these undergo branching decay by orbital electron capture. The parent isotopes are produced in bombardments of thorium with high energy deuterons or helium ions in the 184-inch cyclotron. Chemical identification has been made in all cases where needed, and the alpha-particle energies have been measured through the use of an alpha-pulse analyzer apparatus. The following are the collateral series which have been studied: $Pa^{226} \rightarrow Ac^{222} \rightarrow Fr^{218} \rightarrow At^{214}$ ($4n+2$ mass type); $Pa^{227} \rightarrow Ac^{223} \rightarrow Fr^{219} \rightarrow At^{215}$ ($4n+3$); $Pa^{228} \rightarrow Ac^{224} \rightarrow Fr^{220} \rightarrow At^{216}$ ($4n$); $U^{228} \rightarrow Th^{224} \rightarrow Ra^{220} \rightarrow Em^{216}$ ($4n$); $U^{229} \rightarrow Th^{225} \rightarrow Ra^{221} \rightarrow Em^{217}$ ($4n+1$).

I. INTRODUCTION

THE high energy particles produced in the 184-inch cyclotron make it possible to prepare and study the radioactive properties of many new nuclides with mass numbers on the neutron deficient side of beta-stability. The neutron deficient isotopes of the heaviest elements are unstable toward decay by alpha-particle emission as well as decay by orbital electron capture. Since one of the areas of interest in this laboratory is the study of the radioactive properties of the isotopes of the heaviest elements, and in particular the systematics of the alpha-decay properties, the preparation and characterization of such nuclides has been undertaken.

The present paper describes in some detail the experimental work connected with the identification and measurement of the radioactive properties of 18 new alpha-particle emitting nuclear species. These are distributed among five decay chains which can be referred to as "collateral" to the four heavy radioactive series. The five collateral chains include representatives of each of the four mass number types and hence include series collateral to each of the natural radioactive families, the uranium ($4n+2$), thorium ($4n$), and actinium ($4n+3$) families, and the synthetic neptunium ($4n+1$) family.[1–4]

The data concerning these collateral chains were published previously in summary form[5–7] with very little discussion of the experimental evidence. The present publication presents a documentation of the experimental evidence, including a number of curves which are important in this connection. It should be stated that the data reported here were taken during 1948–1949. Consequently, the energy determinations for the alpha-particles were made with instruments of poorer resolution than those available at the present time. Thus, the energies are less accurate than it would be possible to attain if the entire research were repeated; but this is not contemplated in the present program of the laboratory.

II. PROCEDURE

For the most part in these bombardments, target setups were used which would give a maximum yield of the reaction product for the target material used. Thorium metal foil was bombarded as an internal probe target in the 184-inch cyclotron to produce the four longer-lived series. The time required to dissolve the thorium metal is too long for work with half-lives of the order of two minutes, however, and in these cases thorium nitrate was used as the target material. To further reduce the time between bombardment and counting, use was made of the "jiffy" probe in the 184-inch cyclotron. With it targets were bombarded through the window of a probe tube inserted into the tank of the cyclotron and at the end of bombardment were blown quickly out of the tube by means of compressed air.

After bombardment, the thorium was dissolved in concentrated nitric acid with a small amount of ammonium fluosilicate added to catalyze the reaction, the solution made 6*N* in acid, and a protactinium or uranium fraction separated by one of several chemical procedures,[8] depending on the half-life of the desired isotope and the purification required. The protactinium or uranium parent controls the decay of the other members of the chain which quickly grow into equilibrium with it after the chemical isolation. The alpha-particle decay of these fractions after chemical separation was measured by the use of both standard alpha-particle counting devices and a 48-channel alpha-particle pulse analyzer[9]

* This work was carried out under the auspices of the AEC.

† Present address: Department of Chemistry, University of Michigan, Ann Arbor, Michigan.

[1] English, Cranshaw, Demers, Harvey, Hincks, Jelley, and May, Phys. Rev. **72**, 253 (1947).

[2] Hagemann, Katzin, Studier, Ghiorso, and Seaborg, Phys. Rev. **72**, 252 (1947).

[3] Hagemann, Katzin, Studier, Seaborg, and Ghiorso, Phys. Rev. **79**, 435 (1950).

[4] For summary on neptunium family, see, e.g., G. T. Seaborg, National Nuclear Energy Series, Plutonium Project Record, Vol. 14B, *The Transuranium Elements: Research Papers*, Paper No. 22.3 (McGraw-Hill Book Company, Inc., New York, 1949); Chem. Eng. News **26**, 1902 (1948).

[5] Ghiorso, Meinke, and Seaborg, Phys. Rev. **74**, 695 (1948).

[6] Meinke, Ghiorso, and Seaborg, Phys. Rev. **75**, 314 (1949).

[7] G. T. Seaborg and I. Perlman, Revs. Modern Phys. **20**, 585 (1948).

[8] W. W. Meinke, U. S. Atomic Energy Commission Declassified Documents AECD-2738 and AECD-2750 (August, 1949).

[9] Ghiorso, Jaffey, Robinson, and Weissbourd, National Nuclear Energy Series, Plutonium Project Record, Vol. 14B, *The Transuranium Elements: Research Papers*, Paper No. 16.8 (McGraw-Hill Book Company, Inc., New York, 1949).

equipped with a fast sample-changing mechanism. Through the use of the latter, alpha-particle energies associated with the new collateral alpha-decay chains have been measured.

The collateral chains have been characterized by physical or chemical separation and identification of radioactive end-products of decay which are common both to the chain and to one of the four alpha-radioactive families. When the half-life was too short to allow chemical operations to be performed on a sample, it was possible to separate daughters from their alpha-parents by recoil methods[10] (see Appendix). Many chemical separations have also been made to establish the mass assignments of the series. Such separations[8] have been made for thorium, protactinium, actinium, bismuth, and lead to separate orbital electron capture, beta-, or alpha-decay daughters from the members of the series. In some cases where it has not been possible to perform these separations, assignment has been based on regularities in alpha-decay systematics.[11–13] In many cases where their half-lives and abundances have permitted, individual members of the chains have been studied.

In the next section each series will be discussed individually. The interrelation of each of the series can probably best be seen by reference to a nuclide chart of the heavy region such as is given in Fig. 1. The half-life values given are the most recent available.

III. RESULTS

As stated above, the data for these collateral chains have been previously presented in a preliminary form.[5–7] The experimental results, however, have been reworked completely since the previous reports were made and some additional experimental work has been included. Presented in Table I are the latest half-life and particle energy values (not total disintegration energies) for the five collateral series. Half-life and energy values in parenthesis have been estimated from alpha-decay systematics curves.[11–13] The values presented in this table supersede the values published previously. The radioactive properties of RaE, Po^{210}, AcC, AcC″, ThC, ThC″, ThC′, Po^{213}, and Pb^{209} are the accepted values taken from the literature.[7]

For easy reference, the values for each chain have been combined in Table I. The following discussion treats each chain separately.

A. The Pa^{226} Series

The protactinium fraction from a 150-Mev deuteron bombardment of thorium nitrate in the jiffy probe of the 184-inch cyclotron shows a series of four alpha-particle emitters immediately after bombardment. These activities decay with the 1.8-min half-life of the protactinium parent and appear to be members of a collateral branch of the uranium $(4n+2)$ family as shown by dotted lines in the block diagram of Fig. 2.

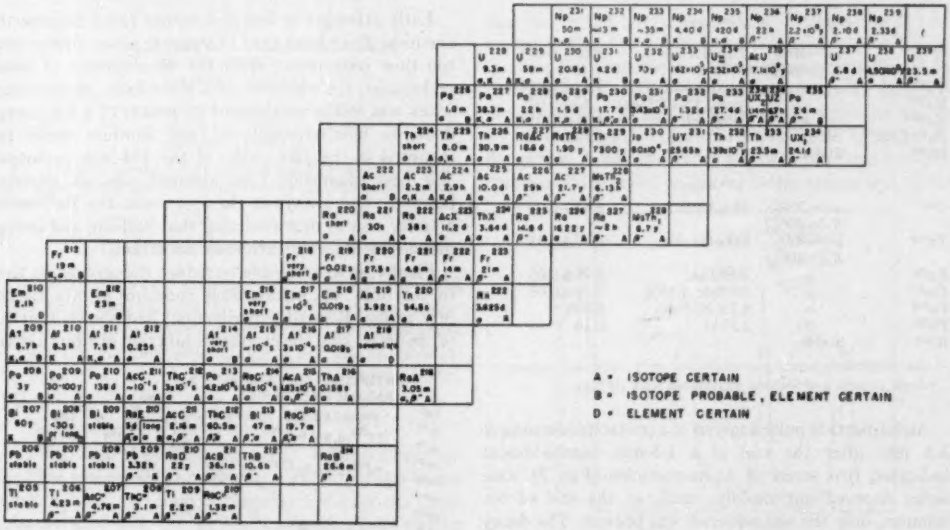

FIG. 1. Nuclide chart for a portion of the heavy region.

[10] Rutherford, Chadwick, and Ellis, *Radiations from Radioactive Substances* (Cambridge University Press, London, 1930), third edition, p. 557.
[11] Perlman, Ghiorso, and Seaborg, Phys. Rev. 74, 1730 (1948).
[12] Perlman, Ghiorso, and Seaborg, Phys. Rev. 75, 1096 (1949).
[13] Perlman, Ghiorso, and Seaborg, Phys. Rev. 77, 26 (1950), and unpublished revisions bringing curves up to date.

TABLE I. Collateral series data.

Nuclide	Type of radiation	Half-life	Energy of radiation (Mev)
		Pa^{226} series	
Pa^{226}	α	1.8±0.2 min	6.81±0.05
Ac^{222}	α	(pred. 30 sec)	6.96±0.05
Fr^{218}	α	(pred. 5×10^{-3} sec)	7.85±0.05
At^{214}	α	(pred. 2×10^{-6} sec)	8.78±0.05
Bi^{210} (RaE)	β^-	5.0 days	1.17
Po^{210}	α	138 days	5.298
Pb^{206}	Stable		
		Pa^{227} series	
Pa^{227}	α (~85%) K (~15%)	38.3±0.3 min	6.46±0.02
Ac^{223}	α (99%) K (1%)	2.2±0.1 min	6.64±0.02
Fr^{219}	α	0.02±0.002 sec	7.30±0.02
At^{215}	α	10^{-4} sec, ±20%	8.00±0.02
Bi^{211} (AcC)	α (99.7%)	2.16 min	6.619
Tl^{207} (AcC″)	β^-	4.76 min	1.47
Pb^{207}	Stable		
		Pa^{231} series	
Pa^{228}	α (~2%) K (~98%)	22±1 hr	6.09±0.02 (75%) 5.85±0.02 (25%)
Ac^{224}	α (~10%) K (~90%)	2.9±0.2 hr	6.17±0.03
Fr^{220}	α	27.5±1.5 sec	6.69±0.03
At^{216}	α	3×10^{-4} sec ±10%	7.79±0.03
Bi^{212} (ThC)	α (34%)	60.5 min	6.081 (27%) 6.042 (70%)
	β^- (66%)		2.20
Tl^{208} (ThC″)	β^-	3.1 min	1.72
Po^{212} (ThC′)	α	3×10^{-7} sec	8.776
Pb^{208}	Stable		
		U^{238} series	
U^{238}	α (~80% K (~20%)	9.3±0.5 min	6.67±0.01*
Th^{234}	α	(pred. 1 sec)	7.13±0.02*
Ra^{230}	α	(pred. 3×10^{-3} sec)	7.43±0.02*
Em^{218}	α	(pred. 10^{-4} sec)	8.01±0.03*
Po^{218} (ThC′)	α	3×10^{-7} sec	8.776
Pb^{206}	Stable		
		U^{235} series	
U^{235}	α (~20%) K (~80%)	58±3 min	6.42±0.02
Th^{231}	α (~90%) K (~10%)	8.0±0.5 min	6.57±0.03
Ra^{223}	α	30±2 sec	6.71±0.03
Em^{219}	α	10^{-3} sec ±10%	7.74±0.03
Po^{215}	α	4.2×10^{-6} sec	8.336
Pb^{209}	β^-	3.32 hr	0.70
Bi^{209}	Stable		

* Orth, Ghiorso, and Seaborg, unpublished work (1950).

Alpha-particle pulse analysis of a protactinium sample 3.3 min after the end of a 1.5-min bombardment indicated two series of alpha-particles (Fig. 3). One series decayed out rapidly, until, at the end of ten minutes, only the second series was present. The decay is shown in Fig. 4 by pulse analysis curves taken during the 10-min period. If the contribution of the 38.3-minute Pa^{227} series (to be discussed in the next section) is subtracted from Fig. 3, the alpha-peaks of the Pa^{226} series remain as in Fig. 5.

The mass type for the parent of the series has not yet been identified through known daughters in the main branch of the radioactive family. The requirements for yield, speed, and purity of samples from the chemical procedure are so stringent that with the present cyclotron beams and bombardment techniques, the task of separating enough 5-day Bi^{210} (RaE) from the decay of this series or of separating Th^{226} from the electron capture branching decay of the parent is almost prohibitively difficult. Furthermore, it has not been possible to date to assign absolutely any alpha-peak to a particular isotope of the series. When the method of formation and half-life of the protactinium parent and the energies of the four members of the series are considered in the light of known alpha-decay systematics, however, it becomes fairly certain that the assignment of isotopes to energies shown in Fig. 5 are valid. On this basis the series decays as follows:

$$Pa^{226} \xrightarrow[1.8\ \text{min}]{\alpha} Ac^{222} \xrightarrow[(\text{predicted } 30\ \text{sec})]{\alpha}$$

$$Fr^{218} \xrightarrow[(\text{pred. } 5\times10^{-3}\ \text{sec})]{\alpha} At^{214} \xrightarrow[(\text{pred. } 2\times10^{-6}\ \text{sec})]{\alpha}$$

$$Bi^{210}\ (\text{RaE}) \xrightarrow[5\ \text{days}]{\beta^-} Po^{210} \xrightarrow[138\ \text{days}]{\alpha} Pb^{206}\ (\text{stable}).$$

1. Pa^{226}

Early attempts to find this isotope failed because the chemical procedures used to separate protactinium were too time consuming. With the development of faster techniques, the existence of a short-lived protactinium series was finally established by means of a full energy deuteron bombardment of 1-mil thorium metal foil mounted in the jiffy probe of the 184-inch cyclotron. The best separation time attained was six minutes, however; and always at the first count the Pa^{227} series activity was so overwhelming that half-life and energy measurements were extremely uncertain.

Finally, it was possible to reduce the separation time to 3.3 min by bombarding thorium nitrate in the jiffy probe. Related experiments[14] had shown that for (d, xn) reactions, the excitation function exhibits a sharp

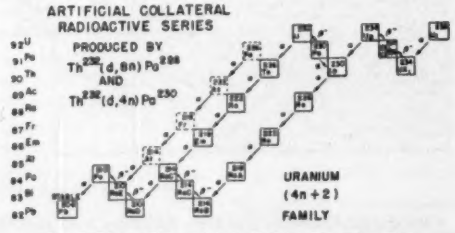

FIG. 2. Block diagram of the Pa^{226} collateral series.

[14] Meinke, Wick, and Seaborg, University of California Radiation Laboratory Report UCRL-868 (September, 1950).

peak which makes the optimum yield of the product isotope very dependent upon the bombarding energy. This allows differentiation between neighboring isotopes in (d, xn) reactions. Bombardments with 150-Mev deuterons resulted in sufficient activity to give satisfactory pulse analyses, one of which is shown in Fig. 3. By following the decay of the longest range alpha-peak (assumed to be At^{214} from systematics), a half-life of 1.8 ± 0.2 min for the Pa^{226} was obtained.

In the further alpha-pulse analysis of the activity remaining after the decay of the Pa^{226} series, it was not possible to detect in the presence of the remaining Pa^{227} series any alpha-peaks due to 30-min Th^{226} and daughters arising from electron capture branching decay of Pa^{226}. Consequently, it is possible to set an upper limit of about one for the K/α branching ratio of Pa^{226}.

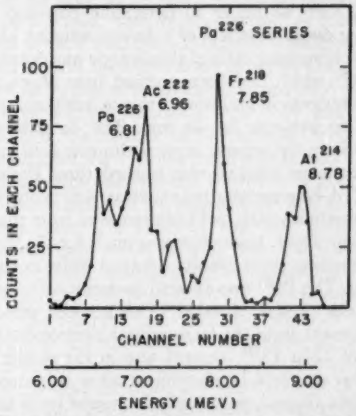

FIG. 3. Alpha-pulse analysis curve of the Pa^{226} series with some Pa^{227} series contamination. The collimated sample was counted for 0.5 min.

2. *Other Members of the Pa^{226} Series*

To date it has not been possible to obtain any data other than the half-life of the Pa^{226} and the alpha-energies of the members of the series. The assignments of mass numbers to these daughter isotopes is made on the basis of alpha-energy *vs* mass number systematics.

B. The Pa^{227} Series

Shortly after 80-Mev deuteron bombardment of thorium, a number of alpha-groups are prominent in the pulse analysis of a protactinium chemical fraction. These groups decay with the 38.3-min half-life of the parent and dominate pulse analyses of protactinium fractions for from five to six hours after the end of bombardment before other alpha-groups make their appearance.

The groups have been definitely assigned to the Pa^{227} series, a collateral branch of the actinium $(4n+3)$ family as shown in the block diagram of Fig. 6. The alpha-pulse

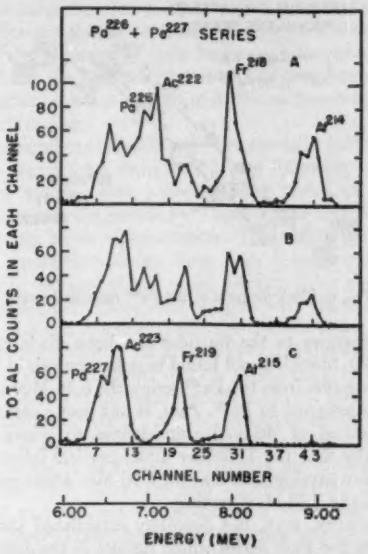

FIG. 4. Alpha-pulse analysis curves showing the decay of the Pa^{226} series, leaving the Pa^{227} series. The curves represent 0.5-min counts of the collimated sample started at the following times after the end of bombardment: A, 3.3 min; B, 6.0 min; C, 10.5 min.

analysis of the five alpha-groups in this series is presented in Fig. 7.

The mass assignment of the series was established by chemically separating electron capture decay products of the first and second members of the series, as well as by the identification of the Bi^{211} (AcC) and Tl^{207} (AcC″) daughters. A half-life value has been obtained for each member of the series and in addition, assignment of the

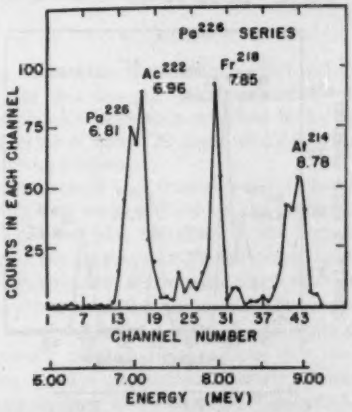

FIG. 5. Resolved alpha-pulse analysis curve of the Pa^{226} series from which the Pa^{227} series peaks shown in Fig. 3 have been subtracted.

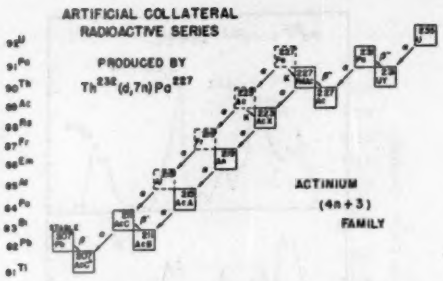

FIG. 6. Block diagram of the Pa^{227} collateral series.

alpha-energies to the nuclides has been made experimentally. Since it is not found in pulse analysis of single recoil samples from the Pa^{227} series, the 6.46-Mev alpha-peak is assigned to Pa^{227}. Also, it has been possible by the method of delayed coincidences to prove electronically that the 7.30-Mev alpha-particle follows the 6.64-Mev particle, and that the 8.00-Mev alpha-particle follows the 7.30-Mev particle.

This work, then, has definitely established that the series is the Pa^{227} series which decays in the following manner:

$$Pa^{227} \xrightarrow[38.3\ \text{min}]{\alpha} Ac^{223} \xrightarrow[2.2\ \text{min}]{\alpha} Fr^{219} \xrightarrow[0.02\ \text{sec}]{\alpha} At^{215} \xrightarrow[10^{-4}\ \text{sec}]{\alpha}$$

$$Bi^{211}\ (AcC) \xrightarrow[2.16\ \text{min}]{\alpha}$$

$$Tl^{207}\ (AcC'') \xrightarrow[4.76\ \text{min}]{\beta^-} Pb^{207}\ (\text{stable}).$$

The branches which arise from orbital electron capture by Pa^{227} and Ac^{223} are not shown.

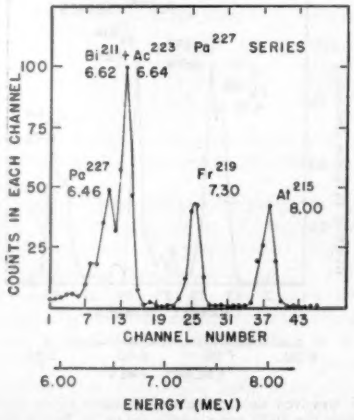

FIG. 7. Alpha-pulse analysis curve of the Pa^{227} series.

1. Pa^{227}

Since it is possible to obtain this isotope in very high yield and since it is the only protactinium isotope in evidence for a period of five or six hours after bombardment, it has been possible to do many experiments with this isotope. The half-life was determined to be 38.3±0.3 min by following the decay of the gross alpha-counts of the series of alpha-emitters. As the main protactinium fraction decayed, aliquot fractions were taken and chemically purified from the daughter radioactivities of 22-hr Pa^{223} also present in the sample (see below); a number of decay points of the Pa^{227} (plus equilibrium daughter products) alpha-activity were taken on each purified aliquot before sufficient daughter activity from the Pa^{223} present made it necessary to purify another aliquot.

By chemically separating a sample of thorium (including Th^{230} as tracer to determine chemical yield) from the decay products of a known amount of Pa^{227}, the K/α branching ratio of this isotope was determined. The Pa^{227} which had been purified from thorium was allowed to decay in a solution of thenoyltrifluoroacetone[15] (TTA) in benzene for 40 min. The daughters were washed from the organic layer with nitric acid and this acidic aqueous solution was washed three times with fresh TTA-benzene solution to extract any protactinium contamination which had been removed from the original organic layer. Correction was made for the time this contaminating protactinium decayed while in the acid solution. The Pa^{227} was allowed to decay only one half-life in the organic solution to reduce the amount of Th^{223} present from the large orbital electron branching decay of 22-hr Pa^{223} (present also in the sample). For a 60-Mev deuteron bombardment when this amount of decay was allowed, pulse analysis showed twice as much Th^{227} as Th^{223} present in the separated daughters. The yield of the 18.6-day Th^{227} in the separated sample indicated a K/α ratio of 0.18±0.02 for Pa^{227}.

Further evidence that the Th^{227} came from the 38.3-min protactinium isotope was obtained when successive separation of thorium from the protactinium sample indicated that the parent of the Th^{227} was decaying with a half-life of about 35 min. The slight discrepancy in half-lives is due to a small loss of parent in the chemical separations.

A double (or second-order) recoil experiment was performed to produce a sample of the well-known nuclide, Bi^{211}, which could be pulse-analyzed free from its parent activities. This was done by first collecting Ac^{223} and daughter atoms by alpha-recoil from Pa^{227} and then Bi^{211} atoms by alpha-recoil from this first recoil sample (the francium and astatine intermediates, of course, do not interfere because of their short half-lives). It was thus possible to observe the Bi^{211} 6.62-Mev alpha-

[15] J. C. Reid and M. Calvin, U. S. Atomic Energy Commission Declassified Document MDDC-1405 (August 13, 1947); also, J. Am. Chem. Soc. 72, 2948 (1950).

particle energy and 2.16-min decay. Furthermore, it was possible by a triple (or third-order) recoil experiment utilizing a very large sample of Pa^{227} to collect enough of the Tl^{207} daughter to follow its 4.76-min decay, and even to make rough aluminum absorption measurements to check its energy. Hence, the assignment of this series to Pa^{227} is established beyond doubt.

Absolute cross sections or relative yields for this isotope have been determined for several methods of production: the $Th^{232}(p, 6n)Pa^{227}$, $Th^{232}(d, 7n)Pa^{227}$, $Th^{232}(\alpha, p8n)Pa^{227}$, and $U^{238}(p, \alpha 8n)Pa^{227}$ reactions.[14] The excitation functions for these reactions have been studied with full energy particles from the 184-inch cyclotron and are reported in detail in another paper.[14]

2. Ac^{223}

Recoil atoms collected from samples containing the Pa^{227} series decayed by alpha-emission with a half-life of about 2.5 min. This value, however, is a composite one due to Ac^{223} and the 2.16-min Bi^{211} daughter. Since the half-lives of these two isotopes are so similar, it was impossible by this method to resolve one from the other.

Another method of attack was more successful in determining the half-life of this isotope. From a plate containing the Pa^{227} series, recoil atoms were collected for ten minutes, long enough to ensure equilibrium between the activity on the sample plate and that on the collector plate. The collector was then removed and successive 1-min recoil samples collected from it over a period of about ten minutes. The decay of the Bi^{211}, the only alpha-activity present on the second-order recoil plates, was followed for about two minutes for each sample. All the counting of successive second-order recoil samples was done on the same alpha-counter and the counts were recorded automatically on tape. The best 2.16-min lines were used to extrapolate the decay rates of each of the second-order recoil plates containing Bi^{211} back to the times of separation from the Ac^{223} parent. These extrapolated values were plotted as ordinates against the time in minutes after removal of the first recoil collecting plate from its Pa^{227} parent. The half-life of Ac^{223} as determined by this method is 2.2 ± 0.1 min. The only assumption made was that the efficiency of recoil was constant during the ten minutes of the experiment. This assumption appears reasonable since the geometry and electric collection field remained the same.

Data on the branching ratio of this isotope were also obtained from recoil experiments. A very large sample of Pa^{227} and daughters (probably about 10^9 or more alpha-counts per minute) was used as the parent for a 10-min collection of recoil fragments. This sample of recoil fragments was allowed to decay for about 15 days and was finally subjected to alpha pulse analysis to determine the amount of Ra^{223} present. The alpha-pulse analysis was somewhat complicated, since the sample also contained Ra^{224} and Ac^{225} as alpha-recoil daughters of Pa^{228} (via Th^{228} and Ac^{224}) and Pa^{229}, respectively.

The activities due to Ra^{224} and Ac^{225} (whose alpha-energies are similar to that of Ra^{223}) were determined from the intensity of their long range daughters, Po^{212} and Po^{213}; the Ra^{223} activity which had been formed from the orbital electron capture of Ac^{223} was then determined by subtraction.

The number of recoiling Ac^{223} atoms collected from the Pa^{227} sample was estimated in the following manner. Recoil samples were collected for a period of several seconds from the parent Pa^{227} sample and then followed for decay in an alpha-counter. The plotted Ac^{223} and Bi^{211} equilibrium decay lines were then extrapolated back to the end of the recoil growth times and these values plotted. Three such samples were taken and the best 38.3-min line drawn through them; a point on this line at the middle of the growth period of the large recoil sample gave an indication of the amount of activity that was recoiling to the collection plate at that time. It was then assumed that 1/7 of this gross alpha-recoil activity was due to Ac^{223} alpha-particles. The reason for this assumption is as follows. Whenever an Ac^{223} atom is recoiled over, there are four alpha-emitting isotopes which may be counted; whenever a Fr^{219} atom recoils over, there is only the one Bi^{211} alpha which may subsequently be counted, since Fr^{219} and At^{215} are very short-lived; and similarly, whenever an At^{215} or a Bi^{211} atom is collected, there is only the possibility of counting the alpha-emission from Bi^{211}. If we assume that the efficiency of recoil is independent of the alpha-energy of the parent atom, then it can be seen that the equilibrium mixture of alpha-activities in the recoil sample will consist of one part due to Ac, one due to Fr, one to At, and four to Bi.

This comparison of the number of atoms decaying by alpha-emission and the number by orbital electron capture shows that the K/α branching ratio for Ac^{223} is ~ 0.01. (Note: This value differs by a factor of 10 from the value presented in the Table of Isotopes.)[7]

3. Fr^{219}

From alpha-decay systematics, a short half-life is expected for this isotope. A determination using the delayed coincidence method described in the Appendix gave a value of about 20 msec which is accurate to within about 10 percent.

In order to check both this value and the feasibility of a rotating disk recoil method for the measurement of short half-lives (also described in the Appendix), a sample containing about 4×10^6 alpha-counts per minute of Pa^{227} was mounted above a disk which was rotating at a speed of one revolution per second. The recoiling Fr^{219} atoms were collected on the disk and some of these consequently emitted alpha-particles into an alpha-counting chamber displaced successively at three different distances from the Pa^{227} sample. The half-life of this francium isotope as determined by this method was approximately 20 msec.

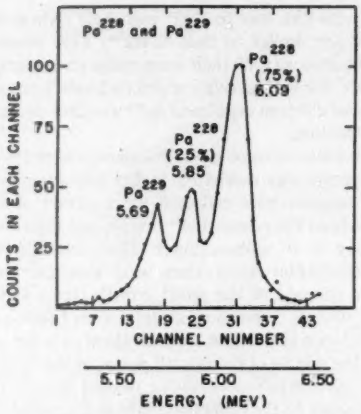

FIG. 8. Alpha-pulse analysis curve of the Pa^{228} and Pa^{229} alpha-groups after complete decay of the Pa^{227} series. This sample was purified from daughter activities immediately before counting.

4. At^{215}

The half-life of this isotope has been determined electronically by the method of delayed coincidences to be about 10^{-4} sec, within about 20 percent.

It is interesting to note that the energy obtained for the At^{215} alpha-particles is several hundred kilovolts less than the 8.4-Mev value reported by Karlik and Bernert[16] for At^{215} as formed by the beta-particle branching decay of Po^{215} (AcA).

C. The Pa^{228} Series

After the Pa^{227} series has decayed, freshly purified protactinium samples exhibit three prominent alpha-peaks in pulse analysis curves, as shown in Fig. 8. Two of these are due to Pa^{228} and the other to Pa^{229}. The isotope Pa^{229} is known[7,17] to be a 1.5-day alpha-emitter and grows the 10.0-day Ac^{225} and subsequent short-lived daughters. Pa^{228} is a new isotope and grows, by alpha-decay, a previously unknown alpha-emitting chain collateral to the thorium ($4n$) family as shown in the block diagram of Fig. 9 (which also includes the U^{228} collateral series which is to be discussed later). In practice, it is difficult to observe the 2.9-hr Ac^{224} and other daughters from the alpha-emission of Pa^{228}. In the present cyclotron bombardments the yields of 17-day Pa^{230} from the (d, $4n$) reaction on thorium were always very much higher than those for the (d, $6n$) reaction; consequently, because of the beta-decay of Pa^{230}, the members of the Pa^{230} series[18] would quickly become prominent and interfere with measurements on the members of the Pa^{228} series.

The alpha-decay daughters of Pa^{228} were separated by recoil experiments. Shown in Fig. 10 is a pulse analysis curve measured on a first recoil sample which has been taken from a sample containing Pa^{228}, Pa^{229}, and Pa^{230} after the daughters of the Pa^{228} had come into equi-

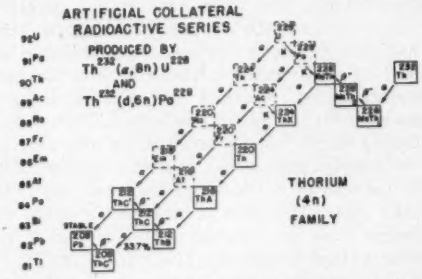

FIG. 9. Block diagram of the Pa^{228} and U^{228} collateral series.

librium with the parent. Here we see the uncontaminated alpha-peaks of Ac^{224} and daughters, since Th^{228} has been allowed to decay completely. Further recoil experiments showed that a 27.5-sec activity followed that due to Ac^{224}, and delayed coincidence experiments showed that the Fr^{220} isotope with the 6.69-Mev alpha-particle is the parent of the At^{216} isotope with the 7.79-Mev alpha-particle. Hence, the Pa^{228} series decays in the following manner:

$$Pa^{228} \xrightarrow[22\ hr]{\alpha} Ac^{224} \xrightarrow[2.9\ hr]{\alpha} Fr^{220} \xrightarrow[27.5\ sec]{\alpha} At^{216} \xrightarrow[3\times10^{-4}\ sec]{\alpha}$$

$$Bi^{212}\ (ThC) \begin{cases} \xrightarrow[34\ percent]{\alpha} Tl^{208}\ (ThC'') \xrightarrow[3.1\ min]{\beta^-} \\ \xrightarrow[66\ percent]{\beta^-} Po^{212}\ (ThC') \xrightarrow[3\times10^{-7}\ sec]{\alpha} \end{cases} Pb^{208}\ (stable).$$

(60.5 min)

[16] B. Karlik and T. Bernert, Naturwiss. 32, 44 (1944).
[17] Hyde, Studier, Hopkins, and Ghiorso, National Nuclear Energy Series, Plutonium Project Record, Vol. 14B, *The Transuranium Elements: Research Papers*, Paper No. 19.17 (McGraw-Hill Book Company, Inc., New York, 1949).
[18] M. H. Studier and E. K. Hyde, Phys. Rev. 74, 591 (1948).

The branches which arise from orbital electron capture by Pa^{228} and Ac^{224} are not shown.

Measurements on a chemically separated lead-bismuth fraction from an equilibrium mixture of the Pa^{228} series confirmed the presence of the Pb^{212} (ThB), Bi^{212} (ThC), and Po^{212} (ThC′) members of the thorium family and hence confirmed the mass assignment of the series.

1. Pa^{229}

In the measurement of the half-life of Pa^{228} there arises the problem of resolution of pulse analysis curves, since the 1.5-day Pa^{229} is always found with Pa^{228} to some extent. Even when a bombardment is planned for maximum Pa^{228} and minimum Pa^{229} yield, there will not be a difference of more than about 20 between the yields of the two isotopes; and by the time the Pa^{228} has decayed for one or two half-lives, the Pa^{229} activity will become appreciable and affect the decay curve; Fig. 8 shows a pulse analysis curve from the protactinium fraction of a typical bombardment.

Since the energies of the Pa^{228} and Pa^{229} are quite close together [6.09 Mev (75 percent) and 5.85 Mev (25 percent) for the two groups of Pa^{228} and 5.69 Mev for Pa^{229}], resolution of consecutive pulse analyses is difficult and inaccurate. A preliminary value of 22 hours was obtained from a rough resolution of several successive pulse analyses taken over a period of two half-lives of the Pa^{228}. In this method, however, there is no good opportunity to estimate the error or to observe trends in the half-life measurements, and it was consequently discarded.

Another method consisted of counting all the alpha-particles in the entire group of peaks representing the Pa^{228} and Pa^{229} from pulse analysis measurements and obtaining the ratio of these counts to long-lived Pa^{231} tracer added at the beginning of the experiment. These counts were taken at about 12-hr intervals and the ratios plotted to represent the composite decay. New samples which had been freshly separated from their daughters were used for each point and thus the use of tracer Pa^{231} was imperative. This chemical separation was necessary in order to remove the Pa^{230} series alpha-particle peaks which tend to obscure the Pa^{228} and Pa^{229} peaks. Figure 12 represents the decay of the sum of the alpha-particles in the Pa^{229} and Pa^{228} peaks, while Fig. 11 shows representative pulse analyses taken at the beginning, in the middle, and near the end of the decay experiment. The dotted line resolution indicated in Fig. 12 represents the intensity of Pa^{229} alpha-particles obtained from the data shown in Fig. 11C (9-day sample) together with a 1.5-day slope corresponding to the half-life of Pa^{229}. This Pa^{229} line was then subtracted from the original points and a line with a slope corresponding to a half-life of 21.8 hr for Pa^{228} was obtained. Other methods of treating the data gave slightly different values for the half-life of Pa^{228}, but all of these

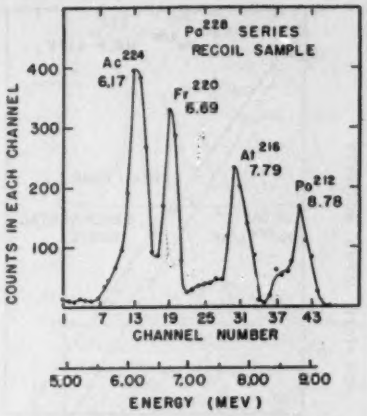

FIG. 10. Alpha-pulse analysis curve of Ac^{224} and alpha-daughters obtained with a recoil sample from Pa^{228}.

values are consistent with a half-life of 22 ± 1 hr for this isotope.

Chemical separation of 1.9-yr Th^{228} after the decay of a known amount of Pa^{228} was made to determine its branching ratio for electron capture. An aliquot of the original Pa^{228} solution was subjected to pulse analysis in order to determine the amount of Pa^{228} present. Tracer

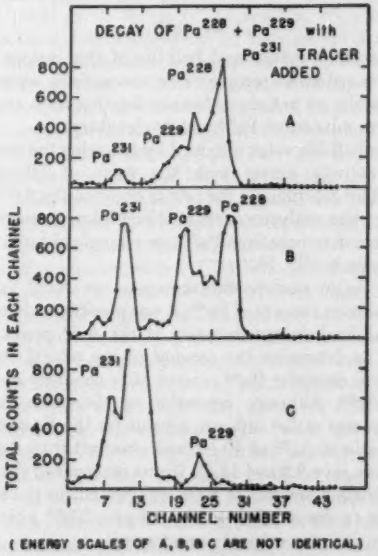

FIG. 11. Alpha-pulse analysis curves showing the decay of the Pa^{228} and Pa^{229} alpha-peaks relative to the long-lived Pa^{231} tracer peak. The curves represent different length counts of the freshly separated sample started at the following times after the end of bombardment: A, 10 hours; B, 3.05 days; C, 9.05 days. (The energy scale has been shifted for curve C.)

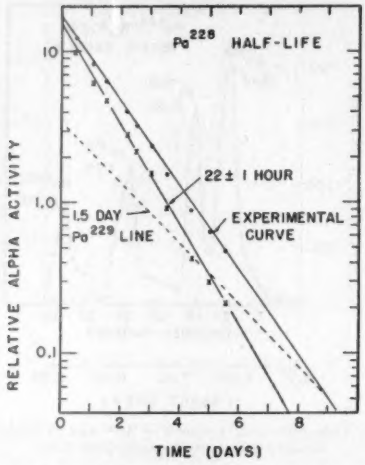

FIG. 12. Determination of the Pa^{228} half-life by measurement of decay of resolved and summed Pa^{228} and Pa^{229} pulse-analysis peaks.

Th^{230} was added and the sample was allowed to decay for six days before thorium was chemically separated. The plates containing the thorium were pulse analyzed to determine the ratio of Th^{228} to Th^{230}. The value obtained for the K/α ratio for this isotope is 53 ± 5.

2. Ac^{224}

The alpha-energy and half-life of this isotope were determined with a sample which was made by separating chemically an actinium-thorium fraction from an equilibrium mixture of Pa^{228} and its daughters.

The half-life value obtained by following the decay of this activity agrees with the value of 2.9 ± 0.2 hr found by determining the rate of decay of the At^{216} peak using pulse analysis curves obtained from measurements on a recoil sample from Pa^{228}; an example of such curves is shown in Fig. 10.

By pulse analysis measurements on recoil samples from a large amount of Pa^{228}, it was possible to determine the alpha-disintegration rate of the Ac^{224} present and later to determine the amount of the orbital electron capture daughter Ra^{224} present after complete decay of the Ac^{224}. Although resolution of the pulse analysis curves was rather difficult, a value for the K/α branching ratio of Ac^{224} of 10 ± 2 was obtained (two determinations gave 8.8 and 11.6). It was determined that only a negligible amount of Ra^{224} was present in the sample owing to the recoil from the 1.9-year Th^{228} which had grown into the original parent sample.

3. Fr^{220}

Experiments on recoil fractions led to a half-life of 27.5 ± 1.5 sec for this isotope. From a large sample of Pa^{228}, recoil samples were collected for short periods of time and followed for gross alpha-decay in a conventional alpha-counter. The resolved decay curve is shown in Fig. 13. In these experiments the contribution of the Ra^{222} which was present in low abundance from the Pa^{230} series was negligible.

4. At^{216}

The half-life for this isotope, as measured by the delayed coincidence method, was found to be about 300 μsec. It is interesting to note the correspondence between the energy of these At^{216} alpha-particles (7.79 Mev) and the energy (7.64 Mev) reported by Karlik and Bernert[19] for At^{216} as formed by the beta-particle branching decay of Po^{216} (ThA). However, there seems to be good reason to doubt the beta-instability of ThA (see Perlman, Ghiorso, and Seaborg[13] for a discussion of this point).

D. The U^{233} Series

Shortly after bombardment of thorium with 120-Mev helium ions, the uranium fraction contains a series of five alpha-emitters which decay with the 9.3-min half-life of the uranium parent, which is apparently a collateral branch of the thorium ($4n$) family as shown in Fig. 9. As this series decays, the 58-min U^{229} series (discussed below) is left from the original mixture as shown in Figs. 14 and 15.

The assignment of masses to this series is difficult, since the only known member of a natural radioactive family present with it is the very short-lived Po^{212} (ThC′).

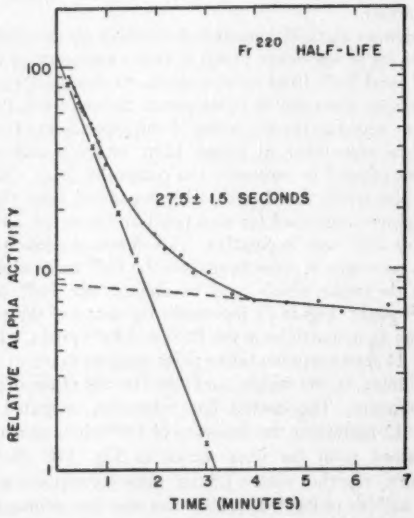

FIG. 13. Determination of the half-life of Fr^{220} from gross decay of recoil samples from a sample containing a large amount of the Pa^{233} series.

[19] B. Karlik and T. Bernert, Naturwiss. 31, 492 (1943).

However, in addition to the energy identification of the high energy Po^{212} alpha-particles, further proof of the mass assignment has been obtained by chemically separating Pa^{228} as the orbital electron capture daughter of the U^{228}. Hence, it is established that this series begins with the U^{228} isotope; and, with the help of alpha-decay systematics, the following decay sequence is suggested:

$$U^{228} \xrightarrow[9.3\ \text{min}]{\alpha} Th^{224} \xrightarrow[(\text{pred. } 1\ \text{sec})]{\alpha}$$

$$Ra^{220} \xrightarrow[(\text{pred. } 3\times10^{-2}\ \text{sec})]{\alpha} Em^{216} \xrightarrow[(\text{pred. } 10^{-4}\ \text{sec})]{\alpha}$$

$$Po^{212}\ (ThC') \xrightarrow[3\times10^{-7}\ \text{sec}]{\alpha} Pb^{208}\ (\text{stable}).$$

The branch arising from the electron capture decay of U^{228} is not shown.

1. U^{228}

The half-life of this isotope was determined as 9.3±0.5 min by following the decay of the alpha-activity in the Th^{224} and Ra^{220} peaks resolved from pulse analysis curves. The decay of the alpha-activity in the Po^{212} peak gave a half-life which was slightly shorter, but within the error of the measurements.

In order to determine the amount of electron capture branching decay of U^{228}, it was necessary to separate chemically Pa^{228} from the decay products of a large sample, after first having taken special precautions to remove by means of TTA-benzene extractions all Pa^{231} formed in the original bombardment. The chemical procedure involved separation of the uranium fraction from a 10-min bombardment of thorium metal through the use of ether extraction from saturated

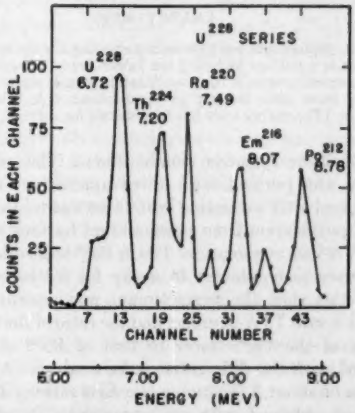

FIG. 14. Alpha-pulse analysis curve of the U^{228} series. Contaminating peaks are those of the U^{229} series. More accurate energy values from another source are given in the text.

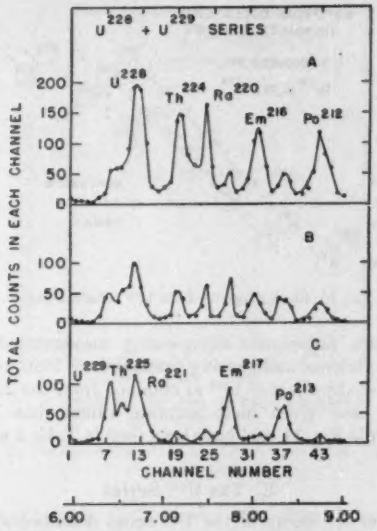

FIG. 15. Alpha-pulse analysis curves showing the decay of the U^{228} series in the presence of the longer-lived U^{229} series. Curves A and B represent 2-min counts, curve C, a 4-min count. Counts of the collimated sample were started at the following times after the end of bombardment: A, 21 min; B, 36 min; C, 65 min.

ammonium nitrate solution; the ether was washed with three portions of saturated ammonium nitrate, and finally the uranium was extracted back into pure water. The water solution was then made 6*N* in nitric acid and was contacted three times with double volumes of TTA-benzene solutions to eliminate any small traces of Pa^{228} which might have come through with the uranium in the ether extraction procedure. Some Pa^{231} was then added as tracer for chemical yield for the subsequent operation, and a small aliquot of the water solution was taken for pulse analysis and determination of the intensity of the U^{228} activity. After standing 20 min, the solution was again contacted with a TTA-benzene solution, this time to extract the daughter Pa^{228}, and the organic layer was evaporated on platinum, flamed, and counted.

It is difficult to obtain a sufficient amount of activity and to make the separations rapidly enough to perform this extraction operation successfully. The results of the experiment are rather indefinite, since the final plate containing the protactinium gave only about 0.4 counts/min of Pa^{228} with 73 percent recovery of the tracer. Consequently, the ratio of K/α reported in Table I as 0.25 may be in error and is presented principally as evidence that there is some orbital electron capture branching in this isotope.

2. Other Members of the U^{228} Series

The half-lives of the other members of this series have not yet been investigated. The assignment of alpha-energies to isotopes has been made from alpha-sys-

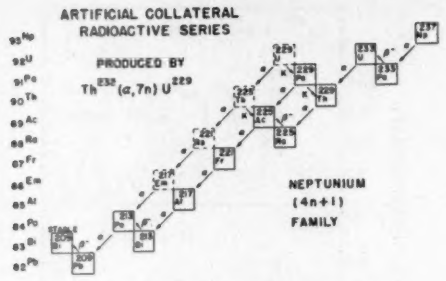

FIG. 16. Block diagram of the U^{229} collateral series.

tematics. Subsequent alpha-energy measurements by Orth, Ghiorso, and Seaborg (unpublished, 1950) on the alpha-decay chain of U^{228} as obtained from the 22-min Pu^{232} have given more accurate values than those shown in Fig. 14, and have been used in Table I of this paper.

E. The U^{229} Series

After the decay of the U^{233} series described above, there is readily apparent a second group of alpha-particle emitters which is collateral to the artificial, neptunium $(4n+1)$, radioactive family[4] (Fig. 16). Alpha-pulse analysis shows a spectrum with three poorly resolved short-range peaks and two longer range ones as shown in Fig. 17. The best values for the energies were obtained from other curves not shown here. This 58-min series dominates the pulse analyses of uranium samples from these thorium bombardments for several hours before finally giving way to the U^{230} series as shown in Fig. 18. Chemical separation of 1.5-day Pa^{229} and 10.0-day Ac^{225} as orbital electron capture daughters of the U^{229} and the Th^{225} isotopes, respectively, proved the mass assignment and decay sequence of this series to be:

$$U^{229} \xrightarrow[58\ \text{min}]{\alpha} Th^{225} \xrightarrow[8.0\ \text{min}]{\alpha} Ra^{221} \xrightarrow[30\ \text{sec}]{\alpha} Em^{217} \xrightarrow[10^{-3}\ \text{sec}]{\alpha}$$

$$Po^{213} \xrightarrow[4.2\times10^{-6}\ \text{sec}]{\alpha} Pb^{209} \xrightarrow[3.32\ \text{hr}]{\beta^-} Bi^{209}\ (\text{stable}).$$

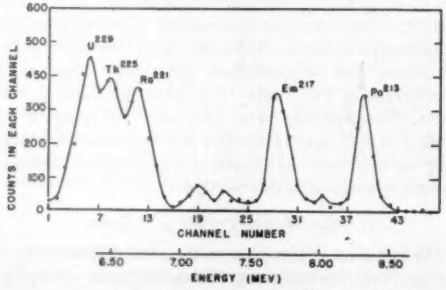

FIG. 17. Alpha-pulse analysis curve of the U^{229} series.

The branches arising from orbital electron capture of the U^{229} and Th^{225} are not shown.

1. U^{229}

The half-life of U^{229} was found to be 58 ± 3 min by following the decay of the alpha-counts in the U^{229}, Th^{225}, and Ra^{221} peaks. The resolved decay curve is shown in Fig. 19.

For the purpose of checking the electron capture branching ratio of this isotope, the daughter Pa^{229} was separated by a chemical procedure patterned after that used for the similar experiment with U^{233}. In order to eliminate any slight effect due to the Pa^{233} daughter of U^{233}, the target was allowed to stand for one hour after

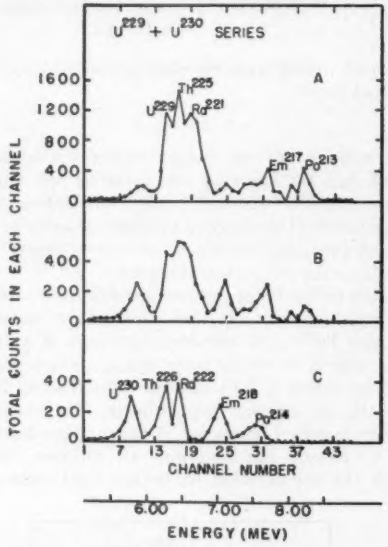

FIG. 18. Alpha-pulse analysis curves showing the decay of the U^{229} series in a mixture including the longer-lived U^{230} series. The curves represent counts of the noncollimated sample started at the following times after the end of bombardment: A, 1 hr; B, 4 hr; C, 8 hr. (The energy scale has been shifted for curve C.)

the end of the cyclotron bombardment. The uranium fraction was purified with three ammonium nitrate washes, and after extraction into water was subjected to further purification from protactinium by four washes with TTA-benzene solution. Tracer Pa^{231} was added and the sample then allowed to decay for 3.5 hr; at the end of this time the protactinium was separated by extraction into TTA-benzene, and the ratio of the alpha-activity of the Pa^{231} tracer to that of Pa^{229} was determined with the differential pulse analyzer. A value for K/α of about 5 (assuming the K/α ratio of Pa^{229} is 100) was obtained with an uncertainty largely dependent on the determination of the initial amount of U^{229} in the sample.

2. Th^{225}

The half-life of Th^{225} was determined by following the decay of the Po^{213} peak in pulse analyses of several recoil samples grown for a short time from a large amount of U^{229}; a value of 8.0±0.5 min was found.

The K/α branching ratio of this isotope was found by a method similar to that used for Ac^{225}. A recoil sample was grown for 3.5 hr from a plate containing the members of the U^{229} series. The short-lived activities were allowed to decay during a period of 9.5 days before an alpha-pulse analysis was made to determine the amount of 10.0-day Ac^{225} that had grown from Th^{225}. The amount of Th^{225} daughter activity which recoiled from the U^{229} plate was determined by several short recoil experiments performed in the same manner as those involving Ac^{225}.

The sample of U^{229} (*ca* 2×10^4 alpha-counts/min) was not as active as is desirable for this type of experiment, however, since only 0.4 alpha-counts/min of Ac^{225} were found on the collection plate originally containing Th^{225} and daughters. The value of 0.12 for the K/α branching ratio of this isotope is thus subject to a large possible error.

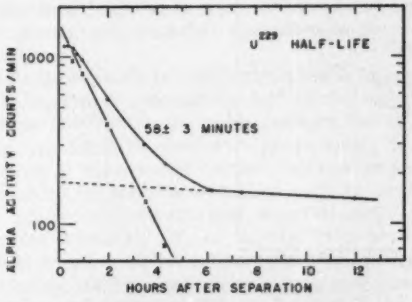

FIG. 19. Determination of the half-life of U^{229} from the decay of the alpha-activity in the U^{229}, Th^{225}, and Ra^{221} peaks from pulse analysis curves shown in part in Fig. 18.

3. Ra^{221}

Two types of recoil experiments were made to measure the 30±2-sec half-life of this isotope. A half-life value of 31.7 sec (Fig. 20) was obtained by the rotating disk method (described in Appendix). These points have been corrected for the decay of the parent during the time of the experiment and also for the 25 percent contamination of 38-sec Ra^{222} introduced from the U^{230} series which was present in the sample with the U^{229} series.

In the other method the recoil sample was transferred manually to an alpha-counter and its decay followed. Counts were taken every 0.05 min and recorded automatically on tape. With a relatively low counting rate and such a short interval between counts, the statistical fluctuations are quite large. In order to minimize these fluctuations, these data have been plotted on an integral curve in Fig. 21. Each count was corrected for background, and the values summed up to a time t. The summation of counts were plotted against t, and the value which they approached was taken as N_∞. In the integral curve, then, the difference between N_∞ (the total number of counts observed on complete decay) and N_t (the total number of counts observed to a certain time t) was plotted. The plot of this quantity on a logarithmic scale against time determines a half-life of 30±2 sec for the activity.

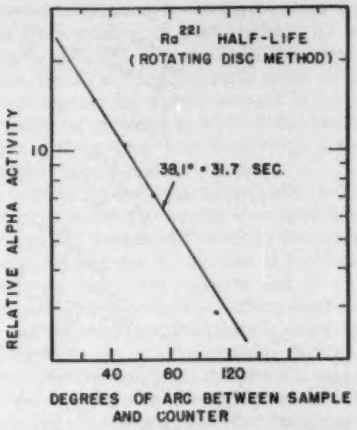

FIG. 20. Determination of the half-life of Ra^{221} by the rotating disk recoil method.

4. Em^{217}

The half-life of this isotope has been determined to be 1 msec, within about 10 percent, by the method of

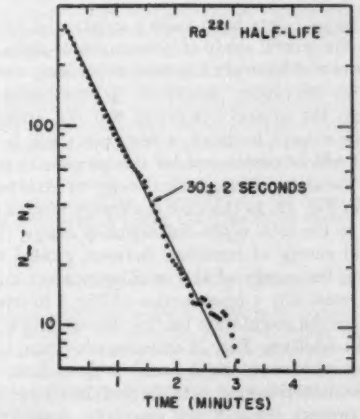

FIG. 21. Decay curve of Ra^{221}. N_∞ = total number of observed counts. N_t = number of observed counts within the time interval t.

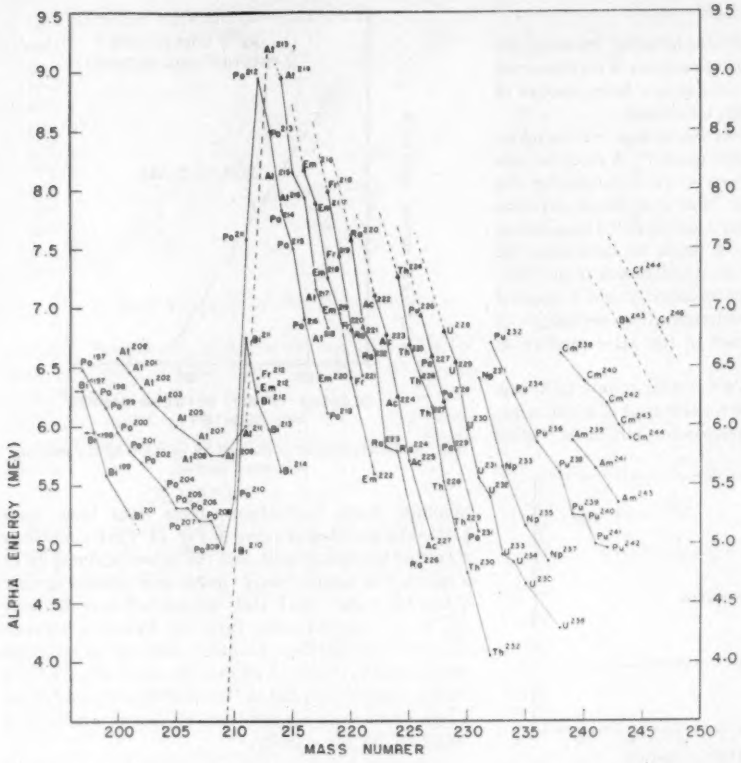

FIG. 22. Alpha-disintegration energy *vs* mass number relationships of the heavy nuclides. △ indicates points which represent data from the research described in the present paper.

counting delayed coincidences (described in Appendix) between the parent Ra^{221} and daughter Em^{217}.

IV. DISCUSSION

The present data have made a substantial contribution to the general study of systematics of alpha-decay properties and have already been extensively used and placed in the proper perspective in this connection.[13] Although the present discussion will not attempt to treat the subject in detail, a few points will be dealt with. It will be convenient for this purpose to use the plot of the alpha-disintegration energy *vs* mass number shown in Fig. 22. In this case the energy plotted corresponds to the total *alpha-disintegration energy*, that is, the total energy of transition between ground states, including the energy of the recoiling product nucleus. This is essentially a reproduction of Fig. 1 in reference 13 and the documentation for the various data is given there. In addition, Fig. 22 includes new data, largely from this laboratory, which brings it up to date.

The points corresponding to the nuclides characterized in the present research are especially designated in Fig. 22 in order to emphasize the manner in which they contribute to the systematics. The data also make an important contribution to the study of the relationship between half-life and alpha-energy, but the curves showing this are not reproduced here, since several are required owing to dependence on the mass number types. Plots showing this relationship for even-even isotopes define for each element regular lines which are close to the curves calculated by selecting a reasonable function for nuclear radius; on the other hand, the nuclei with odd nucleons invariably depart from these curves in the direction which corresponds to prohibition of alpha-decay (reference 13).

It is of interest to predict the radioactive properties of the still undiscovered nuclides which are even more neutron deficient than those studied here. Thus, we can see from extrapolation of the curve corresponding to uranium in Fig. 22 that we might expect an alpha-disintegration energy of some 7.0 to 7.2 Mev for U^{227}. This corresponds to an alpha-emission half-life for this nucleus of the order of a minute, including in the prediction a small factor for the prohibition which should be introduced because of its even-odd character. Since the half-life for orbital electron capture by U^{227} should be substantially longer than this, and since, similarly, the K/α ratio should be small for its daughters,

the U^{227} series should decay mainly as follows:

$$U^{227} \xrightarrow{\alpha} Th^{223} \xrightarrow{\alpha} Ra^{219} \xrightarrow{\alpha}$$

$$Em^{215} \xrightarrow{\alpha} Po^{211}\ (AcC') \xrightarrow{\alpha} Pb^{207}\ (\text{stable}).$$

In a similar manner to that used for U^{227}, the alpha-disintegration energies and half-lives for the daughter isotopes can be predicted; and such considerations lead to the conclusion that these should be about as follows: Th^{223}, 7.5–7.7 Mev, 10^{-1} sec; Ra^{219}, 7.9–8.1 Mev, 10^{-3} sec; Em^{215}, 8.6–8.8 Mev, 10^{-6} sec.

Similar considerations with respect to Pa^{225} lead to the prediction of an alpha-disintegration energy of some 7.2 to 7.4 and a half-life of perhaps 10 sec. The daughters (Ac^{221}, Fr^{217}, At^{213}) in the alpha-emitting decay chain would have increasing alpha-energies and decreasing half-lives in a manner similar, but, of course, different in detail to the above discussed U^{227} series. The prediction of half-lives is less certain here owing to the odd-odd character of the members of the Pa^{225} series and, hence, the greater and somewhat unpredictable degree of prohibition.

In addition, there is uncertainty in the alpha-energy to be expected in a nuclide like At^{213} which decays to a nucleus (Bi^{209}) with the stable configuration of 126 neutrons. Similarly, the curves corresponding to the elements of higher atomic number than astatine probably exhibit the same maximum and minimum as those for astatine and the elements below astatine. Thus, nuclides containing 126, or slightly fewer neutrons, should have low alpha-decay energies and hence relatively long half-lives; and this has already been found to be the case for emanation[20,21] and francium,[21] and also more recently for radium.[22] Observation of corresponding maxima and minima in the curves for the elements higher than radium is a matter of great experimental difficulty because of the problem of producing the nuclides and also because of their relatively short half-lives due to their large neutron deficiency.

Considerations similar to those made for uranium (U^{227}) show that lighter isotopes of elements of atomic number larger than that of uranium (for example, Np^{230}, Pu^{231}, Am^{237}, Cm^{237}, etc.) should have half-lives sufficiently long for observation. A number of these nuclides can, of course, be considered as progenitors of some of the collateral series which are the subject of the present investigation.

No measurements on the radiations accompanying the electron capture process have yet been made on the nuclides in these collateral series which decay by this mechanism in addition to their decay by alpha-emission. The evidence for decay by electron capture comes from the observation of the daughter isotopes which result from this process. The observation and study of the radiations corresponding to electron capture should be possible for a number of these nuclides, for example Pa^{227}, Pa^{228}, Ac^{224}, U^{228}, U^{229}, and Th^{225}. It is interesting to note that the K/α branching ratio seems to decrease with mass number for a given element in the manner which might be expected in view of the much larger variation of alpha-decay rate with energy than is the case for the electron capture process.

It is quite likely, and in fact practically certain, that fine structure in the alpha-particle energies is actually present and has been missed owing to the necessity of measuring the energies in mixtures of alpha-emitters. Further work done more carefully and at higher resolving power should make it possible to observe this. It has become apparent from work done during the last few years that practically all alpha-emitting nuclides exhibit fine structure. The amount of this seems to be greatest, on the average, for the odd-odd species, less for the even-odd and the odd-even, and least for the even-even species. It should be noted that some fine structure was observed for the odd-odd nucleus Pa^{228}; and it is certainly to be expected that it should be especially apparent in its daughter nuclei Ac^{224}, Fr^{220}, and At^{216}.

The predominantly alpha-emitting nuclei Pa^{227} and U^{229}, formed by reactions such as $Th^{232}(p, 6n)Pa^{227}$, $Th^{232}(d, 7n)Pa^{227}$, and $Th^{232}(\alpha, 7n)U^{229}$ are especially suitable for the study of the excitation functions corresponding to these interesting reactions for their production. This has been the subject of another investigation.[14]

We wish to thank James T. Vale and the crew of the 184-inch cyclotron for their assistance in carrying out this work.

APPENDIX

In this research a variety of techniques had to be employed in order to measure the radioactive properties of the isotopes whose half-lives range from days to microseconds. These techniques range from laborious chemical separations of one element from all other elements to electronic methods for measuring short times between two successive alpha-pulses.

For isotopes with half-lives of a day or so, chemical procedures ensure complete separation from even small quantities of contaminating activities. If, on the other hand, the desired isotope has a half-life of less than an hour, the requirement of purity must be made consistent with the requirement for speed of chemical separation and purification. In general, physical methods must be relied upon to measure and identify isotopes of half-lives of less than a minute. Counting techniques must also be geared to the half-life of the substance upon which the measu ements are to be made.

A. Types of Bombardments

In order to obtain the maximum yields in the present work, the internal beam of the cyclotron was used, except when other arrangements could meet a special need (with consequent lowering of yield). The internal beam usually gives about 1 μamp of deuteron and proton current and about one-tenth of this for helium ions.

In general, foils of thorium metal were bombarded either for a time about equal to the half-life of the activity desired or until a sufficient amount of that activity had been produced. The target

[20] Ghiorso, Meinke, and Seaborg, Phys. Rev. **76**, 1414 (1949).
[21] Hyde, Ghiorso, and Seaborg, Phys. Rev. **77**, 765 (1950).
[22] E. K. Hyde and F. F. Momyer (unpublished work, 1950).

foils, measuring about 1.5 by 0.5 inches, were clamped into a holder which could be mounted on the "probe" target of the cyclotron and inserted into the tank to intercept the beam. The energy of the particles which struck the target was determined by the radius at which the leading edge of the target foils were set.

In the first bombardments several 5-mil foils were stacked on each other to increase the reaction yields. Later, however, after it had been found that the ion beam penetrated only a few millimeters back from the leading edge of the target, a target holder was designed in which a target could be bombarded on edge. This holder is put on the end of the 184-inch cyclotron probe in such a way that it requires the beam to traverse the width of the thorium foil instead of its thickness. Hence, for the same weight of target material in foil form, a factor increase of at least ten in yield could be obtained by using this target holder. It was only by the application of this concept of bombarding a target "on edge" that it was possible to obtain sufficient yield in many reactions to obtain the required data.

When the isotopes with long half-lives were being studied, pieces of thorium of 25-mil thickness were used to increase the total yield of the protactinium or uranium. When the time for chemical separation was short, however, thinner pieces of thorium, 5 mils or less in thickness, were used to ensure rapid dissolving.

In some cases, thorium nitrate powder wrapped in aluminum foil was used as the target in order to reduce further the time for dissolution of the target. These bombardments in the vacuum chamber were difficult, however, since often the salt outgassed too much and prevented the attainment of a vacuum sufficiently high to proceed with the bombardment.

B. The "Jiffy Probe"

When it is necessary to decrease the time between the end of the cyclotron bombardment and examination of a sample, use is made of the so-called "jiffy probe." This probe, a long hollow tube with a thin concave aluminum end-window, can be inserted into the tank of the cyclotron. The inside of this tube is kept at atmospheric pressure; hence, the window must be strong enough to withstand the vacuum of the tank. A "rabbit" holding a target is blown by compressed air to a position at the end of the tube as close as possible to the window. At the end of bombardment, the target is blown out through the end of the probe tube with compressed air. Provision is made in the rabbit to hold either a metal target on edge or a small cylinder containing a salt of the element to be bombarded. In the bombardment, the beam current hitting the target is reduced by a factor of at least ten from that attained with the internal beam.

After bombardments of the order of a minute were made with the jiffy probe set-up, the doors of the cyclotron were opened immediately and the target blown out of the probe into a lead carrier. This carrier was then taken to a truck and the combined solution and extraction of the product from the target was made while the truck was being driven some 100 yards to the chemistry building. There the sample was evaporated on platinum and placed in the differential alpha-pulse analyzer by means of a fast sample changing mechanism. This method took a minimum of 3.3 min from cyclotron shutdown to the beginning of the first alpha-pulse analysis for the isolation of protactinium and 4.5 min for the isolation of uranium.

C. Target Chemistry

The thorium targets were very radioactive when removed from the internal beam of the 184-inch cyclotron. Although much of this activity comes from fission products of the thorium which are present in good yield, there is also appreciable radioactivity owing to high yield spallation products. Hence, the first steps in the chemical separation had to be carried out in such a manner as to avoid overexposure to the radiation.

Since the protactinium half-lives vary from a day to minutes, the chemical procedure varied from bombardment to bombardment. For the experiments in which Pa^{227} or Pa^{228} were studied, a single extraction with a solution of 0.4*M* thenoyltrifluoroacetone (TTA)[14] in benzene was sufficient to separate these isotopes from all other alpha-emitters. Zirconium, hafnium, and probably some niobium and iodine fission products are also extracted; but these are all beta-emitting activities and do not affect the alpha-counting. In order to obtain good resolution in pulse analyses of certain protactinium samples with a low intensity of alpha-activity compared to the beta-activity, it was necessary to separate the protactinium from the beta-emitting activities through the use of a further extraction of the protactinium into di-isopropyl ketone.

In general, the chemical procedure for the isolation of Pa^{227} involved solution of the thorium metal in concentrated nitric acid to which a few drops of 0.2*M* ammonium fluosilicate had been added to accelerate this process. This solution was diluted to about 4*N* acid and contacted with an equal volume of TTA-benzene solution. The phases were separated and aliquots of the organic layer containing the protactinium were evaporated on platinum.

A more complicated procedure was used for the isolation of the longer-lived protactinium isotopes. This procedure involved carrying of the protactinium on manganese dioxide, dissolution of this precipitate through the use of hydroxylamine solution and a second co-precipitation on manganese dioxide when needed to reduce the volume; this was followed by extraction of the protactinium into di-isopropyl ketone from acid solution and washing of the ketone layer with water in order to separate small amounts of fission products which might have come through; and finally, extraction of the protactinium into 0.4*M* TTA in benzene solution and the evaporation and flaming of this solution on a platinum plate to give an essentially weightless sample. The co-precipitations with manganese dioxide are instrumental in removing to a very high degree all of the other radioactivities. For the characterization of the Pa^{233} series, however, it was usually necessary to eliminate only the zirconium and niobium fission products through the use of the di-isopropyl ketone extraction procedure which, when combined with the TTA-benzene extraction procedure, provided enough purity for accurate results from the counting of alpha-particles.

For the uranium alpha-emitters, the procedure used by Newton[22] involving ether extraction of the uranium from 10*N* ammonium nitrate solutions was used. Another procedure developed by Crane[8] leads to higher purity uranium fractions, but it was found satisfactory for the present experiments to extract only with ether and wash the ether with several portions of saturated ammonium nitrate solutions before finally re-extracting into water and evaporating the samples on platinum plates.

For the experiments in which the jiffy probe was used with thorium nitrate targets, the salt was dissolved directly in a mixture of the aqueous medium and the organic extracting agent, so that the stirring for dissolution also served as the stirring for extraction.

D. Separation of Daughter Activities

1. Chemical Separation

The usual procedure for separating daughter radioactivities, applicable when the half-lives of the daughters are sufficiently long, is to perform actual chemical separations.[8] Wherever possible in the present work, the daughters were chemically separated in order to definitely prove their atomic number.

Protactinium daughters of uranium isotopes were separated by the TTA-benzene extraction procedures, which were essentially the same as those used for separations from target materials.

Thorium fractions were separated by co-precipitation with zirconium phosphate precipitates, which are quite specific for carrying thorium to the exclusion of other elements in this region. Since this phosphate precipitate is much too bulky to be suitable for pulse analysis experiments, it was metathesized first to the fluoride (using lanthanum fluoride as carrier for the thorium) and then to lanthanum hydroxide, which was finally dissolved in

[22] A. S. Newton, Phys. Rev. 75, 209 (1949).

hydrochloric acid and evaporated as lanthanum chloride containing the thorium activity.

Actinium was separated in several cycles in which it was carried by lanthanum fluoride, metathesized to lanthanum hydroxide, and redissolved in acid. The solution from which the lanthanum fluoride was precipitated contained barium as "holdback" carrier for radium. Thorium was specifically removed in this procedure by co-precipitation on zirconium phosphate which was removed as a "by-product" precipitate.

Bismuth was separated by co-precipitations on lead sulfide, the precipitate being dissolved in hot concentrated hydrochloric acid and then reprecipitated. The lead was finally separated from the bismuth by precipitation as lead sulfate.

2. Separations by Volatilization

Several elements in the heavy region are quite volatile. Hence, in the present work it was possible to remove emanation isotopes by merely heating in a flame a platinum plate containing a series of alpha-emitters. Francium, astatine, and polonium can similarly be at least partially volatilized by "flaming" such a plate. In none of the studies was it necessary to collect the above elements directly after the flaming operation. Instead, the indirect effect of the growth of daughters in the remaining sample was measured as the isotope that had been removed by volatilization grew back into equilibrium with its parent.

3. Recoil Separations

A third and very useful method of separating daughters from the parent activities takes advantage of the recoil imparted to the daughter atom when the parent emits an alpha-particle. When an electric field is imposed between a plate containing the sample and another plate, these recoiling daughter atoms can be collected on the second plate when it is negatively charged. This collector plate, then, is free from the first member of the series present on the original plate, although there may be present on it varying amounts of subsequent members of the series. Similarly, if a second-order recoil transfer is made, in which a further recoil fraction is collected from the first recoil collection plate, neither the first nor second members of the series can be present. This procedure can be extended to third-order or triple recoils, etc., if sufficient activity is available initially. The yield of this type of recoil collection is about 10 percent; higher yields (i.e., up to nearly 50 percent) can be obtained in vacuum without the necessity of an electric field.

An adaptation of this method has made possible half-life determinations on isotopes with values ranging from 30 sec to about 20 msec. Basically, the apparatus consists of a 13-inch diameter rotating metal disk which is wired electrically to act as the collector for recoiling atoms, a sample holder which positions the sample face down over the outer rim of the disk, and an alpha-counting chamber which can also be positioned above the outer rim of the disk. The disk is rotated under the parent sample at a known speed. Recoiling daughter activities are collected along the rim of the disk and the alpha-particles from these activities are counted through the slit window of the alpha-particle counting chamber. By changing the angle between the sample and the chamber, counts of different intensities are registered. The activity obtained at a certain angle is plotted as one coordinate and the angle as the other; thus, the usual type of logarithmic curve can be obtained from which the half-life is determined.

E. Counting Apparatus

Alpha-particles were counted in a standard type argon-filled ionization chamber in which the pulses from electron collection were fed through a fast amplifier and into a scale of 512 counting circuit. Counting losses through coincidence of two or more particles in the chamber for this counting set-up appear to be negligible even at fairly high counting rates.

In order to minimize manual counting operations over long periods of time, an automatic ticker tape recorder was used. This was so arranged that the scaling circuit connected to the alpha-particle or Geiger counting amplification circuits could actuate a counting mechanism which stamped the count totals on a tape recorder. The stamping times could be set at intervals varying from 0.05 to 64 min. This mechanism made possible half-life determinations in a range not easily available for measurement by ordinary manual recording methods.

When counting of beta- or gamma-rays was required, an end-window alcohol-quenched argon-filled Geiger-Müller tube with a window of 3 mg/cm^2 thickness was used in conjunction with a scale of 64 counting circuit.

F. Alpha-Pulse Analysis

Most of the measurements were made through the use of an argon ionization chamber coupled to a 48-channel differential pulse analyzer.[9] A fast sample-changing mechanism on the ion chamber makes it possible to obtain a great deal of data in a short amount of time. Samples are introduced first into a small air lock which can be evacuated and filled with the same gas as that in the ionization chamber without disturbing the main counting volume of the latter. This arrangement reduces the time required for insertion of a sample into the ionization chamber and the actual start of counting. In addition, it is possible to leave the air lock open when extra speed is required and to rely merely on the flow of argon out of the ionization chamber to prevent air from entering. The resolution of the instrument is understandably poorer in the latter case, but is sufficient for some experiments.

Samples are placed on a turntable which can be turned manually from beneath. With the lock open, the table is free to turn to any position. When closed, however, the lock is sealed against the table, keeping the bulk of the chamber at the required gas pressure, while the lock can be kept at any desired vacuum or pressure.

The pulse analyzer itself has 48 electronic channels, each of which selects and counts all pulses within an adjustable energy range. Since these ranges are continuous, when a plot is made of number of counts per channel against channel number, a histogram is obtained of the alpha-spectrum between two particular predetermined energy values. The energy limits of the 48 channels can be varied electronically to give either a general picture of a wide energy region or a more detailed picture of some of the fine points of the spectrum.

In order to obtain good resolution in pulse analyses of the new collateral decay chains, it was found necessary to collimate the alpha-particles emitted by the samples. The chief purpose of such collimation was to reduce the probability of having parent and short-lived daughter alpha-emissions occur nearly simultaneously in the chamber and record, because of the finite resolving time of the amplifier, as a single large pulse. The amplifier-chamber combination used for these investigations was relatively "slow" so that half-lives as long as 200 μsec would cause a certain amount of this delayed coincidence straggling unless collimation were used. The collimators consisted of sieve-like disks of brass with $\frac{1}{16}$-inch diameter holes and varying thicknesses and were placed directly against the samples. The collimator most often used had a transmission of approximately 10 percent.

The alpha-energies determined with the pulse analyzer were all measured by comparison with those occurring in the natural radioactive series, which in turn have been determined accurately with magnetic alpha-ray spectrographs by several independent investigators. Depending on the ease of resolution for each nuclide, the present measurements have probable errors between 10 and 50 kev.

A few limitations of alpha-pulse analysis should be mentioned here. Since thin, almost weightless plates of samples are required, it is almost mandatory that carrier-free chemical separations be made. Thick samples cause poor resolution of the alpha-particle peaks and often make identification of mixtures of peaks im-

possible. In addition, there is a limit to the amount of beta-particle activity that can be tolerated before resolution of the alpha-particle peaks is affected. The resolution in the present apparatus is lessened appreciably when the beta- or electron activity reaches the level of from 10^5 to 10^6 counts per minute of low energy radiation. The tolerance for high energy beta-particles is higher.

G. Very Short Half-Life Determinations

As mentioned previously, the rotating disk method can be applied to determinations of half-lives down to about 20 msec. For half-lives shorter than this, an electronic delayed coincidence measuring apparatus has been used. This instrument was designed and constructed by R. Dorr and H. P. Robinson of this laboratory. The time scale of this apparatus is divided electronically into three equal intervals with a counting dial for each interval. One alpha-pulse can trigger the circuit, and if another pulse follows within the first segment of time, it is recorded on the first dial; within the second segment on the second dial, etc. The apparatus is so designed that it can trigger the circuit only for a certain segment of the pulse analyzer spectrum and record only when pulses occur in another segment of the spectrum. In other words, it can be set to trigger on one peak of a series of alpha-particle emitters and record on another. The time scale of the apparatus can be varied and is suitable for half-lives between 50 μsec and 50 msec. Background correction, of course, has to be made for random counts which are not related as parent-daughter.

PHYSICAL REVIEW VOLUME 81, NUMBER 5 MARCH 1, 1951

Microwave Spectrum of Phosphine, Arsine, and Stibine*

C. C. Loomis† and M. W. P. Strandberg
Research Laboratory of Electronics, Massachusetts Institute of Technology, Cambridge, Massachusetts

(Received October 16, 1950)

The microwave spectrum of the mono-deuterated phosphine (PH_2D), arsine (AsH_2D), and stibine (SbH_2D) has been measured. Although a supposedly pure sample of stibine was prepared, phosphine and arsine proved to be major impurities. They were separated from the sample; the microwave spectrometer was used to monitor the distillation process. The quadrupole fine structure associated with the absorption transitions for AsH_2D is used to illustrate the special assumptions which may be made with these molecules having an axis of charge symmetry. These assumptions allow one to rotate the coordinate system from the charge-symmetry axes to the inertial axes without thereby adding unknown cross derivatives to the descriptions of the dyadic ∇E_m. Interpretation of the spectrum of SbH_2D is more complicated. It is not found possible to fit the theory to the observed lines without making use of the second-order perturbations caused by a nearby level of different symmetry but of the same J. This perturbation involves the cross derivatives which had previously been assumed to be zero. With the assumption of cross derivatives approximately one percent of the diagonal terms, the theory fitted experiment within the experimental error. The electric quadrupole interaction in arsine and stibine is thus determined.

In order to measure the electric dipole moment of arsine and stibine, a slight extension is made to the theory of asymmetric tops in a uniform electric field.

The ground-state inversion splitting is determined to be less than 0.5 Mc/sec for all three molecules.

The rotational transitions observed were such that a determination of the structure of these three molecules is made.

I. INTRODUCTION

THE essential problem which forms the topic of this report is that of verifying the spins assigned to the two stable antimony isotopes and of determining the ratio of their quadrupole moments. Antimony forms one of a small group of stable elements[1] (Hg, Xe, Rb, Ir, Sb) in which the addition of two neutrons changes the spin by one unit. All of the spin assignments to these nuclei have been made by means of measurements of the hyperfine structure of optical spectra. None has as yet been verified by microwave spectroscopy, where the resolution available is sufficient to fix the spin of the nucleus without a doubt. Antimony is of interest, furthermore, because of the recent revival of the shell model for nuclei. On the basis of this model, those nuclei which come just after or just before the closing of a shell should have easily predictable electric and mechanical moments. Since antimony falls in the periodic table just after the closing of a proton shell at 50, a precise determination of its properties is of interest to the theories of shell structure.[2–5]

The nuclear information which one obtains from measurements using the techniques of microwave spectroscopy is contained in the fine structure associated with the absorption lines caused by the transition of a molecule from one rotational state to another. Before the nuclear information can be interpreted, the structure of the molecule must be determined. Consequently, any investigation of nuclear properties carries with it, as a by-product, the determination of the structure of the molecule used.

The only known simple molecule containing antimony and possessing the necessary properties of volatility and a permanent electric dipole moment is stibine; its structure, however, was not known. Before the advent of microwave spectroscopy with its discovery of the

* This work was supported in part by the Signal Corps, the Air Materiel Command, and ONR.

† Now at Los Alamos Scientific Laboratory, Los Alamos, New Mexico.

[1] H. L. Poss, Brookhaven National Laboratory Report 26 (T-10)I (October 1, 1949) (unpublished).

[2] W. Gordy, Phys. Rev. 76, 139 (1949).

[3] C. H. Townes, Phys. Rev. 76, 1415 (1949).

[4] R. D. Hill, Phys. Rev. 76, 998 (1949).

[5] E. Feenberg, Phys. Rev. 77, 771 (1950).

TABLE I. Preliminary molecular data.

Heavy atom	μ (Debye units)	B_ϕ	M_ϕ	$r(A)^a$	ϕ_e	I	$Q(10^{-26}$ cm$^2)$
Pb	0.55	−87.4°	−132.5°	1.42±02	93°±1°	1/2	—
As	0.15	−58.5°	−111.7°	1.53±02	90°±1°	3/2	0.3
Sb^{121}	0.5[a]	−17.0°	−88.5°	1.73±02	90°±1°	5/2	−0.3±0.2
Sb^{123}	0.5[a]	−17.0°	−88.5°	1.73±02	90°±1°	7/2	−1.2±0.2

[a] Estimates.
[b] For phosphine (PH_3), from infrared spectroscopy, $I_3=I_2=6.22\times10^{-40}$ g/cm^2 [G. Herzberg, *Infrared and Raman Spectra* (D. van Nostrand, New York, 1945)].

prevalence of $s-p$ hybridization, Stevenson[6] predicted the structures of the molecules phosphine, arsine, and stibine, using vibrational data, and published covalent radii for the first two and extrapolated to the structure of stibine. He assumed that the stability of the s-orbits in the heavy atom would be such as to make the bonds almost pure p, and therefore the bond angle (the angle formed by any two hydrogens and the heavy atom) would be 90°. He allowed himself a fair amount of latitude, quoting ±1° and ±0.02A. It was not felt, however, that the angle, in particular, could be predicted with that accuracy. The physical properties[7] of this chemical group of molecules, fortunately, have been precisely determined; and in particular the fact has been established that both stibine and arsine are quite unstable at room temperature, disintegrating into hydrogen gas and the metal. The investigation was begun, therefore, with the data of Table I.

Perhaps the simplest transition on which to measure the fine structure due to nuclear quadrupole interaction is the $J=0\rightarrow1$ in a symmetric top. In the case of stibine, however, this theoretical simplicity is not obtained without experimental complexity. The $J=0\rightarrow1$ transition of SbD_3, indeed, comes in the region around 85,000 Mc/sec or roughly three times the frequencies produced by the highest frequency reflex klystrons in general use at the end of the war. Techniques of employing the third harmonics of 11-mm klystrons, however, had been developed by Robert Kyhl while at this laboratory. It was first proposed to search for the $J=0\rightarrow1$ transition of SbD_3 by using these techniques. However, the available sensitivity ($\alpha\sim10^{-6}$) was such that, even with a pure sample of SbD_3 in the absorption cell, the lines would not have been seen if the dipole moment was a factor of two or more smaller than the hoped-for value of 0.5 Debye units.

With these facts in mind, calculations were begun on the variation of transition frequency with structure of the isotopic species SbD_2H and SbH_2D. These molecules fall in the class known as asymmetric tops, for which Cross, Hainer, and King[8] have tabulated the energy levels as a function of J, the two symmetry indices K_{-1} and K_{+1}, and κ, the asymmetry parameter. If one assumes that the bond angle is the same in all four isotopic species, and that the bond distance is not changed by substituting a deuterium for a hydrogen, then great simplification occurs in the calculation of κ. If the coordinate system is set up as in Fig. 1, the molecular dipole moment is along the z' axis, and one is interested in c-type transitions for small ϕ' and a-type for large ϕ'. Since there is no component of the dipole moment along the b axis, b-type transitions have zero intensity. If the energy of the asymmetric top is expressed as

$$E_{J\tau}=\tfrac{1}{2}(a+c)J(J+1)+\tfrac{1}{2}(a-c)E_\tau^J(\kappa),$$
$$a=h^2/2I_a,\quad b=h^2/2I_b,\quad c=h^2/2I_c,\quad \tau=K_{-1}-K_{+1},$$

and $\Delta J=0$ transitions are considered, then

$$h\nu=\tfrac{1}{2}(a-c)[E_\tau^J(\kappa)-E_{\tau'}^J(\kappa)].$$

The quantities $(a-c)/2$ and κ can be obtained as a function of θ from a graph such as that in Fig. 2. Consequently, the transition frequencies can also be plotted as a function of θ. With θ varying only from 90° to 100° possible transitions in the species SbD_2H vary in frequency from 0 to the order of 100,000 Mc, with κ going over almost the whole gamut of values. With SbH_2D, it is quite different, and the frequencies of the first few transitions for the lowest few J values have been plotted in Fig. 3 as a function of θ.

It can be seen that near 90° SbH_2D is an almost symmetric top but one with a dipole moment perpendicular to the symmetry axis. It may also be noted that while SbH_2D is an asymmetric top as determined by its mechanical moments, it is still charge-symmetric about the z' axis.

Since arsine and phosphine, from stability considerations, were likely impurities, the microwave spectra of AsH_2D and PH_2D were calculated and are shown in Figs. 4 and 5.

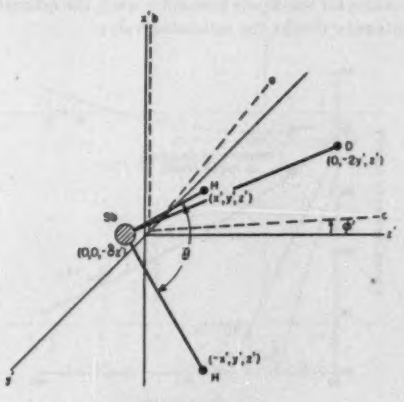

FIG. 1. Molecule-fixed coordinate systems.

[6] D. P. Stevenson, J. Chem. Phys. 8, 285 (1940).
[7] Durant, Pearson, and Robinson, J. Chem. Soc. 1934, 730 (1934).
[8] King, Hainer, and Cross, J. Chem. Phys. 11, 27 (1943).

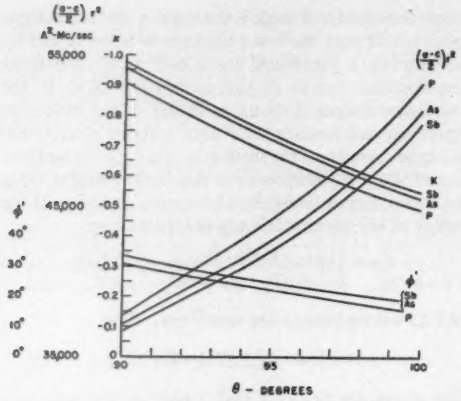

FIG. 2. Molecular parameters vs bond angle.

II. EXPERIMENTAL DATA

PH_2D

The sample (see Appendix 1), though supposedly pure stibine, yielded phosphine for a first fraction as indicated by the spectrometer. The $3_{03}\rightarrow 3_{13}$ line was found and identified by means of the Stark effect. The lack of any fine structure (± 2000 Mc/sec) indicated no quadrupole interaction and a single isotope. Since the transition frequency is such a rapid function of θ, the bond angle can be expressed in the following fashion:

$$\theta = 93.5° - 0.2°\Delta r,$$

Δr = deviation of bond length from 1.419A in 0.01A unit. This determination of θ suffices to determine κ and $(a-c)/2$ so that the dipole moment can be calculated from the Stark effect as 0.55 Debye unit. Furthermore, if this value for the dipole moment is used, the estimated line intensity checks the estimated value.

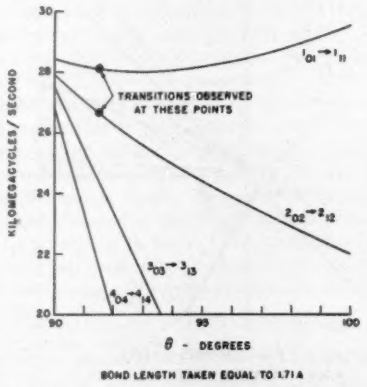

FIG. 3. Transition frequency vs bond angle, SbH_2D.

Following Stevenson's[8] original argument that s orbital stability increased with Z, the region of search for arsine and stibine transitions was thus materially reduced.

AsH_2D

By using the spectroscope to minitor the fractionation, the phosphine was removed from the sample. The next fraction then yielded absorptions due to arsine, AsH_2D. The observed pattern for the $3_{03}\rightarrow 3_{12}$ arsine transition is shown in Fig. 6. This absorption shows nuclear electric quadrupole structure, but, of course, no isotope structure.

The theory of quadrupole coupling in asymmetric tops has been worked out by Knight and Feld[9] and also by Bragg.[10] These authors show that the magnitude of the splitting of each level is a function of the diagonal terms of the dyadic ∇E_{zz} expressed in the coordinates appropriate to the principal axes of the top, and F, the vector sum of I and J. For $J \leqslant 3$ the notation of Bragg's second article[11] is convenient, since the reduced energy matrix can be diagonalized as an explicit function of κ. The theory will be illustrated for $J=1$, where it is particularly simple. In the usual notation:

$$W_{\text{quad}} = eQ\langle V_{zz}\rangle T(F),$$

$$\langle V_{zz}\rangle = \frac{1}{J(J+1)}\left\{V_{aa}\left[J(J+1)+E(\kappa)-(\kappa+1)\frac{\partial E(\kappa)}{\partial \kappa}\right]\right.$$

$$+2V_{bb}\frac{\partial E(\kappa)}{\partial \kappa}$$

$$\left.+V_{cc}\left[J(J+1)-E(\kappa)+(\kappa-1)\frac{\partial E(\kappa)}{\partial \kappa}\right]\right\},$$

$$E(\kappa)_{101} = \kappa - 1, \quad E(\kappa)_{111} = 0,$$

$$T(F) = \frac{\frac{3}{4}C(C+1)-J(J+1)I(I+1)}{2(2J-1)(2J+3)I(2I-1)},$$

$C = F(F+1)-J(J+1)-I(I+1)$, $Q = \langle 3z^2 - r^2\rangle$ nucleus,

substituting:

$$\langle V_{zz}\rangle_{101} = (V_{bb}+V_{cc}), \quad \langle V_{zz}\rangle_{111} = (V_{aa}+V_{cc}),$$

and using Laplace's equation,

$$\langle V_{zz}\rangle_{101} = -V_{aa}, \quad \langle V_{zz}\rangle_{111} = -V_{bb}.$$

In general, the coefficients of the V_{aa}, V_{bb}, V_{cc}, are functions of κ and do not come out as integers. The values which are appropriate for the $3_{03}\rightarrow 3_{12}$ transition

[9] G. Knight and B. T. Feld, R. L. E. Technical Report No. 123 (June 10, 1949) (unpublished).
[10] J. K. Bragg, Phys. Rev. **74**, 533 (1948).
[11] J. K. Bragg and S. Golden, Phys. Rev. **75**, 735 (1949).

in arsine are[12]

$$\langle V_{aa}\rangle_{3_{03}}=[0.907V_{bb}+1.0835V_{cc}],$$
$$\langle V_{aa}\rangle_{3_{13}}=[0.2388V_{bb}+1.2600V_{cc}].$$

Here $\kappa=-0.8625$; θ is 92.02°. θ has been fixed here by the fact that the structure of arsine was precisely determined by using the $1_{01}\rightarrow 1_{11}$ transition frequency.

At this point one could plot a number of patterns using different scales until some of the lines were identified, at which point the scales for the individual levels could be determined by taking differences. It is also possible, by using the charge symmetry of the molecule, to make a very good first guess. If we express the dyadic ∇E_{zz} in the $x'y'z'$ coordinate system of the charge-symmetric axes and then transform to the inertial axes, we get the following expressions:

$$V_{aa}=V_{y'y'}\cos^2\phi'+2V_{y'z'}\sin\phi'+V_{z'z'}\sin^2\phi',$$
$$V_{bb}=V_{x'x'},$$
$$V_{cc}=V_{y'y'}\sin^2\phi'-2V_{y'z'}\sin\phi'\cos\phi'+V_{z'z'}\cos^2\phi'.$$

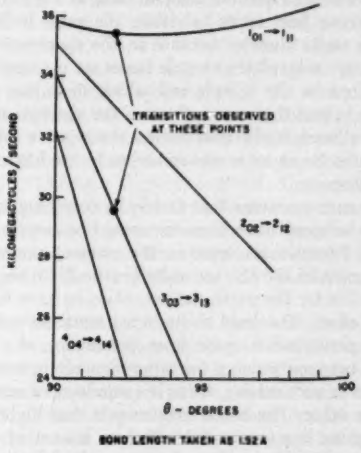

FIG. 4. Transition frequency vs bond angle, AsH_2D.

In the charge-symmetric coordinates the following relations among the elements of ∇E_{zz} obtain:

$$V_{x'y'}=V_{y'z'}=V_{x'z'}=0,$$
$$V_{x'x'}=V_{y'y'}=-\tfrac{1}{2}V_{z'z'}.$$

Reducing the equations for V_{aa}, V_{bb}, V_{cc}, to equations in terms of $V_{z'z'}$ and ϕ' gives

$$V_{aa}=-\tfrac{1}{2}(1-3\sin^2\phi')V_{z'z'},$$
$$V_{bb}=-\tfrac{1}{2}V_{z'z'},$$
$$V_{cc}=-\tfrac{1}{2}(1-3\cos^2\phi')V_{z'z'}.$$

When these values of V_{aa}, and V_{bb}, and V_{cc}, with ϕ' determined from the graph in Fig. 2, were substituted in

[12] Evaluation of $\langle V_{ss}\rangle$ for data reduction has been checked by exact diagonalization.

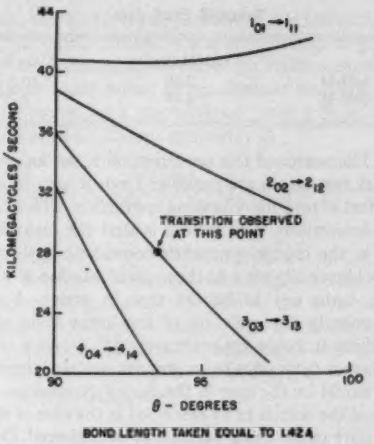

FIG. 5. Transition frequency vs bond angle, PH_2D.

expression for the splitting of the 3_{03} and the 3_{13} levels given above, the pattern which is shown in Fig. 6 resulted. When the center of gravity of the unresolved lines is used, the observed lines fit the theory to within the experimental error of ± 0.2 Mc/sec where $eQV_{z'z'}=-164$ Mc/sec.

As stated above, the $1_{01}\rightarrow 1_{11}$ transition was found and measured and the same transformation of the dyadic ∇E_{zz} applied here. If the angle, as fixed by the undeviated $3_{03}\rightarrow 3_{13}$ line and the undeviated $1_{01}\rightarrow 1_{11}$ line, is used as it was used to fix the pattern of the $3_{03}\rightarrow 3_{13}$ transition, there is a slight discrepancy between the measured and experimental values for the $1_{01}\rightarrow 1_{11}$ transition. This discrepancy can be eliminated by contracting slightly the amount by which the 1_{01} state is

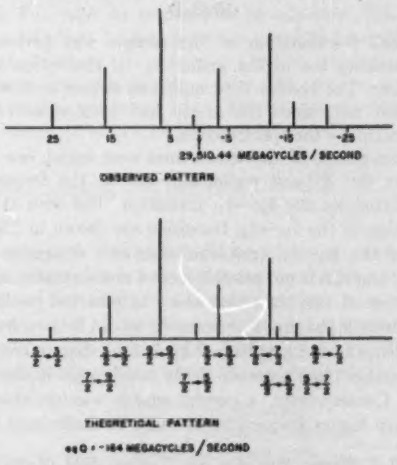

FIG. 6. The $3_{03}\rightarrow 3_{13}$ transition of AsH_2D.

TABLE II. Stark data.

	$\Delta\nu$(Mc/sec)	E(esu/cm)
AsH_2D	2.38	10.5
SbH_2D	4.49	9.79

split. The source of this perturbation is not known, but at least two causes are possible. First, it may be due to the effect of rotation-vibration interaction, which has not been determined. The second is that the cross derivatives in the charge-symmetric coordinate system may not be identically zero. At the angle of rotation $\phi'=29.2°$, which turns out to be the case in arsine, V_{aa} and consequently the splitting of the lower level are approaching 0, being approximately $\frac{1}{3}V_{x'x'}$. As a result a small cross derivative has a proportionately larger effect than would be the case in the $3_{03}\rightarrow3_{13}$ transition.

From the results to be described in the case of stibine, this latter cause seems perhaps to be preferred. One can express this adjustment in either of two ways. ϕ' can be changed from 29.2° to 30.0° with perhaps a change in the effective value of θ from 92.02° to 91.6°. On the other hand, if ϕ' is left unchanged at the value determined by the transition frequencies, $eQV_{x'x'}$ turns out to be 4.7 Mc/sec.

Finally, with the identification of the lines in the $3_{03}\rightarrow3_{13}$ transition of arsine, the Stark splitting of one component in an applied electric field may be measured and the dipole moment computed. The 9/2→9/2 transition, which is also the most intense, was selected and the data of Table II gives a dipole moment of 0.22±0.02 Debye unit, as compared with the value of 0.18 measured by the Debye method.[13] In order to reduce the data to a dipole moment the theory of Golden and Wilson[14] was used, with $J=3$ and $m_J=3$. The justification for this is given in Appendix 3.

SbH_2D

Final fractionation of the sample was performed by making use of the arsine $3_{03}\rightarrow_{13}$ absorption as a minitor. The residue then indicated stibine on a silver nitrate test, since the arsine had been removed as indicated by the spectroscope.

Two groups of absorption lines were found, one just above the K-band region and one at the frequency predicted for the $1_{01}\rightarrow1_{11}$ transition. The lines at the position of the $1_{01}\rightarrow1_{11}$ transition are shown in Fig. 7. Since the $1_{01}\rightarrow1_{11}$ transition does not determine the bond angle, it is not possible from a measurement of the position of this transition alone to plot the predicted quadrupole pattern. Furthermore, as can be seen from a reference to the graphs in Fig. 3, the other transitions fall rather close together if the bond angle is close to 90°. Consequently, a careful search was undertaken toward higher frequencies in order to make sure that there were no other observable lines. None were found within a region of 1500 Mc/sec above and none were found between 28,150 Mc/sec and 26,780 Mc/sec, the position of the next group of lines found below the $1_{01}\rightarrow1_{11}$. Assuming that no lines have been missed, these two groups are the $J=1$ and $J=2$ transitions, respectively; and they fix both the bond angle and the bond length.

It is important that the transitions found at 26,780 Mc/sec be assigned to the correct J value, since they fix the bond angle and therefore the expected quadrupole pattern for the $J=1$ level. Because of the complexity of the $J=2$ quadrupole pattern (there will be 13 lines due to each isotope, completely interlaced, since the isotope shift is of the order of 5 percent of the quadrupole splitting), it would be tedious to measure the frequency of each line and to make a careful estimate of its relative intensity. This is particularly true, since from a qualitative observation of the Stark splitting on each line it could be seen that these Stark components required a stronger field to split out than do those at $J=1$. The use of a strong field tends to vitiate the gains in line intensity made thereby because in the spectrometer as presently designed the electric forces set up mechanical vibrations in the sample cell which modulate the rf energy in just the same fashion as the absorption lines. Weaker Stark fields make useless the relative intensity estimates. Some other means had to be used to identify these lines.

One cannot assume that merely by searching over the region between these lines one would be certain to see the $J=2$ transitions (let us for the moment assume that the lines at 26,780 Mc/sec really are the $J=3$) because it is possible for the particular transition to have the zero Stark effect. The level shifts in a normal second-order Stark perturbation come from the mixing of the two states between which a transition is made in zero field; and, as in such mixing, there is a repulsion of each level by the other. The Stark frequency is thus higher than that of the line in zero field. If there is another energy level nearby to one of the levels involved in the zero-field transition, it also will be mixed in, in proportion to the dipole moment associated with a transition to that

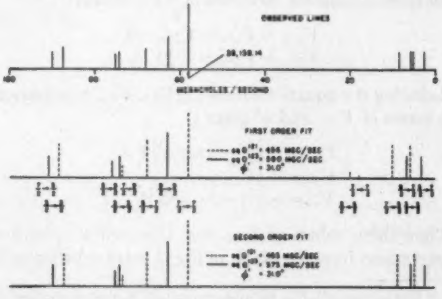

FIG. 7. $1_{01}\rightarrow1_{11}$ transition of SbH_2D.

[13] H. E. Watson, Proc. Roy. Soc. (London) A117, 43 (1927).
[14] S. Golden and E. B. Wilson, J. Chem. Phys. 16, 669 (1948).

level, and will tend to push the affected level away from it. It could, therefore, just cancel or if close enough, completely override the normal Stark effect. If there is no Stark effect, the spectrometer which depends on the Stark effect to modulate the intensity of the main line would detect no absorption. That such a situation could obtain in stibine can be seen from the fact that the level just above the upper of the two levels involved in the transitions desired is approximately 40 times closer to its lower neighbor than the state from which the transition is made.

In order to make sure that no lines have been missed because of the disappearance of the Stark effect, the lines found at 26,780 Mc/sec were tentatively assigned to $J=3$, and the Stark effect for $J=3$ and $J=2$ computed and compared. Assigning the lines to $J=3$ fixes the bond angle at 90.2°, ϕ' at 33.6°, and κ as -0.9677. Using these values, one finds that the Stark effect for $J=3$ and $J=2$ should be nearly equal but of opposite sign, with that for $J=2$ going toward lower frequency and that of $J=3$ going toward higher frequency. Although the Stark effect on the lines found at 26,780 Mc/sec goes toward higher frequency, the fact that the Stark effect on the $J=2$ lines is of the same magnitude makes certain that they would not have been missed in the search previously described. With the lines at 26,780 Mc/sec assigned to $J=2$, the structure of the stibine molecule is fixed at the following values: bond angle, 91.5°; bond length, 1.712A; ϕ', 31.0°; κ, -0.9530. Computing the Stark effect for the $J=2$ lines from these data gives Stark components going toward higher frequency, but a factor of ten less than that observed for the $J=1$ lines. This agrees with the qualitative observations reported above.

Having fixed the structure of the molecule as listed above, the expected quadrupole patterns for the two isotopes can be calculated by using the theory and transformations outlined in the section under arsine (AsH_2D). When this is done, the result is as shown in Fig. 7. It can be seen that the fit is good enough to identify all but one pair of the observed lines both as to isotope and as to F numbers. These patterns are computed for the expected spins of 5/2 and 7/2 for Sb^{121} and Sb^{123}, respectively; the fit is sufficiently good to verify these spin assignments. It can be seen, however, that the ratio of the quadrupole moments is more nearly unity and does not lie in the region of 4 as predicted from the previously published data.[15]

It was not found possible to fit the observed pattern within even a generous error merely by adjusting the magnitude of eqQ and the relative scales of the upper and lower states, as had been done in arsine. It became apparent from an examination of the pattern (by taking differences to determine level spacings) that the trouble was in the 1_{11} level and that an F dependent perturbation was necessary. Because the 1_{10} level is separated 677 Mc from the 1_{11} term compared with the transition frequency of 28,150 Mc/sec, it was immediately suspected. Bragg[16] has included at the end of his article a section on the higher order terms in quadrupole coupling. The matrix element for a perturbation from a level of the same J but of a different symmetry is

$$(J\tau F|H|J\tau' F)=eQ\frac{2J+3}{J}(J\tau J|\nabla E_{zz}|J\tau' J)T(F).$$

In the case of $J=1$, the splitting of each of the three levels is determined by a different diagonal member of ∇E_{zz} expressed in the inertial axes of the molecule. In particular the splitting of the 1_{11} is proportional to V_{bb} and the splitting of the 1_{10} is proportional to V_{cc}. The interaction between them is the average, as calculated by the usual methods,[9] is

$$\langle 2\alpha_{bb}\alpha_{cc}\rangle V_{bc}=3V_{bc}/10.$$

If the cross derivatives are expressed in terms of the charge-symmetric coordinates, they are

$$V_{bc}=V_{x'x'}\cos\phi'-V_{x'y'}\sin\phi',$$
$$V_{ab}=V_{x'y'}\cos\phi'-V_{x'x'}\sin\phi',$$
$$V_{ac}=(V_{y'y'}-V_{x'x'})\sin\phi'\cos\phi'+V_{y'x'}(\sin^2\phi'-\cos^2\phi')$$
$$\simeq-\tfrac{3}{2}V_{x'x'}\sin\phi'\cos\phi'.$$

In originally making the transformation of $\nabla E_{x'x'}$, the cross derivatives in the charge-symmetric system had been assumed to be zero, under the same assumption V_{bc} and V_{ab} would also be zero. V_{ac}, on the other hand, would be quite as large as the diagonal terms. Fortunately, it involves an interaction between the two states which are farthest apart and when calculated turns out to shift the levels by 0.1 Mc or less, which is within the present experimental error.

In order to explain the observed distortion of the 1_{11} level, V_{bc} must be assumed to be non-zero. This assumption is not quite as arbitrary as might first appear because there are two isotopes in identical molecules and therefore any alterations made in the pattern of one must also appear in the other. The quadrupole interaction energy of the 1_{11} level is now expressed as

$$W_{111}\,(\text{quad})=-eV_{bb}QT(F)-\frac{[\frac{1}{2}eV_{bc}QT(F)]^2}{W_{1_{10}}{}^{(0)}-W_{1_{11}}{}^{(0)}}.$$

The changes in the 1_{11} level which are necessary to bring the observed lines into agreement with theory are computed separately for each isotope; their ratio must be as the ratio of the Q's, which can be determined to better than one percent from first-order theory. When this is done, the following results are obtained:

$$[Q^{123}/Q^{121}]^2=1.60\pm0.01,$$
$$eQ^{123}V_{bc}=7.0\pm0.5\text{ Mc/sec},$$
$$eQ^{121}V_{bc}=5.8\pm0.4\text{ Mc/sec},$$
$$[eQ^{123}V_{bc}/eQ^{121}V_{bc}]^2=1.4\pm0.2.$$

[15] K. Murakawa and S. Suwa, Phys. Rev. 76, 433(L) (1949).

TABLE III. Molecular structure.

	Observed		Infrared	Estimate[b]	
	r	θ	θ	r	θ
Phosphine	1.419A[a]	93.5°	99.0°	1.42A	93°
Arsine	1.523A	92.0°	97.5°	1.53A	90°
Stibine	1.712A	91.5°		1.73A	90°

[a] Infrared determination of I_b for PH_3 was used to fix r and θ (reference 6).
[b] Reference 3.

It can be seen that while the errors are large, the assumption of finite cross derivatives is not disqualified. The resulting pattern is shown in Fig. 7.

Having fixed the identity of all the lines in the pattern associated with $J=1$ transition, the dipole moment of the stibine molecule was determined by making measurements on the $7/2 \rightarrow 7/2$ line of Sb^{121}. The data of Table II gives a dipole moment of 0.116 ± 0.003 Debye unit. Again, as in arsine, the theory of Golden and Wilson[14] was applied with $J=1$ and $m_J=1$; the outermost component only was measured. Had this been a normal second-order Stark effect the splitting at the field quoted above would have been of the order of 0.5 Mc/sec. The nearness of 1_{10} level increases the accuracy with which the dipole moment can be determined, from ± 20 percent to the quoted ± 3 percent.

III. DISCUSSION

Molecular Structure

The structure parameters determined in the investigation just described are those numbers which, when fitted into the rigid rotor approximation, give the observed frequencies. Since, at the most, only two groups of lines are measured for each molecule, the system is determined; and the accuracy of the determination is apparently limited only by the measurement of the frequencies. Although the accuracy of frequency measurement is of the order of 1 part in 10^6, the assignment of such accuracy to the structure parameters would be meaningless outside of the particular transition on which they were measured. While not evaluated in this investigation, several known effects may be pointed out which limit the accuracy of the structure determination.

Because these molecules are so light, rotationally speaking, the energy associated with even a low value of angular momentum is high. Consequently, the distortion of the molecule by the rotational motion can be expected to be large. From observations made on such molecules as HDS[22] the effect can be estimated to be of the order of 10 Mc/sec at $J=1$, thus reducing the meaningfulness to 1 part in 10^3. No account, furthermore, has been taken of the zero-point vibrations and in particular of the effect of the one deuterium on the assumption of equal angles and radii. In consideration of the above, it was not felt reasonable to quote the structure to more than three significant figures. See Table III.

The absence of any structure due to inversion doubling must also be taken to mean that the ground-state inversion vibration frequency in all three molecules is less than the line width, about one-half a megacycle.[16]

Dipole Moments

The accuracy of dipole moment determinations by the methods of microwave spectroscopy is ordinarily limited by the precision with which the applied electric field can be measured. In the investigation described above, all the dipole moments were sufficiently small to make the errors quoted those of the frequency measurement. See Table IV.

The previous measurements quoted were all made by Watson,[13] with the spread of the readings indicating the accuracy. It may roughly be said that the use of capacity and temperature techniques at present is limited to dipole moments of 0.5 Debye unit or greater. Consequently, the disagreement shown above with the previously measured value for arsine is not serious. Watson was unable to measure stibine because of its instability.

Quadrupole Coupling

From the fitting process as applied to the antimony pattern, it can be seen that the value of eqQ can be determined to a percent without considering the second-order corrections. The principal reason for the accuracy is that the spread of the pattern is of the order of 100 to 1000 times the error in measuring the frequency. The second-order corrections are, of course, small and nearly symmetrical about the undeviated line. Because the values quoted refer to the charge-symmetry axis of the molecule, the absolute accuracy of an individual determination is only as good as one believes the transformation applied. The ratio of the moments as determined for antimony, however, is independent of this transformation. This ratio, furthermore, is not affected by corrections such as that of approximately 3 percent applied to the ground state of the $J=1$ transition in arsine.

If the transformations are taken as justified the values in Table V are obtained for the various quadrupole couplings in arsine and stibine. It is to be noted that the sign of eqQ changes from arsenic to antimony as expected from the signs of their respective Q's.

TABLE IV. Electric dipole moments.

	Debye units	
	Observed	Previous[a]
Phosphine	0.55 ± 0.01	0.54, 0.56
Arsine	0.22 ± 0.02	0.13, 0.18
Stibine	0.116 ± 0.003	

[a] Reference 13.

[16] Sutherland, Lee, and Wu, Trans. Faraday Soc. **35**, 1373 (1939).

The column headed eQV_{zz} was included as a cautionary measure; these values were not used in the pattern-fitting process. No one, apparently, has considered the possibility that these cross derivatives might be substantial. Consequently, this particular one, which can easily be calculated and is seen to be of the same order of magnitude as that of the diagonal terms, has been displayed. Bragg,[16] although mentioning the possibility of their existence, adds that they probably are nearly zero. Bardeen and Townes[17] have applied second-order corrections from levels of different J values to the quadrupole pattern associated with the $J=3\rightarrow4$ transition in ICN, $K=0$ means the ground vibrational state, while $K=1$ refers to the bending mode, which also produces l-type doubling of the spectral lines. While the theory and the observed lines were in good accord for the ground vibrational state, in the case of $K=1$ the authors mention small unexplained discrepancies. In calculating the theoretical pattern, the authors take into account the substantial perturbations of the levels whose J values differ by ±1 and ±2 and which lie approximately 25,000 Mc away; but apparently they consider the symmetry of the electric field too high for the l doubled levels lying approximately 20 Mc/sec apart to affect each other.

The fact that different corrections are applied to the $J=1$ transitions of arsine and stibine is a discrepancy which needs comment. That the second-order correction, as applied to stibine, is probably too small to be detected in arsine can be seen by taking the following ratios, all derived from the formula for the second-order correction displayed above:

$$(\text{Stibine correction})\ \frac{(eqQ)_{As}^2}{(eqQ)_{Sb}^2}\frac{\Delta W_{Sb}}{\Delta W_{As}}\frac{T(F)_{As}^2}{T(F)_{Sb}^2}$$

$$(\sim 2\ \text{Mc/sec})\ \frac{164^2}{575^2}\frac{770}{2670}\frac{0.250^2}{0.143^2}=0.14\ \text{Mc/sec}.$$

This is smaller than the experimental error of ±0.2 Mc/sec.

No such ratio can explain away the correction applied to the 1_{01} state in arsine, and one is left with the following rationalization. The existence of the cross derivatives depends on the lack of symmetry of the molecular electric field, which is actually surprisingly symmetrical considering the fact that one of the hydrogens in the completely symmetric SbH_3 has been replaced by an atom which is twice as heavy. The increase in bond angle from stibine to arsine with its attendent enhancement of the inertial asymmetry may, therefore, be just sufficient to raise the electric asymmetry to the measureable point.

Quadrupole Moments

Using the ratio of the Q's which has been determined above, the value of the quadrupole moment of one isotope can be determined from the other. Which isotope to select as a standard is a moot question. The quadrupole moments of antimony have been determined from optical spectra by the following method. Tomboulian and Bacher[18] published data on the hyperfine structure of a transition in SbII which they had observed, but they declined to identify the transition. Murakawa and Suwa[15] remeasured a transition previously identified by Badami and from these measurements deduced the value $-0.3\pm0.2\times10^{-24}$ cm^2 for the quadrupole moment Sb^{121}. By identifying the transition reported by Tomboulian and Bacher, Murakawa and Suwa calculate the quadrupole moment of Sb^{123} to be $-1.2\pm0.2\times10^{-24}$ cm^2. The ratio of these two moments is 4 or by taking the maximum error for each it can be reduced to 2, but not to 1.26.

The quadrupole moment of Sb can be calculated by still another method, that suggested by Townes and Dailey,[19] in which a value of $V_{x'x'}$ for a p electron is calculated from atomic data, and the number of contributing p electrons is estimated from the observed structure of the molecule concerned. While no great accuracy is claimed for this method, an attempt can be made to improve all the approximations by comparing the results obtained through incorporation of the same nucleus in several different molecules. In the case of antimony this is not possible, but by the following roundabout path a similar ruse can be used. Iodine, which has only two more protons than antimony, has been measured in several molecules; and its quadrupole moment has been measured from optical spectra. The contributing structures have been analyzed by Townes and Dailey,[19] so that by using the known value of the quadrupole moment one can obtain an estimate of $V_{x'x'}$ for iodine. This can then be converted to antimony by multiplying by the ratio of their effective $Z_{eff}^4=(Z-4)^4$. This figure is on a per-p electron basis. In order to estimate the effective number of p electrons causing the nonspherical field at the nucleus in such a nearly spherical field as must prevail in stibine, use can be made of the fact that arsenic in AsF_3 has been measured and analyzed by Townes and Dailey[19] (see Table VI).

For iodine the average eqQ per p electrons is 2500

TABLE V. Quadrupole coupling constants.

	$eQV_{x'x'}$	$eQV_{y'y'}$	eQV_{bb}	eQV_{aa}
$As^{75}H_2D$	−164	−4.7	<10	105
$Sb^{121}H_2D$	455	<1	±5.8	−302
$Sb^{123}H_2D$	575	<1	±7.0	−381

Units: Mc/sec

	observed	previous[a]
$\frac{Q(Sb^{123})}{Q(Sb^{121})}=$	1.263	~4

[a] Reference 15.

[16] D. H. Tomboulian and R. F. Bacher, Phys. Rev. 58, 52 (1940).
[17] J. Bardeen and C. H. Townes, Phys. Rev. 73, 627 (1948).
[18] D. H. Tomboulian and R. F. Bacher, Phys. Rev. 58, 52 (1940).
[19] C. H. Townes and B. P. Dailey, J. Chem. Phys. 17, 782 (1949).

TABLE VI. Arsenic quadrupole coupling constants.

Molecule	θ	eqQ	No. of p electrons contributing
AsF_3	100°	−235 Mc/sec	−0.4
AsH_2D	92.0°	−164 Mc/sec	−0.28

Mc/sec. If the quadrupole moment is taken[6] as $0.46 \pm 0.15 \times 10^{-24}$ cm², then eq for iodine is 5.4×10^{2} Mc/sec-cm². The ratio of the effective Z_{eff}[4] is 0.847 giving a value of eq for antimony of 4.6×10^{27} Mc/sec-cm². The number of contributing p electrons will certainly not be greater than in arsenic, so that, using the value 0.28, one gets a lower limit. An upper limit may be obtained by assuming that the number of contributing p electrons decreases linearly with θ from the value obtained for arsenic, certainly an outside guess, since the number has increased only to 0.4 at 100°.

The error in the estimates, Table VII, must be at least of the order of 50 percent; but even so the agreement with the optical value of Sb^{121} is astonishingly good.

Finally, one might make the comparison suggested by Gordy.[2] He has pointed out the empirical fact that the ratio of the magnetic moments of two isotopes is nearly the same as that of their quadrupole moments, and that the sense of the ratio depends upon whether the sign of the quadrupole moments is positive or negative. Fortunately, the magnetic moments of the antimony isotopes have recently been measured in two separate places[20,21] and identical answers were obtained.

$$\frac{Q(Sb^{121})}{Q(Sb^{123})}=\frac{-455}{-575}=0.791, \quad \frac{\mu(Sb^{123})}{\mu(Sb^{121})}=1.3191$$

for negative Q's:

$$\mu_1 Q_2/\mu_2 Q_1 = 0.791 \times 1.3191 = 1.043.$$

The average of the examples given by Gordy was 1.12. Townes[5] takes issue with this observation but principally with the extension of the idea by Gordy to predict the quadrupole moments of elements of both different Z and N.

The existence of the isotopic species of molecule SbD_2H and AsD_2H might be pointed out again now that the structure of stibine and arsine are known. While the search for the transitions in these molecules analogous to the ones described in this investigation would have been tedious indeed, it is now a relatively simple task. The usefulness of these molecules lies in two places. First of all, the apparent structure as determined from the microwave measurements will be interesting to compare with that obtained above. Second, the inertial symmetry of these molecules is sufficiently different to make possible the determination, perhaps, of more of the electric field structure than was possible in this investigation alone.

The spectrometer used for this work has been described previously.[22] A table of observed absorptions is given in Table VIII.

TABLE VII. Estimated antimony electric quadrupole moment (units of 10^{-24} cm²).

	Upper	Lower	Previous
Sb^{123}	−0.62	−0.45	−1.2±0.2
Sb^{121}	−0.50	−0.35	−0.3±0.2

TABLE VIII. Observed transition frequencies.

		ν(Mc/sec)	$\alpha(10^{-4}$ cm$^{-1})$
$Sb^{121}H_2D$	5/2→3/2	28,187.74	1.28
	3/2→3/2	unresolved	0.55
$1_{01}\rightarrow 1_{11}$	5/2→7/2	28,168.04	1.31
	7/2→7/2	28,158.14	2.35
	5/2→5/2	unobserved	0.16
	7/2→5/2	28,108.55	1.31
	3/2→5/2	28,105.28	1.28
$Sb^{123}H_2D$	7/2→5/2	28,190.15	1.05
	5/2→5/2	28,175.07	0.57
	7/2→9/2	28,174.48	1.05
$1_{01}\rightarrow 1_{11}$	9/2→9/2	28,162.78	1.65
	7/2→7/2	unobserved	0.07
	9/2→7/2	28,105.80	1.05
	5/2→7/2	28,102.66	1.05

$2_{02}\rightarrow 2_{12}$ lines for $Sb^{123}H_2D$ and $Sb^{121}H_2D$ were observed at 26,780 Mc/sec. α was computed for 100 percent abundance of xH_2D. In this investigation all the values of α should be multiplyed by 0.4.

		ν(Mc/sec)	$\alpha(10^{-4}$ cm$^{-1})$
AsH_2D	1/2→3/2	35,460.08	1.73
	5/2→3/2	35,455.64	1.87
$1_{01}\rightarrow 1_{11}$	3/2→3/2	35,450.51	0.55
	5/2→5/2	35,435.19	4.37
	3/2→5/2	35,430.10	1.87
	1/2→1/2	unobserved	0.35
	3/2→1/2	35,413.79	1.73
	9/2→7/2	29,545.05	1.55
	5/2→7/2	29,539.38	2.00
	3/2→5/2	unresolved	1.48
$3_{03}\rightarrow 3_{13}$	7/2→7/2	29,535.30	11.31
	5/2→5/2	29,526.69	7.65
	7/2→5/2	29,522.64	2.00
	9/2→9/2	29,516.96	17.00
	3/2→3/2	29,507.91	5.93
	7/2→9/2	unresolved	1.55
	5/2→3/2	29,498.52	1.48
		ν(Mc/sec)	$\alpha(10^{-4}$ cm$^{-1})$
PH_2D	$3_{03}\rightarrow 3_{13}$	28,157.72	4.44

APPENDIX 1. PREPARATION OF SAMPLE

The stibine was prepared as follows. An alloy of 80 percent magnesium, 20 percent antimony was powdered and placed in a reaction flask which was connected through a trap at dry-ice and acetone temperature (to remove water vapor) to the sample-collecting trap held at liquid nitrogen temperature. The appro-

[20] W. G. Proctor and F. C. Yu, Phys. Rev. 78, 471 (1950).
[21] Cohen, Knight, and Wentink, Phys. Rev. 79, 191 (1950).
[22] Weiss, Strandberg, Lawrance, and Loomis, Phys. Rev. 78, 202 (1950).

priate acid (DCl for SbD_3 or a mixture of DCl and HCl for SbH_2D) was dripped slowly on the powder. The gas generated was swept gently along with dry nitrogen.

The alloy was prepared by placing the powders in a carbon crucible and heating to a bright-red heat in a hydrogen atmosphere. Antimony sublimes before magnesium melts, so that this heating must be done quickly.

The pure DCl was prepared by collecting the gas given off by the constant boiling mixture of D_2O and P_2O_5 in excess NaCl.

APPENDIX 2. STARK EFFECT IN ASYMMETRIC TOPS WITH QUADRUPOLE COUPLING

The general formulation of the problem for diatomic and linear molecules has been given by Fano,[23] and the extension to symmetric and asymmetric tops is immediate. The calculation in any particular case, however, is tedious, even for a diatomic molecule. For the purpose of the present investigation, the exact position of all of the Stark components is of little consequence, since the only information desired is the dipole moment of the molecule. Because the transitions under consideration above are all $\Delta J=0$, there is one particular Stark component whose position can be calculated with ease by using the published line-strength tables of Cross, Hainer, and King.[24] How this comes about can be seen by considering the general Stark problem.

The general problem is that of calculating the matrix elements of the direction cosines of the molecule-fixed dipole moment to the space-fixed electric field axis. The possibility of accidentally degenerate states will be ignored since it did not happen to occur; consequently there will be no first-order Stark effect. The second-order energy shift of the ith state caused by the mixing of the ith and the jth states is as follows:

$$W_i^{(2)}=\sum_{i\neq j}\frac{|\int\psi_i^*\boldsymbol{\mu}\cdot\mathbf{E}_s\psi_j dV^3|}{W_i^{(0)}-W_j^{(0)}}.$$

If

$$\boldsymbol{\mu}\cdot\mathbf{E}_s=\mu E_s\Phi,$$

then

$$W_i^{(2)}=\mu^2E_s^2\,\Sigma'\frac{|(i|\Phi|j)|^2}{W_i^{(0)}-W_j^{(0)}},$$

and the problem is that of finding a representation in which it is convenient to evaluate the direction cosine elements.

If one of the nuclei in the molecule has a quadrupole moment, it may be coupled to the molecular rotation by the gradient of the molecular electric field at the position of the nucleus. For small coupling energies, $eqQ\ll a$, b, c, (in stibine $eqQ\simeq 10^{-4}$ a, b, or c) the total angular momentum of the molecule F can be considered as the vector sum of two components I and J, the nuclear spin angular momentum and the molecular rotational angular momentum, respectively. The projection of F on a space-fixed axis will be a good quantum number M_F; but because of the coupling now considered, m_I and m_J need not be good quantum numbers. The Stark components whose positions are desired will be characterized by M_F.

It is convenient to expand the wave function in terms of the zero-order wave functions, i.e., those associated with no quadrupole coupling. If there is no coupling, the wave equation must be separable and the zero-order functions are of the following form:

$$\psi(J, m_J)\phi(I, m_I).$$

When F and M_F are the good quantum numbers, each state will be described by a sum of terms each of which is compatible with the F and M_F to be described. The number of terms in each series will be determined by the number of ways the state can be constructed. For $F<J+I$ there may be several terms in the series for each F and M_F.

There is one state whose description is limited to one term. This is the state for which $F=J+I$ and also $M_F=I+J$. For this one state it is sufficient to apply existing theory of the Stark effect in asymmetric tops using the J, M_J representation associated with this one state. In the case of $\Delta J=0$ there is an allowed transition between two states, both of which lend themselves to this simple description. Furthermore, the spectral line associated with this particular transition is the most intense of the pattern. It is on the outermost Stark component of this line, labelled by $F_{max}\rightarrow F_{max}$ in the patterns in Figs. 6 and 7, that the measurements to determine the dipole moment of each molecule were made.

[23] U. Fano, Dept. of Commerce Res. Paper RPI-866, 40 (1948).
[24] Cross, Hainer, and King, J. Chem. Phys. 12, 210 (1944).

Radiative Processes in the Presence of Heavy Nuclei

G. PARZEN
Institute for Nuclear Studies, University of Chicago, Chicago, Illinois
(Received September 15, 1950)

Calculations of the cross sections for bremsstrahlung and pair production are carried out without the use of the Born approximation, but by reducing the calculation of these cross sections to the calculation of the exact elastic scattering of electrons and positrons, the last quantities having been tabulated to some extent. Large deviations from the Born approximation results are obtained in the angular distributions of these radiative processes, but arguments are presented that the Born approximation should yield the integrated cross sections correctly at sufficiently high energies. The failure of the Born approximations for relativistic equations is explained in a purely classical way.

I. INTRODUCTION

IT is known that for radiative processes like bremsstrahlung and pair production in the presence of heavy nuclei, the application of the Born approximation may lead to some error. Exact calculations are very difficult to perform. However, it may be possible to express the cross sections for these processes in terms of the exact elastic scattering cross sections for a coulomb field, which has been tabulated to some extent. This idea is suggested by the usual perturbation calculation whereby the process is visualized as taking place in two steps, one of which is the scattering of the electron by the nucleus. In the following it is shown that this idea can be carried through in the high energy limit, and the calculation of the cross section for these radiative processes is reduced to the calculation of the electron and positron scattering amplitudes.

The results show rather large deviations from the Born approximation expressions for the angular distribution of these processes at the larger angles, but small deviation at the smaller angles where these processes are concentrated. Thus, the corrections to the integrated cross sections (that is, integrated over the angles) are small.

II. THE HIGH ENERGY WAVE FUNCTION

It has been observed that for the scattering of electrons in the presence of heavy elements, it is not correct to apply the Born approximation to the Dirac equation. It has also been pointed out,[1] by investigating the behavior of the phase shifts at high energies, that this breakdown of the Born approximation is not peculiar to the coulomb field, but occurs whenever the potential is strong enough, and is an effect characteristic of relativistic equations.

We shall show that the failure of the Born approximation can be understood and can be corrected, at least theoretically, in a purely classical way. Let us consider a very high energy particle incident in the z direction with velocity v being scattered by a potential $V(\mathbf{r})$ that has no pole. The particle is given a transverse momentum Δp perpendicular to the direction of incidence. If the energy is high enough, we may assume the path of the particle to be almost a straight line parallel to the Z axis. If the particle enters at a distance ρ from the Z axis, then its transverse momentum when it reaches the point (z, ρ) is given by,

$$\Delta p = -\int_{-\infty}^{z} (\partial V/\partial \rho) dt = -(\partial/\partial \rho)(1/v)\int_{-\infty}^{z} V(\rho, z)\cdot dz, \tag{1}$$

where in the integration, $V = V(\mathbf{r}) = V(\rho, z)$, $r = (\rho^2+z^2)^{\frac{1}{2}}$ and the variable ρ is held constant.

Now if the particle is nonrelativistic, as the energy increases, $v \to \infty$ and $\Delta p \to 0$; that is to say, the particle spends so little time near the scatterer that it gets no transverse momentum at all. However, if the particle is relativistic, then as the energy increases, $v \to c$ and the transverse momentum approaches the definite value of

$$\Delta p = -(1/c)\int_{-\infty}^{z} (\partial V/\partial \rho) dz. \tag{2}$$

This has the consequence that the wave function of the relativistic particle, forgetting for the moment the spin variable, cannot approach the form $\exp(ikz)$ at high energies, for this does not give the correct transverse momentum, which can be large if the potential is sufficiently strong. Instead, the wave function will have the form,

$$\psi \underset{k\to\infty}{\to} e^{i(kz+u)}, \tag{3a}$$

u being a function which is independent of the momentum $\hbar k$. If we choose u as given by

$$u = -(1/\hbar c)\int_{-\infty}^{z} V(\rho, z)\cdot dz, \tag{3b}$$

then the expectation value of Δp calculated from ψ will agree with Eq. (2).

We now obtain the result indicated by Eq. (3) more formally. Let us treat at first, a particle which obeys

[1] G. Parzen, Phys. Rev. 80, 355 (1950).

the Klein-Gordon equation,

$$(\nabla^2+k^2-2EV+V^2)\psi=0, \tag{4}$$

where we put $\hbar=c=1$. Let $\psi=\exp[i(kz+u)]$, then we get the equation for u,

$$i\nabla^2u-\text{grad}^2u-2k(\partial u/\partial z)-2EV+V^2=0. \tag{5}$$

We now assume an expansion for u in inverse powers of k,

$$u=u_0+u_1+u_2+\cdots, \tag{6}$$

where u_0 is independent of k, u_1, of order $1/k$, etc. Collecting the lowest power of $1/k$, we get

$$\partial u_0/\partial z=-E\cdot V/k, \tag{7}$$

so that neglecting terms of order $1/k$, we can write,

$$\psi=e^{i(kz+u)}, \quad \partial u_0/\partial z=-V, \tag{8}$$

and

$$u_0=-\int_{-\infty}^{z}V(\rho,z)\cdot dz,$$

where ρ is held constant in the integration. Equation (8) agrees with Eq. (3), if it is remembered that $\hbar=c=1$.

The form of a Dirac wave function at high energies can be obtained by a similar procedure. We write ψ as $\psi_\lambda=a_\lambda\exp[i(kz+u_\lambda)]$, $\lambda=1, 2, 3, 4$, where the a_λ are constants, and substitute in the iterated Dirac equation,

$$(\nabla^2+k^2-2EV+V^2)\psi=i(\alpha\cdot\text{grad}V)\psi. \tag{9}$$

If we expand a_λ and u_λ in powers of $1/k$,

$$\begin{aligned}a_\lambda&=a_\lambda{}^{(0)}+a_\lambda{}^{(1)}+\cdots\\ u_\lambda&=u_\lambda{}^{(0)}+u_\lambda{}^{(1)}+\cdots,\end{aligned} \tag{10}$$

then collecting the lowest power of $1/k$ gives

$$a_\lambda{}^{(0)}[(\partial u_\lambda{}^{(0)}/\partial z)+(EV/k)]=0. \tag{11}$$

For a plane wave in the z direction, with the spin in the $+z$ direction, when $k\to\infty$, the a_λ are given by

$$a_{k0}=\frac{1}{\sqrt{2}}\begin{bmatrix}1\\0\\1\\0\end{bmatrix}; \tag{12}$$

then the solution of Eq. (11) with the correct limiting form is

$$\psi=a_{k0}\exp[i(kz+u_0),$$
$$\partial u_0/\partial z=-V,$$

and

$$u_0=-\int_{-\infty}^{z}V(\rho,z)\cdot dz. \tag{13}$$

III. SOME EXAMPLES OF THE HIGH ENERGY WAVE FUNCTION

Let us consider the gaussian potential $V=V_0\times\exp[-\alpha^2(\rho^2+z^2)]$, then

$$u_0=-V_0\exp(-\alpha^2\rho^2)\cdot\int_{-\infty}^{z}\exp(-\alpha^2z^2)\cdot dz. \tag{14}$$

The phase surfaces of ψ given by $kz+u_0=$constant are no longer plane surfaces, but have a slight curvature near the Z axis, bulging out in $+Z$ direction for a repulsive potential and in the $-Z$ direction for an attractive potential. If we imagine the path of the particle to be perpendicular to these phase surfaces, the curvature of the surfaces will cause the path to deviate from a straight line showing the transverse momentum of Eq. (2).

Let us now consider the coulomb potential $V=Ze^2/(\rho^2+z^2)^{\frac{1}{2}}$. From $\partial u_0/\partial z=-V$, we get,

$$u_0=Ze^2\ln r(1-\cos\theta). \tag{15}$$

This will be recognized as the usual distortion of the plane wave obtained in coulomb scattering. In the derivation of Eq. (15), the indefinite integral was taken as the definite integral diverges. However, Eq. (15) does not give the entirely correct behavior of the coulomb wave function at high energies. Where our derivation breaks down can be easily seen from the classical treatment, where we assumed the path of the particle at high energies to be a straight line. The deviation of the path from a straight line for large impact parameters can be avoided by screening the coulomb field; but since the coulomb field has a pole at the origin, then no matter how high the energy, near the origin the field is strong enough to curve the particle path. We also know from the exact solutions of the Dirac equation for the coulomb field that the wave function has a singularity at the origin which Eq. (15) has not. The error in our power series expansion in $1k$ of ψ probably lies in omitting the higher order terms which, though they go to zero for increasing k, have a singularity at the origin and are not negligible. Thus, we can say that Eq. (15) will represent the wave function well at large distances but not near the origin. The validity of Eq. (15) will be discussed further in Sec. V.

IV. SOME CHECKS OF THE HIGH ENERGY WAVE FUNCTION

As a test of the wave function given by Eq. (3), we can consider what it means in terms of the phase shifts. Let us treat the simpler Klein-Gordon wave function in a central field. We expand ψ in spherical harmonics,

$$\psi=\sum i^l(2l+1)\cdot e^{i\delta_l}\cdot R_l(r)\cdot p_l(\cos\theta), \tag{16}$$

where $R_l(r)$, the radical part of the wave function, has the asymptotic form,

$$R_l(r)\to(kr)^{-1}\cos[kr-\tfrac{1}{2}(l+1)\pi+\delta_l]. \tag{17}$$

Using the orthogonality property of $p_l(\cos\theta)$, we get

$$2\cdot i^l\cdot e^{i\delta_l}R_l(r)=\int_0^\pi e^{i(kr\cos\theta+u)}\cdot p_l(\cos\theta)\sin\theta\cdot d\theta. \quad (18)$$

Now let $r\to\infty$ in Eq. (18) and integrate the right side by parts, dropping terms of higher order than $1/r$, then,

$$2\cdot i^l\cdot e^{i\delta_l}(kr)^{-1}\cdot\cos(kr-\tfrac{1}{2}(l+1)\pi+\delta_l)$$
$$=(ikr)^{-1}e^{i[kr+u(0)]}-(-)^l e^{i[-kr+u(\pi)]}, \quad (19)$$

and thus we get for the phase shifts,

$$\delta_l=-\int_0^\infty V(r)\cdot dr. \quad (20)$$

It has been shown[2] that the phase shift δ_l approaches the quantity $\delta_\infty=-\int_0^\infty V\cdot dr$ when $k\to\infty$. Equation (20) shows that the use of our approximate wave function is in agreement with this result.

Another test is to consider the value of the wave function at the origin. According to Eq. (3),

$$\psi(0)=\exp\left(-i\int_{-\infty}^0 V\cdot dz\right), \quad (21)$$

and as

$$-\int_{-\infty}^0 V\cdot dz=-\int_0^\infty V\cdot dr=\delta_\infty,$$

then

$$\psi(0)=\exp(i\delta_\infty). \quad (22)$$

The mathematics will not be gone into here, but we can show that when $k\to\infty$, $\psi(0)$ does approach $\exp(i\delta\infty)$ if the potential function has no pole at $r=0$.

V. THE EXPRESSION FOR THE SCATTERING CROSS SECTION

For the Dirac equation, the scattering amplitude is given, in relativistic units $\hbar=c=1$, by[1]

$$f(\theta)=(E-\alpha\cdot\mathbf{k}-\beta m)\cdot\int\exp(-i\mathbf{k}\cdot\mathbf{r})\cdot V\cdot\psi\cdot d\tau. \quad (23)$$

Putting $\psi=a_{\mathbf{k}_0}\exp(i\mathbf{k}_0\cdot\mathbf{r})$, a plane wave in the $\mathbf{k}_0$ direction, in Eq. (23) yields the Born approximation, which gives $f(\theta)$ correct to first order in V. However, there are terms which are of higher order in V but do not decrease with increasing energy. That is to say, the Born approximation is the first term in an expansion in V and not in $1/k$, so that it is not correct even at very high energies if the potential is strong enough.

If we substitute the wave function given by Eq. (13) into Eq. (23), we should get an expression which is correct at high energies,

$$f(\theta)=(E-\alpha\cdot\mathbf{k}-\beta m)\cdot a_{\mathbf{k}_0}$$
$$\cdot\int\exp(-i\mathbf{k}\cdot\mathbf{r})\cdot V\cdot e^{i(kz+u)}\cdot d\tau; \quad (24)$$

and the cross section for an unpolarized beam is given by,

$$\sigma(\theta)=E^2(1-v^2\sin^2\tfrac{1}{2}\theta)\cdot|F|^2,$$

where

$$F=(2/4\pi)\cdot\int\exp(-i\mathbf{k}\cdot\mathbf{r})\cdot V\cdot e^{i(kz+u)}\cdot d\tau \quad (25)$$

and

$$u=\int_{-\infty}^z V(\rho\cdot\mathbf{z})\cdot dz.$$

The direct application of Eq. (25) is difficult, for the integral is not easily computed. However, the form is simple and some general relations can be obtained quickly.

By introducing an explicit representation for α and β, and for $a_{\mathbf{k}_0}$, the spin or part of a plane wave in the Z direction with spin in the Z direction, we find[1] for $f_3(\theta,\varphi)$ and $f_4(\theta,\varphi)$,

$$f_3=\tfrac{1}{2}(E+m)(1+\cos\theta)\cdot F, \quad (26a)$$

$$f_4=\tfrac{1}{2}(E+m)\sin\theta\cdot F. \quad (26b)$$

Thus, at high energies,

$$|f_3/f_4|=\cot\tfrac{1}{2}\theta. \quad (27)$$

Relation (27) has the physical significance that, even after scattering, the spin lies along the direction of motion, and an unpolarized high energy beam remains unpolarized after scattering. In the case of the coulomb field, f_3 and f_4 have been calculated exactly by Mott.[3] His formulas in the limit $k\to\infty$ show that $|f_3/f_4|=\cot\tfrac{1}{2}\theta$. However, as the coulomb field has a pole at the origin, we could have expected Eq. (27) to hold only for the smaller angles.

A second immediate relation is the connection between Klein-Gordon scattering and Dirac scattering. The expression for the cross section σ_{KG} for a particle obeying the Klein-Gordon equation is, at high energies and if the potential is not singular at the origin,

$$\sigma_{KG}=E^2\cdot|F|^2 \quad (28)$$

and comparing this with expression (25) for the Dirac scattering of an unpolarized beam, we get

$$\sigma_D=(1-v^2\sin^2(\tfrac{1}{2}\theta)\cdot\sigma_{KG}. \quad (29)$$

VI. THE COULOMB FIELD

It was indicated above that Eq. (13) does not represent the coulomb wave function near the origin. The question arises now as to how well Eq. (25) will give the coulomb cross section. We were unable to do the integral involved, and thus we cannot make a direct comparison of Eq. (25) with the exact coulomb cross section as derived by Mott. However, the correctness of certain general features derivable from Eq. (25) seems to indicate it is fairly reliable for the coulomb

[2] G. Parzen, reference 1. It was shown there for the Dirac equation, but it can be shown to be true for the Klein-Gordon equation as well.

[3] N. F. Mott, Proc. Roy. Soc. (London) A124, 426 (1929).

field. Thus, the relation $|f_1|/|f_0| = \cot\frac{1}{2}\theta$ derived in Sec. IV does hold for the coulomb field. The wave function $\psi = a_{\mathbf{k}_0}\exp[i(kz+u)]$, with $u = Ze^2\ln r(1-\cos\theta)$ does represent the wave function correctly at large distances, and so we would expect Eq. (25) to give the scattering correctly at the smaller angles.

Another property of the exact coulomb cross section is that the ratio σ/σ_R, where $\sigma_R = (\csc^4\frac{1}{2}\theta)/k^2$ is essentially the Rutherford scattering cross section, is independent of energy past about 4 Mev for electrons.[4] According to Eq. (25) the energy dependence of σ/σ_R is given by $(1-v^2\sin^2\frac{1}{2}\theta)$, which is independent of the energy except at angles very close to 180°.

In the following sections we will apply our approximate wave function as given by Eq. (13) to the calculation of bremsstrahlung and pair production in the presence of heavy nuclei. We shall not actually apply Eq. (13) to a coulomb field, but use the form of Eq. (13) to derive certain relationships.

VII. BREMSSTRAHLUNG

In the usual perturbation treatment of bremsstrahlung, it is considered as a two-step process, the emission of a photon and scattering by the nucleus. The breakdown of the Born approximation in treating bremsstrahlung may be thought of as stemming from the application of the Born approximation to the scattering by the nucleus. This indicates that it may be possible to express the bremsstrahlung cross section in terms of the exact coulomb cross section, which has been tabulated fairly well by Bartlett and Watson,[5] and by McKinley and Feshbach.[4]

In order to formulate this idea mathematically, let us set up the exact expression for the bremsstrahlung cross section. Let $\psi(\mathbf{r};\mathbf{p}_0)$ be the wave function for an electron, which is incident with momentum $\mathbf{p}_0$ in the field of a potential $V(\mathbf{r})$. We can write this wave function as[1]

$$\psi(\mathbf{r};\mathbf{p}_0) = a_{\mathbf{p}_0}\exp(i\mathbf{p}_0\cdot\mathbf{r}) + \phi(\mathbf{r},\mathbf{p}_0), \tag{30}$$

where

$$\phi(\mathbf{r},\mathbf{p}_0) = -\frac{1}{4\pi}(E_0 - \boldsymbol{\alpha}\cdot\mathbf{p} - \beta m) \times \int \frac{\exp(ip_0|\mathbf{r}-\mathbf{r}'|)}{|\mathbf{r}-\mathbf{r}'|} V(\mathbf{r}')\psi(\mathbf{r}')\cdot d\tau', \tag{31}$$

and $E_0 = (p_0^2+m^2)^{\frac{1}{2}}$, $\mathbf{p} = -i\,\mathrm{grad}$.

Using the Fourier integral representation of $\exp[ip_0|\mathbf{r}-\mathbf{r}'|]/|\mathbf{r}-\mathbf{r}'|$,

$$\frac{\exp(ip_0|\mathbf{r}-\mathbf{r}'|)}{|\mathbf{r}-\mathbf{r}'|} = \frac{1}{(2\pi)^3}\cdot\int d\mathbf{s}\cdot\exp[i\mathbf{s}\cdot(\mathbf{r}-\mathbf{r}')]\cdot\frac{4\pi}{s^2-p_0^2}, \tag{32}$$

we can write $\phi(\mathbf{r},\mathbf{p}_0)$ as,

$$\phi(\mathbf{r},\mathbf{p}_0) = \frac{1}{(2\pi)^3}\cdot\int d\mathbf{s}\exp(i\mathbf{s}\cdot\mathbf{r})\frac{4\pi}{s^2-p_0^2}\cdot f(\mathbf{s},\mathbf{p}_0), \tag{33}$$

where

$$f(\mathbf{s},\mathbf{p}_0) = -\frac{1}{4\pi}(E_0 - \boldsymbol{\alpha}\cdot\mathbf{s} - \beta m)\cdot\int\exp(-i\mathbf{s}\cdot\mathbf{r})V\psi\,d\tau \tag{34}$$

is a generalization of the scattering amplitude. If $|\mathbf{s}| = p_0$, then $f(\mathbf{s},\mathbf{p}_0)$ is the elastic scattering amplitude for an electron incident in the $\mathbf{p}_0$ direction to be scattered by the potential into the $\mathbf{s}$ direction.

The calculation of the bremsstrahlung cross section for an electron incident with momentum $\mathbf{p}_0$ and scattered to momentum $\mathbf{p}$ while emitting a photon with momentum $\mathbf{k}$ requires the calculation of the matrix element,

$$M = \int\psi^*(\mathbf{r},\mathbf{p})\cdot\exp(-i\mathbf{k}\cdot\mathbf{r})\cdot\alpha_\lambda\cdot\psi(\mathbf{r},\mathbf{p}_0)d\tau, \tag{35}$$

where α_λ is the component of the Dirac $\boldsymbol{\alpha}$-matrix along a polarization direction. Using expression (31) for $\psi(\mathbf{r},\mathbf{p})$ and the Fourier integral expression for $\phi(\mathbf{r},\mathbf{p})$, we can write for M,

$$M = [4\pi/(\mathbf{p}_0-\mathbf{k})^2 - p^2]f^*(\mathbf{p}_0-\mathbf{k},\mathbf{p})\cdot\alpha_\lambda a_{\mathbf{p}_0} + [4\pi/(\mathbf{k}+\mathbf{p})^2 - p_0^2]a_{\mathbf{p}}^*\alpha_\lambda f(\mathbf{k}+\mathbf{p},\mathbf{p}_0) + \int d\tau\cdot\phi^*(\mathbf{r},\mathbf{p})\exp(-i\mathbf{k}\cdot\mathbf{r})\cdot\alpha_\lambda\phi(\mathbf{r},\mathbf{p}_0). \tag{36}$$

At high energies, assuming k, p, and p_0 are of the same order of magnitude, we can show that the third term in Eq. (36) is of order m/p_0 compared with the other two. To compare these terms, substitute into the integrals the asymptotic form of $\phi(\mathbf{r},\mathbf{p}_0), f(\theta)\exp(ip_0r)/r$.

The evaluation of Eq. (36) at high energies reduces them to evaluating $f(\mathbf{s},\mathbf{p}_0)$ at high energies. We will show that $f(\mathbf{s},\mathbf{p}_0)$ can be evaluated in terms of the elastic scattering amplitude.

Using our approximate wave function (13), we can write $f(\mathbf{s},\mathbf{p}_0)$ as,

$$f(\mathbf{s},\mathbf{p}_0) = \tfrac{1}{2}(E_0 - \boldsymbol{\alpha}\cdot\mathbf{s} - \beta m)\cdot a_{\mathbf{p}_0}\cdot F(\mathbf{s},\mathbf{p}_0), \tag{37a}$$

where

$$F(\mathbf{s},\mathbf{p}_0) = (-2/4\pi)\int\exp(-i\mathbf{s}\cdot\mathbf{r})\cdot V(\mathbf{r}) \cdot\exp i[\mathbf{p}_0\cdot\mathbf{r} + u(\mathbf{r},\mathbf{p}_0)]d\tau. \tag{37b}$$

And the function $u(\mathbf{r},\mathbf{p}_0)$ depends only on the direction of $\mathbf{p}_0$, not on the energy of the particle. Now $F(\mathbf{s},\mathbf{p}_0)$ by (37b) depends only on $\mathbf{q} = \mathbf{p}_0 - \mathbf{s}$ and on α the angle between $\mathbf{q}$ and $\mathbf{p}_0$. But the quantity $F(\mathbf{s},\mathbf{p}_0)$, by Eq. (25), is also involved in the calculation of the elastic scattering cross section. In this case, when $|\mathbf{s}| = p_0$, we can write $F(\mathbf{s},\mathbf{p}_0) = F(\theta, E_0)$, θ being the angle of scattering, E_0 the energy of the incident par-

[4] W. A. McKinley, Jr., and H. Feshbach, Phys. Rev. 74, 1759 (1948).

[5] J. H. Bartlett and R. E. Watson, Proc. Am. Acad. Arts Sci. 74, 53 (1940).

ticle, and $q=2p_0\sin\frac{1}{2}\theta$. We can evidently relate $F(\mathbf{s},\mathbf{p}_0)$ to $F(\theta',E_0')$ for any $\mathbf{s}$, and $\mathbf{p}_0$, by choosing θ' and E_0' so as to get the same $\mathbf{q}$ and α. Thus,

$$F(\mathbf{s},\mathbf{p}_0)=F(\theta',E_0')$$

if

$$|\mathbf{q}|=|\mathbf{p}_0-\mathbf{s}|=2p_0'\sin\tfrac{1}{2}\theta' \tag{38}$$

and

$$\tfrac{1}{2}\theta'=\tfrac{1}{2}\pi-\alpha,$$

where α is the angle between $\mathbf{p}_0$ and $\mathbf{q}$.

However, if it so happens that α is larger than 90°, then this situation cannot be duplicated in elastic scattering where α is always less than 90°. By taking the conjugate of Eq. (37b) we can change the direction of $\mathbf{q}$ to $-\mathbf{q}$, which will make an angle of less than 90° with $\mathbf{p}_0$; but we have also changed the sign of $u(\mathbf{r},\mathbf{p}_0)$, which means we must relate $F(\mathbf{s},\mathbf{p}_0)$ to positron scattering rather than to electron scattering. So, in general, if $\alpha\leq 90°$,

$$F(\mathbf{s},\mathbf{p}_0)=F_{el}(\theta',E_0'), \tag{39a}$$

where

$$\theta'/2=\tfrac{1}{2}\pi-\alpha,$$

and

$$q=2p_0'\cos\alpha.$$

If $\alpha\geq 90°$

$$F^*(\mathbf{s},\mathbf{p}_0)=F_{pos}(\theta',E_0'),$$

where

$$\theta'/2=\tfrac{1}{2}\pi-\alpha, \tag{39b}$$

and

$$q=2p_0'\cos\alpha.$$

$F_{el}(\theta',E_0')$ and $F_{pos}(\theta',E_0')$ are the functions involved, according to Eq. (25), in the cross sections for electron and positron scattering, respectively.

Thus, we have reduced the calculation of the bremsstrahlung matrix element M to calculating the elastic scattering amplitudes of both positrons and electrons. To put our result in a form where it can be easily compared with the Bethe-Heitler formula, we note the relationship,

$$\sum_{p'}(a_{p'}a_{p'}^*/E_0-E_{p'})$$
$$=(1/E_0^2-E_{p'}^2)(E_0-\boldsymbol{\alpha}\cdot\mathbf{p}'-\beta m) \tag{40}$$

where $\sum_{p'}$ means summing over the 4 free particle state with the same momentum $\mathbf{p}'$. Now substitute Eqs. (40) and (37) into Eq. (36): we get,

$$M=-(4\pi/2)\{\textstyle\sum_{p'}[(a_p^*a_{p'})(a_{p'}^*\alpha_\lambda a_{p_0})\cdot F^*(p_0-\mathbf{k},\mathbf{p})/$$
$$(E_p-E_{p'})]+\textstyle\sum_{p''}[(a_p^*\alpha_\lambda a_{p''})(a_{p''}^*a_{p_0})F(\mathbf{p}+\mathbf{k},\mathbf{p}_0)/$$
$$(E_{p_0}-E_{p''})]\}, \tag{41}$$

where

$$\mathbf{p}'=\mathbf{p}_0-\mathbf{k},\quad\text{and}\quad\mathbf{p}''=\mathbf{p}+\mathbf{k}.$$

Now let,

$$F(\mathbf{s},\mathbf{p}_0)=(2Ze^2/q^2)H(\mathbf{s},\mathbf{p}_0), \tag{42}$$

where

$$\mathbf{q}=\mathbf{p}_0-\mathbf{s}$$

and $2Ze^2/q^2$ is the Born approximation result for $F(\mathbf{s},\mathbf{p}_0)$. Thus, putting $H(\mathbf{s},\mathbf{p}_0)=1$ in what follows will bring us back to the Born approximation and the Bethe-Heitler formula.

With Eq. (42) and the matrix element (41), we can write the bremsstrahlung cross section as,

$$\sigma(\theta,\varphi,\theta_0)\cdot d\Omega_k d\Omega=(Z^2e^4pEE_0k\cdot d\Omega_k d\Omega/137\pi^2p_0q^4)$$
$$\times|\textstyle\sum\{[(a_p^*a_{p'})(a_{p'}^*\alpha_\lambda a_{p_0})/(E_p-E_{p'})]$$
$$\cdot H^*(\mathbf{p}_0-\mathbf{k},\mathbf{p})+[(a_p^*\alpha_\lambda a_{p''})(a_{p''}^*a_{p_0})/(E_{p_0}-E_{p''})]$$
$$\cdot H(\mathbf{p}+\mathbf{k},\mathbf{p}_0)\}|^2, \tag{43}$$

where $d\Omega$ and $d\Omega_k$ are the solid angles of scattered electron and emitted photon, respectively. Expression (43) differs from the Bethe-Heitler formula[6] by the appearance of the two $H(\mathbf{s},\mathbf{p}_0)$ factors which are equal to unity in the Born approximation. If we perform the indicated sum,[7] we get the result for the bremsstrahlung cross section,

$$d\phi=(Z^2e^4\cdot p\cdot dk\cdot\sin\theta d\theta d\varphi\cdot\sin\theta_0 d\theta_0/2\pi\cdot 137p_0kq^4)$$
$$\times\{Q(\theta,\varphi,\theta_0)|H(\mathbf{p}_0-\mathbf{k},\mathbf{p})|^2+R(\theta,\varphi;\theta_0)$$
$$\times|H(\mathbf{p}+\mathbf{k},\mathbf{p}_0)|^2+E(\theta,\varphi,\theta_0)[H^*(\mathbf{p}_0-\mathbf{k},\mathbf{p})$$
$$\cdot H(\mathbf{p}+\mathbf{k},\mathbf{p}_0)+\text{c.c.}]\}. \tag{44}$$

Here θ, θ_0, and φ are as defined in Heitler.[6]

$$Q=\frac{p_0^2\sin^2\theta_0}{(E_0-p_0\cos\theta_0)^2}(4E^2-q^2)+\frac{2k}{E_0-p_0\cos\theta_0}$$
$$\times[p_0^2\sin^2\theta_0-p_0p\sin\theta\sin\theta_0\cos\varphi$$
$$+k(E+p\cos\theta)] \tag{45a}$$

$$R=\frac{p^2\sin^2\theta}{(E-p\cos\theta)^2}(4E_0^2-q^2)-\frac{2k}{(E-p\cos\theta)}[p^2\sin^2\theta$$
$$-p_0p\sin\theta\sin\theta_0\cos\varphi-k(E_0+p_0\cos\theta_0)] \tag{45b}$$

$$S=\frac{1}{(E-p\cos\theta)(E_0-p_0\cos\theta_0)}\{p_0p\sin\theta\sin\theta_0\cos\varphi$$
$$\times[q^2-3k^2-4E_0E+k(p_0\cos\theta_0-p\cos\theta)]-2m^2k^2\}$$
$$+k\left\{\frac{p^2\sin^2\theta}{E-p\cos\theta}-\frac{p_0^2\sin^2\theta_0}{E_0-p_0\cos\theta_0}\right\}, \tag{45c}$$

where we may note that

$$Q+R+2S=T \tag{45d}$$

[6] W. Heitler, *Quantum Theory of Radiation* (Oxford University Press, London, 1944), second edition, p. 164.

[7] I would like to thank Dr. S. C. Wright for his aid in breaking down the bremsstrahlung formula.

and

$$T=\left[\frac{p^2\sin^2\theta}{(E-p\cos\theta)^2}(4E_0^2-q^2)+\frac{p_0^2\sin^2\theta_0}{(E_0-p_0\cos\theta_0)^2}(4E^2-q^2)\right.$$
$$-\frac{2pp_0\sin\theta\sin\theta_0\cos\varphi}{(E-p\cos\theta)(E_0-p_0\cos\theta_0)}(4E_0E-q^2+2k^2)$$
$$\left.+2k^2\frac{p^2\sin^2\theta+p_0^2\sin^2\theta_0}{(E-p\cos\theta)(E_0-p_0\cos\theta_0)}\right], \quad (45e)$$

and is the expression that occurs in the Bethe-Heitler formula. Thus, putting $H(\mathbf{p}_0-\mathbf{k},\mathbf{p})=H(\mathbf{p}+\mathbf{k},\mathbf{p}_0)=1$ in Eq. (44) will yield the Bethe-Heitler formula.

Assuming the correctness of applying relation (13) to our problem, the only situation in which expression (44) may break down is if in calculating $H(\mathbf{s},\mathbf{p}_0)$, the energy E_0' of the equivalent elastic scattering is small compared with the rest mass. Since $p_0'=q/2\cos\alpha$, this situation can only arise if $q\ll m$, that is, for small θ and θ_0, and also if $\cos\alpha$ is not too small. For small θ and θ_0 we can write as an order of magnitude relation,

$$\tan\alpha\simeq\frac{k\theta_0+p(\theta+\theta_0)}{p_0-p-k+\frac{1}{2}k\theta_0^2+\frac{1}{2}p(\theta+\theta_0)^2} \quad (46)$$

and $q\simeq p_0\theta$. If $p_0\sim p\sim k$, then $\tan\alpha\sim p_0^2\theta_0/m^2$ and $E_0'\sim m$ if θ, $\theta_0\sim(m/p_0)^{\frac{1}{2}}$. In the exceptional case when $p\ll m$, then $E_0'\sim m$ if θ, $\theta_0\sim m/p_0$. Formula (44) will give large deviations from the Bethe-Heitler formula, as much as a factor of five, at the larger angles, but gives very small deviations at the smaller angles $\theta\sim\theta_0\sim m/p_0$ where most of the bremsstrahlung occurs.

As an example, let us consider the case when $\theta_0=0$ and $\theta\gg m/p_0$. In this simple case, $H(\mathbf{p}_0-\mathbf{k},\mathbf{p})=H(\theta',E')$ where $\theta'=\theta$ and $E'=E$ to terms of order m/p_0, and $H(\mathbf{p}+\mathbf{k},\mathbf{p}_0)=H(\theta'',E'')$ where $\theta''=\theta$ and $E''=E_0$. Since $H(\theta,E)$ is independent of energy above 4 Mev for electrons,[4] we can write at $\theta_0=0$, $\theta\gg m/p_0$,

$$H(\mathbf{p}_0-\mathbf{k},\mathbf{p})=H(\mathbf{p}+\mathbf{k},\mathbf{p}_0)=H_{e1}(\theta). \quad (47)$$

Thus, the deviation may be expressed as

$$d\phi/d\phi_{BH}=|H_{e1}(\theta)|^2, \quad (48)$$

where $d\phi_{BH}$ stands for the Bethe-Heitler cross section. $|H_{e1}(\theta)|^2$ is plotted in Fig. 1 for atomic number $Z=82.2$, and one can see clearly the large deviation for large θ when $\theta_0=0$. The neglect of screening should not be important in a result like Eq. (48), for we have restricted ourselves to the larger angles where the screening should have little effect.

Although the Born approximation leads to large errors in the angular distribution of the bremsstrahlung, this is not so after the cross section has been integrated over the angles θ, θ_0, and φ. Our formula (44) shows that the integrated cross section as obtained by the Born approximation has a percentage error which is at most

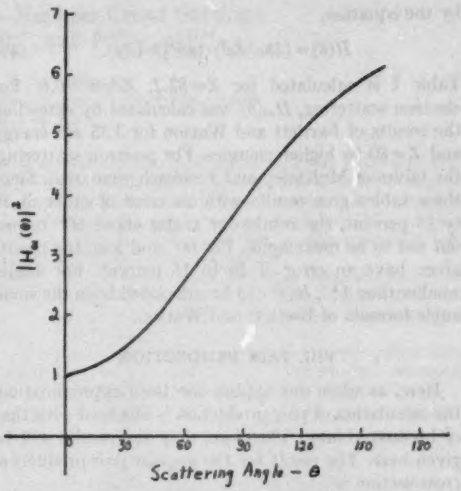

FIG. 1. $|H_{e1}(\theta)|^2$, the ratio of the exact coulomb cross section to the Born approximation cross section, plotted as a function of the scattering angle θ for $z=82.2$ at high energies.

the order of $(m/p_0)^{\frac{1}{2}}$. This results from the fact that the percentage deviation expected at angles $\theta\sim\theta_0\sim m/p_0$, where the bremsstrahlung is greatest, is only of the order of m/p_0. We placed the error at $(m/p_0)^{\frac{1}{2}}$ instead of (m/p_0), because our expression (44) does not hold for angles smaller than $\sim(m/p_0)^{\frac{1}{2}}$.

We have not taken screening into account. However, one might expect this result, that the Born approximation leads to little error in the integrated cross section at high energies, to carry over when screening is included. For, as the above calculation indicates, the Born approximation will give the small angle bremsstrahlung correctly and thus also the integrated cross section.

In Table I, we have tabulated $H(\theta)$, so that using relations (39), (42), and (44), the bremsstrahlung cross section can be calculated at different values of θ, θ_0, and φ. $H(\theta)$ is independent of energy, for sufficiently high energies and is related to the function[4,5] $G(\theta)$ which occurs in the calculation of coulomb scattering

TABLE I. $H_{e1}(\theta)$ is the ratio of the exact scattering amplitude to the Born approximation expression for the scattering amplitude of electrons in a coulomb field where $Z=82.2$ and $Ze^2/\hbar c=0.6$. $H_{pos}(\theta)$ is the corresponding quantity for positron scattering. For high enough energies, $H(\theta)$ is independent of energy.

	$H_{e1}(\theta)$		$H_{pos}(\theta)$	
θ	Real	Imaginary	Real	Imaginary
15°	−0.211	−1.05		
30°	0.820	−0.890	−0.26	−0.92
45°	1.34	−0.389	−0.62	−0.69
60°	1.60	0.128	−0.82	−0.47
90°	1.72	0.994		
120°	1.68	1.54		
150°	1.56	1.89		

by the equation,

$$H(\theta)=(2\hbar c/Ze^2)\cdot\tan^2\tfrac{1}{2}\theta\cdot G(\theta). \tag{49}$$

Table I is calculated for $Z=82.2$, $Ze^2/\hbar c=0.6$. For electron scattering, $H_{el}(\theta)$ was calculated by extending the results of Bartlett and Watson for 3.35 mc^2 energy and $Z=80$ to higher energies. For positron scattering, the tables of McKinley and Feshbach were used. Since these tables give results with an error of order of 10 to 15 percent, the results for angles above 60° turned out not to be meaningful. For 60° and less, the results given have an error of 10 to 15 percent. For angles smaller than 15°, $H(\theta)$ can be calculated from the small angle formula of Bartlett and Watson.

VIII. PAIR PRODUCTION

Here, as when one applies the Born approximation, the calculation of pair production is identical with that of bremsstrahlung. Therefore, only the results will be given here. The result for the angular pair-production cross section is

$$d\phi=-(Z^2e^4p_+p_-dE_+\sin\theta_+\sin\theta_-d\theta_+d\theta_-d\varphi_+/2\pi\cdot 137k^3q^4)$$
$$\times\{Q(\theta_+,\varphi_+,\theta_-)|H(\mathbf{p}_--\mathbf{k},-\mathbf{p}_+)|^2+R(\theta_+,\varphi_+,\theta_-)$$
$$\times|H(-\mathbf{p}_++\mathbf{k},\mathbf{p}_-)|^2+S(\theta_+,\varphi_+,\theta_-)$$
$$\times[H^*(\mathbf{p}_--\mathbf{p},-\mathbf{p}_+)\cdot H(-\mathbf{p}_++\mathbf{k},\mathbf{p}_-)+\text{c.c.}]\}, \tag{50}$$

where the same notation is used as by Heitler.

$$Q=\frac{p_-^2\sin^2\theta_-}{(E_--p_-\cos\theta_-)^2}(4E_+^2-q^2)+\frac{2k}{E_--p_-\cos\theta_-}$$
$$\times[p_-^2\sin^2\theta_-+p_+p_-\sin\theta_+\sin\theta_-\cos\varphi_+$$
$$-k(E_++p_+\cos\theta_+)] \tag{51a}$$

$$R=\frac{p_+^2\sin^2\theta_+}{(E_+-p_+\cos\theta_+)^2}(4E_-^2-q^2)+\frac{2k}{E_+-p_+\cos\theta_+}$$
$$\times[p_+^2\sin^2\theta_++p_-p_+\sin\theta_+\sin\theta_-\cos\varphi_+$$
$$-k(E_-+p_-\cos\theta_-)] \tag{51b}$$

$$S=-\frac{1}{(E_--p_-\cos\theta_-)(E_+-p_+\cos\theta_+)}$$
$$\times\{-p_-p_+\sin\theta_-\sin\theta_+\cos\varphi_+[q^2-3k^2+4E_-E_+$$
$$+k(p_-\cos\theta_-+p_+\cos\theta_+)-2m^2k^2\}$$
$$-k\left\{\frac{p_+^2\sin^2\theta_+}{E_+-p_+\cos\theta_+}+\frac{p_-^2\sin^2\theta_-}{E_--p_-\cos\theta_-}\right\}, \tag{51c}$$

where again we may note that

$$Q+R+2S=T \tag{51d}$$

and

$$T=\frac{p_+^2\sin^2\theta_+}{(E_+-p_+\cos\theta_+)^2}(4E_-^2-q^2)$$
$$+\frac{p_-^2\sin^2\theta_-}{(E_--p_-\cos\theta_-)^2}(4E_+^2-q^2)$$
$$+\frac{2p_+p_-\sin\theta_+\sin\theta_-\cos\varphi_+}{(E_+-p_+\cos\theta_+)(E_--p_-\cos\theta_-)}(4E_+E_-+q^2-2k^2)$$
$$-2k^2\frac{p_-^2\sin^2\theta_-+p_+^2\sin^2\theta_+}{(E_--p_-\cos\theta_-)(E_+-p_+\cos\theta_+)} \tag{51e}$$

and is the expression that occurs in the Born approximation formula.[6]

In the past experiments on high energy bremsstrahlung and pair production in the presence of heavy nuclei, only the integrated cross sections were measured. The deviations from the Born approximation obtained were of the order of 10 percent at energies of the order of 20 Mev. Of course, one must take screening into account in calculating the integrated cross section. However, as mentioned above, our calculations lead us to believe that when screening is included, we would expect the Born approximation to be in error by at most of the order of $(m/p_0)^1$. This is not in contradiction with the measured deviations.

To repeat, the one weakness in the above treatment seems to be the application of our high energy wave function [Eq. (13)] to the coulomb field which has a pole at the origin. However, the general nature of our results should still be valid in any case. The basis for our remarks concerning the integrated cross sections is not affected as our high energy wave function should give small angle scattering correctly. The large deviations from the Born approximation results obtained at the larger angles should still be expected, although they may not be given entirely correctly by our formulas.

In Eq. (35), $\psi^*(\mathbf{r},\mathbf{p})$ should really have an ingoing scattered wave. However our results are independent of this point.

[6] Reference 6, p. 196.

Determination of the Photo-Nuclear Cross Sections $S^{32}(\gamma, d)P^{30}$, $S^{32}(\gamma, np)P^{30}$, and $P^{31}(\gamma, n)P^{30}$

L. KATZ AND A. S. PENFOLD
Betatron Group, University of Saskatchewan, Saskatoon, Saskatchewan, Canada
(Received September 14, 1950)

The photo-nuclear cross sections for the gamma-deuteron and gamma-neutron proton, reactions of the parent isotope S^{32} were measured. An attempt was made to discover whether these reactions are sufficiently strong to offer enough competition to the gamma-neutron reaction to account for the shape of the latter cross section. Sulfur samples were irradiated in the photon beam from the University of Saskatchewan's 22-Mev betatron and an activity curve was obtained. The activity curve was analyzed to give a cross-section curve that had a peak value at 26 Mev and an indication of the possible existence of another peak at 24 Mev. The observed threshold energy was 19.15±0.20 Mev, a value that is consistent with the calculated value for a gamma-deuteron reaction. The cross-section curve can be interpreted to be the result of a superposition of a gamma-deuteron cross section and a gamma-neutron proton, cross section with peak values of 0.7±0.1 and 1.5±0.2 millibarns, respectively. The half-width energy of the combined cross-section curve was roughly 3 Mev. The integrated cross section gave a value of 4 millibarns-Mev and it is estimated that this value is too low to offer appreciable competition to the gamma-neutron reaction.

The gamma-neutron cross section from the parent isotope P^{31} was also measured. This curve had a threshold at 12.4±0.2 Mev and the peak occurred at 19 Mev. The peak value was 17±2 millibarn and a half-width energy of 7.6 Mev.

It is observed that all cross sections for photo-nuclear disintegrations so far measured in this laboratory show an energy interval of about 6 Mev between threshold and peak.

I. INTRODUCTION

RECENT measurements[1-3] of (γ, n) cross sections of nuclides have shown that the cross section *versus* energy curves have shapes similar to resonance curves; that is, they are peaked. In general, the half-width energy of a gamma-neutron cross section can be taken to be of the order of 6 Mev.

In the light of the present conceptions of nuclear level spacing, an explanation based on a simple resonance theory is not possible. If the observed cross section is due to resonance over a single nuclear energy level, the separation of the levels would need to be of the order of 36 Mev. Experiments[3] have shown the existence of only one peak for the $Cu^{63}(\gamma, n)$ reaction over the energy range from 10 to 100 Mev.

According to the continuum theory of nuclear reactions, one assumes that contributions to the reaction come from a great many nuclear levels. This theory is based on the Bohr assumption that a nucleus absorbs an incident particle a to form a compound nucleus and the compound nucleus subsequently decays with the emission of a particle b. The mode of decay is assumed to be independent of the mode of formation. The cross section for the reaction can then be expressed, following Blatt and Weisskopf,[4] as:

$$\sigma(a, b)=\sigma_a(a)G_a(b), \tag{1}$$

where σ_a is the probability of forming the compound nucleus and is equal to the product of the probability that the particle will reach the nuclear surface and the sticking functions; G_a is the probability that the nucleus decays with the emission of a particle b.

$$G_a=\frac{\text{probability for the emission of } b}{\Sigma \text{ probabilities for decay by all modes}}$$

$$=F_b/\Sigma_a F_a. \tag{2}$$

According to the calculations of Weisskopf and Ewing,[5] the F_a functions increase monotonically with energy.

Thus, a cross-section curve for a particular reaction can exhibit a peak only if the denominator of Eq. (2) becomes large beyond a certain energy owing to the effect of strongly competing reactions or $\sigma_a(a)$ exhibit this energy dependence.

It was suggested by Wäffler and Hirzel[6] that a $(\gamma, 2n)$ reaction might supply sufficient competition to the (γ, n) process to account for the shape of the latter cross section. Measurements in our laboratory indicate that at least for Cu^{63} this reaction is insignificant in the required energy range.

It was therefore of some interest to determine whether sufficient competition could be supplied by (γ, d) and (γ, np) reactions.

II. DISCUSSION OF THE EXPERIMENT

The isotope S^{32} was chosen for a target. The (γ, n) reaction gives the short-lived S^{31} isotope, whose activity dies away quickly, while the (γ, d) reaction gives P^{30}, with the convenient half-life of 2.55 min. Cadmium shielding was used to eliminate the 5-min sulfur activity formed by slow neutron absorption. All other unwanted contributions to the activity were found to be negligible.

Sulfur flowers were heated to the liquid state and poured into a one-inch diameter glass tube. The result-

[1] Johns, Katz, Douglas, and Haslam, Phys. Rev. **80**, 1062 (1950).
[2] B. C. Diven and G. M. Almy, Phys. Rev. **80**, 407 (1950).
[3] G. C. Baldwin and G. S. Klaiber, Phys. Rev. **73**, 1156 (1948).
[4] J. M. Blatt and V. F. Weisskopf, *The Theory of Nuclear Reactions*, Technical Report No. 42, Laboratory for Nuclear Science and Engineering, M.I.T.
[5] V. F. Weisskopf and D. H. Ewing, Phys. Rev. **57**, 472 (1940).
[6] H. Wäffler and O. Hirzel, Helv. Phys. Acta **21**, 200 (1948).

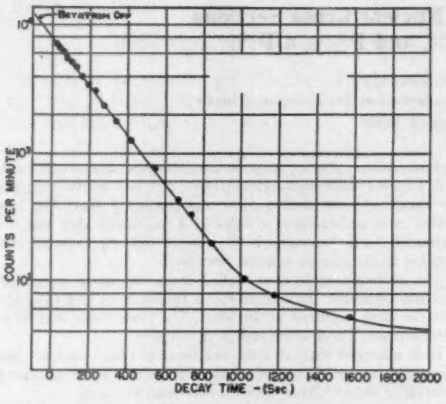

FIG. 1. Decay curve of P^{30}. The maximum energy of the betatron was 24 Mev. The dose rate was 538 r/min and the irradiation time was 8 min. The measured half-life is 2.62 min. Subtraction of the slight amount of unidentified long-lived activity gives a half-life in good agreement with the listed value of 2.55 min.

ing cylinder was cut into samples of thickness equal to the diameter of a Victoreen r-meter. The samples weighed about nine grams each.

The samples were irradiated in the photon beam from the University of Saskatchewan's 22-Mev betatron.

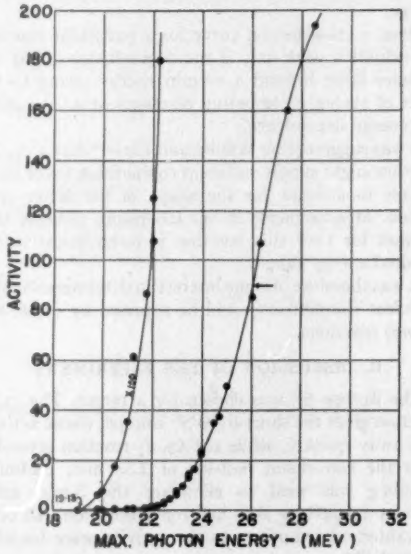

FIG. 2. Activation curve for the reaction $S^{32}(\gamma, {}^{*}{}_{d}{}^{p})P^{30}$ as obtained with the betatron. The ordinates of the figure are in arbitrary units, but the point at 26 Mev corresponds to 22×10^{-19} events/100r/atom. The region immediately above the threshold is re-drawn to a 100× scale. The threshold energy is 19.15±0.20 Mev.

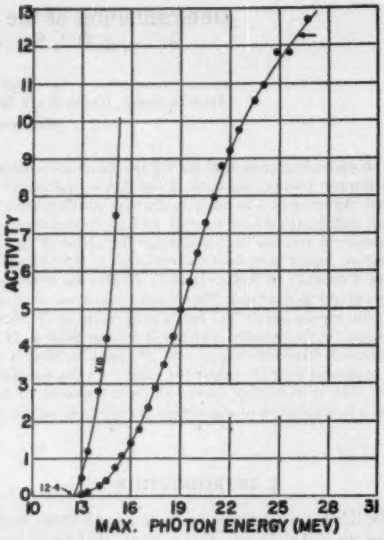

FIG. 3. Activation curve for the reaction $P^{31}(\gamma, n)P^{30}$ as obtained with the betatron. The units of the ordinates are arbitrary but the point at 26 Mev corresponds to 63×10^{-19} events/100r/atom. The region immediately above the threshold is re-drawn to a 10× scale. The threshold energy is 12.4±0.2 Mev.

The experimental arrangement was similar to that described in a previous paper.[1]

Horizontally, the samples subtended the same angle to the x-ray source as did the r-meter used for monitor calibration. In the vertical direction they subtended about twice the angle of the r-meter. This arrangement is suitable if it is assumed that the x-ray beam swings a negligible amount (with temperature, pressure, etc.) in the vertical plane during irradiation.

The maximum energy of the betatron bremsstrahlung was held constant to within 0.1 Mev through the use of an integrator-expander circuit[7] for energies up to 25 Mev. The energy calibration was based on the thresholds for (γ, n) reactions in Cu^{63} and C^{11} as reported by McElhinney.[8] Points above 25 Mev were taken at night, when the line frequency was particularly stable, the energy being determined from the voltage induced in a leg turn on the betatron. The betatron monitor was calibrated against the r-meter, both before and after each irradiation, and the samples were counted on thin plastic films in front of the window of an end-on Geiger counter.

Decay curves were taken with the use of an automatic time-stamping device and the saturated 2.55-min activity per gram per 100 r (measured in Lucite) was obtained at each energy. A sample decay curve is shown

[7] Katz, McNamara, Forsyth, Haslam, and Johns, Can. J. Research 28, 93 (1950).

[8] McElhinney, Hanson, Becker, Duffield, and Diven, Phys. Rev. 75, 542 (1949).

in Fig. 1. The resulting activity curve is shown in Fig. 2. A threshold energy of 19.15±0.20 Mev was obtained.

Smaller sulfur disks were cast to determine the absolute ordinates of Fig. 1. Corrections for self-absorption, backscattering, etc., were made and the counting geometry factor was determined by comparison with a standard RaE source.

Similar experimental arrangements, but powdered samples, were used to determine the activations curve for the reaction $P^{31}(\gamma, n)P^{30}$. This curve is shown in Fig. 3.

The measured gamma-neutron threshold is 12.4±0.2 Mev, a value in excellent agreement with a recent measurement by McElhinney, *et al.*[8]

The two cross-section curves were obtained from the pure[9] β^+ activity curves through the use of a progressive-smoothing method previously described.[1] This analysis yielded points on the cross-section curve one Mev apart.

III. DISCUSSION OF THE (γ, n) CROSS SECTION

The (γ, n) curve for P^{31} has the same general features, with one exception, as had been observed previously for other (γ, n) reactions. The exception is the steep rise and large tail of the cross-section curve (Fig. 4). It has a peak value of 17±2 millibarns. The half-width is 7.5 Mev, and the peak occurs 6.6 Mev above the threshold. The value of the cross section rises very steeply near the threshold. The integrated cross section is 120 mb-Mev.

The neutron yield/mole/r for the gamma-neutron reaction at 18 and 22 Mev has been calculated. These calculations gave values of 1.1×10^5 and 2.92×10^5, respectively. This is in very good agreement with the values of 1.1×10^5 and 3.2×10^5 obtained by Price and Kerst.[10]

IV. DISCUSSION OF THE $(\gamma, {}^*d^*)$ CROSS SECTION

An attempt was made to calculate the value of the (γ, d) threshold energy using known values of reaction energies and decay energies. The values were taken from Mattauch and Flammersfeld's tables,[11] Seaborg's tables,[12] and the paper on thresholds by McElhinney, *et al.*[8]

Table I gives the reactions, reaction energies, and decay energies used in the calculations. Four separate paths of calculation were chosen as indicated in Fig. 1 of a recent letter to the editor by one of the authors.[13] of 272.12 Mev.

The four paths of calculation yielded values of 18.98, 19.27, 19.17, and 18.89 Mev. The mean value of these is 19.08 Mev, and it is in excellent agreement with our experimentally determined value of 19.15 Mev.*

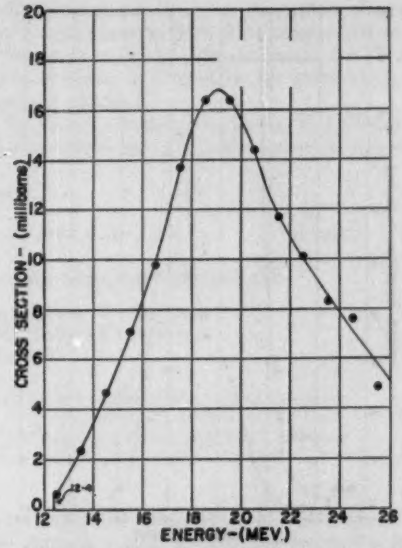

FIG. 4. Cross-section curve for the reaction $P^{31}(\gamma, n)P^{30}$. The curve shows one peak with a maximum value of 16.6 mb and a half-width of 7.6 Mev. A finite beginning of 0.5 mb is evident. The peak occurs 6.6 Mev above the threshold.

The (γ, np) threshold is higher than the (γ, d) threshold by the amount of the binding energy[14] of the

TABLE I. Nuclear data used in the calculations.

Reaction	Reaction energy (Mev)	Decay energy (Mev)
$S^{31}\xrightarrow{\beta^+}P^{31}$		3.85
$P^{30}\xrightarrow{\beta^+}Si^{30}$		3.50
$S^{32}(\gamma, n)S^{31}$	−14.8	
$P^{31}(\gamma, n)P^{30}$	−12.35	
$Si^{30}(d, n)P^{31}$	3.38	
$Al^{27}(\alpha, n)P^{30}$	−2.93	
$Si^{30}(d, n)P^{31}$	4.56	
$Al^{27}(\alpha, P)Si^{30}$	2.26	
$S^{32}(n, \alpha)Si^{29}$	1.2	

[9] C. Magnan, Ann. de physique **15**, 5 (1941).
[10] G. A. Price and D. W. Kerst, Phys. Rev. **77**, 806 (1950).
[11] J. Mattauch and A. Flammersfeld, "Isotopic report," special issue of the Z. Naturfor., 1949.
[12] G. T. Seaborg and I. Pearlman, Revs. Modern Phys. **20**, 585 (1948).
[13] A. S. Penfold, Phys. Rev. **80**, 116 (1950).

* The measured threshold for the (γd) reaction would normally be expected to be above that calculated from mass differences because of barrier effects. Recent discussions between one of the authors (L. K.) and Mr. A. G. W. Cameron of this laboratory has led them to propose the following process to account for the good agreement between the measured and calculated thresholds. It may also account for the large $(\gamma d)/(\gamma p)$ ratio in copper found by P. R. Byerly and W. E. Stephens [Phys. Rev. **81**, 473 (1951)].

The (γ, d) process near the threshold may be visualized as similar to an inverse Oppenheimer-Phillips process. The photon energy is assumed to be largely absorbed by the proton of a "deuteron" in the nucleus. The proton thus excited may penetrate the coulomb barrier relatively easily and more radially outward. A redistribution of energy may then take place in which the neutron remaining inside the nucleus is raised far enough to escape from the remaining potential well. The deuteron would thus escape in two stages, and the product of the separate probabilities for each stage may well be much greater than the probability for the penetration of the coulomb barrier by the deuteron as a unit.

[14] R. E. Bell and L. G. Elliot, Phys. Rev. **79**, 282 (1950).

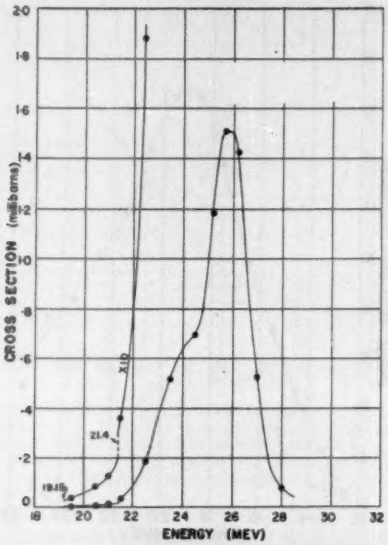

FIG. 5. Cross-section curve for the reaction $S^{32}(\gamma, {}^6d^p)P^{30}$. The curve shows two peaks and is interpreted to be the superposition of a (γ, d) and a (γ, np) cross section. The enlarged plot of the region near the threshold shows a discontinuity. This is believed to be the result of a small finite beginning of the (γ, np) cross section, similar to that for the (γ, d) cross section. The maximum value of the (γ, np) cross section is 1.5 mb and the maximum value of the (γ, d) cross section is somewhat smaller than 0.7 mb.

deuteron; 2.230 Mev. Thus the (γ, np) threshold occurs at 21.4 Mev.

It is to be noted that the curve of Fig. 5 exhibits a small "finite" beginning of 0.03 mb. Such a rapid rise of cross section near the threshold has been observed by us in all (γ, n) reactions investigated and is to be expected for these reactions from theoretical considerations.

Since the (γ, d) cross-section curve has a "finite" beginning, it is reasonable to assume that a (γ, np) curve would have a finite value also. In fact, one can imagine that a discontinuity, corresponding to this quantity, occurs between 21 and 21.5 Mev in Fig. 5.

It is also noted that the cross-section curve exhibits a bump in the neighborhood of 24 Mev. None of the (γ, n) cross-section curves examined by the authors have exhibited this shape; and they take it to indicate the presence of two reactions, (γ, d) and (γ, np). The peak value for the cross sections may be estimated at about 0.7 ± 0.1 mb for (γ, d) and 1.5 ± 0.2 mb for (γ, np).

To estimate the total plot cross section in S^{32} including all reactions, the following computations were made. A recent paper by Wäffler and Hirzel[8] lists the value of the cross section for the reaction $S^{32}(\gamma, n)S^{31}$ as 0.041 that of the value for the reaction $Cu^{63}(\gamma, n)Cu^{62}$ at 17.5 Mev. According to measurements made in our laboratory[1] the peak of the $Cu^{63}(\gamma, n)Cu^{62}$ cross section occurs at about 17.5 Mev and has the value of 110 mb. Since the threshold for the $S^{32}(\gamma, n)S^{31}$ reaction occurs at 12.35 Mev and by analogy to a typical (γ, n) curve, the value of the $S^{32}(\gamma, n)S^{31}$ cross-section curve at the peak may be estimated to be of the order of $110\times0.041\times2=9$ mb (the factor of 2 being included to correct for the position of the peak). If we assume that the half-width for this reaction is approximately 6 Mev, then the integrated cross section for the (γ, n) reaction is 54 mb-Mev. From Fig. 5 the value of the integrated $(\gamma, d)+(\gamma, np)$ cross sections is 4.1 mb-Mev.

For the integrated (γ, p) cross section from S^{32} one can make an estimate of 1/10 that of the gamma-neutron value.† This is probably a liberal estimate[15] (Curtis and Hornbostel[16] find (γ, p) for rhodium to be ≈0.4 mb).

Recent measurements at Chalk River[17] indicate that the integrated (γ, α) cross section can be estimated to be around 3 mb-Mev. The (γ, γ') reaction is believed to be small. Thus adding these values we find

$$\sum_b \int \sigma(\gamma, b)dE=66 \text{ mb-Mev}.$$

According to the theory of Levinger and Bethe[18] the "resonance" shape of the cross-section curve is due to the resonance nature of $\sigma_a(a)$ of Eq. (1) and the value of the integrated cross section summed over all possible decay modes is

$$\sum_b \int \sigma(\gamma, b)dE=0.015(1+0.8x)A. \qquad (3)$$

where x is the fraction of attractive exchange forces contributing. With $x=0$, and for our case of $A=32$, Eq. (3) gives 480 mb-Mev, a value which is not in agreement with our estimates.

We conclude that the combined effects of the (γ, d) and (γ, np) reactions are not so great as to offer an appreciable amount of competition to the (γ, n) reaction, nor does the measured integrated cross section summed over all photon reactions agree with the theory of Levinger and Bethe. Perhaps the mode of decay of the compound nucleus cannot be assumed to be independent of the mode of formation. Arguments in support of this conclusion were recently advanced by Weisskopf.[19]

Workers in our laboratory have measured the (γ, n) cross sections for Cu^{63}, Cu^{65}, Ta^{181}, Sb^{123}, Sb^{121}, P^{31}, and Zn^{64} (unpublished). These cross sections, along with the $(\gamma, {}^6d^p)$ cross sections of this paper all show one notice-

† Recent measurements indicate that the integrated (γ_p) and (γ, n) cross sections are about equal in this region of the periodic table. Our conclusion regarding the relative magnitudes of the measured and theoretical integrated cross sections will not be altered by this change.

[15] L. I. Schiff, Phys. Rev. **73**, 1311 (1948).
[16] Curtis, Hornbostel, Lee, and Salant, Phys. Rev. **77**, 290 (1950).
[17] C. H. Millar and A. G. W. Cameron (to be published).
[18] J. S. Levinger and H. A. Bethe, Phys. Rev. **78**, 115 (1950).
[19] V. F. Weisskopf, Helv. Phys. Acta **XXIII**, 187 (1950).

able similarity. The energy interval between the threshold and the peak value is always about 6 Mev.

The arguments which have been presented might be summed up as follows.

(a) The idea of competing reactions cannot account for the experimentally observed shape of photo-nuclear cross-section curve of S^{32}.

(b) A resonance theory might explain the results, but it would have to differ from present theories.

The authors would like to thank the Canadian National Research Council for the grant which made this work possible.

They would also like to thank Mr. H. J. Moody, who measured the phosphorous gamma-neutron cross section.

PHYSICAL REVIEW VOLUME 81, NUMBER 5 MARCH 1, 1951

Microwave Spectrum and Molecular Structure of GeF_3Cl

WALLACE E. ANDERSON,* JOHN SHERIDAN,† AND WALTER GORDY
Department of Physics, Duke University,‡ Durham, North Carolina

(Received November 24, 1950)

Measurements of the microwave rotational lines of four different transitions yield B_0 values in Mc/sec as follows: 2168.52 for $Ge^{70}F_3Cl^{35}$, 2167.53 for $Ge^{70}F_3Cl^{37}$, 2166.60 for $Ge^{74}F_3Cl^{35}$, 2108.13 for $Ge^{70}F_3Cl^{37}$, 2107.04 for $Ge^{72}F_3Cl^{37}$, and 2105.98 for $Ge^{74}F_3Cl^{37}$. For all these forms $D_J \approx 0.6$ kc/sec and $D_{JK} < |1|$ kc/sec. The molecular dimensions obtained for GeF_3Cl are $\angle FGeF = 107.7° \pm 1.5°$, $d_{Ge-F} = 1.688 \pm 0.017$A, and $d_{Ge-Cl} = 2.067 \pm 0.005$A.

I. INTRODUCTION

THE structures of but few germanium compounds are known. Only three germanium halides, $GeCl_4$, $GeBr_4$, and GeI_4, have been measured with electron diffraction.[1] Recently, structural determinations of GeH_3Cl and GeH_3Br have been made by microwave spectroscopy.[2] The present study reports the determination of the structure of GeF_3Cl by the latter method.

II. PROCEDURE

Most of the observations were made with a Stark modulation spectrograph[3] employing 100-kc sine wave modulation superimposed on a dc bias. The cell was 20 ft in length and was of brass X band guide with a center electrode of brass supported by Teflon strips. For the most abundant isotopic combinations measurements were also made with a video-type spectrometer[4] which did not employ Stark modulation. The dipole moment could not be evaluated with the type of modulation employed. It is evidently small, as the intensities of the rotational lines were very weak. We hope to measure the dipole moment later with an improved cell and square wave modulator. All measurements were made with frequency markers monitored by station WWV. The accuracy was limited by distortions of the Stark modulating system and by the unresolved structure of the lines.

III. RESULTS

Table I lists the frequencies measured for the different transitions. Table II gives the most probable values for B_0 for the different species and the moments of inertia, I_B, calculated from these with $h = 6.62373 \times 10^{-27}$ erg sec. The values of D_J and D_{JK} are too small to be

TABLE I. Observed rotational frequencies of GeF_3Cl.

Species	Transition $J \rightarrow J'$	Frequency Mc/sec
$Ge^{70}F_3Cl^{35}$	6→7	30,358.62±0.30
	7→8	34,694.71±0.40
	8→9	39,031.91±0.30
$Ge^{70}F_3Cl^{37}$	6→7	30,344.56±0.30
	7→8	34,679.32±0.30
	8→9	39,014.14±0.30 (Stark)
	8→9	39,013.81±0.20 (Video)
$Ge^{74}F_3Cl^{35}$	6→7	30,332.58±1.00
	7→8	34,664.55±0.30
	8→9	38,996.79±0.30 (Stark)
	8→9	38,996.78±0.20 (Video)
$Ge^{70}F_3Cl^{37}$	6→7	29,512.96±0.30
	7→8	33,728.15±0.80
	8→9	37,945.47±0.90
$Ge^{72}F_3Cl^{37}$	6→7	29,497.57±0.30
	7→8	33,711.21±0.30
	8→9	37,925.87±0.90
$Ge^{74}F_3Cl^{37}$	6→7	29,482.88±0.30
	7→8	33,694.43±0.30
	8→9	37,905.91±0.30

* Present address: Department of Physics, The Citadel, Charleston, South Carolina.
† On leave from the Department of Chemistry, University of Birmingham, England.
‡ The research reported in this document has been made possible through support and sponsorship extended by the Geophysical Research Directorate of the Air Force Cambridge Research Laboratories. It is published for technical information only and does not represent recommendations or conclusions of the sponsoring agency.
[1] P. W. Allen and L. E. Sutton, Acta Cryst. 3, 46 (1950).
[2] Dailey, Mays, and Townes, Phys. Rev. 76, 137 (1949); Sharbaugh, Pritchard, Thomas, Mays, and Dailey, Phys. Rev. 79, 189 (1950).
[3] McAfee, Hughes, and Wilson, Rev. Sci. Instr. 20, 821 (1949); A. H. Sharbaugh, Rev. Sci. Instr. 21, 120 (1950).
[4] W. Gordy and M. Kessler, Phys. Rev. 71, 640 (1947).

TABLE II. Molecular constants of GeF_3Cl.

	B_0 (Mc/sec)[a]	D_J (kc/sec)	D_{JK} (kc/sec)	I_B (g-cm² ×10⁻⁴⁰)[b]
$Ge^{70}F_3Cl^{35}$	2168.52	0.6	<|1|	386.8_{56}
$Ge^{72}F_3Cl^{35}$	2167.53	0.6	<|1|	387.0_{32}
$Ge^{74}F_3Cl^{35}$	2166.60	0.6	<|1|	387.1_{99}
$Ge^{70}F_3Cl^{37}$	2108.13	0.6	<|1|	397.9_{38}
$Ge^{72}F_3Cl^{37}$	2107.04	0.6	<|1|	398.1_{44}
$Ge^{74}F_3Cl^{37}$	2105.98	0.6	<|1|	398.3_{44}

[a] With D_J =0.6 kc/sec. [b] With h =6.62373×10⁻²⁷ erg sec.

evaluated precisely, but fairly accurate upper limits of these constants can be set. Because of the strong interactions of the nonbonded halogens and because of the relatively large values of both I_A and I_B, the very small centrifugal stretching constants observed (Table II) are not surprising. Likewise, an upper limit of about 50 Mc can be set for the magnitude of the nuclear coupling eQq of Cl^{35}, but none of the high J lines observed could be resolved sufficiently to obtain a specific value for this constant. A few lines of the hyperfine structure of $Ge^{73}F_3Cl^{35}$ could be seen, but the spectrum of this species was too weak to yield enough data for an analysis. Recent microwave measurements on GeH_3Cl by Townes, Mays, and Dailey[5] have shown that the Ge^{73} nucleus has a large quadrupole moment and a spin of 9/2.

All three structural parameters of the molecule can be calculated from any three of the six isotopic combinations studied, provided that substitutions for both Ge and Cl are included. The three most widely spaced lines of species $Ge^{70}F_3Cl^{35}$, $Ge^{74}F_3Cl^{35}$, and $Ge^{74}F_3Cl^{37}$ were chosen as the ones from which to calculate the structure, and the values thus determined were used to calculate B_0 values for the other three species. These were found to agree within the estimated limits of error in the measurements. Therefore, the accuracy of the determination is probably in this instance limited by the measurements rather than by zero-point vibrational energies. The values of d_{Ge-F} and angle FGeF (Table III) depend heavily upon the frequency separation of the lines used for $Ge^{70}F_3Cl^{35}$ and $Ge^{74}F_3Cl^{35}$, which is accurate to only 1.5 percent. Because the structural parameters depend on the square root of the moments of inertia, these values are accurate to about one percent. Since the center of gravity of the molecule is near the Ge nucleus, the GeCl distance depends almost completely upon the square root of the differences between the moments of inertia, I_B, for the molecules

TABLE III. Molecular dimensions.

	∠FGeF	d_{Ge-F}	d_{Ge-Cl}
GeF_3Cl	107.7°±1.5°	1.688±0.017A	2.067±0.005A

[5] Townes, Mays, and Dailey, Phys. Rev. 76, 700 (1949).

with different Cl isotopes, which are accurate to better than 0.1 percent.

Table IV compares the bond lengths in GeF_3Cl and related molecules with those estimated from the Schomaker-Stevenson rule[6] $d=r_1+r_2-0.09|x_1-x_2|$. In this relation (r_1+r_2) is the added single bond covalent radii and $-0.09|x_1-x_2|$ is an empirically determined correction for the shortening of the bond caused by the resonance of the covalent forms with the ionic forms. The factor (x_1-x_2) represents the electronegativity difference of the bonded atoms. Because of the low electronegativities of Ge and Si in comparison with the halogens, there is a considerable shortening of the Si(Hal) or Ge(Hal) bonds caused by this resonance. For GeCl bonds the Schomaker-Stevenson correction seems to account for practically all of the observed bond shortening. This is even true approximately for the GeF bond, in which 85 percent of the observed shortening of 0.25A is accounted for by the correction for ionic character. It is interesting that this correction for partial ionic character does not account for the observed bond shortening in SiF_3Cl nearly so well as in GeF_3Cl, nor even as in CF_3Cl. This extra shortening for bonds to Si

TABLE IV. Comparison of interatomic distances in GeF_3Cl and related molecules with those estimated from covalent radii.

MF_3Cl	MF distance in A Obs	MF distance in A Calc[a]	MCl distance in A Obs	MCl distance in A Calc[a]
GeF_3Cl	1.68_8	1.73	2.067	2.09
SiF_3Cl	1.55_9[b]	1.69	2.00[b]	2.05
CF_3Cl	1.323[c]	1.38	1.765[c]	1.74

[a] Calculated with the Schomaker-Stevenson rule, reference 6.
[b] J. Sheridan and W. Gordy, Phys. Rev. 77, 719 (1950).
[c] D. K. Coles and R. H. Hughes, Phys. Rev. 76, 858 (1949).

is also shown in $Si(Hal)_4$ compounds measured by electron diffraction.[1] A simple explanation for the exceptional behavior of Si is possible on the basis of resonance contributions of double bonded structures of the type

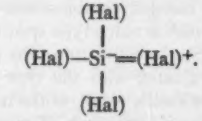

Such resonance is not possible with carbon compounds because of the unavailability of a d orbital in the valence shell, and it is not very important in Ge compounds because of the decreasing tendency of atoms to form double bonds with increasing size. That Si forms double bonds more readily than does Ge is also revealed by the relative nuclear quadrupole couplings of Cl in SiH_3Cl and GeH_3Cl. On the basis of ionic character alone, one would expect the Cl coupling in SiH_3Cl to be greater than that in GeH_3Cl, whereas it is observed to be lower.[7] The Cl coupling would be lowered by the

[6] V. Schomaker and D. P. Stevenson, J. Am. Chem. Soc. 63, 37 (1941).
[7] See reference 2, also A. H. Sharbaugh, Phys. Rev. 74, 1870 (1948).

double bond character as well as by the ionic character of the bond. Pauling[8] has suggested resonance with various double bonded structures as a possible cuase for the bond shortening in molecules of the above type. However, because he neglected the shortening caused by resonance with ionic structures, his treatment overemphasizes the contributions from double bonded structures. It is of interest that $\angle$FGeF in GeF_3Cl, 107.7°, is nearly tetrahedral like the corresponding one,[1] $\angle$FSiF, in SiF_3Cl. Pauling[8] has pointed out that partial double bond character seems to have little influence on bond angles.

[8] L. Pauling, *Nature of the Chemical Bond* (Cornell University Press, Ithaca, 1939), Ch. VII, p. 210.

PHYSICAL REVIEW VOLUME 81, NUMBER 5 MARCH 1, 1951

The Spectrum of Iodine Excited in the Presence of Argon

PUTCHA VENKATESWARLU*
Department of Physics, University of Chicago, Chicago, Illinois
and
Division of Physics, National Research Council, Ottawa, Canada
(Received August 15, 1950)

Iodine vapor was excited by an uncondensed transformer discharge in the presence of argon. A new band system λ2785–2750A is recorded. In addition a large number of new bands are found in the band systems λ3455–3015A, λ2730–2520A, and λ4420–4000A reported by earlier workers. These band systems are analyzed and explained in terms of the fairly well-established term scheme of the iodine molecule. The absorption data in the region λ2000–3500A are discussed in the light of the present results.

I. INTRODUCTION

THE electrical and fluorescent excitations of iodine vapor are known to give a discrete band system in the visible region and a number of groups of semicontinuous (or diffuse) bands in the region λ4800 to 2400A. The discrete band system is due to a transition from the upper electronic state $\sigma_g^2\pi_u^4\pi_g^3\sigma_u$, $0_u^+(^3\Pi_u)$ to the ground state. The groups of semicontinuous bands were explained in earlier papers by the present author[1] as due to transitions from various stable upper electronic states to various repulsive lower states dissociating into $^3P+^3P$ iodine atoms. It was known by experiments of earlier workers[2–4] that the spectrum obtained by fluorescent excitation of a mixture of iodine and nitrogen is different from the fluorescent spectrum of pure iodine vapor. Elliott[4] obtained four band systems in the regions λ4630 to 4440A, 4321 to 4041A, 3450 to 3040A, and 2730 to 2520A. Since these band systems were obtained only in the presence of nitrogen, it was not clear which of them were actually due to the I_2 molecule. Hence, the discussion of these band systems was omitted by the present author in his earlier papers on the iodine molecule. Recently, Professor Mulliken kindly showed to the author an unpublished spectrogram which was taken a number of years ago on a medium quartz spectrograph by exciting iodine vapor by active nitrogen. It appears from the spectrum that the effect of active nitrogen on iodine vapor is the same as that of the fluorescent excitation of iodine vapor in the presence of nitrogen.

Waser and Wieland[5,6] excited iodine vapor in the presence of argon by a high frequency discharge and reported the last three of the above four band systems obtained by Elliott in fluorescence in the presence of nitrogen. The first system (λ4630 to 4440A) was attributed by them to IN. They gave the vibrational formulas for the bands of the second and fourth systems but not of the third (λ3450 to 3040A), for which, apparently, they accepted Elliott's analysis. The latter appears to be quite uncertain, since out of the 73 bands reported by Elliott in the region 3450 to 3040A, 27 bands were not classified in his vibrational scheme. Further, the constants used by Waser and Wieland for the lower state of the fourth system (λ2730 to 2520A), which represents the ground state of the iodine molecule, are different from those obtained by Rank[7] from the resonance spectral data of iodine. These constants used by Waser and Wieland do not fit in with the resonance spectral data; and, therefore, it has become necessary to analyze also the band system λ2730 to 2520A.

Because of these reasons, a reinvestigation of the spectrum of iodine excited in the presence of argon was made by the present author. The band systems reported by Elliott and by Waser and Wieland, together with a new band system here obtained, were then analyzed and interpreted in accordance with the fairly well-established term scheme[8,9] of the iodine molecule.

* National Research Laboratories, Postdoctorate Fellow.
[1] P. Venkateswarlu, Proc. Indian Acad. Sci. 24A, 480 (1946); 25A, 119, 133 (1947).
[2] O. Oldenberg, Z. Physik 25, 136 (1924).
[3] F. Duschinsky and P. Pringsheim, Physica 2, 923 (1935).
[4] A. Elliott, Proc. Roy. Soc. (London) 174A, 273 (1940).
[5] J. Waser and K. Wieland, Nature 160, 643 (1947).
[6] K. Wieland, Victor Henri Memorial Volume 229, 1947–48.
[7] D. H. Rank, J. Opt. Soc. Am. 36, 239 (1946).
[8] R. S. Mulliken, Phys. Rev. 46, 549 (1934).
[9] R. K. Asundi and P. Venkateswarlu, Indian J. Phys. 21, 101 (1947).

TABLE I.* Band heads and vibrational analysis of the band system λ3455 to 3015A.

Skorko absorption	Present experiments (electrical excitation of I_2+ argon) λ_{air}	ν_{vac}	v', v''	ν_{calc}
	3454.4*f*	28940	2,62	28940
	3452.3	28958	0,60	28957
	3450.2	28976	11,71	28975
	3448.3*f*	28992	12,72	28991
	3446.7	29005	13,73	29009
	3444.1	29027	14,74	29031
	3442.0	29045	3,62	29042
	3440.6	29056	15,75	29054
	3439.7	29064	11,70	29062
			1,60	29060
	3438.1*f*	29078	12,71	29075
	3437.3	29084	16,76	29080
	3436.3*f*	29093	13,72	29091
	3432.0*f*	29129	15,74	29130
	3430.0	29146	4,62	29144
	3427.6*f*	29167	2,60	29163
	3425.0	29189	0,58	29190
	3424.0*f*	29197	14,72	29191
	3422.9	29207	15,73	29208
3419	3419.1*f*	29239	10,67	29239
			6,63	29241
	3417.5	29253	4,61	29254
			12,69	29252
	3416.4	29262	13,70	29262
	3415.4	29271	14,71	29275
	3413.5*f*	29287	15,72	29290
	3412.8	29293	1,58	29293
	3411.7	29303	19,77	29306
	3409.4*f*	29322	17,74	29328
	3406.3*f*	29349	6,62	29348
			12,68	29345
	3405.7	29354	13,69	29352
			5,61	29356
	3404.5	29364	4,60	29367
			14,70	29362
3403	3403.1*f*	29377	19,76	29376
	3402.4	29383	3,59	29380
	3401.9	29387	16,72	29389
	3400.3*f*	29401	20,77	29404
	3399.5	29408	17,73	29406
			1,57	29412
	3397.5*f*	29425	18,74	29427
	3395.9	29439	9,64	29439
			11,66	29438
			12,67	29440
	3394.7*f*	29449	7,62	29450
			13,68	29445
	3393.2	29462	15,70	29461
	3391.5*f*	29477	20,76	29474
	3389.0*f*	29499	3,58	29498
3386	3385.6	29528	19,74	29528
	3384.1	29541	13,67	29540
			10,64	29540
	3382.2*f*	29558	0,55	29556
			7,61	29560
	3381.5*f*	29564	16,70	29560
	3379.6*f*	29581	5,59	29584
	3377.3*f*	29601	4,58	29600
	3374.5*f*	29626	20,74	29623
	3371.8*f*	29649	10,63	29646
			9,62	29652
3369	3369.2*f*	29672	7,60	29673
	3367.9*f*	29684	19,72	29685
			6,59	29686
			0,54	29682
	3366.4	29697	23,77	29698
			20,73	29701
	3365.2	29707	5,58	29702
	3363.8	29720	4,57	29719
	3362.4*f*	29732	13,65	29738
	3360.7	29747	11,63	29747
	3359.1*f*	29761	2,55	29762
			9,61	29762
	3358.6	29766	19,71	29770
	3357.8*f*	29773	8,60	29774
	3356.3*f*	29786	1,54	29785
			7,59	29788
	3354.2*f*	29805	6,58	29804
3353	3353.0	29815	0,53	29811
	3352.3	29822	5,57	29821
	3351.0	29833	15,66	29837
	3349.8	29844	4,56	29841
	3348.2*f*	29858	19,70	29856
	3346.2*f*	29876	9,60	29875
	3343.4	29901	22,73	29897
	3342.0	29914	1,53	29914
3339	3338.4	29946	13,63	29947
			0,52	29941
	3336.7*f*	29961	11,61	29964
	3335.3*f*	29974	10,60	29976
	3333.3	29992	3,54	29990
			9,59	29990
	3331.9	30004	8,58	30007
	3330.1	30021	2,53	30016
	3329.2	30029	7,57	30025
3327	3327.9	30040	15,64	30040
	3325.6	30061	12,61	30064
	3324.8	30068	5,55	30068
	3324.2	30074	0,51	30074
			11,60	30077
	3317.6	30134	17,65	30135
	3316.3	30145	15,63	30146
	3315.6	30152	14,62	30154
	3313.9	30167	13,61	30164
	3312.2	30183	1,51	30177
	3311.1	30193	5,54	30194
			11,59	30192
3309	3309.0	30212	0,50	30212
	3307.1	30229	9,57	30227
	3305.8	30241	16,63	30245
	3304.3	30255	15,62	30253
	3303.0	30267	14,61	30264
	3302.1	30275	7,55	30272
	3300.2	30293	12,59	30292
	3299.0	30304	11,58	30310
3295	3296.2	30329	10,57	30328
	3294.1	30349	0,49	30346
			9,56	30349
	3292.6	30362	15,61	30363
	3291.1	30376	14,60	30377
			8,55	30373
	3290.0	30386	3,51	30382
	3288.5	30400	7,54	30398
	3287.0	30414	2,50	30415
	3286.1	30422	6,53	30425
	3285.0	30433	19,64	30435
3283	3284.0	30442	18,63	30443
	3282.2	30459	16,61	30462
	3279.9	30480	4,51	30484
	3278.6	30492	14,59	30492
	3278.0	30498	8,54	30499
	3276.6	30511	13,58	30510
	3274.7	30528	7,53	30527
			12,57	30529
3273	3271.7	30556	6,52	30555
			2,49	30552
	3271.2	30561	17,61	30561
	3269.5	30577	10,55	30575
	3267.6	30611	14,58	30610
	3264.5	30624	0,47	30627
3263	3263.4	30634	21,64	30630
	3262.2	30645	19,62	30648
	3261.8	30649	12,56	30651
	3260.9	30658	7,52	30657

* The bands marked *f* have been observed also in the fluorescence of I_2+N_2 by Elliott.

TABLE I.*—(*Continued*).

Skorko absorption	Present experiments (electrical excitation of I_3^+ argon) λ_{air}	ν_{vac}	v', v''	ν_{calc}
			3,49	30654
	3259.6	30670	17,60	30674
	3258.9	30676	11,55	30676
	3257.9	30686	6,51	30688
	3256.2	30702	10,54	30701
3253	3253.6	30726	9,53	30729
	3251.4	30747	20,62	30746
	3249.4	30766	0,46	30770
	3248.4	30776	12,55	30776
3245	3245.7	30801	11,54	30802
	3243.6	30821	6,50	30823
	3241.9	30837	2,47	30833
	3240.9*f*	30847	21,62	30844
	3239.7	30858	5,49	30858
			9,52	30859
3238	3237.7*f*	30877	13,55	30876
	3236.2	30892	8,51	30891
	3234.8*f*	30905	12,54	30902
	3233.7	30915	0,45	30915
	3232.1	30931	11,53	30931
	3230.2*f*	30949	15,56	30950
	3228.8	30962	10,52	30960
			6,49	30960
3228	3227.7	30973	2,46	30976
	3224.3*f*	31006	18,58	31006
	3222.7*f*	31021	1,45	31018
3219	3220.4*f*	31043	23,62	31038
	3218.1	31065	0,44	31062
	3217.1	31075	15,55	31075
			3,46	31078
	3214.5*f*	31100	6,48	31100
	3213.5	31110	26,64	31114
	3212.2*f*	31122	2,45	31121
3211	3210.8	31136	5,47	31139
	3209.6*f*	31148	17,56	31148
	3208.6	31157	12,52	31161
	3203.1	31211	0,43	31211
3199	3200.1*f*	31240	6,47	31241
	3197.7*f*	31263	9,49	31264
	3195.2	31288	12,51	31294
	3193.0	31309	1,43	31314
	3191.7	31322	20,57	31321
			4,45	31325
3188	3189.7*f*	31342	7,47	31343
	3186.2	31376	23,59	31376
	3184.7*f*	31391	13,51	31394
	3184.0	31398	17,54	31399
	3182.7	31411	2,43	31417
	3181.7	31421	27,62	31422
3180	3180.3	31435	26,61	31437
	3179.1*f*	31446	8,47	31444
	3177.6	31461	15,52	31460
	3173.1*f*	31506	10,48	31505
3171	3169.9*f*	31538	21,56	31541
	3167.6	31561	16,52	31559
	3166.8	31569	2,42	31568
	3166.0*f*	31576	5,44	31574
	3164.4	31592	15,51	31593
	3163.4	31602	11,48	31606
	3162.3	31613	1,41	31617
			23,57	31613
3161	3161.2	31624	4,43	31621
	3160.0	31636	7,45	31631
	3159.5*f*	31641	10,47	31646
	3154.8	31689	9,46	31688
	3151.7	31720	2,41	31720
3151	3150.4*f*	31733	8,45	31732
	3146.7*f*	31770	4,42	31772
	3142.3	31815	30,61	31817
3141	3140.6*f*	31832	9,45	31833
	3137.1*f*	31867	15,49	31865
	3134.0	31899	26,57	31902
	3133.2*f*	31907	14,48	31906
3132	3130.9*f*	31930	1,39	31929
			7,43	31927
	3128.6*f*	31954	20,52	31953
	3127.9	31961	24,55	31957
			16,49	31964
3123	3124.9*f*	31992	12,46	31990
	3121.4*f*	32028	5,41	32026
			8,43	32028
	3119.4	32048	14,47	32047
	3118.5	32057	25,55	32053
	3117.5	32068	29,58	32069
	3116.3	32080	4,40	32079
			10,44	32081
3112	3113.1*f*	32113	23,53	32115
	3105.3	32194	2,38	32191
3105	3104.1	32206	17,48	32203
	3099.9	32250	1,37	32246
3095	3096.4*f*	32286	6,40	32283
	3092.7	32325	21,50	32319
	3088.1*f*	32373	27,54	32370
3084	3083.8*f*	32418	22,50	32416
	3082.2	32435	15,45	32434
	3081.1	32447	18,47	32443
			3,37	32451
3076	3075.9*f*	32501	27,53	32499
3067	3067.3*f*	32593	28,53	32595
			6,38	32597
3059	3058.9*f*	32682	13,42	32682
3052	3053.7*f*	32738	21,47	32737
	3048.7*f*	32791	23,48	32790
	3045.3	32828	19,45	32829
3042	3043.0	32853	28,51	32858
	3040.5*f*	32880	15,42	32881
			21,46	32880
	3037.8	32909	9,38	32903
3035	3032.8	32963	8,37	32960
3029	3027.3	33023	21,45	33025
	3019.7	33106	11,38	33105
	3014.6	33162	10,37	33162

II. EXPERIMENTAL RESULTS AND VIBRATIONAL ANALYSIS

The iodine vapor was excited in the presence of argon (5 to 60 mm) by an uncondensed transformer discharge and the spectrum obtained was photographed on large and medium Hilger quartz spectrographs. The spectrum of iodine without the introduction of argon was also taken on the same plates for comparison. The discrete band system 6700 to 5000A, which one obtains in all kinds of excitation of pure iodine vapor is absent in the experiments with the mixture of iodine and argon. The several groups of semicontinuous bands obtainable in fluorescence or by electrical excitation of pure iodine vapor, discussed previously,[1] are all absent except for the three bands at 4747, 4662, and 4575A. However, some diffuse bands which were not obtainable in the excitation of pure iodine vapor appear in the present experiments with the mixture of iodine and argon. They are at 5100, 3524, 3481, 2880, 2868, 2857, 2847, 2836, and 2825A. Some of these bands were obtained by Elliott and by Waser and Wieland. These bands are presumably due to transitions from upper stable elec-

TABLE II. Band heads and vibrational analysis of the band system λ2785 to 2750A.

Intensity	λ_{air}	ν_{obs}	v', v''	ν_{calc}
1	2784.5	35903	5,62	35904
2	2779.8	35963	0,57	35959
5	2776.0	36012	5,61	36014
2	2775.3	36022	4,60	36023
5	2774.6	36031	3,59	36035
?	2773.2	36049	2,58	36049
6	2772.1	36063	1,57	36063
2	2771.4	36072		
½	2770.3	36086	0,56	36081
3	2769.4	36098	9,64	36103
			10,65	36103
?	2768.7	36107	8,63	36106
6	2768.2	36114	6,61	36117
			7,62	36111
1	2767.3	36126	5,60	36127
3	2765.4	36150	3,58	36153
3	2764.1	36167	2,57	36168
2	2762.8	36184	1,56	36185
2	2762.4	36190		
?	2761.5	36202	11,65	26205
			10,64	26206
2	2760.1	36220	7,61	36221
1	2759.3	36230	6,60	36230
1	2758.6	36240	5,59	36242
?	2757.5	36254	4,58	36254
4	2756.1	36272	3,57	36272
?	2755.0	36287	2,56	36290
1	2750.7	36344	6,59	36345
?	2748.3	36375	4,57	36375

tronic levels to repulsive states dissociating into $^2P+^2P$ iodine atoms. We hope to discuss these bands in a later paper.

Beside the above bands, there are four band systems in the regions: (1) 4420 to 4000A, (2) 3455 to 3015A, (3) 2785 to 2750A, and (4) 2730 to 2520A. Of these, the system λ2785 to 2750A is new, and the other three are the same as those obtained by earlier workers,[4,5] except that a large number of additional bands belonging to these systems are found in the present work. The band heads of all these systems are degraded to longer wavelengths.

The band system λ3455 to 3015A is very extensive, and its band heads are very close to one another. The wavelengths and wave numbers of the band heads in this system are given in Table I. All the bands were found to fit into a single vibrational scheme and could be expressed by the formula,

$$\nu = 39131 + (103.0v' - 0.1v'^2 - 0.001v'^3) - (213.798v'' - 0.614v''^2 - 0.000932v''^3 - 0.0000187v''^4),$$

with $v' = 0$–30 and $v'' = 37$–77. The constants of the lower state of the system which represents the ground state of the iodine molecule are those obtained by Rank[7] from the resonance spectral data. The (v', v'') values and the corresponding wave numbers calculated from the above formula are given in Table I.

The band system λ2785 to 2750A is not extensive, and it is weaker than the 3455–3015A system. The band heads of this system are also quite close to one another. The wavelengths and the wave numbers of the bands, together with their estimated intensities, are given in Table II. The bands could be fairly well represented by the formula,

$$\nu = 45781 + (104.5v' - 0.1v'^2) - (213.798v'' - 0.614v''^2 - 0.000932v''^3 - 0.0000187v''^4),$$

with $v' = 0$–11 and $v'' = 56$–65. The lower state is again the ground state of the iodine molecule. The (v', v'') values and the corresponding wave numbers calculated according to the above equation are also given in Table II.

The vibrational scheme of the band system λ2730 to 2520A is shown in Table III. The bands could be well

TABLE III.* The vibrational scheme of the band system λ2730–2520A.

v' \ v''	45	50	55	60	65
0	38932 (145) 38787 (144, 100) 38643 (141, 96) 38502 (136, 99) 38366 (136, 94) 38230 (133, 86) 38097 (133, 95) 37961 (136, 95) 37834 (127, 95) 37706 (128, 90) 37580 (126, 123) 37457 (93)	37088 (110) 36978 (112) 36866 (93)		
	38887 (148) 38739 (148, 95) 38591 (138, 96) 38460 (131, 95) 38326 (134, 95) 38192 (134, 93) 38056 (136, 127) 37929 (91) 37796 (133, 94) 37550 (97) 37425 (125, 100)	37071 (112) 36959 (87) 36746 (92) 36631 (115)		
2	39275 (91) 39121 (154, 94) 38834 (98, 137) 38697 (142) 38555 (134) 38421 (136) 38285 (136) 38020 (97, 130) 37890 (130) 37647 (122) 37525	37056 (116) 36940 (102) 36838	36631	
	39366 (151) 39215 (146, 90) 39049 (95, 137) 38932 (96, 87) 38250 (91, 133) 38117 (96, 126) 37991 (133) 37860 (130) 37613 (88) 37502	36823 (99)		
4	39605* (149) 39456 (146) 39310 (143, 91) 39167 (148) 39019 (148) 38341 (128) 38213	37354	36922	
	39250	38973	37337	37220	
6	38391	37712 (125, 99) 37647	37316	37106 (91) 36992* (114, 98) 36894
		37746		37197	
8					37176
	39767		37580	37367 (90)	
10				37457	

* The bands marked * are from Elliott's data in fluorescence.

TABLE IV.* The vibrational scheme of the band system λ4420–4000A.

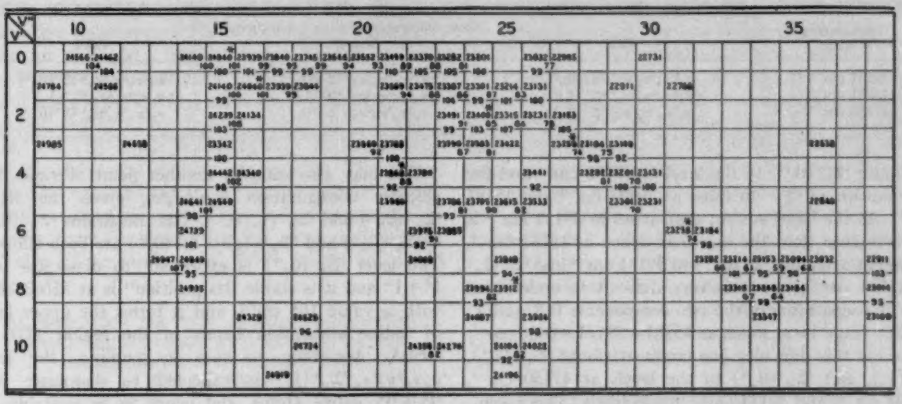

* The bands marked * are from Elliott's data in fluorescence.

represented by the expression,

$$\nu = 47150 + (96.21v' - 0.49v'^2) - (213.798v'' - 0.614v''^2 - 0.000932v''^3 - 0.0000187v''^4),$$

with $v' = 0$–10 and $v'' = 43$–66. The lower state of the band system is again the ground state of the molecule. We see from the equation that the present analysis of this system does not change the vibrational constants[5] of the upper level, but changes its position[9a] to 47150 cm^{-1} from the previous value 46441 cm^{-1} obtained by Waser and Wieland.[5]

Waser and Wieland, as mentioned above, gave the vibrational formula for the bands of the system λ2730 to 2520A, but have not yet published their experimental data and their vibrational analysis. The vibrational scheme of this band system as obtained from the present work is therefore shown in Table IV. The following formula of Waser and Wieland represents fairly well the bands of this system:

$$\nu = 25757.2 + (101.88v' - 0.3v'^2) - (126.57v'' - 0.75v''^2 - 0.0033v''^3).$$

Bands with $v' = 0$–11 and $v'' = 9$–38 are recorded in the present work. The lower state of this system is the $\sigma_g^2\pi_u^4\pi_g^3\sigma_u$, $0_u^+(^3\Pi)$ state at 15598 cm^{-1}.

III. ELECTRONIC TRANSITIONS INVOLVED

According to the vibrational analyses discussed above, three of the band systems have their upper electronic levels at 39131 cm^{-1}, 45781 cm^{-1}, and 47150 cm^{-1}, respectively, and have the ground state of the iodine molecule as their lower state. The fourth system in the region λ4420 to 4000A has its upper level at 15598+25757=41355 cm^{-1} and its lower level at 15598 cm^{-1}. The lower level in this case, as mentioned above, is well known to be $\sigma_g^2\pi_u^4\pi_g^3\sigma_u$, $0_u^+(^3\Pi_u)$, which dissociates into $^2P_{\frac{1}{2}}+^2P_{\frac{1}{2}}$ iodine atoms. Therefore, the upper state according to the selection rules should be 0_g^+ or 1_g. A consideration of the electronic term scheme of the iodine molecule, discussed in earlier papers and shown to some extent in Table VII, shows that the upper state of the band system is very probably a 0_g^+ state corresponding to $\sigma_g^2\pi_u^2\pi_g^4\sigma_u^2\,{}^1\Sigma_g^+$. This state is predicted[1,3] to be stable because it dissociates probably into ions $I^+(p^4, {}^1D)+I^-(p^6, {}^1S)$, while its very low ω_e (102 cm^{-1}) is understandable in view of the presence of two strongly antibonding electrons (σ_u^2).

We now consider the probable electronic terms for the three levels at 39131 cm^{-1}, 45781 cm^{-1}, and 47150 cm^{-1}. The electron configuration $\sigma_g^2\pi_u^3\pi_g^3\sigma_u^3$ gives rise among others to the terms $^1\Sigma_u^+(0_u^+)$, $^3\Sigma_u^-(0_u^+, 1_u)$, and $^1\Delta_u(2_u)$, the symbols in the parentheses being those for case c type coupling. These terms are predicted to dissociate into ions $I^+ + I^-$, and so are expected to be stable. The remaining terms of the configuration are predicted to dissociate into $^2P+^2P$ atoms, and so (in view of their height) should be unstable. For case a coupling the only possible transition from the above terms to the ground state $^1\Sigma_g^+(0_g^+)$ is that from $^1\Sigma_u^+(0_u^+)$. However, in the iodine molecule, where we expect a strong tendency towards case c coupling, the transitions $^3\Sigma_u^-(0_u^+, 1_u) \rightarrow {}^1\Sigma_g^+(0_g^+)$ are also allowed.

The fact that the three observed levels under consideration have vibrational frequencies of the same magnitude suggests that the electronic terms responsible for these levels arise from the same configuration, presumably $\sigma_g^2\pi_u^3\pi_g^3\sigma_u^3$. Then the low ω_e values observed for these three levels will be in harmony with the presence of the two strongly antibonding σ_u electrons. Assuming that $^1\Sigma_u^+$ is above $^3\Sigma_u^-$, one could

[9a] Dr. Wieland, in a recent private communication to Dr. Herzberg, mentioned that the position of the upper level of the above band system has probably to be changed from 46441 cm^{-1} to 47151 cm^{-1}, which is in perfect agreement with the above result. The author wishes to express his thanks to Dr. Herzberg for this information.

TABLE V. Identification of electronic terms.

Position of the levels	Three different possible electronic terms		
	First	Second	Third
39131 cm^{-1}	$\sigma_g^2\pi_u^3\pi_g^3\sigma_u^2\ ^3\Sigma^-(0_u^+)$	$\sigma_g^2\pi_u^3\pi_g^3\sigma_u^2\ ^1\Sigma^+(0_u^+)$	$\sigma_g^2\pi_u^3\pi_g^3\sigma_u^2\ ^3\Sigma^-(0_u^+)$
45781 cm^{-1}	$\sigma_g^2\pi_u^3\pi_g^3\sigma_u^2\ ^3\Sigma^-(1_u)$	$\sigma_g^2\pi_u^3\pi_g^3\sigma_u^2\ ^3\Sigma^-(1_u)$	$\sigma_g\pi_u^4\pi_g^3\sigma_u\ ^3\Sigma^+(1_u)$
47150 cm^{-1}	$\sigma_g^2\pi_u^3\pi_g^3\sigma_u^2\ ^1\Sigma^+(0_u^+)$	$\sigma_g^2\pi_u^3\pi_g^3\sigma_u^2\ ^3\Sigma^-(0_u^+)$	$\sigma_g^2\pi_u^3\pi_g^3\sigma_u^2\ ^1\Sigma^+(0_u^+)$

attribute $^1\Sigma_u^+(0_u^+)$ to the level at 47150 cm^{-1} and the components of $^3\Sigma_u^-$ to those at 39131 cm^{-1} and 45781 cm^{-1}. As the band system that arises in 39131 cm^{-1} is more intense than the one that arises in 45781 cm^{-1}, we might attribute $^3\Sigma^-(0_u^+)$ to 39131 cm^{-1} and $^3\Sigma^-(1_u)$ to 45781 cm^{-1}; but it is very difficult to understand how the separation of the two components 0_u^+ and 1_u of $^3\Sigma_u^-$ could be as much as 45781−39131=6650 cm^{-1}. To avoid this difficulty one might attribute $^3\Sigma_u^-(0_u^+)$, $^3\Sigma^-(1_u)$, and $^1\Sigma_u^+(0_u^+)$ to the levels at 47150 cm^{-1}, 45781 cm^{-1}, and 39131 cm^{-1}, respectively. This assignment is in good agreement with the observed relative intensities of the respective band systems; i.e., the 39131 system is most intense and the 45781 system is weakest of the three. Further, the component separation of $^3\Sigma_u^-$ will be 47150−45781=1369 cm^{-1}, which appears to be reasonable for the case c coupling. The only questionable point about this assignment is that the relative positions of $^3\Sigma_u^-$ and $^1\Sigma_u^+$ are reversed; i.e., $^3\Sigma_u^-$ is above $^1\Sigma_u^+$. Recknagel[10] has worked out the relative positions of $^1\Sigma^+$ and $^3\Sigma^-$ for the configurations $\pi^3\pi'$ and $\pi\pi'$. For the configuration $\pi\pi'$, $^3\Sigma^-$ is lower than $^1\Sigma^+$; and for the configuration $\pi^3\pi'$, $^3\Sigma^-$ is higher than $^1\Sigma^+$. However, the relative positions of $^3\Sigma$ and $^1\Sigma$ of the configuration $\sigma_g^2\pi_u^3\pi_g^3\sigma_u^2$ have not been calculated so far. But one will presumably expect in simple molecules that the $\sigma_g^2\pi_u^3\pi_g^3\sigma_u^2$ case will be similar to $\pi\pi'$; i.e., $^3\Sigma^-$ will be lower than $^1\Sigma^+$. However, in the case of iodine molecules, it is conceivable that the calculations for $\sigma_g^2\pi_u^3\pi_g^3\sigma_u^2$ may show that $^3\Sigma^-$ is higher than $^1\Sigma^+$. Therefore, the assignment of $^3\Sigma^-(0_u^+)$, $^3\Sigma^-(1_u)$, and $^1\Sigma_u^+(0_u^+)$ to the levels at 47150 cm^{-1}, 45781 cm^{-1}, and 39131 cm^{-1}, respectively, appears to be reasonable.

TABLE VI. Alternative configurations in I_2 for dissociation into atoms in ^2P states.

Dissociation products	Odd electron terms derived according to case c type coupling	Case A: The electron configurations of odd unstable states if $\sigma_g\pi_u^4\pi_g^4\sigma_u\ ^2\Sigma_u^+(1_u)$ does not dissociate into $^2P_{1/2}+^2P_{1/2}$ atoms and so is stable	Case B: The electron configurations of odd unstable states if $\sigma_g\pi_u^4\pi_g^4\sigma_u\ ^2\Sigma_u^+(1_u)$ dissociates into $^2P_{1/2}+^2P_{1/2}$ atoms and so is unstable
$^2P_{1/2}+^2P_{1/2}$	0^-, 1	$\sigma_g^2\pi_u^3\pi_g^3\sigma_u^2\ ^1\Sigma^+(1_u)$ $\sigma_g^2\pi_u^3\pi_g^3\sigma_u^2\ ^1\Sigma^+(0_u^-)$	$\sigma_g\pi_u^4\pi_g^3\sigma_u\ ^3\Sigma^+(1_u)$ $\sigma_g\pi_u^4\pi_g^3\sigma_u\ ^3\Sigma^+(0_u^-)$
$^2P_{3/2}+^2P_{1/2}$	0^-, 1, 1, 2 0^+ (stable)	$\sigma_g^2\pi_u^3\pi_g^3\sigma_u^2\ ^1\Sigma^-(0_u^-)$ $\sigma_g^2\pi_u^3\pi_g^3\sigma_u^2\ ^1\Delta(1_u)$ $\sigma_g^2\pi_u^3\pi_g^3\sigma_u^2\ ^1\Delta(2_u)$ $\sigma_g^2\pi_u^4\pi_g^2\sigma_u\ ^1\Pi(1_u)$	$\sigma_g^2\pi_u^3\pi_g^3\sigma_u^2\ ^3\Delta^+(0_u^-)$ $\sigma_g^2\pi_u^3\pi_g^3\sigma_u^2\ ^3\Sigma^+(1_u)$ $\sigma_g^2\pi_u^3\pi_g^3\sigma_u^2\ ^3\Delta(1_u)$ $\sigma_g^2\pi_u^3\pi_g^3\sigma_u^2\ ^3\Delta(2_u)$

[10] A. Recknagel, Z. Physik 87, 396 (1934).

One may also consider another point of view. The electron configuration $\sigma_g\pi_u^4\pi_g^4\sigma_u$ gives the terms $^1\Sigma_u^+(0_u^+)$ and $^3\Sigma_u^+(1_u, 0_u^-)$. The transitions $^1\Sigma_u^+(0_u^+) \leftrightarrow ^1\Sigma_g^+(0_g^+)$ and $^3\Sigma_u^+(1_u) \leftrightarrow ^1\Sigma_g^+(0_g^+)$ are both allowed. The level $^1\Sigma_u^+(0_u^+)$ is expected[11] to dissociate into $I^+ + I^-$ and it is stable. Its position[11] is at 51683 cm^{-1} with ω value 165 cm^{-1}, and it forms the upper level of iodine absorption bands in the region 1770 to 1950A. According to case a coupling, the level $\sigma_g\pi_u^4\pi_g^4\sigma_u\ ^3\Sigma_u^+(1_u)$ is expected to dissociate into $^2P_{\frac{1}{2}}+^2P_{\frac{1}{2}}$ iodine atoms, and hence to be unstable. In the case of the iodine molecule, one might expect that $\sigma_g\pi_u^4\pi_g^4\sigma_u\ ^3\Sigma_u^+(1_u)$ will go to higher dissociation products to avoid crossing the $\sigma_g^2\pi_u^3\pi_g^3\sigma_u^2\ ^1\Sigma_u^-(1_u)$. In this case the latter will dissociate into $^2P_{\frac{1}{2}}+^2P_{\frac{1}{2}}$ atoms, and so be an unstable state, and $\sigma_g\pi_u^4\pi_g^4\sigma_u\ ^3\Sigma_u^+(1_u)$ will be a stable state. Then we will have $\sigma_g^2\pi_u^3\pi_g^3\sigma_u^2\ ^3\Sigma_u^-(0_u^+)$, $\sigma_g\pi_u^4\pi_g^4\sigma_u\ ^3\Sigma_u^+(1_u)$, and $\sigma_g^2\pi_u^3\pi_g^3\sigma_u^2\ ^1\Sigma_u^+(0_u^+)$ for the three levels at 39131, 45781, and 47150 cm^{-1}, respectively. The validity of this assignment is somewhat doubtful, since, according to it, $\sigma_g\pi_u^4\pi_g^4\sigma_u\ ^3\Sigma_u^+(1_u)$ is at 45781 cm^{-1} and its ω value is 104.5 cm^{-1}, whereas the ω value of $^1\Sigma_u^+(0_u^+)$ at 51683 cm^{-1} from the same configuration is 165 cm^{-1}. Moreover, the value 104.5 cm^{-1} is much nearer to the ω values 103.0 and 96.2 cm^{-1} of the other two states arising from the configuration $\sigma_g^2\pi_u^3\pi_g^3\sigma_u^2$. This difference in ω value of the two states, 0_u^+ at 51683 cm^{-1} and 1_u at 45781 cm^{-1}, can be understood if they dissociate into different components of $I^+ + I^-$. For example, we know that the vibrational frequencies of $^3\Pi(0_u^+)$ and $^3\Pi(1_u)$ of the configuration $\sigma_g^2\pi_u^4\pi_g^3\sigma_u$ are 128 cm^{-1} and 44 cm^{-1}, respectively. This is because $^3\Pi(0_u^+)$ dissociates into $^2P_{\frac{1}{2}}+^2P_{\frac{1}{2}}$ iodine atoms and $^3\Pi(1_u)$ dissociates into $^2P_{\frac{1}{2}}+^2P_{\frac{1}{2}}$ iodine atoms. Thus, there are three different possible ways of identifying the electronic terms at 39131, 45781, and 47150 cm^{-1}, which are summarized in Table V.

The rotational analysis of the band systems, which requires quite large resolution instruments, will show which one of the three possible configurations in Table V is correct. However, from the considerations of relative intensities of the band systems, the vibrational frequencies of the three levels, and their relative mutual separation, we prefer the second assignment, which is included in Table VII.

If one accepts the second assignment, a change in the assignment of electronic terms for the odd unstable states, dissociating into $^2P+^2P$ iodine atoms, is neces-

[11] P. Venkateswarlu, Proc. Indian Acad. Sci. 24A, 473 (1946).

sary, as those assignments in the earlier papers[1] were made with the assumption that $\sigma_g\pi_u^4\pi_g^4\sigma_u\,{}^3\Sigma_u^+(1_u)$ would be a stable state.[11] The two alternative configurations for the odd unstable states dissociating into ${}^2P+{}^2P$ iodine atoms are given in Table VI for the cases (A) if $\sigma_g\pi_u^4\pi_g^4\sigma_u\,{}^3\Sigma_u^+(1_u)$ dissociates into higher dissociation products, say I^++I^-, and hence is a stable state, and (B) if $\sigma_g\pi_u^4\pi_g^4\sigma_u\,{}^3\Sigma_u^+(1_u)$ dissociates into ${}^2P_{\frac{1}{2}}+{}^2P_{\frac{1}{2}}$ atoms and is therefore unstable. The assignment (A) was adopted in the earlier papers[1] by the writer, but the assignment (B) is to be preferred to (A) if one accepts the second possible configuration given in Table VI for the levels at 39131, 45781, and 47150 cm^{-1}.

IV. REMARKS ON THE KIMURA-MIYAMISHI, PRINGSHEIM-ROSEN, AND SKORKO BANDS IN ABSORPTION IN THE REGION 2000 TO 3500A

In an earlier paper[12] the present author arranged the Pringsheim-Rosen, Kimura-Miyanishi (P-R, K-M) bands in one vibrational scheme; but the wave number separations were so irregular that no equation was developed for the bands. However, with the assumption that the P-R, K-M bands are all due to a single electronic transition from the ground state, the upper electronic level was extrapolated to be 44900 cm^{-1}. According to the present experiments, we have a level at 45781 cm^{-1} which forms the upper level of the band system λ2785 to 2750A discussed above. Though one might argue that, in view of the large extrapolation involved, the position of the level extrapolated from the analysis of the P-R, K-M bands coincides roughly with the position of the level at 45781 cm^{-1}, it is uncertain whether all the P-R, K-M bands have this upper level. For (1) the ω-value for the single vibrational scheme of the P-R, K-M bands was about 90 cm^{-1}, and the present level has $\omega=104.5$ cm^{-1}; (2) as stated above, the wave number separations in the analysis of the P-R, K-M bands were irregular and no equation had been developed. Further, we see that all the transitions from the ground state to the states at 47150 cm^{-1}, 45781 cm^{-1}, and 39131 cm^{-1} are possible in absorption, since the reverse transitions do occur in emission. These transitions in absorption can be expected to give rise to the bands in the region 2000A to 3500A. It is probably for this reason that the attempts so far made to develop a single vibrational scheme for all the P-R, K-M, and Skorko[13,14] bands did not succeed. Future reinvestigation of the absorption spectra of iodine in the region 2000 to 3500A at varying temperatures from room temperature to 1300°C and the reanalysis of all the absorption bands in that region may show definitely the existence of the above three transitions in absorption. With the present knowledge about the iodine molecule we can say that the P-R, K-M bands are due to the overlapping of transitions from the ground state to the two levels at 45781 cm^{-1} and 47150 cm^{-1}; and the Skorko bands to a transition from the ground state to the one at 39131 cm^{-1}. The wavelengths of the Skorko bands in absorption are included in Table I, where the emission bands from the level at 39131 cm^{-1} to the ground state are given. The agreement of the wavelengths confirms the above statement with regard to the transition of the Skorko bands. Therefore, the tentative explanation suggested for these Skorko bands in an earlier paper[12] must be abandoned.[14a]

For convenience, the positions of all the stable electronic levels of the I_2 molecule observed either in absorption or emission, their term designations and probable electron configurations are given in Table VII together with their vibrational frequencies.

The Absence of the Band System λ6700 to 5000A

As mentioned in the beginning, the discrete band system λ6700 to 5000A which is due to a transition from 0_u^+ to the ground state, is absent in the excitation of the mixture of argon and iodine. Normally, when there is no foreign gas, the molecules which are excited to 0_u^+ come back to the ground state giving the discrete band system. However, when foreign gas is introduced, the excited molecules in the 0_u^+ state very probably go over, by collisions, to the repulsive state 0_u^- which either touches or crosses the 0_u^+ and dissociate into ${}^2P_{\frac{1}{2}}+{}^2P_{\frac{1}{2}}$ iodine atoms as suggested by Van Vleck[15] in explaining the magnetic quenching of iodine fluorescence and Turner's fluorescence experiments[16] in a mixture of iodine and argon. Turner[16] also reported that he compared the spectra in the visible region of the discharges in pure iodine and in iodine and argon mixtures. All bands of wavelength longer than 5440A were reported to appear to have normal intensities, while the bands of shorter wavelength were considerably weakened in spectra of the mixture, but in the present experiments the whole band system is absent. The difference between the present experimental results and those of Turner may be due to the higher pressure of argon used in the present experiments.

The other characteristic features of the spectrum of the mixture of iodine and argon, as already described, are (1) the absence of certain groups of semicontinuous emission bands which are present when iodine is excited alone and which arise in levels whose r_e values are not very different from the r_e values of the ground state, and (2) the presence of the four band systems which arise

[11] P. Venkateswarlu, Indian J. Phys. 21, 43 (1947).
[13] Skorko, Nature 131, 366 (1933).
[14] Skorko, Acta Phys. Polonica 3, 191 (1934).

[14a] The explanation given in the earlier papers (references 9 and 12) for the continua in absorption at 3413A and 3263A still holds good. They are not due to the same transition as the narrow absorption bands (Skorko bands discussed above).
[15] J. H. Van Vleck, Phys. Rev. 40, 544 (1932).
[16] L. A. Turner, Phys. Rev. 38, 574 (1931).

TABLE VII. Observed stable electronic states of iodine molecule.

Electron configuration	Electron states: Case a or b type coupling	Electron states: Case c or $\Omega \rightarrow s$ coupling	Name	Position of the levels[a] T_e in cm^{-1}	ω_e in cm^{-1}	Probable dissociation products if there is to be no effect of crossing[a]	Remarks
$\sigma_g\pi_u^3\pi_g^4\sigma_u^2$	$^1\Pi_u$	1_u	Q	64329	(93)	$5p^4\,^1D_2+5p^6\,^1S_0$	J, K, M, N, O, P, and Q form the upper levels of the seven groups of bands obtained by Cordes[b] in absorption in the region 1770–1500A. The wave number separations in all these seven groups are very irregular, and so the positions and frequencies of these levels are to be taken as doubtful until they are confirmed by future experiments.
$[\sigma_g^2\pi_u^4\pi_g^3\,^2\Pi_{\frac{1}{2}}]\sigma_u\,6p$		$\Pi_{1,0u^+}$	P	62802	(297)	$ex+5p^6\,^2P$	
$\sigma_g\pi_u^3\pi_g^4\sigma_u^2$	$^3\Pi_u$	0_u^+	O	61824	(96)	$5p^4\,^3P_0+5p^6\,^1S_0$	
$[\sigma_g^2\pi_u^3\pi_g^4\,^2\Pi_{\frac{1}{2}}]\sigma_g\,6s$		$\Pi_{1,0u^+}$	N	59217	(212)	$ex+5p^6\,^2P$	
$\sigma_g\pi_u^3\pi_g^4\sigma_u^2$	$^3\Pi_u$	1_u	M	58937	(203)	$5p^4\,^3P_1+5p^6\,^1S_0$	
$\sigma_g\pi_u^4\pi_g^3\sigma_u^2$	$^1\Pi_g$	1_g	L	58578	120	$5p^4\,^1D_2+5p^6\,^1S_0$	Three groups of diffuse emission bands arise in this level (reference 1).
$[\sigma_g^2\pi_u^4\pi_g^3\,^2\Pi_{\frac{1}{2}}]\sigma_u\,6p$		$\Pi_{1,1u}$	K	57794	(246)	$ex+5p^6\,^2P$	$X \rightarrow K$ gives part of absorption bands in the vacuum region.
$[\sigma_g^2\pi_u^3\pi_g^4\,^2\Pi_{\frac{1}{2}}]\sigma_g\,6s$		$\Pi_{1,1u}$	J	56933	(207)	$ex+5p^6\,^2P$	$X \rightarrow J$ gives part of absorption bands in the vacuum region.
$[\sigma_g^2\pi_u^4\pi_g^3\,^2\Pi_{\frac{1}{2}}]\sigma_g\,6s$		$\Pi_{1,1g}$	I	56000	(360)	$ex+5p^6\,^2P$	Five groups of semicontinuous bands arise in this level (reference 1). The abnormally high value for the frequency separation (360 cm^{-1}) for these bands may be partly only apparent and due to the shape of the repulsion curves of the lower states of these bands.
$\sigma_g\pi_u^4\pi_g^4\sigma_u$	$^1\Sigma_u^+$	0_u^+	H	51683	164.5	$5p^4\,^1S_0+5p^6\,^1S_0$	$X \rightarrow H$ gives Cordes absorption bands λ1950–1770[11]. Five groups of semi-continuous bands in emission (reference 1) arise in this level H.
$\sigma_g\pi_u^4\pi_g^3\sigma_u^3$	$^3\Pi_g$	1_g	G	51528	215	$5p^4\,^3P_1+5p^6\,^1S_0$	Five groups of diffuse semicontinuous emission bands arise in G and have for their lower levels different repulsive states dissociating into $^3P+^3P$ iodine atoms (references 1 and 9).
$\sigma_g^2\pi_u^3\pi_g^3\sigma_u^2$	$^3\Sigma_u^-$	0_u^+	F	47150	96.2	$5p^4\,^3P_2+5p^6\,^1S_0$	$X \leftrightarrow F$ gives emission bands 4420–4000A in the presence of a foreign gas and also probably part of P-R, K-M absorption bands.
$\sigma_g^2\pi_u^3\pi_g^3\sigma_u^2$	$^3\Sigma_u^-$	1_u	E	45781	104.5	$5p^4\,^3P_2+5p^6\,^1S_0$	$X \leftrightarrow E$ gives emission bands 2785–2750A in the presence of a foreign gas, and also probably part of P-R, K-M absorption bands.
$\sigma_g^2\pi_u^3\pi_g^4\sigma_u^2$	$^1\Sigma_g^+$	0_g^+	D	41355	101.9	$5p^4\,^1D_2+5p^6\,^1S_0$	$D \rightarrow B$ gives emission bands 2730–2520A in the presence of a foreign gas.
$\sigma_g^2\pi_u^3\pi_g^3\sigma_u^2$	$^1\Sigma_u^+$	0_u^+	C	39131	103.0	$5p^4\,^1D_2+5p^6\,^1S_0$	$X \leftrightarrow C$ gives emission bands 3455–3015A in the presence of a foreign gas, and absorption bands recorded by Skorko at high temperatures.
$\sigma_g^2\pi_u^3\pi_g^3\sigma_u$	$^3\Pi_u$	0_u^+	B	15598	126.6	$5p^5\,^2P_{\frac{1}{2}}+5p^5\,^2P_{\frac{1}{2}}$	$X \leftrightarrow B$ gives absorption bands 8600–4300A and emission bands 6700–5000A (reference 9).
		1_u	A	11803	44	$5p^5\,^2P_{\frac{1}{2}}+5p^5\,^2P_{\frac{1}{2}}$	$X \rightarrow A$ gives absorption bands in the region 9300–8375A (reference 9).
$\sigma_g^2\pi_u^4\pi_g^4$	$^1\Sigma_g^+$	0_g^+	X	0	213.8	$5p^5\,^2P_{\frac{1}{2}}+5p^5\,^2P_{\frac{1}{2}}$	Ground state.

[a] In column 7 of this table, "ex" stands for an excited neutral atom of the configuration of the type $5p^4\,6p$ or $5p^4\,6s$. The positions of the levels in column 5 represent the heights of the zero vibrational levels of the respective states over that of the ground state.
[b] H. Cordes, Z. Physik 97, 603 (1935).

in levels with smaller ω_s values and hence larger r_s values than those of the ground state. This shows that collisions with the foreign gas the make molecules in the higher excited states go over into lower excited electronic states in the energy range 39131 to 47150 cm^{-1}, with larger r_s values and smaller ω_s values, in the manner discussed by Wieland.[6]

The author wishes to express his thanks to Dr. R. S. Mulliken and Dr. G. Herzberg for their kind interest in the work.

PHYSICAL REVIEW VOLUME 81, NUMBER 5 MARCH 1, 1951

Relation between Lattice Vibration and London Theories of Superconductivity

J. BARDEEN
Bell Telephones Laboratories, Murray Hill, New Jersey
(Received November 2, 1950)

A gas of noninteracting electrons of small effective mass, m_{eff}, has a large diamagnetic susceptibility. It is shown that the London phenomenological equations of superconductivity follow as a limiting case when m_{eff} is so small that the Landau-Peierls theory yields a susceptibility $<-1/4\pi$. Justification is given for the use of an effective mass, $m_s \sim 10^{-4} m$, for superconducting electrons in the lattice-vibration theory of superconductivity. This value is sufficiently small to show that the theory gives the London equations and, as a consequence, the typical superconducting properties. The concentration of superconducting electrons, n_s, is smaller than the total electron concentration, n, by about the same ratio as the effective masses, so that $n_s/n \sim m/m_s$, and thus the penetration depth is of the same order as that given by the usual London expression.

I. INTRODUCTION

A THEORY of superconductivity based on interactions between electrons and lattice vibrations has been discussed in two previous communications.[1,2] The second of these (to be denoted by the letters WF), deals with wave functions for superconducting electrons. Fröhlich[3] has independently developed a theory along similar lines. These earlier papers have been concerned primarily with the energy of the lowest state of a superconductor and have not discussed in any detail how the electrodynamic characteristics of the superconducting state—perfect diamagnetism and infinite conductivity—follow from the model. We shall show here that the theory leads to the London phenomenological equations[4] in the manner indicated in our earlier papers.

The present theory is similar in many respects to one suggested some years ago by the author.[5] In the earlier theory it was proposed that in the superconducting state there is a small distortion of the lattice which produces Brillouin zone boundaries with small energy gaps, $\sim \kappa T_c$ (T_c = transition temperature) at the Fermi surface. There would be a resultant decrease in energy of electrons in states on the low energy side of the gap. Associated with the small energy gap is a small effective mass ratio, $\sim \kappa T_c/E_F$, for electrons with energies near the Fermi surface, E_F. It was shown that a sufficiently large diamagnetism for superconductivity will occur if there is a sufficient number of electrons of small effective mass. The difficulty with the theory as formerly proposed is that it appears that the energy required to distort the lattice and so to produce the zone boundaries is larger than the energy gained by the electrons.

In the present theory, zero-point vibrations replace the small permanent distortion of the lattice. The effective mass of the superconducting electrons is small as in the earlier theory, and we have suggested[1,2] that the explanation of the superconducting properties in terms of a large diamagnetic effect of the electrons is similar.

It has been recognized for some years that the Meissner effect ($\mathbf{B}=0$), is a more basic property of the superconducting state than infinite conductivity ($\mathbf{E}=0$), although, from a purely macroscopic point of view, neither one is a consequence of the other. Both follow from the London equations which can be derived most readily from a consideration of the magnetic properties.

From a formal point of view, a perfect diamagnetism can be described by a diamagnetic susceptibility equal to $-1/4\pi$. Landau[6] has shown that, as a consequence of quantum theory, a gas of free noninteracting electrons obeying Fermi-Dirac statistics has a diamagnetic susceptibility:

$$\chi_0 = -(n/2E_F)(e\hbar/2mc)^2 = -n\mu^2/2E_F, \quad (1.1)$$

Here n is the number of electrons/cm^3, E_F is the

[1] J. Bardeen, Phys. Rev. 79, 167 (1950).
[2] J. Bardeen, Phys. Rev. 80, 567 (1950) (referred in the text as WF).
[3] H. Fröhlich, Phys. Rev. 79, 845 (1950).
[4] F. and H. London, Physica 2, 341 (1935).
[5] J. Bardeen, Phys. Rev. 59, 928 (A) (1941). This work, done while the author was at the University of Minnesota, was interrupted by the war and was never published in full.
[6] L. Landau, Z. Physik 64, 629 (1930).

maximum energy of the Fermi distribution and μ is the Bohr magneton. Landau's theory was later extended by Peierls[7] to apply to electrons with Bloch-type wave functions appropriate to motion in a periodic field of a crystal lattice. The effect of the periodic field is to introduce an appropriate effective mass instead of the ordinary mass in (1.1). If the effective mass is made sufficiently small, Eq. (1.1) will yield values for $\chi_0 < -1/4\pi$. If values of n and E_F characteristic of ordinary metals are inserted in (1), the expression gives values of χ_0 of the order of 10^{-7} to 10^{-6}, in agreement with observed susceptibilities. To get a value smaller than $-1/4\pi$ would require an effective mass of 10^{-3} m or smaller.

Wave functions for superconducting electrons (see WF) are linear combinations of Bloch states which lie within a small energy $\Delta \sim \kappa T_c$ of the Fermi surface. It has been pointed out that these wave functions correspond to a small effective mass, of the order of $(\Delta/E_F)m$. The concentration of superconducting electrons, n_s, is a small fraction, of the order of (Δ/E_F), of the total concentration, n, but the effective Fermi energy of the superconducting electrons, E_s, is of the order of Δ so that

$$n_s/E_s \sim n/E_F. \tag{1.2}$$

The condition for a perfect diamagnetism is then

$$(n_s\mu^2/2E_s)(m/m_{eff})^2 \sim (n\mu^2/2E_F)(E_F/\Delta)^2 > 1/4\pi. \tag{1.3}$$

In the derivation of (1.1) it is assumed that the magnetic field is uniform throughout the specimen. Actually, the magnetic field in a perfect diamagnetic or superconductor is confined to a thin surface layer. It is necessary to reinvestigate the problem with this in mind; we shall show that one is then led to the London phenomenlogical theory. In other words, we shall show that the London theory is the limiting case of a large diamagnetism of the Landau-Peierls type.

In the ordinary theory of diamagnetism, the electrons are in quantized states which correspond to the classical circular orbits of an electron in a magnetic field. Circular orbits in the interior of the specimen give a large diamagnetic moment which is cancelled to a large extent by electrons in boundary orbits whose moment is in the opposite direction.[8] We shall show that when (1.3) is fulfilled, the magnetic field and associated currents are confined to the penetration depth of the London theory and there are no quantum states which correspond to circular or to boundary orbits. The wave functions of the electrons are only slightly modified by the magnetic field.

The connection with the phenomenological theory follows the general approach anticipated by London.[9] London has pointed out that it is convenient to choose the gauge in the vector potential, $\mathbf{A}$, in such a way that the normal component vanishes at a free surface and such that the divergence of $\mathbf{A}$ vanishes everywhere:

$$\mathrm{div}\mathbf{A}=0; \quad \mathbf{A}_\perp = 0 \text{ on the surface.} \tag{1.4}$$

These conditions determine $\mathbf{A}$ uniquely in a simply connected body. In a multiply connected body, such as a ring, an additional quantity, related to the flux through the ring, must be specified. This additional freedom permits the description of persistent currents by the theory. In a body of macroscopic size, $\mathbf{A}$ is confined to a thin surface layer and is parallel to the surface.[10]

In quantum theory, the average velocity of an electron of charge $(-e)$ is given by the average value of

$$\mathbf{v}=[(\mathbf{p}+e\mathbf{A}/c)/m]_{av} \tag{1.5}$$

over the wave function. If it is assumed that the wave functions are not altered by the field (with the above choice of gauge), the average value of $\mathbf{p}$ will be zero and the current density at a position $\mathbf{R}$ will be given by[9]

$$\mathbf{j}(\mathbf{R}) = -n(\mathbf{R})e\mathbf{v}(\mathbf{R}) = -(e^2/mc)n(\mathbf{R})\mathbf{A}(\mathbf{R}), \tag{1.6}$$

where $n(\mathbf{R})$ is the concentration of electrons at $\mathbf{R}$. The curl of (1.5) gives the London phenomenological equation:

$$\mathrm{curl}\Lambda\mathbf{j} = -\mathbf{B}/c, \tag{1.7}$$

where the parameter Λ of the theory is evaluated to be:

$$\Lambda = m/ne^2. \tag{1.8}$$

The penetration depth, d, of the London theory is

$$d = (mc^2/4\pi e^2 n)^{\frac{1}{2}}. \tag{1.9}$$

As London points out,[9] the wave functions of the electrons will be modified by the field so that (1.6) is an over-simplification. He states that it would be "sufficient to show that a state would be established in which the eigenfunctions of a fraction of the electrons are prevented from coiling when the system is brought into a magnetic field, but stay essentially as they are without magnetic field, as if frozen." We may interpret this statement as being equivalent to the one made above: that in a superconductor "there are no quantum states which correspond to the classical circular or to the boundary orbits."

We shall show in (1.6) and (1.8), that the quantum states actually are modified by the field in such a manner as to introduce an effective mass instead of the ordinary electron mass. However, since m_{eff}/n_s is of the order of m/n, the values of Λ and of the penetration depth are of the same order as given by (1.8) and (1.9). It is well known that observed penetration depths are in general agreement with (1.9) as to order of magnitude.

[7] R. Peierls, Z. Physik **80**, 763 (1933).

[8] For an excellent discussion of this problem, see J. H. Van Vleck, *Electric and Magnetic Susceptibilities* (Oxford University Press, London, England, 1932).

[9] F. London, Proc. Roy. Soc. (London) **A152**, 24 (1935); Phys. Rev. **74**, 562 (1948).

[10] For a justification for this choice of gauge, see J. Bardeen, Phys. Rev. **81**, 469 (1951).

II. RELATION BETWEEN THE LANDAU-PEIERLS AND THE LONDON THEORIES

We are concerned in this section with the relation between the Landau-Peierls theory[6,7] of diamagnetism and the London theory for a model in which we make the *ad hoc* assumption that the electrons have a small effective mass. The justification for the application to superconducting electrons will be given in following sections. We shall here assume simply that the electrons have an effective mass which is smaller than normal and work out the consequences.

In the Bloch theory, the effective mass is a tensor rather than a scalar. If the energy of an electron with wave vector $\mathbf{k}$ is $\epsilon(\mathbf{k})$, the effective mass is defined by[11]

$$1/m_{eff}=\hbar^{-2}\,\mathrm{grad}_{\mathbf{k}}\,\mathrm{grad}_{\mathbf{k}}\,\epsilon(\mathbf{k}). \tag{2.1}$$

For example, for motion in the x-direction,

$$(1/m_{eff})_{xx}=\hbar^{-2}\partial^2\epsilon(\mathbf{k})/\partial k_x^2. \tag{2.2}$$

For simplicity, we shall take a model for which

$$\epsilon(\mathbf{k})=(\hbar^2/2m)(\alpha_1k_x^2+\alpha_2k_y^2+\alpha_3k_z^2). \tag{2.3}$$

The coefficients, α_i, are the effective mass ratios:

$$\alpha_1=m/(m_{eff})_{xx},\ \text{etc.} \tag{2.4}$$

Peierls' expression for the diamagnetic susceptibility for electrons with energies given by (2.3) is

$$\chi=-\tfrac{1}{2}n_e\mu^2\alpha_1\alpha_2/E_e, \tag{2.4'}$$

where n_e is the number of electrons per unit volume for which (2.3) holds and E_e is the maximum value of $\epsilon(\mathbf{k})$ in the Fermi distribution. It is assumed that the magnetic field is in the Z-direction.

If α is large, a Brillouin zone with energies given by (2.3) can accommodate only a small number of electrons; if the states are filled to a maximum energy E_e:

$$n_{zone}=(1/3\pi^2)(3mE_e/\hbar^2)^{\frac{3}{2}}(\alpha_1\alpha_2\alpha_3)^{-\frac{1}{2}}. \tag{2.5}$$

We shall not restrict n_e to the small value given by (2.5), but shall suppose that there is a sufficient number of zones to accommodate any desired number, n_e, of electrons.

The condition that $\chi<-1/4\pi$, corresponding to a perfect diamagnetic, is:

$$n_e\mu^2\alpha_1\alpha_2/E_e>1/2\pi. \tag{2.6}$$

We shall show that (2.6) is equivalent to the condition for the validity of the London theory, and that the wave functions of the electrons are not modified very much by the magnetic field. When (2.6) applies, it is no longer permissible to assume that the magnetic field is uniform in the specimen. The current density and magnetic field should be determined by a self-consistent field procedure. The current flow depends on the magnetic field which in turn is determined in part by the current flow. We first calculate the current under the assumption that the wave functions are not altered very much by the field. The penetration of the field into the specimen then follows from the London theory. We shall then show that if (2.6) is satisfied, the wave functions are not significantly altered so that the initial assumption is justified.

We consider a metal whose surface is the plane $x=0$. The magnetic field, $\mathbf{B}$, has only a Z-component and decreases from a value B_0 at $x=0$ to zero in the interior in the case of a perfect diamagnetic. It is most convenient to choose the vector potential $\mathbf{A}$ in such a way that

$$A_x=A_z=0, \tag{2.7}$$

while $A_y(x)$ is independent of y and z. Then B, which depends only on x, is given by:

$$B_x=B_y=0,\quad B_z(x)=\partial A_y/\partial x. \tag{2.8}$$

The equation which determines $\mathbf{A}$ from the current density, $\mathbf{j}$, is:

$$d^2A_y/dx^2=-4\pi j_y/c. \tag{2.9}$$

We next consider how j_y depends on $\mathbf{A}$. The wave function, ψ_k, is of the form:

$$\psi_k=\exp[i(k_yy+k_zz)]\cdot f(x). \tag{2.10}$$

As the effective mass for motion in the y-direction is m/α_2, the y-component of current density for an electron in the state ψ_k is

$$-(\alpha_2e/m)[\hbar k_y+(e/c)A_y]\psi_k^*\psi_k. \tag{2.11}$$

If the wave function for the state $+k_y$ does not differ appreciably from that for $-k_y$, the sum over k_y vanishes and the total current density is

$$j_y=-(\alpha_2e^2/mc)n_eA_y, \tag{2.12}$$

where

$$n_e=\Sigma\psi_k^*\psi_k \tag{2.13}$$

is the concentration of electrons, which we shall assume to be constant.

When (2.12) is inserted into (2.9), there results an equation of the form:

$$\partial^2A_y/\partial x^2=A_y/d^2, \tag{2.14}$$

where d is the penetration depth of the London theory:

$$d=(mc^2/4\pi\alpha_2e^2n_e)^{\frac{1}{2}}. \tag{2.15}$$

The appropriate solution of (2.14) is:

$$A_y=-B_0de^{-x/d}. \tag{2.16}$$

Under what conditions is it valid to assume, as we have done above, that the wave function for the state $+k_y$ is nearly the same as that for $-k_y$? The wave equation for the electron is

$$(1/2m)[\alpha_1p_x^2+\alpha_2(p_y+eA_y/c)^2+\alpha_3p_z^2]\varphi=E\varphi. \tag{2.17}$$

We may set $p_y=\hbar k_y$ and $p_z=\hbar k_z$, so that (2.17) reduces

[11] See, for example, F. Seitz, *Modern Theory of Solids* (McGraw-Hill Book Company, Inc., New York, 1940), p. 316.

to an equation in x alone. The difference between the second term of (2.17) and $\alpha_2 p_y^2/2m$ is an effective potential, V_e, which is large only near the surface:

$$V_e=(\alpha_2/2m)[(p_y+eA_y/c)^2-p_y^2]. \quad (2.18)$$

The potential is negative (attractive) if p_y is opposite in sign to eA_y/c and is a minimum at a position $x=x_0$ such that

$$p_y+eA_y(x_0)/c=0. \quad (2.19)$$

In the usual theory of diamagnetism, the state corresponding to this value of p_y is localized near $x=x_0$. States localized very close to the surface correspond to boundary orbits whose moments nearly cancel those of states localized in the interior.[12] We shall show that if (2.6) is satisfied, there are no localized quantum states either at the boundary or in the interior, and that the wave function does not depend very much on the sign of k_y.

The maximum negative potential at the surface occurs when p_y has its maximum value given by

$$\alpha_2 p_y^2/2m=E_s. \quad (2.20)$$

The value of V_e is then $-E_s$ at $x=0$, and the negative potential extends over a distance of the order of the penetration depth, d. This potential will not affect the wave function very much, and there will be no stationary state if

$$\int p_x dx<\hbar, \quad (2.21)$$

where p_x is computed classically for an energy $E=E_s$. If (2.21) is satisfied, the change in phase of the wave function in the W.K.B. approximation is less than one radian. The value of p_x is 0 for $x>\sim d$ and is

$$p_x\sim(2mE_s/\alpha_1)^{\frac{1}{2}} \text{ for } x<\sim d. \quad (2.22)$$

Condition (2.21) is then approximately

$$(2mE_s/\alpha_1)^{\frac{1}{2}}d<\hbar,$$

or

$$\alpha_1\hbar^2/2mE_sd^2>1. \quad (2.23)$$

With use of (2.15) for d, this relation becomes

$$n_s\mu^2\alpha_1\alpha_2/E_s>1/8\pi, \quad (2.24)$$

which, except for a numerical factor, is the same as (2.6).

We have thus shown that when the Landau-Peierls theory indicates a perfect diamagnetism, there are no bound states and the wave functions of the electrons are not altered very much by the field near the surface. The conditions for the London theory are satisfied.

III. EFFECTIVE MASS OF SUPERCONDUCTING ELECTRONS

We have shown in WF that the wave functions of the superconducting electrons are linear combinations of Bloch states, ψ_k, which have energies in the range between $E_F-\epsilon_1$ and $E_F+\epsilon_1$ where E_F is the energy of the Fermi surface of the normal metal at $T=0°K$. In WF they were taken to be of the form

$$\Psi_k=c_k\psi_k+\Sigma_{k'}c_{k'}[q_{kk'}/(q_{kk'})_{rms}]\psi_{k'}. \quad (3.1)$$

Here, $q_{kk'}$ is the amplitude of the normal mode whose wave vector connects the states $\mathbf{k}$ and $\mathbf{k}'$. The states ψ_k have energies in the range between E_F and $E_F+\epsilon_1$, and the states $\psi_{k'}$ have energies between $E_F-\epsilon_1$ and E_F. There is one superconducting state for each ψ_k. The value of ϵ_1 is chosen to make the energy a minimum when interactions between electrons and normal modes are taken into account and is presumably of the order of kT_c.

The equations which determine the coefficients c_k and $c_{k'}$ are Eqs. (3.20) of WF:

$$c_k\epsilon_k+\Sigma_{k'}c_{k'}M_{k'k}=E_kc_k, \quad (3.2a)$$

$$c_{k'}(\epsilon_{k'}+\hbar\omega_{kk'})+c_kM_{kk'}=E_kc_{k'}, \quad (3.2b)$$

in which ϵ_k and $\epsilon_{k'}$ are the energies of the Bloch states, E_k is the energy of the superconducting state, Ψ_k, and $M_{kk'}$ is the matrix element and $\omega_{kk'}$ the angular frequency for the normal mode kk'. Equation (3.2b) can be solved for $c_{k'}$:

$$c_{k'}=M_{kk'}c_k/(E_k-\epsilon_{k'}-\hbar\omega_{kk'}). \quad (3.3)$$

When (3.3) is inserted into (3.2a), there results an equation for E_k:

$$\Sigma\frac{|M_{kk'}|^2}{E_k-\epsilon_{k'}-\hbar\omega_{kk'}}=E_k-\epsilon_k. \quad (3.4)$$

In order to get an approximate solution of (3.4) we shall replace $\epsilon_{k'}+\hbar\omega_{kk'}$ by an average value, ϵ'. Equation (3.4) then reduces to

$$(E_k-\epsilon_k)(E_k-\epsilon')=\Delta^2, \quad (3.5)$$

where

$$\Delta^2=\Sigma_{k'}(M_{kk'})^2. \quad (3.6)$$

The solution of (3.5) is familiar from the theory of nearly free electrons in metals:

$$E_k=\tfrac{1}{2}(\epsilon_k+\epsilon')\pm\tfrac{1}{2}[(\epsilon_k-\epsilon')^2+4\Delta^2]^{\frac{1}{2}}. \quad (3.7)$$

The low energy state, which is the one of interest, is that with the negative sign. For $|\epsilon_k-\epsilon'|<2\Delta$, the approximate solution of (3.7) is[13]

$$E_k=\tfrac{1}{2}(\epsilon_k+\epsilon')-\Delta-[(\epsilon_k-\epsilon')^2/8\Delta]. \quad (3.8)$$

[12] E. Teller, Z. Physik 67, 311 (1931).

[13] *Note added in proof.*—It has been pointed out to the author by J. H. Van Vleck (private communication) that a lower energy is obtained if the ψ_k are taken in the range between $E_F-\epsilon_1$ and E_F and the $\psi_{k'}$ in the range between E_F and $E_F+\epsilon_1$. The difference is small when $|\epsilon_k-\epsilon'|<2\Delta$ so that (3.8) may be used. This condition is equivalent to the criterion for superconductivity given by Eq. (4.17) of WF and is required to get a small effective mass for the superconducting electrons. The approximation $(E_k)_{kk}=(1/2)(\epsilon_k+\epsilon')_{kk}-\Delta$ used in WF is independent of whether the states ψ_k are taken in the high energy or the low energy range.

We shall see in Sec. IV that the effective mass should be computed from energy changes which involve shifts of $\mathbf{k}$ and all the $\mathbf{k}'$ by the same small vector displacement $\mathbf{K}$ in $\mathbf{k}$-space. The normal modes which connect $\mathbf{k}$ and $\mathbf{k}'$ are then unchanged, since they depend only on the vector displacement between $\mathbf{k}$ and $\mathbf{k}'$. We also want to consider virtual shifts in which it is assumed that the matrix elements $M_{kk'}$ are independent of $\mathbf{K}$. The effective mass tensor is defined by

$$[(m_{ij})^{-1}]_{ij}=\hbar^{-2}(\partial^2 E_k/\partial K_i \partial K_j)_{K=0}. \tag{3.9}$$

In differentiating (3.8), with respect to K to get the effective mass, we therefore assume that Δ and $(\hbar\omega_{kk'})_{av}$ are independent of $\mathbf{K}$. The largest contribution comes from differentiation of the third term of (3.8);

$$[(m_{ij})^{-1}]_{ij}\sim\frac{\hbar^{-2}}{4\Delta}\left[\frac{\partial\epsilon_k}{\partial K_i}-\left(\frac{\partial\epsilon_{k'}}{\partial K_i}\right)_{av}\right]\left[\frac{\partial\epsilon_k}{\partial K_j}-\left(\frac{\partial\epsilon_{k'}}{\partial K_j}\right)_{av}\right]. \tag{3.10}$$

We can use the free electron approximation,

$$\epsilon_k=\hbar^2k^2/2m, \tag{3.11}$$

to estimate the order of magnitude of (3.10). Since the angles between $\mathbf{k}$ and $\mathbf{k}'$ are in general large, each of the factors is of the order of

$$\left[\frac{\partial\epsilon_k}{\partial K}-\left(\frac{\partial\epsilon_{k'}}{\partial K}\right)_{av}\right]\sim\frac{\partial\epsilon_k}{\partial K}\sim\frac{\hbar^2k_0}{m}, \tag{3.12}$$

where k_0 is the magnitude of $\mathbf{k}$ on the Fermi surface. Thus we have

$$(m_{ii})^{-1}\sim(\hbar^2/4\Delta)(\hbar^2k_0/m)^2\sim m^{-1}(E_F/2\Delta). \tag{3.13}$$

As $\Delta\sim kT_c\sim10^{-4}$ ev and E_F is several ev, $(m_{ii})^{-1}$ is of the order of $10^{-4}\,m$. A similar estimate was obtained by a slightly different procedure in WF.

IV. CURRENT FLOW IN THE LONDON THEORY

It is not at once evident that an effective mass should be used in the expression (1.5) for the current density in the London theory, because it is the ordinary mass which appears in the expression (1.4) for the average velocity. We shall derive an expression for the current density, sufficiently general to apply to superconducting as well as to Bloch wave functions, in order to show why the effective mass appears.

The hamiltonian for an electron interacting with the normal modes can be expressed in the form (WF):

$$(H_e+H_L+H_I)\psi=E\psi, \tag{4.1}$$

where H_e is the hamiltonian for the electrons with the ions in their equilibrium positions, H_L is that for the vibrations and H_I represents the interaction terms between the electron and normal modes.

We again consider a metal with a surface at $x=0$ subject to a magnetic field in the Z-direction. The vector potential may be defined as in (2.7), so that

$$H_e=(1/2m)[p_x^2+(p_y+eA_y/c)^2+p_z^2]+V(r), \tag{4.2}$$

where the subscript i represents the ith electron. Since A_y is a function only of the x coordinate, the periodicity in the y and z-directions is not destroyed.

A typical term of H_I is of the form

$$q_sV_s(r), \tag{4.3}$$

where q_s is the amplitude of a mode with wave vector s and $V_s(r)$ gives the interaction for unit amplitude.

The superconducting states can still be designated by k_y and k_z, but it is in general necessary to replace k_x by a different quantum number which need not be specified. The wave function is then of the form

$$\psi(r, q_s)=\exp[i(k_yy+k_zz)]\cdot U_k(r, q_s). \tag{4.4}$$

Owing to the interaction terms, the complete hamiltonian is not periodic, so that $U(r)$ is not periodic, as it would be for Bloch functions. There are, however, various ways in which U_k may be so specified as to express a wave function in the form (4.4). One might require, for example, that when U is expanded in a power series in the q_s's, the term independent of the q_s's be periodic. In other words, U_k should be periodic when all the q_s's are set equal to zero.

If (4.4) is substituted into (4.1), the following equation is obtained for U_k:

$$\left[\frac{\hbar^2}{2m}(k_y^2+k_z^2)+\frac{e\hbar k_y}{m}\left(p_y+\frac{e}{c}A_y\right)\right]U$$
$$+\left[\frac{\hbar^2p^2}{2m}+V+H_L+H_I\right]U=EU. \tag{4.5}$$

Let us now change k_y to $k_y+\Delta k_y$, and treat the terms in Δk_y as a perturbation. Terms linear in Δk_y are

$$(\hbar\Delta k_y/m)(\hbar k_y+p_y+eA_y/c). \tag{4.6}$$

We suppose that the interaction terms remain unchanged. The change in energy, ΔE, corresponding to the change Δk_y can be obtained by first-order perturbation theory. It is required that U_k be of the form specified above so that k_y does not enter into the boundary conditions for U_k. There results:

$$\Delta E/\Delta k_y=(\hbar/m)\int U_k^*(\hbar k_y+p_y+eA_y/c)U_k\,d\tau,$$
$$=(\hbar/m)\int\psi_k^*(p_y+eA_y/c)\psi_k\,d\tau. \tag{4.7}$$

The term on the right is just $\hbar$ times the average velocity v_y. Thus, just as for ordinary Bloch functions, we have

$$v_y=\partial E/\hbar\partial k_y. \tag{4.8}$$

This equation is valid if the change in energy is computed by assuming that the interaction terms remain

unchanged. This requires that when k_y in a wave function of the form (3.1) is changed to $k_y+\Delta k_y$, k_y' must be increased to $k_y'+\Delta k_y$. The normal modes will then be unchanged. Furthermore, in computing the change in energy, it must be assumed that $M_{kk'}$ depends only on the vector displacement between $\mathbf{k}$ and $\mathbf{k}'$. Even if this latter condition is not satisfied, we can consider virtual displacements in which it is. Equation (4.8) will then be valid if the energy is calculated for such virtual displacement.

We shall now suppose that $A_y(x)$ is such that the wave functions are not altered very much by the field. The conditions for the London theory are then satisfied. We may then treat the terms in A_y as a perturbation and calculate the energy, E_{k1}, arising from the magnetic field by first-order perturbation theory. The total energy is

$$E_k=E_{k0}+E_{k1}+\cdots, \tag{4.9}$$

where E_{k0} is the energy for a wave function Ψ_{k0} corresponding to zero field and

$$E_{k1}=\frac{1}{2m}\int\Psi_{k0}^*\left[\frac{2e}{c}p_yA_y+\frac{e^2}{c^2}A_y^2\right]\Psi_{k0}d\tau. \tag{4.10}$$

The average velocity of the electron can be obtained by use of (4.8)

$$v_y=[(\partial E_{k0}/\partial k_y)+(\partial E_{k1}/\partial k_y)]/\hbar. \tag{4.11}$$

The change in energy with k_y is to be computed as required for (4.8) to hold. This expression is accurate to terms of the second order in the wave function.

The expression for E_{k1} can be simplified if it is assumed that A_y is a slowly varying function which can be treated as a constant while the integration is carried out over a unit cell. We can then use (4.8) to replace p_y/m by v_y for zero field, and obtain

$$E_{k1}=\int\left(\frac{e}{c}\frac{\partial E_{k0}}{\partial k_y}A_y+\frac{e^2}{2mc^2}A_y^2\right)\Psi_{k0}^*\Psi_{k0}d\tau. \tag{4.12}$$

If we now make the reasonable assumption that the average value of $\Psi_{k0}^*\Psi_{k0}$ over a cell is independent of changes in k_y, we find

$$v_y=\frac{1}{\hbar}\frac{\partial E_{k0}}{\partial k_y}+\int\frac{e}{\hbar^2c}\frac{\partial^2E_{k0}}{\partial k_y^2}A_y\Psi_{k0}^*\Psi_{k0}d\tau. \tag{4.13}$$

The first term gives the normal current which averages to zero, and the second term is that arising from the magnetic field. It is similar to that used by London except that an effective mass, given by

$$(m_{eff})^{-1}=\hbar^{-2}\partial^2E_{k0}/\partial k_y^2, \tag{4.14}$$

replaces the ordinary electron mass. The current density which arises from the magnetic field is

$$j_y=-(e^2/\hbar^2c)(\partial^2E_{k0}/\partial k_y^2)A_y\sum\Psi_{k0}^*\Psi_{k0}, \tag{4.15}$$

where the sum is over all occupied states. This completes the proof that an effective mass should be used in London expressions for the current density.

V. JUSTIFICATION FOR USE OF EFFECTIVE MASS

There remains to discuss the justification for using an effective mass, m/α_1, in the condition for the validity of the London theory, (2.3), which came from Eq. (2.17) and following. The method of the effective mass has been used for the discussion of the motion of electrons in a slowly varying potential, V_s, superimposed on the periodic potential of the crystal lattice. In an energy band in which the energies are given by an expression of the form (2.3) it is possible to omit the periodic potential and calculate a wave function from the equation:

$$[(2m)^{-1}(\alpha_1p_x^2+\alpha_2p_y^2+\alpha_3p_z^2)+V_s]\varphi=E\varphi. \tag{5.1}$$

To a close approximation, the true wave function is

$$\psi=\varphi(r)\psi_0(r), \tag{5.2}$$

where $\psi_0(r)$ is the Bloch function for $k=0$. The method can be applied to slowly varying magnetic fields, in which case φ is a solution of (2.17).

One way to get the appropriate effective mass for motion, say, in the x-direction is to compare the energy of a Bloch function with a sinusoidal modulation with that of the corresponding plane wave. Such a function is

$$\psi=-\tfrac{1}{2}i(\psi_{k+a}-\psi_{k-a})\simeq\sin ax\psi_k, \tag{5.3}$$

for which the energy is approximately:

$$\begin{aligned}E&=\tfrac{1}{2}[\epsilon(k+a)+\epsilon(k-a)]\\&=\epsilon(k)+\tfrac{1}{2}a^2\partial^2\epsilon/\partial k_x^2.\end{aligned} \tag{5.4}$$

If the added energy is compared with $\hbar^2a^2/2m$, it can be seen that the effective mass is $\hbar^{-2}\partial^2\epsilon(k)/\partial k_x^2$, as given by (2.2).

The added energy is that required to localize a wave function centering about ψ_k within a distance π/a. The above argument can be extended without modification to apply to superconducting wave functions. The change in energy with k should then be computed on the assumption that the interaction terms remain unchanged, as discussed below (4.7) for application to the calculation of average velocity. It should be noted that in our model the effective mass is negative so that the hole theory should be used for the superconducting electrons.

The Mobility and Life of Injected Holes and Electrons in Germanium

J. R. HAYNES AND W. SHOCKLEY
Bell Telephone Laboratories, Murray Hill, New Jersey
(Received October 26, 1950)

The mobilities of holes injected into *n*-type germanium and of electrons injected into *p*-type germanium have been determined by measuring transit times between emitter and collector in single crystal rods. Strong electric fields in addition to those due to injected current were employed so that spreading effects due to diffusion were reduced. The mobilities at 300°K are 1700 cm²/volt-sec for holes and 3600 cm²/volt-sec for electrons with an error of probably less than five percent. The value for electrons is about 20 percent higher than the best estimates obtained from the conventional interpretation of the Hall effect and the difference may be due to curved energy band surfaces in the Brillouin zone. Studies of rates of decay indicate that recombination of holes and electrons takes place largely on the surface of small samples with constants varying from 10^2 to $>10^4$ cm/sec for special treatments.

I. INTRODUCTION

As a result of new experimental techniques[1] developed in connection with the transistor[2] program, the speed with which holes and electrons drift in electric fields in germanium can now be measured with an accuracy sufficient to determine their mobilities to within a few percent. The basic phenomena which permit these new experiments to be performed are those of carrier injection[3] and collector action;[2] with the aid of the former, holes or electrons can be injected at a given place and time, and with the aid of the latter their arrival time at another point can be determined.

It should be emphasized that transit time measurements determine drift mobility in a very direct way. Hall effect measurements, which have previously been used to determine mobilities in semiconductors, are quite indirect. The relationship between Hall mobility, defined by the angle between current and electric vectors in unit magnetic field, and true mobility involves the detailed nature of the scattering processes and energy band shapes and only under special conditions does the ratio have the conventional value of $3\pi/8$. It now appears probable that a real deviation from the simple ratio $3\pi/8$ occurs for electrons in germanium and that this is associated with energy band shapes.[4]

II. SIMPLE CIRCUIT ARRANGEMENT FOR MOBILITY STUDIES

The essence of the technique described in this paper is incorporated in the circuit[5] shown in Fig. 1. A rod of *n*-type germanium, cut from a single crystal, is provided with rhodium-plated contracts at either end for good electrical contact. A battery is placed in series with these plated contacts so that a direct current I_B, called the sweeping current, flows downward in the crystal producing electric field in the same direction. Four phosphor bronze points are placed in contact with the germanium with the aid of a micromanipulator. A relay and a battery are placed in series with the point e so that when the relay is closed a current I_e flows from the point into the germanium making this point an emitter of positive holes. In series with the point C is placed a resistance R_1 and a battery, so that this point is biased negatively with respect to the germanium, as is a collector in a type A transistor. The other two points P_1 and P_2 are used as probes to measure the potential difference in the germanium crystal between the emitter and collector points. The input amplifier of a cathode-ray oscilloscope is connected across the resistance R_1. This resistance has a value which is small compared with the impedance of the collector point so that the voltage applied to the oscilloscope is proportional to the admittance of the point. At a certain instant of time a positive pulse of current is applied to the emitter point by closing the relay. Holes enter the crystal at this time and are swept down to the collector in the electric field produced by the combined

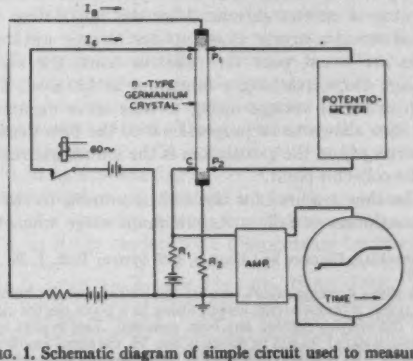

FIG. 1. Schematic diagram of simple circuit used to measure mobility of injected holes and electrons.

[1] Shockley, Pearson, and Haynes, Bell System Tech. J. **28**, 344 (1949).
[2] J. Bardeen and W. H. Brattain, Phys. Rev. **74**, 230 (1948); **75**, 1208 (1949).
[3] E. J. Ryder and W. Shockley, Phys. Rev. **75**, 310 (1947). J. N. Shive, Phys. Rev. **75**, 689 (1949). J. R. Haynes and W. Shockley, Phys. Rev. **75**, 691 (1949).
[4] Pearson, Haynes, and Shockley, Phys. Rev. **78**, 295 (1950).
[5] This circuit is drawn for the study of the behavior of injected holes in *n*-type germanium. It is equally well adapted to the study of injected electrons in *p*-type germanium. For this purpose it is only necessary to reverse the polarity of the batteries.

FIG. 2. Photograph of characteristic obtained on cathode-ray tube. Oscilloscope synchronized to start of hole injection.

FIG. 3. Photograph of characteristic obtained on cathode-ray tube. Oscilloscope synchronized to stop of hole injection.

currents I_B and I_e. When they arrive at the collector, they produce a measurable signal on the oscilloscope.

III. FORM OF SIGNAL OBTAINED AND TRANSIT TIME

A photograph of the signal obtained with the oscilloscope synchronized to the start of hole injection is shown in Fig. 2. The dots on the oscilloscope trace are 10 μsec marker intervals. A small initial rise can be observed. This rise is due to the added emitter current and is produced by the consequent increased voltage drop in the segment of the germanium crystal between the collector point and ground. After this initial rise, the signal remains constant for 60 μsec. During this time the injected holes are moving down the crystal from the emitter point, which was placed a centimeter away from the collector. When the holes arrive at the collector, the voltage applied to the oscilloscope rises slowly to a maximum at 120 μsec. This increase in voltage, which is made by the circuit to be proportional to the increase in collector current, has been shown to be also proportional to the hole density arriving at the collector point.[6]

The hole injection from the emitter point stops abruptly when the relay is opened. The photograph shown in Fig. 3 was obtained with the oscilloscope synchronized to this time. The initial short drop which occurs when the relay opens is analogous to the initial rise obtained at the start of hole injection and is due to the stop of emitter current. After this initial drop the signal remains nearly constant[7] for 60 μsec until the holes are swept past the collector when the signal voltage drops, reaching a minimum in 120 μsec. This drop in signal voltage owing to hole wave departure has been shown to be proportional to the hole density departing from the germanium is the immediate region of the collector point.[6]

The time required for the emitter current to rise to its maximum or fall to its minimum value when the relay was closed or opened was found by connecting the oscilloscope across R_2 instead of R_1 (Fig. 1). Although this time was shown to be a small fraction of a microsecond, the hole arrival and departure wave fronts are seen to be spread out over some 30 μsec. This "softening" of these waves has been found to be quantitatively that to be expected from random diffusion. When the emitter current is made sufficiently small so that the conductivity modulation can be neglected,[8] the shape of these characteristics[9] is given by the customary integral of the error function, such as is met with in heat flow problems, and diffusion takes place to equal degrees behind and ahead of the average portion of the wave fronts. For this reason the transit time required for the holes to pass from the emitter to the collector has been taken as the time at which the wave reaches half-maximum on arrival and half-minimum on departure.

IV. ELECTRIC FIELD ASSOCIATED WITH MEASURED TRANSIT TIME

The electric field in the germanium crystal during the time that the hole arrival characteristic was obtained (Fig. 2) was somewhat greater than that for the hole departure wave characteristic (Fig. 3), because the current flowing in the crystal was greater in the first case by an amount equal to the emitter current. In Sec. XI we shall show that, owing to conductivity modulation of the germanium, the electric field experienced by the wave front is never quite constant. Since, however, conductivity effects are minimized by using small values of the emitter current, the steady-state values of the electric field obtained with and without an emitter current are closely those experienced by the holes in the arrival and departure waves. These steady-state electric fields were determined by measuring the steady-state voltages between the probe points P_1 and P_2 with a potentiometer and dividing by the distance

[6] Shockley, Pearson, ann Haynes, Bell System Tech. J. 28, 344 (1949).

[7] A slight decrease occurs because the transit time for holes in the crystal is progressively longer, owing to a lower electric field, since the emitter current has been removed. This results in a decreasing signal. As will be shown in Sec. VI, the signal amplitude decreases with transit time due to recombination of holes and electrons.

[8] The shape of these wave fronts when conductivity modulation is important has been investigated theoretically by C. Herring, Bell System Tech. J. 28, 401 (1949).

[9] In cases where the diffusion spread is comparable to the mean life of the injected carriers correction must be made for wave front alteration due to recombination. The correction factor required is $\exp(t/\tau)$, where t is the transit time and τ is the mean life of the holes.

between them. This method of measuring the electric field involves, of course, the further assumption that the sample is homogeneous. The validity of this assumption is discussed in Secs. VIII and XI.

V. CALCULATION OF THE MOBILITY

Since we can measure the transit time from emitter to collector, the transit distance, and the electric field, we can calculate the mobility of the injected holes in this sample of n-type germanium.

The mobility of a charged particle moving in an electric field is by definition, $\mu=v/E$, where v is the velocity of the particle and E is the electric field intensity. The average velocity of the holes is equal to the distance of the emitter from the collector L, divided by the transit time t or $\mu=L/Et$. Since $E=V/L$, where V is the voltage between the emitter and collector, $\mu=L^2/Vt$. Further, if t_1 is the transit time measured from the hole arrival wave, t_2 the transit time measured from the hole departure wave, V_1 the voltage between the probe points with current I_e+I_B, and V_2 the voltage with current I_B only, we may calculate two values of mobility, $\mu_1=L^2/V_1t_1$ and $\mu_2=L^2/V_2t_2$. As will be shown in Sec. XI, the true value of μ lies between μ_1 and μ_2, which approach each other as the emitter current is reduced.

VI. LIFETIME

In addition to having a uniform electric field it is necessary to have a long lifetime for the injected carriers (either holes or electrons), since otherwise no appreciable signal will arrive at the collector point.

The lifetime can be determined by measuring the amplitude of the signal arriving at the collector point as the distance between the emitter and collector points is changed keeping I_B and I_e constant. This in effect changes the time which the carriers spend in the crystal before arriving at the collector.

Early measurements showed that injected holes in n-type germanium recombine with excess electrons so that, if N_0 is the original number of injected holes, there will exist after time t a number $N=N_0\exp(-t/\tau)$, where τ is the lifetime of a positive hole.[10] Later experiments show that this exponential law is obeyed well for injected electrons in p-type germanium.

The measurement of the lifetime of the carriers using crystals of various cross section shows that the lifetime of either injected holes or electrons decreases as the cross-sectional dimensions are decreased in a manner which is consistent with the view that injected carriers are recombining both in the volume and on the surface of the germanium.[11] We may therefore write $1/\tau=(1/\tau_v)+(1/\tau_s)$, where τ is the measured lifetime, τ_v the lifetime of the carriers in the volume of the germanium, and τ_s the effective lifetime due to surface recombination only.

Using crystals of large cross-sectional dimensions (0.4 cm) made by the crystal-pulling technique of Teal and Little,[12] lifetimes of the carriers as long as 200 μsec are obtained with both n and p type germanium.[13] Even with these large samples the carriers may still be recombining largely on the surface, so that it can only be concluded that the lifetime of the injected carriers is at least 200 μsec in the bulk material and probably is considerably greater.[14] The volume recombination rate can be increased by heating the crystals to a high temperature (above 500°C) and quenching. It can also be increased by bombardment of the crystal with alpha-particles or deuterons.

The surface recombination has been investigated using crystals produced by the pulling technique. These crystals are cut into samples having cross-sectional dimensions of the order of a half-millimeter. With these dimensions the carriers diffuse to the surface so rapidly that surface recombination dominates the measured lifetime.

Measurements show that the surface recombination rate depends on surface treatment. Using a sandblasted surface on a sample with cross-sectional dimensions of $7.59\times10^{-2}\times4.71\times10^{-2}$ cm the measured lifetime was 4 μsec. This value agrees with that predicted by the formula (see Appendix) derived on the assumption that every carrier which arrives at the surface disappears immediately. This formula is

$$1/\tau=(1/\tau_v)+D\pi^2(B^{-2}+C^{-2}),$$

where D is the appropriate diffusion constant and $2B$ and $2C$ the width and thickness of the rod. With a smoothly etched surface the measured lifetime of the carriers may be increased to about 30 μsec, showing that the carriers do not recombine immediately on reaching the surface.

Surface recombination can also be altered by chemical treatment. Work in collaboration with R. D. Heidenreich has shown that a recombination rate as high as that achieved by sandblasting the surface can be obtained by simply heating the sample in tap water or distilled water containing zinc ions. On the other hand, placing the sample in a solution of SbOCl with a positive polarity on the crystal increases the life of the carriers to the order of 100 μsec. Reversing the polarity reduces the measured lifetime to a value as low as that produced by sandblasting.

Recombination at the surface may be expressed in terms of a quantity having the dimensions of a velocity, as if the carriers were disappearing by flowing

[10] A discussion of the results of early measurements of lifetime will be found in reference 3.

[11] Reference to the recombination of holes, electrons on the surface as well as the interior of germanium volume will be found in H. Suhl and W. Shockley, Phys. Rev. 75, 1617 (1949).

[12] G. K. Teal and J. B. Little, Phys. Rev. 78, 647 (1950).

[13] Nearly all crystals examined which have been grown by this method display these long volume lifetimes. Crystals produced by other methods exhibit volume lifetimes usually less than 200 μsec. In one case a volume lifetime as short as 5 μsec was observed.

[14] A possible explanation of these long lifetimes is given in reference 3.

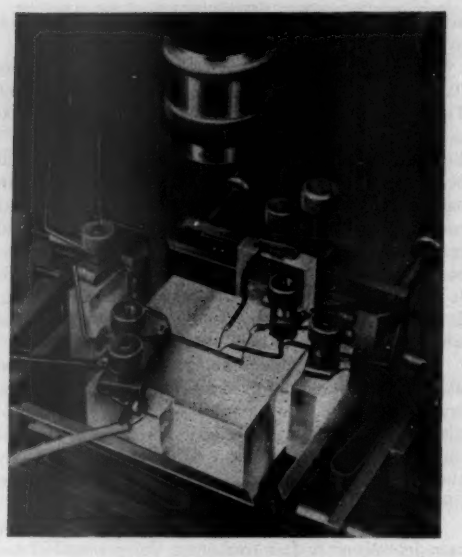

FIG. 4. Photograph of apparatus used to place metal points on germanium single crystal.

out of the surface. (See Appendix.) Values of this surface velocity have been obtained which range from 10^2 to $>10^4$ cm/sec, depending upon the kind of surface treatment.

VII. FABRICATION AND UNIFORMITY OF SAMPLES

Use has been made of this knowledge of surface recombination of injected carriers in the fabrication of the samples used for mobility measurement. Near the end electrodes it is desirable to have a short lifetime so that carriers injected from the electrodes do not enter the central portion of the sample and alter the resistivity. On the other hand, in the central portion of the crystal a long lifetime is desirable, not only so that the emitter may be placed at considerable distances from the collector, but also so that the shape of the signal received is negligibly affected by carrier recombination during the time of wave arrival and departure.

The cross-sectional dimensions of the samples were chosen to give sufficiently long lifetimes of the carriers in the central portion of the crystal without demanding the use of large currents to produce appropriate electric fields. Only single crystals were used, because of the uncertainty of the magnitude of the electric field in the neighborhood of grain boundaries.

In accordance with these considerations the samples were cut, ground, and polished into rectangular rods having dimensions of roughly $2.5\times0.05\times0.05$ cm. Approximately 0.2 cm of each end of the rod was then sandblasted and a section approximately 0.05 cm nearest each end was plated with rhodium. This left about 0.15 cm of sandblasted surface adjacent to each electrode to act as a recombination surface for carriers injected from the electrodes. The central portion of the rod was then etched for approximately one minute in CP-4 etch[15] and rinsed in methyl alcohol. Finally the rod was immersed in a solution of SbOCl with 1.5 volts positive potential on the rod for 5 minutes and again rinsed in methyl alcohol.[16]

The finished sample, mounted on a plastic block and surrounded by four micromanipulators, is shown in Fig. 4. The scale of the photograph can be judged from the microscope objective seen at the top and from the fact that the germanium crystal is 2.5 cm long. Four contact points, each controlled by a micromanipulator, may be seen contacting the sample. One of the points on the left was used as an emitter and one on the right was used as a collector, the other two being used as voltage probe points.

Only germanium crystals having a high degree of perfection were used. In order to make certain that the passage of the current I_B results in a uniform electric field all of the samples used have been probed to insure that in each the voltage drop is a nearly linear function of the distance along the crystal. Typical voltage distance plots are shown in Fig. 5 for four different samples, details of the individual specimens being given in the legend. It will be observed that some are n-type and some or p-type. One of the most satisfactory of the latter samples was produced by the addition of gallium to the melt from which the crystals are widthdrawn.

VIII. TEMPERATURE OF SAMPLES DURING MOBILITY MEASUREMENTS

Since the mobility is a function of temperature, it is important to know the temperature of the germanium crystal during mobility measurements. It has been

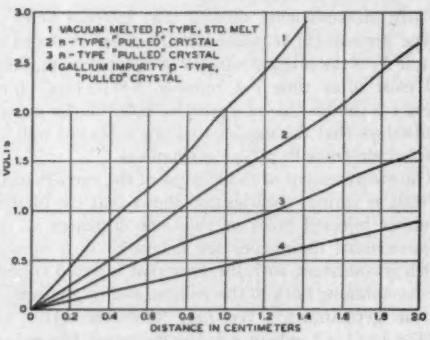

FIG. 5. Voltage as a function of distance along axes of typical samples for a current of 1.0 milliampere.

[15] The composition of CP-4 etch is as follows: 15 cc CH_3COOH, 25 cc concentrated HNO_3, 15 cc 48 percent HF, and 0.3 cc Br.

[16] This treatment was developed in collaboration with R. D. Heidenreich.

shown by Wilson[17] and more generally by Sietz[18] that, in the temperature range where the mobility is determined by lattice scattering in a nonpolar substance such as germanium or silicon, the mobility should vary at $T^{-\frac{3}{2}}$ for the nondegenerate case. This theoretical law has been confirmed by numerous observers including Pearson and Bardeen,[19] who found the predicted Hall coefficient variation with temperature in silicon, and by Pearson in his studies of germanium.[20] This work further shows that in both silicon and germanium the $T^{-\frac{3}{2}}$ law is not obeyed at low temperatures, since impurity scattering becomes important. However, Pearson's measurements of Hall coefficient and conductivity of the samples used in these drift mobility experiments show that the purity of these crystals is such that the law is closely obeyed for temperatures higher than 90°K. In correcting the measured values of drift mobility to a common temperature; therefore, it certainly seems fair to assume this law over the very limited range of from 295° to 310°K used.

The temperatures of the germanium samples during mobility measurements were determined by making use of the observation that a thermometer bulb coated with a thin coating of ceresin wax changed its luster abruptly at 51°C. The procedure used was to increase the current through a sample previously prepared with a thin coating of ceresin until the luster change occurred. It was then assumed that the temperature for lower values of current was proportional to the heat dissipated in the crystal, or that the increase in the temperature of the sample above ambient, $\Delta T = k(I_B)^2$. At the melting point of the wax (51°C) ΔT is known and I_B can be measured so that k, the proportionality constant, can be evaluated. In the measurements of drift mobility just described, the relay is closed for only half the time. The temperature of the sample under these conditions is

$$T = T_0 + \tfrac{1}{2}kI_B^2 + \tfrac{1}{2}k(I_e + I_B)^2,$$

where T_0 is the ambient temperature.

Although the error in these measurements may be as high as 10 percent, ΔT was never greater[21] than 10°C, so that the temperature of the sample was determined to within a degree Centigrade. This doubt of 1°C in the sample temperature corresponds to a maximum uncertainty of only 0.4 percent in the mobility due to this cause.

[17] H. A. Wilson, *Theory of Metals* (Cambridge University Press, Cambridge, 1936), p. 211.
[18] F. Sietz, Phys. Rev. 73, 549 (1948).
[19] G. L. Pearson and J. Bardeen, Phys. Rev. 75, 865 (1949).
[20] The justification of the use of the variation of mobility with temperature as determined by the measurement of the Hall coefficient and the conductivity supposes only that for a single sample the mobility so derived is proportional to the true mobility.
[21] In the measurements using pulse techniques (to be described later) ΔT never exceeded 3°C with an even lower uncertainty in temperature and mobility.

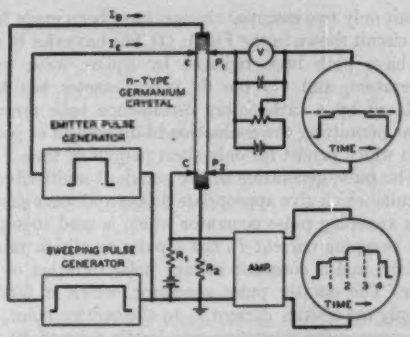

FIG. 6. Schematic diagram of circuit used to obtain more accurate measurements of mobility.

IX. DIFFUSION AND ELECTRIC FIELD DISPLACEMENT

It is desirable to make the electric field in the crystal as high as possible in order to minimize the ambiguity in transit time due to diffusion.

The relative effect of diffusion and applied voltage may be estimated from the following considerations. The distance which a hole (or electron) diffuses in time t is given by the usual diffusion formula, $l^2 = Dt = kT\mu t/e$, where D is the diffusion constant, k is Boltzman's constant, T is the absolute temperature, and e is the electronic charge. On the other hand, the distance that it travels in an electric field, $L = \mu Et$. If L is made equal to the distance from the emitter to the collector and V is the potential difference in the crystal between the position of the emitter and collector points, then $E = V/L$ and $L^2 = \mu Vt$. The ratio of these two distances is, therefore, $l/L = (kT/eV)^{\frac{1}{2}}$. Since the room temperature $kT/e = 1/40$ electron volt, $l/L = 1/6V^{\frac{1}{2}}$.

It is evident, therefore, that the voltage difference between the emitter and collector in the germanium crystal should be made as large as possible in order to obtain maximum accuracy in the determination of the carrier transit time. At the same time it is essential to avoid raising the temperature of the crystal much above ambient because of the difficulty of measuring the temperature rise accurately. Both of these criteria, however, may be met by pulsing I_B as well as I_e so that the duty cycle of these currents is made a small fraction.

X. CIRCUIT FOR MORE ACCURATE DETERMINATION OF TRANSIT TIME

While the simple circuit shown in Fig. 1 gave results which could be repeated within fairly close limits and which are entirely consistent with those obtained using the pulse techniques (described below), the results obtained with the latter are much to be preferred, since the transit times of the carriers are determined with considerably greater accuracy.

The circuit used which takes advantage of these pulse techniques is shown schematically in Fig. 6. In this

circuit only two essential changes have been made from the circuit shown in the Fig. 1. (1) The batteries B_1 and B_2 have both been replaced by square wave pulse generators, and (2) the dc potentiometer has been replaced by a cathode-ray oscilloscope tube arrangement permitting the evaluation of differences of potentials which persist for only short periods of time.

The pulse generators utilize standard multi-vibrator circuits which give appropriate delays and wave shapes. The sweeping pulse generator which is used to supply the sweeping current I_B has a pulse repetition rate of 38/sec, and a constant voltage pulse duration of 200 μsec. The emitter pulse generator, which is used to supply the emitter current I_e to the emitter point, has the same pulse repetition rate but is delayed 40 μsec behind the sweeping pulse and has a constant voltage duration of only 120 μsec. Both generators have a rise time of the order of 0.25 μsec.

The resulting sequence of events is as follows:

(1) The sweeping pulse generator initiates a constant voltage across the ends of the sample giving rise to nearly constant sweeping current, I_B.

(2) After a delay of 40 μsec the emitter pulse generator produces a constant voltage giving rise to a nearly constant emitter current, I_e.

(3) The emitter pulse generator is turned off, and I_e is reduced to a value very close to zero.

(4) After a delay of an additional 40 μsec the sweeping pulse generator is turned off, and the sweeping current is also reduced to a value close to zero.

The shape of the approximate resultant voltage gradient in the crystal is shown schematically on the cathode-ray tube potentiometer trace (upper right). The vertical deflecting plates of this tube are directly connected to two probe points through low capacitance leads. A variable potential source obtained with a battery and potentiometer is inserted in one of these leads. The value of this inserted potential was read directly on a voltmeter. The horizontal deflecting plates of this tube are connected to a linear time sweep which is synchronized to the sweeping pulse generator.

The procedure used in the measurement of the potential difference in the crystal between the emitter and collector points was as follows. With the voltmeter reading zero volts, the probe point P_1 was removed from the crystal and connected to P_2, which was placed opposite to the collector point as shown in the figure. This point was then "formed" [22] to lower its impedance. Under these conditions a nearly straight line trace down the center of the tube was obtained as indicated by the dotted line shown in Fig. 6. This zero potential line was traced carefully on the tube. The point P_1 was then placed opposite to the emitter point and also "formed." The measurement of the potential between P_1 and P_2 for any part of the characteristic was then found by simply bringing that part of the voltage characteristic to the zero potential line by adjusting the potentiometer. At the required instant of time, therefore, the deflecting plates of the cathode-ray tube are at the same voltage and the potential of P_1 differs from P_2 by an amount equal to that of the voltmeter reading.

The cathode-ray tube used was a Dumont 5X low capacitance and high sensitivity tube. Capacitance of both the leads and the inserted potential source were held to a minimum so that the time constant of the circuit was of the order of 0.5 μsec. This circuit is therefore capable of measuring the true potential difference in the germanium crystal at times of the order of a few microseconds after voltage changes in it occur.

The circuit used to measure the relative hole concentration at the collector point C as well as the current through the bridge is shown in the lower right of Fig. 6. It consists simply of a wide band amplifier and oscilloscope as before. When the amplifier was connected across R_1, as shown, the hole arrival and departure wave was displayed on the oscilloscope as indicated schematically. The four important parts of this characteristic are shown. The initial rise of this characteristic is due simply to the voltage produced between the collector point and ground by the sweeping current I_B introduced by the sweeping pulse generator. The emitter pulse starts at 1 and produces a further rise since additional current is introduced. At 2 the hole wave arrives, the wave front being now quite sharp due to the comparatively high voltage between the emitter and collector points. The emitter current is cut off at 3 giving a sharp drop in the characteristic. At 4 the characteristic due to hole wave departure, also quite sharp, is obtained. A short time later the sweeping pulse is removed and the characteristic returns to its initial voltage.

The time represented by the distance 1 to 2 is the transit time of the injected carriers with currents I_e and I_B flowing and the time represented by the distance 3 to 4 is the transit time with I_B only.

The currents I_e and I_B were measured by connecting the amplifier across R_2, instead of R_1, so that the voltage across this resistance as a function of time could be determined. The temperature of the sample during measurement was then computed as described in Sec. VIII.

XI. TECHNIQUES AND ERRORS

It is possible to measure the mobility to a high order of accuracy with this circuit, since the ambiguity in the transit time of the carriers is reduced to a negligible value. In a typical example the time required for the fastest carriers to arrive was 20 μsec, while the diffusion spread from 0.1 to 0.9 maximum was only 1.5 μsec. The error in the measurement of the time of arrival of the half-maximum in this case was less than 0.1 μsec as estimated using one microsecond marker intervals previously calibrated with standard frequencies. Con-

[22] J. Bardeen and W. H. Brattain, Phys. Rev. **75**, 1208 (1949); W. G. Pfann and J. H. Scaff, Phys. Rev. **76**, 452 (1949); and J. Bardeen and W. G. Pfann, Phys. Rev. **77**, 401 (1950).

sequently, the error in measuring the transit time was less than 0.5 percent.

The transit distance from emitter to collector was usually of the order of 1 cm. This distance was measured with a microscope equipped with an optical micrometer calibrated with standard scales. Measurements showed that readings could be repeated to well within 2×10^{-3} cm giving a maximum error of 0.2 percent in the measurement of L.

The voltage between the probe points could be repeated with differences of less than 0.1 volt. Since the absolute values of these voltages were always in the neighborhood of 20 volts, and were read on a calibrated voltmeter, errors due to the measurement of the potential difference were less than 0.5 percent.

Some ambiguity exists, however, in the electric field to be associated with the measured transit time. This is because, owing to conductivity modulation of the germanium by the injected carriers, the electric field is constantly changing during hole wave arrival and departure. The state of affairs is indicated by the characteristic obtained on the oscilloscope tube connected to the probe points P_1 and P_2. Such a characteristic typical of those obtained using large emitter currents is shown in the drawing of Fig. 7. The initial rise at A is produced by the start of the sweeping current I_B. After this initial rise the characteristic remains constant until an additional rise is produced by the start of emitter current I_e at B. At this time carriers are injected into the germanium crystal with a resultant progressive decrease in the resistance of the crystal between the probe points P_1 and P_2. The currents in the crystal remain substantially constant, owing to the high impedance of the pulse generators, so that the voltage falls. This decrease in resistance and consequent decrease in the voltage between the probe points continues as the carrier wave advances until at F the wave front passes P_2. A semi-steady-state voltage and electric field between the emitter and collector then exists until the emitter current is removed at G. In consequence of this, the voltage drops abruptly. I_B is now the only current flowing in the crystal. The value of the voltage produced initially by this current is, however, less than that obtained at the start of the sweeping current, since the region between the probe points is now filled with injected carriers, and recovery is only complete when the last of the injected carriers in the departure wave flows past P_2 at H.

It is possible in principle to solve the equations for the leading and trailing edges of the carrier wave exactly, taking into account diffusion and conductivity modulation. This problem has not been dealt with completely theoretically at the present time although certain phases of it have been examined in considerable detail by Herring.[23] However, it is possible to eliminate the effects of conductivity modulation by suitable experimental conventions.

[23] C. Herring, Bell System Tech. J. 28, 401 (1949).

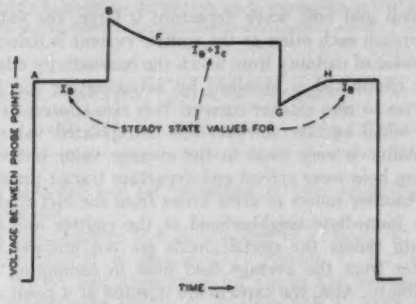

FIG. 7. Characteristic of voltage between emitter and collector points as a function of time, showing effects of conductivity modulation. (Emitter current large.)

The convention used has been to associate the transit time with the final or semi-steady-state value of the voltage obtained with the appropriate currents flowing in the crystal. For the transit time due to carrier wave arrival this voltage is F of Fig. 7. This value is obviously too low and the resultant electric field calculated by V/L will also be too low, leading to a mobility which is too high. On the other hand, by using this convention, the voltage associated with the transit time obtained from the carrier departure wave is H, a voltage which is obviously too high leading to a mobility which is too low. The true mobility, therefore, lies always between the value obtained using the transit time due to carrier wave arrival and that obtained with carrier wave departure. Since these effects, owing to carrier injection modulation of the crystal resistance, decrease as the injected currents decrease, the difference between the mobility calculated using carrier wave arrival and that obtained using carrier wave departure approaches zero as the injected current approaches zero, with assurance that the desired value always lies between the two.

A plot of the values of mobility so obtained is shown in Fig. 8. Here the apparent mobility for injected holes in n-type germanium is plotted as a function of the emitter current. While for large emitter currents the difference in the values obtained using the transit time and conventional voltage associated with hole wave

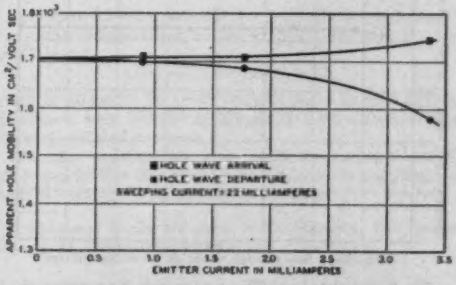

FIG. 8. Calculated mobility as a function of emitter current.

arrival and hole wave departure is large, the values approach each other as the emitter current is reduced. A value of mobility from which the conductivity effects are eliminated is obtained by extrapolating the two curves to zero emitter current. It is also apparent that for small emitter currents this extrapolated value of mobility is very close to the average value obtained using hole wave arrival and departure transit times.

Another source of error arises from the fact that in the immediate neighborhood of the emitter and collector points the electric fields are not uniform and differ from the average field used in computing the mobility. Also, the carriers are injected at a point and collected at a point, so that, in the vicinity of the emitter and collector, the paths of the carriers are curved. As a result of these local disturbances there will be end effects which should become progressively less important as the distance between the emitter and collector points is increased. The extent of these effects is shown in Fig. 9, in which we have plotted the average values of mobility obtained using small emitter currents, as a function of the spacing between the emitter and the collector points. As is seen, the end effects appear to be entirely negligible for spacings greater than a centimeter.

The measurements of mobility on a single sample were reproducible to within 0.6 percent, which is in agreement with the estimates of the errors involved in the measurement of transit time voltage, and spacing between the emitter and collector. However the values of the mobility obtained using different crystals of germanium had a spread more than 10 times as great. This indicates that by far the greatest error is introduced by the assumption that the electric field is everywhere uniform and equal to V/L. As is seen from Fig. 5 this is only approximately true. Since any deviation from linearity in these characteristics results in a calculated mobility which is too low by an amount which depends on the shape of the particular characteristic, an individual correction factor must be applied to each sample. This correction factor is found by dividing these characteristics in the section between the position of the collector and that of the emitter into a number of small segments l_i for each of which the field is substantially uniform and the voltage is V_i. Then the transit time for each segment is $l_i=l_i^2/V_i\mu$, so that

$$\mu\Delta l_i=\Sigma l_i^2/V_i.$$

Since $\Sigma t_i=t$, the total transit time, this value of μ can be expressed in terms of the uncorrected mobility, $\mu'=l^2/Vt$, as follows:

$$\mu=(\Sigma l_i^2/V_i)/t=[(\Sigma l_i^2/V_i)V/l^2]\mu'.$$

The correction factor, in square brackets, can be determined from voltage *versus* distance plots.

The application of this correction factor reduced the variation in the values of mobility obtained using different samples. A residual spread, however, of nearly six percent persisted. It is felt that this is due to deviations from a uniform field on a smaller scale, which are extremely difficult to measure experimentally.

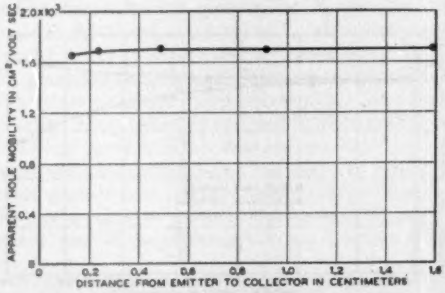

FIG. 9. Calculated mobility as a function of separation of emitter and collector points.

XII. RESULTS

The average value of the mobility of holes in germanium obtained using four different samples was 1700 cm²/volt-sec. The average mobility of electrons using three samples of p-type germanium was 3600 cm²/volt-sec. These values were obtained using samples of crystals grown in different ways and having values of specific resistance ranging from 1.5 to 6 ohm-cm. Too few samples have so far been examined to be certain of the accuracy of the results. However, the maximum spread of these values (obtained with n-type samples) was less than six percent. It is felt, therefore, that the average values have an error of less than five percent.

XIII. REVIEW OF METHODS OF MEASURING MOBILITY

As has been pointed out previously,[24] the values for the mobility determined in various ways need not necessarily agree. We can at present distinguish between four experimental methods of measuring mobility and three theoretical definitions, the latter being described as follows.

μ_m=*microscopic mobility*. This is the mobility of a charge carrier in the conduction band or valence-bond band and is the conventional concept.

μ_d=*drift mobility*. This is the drift velocity that a carrier would have in unit field allowing for trapping. For example, if an injected hole spent only half its time in the valence-bond band and the other half trapped on acceptors, μ_d would be $\frac{1}{2}\mu_m$.

μ_H=*Hall mobility*=$R\sigma$. For spherical energy surfaces in the Brillouin zone and degenerate statistics, as in a metal, theory predicts that $\mu_H=\mu_m$. For spherical energy surfaces, a mean free path independent of direction and energy, and a maxwellian distribution of velocities, $\mu_H=(3\pi/8)\mu_m$. If the energy surfaces are concave, theory predicts that $\mu_H=A(3\pi/8)\mu_m$, where A

[24] Pearson, Haynes, and Shockley, Phys. Rev. 78, 295 (1950).

may be less than unity or even negative. For negative values of A, we would have *anomalous electrons* and *anomalous holes*. An injected anomalous hole would move towards the negative terminal, yet a p-type sample conducting by such holes would give the Hall effect ordinarily attributed to electrons. Evidence that holes and electrons in germanium are not anomalous is furnished by the sign of the Suhl effects[25] and the consistency of the Hall effect with (1) motion of injected carriers, (2) sign of rectification, and (3) thermoelectric power and (4) valence of added impurities.

Experimentally, the Hall effect and the drift velocity should measure the quantities described by the preceding theoretical concepts for μ_H and μ_d. In addition, a *conductivity mobility* μ_σ can be measured by adding known amounts of impurity which thus adds known numbers of carriers;[26] from these known numbers and the measured conductivity a mobility can also be determined. In germanium at room temperature, the fraction of the carriers trapped on donors and acceptors is negligible, and μ_d, μ_m, and μ_σ should all be equal. The sum of the drift mobility for electrons μ_{dn} and μ_{dp} for holes may also be determined from photo-conductivity experiments assuming 100 percent quantum efficiency. In this determination it is assumed that each photon absorbed creates one hole-electron pair which persists on the average for the lifetime of a hole which may be independently measured.[27] Since the quantum efficiency can be less than 100 percent, this measurement gives a lower limit for

$$\mu_{dn}+\mu_{dp}.$$

The values of mobility obtained in these ways are shown in the Table I. All of the values except that of μ_σ were obtained on the same samples. The Hall effect data, however, correspond to the normal carriers rather than the injected carriers. It is seen that the data in the last three columns, which should correspond to μ_d, are consistent within the experimental accuracy. There appears to be a real discrepancy, however, between the Hall effect data for electrons and the other data. It is proposed that this discrepancy is due to curvatures of the energy surface in the Brillouin zone as discussed above.

Further evidence for nonspherical surfaces is furnished by magnetoresistance effects in germanium.[28,29]

At lower temperatures, appreciable trapping of injected carriers may take place and deviations of μ_d from μ_m should occur. Observations of such effects may furnish a useful tool for investigation trap densities in germanium.

TABLE I. Mobilities in cm²/volt-sec in germanium at 300°K.

	$(8/3\pi)\mu_H$	μ_d	μ_σ	Photo-conductivity
Electrons	2600±300	3600±180	3350±400	——
Holes	1700+500−100	1700±90	——	——
Sum	4300+800−400	5300±270	——	≧5300±500

We are indebted to F. S. Goucher, W. L. Bond, R. D. Heidenreich, H. R. Moore, G. L. Pearson, G. K. Teal, and W. W. Van Roosbroeck for advice and help with the experiments and to J. Bardeen and F. Seitz for stimulating discussions of the theory and to W. C. Westphal who prepared the specimens and took many of the data.

APPENDIX A1. RECOMBINATION FORMULAS

We shall treat the case of holes injected into n-type germanium below; the formulas for electrons injected into p-type are obtained by a suitable change of subscripts.

A hole injected in a filament may recombine either in the interior or on the surface. These processes lead to a set of eigenfunctions for hole density ϕ, as a function of y and z, the transverse dimensions. These functions satisfy the continuity equation in which τ_p is the body lifetime for holes and D_p is the diffusion constant;

$$\partial\phi/\partial t=-(\phi/\tau_p)+D_p[(\partial^2\phi/\partial y^2)+(\partial^2\phi/\partial z^2)].$$

The eigenfunctions must also satisfy the boundary conditions

$$s\phi=\mp D_p(\partial\phi/\partial y) \text{ at } y=\pm B,$$
$$s\phi=\mp D_p(\partial\phi/\partial x) \text{ at } z=\pm C,$$

where s is surface recombination velocity and B and C are half-widths of the filament.[30] The solution for ϕ which decays most slowly is

$$\phi=\exp(-1/\tau)\cos(by)\cos(cz),$$

where in order to satisfy the boundary conditions,

$$bB\tan(bB)=sB/D_p, \quad cC\tan(cC)=sC/D_p.$$

Letting b_0 and c_0 represent the smallest solutions of these equations, we find that

$$1/\tau=(1/\tau_p)+D_p(b_0^2+c_0^2).$$

For the case in which sB/D_p and sC/D_p are $\gg 1$, $bB=\pi/2$ and

$$1/\tau=(1/\tau_p)+D_p(\pi/2)^2(B^{-2}+C^{-2}),$$

this being the formula found valid for sandblasted surfaces for which s is 10^4 cm/sec so that, for example,

$$sB/D_p>10^4\times(2.5\times10^{-3})/44>6$$

for a filament 0.5 mm square and $(1/\tau)-(1/\tau_p)$ is about $(3\ \mu\text{sec})^{-1}$. For a long lifetime surface, so that $sB/D_p\ll 1$, the value of b_0B is $(sB/D_p)^{\frac{1}{2}}$ and

$$(1/\tau)-(1/\tau_p)=(s/B)+(s/C),$$

which is $(60\ \mu\text{sec})^{-1}$ for $s=200$ cm/sec. For a filament of these dimensions, body lifetimes of 100 μsec or more contribute little to the recombination process.

The other eigenfunctions decay much more quickly and die out so rapidly that they need not be considered in analyzing lifetimes in filaments by the methods of this paper.

[25] H. Suhl and W. Shockley, Phys. Rev. 75, 1617 (1949).
[26] Pearson, Struthers, and Theuerer, Phys. Rev. 75, 344 (1949) and 77, 809 (1950).
[27] The data used are those of F. S. Goucher, Phys. Rev. 78, 646 (1950), who assumed drift mobilities of 1700 and 3600 and found 100 percent quantum efficiency. In this analysis we assume efficiencies ≤100 percent and deduce the sum of the mobilities.
[28] G. L. Pearson, Phys. Rev. 78, 646 (1950).
[29] H. Suhl, Phys. Rev. 78, 646 (1950).
[30] Additional details are given in W. Shockley, Bell System Tech. J. 28, 435 (1949), Appendix V.

The Theory of the Separation of Isotopes by Thermal Diffusion

SUDHANSU DATTA MAJUMDAR
Institute of Nuclear Physics, University College of Science, Calcutta, India
(Received July 25, 1950)

The time-dependent partial differential equation of the "separation column" of Clusius and Dickel has been solved exactly. Only an approximate solution, subject to the restriction that the fractional concentration c is everywhere small compared to unity, was known previously. The present work makes a comparison between theory and experiment possible over the full range of concentration values.

I. INTRODUCTION

THOUGH Chapman[1] had suggested as early as 1919 that the phenomenon of thermal diffusion discovered theoretically by Enskog and himself might be used for separating isotopes, attempts in this direction did not meet with success till Clusius and Dickel[2] pointed out that convection currents could be utilized for greatly enhancing the effect. The apparatus used by them consisted of a long vertical tube closed at both ends with an axial hot wire which could be maintained at any desired temperature by passing an electric current. Introduction of the gaseous mixture of isotopes into this tube gave rise to convection currents rising near the axis and descending near the cooled wall of the tube. When the tube was allowed to remain in this condition for a sufficiently long time, the combined effect of convection and thermal diffusion led to a partial separation of the two constituents of the mixture. The theory of the operation of the "separation column," as it is called, has been worked out by a number of authors. The most notable among them are Waldmann,[3] Furry,[4,5] Jones,[4,5] Onsager, and Debye.[6] The various treatments, though they differ somewhat, lead ultimately to the same transport equation

$$q=Hc(1-c)-K\partial c/\partial z, \tag{1}$$

where q is the transport of the lighter isotope up the tube in g/sec, c is the fractional number density of the molecules of the lighter isotope, H, K are constants[4] depending on the nature of the gaseous mixture and the specifications of the column, and z is the height in cm of any cross section of the column from its lower end. A similar equation holds for the transport of the heavier isotope down the tube.

Equation (1) will fail to hold, of course, near the two ends of the column where the convection current turns round; but, as these regions occupy only a small part of the total length, little error is committed by assuming it to be valid throughout the entire length of the column. Conservation of mass then leads to the equation of continuity

$$\mu\partial c/\partial\tau=-\partial q/\partial z, \tag{2}$$

where μ is the mass of gas in unit length of the column and τ is the time in sec.

Combining Eqs. (1) and (2), and denoting partial differentiation by a subscript, we have

$$\mu c_\tau=-H(1-2c)c_z+Kc_{zz}. \tag{3}$$

This is the basic equation of the separation column. Its solution subject to the appropriate boundary conditions gives the concentration distribution along the column as a function of time. Both Debye[6] and Bardeen[7] have treated this equation with the restriction that c is small compared to unity, so that the term c^2 in Eq. (1) can be neglected. On this assumption the simplified form of the transport equation is

$$q=Hc-Kc_z \tag{4}$$

and that of the equation of continuity is

$$\mu c_\tau=-Hc_z+Kc_{zz}. \tag{5}$$

Equation (5) can be solved easily with the help of the standard theory of linear differential equations; but very often the experimental conditions necessitate a more complete discussion of the differential equation (3) without the above restriction on the values of c. In this paper we shall show that it is possible to solve the equation completely by reducing it to the linear form by means of a suitable transformation. Before proceeding to demonstrate this it will be convenient to bring Eq. (3) into the dimensionless form,

$$c_t=-(1-2c)c_x+c_{xx}, \tag{6}$$

by the substitutions,

$$x=Hz/K, \quad t=H^2\tau/\mu K.$$

The same substitutions transform Eq. (1) into

$$q/H=c(1-c)-c_x \tag{7}$$

and the simplified Eqs. (4) and (5) into

$$q/H=c-c_x \tag{8}$$

and

$$c_t=-c_x+c_{xx}. \tag{9}$$

[1] S. Chapman, Phil. Mag. **38**, 182 (1919).
[2] K. Clusius and G. Dickel, Z. physik. Chemie **B44**, 397 (1939).
[3] L. Waldmann, Z. Physik **114**, 53 (1939).
[4] R. C. Jones and W. H. Furry, Revs. Modern Phys. **18**, 151 (1946). This problem is stated on page 178.
[5] W. H. Furry and R. C. Jones, Phys. Rev. **69**, 459 (1946).
[6] P. Debye, Ann. Physik **36**, 284 (1939).
[7] J. Bardeen, Phys. Rev. **57**, 35 (1940).

II. TRANSFORMATION OF EQ. (6)

To linearize Eq. (6) we first make the substitution $c=\frac{1}{2}+v_x$, obtaining

$$v_{xt}=(v_x^2)_x+v_{xxx}.$$

Integration with respect to x yields

$$f(t)+v_t=v_x^2+v_{xx},$$

where $f(t)$ is an arbitrary function of t. Since the addition of an arbitrary function of time to v leaves c unaltered, we can absorb $f(t)$ in v and write simply

$$v_t=v_x^2+v_{xx}. \tag{10}$$

Next we make the substitution $v=\phi(w)$ in Eq. (10), where the functional form ϕ is to be suitably chosen. This gives

$$v'w_t=(v')^2w_x^2+v''w_x^2+v'w_{xx},$$

where $v'=dv/dw$, and $v''=d^2v/dw^2$. If the functional form be so chosen that

$$(v')^2+v''=0, \tag{11}$$

then this equation reduces to

$$w_{xx}=w_t, \tag{12}$$

which is the familiar equation of ordinary diffusion in one dimension.

A solution[6] of Eq. (11) is $v=\ln w$. Thus, the substitution

$$c=\tfrac{1}{2}+w_x/w \tag{13}$$

transforms the nonlinear equation (6) in c into a linear equation in w. The same substitution transforms the transport equation (7) into

$$q/H=\tfrac{1}{4}-w_{xx}/w. \tag{14}$$

First, we shall make use of the function w in deriving the solution for the steady state which corresponds to constant q. By Eqs. (12) and (14),

$$\tfrac{1}{4}b^2=\tfrac{1}{4}-q/H=w_{xx}/w=w_t/w,$$

whence

$$w=\exp(b^2t/4)\cdot g(x).$$

If Eq. (12) is to be satisfied by w, $g(x)$ must be of the form $Ae^{bx/2}+Be^{-bx/2}$. The relation (13) then gives

$$c=\tfrac{1}{2}+\tfrac{1}{2}b(Ae^{bx/2}-Be^{-bx/2})/(Ae^{bx/2}+Be^{-bx/2}).$$

In the special case, $q=0$,

$$c=\tfrac{1}{2}+\tfrac{1}{2}\tanh\tfrac{1}{2}(x-x_0).$$

The expression for w in terms of c is, by Eq. (13),

$$w=g(t)\exp\left[-\tfrac{1}{2}x+\int_l^x c\,dx\right], \tag{15}$$

where lK/H is the length of the column, and $g(t)$ is an arbitrary function of time. The expression for w in terms of c therefore contains an arbitrary function of time as a multiplier. But the condition that w is to satisfy the differential equation (12) instead of an equation of a more general type obtained by direct substitution of Eq. (13) in Eq. (6), determines $g(t)$ up to a constant factor which still remains arbitrary. This can be seen in the following way: by Eqs. (14), (15), and (2),

$$w_{xx}=[\tfrac{1}{4}-H^{-1}q(x,t)]w$$

and

$$w_t=\left\{[g'(t)/g(t)]+\int_l^x c_t\,dx\right\}w$$

$$=\{[g'(t)/g(t)]-H^{-1}q(x,t)+H^{-1}q(l,t)\}w.$$

Therefore, if Eq. (12) is to hold, we must have

$$g(t)=A\exp\left[(t/4)-H^{-1}\int_0^t q(l,t)dt\right];$$

where the constant A is arbitrary. Hence, the expression (15) can be written as

$$w=A\exp\left[(t/4)-H^{-1}\int_0^t q(l,t)dt-(x/2)+\int_l^x c\,dx\right]. \tag{16}$$

This expression will be required later in deriving some important results.

III. THE INITIAL AND BOUNDARY CONDITIONS

We now proceed to discuss the initial and the boundary conditions of the problem. Linearization of the differential equation alone will not be sufficient to make the problem solvable unless the boundary conditions also assume a linear form. Fortunately, this requirement is fulfilled in the two most important cases discussed below.

In the first case the column is closed at both ends, so that the boundary conditions are $q=0$ at both $x=0$ and $x=l$; that is,

$$w_{xx}=\tfrac{1}{4}w, \quad \text{at } x=0 \text{ and } x=l. \tag{17}$$

This will be referred to as Problem (I).

In the second case the column is closed at the upper end and is connected to a reservoir of infinite capacity at the lower end, so that the concentration there remains constant and equal to c_0, the concentration in the reservoir. The corresponding boundary conditions are

$$\left.\begin{aligned} -w_x&=(\tfrac{1}{2}-c_0)w=\sigma w, && \text{at } x=0\\ w_{xx}&=\tfrac{1}{4}w, && \text{at } x=l \end{aligned}\right\}. \tag{18}$$

and

This will be referred to as Problem (II).

[6] This transformation was used by the author in a previous paper (S. D. Majumdar, Phys. Rev. 72, 393 (1947)) to linearize an equation occurring in the general theory of relativity.

The initial concentration will be taken to be constant throughout the length of the column. This is the only case which occurs in practice. If we take $A=\exp(c_0 l)$ in Eq. (16), the corresponding initial condition for w comes out to be

$$w(x,0)=\exp[-x/2+c_0 x]=e^{-\sigma x}, \quad \text{at } t=0. \tag{19}$$

When Eq. (12) has been solved in conformity with the initial condition (19) and the boundary conditions (17) or (18), Eq. (13) enables us to obtain the expression for c in terms of x and t, which, in the cases discussed here, comes out in the form of a ratio of two infinite series. In the special case, $c \ll 1$, a simplified expression for c can be obtained by the following considerations.

In both the cases considered here $q(l,t)=0$ for all values of t. Hence the relation (16) reduces to

$$w=A\exp\left[(t/4)-(x/2)+\int_l^x c\,dx\right],$$

whence

$$\exp\left[\int_l^x c\,dx\right]=A^{-1}\exp[-(t/4)+(x/2)]w.$$

If cl is small compared to unity, the left-hand side may be set approximately equal to $1+\int_l^x c\,dx$, whence, on differentiation,

$$c=A^{-1}e^{-t/4}(e^{x/2}w)_x. \tag{20}$$

The expression for c thus obtained will agree (for small c) with the solution of the simplified Eq. (9) to a first approximation, but not exactly.

Though the relation (20) has been derived by a process of approximation, it is interesting to note that, when substituted in the simplified Eq. (9), it transforms the latter *rigorously* into an equation of ordinary diffusion for w. The substitution (20) therefore leads to an alternative method for solving Eq. (9). Substituting Eq. (20) in Eq. (9) and integrating with respect to x, we have

$$w_{xx}=w_t+h(t)e^{-x/2}.$$

Here also the arbitrary function $h(t)$ can be set equal to zero without any loss of generality, so that we have, as in the previous case,

$$w_{xx}=w_t.$$

After these preliminary discussions it is easy to obtain the solutions in an explicit form with the help of the standard theory of linear differential equations. We shall discuss Problem (II) in some detail because of its greater practical importance.

IV. DISCUSSION OF PROBLEM (II)

The discussion of Problem (II) is perhaps a little simplified by the introduction of a function u defined by

$$u=w-\exp[\sigma^2 t-\sigma x],$$

which satisfies the same differential equation,

$$u_{xx}=u_t, \tag{21}$$

but with the altered initial and boundary conditions,

$$u(x,0)=0, \quad \text{at } t=0, \tag{22}$$

$$\left.\begin{aligned} -u_x&=\sigma u, && \text{at } x=0\\ u_{xx}&=\tfrac{1}{4}u+(\tfrac{1}{4}-\sigma^2)\exp[\sigma^2 t-\sigma l], && \text{at } x=l \end{aligned}\right\}. \tag{23}$$

Equation (21) is solved most conveniently by making use of a Laplace transformation.[9] We multiply both sides of Eqs. (21) and (23) by $e^{-\gamma t}$, where $\Re(\gamma)$ is sufficiently large, and integrate over t from 0 to ∞, obtaining

$$v_{xx}-\gamma v=0, \tag{24}$$

$$\left.\begin{aligned} -v_x&=\sigma v, && \text{at } x=0\\ v_{xx}&=\tfrac{1}{4}v+e^{-\sigma l}\gamma(\tfrac{1}{4}-\sigma^2)/(\gamma-\sigma^2), && \text{at } x=l \end{aligned}\right\}, \tag{25}$$

where $v(x,\gamma)$ is the adjoint function,

$$\gamma^{-1}v(x,\gamma)=\int_0^\infty u(x,t)e^{-\gamma t}dt.$$

The solution of the ordinary differential equation (24), with the boundary conditions (25), is

$$v(x,\gamma)=\frac{\gamma(\tfrac{1}{4}-\sigma^2)e^{-\sigma l}}{(\gamma-\tfrac{1}{4})(\gamma-\sigma^2)}\cdot\frac{e^{-s(l-x)}+\epsilon(s)e^{-s(l+x)}}{1+\epsilon(s)e^{-2sl}}, \tag{26}$$

where $s=\sqrt{\gamma}$ and $\epsilon(s)=(s+\sigma)/(s-\sigma)$.

Though the function $s=\sqrt{\gamma}$ has a branch point at $\gamma=0$, it is easy to verify that $v(x,\gamma)$ (looked upon as a function of γ alone) is a meromorphic function *devoid of branch points*. Its only singularities are simple poles at $\gamma=\frac{1}{4}$, $\gamma=\sigma^2$, and $\gamma=s_n^2$, where s_n is a root of the equation

$$\exp(2s_n l)=(\sigma+s_n)/(\sigma-s_n); \tag{27}$$

that is, of the equation,

$$\tanh s_n l=s_n/\sigma. \tag{28}$$

At $\gamma=0$, however, there is usually no singularity. Roots of Eq. (28) occur in pairs of opposite signs. Depending on the value of σl, there may or may not be any real[10] root other than the one at $s=0$; but there are always an infinite number of pure imaginary[11] roots. Moreover, an examination of Eq. (27) shows that there exists a real number α_0 such that $\Re(s_n)<\alpha_0$ for all values of n.

The adjoint function $v(x,\gamma)$ is of the familiar type occurring in the theory of partial differential equations,

[9] R. Courant and D. Hilbert, *Methoden der Mathematischen Physik*, Bd. II (Verlag. Julius Springer, Berlin, 1937).

[10] If $\sigma l<1$ (which includes the case $\sigma l<0$), there is no real root. If $\sigma l>1$, there is a pair of real roots $\pm s_r$ lying between $-\sigma$ and $+\sigma$. In this case $(s_r)^2<\sigma^2<\frac{1}{4}$. If $\sigma l=1$, there is a triple root at $s=0$, which must be taken into account in evaluating residues.

[11] It can be proved that Eq. (27) has no complex roots with nonvanishing real and imaginary parts. This circumstance considerably reduces the labor of numerical evaluation of the roots.

and satisfies all the conditions necessary for the validity of the inversion formula,

$$u(x,t)=(1/2\pi i)\int_{\alpha-i\infty}^{\alpha+i\infty}\gamma^{-1}v(x,\gamma)e^{\gamma t}d\gamma, \qquad (29)$$

where the path of integration L is a straight line parallel to the imaginary axis and lying in the region $\Re(\gamma)>\frac{1}{4}$. The function $u(x,t)$ thus obtained is the required solution of the differential equation $u_{xx}=u_t$ satisfying Eqs. (22) and (23). To bring it into a form suitable for numerical work we must remove γ by carrying out the integration on the right-hand side of Eq. (29). It can be easily verified that on a system of parabolic contours C_n, bounded on the right by the straight line L, and satisfying the equation $Im(s)=\pm n\pi/l$, this integral tends to zero as n tends to infinity. The value of the integral on L is therefore equal to $2\pi i$ times the sum of the residues at the poles of the integrand. The solution of Problem (II) is thus obtained in the form of an infinite series,

$$w(x,t)=\frac{\exp[-\sigma l+t/4][c_0e^{x/2}+(1-c_0)e^{-x/2}]}{[c_0e^{l/2}+(1-c_0)e^{-l/2}]}$$
$$+\sum_n\frac{(\frac{1}{4}-\sigma^2)8s_n\exp[-\sigma_1'+s_n^2t]\sinh s_n(l-x)}{\sigma(1-4s_n^2)\{1-\sigma l(1-s_n^2/\sigma^2)\}}. \qquad (30)$$

For the reasons previously stated the root $s=0$ makes no contribution to the series unless $\sigma l=1$. Since two roots $\pm s_n$ of opposite signs correspond to the same pole in the γ-plane, only one of them should be included in the summation.

The above solution assumes a particularly simple form if we start with a mixture of two isotopes in equal proportions.

The same procedure leads to the following solution[12] of Problem (I)

$$w(x,t)=e^{t/4}[(e^{\sigma l}-1)e^{x/2}+(e^l-e^{\sigma l})e^{-x/2}]/(e^l-1)$$
$$+\sum_n\frac{2q_n(\frac{1}{4}-\sigma^2)}{l(\frac{1}{4}+q_n^2)(\sigma^2+q_n^2)}\cdot[1-(-1)^ne^{-\sigma l}]$$
$$\times\exp(-q_n^2t)\sin q_nx,$$

where $q_n=n\pi/l$, and n runs over all positive integral values.

V. COMPARISON WITH EXPERIMENT

The solutions worked out in the preceding paragraphs hold for a single column only. In practice a number of columns are usually connected in series by tubes in which a convective circulation of the gas is maintained by non-uniform heating. These connecting tubes act like reservoirs and invariably cause delay in the establishment of equilibrium. This more general case does not lend itself so easily to an exact mathematical treatment. It is desirable that experiments should be performed with a single column over a wide range of concentrations for a more complete test of the theory of Furry and Jones. Meanwhile, we proceed to compare the results obtained here with the experimental data of Clusius and Dickel[2] on the rate of separation of oxygen from air. Their column had the following specifications:

Length of the column = 295 cm;
Radius of the outer tube = 0.42 cm;
Radius of the hot wire = 0.02 cm;
Temperature of the outer tube = 293°K;
Temperature of the hot wire = 923°K.

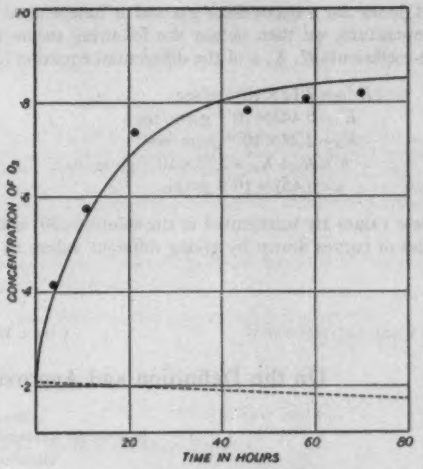

FIG. 1. Theoretical curve for $\alpha=0.014$ and the experimental points of Clusius and Dickel reference 2).

The upper end of the column was connected with a large reservoir and the whole system filled with air at atmospheric pressure. In course of separation the concentration of O_2 in the reservoir fell from its normal value 0.209 to 0.174. The mean, 0.191, of these two is taken to be the initial concentration c_0. Since in the equilibrium condition the concentration of O_2 varied from 0.174 to 0.83 along the column, calculations are carried out for a mixture of N_2 and O_2 in equal proportions. For such a mixture[13] at 20°C:

The coefficient of viscosity[14,15] $\eta=1.88\times10^{-4}$ poise, and η varies as $T^{0.756}$;

The density $\rho=1.25\times10^{-3}$ g/cm³;

The coefficient of diffusion $D=1.44\eta/\rho$ cm²/sec $=0.216$ cm²/sec.

Making use of the tables and formulas given by Furry

[12] Substituting this solution in Eq. (16) and putting $x=0$, we get for all values of t the expected result $\int_0^l c\,dx=c_0l$.

[13] The notation of reference 4 is used throughout this section.

[14] M. Trautz and K. G. Sorg, Ann. Physik 10, 81 (1931).

[15] M. Trautz and R. Heberling, Ann. Physik 10, 155 (1931).

and Jones[4] for a maxwellian gas and α independent of temperature, we then obtain the following values for the coefficients H, K, μ of the differential equation (3):

$$H/\alpha = 2.12\times10^{-4} \text{ g/sec};$$
$$K_s = 0.443\times10^{-4} \text{ g-cm/sec};$$
$$K_d = 2.28\times10^{-4} \text{ g-cm/sec};$$
$$K = K_s + K_d = 2.72\times10^{-4} \text{ g-cm/sec};$$
$$\mu = 0.487\times10^{-4} \text{ g/cm}.$$

These values are substituted in the solution (30) and a series of curves drawn by giving different values to α. Of these the curve for $\alpha = 0.014$ which fits best with the experimental points is reproduced in Fig. 1. This may be compared with the value 0.018 found by Waldmann[16] by another method.

In conclusion I wish to thank Professor M. N. Saha, F.R.S., for acquainting me with this subject and for his interest, Professor N. R. Sen for having kindly gone through the paper, Dr. U. C. Guha for his friendly cooperation in checking the calculations, and the National Institute of Sciences of India for the Fellowship.

[16] L. Waldmann, Z. Naturforsch. 1 (1946).

PHYSICAL REVIEW VOLUME 81, NUMBER 5 MARCH 1, 1951

On the Definition and Approximation of Feynman's Path Integrals

CÉCILE MORETTE*†
Institute for Advanced Study, Princeton, New Jersey
(Received July 10, 1950)

A general and compact expression for Feynman's path integral has been obtained. A classical method is given for the computation of such expressions. The example of a Dirac particle in a constant external electromagnetic field is treated by this method.

I. INTRODUCTION

IN order to treat problems involving action at a distance, Feynman has proposed a lagrangian form of quantum mechanics.[1] In this formulation the probability amplitude $K(x^B, x^A)$ for a particle to go from a space-time point x^A to a space-time point x^B is postulated to be given by an expression of the form:

$$K(x^B, x^A) = \int \exp(iS[x]/\hbar)d(\text{paths}), \qquad (1)$$

the integral being extended over all paths, $x(\tau)$ from x^A to x^B. In this paper we give a general and compact definition for this integral, and we give also a classical method for computing an approximate expression for it.

We make use of the following notation:

$x(\tau)$ is the parametric representation of a world line

$$x = x_\mu. \quad \mu = 1, 2, 3, 4. \quad \tau = \text{proper time}.$$

$\dot{x}(\tau) = dx(\tau)/d\tau$.
$\bar{x}(\tau)$ is the classical path.
$x^k \equiv x(\tau^k)$.
$\epsilon = \tau^{k+1} - \tau^k$.

$$S[x] = \int_{\tau^A}^{\tau} L\{x(\tau), \dot{x}(\tau)\}d\tau;$$

$S[x]$ is a functional of the function $x(\tau)$.
$\bar{S} = S[\bar{x}]$; $\bar{S}$ is the classical action.

II. DEFINITION OF THE PATH INTEGRALS

In Feynmans' work[1] the definition of the path integrals involves an infinite product of "normalization factors." For his purposes Feynman determined these normalization factors in the cases in which the potential is velocity independent and gave their expressions in rectangular coordinates; and he indicated also the existence of a relationship between these factors and the action, S. We shall give here the general formula for the normalization factors valid for all actions and all frames of reference; moreover, we shall give a compact expression for the infinite product of the normalization factors. We shall give first the general formula for $K(x^{k+1}, x^k)$ for two points corresponding to an interval $\tau^{k+1} - \tau^k = \epsilon$ infinitesimally small; then we shall obtain $K(x^B, x^A)$ by iteration. (The essential formulas are given before their proofs.)

$$\text{①} \quad K(x^{k+1}, x^k) = \exp[(i/\hbar)\bar{S}(x^{k+1}, x^k)] \times (2\pi\hbar i)^{-l/l}(\det_{\mu\nu} a^{\mu\nu}{}_{k+1,k})^{\frac{1}{2}}. \quad (2)$$

Here l is the number of degrees of freedom ($l = 4$ in the actual case),

$$a^{\mu\nu}{}_{k+1,k} \equiv \partial^2\bar{S}/\partial x_\mu{}^{k+1}\partial x_\nu{}^k$$

$\det_{\mu\nu}$ means the determinant with respect to the indices μ and ν.

* Chargée de Recherches du Centre National de la Recherche Scientifique.
† Now at Institut Henri Poincaré, Paris.
[1] R. P. Feynman, Revs. Modern Phys. **20**, 367 (1948), hereafter called I. Following the suggestion made in paragraph 14 of I, we have defined a path $x(\tau)$ by four functions $x_\mu(\tau)$ of a parameter τ; the formulas of I are still valid, the quantities $\psi(x, \tau) = \exp(iMc/2\hbar)\psi(x)$ replacing the wave function $\psi(x)$. A proof of this fact is given in connection with the example studied below. For a more complete study of a formalism of relativistic quantum mechanics introducing the wave function $\psi(x, \tau)$, see E. C. G. Stueckelberg, Helv. Phys. Acta **14**, 588 (1941), and **15**, 23 (1942).

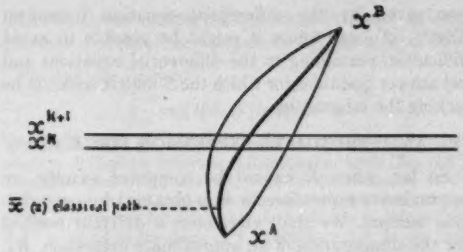

FIG. 1. A world line is defined by its parametric representation $x(\tau)$ the world line of the classical path is $\bar{x}(\tau)$.

Proof of formula (2). Feynman defined $K(x^{k+1}, x^k)$ as follows[1]

$$K(x^{k+1}, x^k) = \exp[iS(x^{k+1}, x^k)/\hbar](1/\mathfrak{c}^{k+1,k}) \quad (3)$$

and computed the normalization factor $\mathfrak{c}^{k+1,k}$ for special cases. We shall determine $|\mathfrak{c}^{k+1,k}|$ in a general way by the unitary condition,

$$\int_{-\infty}^{+\infty} K^*(x^{k+1}, x^k) K(x^{k+1}, x'^k) dx^{k+1} = \delta(x^k - x'^k). \quad (4)$$

By substitution of Eq. (3) into Eq. (4), one obtains:

$$\int_{-\infty}^{+\infty} \exp[-i[S(x^{k+1}, x^k) - S(x^{k+1}, x'^k)]/\hbar] \times |\mathfrak{c}^{k+1,k}|^{-2} dx^{k+1} = \delta(x^k - x'^k). \quad (5)$$

The calculation of $\mathfrak{c}^{k+1,k}$ goes then as follows. Let us expand S in a Taylor series:

$$S(x^{k+1}, x^k) = S(x^{k+1}, x^{k+1}) + (x^k - x^{k+1})(\partial S/\partial x^k)(x^{k+1}, x^{k+\tau}) \quad 0 \leqslant \tau \leqslant 1. \quad (6)$$

By use of the classical relation:

$$\partial S(x^{k+1}, x^k)/\partial x^k = p^{k+1,k}(x^{k+1}, x^k) \quad (7)$$

[the momentum $p^{k+1,k}$ is tangent to the classical path: $x^k \to x^{k+1}$ (Figs. 1 and 2) at the point x^k and is orientated in the same direction as the path], and by use of the following change of variable:

$$x^{k+1} \to p^{k+1,k} \quad (8)$$

$$dx^{k+1} \to J(x^{k+1};\ p^{k+1,k}) dp^{k+1,k} = |\det_{\mu\nu} a^{\mu\nu}{}_{k+1,k}|^{-1} dp^{k+1,k}, \quad (9)$$

(J is the jacobian associated with the change of variables (8)) Eq. (5) becomes:

$$\int_{-\infty}^{+\infty} \exp[-(i/\hbar)[(x^k - x'^k)p^{k+1,k} + 0(x^k - x'^k)^2]] |\mathfrak{c}^{k+1,k}|^{-2} |\det_{\mu\nu} a^{\mu\nu}{}_{k+1,k}|^{-1} dp^{k+1,k} = \delta(x^k - x'^k). \quad (10)$$

When the distances $|x^{k+1} - x^k|$ and $|x^{k+1} - x'^k|$ are smaller than $\epsilon\sqrt{2}$, the exponent in Eq. (10) reduces to its first term (in the limit $\epsilon \to 0$).

However, when the distances $|x^{k+1} - x^k|$ and $|x^{k+1} - x'^k|$ are larger than $\epsilon\sqrt{2}$ and when S does not contain $\dot{x}$ to powers larger than two,[2] Feynman has shown that the contributions of the corresponding actions cancel each other. We shall restrict ourselves

[2] The action functions studied so far do not involve $\dot{x}$ to powers larger than 2; nevertheless, such possibilities may be of interest. A more elaborate proof is then needed to determine $\mathfrak{c}^{k+1,k}$ (see reference 4).

FIG. 2. Figure 2a shows a path defined by successive points and Fig. 2b shows the same path defined by successive tangents. Between two given points infinitisimally close to each other, the path followed by the particle is the classical path, i.e., a definite one; hence, it is possible to go from a point description to a tangent description of the path.

to such actions. Consequently, in the limit $\epsilon \to 0$ Eq. (10) tends towards the following equation:

$$\int_{-\infty}^{+\infty} \exp[(i/\hbar)(x^k - x'^k)p^k] |\mathfrak{c}^{k+1,k}|^{-2} |\det_{\mu\nu} a^{\mu\nu}{}_{k+1,k}|^{-1} dp^k = \delta(x^k - x'^k); \quad (11)$$

and the result is

$$|\mathfrak{c}^{k+1,k}|^{-1} = h^{-2} |\det_{\mu\nu} a^{\mu\nu}{}_{k+1,k}|^{\frac{1}{2}}. \quad (12)$$

Van Hove has shown that[3,4]

$$\mathfrak{c}^{k+1,k} = \exp[i\pi l/4] |\mathfrak{c}^{k+1,k}| \quad (13)$$

In the actions considered so far, all the off-diagonal terms vanish:

$$(\mathfrak{c}^{k+1,k})^{-1} = \prod_\mu (ih)^{-1} a^{\mu\mu}{}_{k+1,k} \equiv \prod_\mu (c_\mu{}^{k+1,k})^{-1}. \quad (14)$$

One can readily check the value of $\mathfrak{c}^{k+1,k}$ obtained by Feynman for actions expressed in cartesian coordinates where the potential is velocity independent; namely,

$$c_\mu{}^{k+1,k} = (ih\epsilon/Mc)^{\frac{1}{2}}. \quad (15)$$

② $K(x^B, x^A)$

$$= \lim_{n \to \infty} \int_{-\infty}^{+\infty} \cdots \int_{-\infty}^{+\infty} \exp\left[\frac{i}{\hbar} \sum_{k=0}^{n-1} S(x^{k+1}, x^k) J^k\right] \times J^k(x^0,\ p^{1,0}/ih \cdots p^{n,n-1}/ih;\ x^0 \cdots x^n) \times \prod_{k=0}^{n} dx^k \delta(x^0 - x^A) \delta(x^n - x^B). \quad (16)$$

Proof of Eq. (16). The straightforward iteration of Eq. (3) leads to the value of $K(x^B, x^A)$ given in I;

[1] We are greatly indebted to Dr. Van Hove for giving us formula 12 before publication and for very many helpful discussions in the course of this work. For a more general study of Eq. (2) we refer the reader to a work of Dr. Van Hove (unpublished as yet).

The square root of the determinant in formula (2) has appeared already in another connection in a work of Jordan, Physik 38, 513 (1926), and a work of J. H. Van Vleck, Proc. Nat. Acad. Sci. 14, 178 (1928).

[3] Equation (12) justifies Feynman's remark in I, reference 15; it enables us to generalize the very useful Eqs. (58) and (46) of I, one of which we shall need later on.

The definition of the hamiltonian:

$$H_k = (\partial/\partial\tau^k)[S(x^{k+1}, x^k) - \ln \mathfrak{c}^{k+1,k}]. \quad (A)$$

The equivalence of two functionals:

$$\partial f/\partial x^k \underset{S}{\leftrightarrow} -f(\partial/\partial x^k)\{[iS(x^{k+1}, x^k)/\hbar] + [iS(x^k, x^{k-1})/\hbar] - \ln \mathfrak{c}^{k+1,k} \mathfrak{c}^{k,k-1}\}. \quad (B)$$

namely,

$$K(x^B, x^A) = \lim_{n\to\infty} \int_{-\infty}^{+\infty} \cdots \int_{-\infty}^{+\infty} \exp\left[\frac{i}{h}\sum_{k=0}^{n-1} \bar{S}(x^{k+1}, x^k)\right]$$

$$\times \prod_{k=0}^{n-1} (\epsilon^{k+1,k})^{-1} \prod_{k=0}^{n} dx^k \delta(x^0 - x^A)\delta(x^n - x^B). \quad (17)$$

The limits of integration of the x^k are fixed by the boundary conditions; for definiteness, we take them equal to $+\infty$ and $-\infty$.

We shall show that the untractable product $\prod_{k=0}^{n-1} (\epsilon^{k+1,k})^{-1}$ is equal to the square root of a jacobian;[5] this jacobian corresponds to the following change in the description of a path, namely, the change from a tangent description to a point description.

Let us study the following change of $4(n+1)$ variables:

$$\begin{matrix} x^0 \to x^0 \\ p^{1,0}(x^1, x^0)/ih \to x^1 \\ \cdots\cdots\cdots\cdots \\ p^{n,n-1}(x^n, x^{n-1})/ih \to x^n, \end{matrix} \quad (18)$$

where the $p^{k+1,k}$ are given by Eq. (7), to which corresponds the following jacobian:

$$J(x^0, p^{1,0}/ih \cdots p^{n,n-1}/ih; x^0 \cdots x^n)$$

$$= \begin{vmatrix} J(x^0; x^0) & & & \\ J(p^{1,0}/ih; x^0) & J(p^{1,0}/ih; x^1) & & \\ & & 0 & \\ 0 & & & \\ & & & J(p^{n,n-1}/ih; x^{n-1}) J(p^{n,n-1}/ih; x^n) \end{vmatrix}. \quad (19)$$

This compound determinant is equal to the product of its diagonal elementary determinants:

$$J(x^0, p^{1,0}/ih \cdots p^{n,n-1}/ih; x^0 \cdots x^n) = \prod_{k=0}^{n-1} J(p^{k+1,k}/ih; x^k). \quad (20)$$

According to Eqs. (8) and (12),

$$J^1(x^0, p^{1,0}/ih \cdots p^{n,n-1}/ih; x^0 \cdots x^n) = \prod_{k=0}^{n-1} (\epsilon^{k+1,k})^{-1}. \quad (21)$$

$$\textcircled{8}\quad K(x^B, x^A) = \int \exp[iS[x(\tau)]/h] J^1 \times [p(\tau)/ih; x(\tau)] d[x(\tau)], \quad (22)$$

where the integral is extended over all allowed paths, $x(\tau)$, from x^A to x^B. Equation (22) is merely the transcription of Eq. (16), where the notion of a functional as the limit of a function of n variables when $n \to \infty$ has been introduced. Incidentally, Eq. (22) is manifestly dimensionless.

We have thus obtained a mathematical expression for Eq. (1); consequently, we hope to be able to study more simply and more deeply both the mathematical and physical questions raised in connection with Eq. (1).[5] In particular, on the one hand, expression (1) gives more information than does the S-matrix $K(+\infty, -\infty)$; on the other hand, it is possible to choose actions for which Eq. (1) is not equivalent to the detailed information given by the differential equation formalism $K(x^{k+1}, x^k)$, and hence it might be possible to avoid difficulties pertaining to the differential equations and yet answer questions for which the S-matrix seems to be lacking the information.

[5] We are happy to acknowledge a very interesting discussion with Professor von Neuman in connection with this point.

III. AN APPROXIMATE EXPRESSION FOR $K(x^B, x^A)$

So far, when K cannot be computed exactly, an approximate expression for it is obtained by perturbation method. We shall give, now, a different method for the computation of an approximate expression, K_a, for the exact expression, K; the method is quite general and leads to a result such that $K - K_a = 0(h)$.

A *Rule*:

Let S_a be the first two terms of the Taylor expansion of S around its extremal value. K_a is obtained by substitution of S_a for S in the equation of definition of K, Eq. (22) or (16).

B *Method*:

Let us first write Eq. (22) explicitly for K_a. Let $\bar{x}(\tau)$ be the function which makes $S[x]$ minima, namely, the classical path,

$$\delta S[\bar{x}] = 0 \quad (23)$$

$$S[\bar{x}] = \bar{S}(x^B, x^A). \quad (24)$$

Set

$$x(\tau) = \bar{x}(\tau) + \chi(\tau); \quad (25)$$

it follows

$$\chi(\tau^A) = \chi(\tau^B) = 0. \quad (26)$$

The Taylor expansion of S around its extremal value is given by:

$$\begin{aligned} S[x] &= S[\bar{x}] + (1/2!)\delta^2 S[\bar{x}] + (1/3!)\delta^3 S[\bar{x}] + \cdots \\ S_a[x] &\equiv S[\bar{x}] + (1/2!)\delta^2 S[\bar{x}]. \end{aligned} \quad (27)$$

or more briefly,

$$S_a \equiv \bar{S} + (1/2!)\delta^2 \bar{S} \quad (28)$$

$$\delta^2 \bar{S} = \int_{\tau^A}^{\tau^B} [(\partial^2 L/\partial x_\mu \partial x_\nu)|_{x=\bar{x}} \chi_\mu \chi_\nu + 2(\partial^2 L/\partial x_\mu \partial \dot{x}_\nu)|_{x=\bar{x}} \chi_\mu \dot{\chi}_\nu + (\partial^2 L/\partial \dot{x}_\mu \partial \dot{x}_\nu)|_{x=\bar{x}} \dot{\chi}_\mu \dot{\chi}_\nu] d\tau. \quad (29)$$

The second variation $\delta^2 \bar{S}$ is quadratic in the function of integration, χ.

Set

$$J[p_a(\tau)/ih; x(\tau)] \equiv J_a. \quad (30)$$

J_a is independent of χ and involves only the second functional derivative of S_a. The second functional derivative of $\bar{S}$ is zero and that of $\delta^2 S$ is a constant with respect to the function of integration.

$$K_a = \exp[i\bar{S}/h] \int_{x^A}^{x^B} \exp[i\delta^2 \bar{S}/2h] J_a^1 d[x]. \quad (31)$$

The two circumstances $\delta^2\bar{S}$ quadratic in x, and J_α independent of x, make the computation K_α always possible.

We shall now compute:[6]

$$\int_{x^A}^{x^B} \exp[i\delta^2\bar{S}/2\hbar]J_\alpha\mathcal{D}[x]=A_\alpha. \tag{32}$$

Though it should be possible to evaluate A_α from Eq. (32), we resort to the limiting definition of functional integrals [Eq. (16)]. The calculation of A_α amounts, then, to the evaluation of the flattening of successive gaussian curves; more precisely, we establish a recurrence formula giving the result of $k+1$ integrations A_α^{k+1} in terms of the result of k integrations A_α^k. In the limit $n\to\infty$, $A_\alpha^n\to A_\alpha$.

Because of Eq. (29) A_α can be written as follows:

$$A_\alpha=\lim_{n\to\infty}\int\cdots\int\exp\left[\frac{i}{\hbar}\sum_{k=0}^{n}\alpha^k(x^k-\beta^k)^2\right]\prod_{k=1}^{n-1}dx^k/c_\alpha. \tag{33}$$

c_α is the common value of $c_\alpha^{k+1,k}$ when the interval $\tau^B-\tau^A$ is divided in equal parts; $c_\alpha^{k+1,k}$ stands to J_α as $c^{k+1,k}$ to $J\cdot\beta^k$ is a linear homogeneous function of x^{k+1} α^k is obtain by a recurrence formula when one writes $\delta^2\bar{S}$ as a sum of successive squares $(x^l-\beta^l)^2$ (successive means increasing value of l). This recurrence formula is particularly easy to find because, x^0 and x^n being zero, the first term has the same structure as the following ones. α^k is function of α^{k-1}, the coefficients of x^k and $\dot{x}^k$, i.e., x^A, x^B, τ^k, ϵ, and the constants appearing in S: it is important to notice that α^k is real and independent of $\hbar$. The result A_α^{k+1} of $(k+1)$ integration is equal to

$$A_\alpha^{k+1}=A_\alpha^k\Pi_\mu 2\pi\hbar i/\alpha_\mu^{k+1}c_{\alpha\mu}. \tag{34}$$

As $A_\alpha^{k+1}\to A_\alpha^k$ in the limit $n\to\infty$, a natural change of variable is

$$\alpha_\mu^{k+1}=\lambda_\mu^{k+1}+2\pi\hbar i/c_{\alpha\mu}, \tag{35}$$

where λ_μ^{k+1} is given by an equation of the following structure:

$$\lambda_\mu^{k+1}-\lambda_\mu^k=\epsilon f_\mu(\lambda^k,\tau^k,x^A,x^B)+0(\epsilon), \tag{36}$$

and the limit,[7]

$$d\lambda_\mu/d\tau=f_\mu(\lambda,\tau,x^A,x^B), \tag{37}$$

the constant of integration is determined by Eq. (35) for $k+1=0$. Consequently, in the limit, Eq. (34) is written

$$dA_\alpha/d\tau=A_\alpha F(\tau,x^A,x^B)$$

$$A_\alpha=\text{const}\exp\left[\int_{\tau_A}^{\tau_B}Fd\tau\right]. \tag{38}$$

The constant of integration is determined by the condition

$$A_\alpha(\epsilon)=c_\alpha^{-1}. \tag{39}$$

Nature of the approximation:

This approximation is, in functional analysis, the analog to the approximation of the osculatrix parabola in function theory (see, for instance, the Darwin-Fowler method in statistical mechanics). We shall show that K_α is equal to the value obtained by the WKB method, when the lagrangian formulation reduces to the hamiltonian formulation of quantum mechanics; that is, when hamiltonian equations of motion exist. In the WKB method,[8] the wave function ψ is written in the form:

$$\psi=\exp\{(i/\hbar)[S^0+(\hbar S^1/i)+0(\hbar)]\}, \tag{40}$$

and approximated by

$$\psi_\alpha=\exp[iS^0/\hbar]\exp[S^1]. \tag{41}$$

We shall show that $\psi_\alpha=K_\alpha$.

As is well known, $S^0=\bar{S}$; we shall show that A_α, like $\exp[S^1]$, is real and independent of $\hbar$ up to a multiplicative constant,[9] this constant is the same for A_α and $\exp[S^1]$; moreover, $K-K_\alpha=0(\hbar)$.

(a) A_α is real and independent of $\hbar$. One observes from Eq. (14) and (34) that the result of each integration is independent of i and $\hbar$; moreover, as $x^A=x^B=0$, there is no phase term left after integrations (33).

(b) $\exp[S^1]$ and A_α are real and independent of $\hbar$ up to a constant of integration: this constant is determined by the same condition, namely, the normalization condition (39) and (4).

(c) $K-K_\alpha=0(\hbar)$. Set:

$$K=\exp[i\bar{S}/\hbar]A \tag{42}$$

and compare A with A_α. Make the change of variable:

$$x\to\hbar^{\frac{1}{2}}y \tag{43}$$

which implies $\beta\to\hbar^{\frac{1}{2}}b$, b being independent of $\hbar$. Then,

$$A^1=A^0\int\exp[ic^1(y^1-b^1)^2][1+i\hbar^{\frac{1}{2}}(1/3!)\delta^3S(y^0,y^1)+0(\hbar)]dy^1/\hbar^{\frac{1}{2}}c^{1,0}. \tag{44}$$

If we assume that S does not contain $\dot{x}$ to powers larger than 2, δ^3S is proportional to ϵ; hence,

$$A^2=A^0[A_\alpha{}^1+\epsilon 0(\hbar)f(\tau^1)]. \tag{45}$$

By iteration and keeping at each step only the term of lower degree in $\hbar$, one gets

$$A=A_\alpha\left[1+0(\hbar)\int_{\tau_A}^{\tau_B}f(\tau)d\tau\right]. \tag{46}$$

Consequently, the method given here for computing an approximate expression for K is in the lagrangian formalism, the equivalent of the WKB method.[10]

Remark: When the lagrangian is a linear, bilinear, or quadratic function x_μ and $\dot{x}_\mu$, $S_\alpha=S$; hence, $K_\alpha=K$. In this case A_α is function of τ alone: the coefficients of x_μ and $\dot{x}_\mu$ are constant and Eq. (37) becomes $d\lambda_\mu/d\tau=f_\mu(\lambda)$. Incidentally, it is then not necessary to solve the equation of motion in order to write $\delta^2\bar{S}$ explicitly, Similarly, it can be shown directly that when $\psi=\psi_\alpha$. $\exp[S^1]$ is a function of τ alone.

---

[6] The computation of the path integral for exponential of quadratic functions has already been given [R. P. Feynman, Ann Arbor, Summer Symposium, 1949]. The method described here is that used by Feynman in his thesis (Princeton University, 1942) in the study of a forced harmonic oscillator.

At this stage, the order of the variables x^k (order according to increasing or decreasing k) is irrelevant, but the transcription of the results in terms of operators of the usual quantum mechanics requires such an ordering. For this reason, we prefer the method here described to other methods often used in statistical mechanics.

[7] In the case $L=(M\dot{x}^2/2\epsilon)-V(x)$ for instance, Eq. (37) becomes:

$$d\lambda/d\tau=(2\epsilon\lambda^2/M)-\tfrac{1}{2}\partial^2V/\partial x^2\big|_{x=\bar{x}(\tau)}\quad\text{(Riccati equation)}.$$

[8] See, for instance W. Pauli, *Handbuch der Physik* 2 Aufl. Band 24, 1 Teil (Verlag. Julius Springer, Berlin, 1933), p. 166.

[9] In the WKB method, $\exp[S^1]$ is given as the solution of a differential equation (namely the continuity equation). It is not possible to see directly which differential equation is satisfied by A_α for the following reason. In Eq. (32) x^A and x^B are involved; hence, the knowledge of the system at time s is not sufficient to determine the knowledge of the system at time $\tau+d\tau$.

[10] In spite of the fact that with the change of variable (43), the ratio of the $(n+1)$th variation to the nth variation goes to zero with $\hbar$, we are not in a position to ascertain that each successive approximation in the Taylor expansion of S corresponds to the successive approximations of the WKB method.

As a working example, we treat here the motion of a Dirac particle in a constant external electromagnetic field. The choice of this example does not imply that Feynman's formalism is restricted to problems pertinent to the first quantization.

The action S for such a system is

$$S=\int[(Mc/2)(\dot{x})^2+(e/2c)(\gamma\cdot\dot{x})(\gamma\cdot\mathfrak{A})]d\tau, \tag{47}$$

where $\mathfrak{A}$ is the four-potential vector of the electromagnetic field and γ are the 4×4 Dirac matrices. The fulfillment of the two following conditions justifies Eq. (47).

(a) $\delta S=0$ gives, in spite of the γ-matrices, the Lorentz equations.

(b) the corresponding wave function is the Dirac wave functions, more precisely the product $\exp[iMc\tau/2\hbar]$ by the square of the Dirac equation.

The procedure to obtain the wave function corresponding to a given action is established in paragraph 6 of I when the paths are defined by three space functions (x_1, x_2, x_3) of the time, x_4. The transposition of this procedure when the paths are defined by four space-time functions x_μ of the proper time τ leads to the following results:

$$\psi(x^{b+1}, \tau^{b+1})=\int \exp[(i/\hbar)\mathcal{S}(x^{b+1}, x^b)]J^{\frac{1}{2}}\psi(x^b, \tau^b)dx^b. \tag{48}$$

By expanding both sides of Eq. (48) and equating terms of two first-order in $(\tau^{b+1}-\tau^b)$, one obtains

$$\psi(x^{b+1}, \tau)=\psi(x^{b+1}, \tau)$$
$$(2i\hbar c/\hbar)\partial\psi/\partial\tau=[\gamma_\mu[(\partial/\partial x_\mu)-(ie/\hbar c)\mathfrak{A}_\mu]]^2\psi; \tag{49}$$

hence,

$$\psi(\tau, \tau)=\exp[iMc\tau/2\hbar]\psi(x). \tag{50}$$

A supplementary condition is necessary to eliminate the unwanted solutions introduced by the use of the square of the Dirac operator instead of the Dirac operator itself.

We shall proceed to evaluate K; as $K=K_0$, we can compute K by the method given in part B of this section. The following equations are merely the values of the quantities defined there when the action is given by Eq. (47).

$$\delta\mathcal{S}(x^{b+1}, x^b)=\epsilon[Mc[[(x_\mu{}^{b+1}-x_\mu{}^b)/\epsilon]$$
$$+2e(x_\nu{}^{b+1}-x_\nu{}^b)x_\rho{}^b(\partial\mathfrak{A}_\mu/\partial x_\rho)/\epsilon c]$$
$$+(e/c)\gamma_\mu\gamma_\nu[[(x_\mu{}^{b+1}-x_\mu{}^b)x_\rho{}^b(\partial\mathfrak{A}^\nu/\partial x_\rho)/\epsilon]$$
$$-x_\rho{}^{b+1}(\partial\mathfrak{A}^\nu/\partial x_\rho)(x_\mu{}^{b+1}-x_\mu{}^b)/\epsilon]], \tag{29a}$$

$$c_\mu=(2\pi\hbar i\epsilon/Mc)^{\frac{1}{2}}. \tag{15a}$$

With the use of Eq. (24) of I, we can write

$$[(x_\mu{}^{b+1}-x_\mu{}^b)x_\rho{}^b/\epsilon]-x_\rho{}^{b+1}(x_\mu{}^{b+1}-x_\mu{}^b)/\epsilon=\hbar\delta_{\mu\rho}/iM.$$

Thus, in Eq. (22) the terms involving γ's can be taken out of the integral[11]

$$K_D=MK_{KG}$$

[11] If that part of the exponent which is under the integral sign is a matrix, one can break the integrals into integrals over scalars; for instance,

$$\int \exp[i\Gamma_\mu f^\mu[x]]J^{\frac{1}{2}}d[x],$$

where the Γ_μ's are products of γ's such that

$$\Gamma_\mu\Gamma_\nu+\Gamma_\nu\Gamma_\mu=\pm2\delta_{\mu\nu}$$

is equal to

$$\int{}^{\cosh}_{\cos}(\Sigma_\mu f^{\mu 2}[x])^{\frac{1}{2}}J^{\frac{1}{2}}d[x]$$
$$+\Gamma_\mu\int\{f^\mu[x]/(\Sigma_\mu f^{\mu 2}[x])^{\frac{1}{2}}\}{}^{\sinh}_{\sin}(\Sigma_\mu f^{\mu 2}[x])^{\frac{1}{2}}J^{\frac{1}{2}}d[x].$$

This last expression does not involve Γ's in the integrand though it might be hard to evaluate.

It is a pleasure to thank Dr. Bruria Kaufmann on this point. See also O. Klein, Z. Physik 80, 792 (1933). The author has enjoyed several interesting conversations with Professor Klein on this subject.

where K_D and K_{KG} means the amplitude probability for a Dirac and a Klein-Gordon particle respectively.

$$M=\exp[(e/2Mc)\gamma_\mu\gamma_\nu I_{\mu\nu}(A, B)]$$
$$=\cos\{(e/2Mc)\{\Sigma_{\mu\nu}[I_{\mu\nu}(A, B)]^2\}^{\frac{1}{2}}\}$$
$$+[\gamma_\mu\gamma_\nu I_{\mu\nu}(A, B)/\{\Sigma_{\mu\nu}[I_{\mu\nu}(A, B)]^2\}^{\frac{1}{2}}]$$
$$\cdot\sin\{(e/2Mc)\{\Sigma_{\mu\nu}[I_{\mu\nu}(A, B)]^2\}^{\frac{1}{2}}\},$$

$$I_{\mu\nu}(A, B)=\int_A^B F_{\mu\nu}d\tau.$$

For simplicity, let us consider a constant electric field, $\mathcal{E}$, the problem being not essentially more difficult for a constant arbitrary field. Set

$$\mathfrak{A}_3=-i\mathcal{E}x_4 \quad \mathfrak{A}_1=\mathfrak{A}_2=\mathfrak{A}_4=0$$

Then, the coefficients α^b introduced in Eq. (33) are

$$\alpha_\mu{}^b=Mc/\epsilon-M^2c^2/4e^2\alpha_\mu{}^{b-1}-e\mathcal{E}/4c\alpha_\mu{}^{b-1} \qquad \mu=3, 4$$
$$\alpha_\nu{}^b=(Mc/\epsilon)-(Mc/2\epsilon)^2(\alpha_\nu{}^{b-1})^{-1}; \qquad \nu=1, 2$$

hence,

$$d\lambda_\mu/d\tau=-(2\lambda_\mu{}^2/Mc)-(e\mathcal{E})^2/8Mc^3$$
$$d\lambda_\nu/d\tau=-2\lambda_\nu{}^2/Mc. \tag{37a}$$

As is already known,[12] one finds that in the coordinates 3, 4, the particle behaves like a complex harmonic oscillator of frequency $2\omega=e\mathcal{E}/Mc^2$ and in the coordinates 1, 2, it behaves like a free particle:

$$K_{KG}(x^B, x^A)=[\omega/2\pi\hbar i\sin\omega(\tau^B-\tau^A)]$$
$$\times[Mc/2\pi\hbar i(\tau^B-\tau^A)]\exp[i\mathcal{S}/\hbar].$$

The classical action $\mathcal{S}$ is equal to

$$(Mc\tau/2)+[Mc(\omega x_3{}^A-i\dot{x}_4{}^A)(-\dot{x}_3{}^A\cosh\alpha\tau-i\dot{x}_4{}^A\sinh\alpha\tau)/\omega]$$
$$+Mc\{-i\dot{x}_3{}^A\dot{x}_4{}^A\cosh2\alpha\tau$$
$$-\tfrac{1}{2}[(\dot{x}_3{}^A)^2-(\dot{x}_4{}^A)^2]\sinh2\alpha\tau+\tau\}/2\omega,$$

taken between the limits $\tau=\tau^A$ and $\tau=\tau^B$. τ can be eliminated from K with the help of the following relation:

$$\omega(\tau-\tau^A)=\sinh^{-1}[-i\omega(x_4-x_4{}^A)-\dot{x}_3{}^A]-\sinh^{-1}(-\dot{x}_3{}^A).$$

$\dot{x}_3{}^A$ and $\dot{x}_4{}^A$ can be expressed in terms of $(dx_3/dx_4)^A=x_3{}'^A$, which in turn can be expressed in terms of $x_3{}^B$ and $x_4{}^B$ by the following equations:

$$\dot{x}_3{}^A=x_3{}'^A[1+(x_3{}'^A)^2]^{-\frac{1}{2}}$$
$$\dot{x}_4{}^A=[1+(x_3{}'^A)^2]^{-\frac{1}{2}}$$
$$\{\omega x_3{}^B-\omega x_3{}^A+i[1+(x_3{}'^A)^2]^{-\frac{1}{2}}\}^2$$
$$+\{\omega x_4{}^B-\omega x_4{}^A-x_3{}'^A[1+(x_3{}'^A)^2]^{-\frac{1}{2}}\}^2-1=0$$

Strueckelberg[13] and Feynman[14] have shown independently that the motion of a positive electron is the same as the motion of a negative electron going backwards in time. In a constant field, $x_4-x_4{}^A$ is always of the same sign as $\dot{x}_4{}^A$, the x_4 direction of the path cannot be reversed and there is no pair creation or pair annihilation. But if there is a potential difference (in time or space) equal to a least $2Mc^2$ within a distance equal to $\hbar/Mc^2$ (time) or $\hbar/Mc$ (space), it has been shown that the present formalism describes adequately the phenomenon of pair creation and annihilation by a time potential barrier[13] or by a space potential barrier;[15] then the classical path is reflected at a time potential barrier or refracted with reversal of time at a space potential barrier.

I wish to thank Professor Oppenheimer for the hospitality extended to me at the Institute and for the interest he has taken in my work.

[12] See, for instance, L. Landau, Physik 64, 629 (1930), for the case of a constant magnetic field; thus, the indices 1, 2 replace the indices 3, 4 and vice versa.

[13] See references given in footnote 1.

[14] R. P. Feynman, Phys. Rev. 76, 749 (1949).

[15] R. P. Feynman, Phys. Rev. 74, 943 (1948).

Fluorescence of Solutions Bombarded with High Energy Radiation (Energy Transport in Liquids)

Part II*

HARTMUT KALLMANN AND MILTON FURST
Physics Department, New York University, Washington Square, New York, New York

(Received October 23, 1950)

In organic solutions containing fluorescent molecules a considerable part of the high energy radiation absorbed in the bulk material is transformed into light emitted by the fluorescent molecules. There is a transfer of excitation energy from the bulk material to these molecules which reaches its maximum at concentrations of approximately 1 g/l and higher. Experiments with mixed solvents are described where relatively small concentrations (several mole percent) especially of naphthalene and *o*-diphenylbenzene act in some way as a second solvent. The excitation energy can be localized by investigating the fluorescence of these mixed solvents when different fluorescent solutes are added. It is found that the energy migrates from the original solvent to the second solvent and then to the fluorescent molecule. This intermediate energy transfer can change the light emission curve completely. From this change the dependence of the light emission on internal and self-quenching could be determined. Besides this internal energy transfer, an energy transfer via radiation occurs which is described in detail by studying the absorption of the fluorescent light inside the solution by adding small amounts of a second solute of the order of 0.1 g/l. Such small amounts change the light intensity considerably and shift the spectrum to the spectrum of the second solute. Photographs and data of the spectral distribution of such solutions are presented, which show that such drifts already occur with very small amounts of the second solute.

A. INTRODUCTION

In a previous paper, experiments on the light emission of dilute organic solutions excited by high energy radiation were described, and a theory was developed to explain the phenomena observed.[1] It was found that small amounts of solute molecules (of the order of 1 g/l) are already enough to increase the light emission of the pure solvent by as much as a factor of 35 and probably more. This phenomenon was explained by assuming a transfer of energy from the excited solvent molecules to the solute molecules. It was shown that the direct excitation of the same amount of solute as was present in the solution produced much smaller light emission than was observed in these experiments and therefore, could not be responsible for the large amount of light emitted. The energy transfer to the solute molecule was described as a competition between two processes: (1) the migration of the excitation energy through the solvent and its trapping by the solute molecule, and (2) the process of quenching the excitation energy in the solvent. These processes are described by means of a quenching probability $1/\tau_q$ which is inherent to the solvent, and a trapping probability $1/\tau_t$ which is a function of the concentration of the solute. In first approximation, $1/\tau_t$ was put equal to αc, where c is the concentration of the solute and α is a coefficient depending on both the solute and the solvent. The number, n, of excited solute molecules per second was given by

$$n=\alpha\tau_q c n_E(1+\alpha\tau_q c)^{-1}, \qquad (1)$$

where n_E represents the number of solvent molecules directly excited per unit time. The intensity of the light emitted is then given by n times a factor which stems from the competition of three processes: the process of light emission by the solute molecule described by the probability $1/\tau_e$, the process of internal quenching (transformation of excitation energy into heat inside the solute molecule) described by the probability $1/\tau_i$ ($1/\tau_q$ has essentially the same physical significance of internal quenching as $1/\tau_i$ except that $1/\tau_q$ refers to the solvent molecule whereas $1/\tau_i$ refers to the solute), and the process of so-called self-quenching (interaction of solute molecules of the same kind) described by the probability $1/\tau_s$, which is as a first approximation also proportional to the concentration; i.e., equal to βc, where β depends on both the solute and the solvent. The radiation from the solvent is neglected in this development. The internal quenching probability is inherent to the solute molecule, but in some degree it depends on the surroundings of the molecule and, therefore, depends also on the solvent. In special cases it may even depend on the concentration of the solute. The final formula for light emission is given by (2), which is essentially the same expression as (2) of the previous paper:

$$I=\alpha\tau_q c n_E(1+\alpha\tau_q c)^{-1}[1+(\tau_q/\tau_i)+\beta\tau_q c]^{-1}. \qquad (2)$$

The general shape of the light emission curve as a function of the concentration in most cases can be explained by this theory. It was found, however, that in several cases an additional phenomenon occurs; it was observed that very small concentrations of an additional solute (of the order of 0.5 g/l and less) could decrease the light emission considerably. This attenuation was attributed to an absorption of the light emitted from the first solute by the second solute and only

* This work was supported by the Signal Corps Engineering Laboratories, Fort Monmouth, New Jersey.

[1] H. Kallmann and M. Furst, Phys. Rev. 79, 857 (1950).

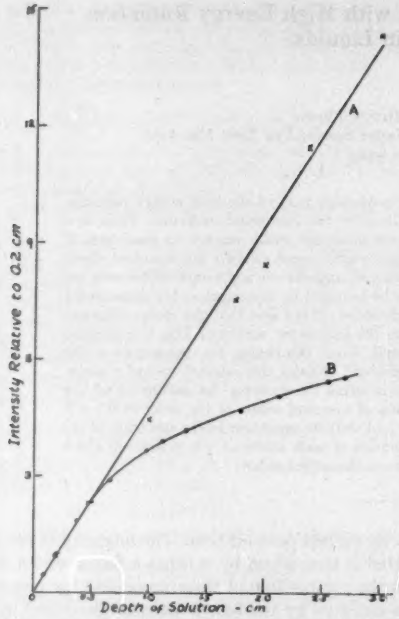

FIG. 1. Standard absorption curves.

partial retransformation of the energy into light. The rest of this energy is transformed into heat by the internal quenching in the second solute molecule.

Sections B and C are concerned with experiments bearing out the theory proposed in that paper. In Sec. B particularly the absorption of the fluorescent light in the solution is determined directly, whereas in Sec. C the emission spectra of a number of crystals and solutions is found. These latter spectra and their shift by small amounts of "impurities," play an important role in the theory. Solutions with strong absorption always show shifts of the spectrum of the emitted light of the original solution to that of the spectrum of the absorbing solute.

Section D describes experiments with mixed solutions where practically no absorption energy occurs, but where the maximum intensity of the emitted light and the concentration for maximum intensity are changed by the addition of fairly small amounts of an additional solute. Here one must assume a new process of energy transfer which, however, fits very well into the general scheme proposed in this paper. By means of these experiments one is able to follow the transfer processes in greater detail.

The experiments on absorption indicate that in some cases an energy transfer from the first solute to the second solute via radiation occurs. The question of whether such energy transfer by radiation may also be responsible for the energy transfer from the solvent to the solute then arises. Since the radiation of the pure solvent is small compared with that of the solution, the energy transfer could be achieved only by means of radiation if the radiation emitted by this pure solvent is already strongly absorbed by the solvent itself within thicknesses considerably smaller than one millimeter. Otherwise, the small radiation of larger amounts of the pure solvent and the strong radiation of the same amount of solution could not be explained. Although the absorption experiments described in Sec. B do not indicate such a strong absorption, it may be that such an absorption could be overlooked, since a very thin layer of the pure solvent emits only a very small amount of radiation. Experiments described in Sec. D clearly prove that the energy transfer from the solvent to the solute does not occur by radiation. They indicate that another mechanism of energy transfer, for instance, such as that described in our previous paper, exists.

B. ABSORPTION EXPERIMENTS

In the previous paper (Table V) experiments were described showing that the intensity of a xylene-terphenyl solution was greatly attenuated by the addition of 0.1 g/l of anthracene. If this attenuation is caused by an absorption of the terphenyl radiation inside the solution, the ratio of the light intensities emitted by a pure xylene-terphenyl solution to that emitted by the contaminated solution should depend on the thickness of the solution under investigation. In a solution with small thickness the light has a smaller chance of being absorbed; and, therefore, the ratio of the light intensities of two solutions, one without and one with the absorber, should depend on the thickness and should approach unity for very small thicknesses of solutions. In the experimental arrangement described in the previous paper the intensity of the solution is not a linear function of the thickness of the solution, since the geometrical factor for different parts of the solution with respect to the source of radiation is not constant and the container has reflecting walls. To determine the effect of these factors, the intensity of the solution was measured as a function of the thickness of the solution with a 100-millicurie source relatively far away from the solution in a nonreflecting beaker. For this experiment the geometrical factor for all thicknesses of solutions was approximately the same, and if no absorption exists, the curve should be a straight line. Curve *A* in Fig. 1 clearly indicates that for a xylene-terphenyl solution practically no absorption exists. For checking other solutions, it was desirable to avoid using the strong 100-mc source. Therefore, the same xylene-terphenyl solution was measured as a function of the thickness in the old arrangement (but with an oxidized nonreflecting brass beaker instead of the porcelain beaker[2]) with the variable geometric factor. These measurements are

[2] A nonreflecting beaker was used, since it was found that by shifting the wavelength of the emitted radiation a difference in the reflection factor occurred.

represented by Curve *B* of Fig. 1. The ratio of these two curves gives the average geometrical factor for each depth of solution. To determine the absorption of other solutions, measurements were made with the old arrangement using the brass beaker, and the results compared with those of curve *B*. This xylene+terphenyl solution curve served as a standard for all other solutions. A typical experiment is described in Fig. 2, where *A* is the standard curve and curve *B* describes the light intensity curve as a function of the thickness in a xylene-terphenyl 1 g/l solution with an additional amount of 0.1 gram of anthracene per liter. Curve *B* is close to curve *A* for small thicknesses. The strong deviation for larger depths shows that anthracene absorbs the terphenyl radiation. As a further check that these deviations are due to absorption, an experiment was performed using two beakers, one above the other, the top one having a transparent bottom. The lower beaker contained a highly fluorescent terphenyl solution. The upper beaker was filled first with pure xylene; this xylene produced only a very slight attenuation. Then 0.1 g/l anthracene was dissolved in the solvent in the upper beaker, and the intensity of the terphenyl solution went down to 0.2 of its original value.

These absorption methods have been used to check whether solvents or solutions have their light emission attenuated by absorption through impurities and thus whether the fluorescence can be improved by further purification.[3] A typical example is *o*-xylene of the highest purity obtainable commercially. With terphenyl this solvent exhibited a 20 percent smaller intensity than did the commercial ordinary xylene; our absorption check indicated noticeable absorption, larger than terphenyl in xylene. A comparison with a solution using *o*-xylene from a standard sample of the Bureau of Standards showed the same light emission with terphenyl as with ordinary xylene and the absorption check indicated much smaller absorption. This experiment shows that the commercially available *o*-xylene gives smaller readings than the normal xylene as a consequence only of absorption by impurities present. Some of our results are collected in Table I. They indicate that most of the solvents have some absorption in the ultraviolet in the region around 3000A, but little absorption for wavelengths above 3400A as was checked by the absorption curves of these solvents with terphenyl. All our solvents are checked with terphenyl (if it is soluble enough); and if they indicate no absorption with terphenyl radiation, these solvents are considered to be purified enough (for radiation around and above 3500A). Additional purification would give no increase in light emission of the solute. The absorption observed in the ultraviolet seems to stem partly from unknown impurities. This was indicated by the following observation. If the light above about 3300A was observed separately from the light emitted in the spectral range below 3300A (by means of a glass filter), it was always observed that the light more to the ultraviolet was attenuated by absorption, but that the light more to the visible showed little attenuation and in several cases even exhibited an increase in intensity above the values of the standard absorption curve. This seems to indicate that some light was transformed from the ultraviolet to the visible region.

The amount of absorption in the ultraviolet range is, however, not strong enough to explain the energy transfer from the solvent to the solute by radiation as can be seen, for example, from the values in Table I for benzene, which has an absorption curve in the ultraviolet fairly close to the standard curve. If the light emitted by the pure solvent were strongly enough absorbed to explain a radiation energy transfer in the solvent, a practically constant light intensity or even a decrease should be expected for thicknesses greater than about one millimeter.

Table I indicates that the absorption increases toward the ultraviolet. Benzene and phenylcyclohexane are the solvents which indicate the smallest absorption in the ultraviolet. This may be the reason why durene, with large ultraviolet fluorescence, gives the largest light emission in these solvents. How far the absorption in the "so-called" pure solvent comes from the solvent molecule itself is still an open question. With increasing wavelength the absorption decreases, as is evidenced by the fact that for the terphenyl radiation several solvents already show practically no absorption. Mesitylene,

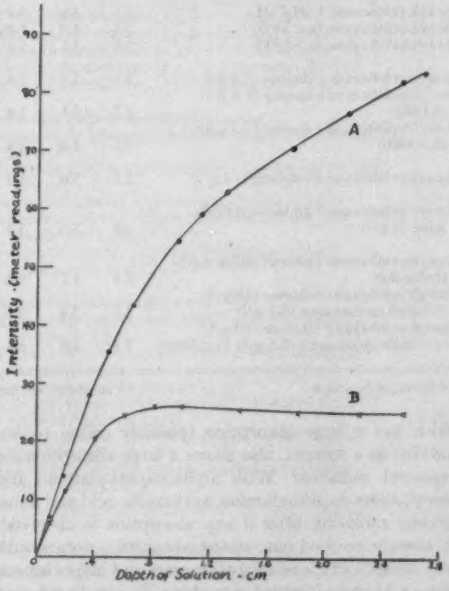

FIG. 2. Absorption in xylene+terphenyl (1 g/l)+anthracene (0.1 g/l).

[3] H. Kallmann and M. Furst, Nucleonics 7, 69 (1950).

TABLE I. Absorption.

Solution	Depth cm	Approximate relative intensity to 0.2 cm: Solution	Approximate relative intensity to 0.2 cm: Standard
Benzene	2.5	4.8	5.4
Benzene ($\lambda<3300$)	2.5	3.9	5.4
Benzene ($\lambda>3300$)	2.5	6.7	5.4
Benzene+durene (20 g/l)	2.6	4.4	5.5
Benzene+durene (20 g/l) ($\lambda<3300$)	2.6	3.8	5.5
Benzene+durene (20 g/l) ($\lambda>3300$)	2.6	7.2	5.5
Benzene+phenol (5 g/l)	2.6	2.9	5.5
Benzene+phenol (5 g/l) ($\lambda<3300$)	2.6	2.3	5.5
Benzene+phenol (5 g/l) ($\lambda>3300$)	2.6	3.3	5.5
p-dioxane	1.9	3.2	4.9
p-dioxane ($\lambda<3300$)	1.9	1.6	4.9
p-dioxane ($\lambda>3300$)	1.9	5.6	4.9
p-dioxane+terphenyl (5 g/l)	1.9	4.0	4.9
iso-durene[a]	1.3	2.2	4.1
iso-durene[a] ($\lambda<3300$)	1.3	2.1	4.1
iso-durene[a] ($\lambda>3300$)	1.3	3.0	4.1
iso-durene+terphenyl (4 g/l)	1.1	3.4	3.9
Mesitylene	2.6	1.8	5.5
Mesitylene ($\lambda<3300$)	2.6	1.0	5.5
Mesitylene ($\lambda>3300$)	2.6	2.4	5.5
Mesitylene+terphenyl (5 g/l)	2.6	1.4	5.5
Paraffin oil $H-(CH_2)_n-H$	2.5	2.9	5.4
Paraffin oil ($\lambda<3300$)	2.5	1.3	5.4
Paraffin oil ($\lambda>3300$)	2.5	6.0	5.4
Phenylcyclohexane $C_6H_5C_6H_{11}$	2.5	3.6	5.4
Phenylcyclohexane ($\lambda<3300$)	2.5	3.3	5.4
Phenylcyclohexane ($\lambda>3300$)	2.5	5.7	5.4
Phenylcyclohexane+durene (7.5 g/l)	2.5	3.5	5.4
Phenylcyclohexane+durene (7.5 g/l) ($\lambda3300$)	2.5	3.1	5.4
Phenylcyclohexane+durene (7.5 g/l) ($\lambda>3300$)	2.5	5.4	5.4
Phenylcyclohexane+terphenyl (4 g/l)	2.3	5.0	5.2
Phenylcyclohexane+alpha-naphthylamine (1 g/l)	2.5	5.3	5.4
Phenylcyclohexane+phenyl alpha-naphthylamine	2.4	4.7	5.3
Phenylcyclohexane+durene (10 g/l) +o-diphenylbenzene (0.5 g/l)	2.5	2.4	5.4
Phenylcyclohexane+durene (10 g/l) +o-diphenylbenzene (0.5 g/l) ($\lambda<3300$)	2.5	1.8	5.4
Phenylcyclohexane+durene (10 g/l) +o-diphenylbenzene (0.5 g/l) ($\lambda>3300$)	2.5	7.3	5.4
Phenetole+phenyl alpha-naphthylamine (5.5 g/l)	2.5	4.9	5.4
Xylene	2.5	3.2	5.4
Xylene ($\lambda<3300$)	2.5	2.6	5.4
Xylene ($\lambda>3300$)	2.5	4.1	5.4
Xylene+phenyl alpha-naphthylamine (7.5 g/l)	2.6	4.3	5.5
o-xylene[a]	1.4	3.1	4.3
o-xylene[a] ($\lambda<3300$)	1.4	3.1	4.3
o-xylene[a] ($\lambda>3300$)	1.4	3.1	4.3
o-xylene[a]+terphenyl (6.5 g/l)	1.2	3.5	4.0
o-xylene (commercial+terphenyl (7 g/l)	1.2	2.9	4.0
o-xylene (commercial)	2.5	2.9	5.4
o-xylene (commercial) ($\lambda<3300$)	2.5	1.0	5.4
o-xylene (commercial) ($\lambda>3300$)	2.5	4.5	5.4
Xylene+anthranilic acid	2.6	5.2	5.5
Xylene+terphenyl (1 g/l)[b]	2.6	5.5	5.5
Xylene+terphenyl (1 g/l)+naphthalene (280 g/l)	2.6	4.4	5.5
Xylene+anthracene (2 g/l)	2.6	5.3	5.5
Xylene+alpha-naphthylamine (2 g/l)	2.6	5.2	5.5
Xylene+alpha-naphthylamine (2 g/l) +anthracene (0.08 g/l)	2.6	4.4	5.5
Xylene+fluoranthene (35 g/l)	1.9	4.4	4.9
Xylene+fluoranthene (35 g/l)+o-diphenylbenzene (20 g/l)	1.9	4.3	4.9
Xylene+terphenyl (1 g/l)+anthracene (0.1 g/l)	2.6	2.3	5.5
Xylene+terphenyl (1 g/l)+naphthacene (0.05 g/l)	2.5	4.1	5.4
Phenylcyclohexane+durene (10 g/l) +naphthalene (0.5 g/l)	2.0	2.8	5.0
Phenylcyclohexane+durene (10 g/l) +naphthalene (0.5 g/l) ($\lambda<3300$)	2.0	1.6	5.0
Phenylcyclohexane+durene (10 g/l) +naphthalene (0.5 g/l) ($\lambda>3300$)	2.0	4.9	5.0

[a] Bureau of Standards.

[b] Standard—see figures.

which has a large absorption (possibly owing to impurities) as a solvent, also shows a large absorption for terphenyl radiation. With alpha-naphthylamine and phenyl alpha-naphthylamine, anthranilic acid and fluoranthene radiation little if any absorption is observed. As already pointed out, strong absorption occurs with very small additions of anthracene and naphthacene because of their internal quenching. It was found that many substances, especially those emitting light of longer wavelengths, have a variation with depth in different solvents similar to that of the standard curve. This can be considered as an independent check on the reliability of the absorption measurements. Only small absorption of the terphenyl radiation by as much as 280 g/l of naphthalene is found, although in this case the intensity went down by a factor of about 10. Also, the addition of o-diphenylbenzene to a fluoranthene solution produces practically no additional absorption,

though it does decrease the light emission noticeably (see Sec. D).

Table II describes how known "impurities" influence the intensity of these solutions. They show that many solutions are influenced by the addition of small amounts of other solutes. Absorption was always found if the attenuation already occurs with a very small concentration of the second solute (smaller than 0.5 g/l) as, for example, the cases of xylene solutions of alpha-naphthylamine or terphenyl by the addition of small amounts of anthracene. Some substances produce no attenuation at all, for instance, the addition of terphenyl to a xylene plus alpha-naphthylamine solution. With others, strong attenuating effects occur only with comparatively large concentrations of the second solute as in the addition of large amounts of naphthalene or *o*-diphenylbenzene to some of these solutions. Most of the attenuation in these latter cases does not stem from absorption but from other effects which will be described in Sec. D. With some substances, like diphenyl hexatriene, an addition of naphthalene or *m*-diphenylbenzene even, an increase in light output occurs (see also Table V of reference 1). A tentative explanation will be given in Sec. D.[4]

Table II. Effects of known impurities.

Solution	Relative intensity
Xylene+alpha-naphthylamine (2 g/l)	0.19
Xylene+alpha-naphthylamine (2 g/l)+anthracene (0.04 g/l)	0.14
Xylene+alpha-naphthylamine (2 g/l)+anthacene (0.1 g/l)	0.13
Xylene+alpha-naphthylamine (2 g/l)+diphenyl (0.5–2 g/l)	0.19
Xylene+alpha-naphthylamine (1 g/l)+naphthalene (10 g/l)	0.075
Xylene+alpha-naphthylamine (1 g/l)+naphthalene (100 g/l)	0.019
Xylene+terphenyl (2 g/l)	0.39
Xylene+terphenyl (2 g/l)+anthacene (0.01 g/l)	0.21
Xylene+terphenyl (2 g/l)+anthracene (0.05 g/l)	0.15
Xylene+terphenyl (2 g/l)+fluoranthene (0.03 g/l)	0.16
Xylene+terphenyl (2 g/l)+o-diphenylbenzene (0.5 g/l)	0.33
Xylene+terphenyl (2 g/l)+o-diphenylbenzene (20 g/l)	0.09
Xylene+terphenyl (2 g/l)+naphthalene (0.3 g/l)	0.37
Xylene+terphenyl (2 g/l)+naphthalene (100 g/l)	0.060
Xylene+terphenyl (2 g/l)+anthranilic acid (0.1 g/l)	0.32
Xylene+phenyl alpha-naphthylamine (7.5 g/l)	0.24
Xylene+phenyl alpha-naphthylamine (7.5 g/l) +anthracene (0.1 g/l)	0.21
Xylene+phenyl alpha-naphthylamine (7.5 g/l) +anthracene (0.5 g/l)	0.16
Xylene+phenyl alpha-naphthylamine (2 g/l)	0.30
Xylene+phenyl alpha-naphthylamine (2 g/l) +fluoranthene (0.05 g/l)	0.24
Xylene+phenyl alpha-naphthylamine (2 g/l) +fluoranthene (0.2 g/l)	0.19
Xylene+anthranilic acid (3 g/l)	0.23
Xylene+anthranilic acid (3 g/l)+anthracene (0.5 g/l)	0.16
Xylene+anthranilic acid (3 g/l)+anthracene (3 g/l)	0.09
Xylene+fluoranthene (3 g/l)	0.12
Xylene+fluoranthene (3 g/l)+anthranilic acid (0.5 g/l)	0.12
Xylene+fluoranthene (3 g/l)+anthranilic acid (2 g/l)	0.12
Xylene+fluoranthene (3 g/l)+anthracene (0.5 g/l)	0.12
Xylene+fluoranthene (3 g/l)+anthracene (2 g/l)	0.11
p-dioxane+alpha-naphthylamine (2 g/l)	0.11
p-dioxane+alpha-naphthylamine (2 g/l)+naphthalene (30 g/l)	0.10
p-dioxane+alpha-naphthylamine (2 g/l)+naphthalene (100 g/l)	0.078
p-dioxane+phenyl alpha-naphthylamine (10 g/l)	0.11
p-dioxane+phenyl alpha-naphthylamine (10 g/l) +anthranilic acid (0.5 g/l)	0.10
p-dioxane+phenyl alpha-naphthylamine (10 g/l) +anthranilic acid (5 g/l)	0.09
Xylene+diphenylhexatriene (0.9 g/l)	0.21
Xylene+diphenylhexatriene (0.9 g/l)+m-diphenyl-benzene (0.5 g/l)	0.215
Xylene+diphenylhexatriene (0.9 g/l)+m-diphenyl-benzene (10 g/l)	0.245
Xylene+diphenylhexatriene (1 g/l)	0.22
Xylene+diphenylhexatriene (1 g/l)+phenyl alpha-naphthylamine (0.5 g/l)	0.24
Xylene+diphenylhexatriene (1 g/l)+phenyl alpha-naphthylamine (3 g/l)	0.26
Xylene+diphenylhexatriene (1 g/l)+phenyl alpha-naphthylamine (7 g/l)	0.24

C. SPECTRAL DISTRIBUTION OF DIFFERENT SOLUTIONS AND POWDERS

To clarify the processes occuring in these solutions, measurements of the spectral distributions of the emitted light were carried out. Two different experimental arrangements were used; the first arrangement with which most of the spectra presented here were obtained consists of a highly reflecting silver tube of 10-cm length and about 2-cm diameter with a transparent quartz plate at one end which was placed directly in front of the slit of a quartz spectrograph. The solution was excited by a 100-millicurie gamma-source placed directly under the tube containing the solution. The photographic plate in the spectrograph was screened from the direct radiation of the source by some lead plates in order to reduce fogging. With this arrangement spectra of the emitted light of nearly all of the better solutions could be obtained by exposure for 16 hours; some weaker solutions required an exposure of 64 hours. This arrangement with a long tube is good for showing shifts in the emission spectra caused by absorption effects. Thus, if the solution contains even small amounts of impurities, the spectrum of the impurity could appear stronger than that of the original solution if the absorption theory is correct. The other experimental setup has been used to minimize absorption effects. In this case a very small amount of solution was used and the solution placed immediately above the slit of the spectroscope. The solution was energized by a polonium alpha-particle source of 10-millicurie strength. With this source, spectra could be obtained from the best solutions within five hours; fog was completely absent from these plates.

[4] These tables include substances giving considerable fluorescence, which were not mentioned in previous papers. Since the submission of the last paper many new solutions have been investigated. A summary of these results may be published soon.

TABLE III. Spectral ranges of different solutions and crystals.

Substance	Approximate emission spectral range (Angstroms)
Anthracene crystal	4200–4700
Xylene+anthracene (1.5 g/l)	3900–4400
Naphthalene crystal	3300–3800
Xylene+naphthalene (20 g/l)	3200–3800
Durene crystal[a]	2900–3300
Phenylcyclohexane+durene (4 g/l)	2800–3500
Phenylcyclohexane+durene (4 g/l)+fluoranthene (0.1 g/l)	4000–5000
Phenylcyclohexane+durene (4 g/l)+fluoranthene (1 g/l)	4000–5000
Phenylcyclohexane (α-particles)	2700–3100
Xylene+fluoranthene (3 g/l)	4100–5000
Tetrahydronaphthalene+fluoranthene (3 g/l)	4200–5500
Phenylcyclohexane+terphenyl (3 g/l)	3200–4100
Phenylcyclohexane+terphenyl (1 g/l) (α-particles)	3150–4000
Xylene+terphenyl (1 g/l)	3250–4000
Xylene+terphenyl (1 g/l)+anthranilic acid (0.1 g/l)	3600–4400
Xylene+terphenyl (2 g/l)+anthracene (0.05 g/l)	3800–4400
p-cymene+terphenyl (2.5 g/l)	3300–4000
Phenylcyclohexane+terphenyl (3 g/l)+diphenylhexatriene (trace)	3200–4800
Tetrohydronaphthalene+terphenyl (5 g/l)	3500–4000
Terphenyl crystal	3600–4300
Xylene+m-diphenylbenzene (15 g/l)	3200–4000
Xylene+m-diphenylbenzene (15 g/l)(α-particles)	3200–3800
Xylene+anthranilic acid (3 g/l)	3600–4400
Xylene+diphenylhexatriene (0.6 g/l)	4000–5500
Phenylcyclohexane+diphenylhexatriene (1 g/l) (α-particles)	3900–5500
Xylene+α-naphthylamine (2 g/l)	3600–4400
Xylene+β-naphthylamine (2 g/l)	3700–4300
Xylene+α-naphthylamine (2 g/l)+anthracene (0.1 g/l)	3800–4400
Phenylcyclohexane+phenyl α-naphthylamine (1 g/l)	3700–4500
Xylene+phenyl α-naphthylamine (2 g/l)	3200–4500
Xylene+phenyl α-naphthylamine (2 g/l)+fluoranthene (0.2 g/l)	3900–4500
p-dioxane+phenyl α-naphthylamine (5 g/l)	3900–4500
Aniline+phenyl α-naphthylamine (1.5 g/l) (α-particles)	3800–4500
Phenanthrene powder (α-particles)	3800–4400
Phenylcyclohexane+phenanthrene (7 g/l) (α-particles)	3800–4100
Phenylcyclohexane+carbazole (1 g/l) (α-particles)	3400–3800
Phenylcylohexane+diphenylbutadiene (1 g/l) (α-particles)	3600–4200
Phenylcyclohexane+o-diphenylbenzene (20 g/l) (α-particles)	3600–4500

[a] The durene crystal of one-cm cube was prepared for us by Mr. J. Zar.

The results are listed in Table III in which the range of the more intense part of the spectrum is indicated. For comparison purposes, the spectrum of the crystal was also determined for some substances. Terphenyl and anthracene spectra using x-rays and light have recently been published by Harrison and Reynolds.[5] Our spectra of these substances obtained with gamma-rays agree closely with their spectra, thus indicating that they do not strongly depend on the kind of excitation (see also end of this section).

The comparison between the pure crystal and the solution indicates that the solution spectrum is in some cases broader than the spectrum of the pure crystal and somewhat shifted to the ultraviolet. Special notice should be given to the results with naphthalene. The naphthalene crystal was a large clear crystal and gave a spectrum between 3300 and 3800A. The same crystal was tested on a multiplier tube and compared with an anthracene crystal. Its peak intensity was about 40 percent of that of anthracene. In this case we can conclude from the spectrum that the light emitted from this crystal was the light of the naphthalene and not from any impurity, since this spectrum of the crystal coincides so closely with the spectrum of a xylene+naphthalene solution that it could not be excited by energy transfer inside the crystal from the bulk material to an unknown impurity. Energy transfer to small amounts of additional material occur with larger probability only if the emission spectrum of the additional material is far enough toward longer wavelengths from the emission spectrum of the bulk material; otherwise, no trapping of the excitation energy can occur in the additional molecules. These ideas are supported by an experiment described in Sec. D.

These spectra further support the idea that the effects of small amounts of additional material stem from absorption. Table III indicates that the spectrum of 4 g/l of durene in a phenylcyclohexane solution ranges from 2800 to 3500A. With 0.1 g/l of fluoranthene added to this solution, the spectrum is already completely shifted to the fluoranthene spectrum (see Table III). With 0.05 g/l of anthracene added to a xylene-terphenyl solution of 2 g/l the spectrum was completely removed from the region of terphenyl to that of anthracene. With such a small amount of anthracene alone, no spectrum at all

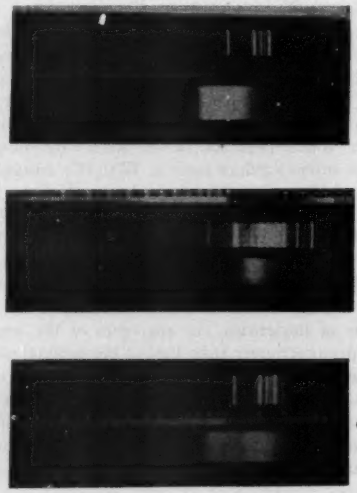

FIG. 3. (a) Terphenyl solution. (b) Terphenyl solution +0.1 g/l anthranilic acid. (c) Terphenyl solution+trace of diphenylhexatriene.

[5] F. B. Harrison and G. T. Reynolds, Phys. Rev. 79, 732 (1950).

would be obtained for the same duration of exposure. A similar result was obtained by adding 0.1 g/l of anthranilic acid to a xylene-terphenyl solution; the spectrum is completely shifted to the region of the anthranilic acid. Figure 3 gives some typical spectra obtained; Fig. 3a presents the spectrum of a terphenyl solution, 3b the spectrum of a terphenyl solution with 0.1 g/l anthranilic acid added, it shows the complete shift to the anthranilic acid spectrum, 3c gives the spectrum of a terphenyl solution with a trace of diphenylhexatriene. Here both spectra, that of terphenyl and that of diphenylhexatriene, appear in agreement with results obtained from absorption measurements.

A special search has been made with this method for substances excited by gamma-radiation which gives an emission more to the visible. The best substance found is diphenylhexatriene, which gives a high intensity and a spectrum of which reaches to about 5500A. Another substance with fairly good light efficiency in the same region is fluoranthene. This absorption phenomenon may be helpful in scintillation counter work. It gives the possibility of shifting the spectra of a given solution to the visible by using only very small amounts of a substance. This may be of advantage for the reason that the intensity of the emitted light in the visible can, in some cases, be made even larger than by using this substance directly, since the self-quenching effect can thus be avoided. In cases where the substance contains small amounts of quenching impurities, the effects of these impurities may be minimized by the absorption method. Finally, some of these substances are rather costly, and the absorption method is less expensive.

The spectra of the pure solvents would be too weak to be observed with the long tube arrangement because the fog produced by the gamma-radiation is too high. With the arrangement using alpha-particles for excitation such measurements can be made. Phenylcyclohexane has an emission spectrum betweem 2700 and 3100A. It appears that the spectra excited by alpha-particle excitation coincide fairly closely with the spectra taken with the gamma-radiation arrangement, provided that no absorption occurs.

D. EXPERIMENTS WITH MIXED SOLUTIONS

As was indicated in Sec. B, quite different effects occur in mixed solutions. All of these effects seem to be complicated by the absorption of the light emitted from one substance by the other substances. To find out more about these processes in mixed solutions we have used two substances in which little if any absorption occurs. These substances are naphthalene and *o*-diphenylbenzene. The emission and absorption spectra of naphthalene are so similar to those of terphenyl that no absorption of the terphenyl radiation can occur. Since most of the substances under investigation have emissions of longer wavelengths than those of terphenyl, the light emitted by them cannot be absorbed by naphthalene. Only substances like durene have an emission

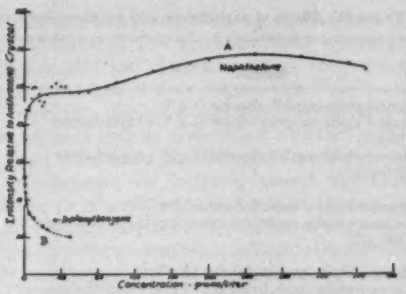

FIG. 4. Naphthalene and *o*-diphenylbenzene in xylene.

spectrum which could be absorbed by naphthalene. These conclusions are verified with solutions containing naphthalene; the durene emission is decreased by absorption, but not the light emitted by most of the other substances investigated. *O*-diphenylbenzene also has an absorption spectrum similar to that of *p*-diphenylbenzene (terphenyl) and, therefore, cannot absorb the emission of most of the substances used in these experiments.

Either of these substances added to the solvents under investigation were found to emit only a very small amount of light. For example, naphthalene in xylene has a maximum intensity of 1/15 of a corresponding terphenyl solution; *o*-diphenylbenzene perhaps emits no light at all; it even weakens the small light intensity emitted by the pure solvent. The light emission curves of naphthalene and of *o*-diphenylbenzene in xylene are given respectively by curves *A* and *B* of Fig. 4. The light curve of naphthalene gives the intensity of a solution for the same amount of xylene.† There is a sharp increaseat small concentrations and a leveling off at about a concentration of 5 g/l. Since the density of the solution is practically unchanged by the addition of naphthalene, and since the parts of the solution remote from the source in this case contribute but little to the total intensity, this increase in emitted radiation is only very slightly due to the larger amount of substance used in the naphthalene experiments. This curve coincides in its general shape with the curves published by Ageno, Chiozzotto, and Querzoli.[6] It may be noted that the values near the leveling-off concentration show a noticeable fluctuation. The *o*-diphenylbenzene curve shows a decrease in intensity with concentration. Measurements taken with a previous sample of *o*-diphenylbenzene obtained from the same company showed, however, another type of variation. There was a small gradual increase in intensity over a large range of concentration but no sharp rise at small concentration

† *Note added in proof.*—It may be that the small light output of the naphthalene solution is due to oxygen in the solution, since a characteristic quenching by oxygen of naphthalene *radiation* is reported in the literature. However, the measurements below indicate that the *energy* is not quenched.

[6] Ageno, Chiozzotto, and Querzoli, Phys. Rev. 79, 720 (1950).

TABLE IV. Effects of naphthalene and o-diphenylbenzene.

Solution	Relative intensity
Xylene+alpha-naphthylamine (1 g/l)	0.18
Xylene+alpha-naphthylamine (1 g/l)+naphthalene (10 g/l)	0.075
Xylene+alpha-naphthylamine (1 g/l)+naphthalene (100 g/l)	0.019
p-dioxane+alpha-naphthylamine (2 g/l)	0.11
p-dioxane+alpha-naphthylamine (2 g/l)+naphthalene (100 g/l)	0.08
Toluene+alpha-naphthylamine (1 g/l)	0.18
Toluene+alpha-naphthylamine (1 g/l)+naphthalene (100 g/l)	0.04
Xylene+anthracene (1.5 g/l)[a]	0.07
Xylene+anthracene (1.5 g/l)[a]	0.07
Xylene+anthracene (4 g/l)+o-diphenylbenzene (50 g/l)[a]	0.023
Xylene+anthracene (1.5 g/l)+naphthalene (230 g/l)[a]	0.07
Xylene+phenyl alpha-naphthylamine (2 g/l)[a]	0.31
Xylene+phenyl alpha-naphthylamine (9 g/l) +o-diphenylbenzene (50 g/l)[a]	0.11
Xylene+anthranilic acid (2 g/l)[a]	0.24
Xylene+anthranilic acid (2 g/l)+naphthalene (20 g/l)[a]	0.24
Xylene+anthranilic acid (4 g/l)+o-diphenylbenzene	0.075
p-cymene+anthranilic acid (4 g/l)[a]	0.17
p-cymene+anthranilic acid (3 g/l)+naphthalene (20 g/l)[a]	0.20
Xylene+fluoranthene (3–8 g/l)[a]	0.13
Xylene+fluoranthene (3–8 g/l)+naphthalene (20 g/l)[a]	0.13
Xylene+fluoranthene (18–35 g/l)+o-diphenylbenzene (20 g/l)[a]	0.09
p-cymene+fluoranthene (7 g/l)[a]	0.11
p-cymene+fluoranthene (20 g/l)+o-diphenylbenzene (20 g/l)[a]	0.082
Phenylcyclohexane+terphenyl (2.5 g/l)	0.38
Phenylcyclohexane+terphenyl (2.5 g/l)+o-diphenyl-benzene (0.5 g/l)	0.29
Phenylcyclohexane+terphenyl (2.5 g/l)+o-diphenyl-benzene (5 g/l)	0.095
Xylene+m-diphenylbenzene (0.5 g/l)	0.056
Xylene+m-diphenylbenzene (0.5 g/l)+o-diphenyl-benzene (1 g/l)	0.044
Xylene+m-diphenylbenzene (0.5 g/l)+o-diphenyl-benzene (10 g/l)	0.014
Phenylcyclohexane+durene (5 g/l)	0.057
Phenylcyclohexane+durene (5 g/l)+o-diphenylbenzene (0.5 g/l)	0.015
Xylene+diphenylhexatriene (1.5 g/l)[a]	0.235
Xylene+diphenylhexatriene (1 g/l)+naphthalene (20 g/l)[a]	0.24
Xylene+diphenylhexatriene (2.5 g/l)+o-diphenyl-benzene (20 g/l)[a]	0.069
Xylene+diphenylhexatriene (1 g/l)+naphthalene (100 g/l)	0.28
Xylene+terphenyl (2 g/l)	0.39
Xylene+terphenyl (2 g/l)+naphthalene (0.3 g/l)	0.37
Xylene+terphenyl (2 g/l)+naphthalene (100 g/l)	0.08
Xylene+terphenyl (7 g/l[b])+naphthalene (20 g/l)[a]	0.24
Xylene+terphenyl (2 g/l)+o-diphenylbenzene (0.1 g/l)	0.37
Xylene+terphenyl (2 g/l)+o-diphenylbenzene (20 g/l)	0.24
Xylene+terphenyl (7 g/l[b])+o-diphenylbenzene (20 g/l)[a]	0.17

[a] Approximate maximum intensity. [b] Saturated.

as with the naphthalene curve. The difference between the two samples was due most likely to a small amount

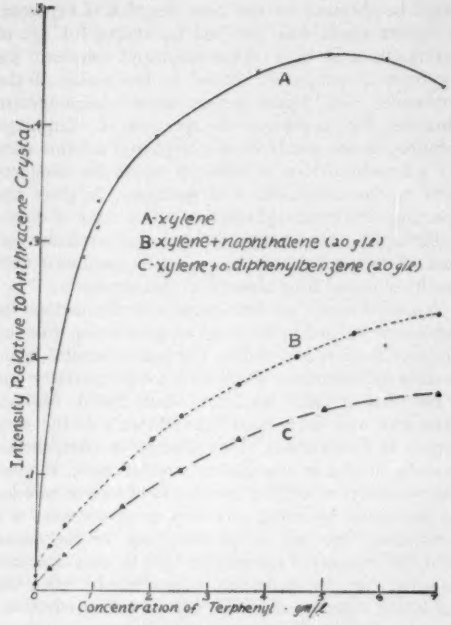

FIG. 5. Terphenyl solutions.

of a fluorescent contamination in the more fluorescent sample of *o*-diphenylbenzene. This assumption was borne out by obtaining a spectrum of the more fluorescent solution with the aid of α-particles. It was found to extend to 4500A. It may be mentioned that both types of *o*-diphenylbenzene solutions showed no difference of behavior with respect to the addition of different fluorescent material.

Similar curves are found when these substances are dissolved in other solvents. Since the emission spectra of these substances are close to that of terphenyl [for naphthalene this is proved by our experiments of Sec. C and for *o*-diphenylbenzene it can be derived from the experimental fact that the absorption spectra of o-diphenylbenzene and *p*-diphenylbenzene (terphenyl) nearly coincide], the possibility of energy transfer to these substances should be as good as for terphenyl itself. Since, however, the intensities are much lower, the idea presents itself that the energy still goes over to these molecules but is quenched before the light is emitted. According to Eq. (2) this would mean a very small value τ_i for these substances.

To test this idea and to find out what happens to the excitation energy in these solutions with naphthalene and *o*-diphenylbenzene, we have introduced into them molecules of other solutes normally highly fluorescent in pure solvents. The results are collected in Table IV and Figs. 5, 6, 7, and 8. These experiments show that for the fluorescent substances with emission spectra

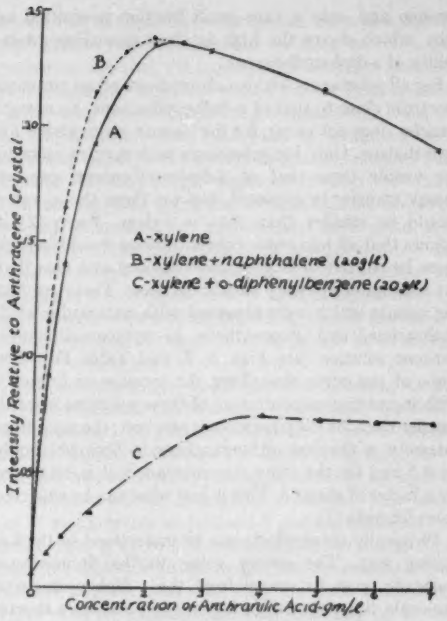

FIG. 6. Anthranilic acid solutions.

close to those of naphthalene or *o*-diphenylbenzene, the light intensity is much smaller in these solutions than in the pure solvent. With large naphthalene or *o*-diphenylbenzene concentrations the light emission, for example, of a terphenyl solution, is strongly suppressed for a given concentration of terphenyl. The intensity continues to go down with increasing naphthalene or *o*-diphenylbenzene concentration and approaches the light emission of these substances without terphenyl (see Table IV and Fig. 5). Phenyl alpha-naphthylamine is not as strongly attenuated as terphenyl. It must be emphasized that strong changes are already achieved with the relatively small concentration of one percent of these solutes. These effects are not caused by absorption as can be seen from absorption curves taken with these solutions. With substances such as fluoranthene, anthracene, anthranilic acid, and diphenyl hexatriene, having emission spectra more toward the visible than terphenyl, the results are completely different. In naphthalene solutions the light emission is only slightly affected; practically the same light emission curves as functions of the concentration are obtained if these substances are dissolved in xylene-naphthalene solutions instead of pure xylene. In some cases even a slight increase in light emission is observed (see Fig. 8 and Table IV).

With *o*-diphenylbenzene-xylene solutions, however, the light emission curves of these substances are greatly changed; all their maximum concentrations are shifted to higher concentrations even by small amounts of *o*-diphenylbenzene. The maximum light intensities of anthranilic acid and of anthracene are more strongly reduced than that of fluoranthene (see Figs. 6 and 7 and Table IV). Similar results are obtained with different solvents such as cymene and dioxane; only the quantitative behavior is different. For dioxane with *o*-diphenylbenzene, for instance, phenyl alpha-naphthylamine gives a relatively higher light emission than in a xylene-*o*-diphenylbenzene solution as compared to the reading in the pure solvent; but again the maximum concentration is shifted to larger concentrations (see Table IV).

There are two possible explanations for these effects based on Eq. (2). The first assumes that the internal quenching constants τ_i of naphthalene and of *o*-diphenylbenzene are much smaller than those of terphenyl, anthranilic acid, and other fluorescent substances. This means that the excitation energy is mostly internally quenched before it can be emitted as light. The transfer of excitation energy from the solvent to these molecules may be of the same order of magnitude as for terphenyl or for other substances. With 20 grams or more per liter of naphthalene or *o*-diphenylbenzene a considerable amount of excitation energy is transferred from the solvent to these molecules. If now other molecules which are highly fluorescent are introduced in small concentrations, the energy passes first to the naphthalene or the *o*-diphenylbenzene molecules and then from these molecules to the fluorescent molecules. For this latter

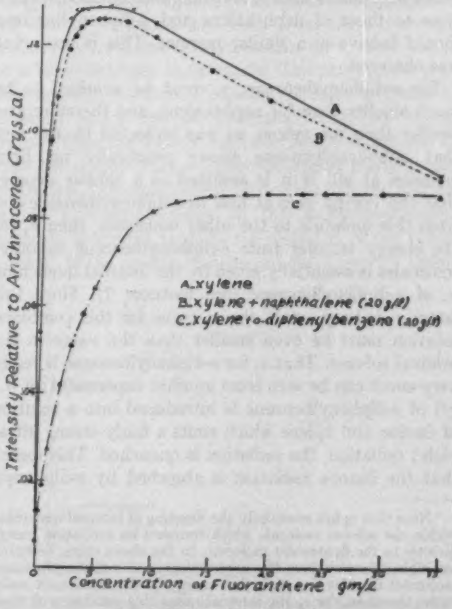

FIG. 7. Fluoranthene solutions.

energy transfer the coefficient α and the constant τ_q in Eq. (1) are those belonging to naphthalene or *o*-diphenylbenzene and not to xylene.[7] If we now assume that $\alpha\tau_q$ is practically the same for naphthalene as for xylene, the behavior of anthranilic acid, anthracene, and fluoranthene in naphthalene solutions can be understood. For terphenyl, however, it cannot be assumed that α is still the same for the energy transfer from naphthalene to terphenyl as from xylene to terphenyl, since the emission spectra of terphenyl and naphthalene are too close to each other. There is then little trapping of the excitation energy by the terphenyl molecule, since the energy can also go back from the terphenyl to the naphthalene. Thus terphenyl can draw most of its energy only from the xylene. If the terphenyl concentration is high enough, the energy transfer from the xylene will be divided between naphthalene and terphenyl, and a certain amount of energy will still go directly to the terphenyl molecule and be emitted as light by this molecule. Therefore, the light emitted by such a solution should depend strongly on the concentration ratio of terphenyl and naphthalene or terphenyl and *o*-diphenylbenzene and should increase with an increase of this ratio until self-quenching becomes considerable. As a consequence, the maximum in such solutions is shifted toward higher concentrations of the fluorescent molecules. This occurs also with naphthalene, where other substances such as diphenyl hexatriene exhibit a shift to smaller concentration, since in this case $\alpha\tau_q$ is larger than for the original solvent. Other substances with absorption and emission spectra close to those of naphthalene and *o*-diphenylbenzene should behave in a similar manner. This is just what was observed.

For *o*-diphenylbenzene, τ_i must be assumed to be much smaller than for naphthalene, and therefore also smaller than for xylene, as was indicated by the fact that *o*-diphenylbenzene shows practically no light emission at all. If it is assumed in a similar manner that the energy goes at first to *o*-diphenylbenzene and from this molecule to the other molecules, then τ_q for the energy transfer from *o*-diphenylbenzene to other molecules is essentially given by the internal quenching τ_i of *o*-diphenylbenzene (see footnote 7). Since this latter τ_i is very small, the τ_q value for this combined solution must be even smaller than the value in the original solvent. That τ_i for *o*-diphenylbenzene is really very small can be seen from another experiment: if 0.1 g/l of *o*-diphenylbenzene is introduced into a solution of durene and xylene which emits a fairly strong ultraviolet radiation, the radiation is quenched. This means that the durene radiation is absorbed by *o*-diphenylbenzene and only a very small fraction re-emitted as light, which shows the high internal quenching probability of *o*-diphenylbenzene.

For all substances with an absorption and an emission spectrum close to that of *o*-diphenylbenzene, an energy transfer does not occur, for the reasons given above for naphthalene. Only for substances with spectra more to the visible than that of *o*-diphenylbenzene can an energy transfer be expected, but for these the τ_q value should be smaller than that in xylene. From (2) it follows that all maximum concentrations should in such cases be shifted to larger concentrations and also that the maximum intensity should decrease. These are just the results which were observed with anthranilic acid, anthracene, and fluoranthene in xylene-*o*-diphenylbenzene solution (see Figs. 6, 7, and Table IV). The slope of the curve describing the increase of intensity with increasing concentration of these solutions is much smaller than for the pure solvent solution; the maximum intensity in the case of fluoranthene is diminished only by 1.5 and for the other two substances it is decreased by a factor of about 3. This is just what can be expected from formula (2).

Physically these effects can be understood in the following way. The energy going to the fluoranthene molecule must be drawn from the *o*-diphenylbenzene molecule. Since the excitation energy possesses a shorter lifetime in this molecule (because of the large internal quenching) than in the xylene molecule, a higher concentration of fluoranthene is needed to draw the same amount of energy from *o*-diphenylbenzene than from xylene. With higher concentration of fluoranthene self-quenching is increased; but if the self-quenching effect is not too large, the maximum intensity will not be diminished too strongly. In anthranilic acid and also in anthracene the same effect occurs; but since the self-quenching of these substances is comparatively high, the maximum value of the light emission is smaller in *o*-diphenylbenzene than in xylene. The smaller self-quenching of fluoranthene can be deduced from the flatness of its light curve after the maximum concentration in xylene solutions is reached.

The other possibility of explaining the behavior of these mixed solutions would be to assume, in order to account for the small light emission of the solutions of naphthalene and *o*-diphenylbenzene in xylene and other solvents, that practically no energy transfer to the naphthalene molecule or the *o*-diphenylbenzene molecule occurs. However, we can find no good theoretical reason for such an abnormal behavior of these substances. Nevertheless, on this assumption one could perhaps partly account for the behavior of the mixed solutions with naphthalene. According to this idea, the additional fluorescent molecules in these solutions draw their energy entirely from the xylene. The fact that those molecules, having emission spectra near that of naphthalene, show a strong decrease in intensity could be explained by the further assumption that there is an

[7] Note that τ_q has essentially the meaning of internal quenching within the solvent molecule which transfers its excitation energy directly to the fluorescent molecule. In the above cases, however, for high concentrations the naphthalene and *o*-diphenylbenzene molecules transfer the excitation energy to the fluorescent molecules; therefore, for τ_q the internal quenching constants of these molecules must be used.

interaction between these fluorescent molecules and the naphthalene molecules similar to that between like molecules, and that the naphthalene molecule quenches the radiation of molecules with a similar light emission spectrum by the mechanism of self-quenching. Thus, the light emission of such molecules is weakened with increasing naphthalene concentration. Substances with emission spectra strongly displaced towards the visible from the emission spectrum of naphthalene, however, are not influenced by naphthalene and some self-quenching mechanism, since their spectra are too different from each other. Therefore, these substances are only slightly influenced in their light emission even by large concentrations of naphthalene, since it is assumed in this explanation that they draw all their energy directly from xylene.

Such an assumption would not hold, however, for the *o*-diphenylbenzene solution since here already relatively small amounts of *o*-diphenylbenzene (1 mole percent solution) strongly influence the shape of the light curve in such a way as to reduce the light intensity for a given concentration of the fluorescent molecule. This effect can be much better understood if one assumes that the energy first goes to the *o*-diphenylbenzene and then from this molecule to the respective fluorescent molecule. We suppose, however, that the same mechanism is also valid for naphthalene. That this may be so can be seen from experiments with *p*-cymene as the initial solvent, and additional amounts of naphthalene. In such a solution the fluorescence of anthranilic acid is already increased by small amounts of naphthalene, and the light concentration curve is shifted to the left. This means that in this case the internal quenching probability of naphthalene $1/\tau_i$ is smaller than for the cymene molecule. Therefore, the energy transfer via the naphthalene molecule is more effective than the direct energy transfer from cymene to the anthranilic acid molecule. Another hint in this direction may be seen in the fact that diphenylhexatriene in xylene also shows the effect of increasing intensity with larger amounts of naphthalene (Fig. 8). The addition of m-diphenylbenzene has also been found to produce an even slightly greater increase in the intensity of diphenylhexatriene. Thus, the first mechanism of the energy transfer taking place via the additional solute molecule seems to provide the more adequate explanation.

The advantage of using just these mixed solutions for exploring the mechanism of energy transfer lies in the fact that small amounts of additional substances already strongly influence the shape of the light curve (see Figs. 5 to 8, and Table IV), and give comparatively no light emission of their own, so that they do not mask the main fluorescence. There are several parameters describing the light emission from the fluorescent molecule in solution (Sec. A); most of them depend on the properties of the solvent, but they should change only slightly if the solvent is also changed only slightly by a relatively small percentage of added naphthalene or *o*-diphenylbenzene. If the idea of energy transfer to these substances from the initial solvent and its further transfer from these molecules to the fluorescent solutes is correct, then $\alpha\tau_0$ in (2) has to be chosen for the transfer from naphthalene or *o*-diphenylbenzene and not from the original solvent. Since the energy transfer to naphthalene and *o*-diphenylbenzene already occurs at small concentration, this factor $\alpha\tau_0$ goes over from the original value to the values inherent in these molecules even when only small amounts of such molecules are added. The other constants indicated are not changed by small amounts of additional substances and especially the self-quenching coefficient β may be influenced only very slightly as long as the emission spectra of the different molecules are not close to each other.

There is another point which is explained by these experiments, namely, that the possibility of energy transfer from the solvent to the molecule by radiation is ruled out. If there should be some hidden radiation which is already strongly absorbed within small thicknesses of solution, then this radiation would go over to the naphthalene or *o*-diphenylbenzene molecule by absorption since radiation strongly absorbed in xylene is still more strongly absorbed by *o*-diphenylbenzene. *O*-diphenylbenzene, however, quenches any absorbed radiation, as is proved by the experiments of adding *o*-diphenylbenzene to phenylcyclohexane solutions of durene. The durene radiation is already completely quenched by small amounts of *o*-diphenylbenzene. If the energy in the pure solvent could go to the *o*-diphenylbenzene by radiation and then from the *o*-diphenylbenzene by radiation to another substance, there should be a large decrease in intensity. The experiment with fluoranthene, however, shows only a slight decrease in intensity which can be understood only by energy transfer from the solvent itself and not by radiation. To draw the energy from *o*-diphenylbenzene, a larger concentration of fluoranthene is needed because the lifetime of the excitation energy in the *o*-diphenylbenzene molecule is shorter than in the molecule of the initial solvent. If the energy transfer should occur via radia-

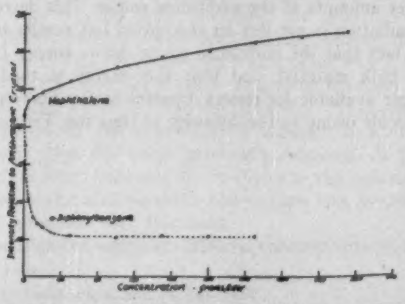

FIG. 8. Effect of naphthalene and *o*-diphenylbenzene on xylene +diphenylhexatriene (1 g/l).

tion, the increased concentration of fluoranthene would not accelerate the transfer from *o*-diphenylbenzene to fluoranthene.

E. SUMMARY

The experiments with naphthalene and *o*-diphenylbenzene solutions seem to us to provide proof for our ideas on energy transfer, and the method of adding fluorescent molecules to such solutions appears to make it possible to localize the excitation energy. The fact that these solutions have practically no radiation of their own, but can, nevertheless, still produce considerable light emission with some other fluorescent molecules can be looked upon as a support for our ideas in connection with the mechanism of energy transfer in fluorescent solutions. In particular, they demonstrate that only those fluorescent molecules with an emission spectrum of larger λ than that of the transferring molecule show the phenomenon of increased light emission when the solvent is irradiated by γ-radiation. They further indicate the importance of the quenching factor τ_q for the maximum intensity and the maximum concentration, and show that τ_q for the solvent, and τ_i for the solute have the same physical significance of internal quenching. Finally, they also demonstrate the importance of the self-quenching mechanism on the emitted light intensity.

It was found that three types of fluorescent materials can be distinguished in mixed solutions containing an "additional solute," such as naphthalene or *o*-diphenylbenzene, producing only a small light emission of their own. The *first* type has emission and absorption spectra of shorter wavelengths than most of the absorption spectrum of the additional solutes. The fluorescence of these materials is strongly decreased by very small amounts of the additional solute as a consequence of the absorption of the fluorescent light by these molecules and its internal quenching. Durene is an example of this type of fluorescent molecule if naphthalene or *o*-diphenylbenzene is added. The *second* type of fluorescent material has absorption and emission spectra close to those of the additional solute. The light emission of these fluorescent molecules is strongly decreased by larger amounts of the additional solute. This decrease in radiation is not due to absorption but results from the fact that the additional solute draws energy from the bulk material, and that this energy is then no longer available for energy transfer to the fluorescent molecule owing to the difficulty of trapping. Terphenyl and *m*-diphenylbenzene are molecules of this type. The *third* type of fluorescent molecule has an emission spectrum consisting of considerably longer wavelengths than those of the additional solutes. As a consequence they can also draw excitation energy from the additional solutes and then trap this energy if the concentration of the additional solute is comparable or higher than that of the fluorescent molecule. In this case the energy transfer occurs in two steps. First, an energy transfer occurs from the original solvent to the additional solute molecules and then from these molecules to the fluorescent molecules. In this sense the additional solute acts in some way as a second solvent. The intensity of the fluorescent light depends strongly on the internal quenching of the additional solute. Anthranilic acid and diphenylhexatriene belong to this group of substances when naphthalene or *o*-diphenylbenzene is added.

Similar effects may also occur in all mixed solutions if the additional solutes emit considerable light by themselves. In these cases, however, the special effects mentioned above are masked by the comparatively strong light emission of the additional solutes.

This article deals with the mechanism of energy transfer in fluorescent materials. In this connection, however, some other concepts are disclosed by these measurements which may be of some interest. One in particular is that these measurements show that the differences in light emission from various fluorescent molecules is not so much due to a change in the probability of light emission, $1/\tau_e$, but is mostly affected by a change in the internal quenching $1/\tau_i$. This internal quenching probability is very sensitive to structural changes in the molecules as can be seen from the comparative measurements with *p*-, *m*-, and *o*-diphenylbenzene, all of which have approximately the same absorption and emission spectra (the *o*-diphenylbenzene emission was not obtained). In these cases the change in the configuration of the three benzene rings produces changes in the quenching probability by an order of magnitude. The measurements also show that this probability is dependent on the solvent.[8] Some of the variations in different solvents stem from this influence on the internal quenching probability. The measurements with naphthalene and *o*-diphenylbenzene indicate that the internal energy transfer is by no means limited to fluorescent molecules but generally also with nonfluorescent molecules.

[8] E. J. Bowen and A. Norton, Trans. Faraday Soc. 35, 44 (1939).

Polarizabilities of Ions in Perovskite-Type Crystals

SHEPARD ROBERTS
General Electric Research Laboratory, Schenectady, New York
(Received August 24, 1950)*

Each type of ion is shown to have very nearly the same polarizability in different crystals of the perovskite type as well as in the diagonal cubic types reported previously. This conclusion is based on dielectric constant data for several titanates and zirconates and $KMgF_3$. The values of ionic polarizability are roughly proportional to the cube of the radius for ions in the same valence series.

I. INTRODUCTION

IN recent papers[1,2] the author proposed a theory of dielectric constants of simple crystals essentially based on the following familiar postulates:

(1) The electric field tending to polarize a given ion is that at its center produced by conditions external to the given ion.

(2) The induced electric moment of a given ion acts on other ions in the crystal like a central point dipole.

At frequencies low enough to avoid inertia effects, and at low field strengths, the ratio of the effective dipole moment to the polarizing field is constant for a given ion in a given crystal. This constant ratio is called the dielectric polarizability. In order to clarify the distinction between the polarizability as here defined and the very different but more usual concept of electronic or optical polarizability, a further discussion is given in Appendix I.

On the basis of dielectric constant data of a large number of compounds, it was shown[1] that the polarizability of each type of ion is very nearly the same in different crystals—subject to certain symmetry requirements. The criterion for testing this condition was the additivity relation:

$$\alpha=\sum \alpha_i, \tag{1}$$

where $\sum \alpha_i$ is the sum of the polarizabilities of all ions in the molecule or chemical formula, and α is calculated as follows:

$$\alpha=3V(K-1)/(K+2), \tag{2}$$

where V is the volume per molecule or chemical formula, and K is the dielectric constant. Equation (1) is rigorous only when applied to crystals of "diagonal cubic" symmetry, such as NaCl, CsCl, CaF_2, and cubic ZnS, but not to perovskite-type crystals. Nevertheless, it does appear to "work" deceptively well when applied to certain titanates of the perovskite-type. The value of K employed in Eq. (2) should be determined under symmetry conditions such that the static local field tending to polarize each ion is zero and its electric moment vanishes.

A detailed analysis of perovskite-type crystals and barium titanate in particular was given by Slater,[3] making implicit use of the postulates mentioned above. Slater apparently did not accept the conclusion that the polarizability of a given ion is very nearly the same in different crystals. He allowed only that the polarizability of the titanium ion is "not larger in order of magnitude than that usually found." His treatment actually implied that the looseness of the titanium ion should have a dominant effect on its polarizability in barium titanate. This looseness arises because the space available for titanium in the middle of an oxygen octahedron is slightly too large. Titanium was then treated as though it had special properties not shared by other ions.

In the following discussion it will be shown that Eq. (1) is valid to a rough approximation even in barium titanate in which the detailed picture is much different than that used in deriving (1). It will also be shown that the polarizability of titanium is substantially the same in strontium titanate, in which no excess space is available. It will likewise be shown that the ferroelectric nature of lead zirconate can be satisfactorily explained by reasonable values of the polarizability of zirconium and lead which agree with other data. In addition, the newly reported dielectric constants of $KMgF_3$ and $BaZrO_3$ will be shown to be consistent with the present theory.

II. EXPERIMENTAL EVALUATION OF POLARIZABILITIES

Dielectric constants and unit cell volumes of the perovskite crystals being considered are shown along with similar data for a number of diagonal cubic crystals in Table I. This table indicates a new value, 34 ± 3, for the dielectric constant of BaO, which was obtained by Sproull and Bever of Cornell University.[4] This result appears to be well substantiated although it is very different from the value previously supposed. It has therefore been necessary to re-evaluate the polarizabilities of the alkaline-earth and oxygen ions in order to be consistent with this result.

The negative values of dielectric constant quoted for

* Revised manuscript received November 27, 1950.
[1] S. Roberts, Phys. Rev. **76**, 1215 (1949).
[2] S. Roberts, Phys. Rev. **77**, 258 (1950).
[3] J. C. Slater, Phys. Rev. **78**, 748 (1950).
[4] Private communication; also mentioned in oral presentation by R. L. Sproull, Phys. Rev. **75**, 1282 (1949).

TABLE I. Experimental data and polarizabilities.

	(1) K	(2) V (A^3)	(3) α (A^3)	(4) $\Sigma\alpha_i$ (A^3)
MgO	9.8	18.52	41.4	43.0
CaO	11.8	27.65	64.9	66.9
SrO	13.3	33.16	79.9	81.1
BaO	34	41.59	114.4	108.8
CaF_2	8.43	40.47	86.5	84.5
SrF_2	7.69	48.27	99.9	98.7
BaF_2	7.33	59.29	120.8	126.4
$SrTiO_3$	295	59.54	176.8	160.1
$BaTiO_3$	−1860	64.36	193.3	187.8
$BaZrO_3$	43	73.51	205.7	191.8
$PbZrO_3$	−950	71.00	213.6	206.5
$KMgF_3$	8.5	63.04	135.1	127.8

$BaTiO_3$ and $PbZrO_3$ correspond to the unstable cubic form and are obtained from published data[5] by extrapolating the Curie-Weiss law, valid in the cubic region, down to 25°C. The values of dielectric constant of $SrTiO_3$ and $BaZrO_3$ were determined on ceramic specimens and include a correction for porosity. The dielectric constant of $KMgF_3$ was estimated (8.5±0.5) by S. I. Reynolds of this laboratory by examining the motion of small crystal grains in carefully dried dielectric liquids of various dielectric constants, while applying a non-uniform electric field.

The calculation of the cell volume of the titanates and zirconates is based on the measurements of Megaw,[6] while that of $KMgF_3$ is determined from the value $a_0=(3.980\pm0.002)$A measured by B. F. Decker of this laboratory.

The third column in Table I shows the polarizability in cubic angstroms, calculated from the dielectric constant and unit cell volume by means of Eq. (2).

A revised list of the dielectric polarizabilities of ions is shown in Table II. The values for halide ions are taken directly from reference 1, and those for the alkali ions are modified only slightly so as to be in better agreement with reference 2. The polarizabilities of the alkaline earth ions and oxygen are adjusted to a somewhat greater extent in order to comply with the new result for barium oxide. Values for titanium and zirconium are averages of the results calculated in this paper. The polarizability of lead is uncertain, since it was determined from dielectric constants of crystals (PbO, $PbCl_2$, and PbI_2) which lack diagonal cubic symmetry.

TABLE II. Dielectric polarizabilities of ions in cubic angstroms.

Li^+	11.7	Mg^{++}	9.0
Na^+	19.7	Ca^{++}	32.9
K^+	41.4	Sr^{++}	47.1
Rb^+	57.3	Ba^{++}	74.8
Cs^+	71.5	Ti^{++}	11.0
F^-	25.8	Zr^{++}	15.0
Cl^-	62.8	$O^=$	34.0
Br^-	81.0		
I^-	109.4	Pb^{++}	(89.5)

The sums of the appropriate ionic polarizabilities shown in Table II are calculated for each of the various compounds of Table I and are shown in the fourth column of that table. These values are in satisfactory agreement (five percent tolerance) with the results shown in column three for the diagonal-cubic crystals. The use of Eq. (1) evidently introduces a somewhat larger error in estimation of the values of α in perovskite-type crystals, although the difference could be much greater in more extreme cases.

III. CALCULATED RESULTS FOR PEROVSKITE CRYSTALS

A more accurate and more detailed treatment of perovskite crystals is that considered by Van Santen and Opechowski,[7] and more recently by Slater.[3] The mathematical details of this treatment are summarized in Appendix II.

By this method a different field constant, β_i, is calculated for each ion signifying the ratio of the actual field acting on the given ion to the Lorentz internal field, $F=E+P/3\epsilon_0$. The polarizabilities of the various ions are likewise designated by numerical subscripts, α_2 being the polarizability of titanium or zirconium. The values of α_2 are calculated by making use of the given values of α and the polarizabilities of the other ions as listed in Table II. The resulting values of α_2 and the internal field constants β_i are shown in Table III.

Table III indicates a slightly smaller polarizability for Ti in $SrTiO_3$ than in $BaTiO_3$. Such a difference is not inconsistent with the approximate nature of the theory; however, it may also be attributed to considerations such as those outlined by Slater. In any event, the small difference indicates that looseness of the titanium ion is not the dominant factor controlling its polarizability in barium titanate. It may also be noticed that a similar difference is observed in the polarizability of zirconium in $BaZrO_3$ and $PbZrO_3$, although there is no question of "looseness" in either.

The values of the field constants in each of the compounds of Table III show that there is a strong interaction between the ions in the sites corresponding to titanium and its oxygen neighbor in the field direction. Lead zirconate is strikingly different from the others in that the corresponding ions are polarized in reverse to the normal internal field direction. This fact may attempt to explain some of the differences in structure and properties of lead zirconate as compared with barium titanate. For example, the observation that the tetragonal unit cell, or pseudo-cell as the case may be, of lead zirconate has an axial length shorter than its lateral

[5] S. Roberts, J. Am. Ceram. Soc. **33**, 63 (1950).
[6] H. D. Megaw, Proc. Phys. Soc. (London) **58**, 133 (1946).
[7] J. H. Van Santen and W. Opechowski, Physica **14**, 545 (1948).

dimensions, or $c_0/a_0<1$, while barium titanate, to the contrary,[6] has $c_0/a_0>1$, may be related to this internal field reversal and to the relatively greater total polarization of the remaining ions.

The values calculated for α_2 in the above manner do not depend too critically on the choice of the polarizabilities of the other ions. For example, Slater[3] in calculating the polarizability of titanium in barium titanate used the author's[1] former published value 30.0 for the polarizability of oxygen and a surprisingly low value, 24.42, for the polarizability of barium. Even so, his result for titanium was only 14.26 as compared with our value of 12.1. On the other hand, the internal field constants β_i are very sensitive to small changes in the values of α_i. For this reason, not too much reliance should be placed on the specific values of β_i shown in Table III.

It is instructive to compare the polarizabilities of ions *versus* their radii. Figure 1 shows such a comparison for the ions listed in Table II. Two values of radius are indicated in this figure, namely, those due to Pauling, by crosses, and those due to Goldschmidt, by circles. The values are taken from a table on p. 268 of the book by Mott and Gurney.[6] For ions of equal valence the polarizability is roughly proportional to the cube of the radius, or to the volume. There are definite exceptions to this rule of the same order of magnitude as the differences between the two values of the radii.

IV. CONCLUSIONS

Dielectric constants of all ionic crystals having diagonal cubic or perovskite symmetry appear to be consistent with an interpretation based on the following considerations.

(1) The electric field tending to polarize a given ion is that at its center produced by conditions external to the given ion.

(2) The electric moment of a given ion acts on other ions in the crystal like a central point dipole.

(3) The dielectric constant is determined under symmetry conditions such that the local field tending to polarize each ion is zero and its electric moment vanishes.

(4) The ratio of the electric moment to the polarizing field is a nearly invariant property of an ion, called its "dielectric polarizability." This value of polarizability is defined under conditions of constraint only by the neighboring ions. It is appreciably different from the "electronic polarizability," which involves restraint of the nucleus by its own inertia.

Several of the substances considered, namely, LiBr, LiI, and $BaTiO_3$, are thought to contain cations which are smaller than the available space. Nevertheless, the results indicate that this fact, if true, has no more than a minor effect on the polarizability of these ions.

[6] N. F. Mott and R. W. Gurney, *Electronic Processes in Ionic Crystals* (Oxford University Press, London, 1940).

TABLE III. Calculated polarizabilities and field constants.

	α_2 (Ti, Zr)	β_1 (Sr, Ba)	β_2 (Ti, Zr)	β_4 (O_x, O_y)	β_5 (O_z)
$SrTiO_3$	9.9	0.17	3.9	0.57	2.69
$BaTiO_3$	12.1	−2.14	11.9	−0.83	7.79
$BaZrO_3$	15.9	0.095	4.14	0.36	3.19
$PbZrO_3$	14.2	2.26	−3.33	1.84	−1.94
$KMgF_3$	11.0	0.76	1.82	0.80	1.64

APPENDIX I

In order to study the effect of an electric field on a single isolated ion, it is necessary to support the ion mechanically, since it has a net charge and experiences an electrostatic force. The electric moment is produced by the displacement of the charged particles constituting the ion relative to their zero-field positions. In a recent paper,[2] the author showed that the magnitude of the induced electric moment depends critically on how the ion is held. If it is held by restraining the motion of its external boundary, then the electric moment will generally be much greater than that produced if the nucleus instead is held fixed.

The restraint on the boundary corresponds to that imposed by adjacent ions on each other in a crystal. Evidence for such restraint can be found in the constancy of ionic radii in crystals. The restraint of the nucleus occurs when a free ion is placed in a field which oscillates so rapidly that the inertia of the nucleus effectively prevents it from moving. In this way it can be seen that the dielectric polarizability defined under the conditions of restraint of the boundary is appropriate for interpreting the dielectric constants of crystals and is, or may be, radically different

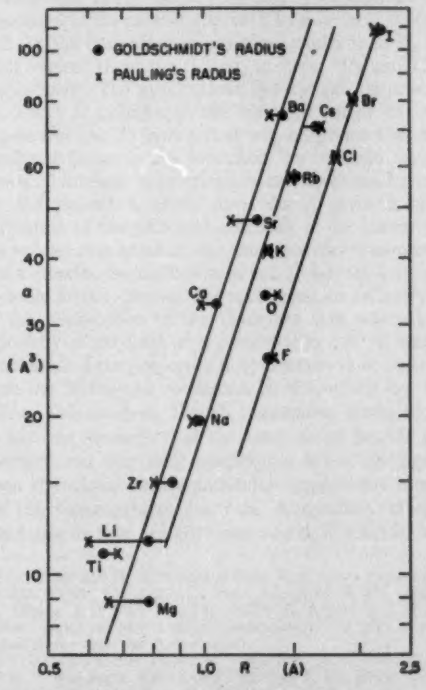

FIG. 1. Dielectric polarizabilities *versus* ionic radii.

from the electronic or optical polarizability defined under the conditions of nuclear restraint. The latter is valid for isolated ions measured at optical frequencies. The polarizabilities of ions in crystals at optical frequencies were shown to be even somewhat smaller than the electronic polarizabilities defined above, owing to the additional mutual restraint of their boundaries.

APPENDIX II

In diagonal cubic crystals, that is, in cubic crystals in which a rhombohedral unit cell can be constructed having all the ions on its diagonal, the local field acting on each ion is the same. It is

$$F_i = E + \Sigma P_j/3\epsilon_0 = (K+2)E/3, \tag{3}$$

where E is the external electric field, P_j is the dipole moment per unit volume of the jth ion, and ϵ_0 is the permittivity of space.

In perovskite-type crystals, a different field is effective for each ion, as distinguished by different values of β_i.

$$F_i = \beta_i(K+2)E/3. \tag{4}$$

In terms of the various components of polarization the local field at the ith ion is alternatively

$$F_i = E + (1/3\epsilon_0)\,\Sigma_j(f_{ij}+1)P_j, \tag{5}$$

where each f_{ij} is a matrix element calculated from the geometrical arrangement of the ions.

The numerical subscripts, 1 to 5, are assigned in the following order: Ba, Ti, O_x, O_y, and O_z, in which O_z is the oxygen ion having its nearest Ti neighbor in the z-direction, etc. If the electric field is applied in the z-direction, then the resulting matrix for f_{ij} is

$$(f_{ij}) = \begin{bmatrix} 0 & 0 & +1.0346 & +1.0346 & -2.0692 \\ 0 & 0 & -3.5908 & -3.5908 & +7.1816 \\ +1.0346 & -3.5908 & 0 & -2.0692 & +1.0346 \\ +1.0346 & -3.5908 & -2.0692 & 0 & +1.0346 \\ -2.0692 & +7.1816 & +1.0346 & +1.0346 & 0 \end{bmatrix}.$$

In calculation of the above matrix, values of $4\pi(f_{ij}+1)/3$ were taken from a paper by McKeehan[9] as determined by the method of Ewald.

Instead of Eq. (1), a different relation is valid between the macroscopic polarizability α and the ionic polarizabilities α_i:

$$\alpha = 3V(K-1)/(K+2) = \Sigma\,\alpha_i\beta_i = \Sigma\,\gamma_i, \tag{6}$$

in which the last equality is taken as a definition of γ_i. The values of γ_i are solutions of a series of simultaneous equations:

$$(1/\alpha_i)\gamma_i - \Sigma_j(f_{ij}/3V)\gamma_j = 1. \tag{7}$$

Equations (6) and (7) are then sufficient to replace Eq. (1) in calculation of the relation between the various polarizabilities in perovskite-type crystals.

[9] L. W. McKeehan, Phys. Rev. 43, 913 (1933).

On the Theory of Spin Waves in Ferromagnetic Media

CONYERS HERRING AND CHARLES KITTEL
Bell Telephone Laboratories, Murray Hill, New Jersey
(Received November 6, 1950)

The theory of spin waves, leading to the Bloch $T^{\frac{3}{2}}$ law for the temperature variation of saturation magnetization, is discussed for ferromagnetic insulators and metals, with emphasis on its relation to the theory of the energy of the Bloch interdomain wall. The analysis indicates that spin-wave theory is of more general validity than the Heitler-London-Heisenberg model from which it was originally derived. Many properties of spin waves of long wavelength can be derived without specialized assumptions, by a field-theoretical treatment of the ferromagnetic material as a continuous medium in which the densities of the three components of spin are regarded as amplitudes of a quantized vector field. As applications, the effects of anisotropy energy and magnetic forces are calculated; and it is shown that the Holstein-Primakoff result for the field dependence of the saturation magnetization can be derived in an elementary manner. An examination of the conditions for validity of the field theory indicates that it should be valid for insulators, and probably also for metals, independently of any simplifying assumptions. The connection with the itinerant electron model of a metal is discussed; it appears that this model is incomplete in that it omits certain spin wave states which can be proved to exist, and that when these are included, it will yield both a magnetization reversal proportional to $T^{\frac{3}{2}}$ and a specific heat proportional to T. Incidental results include some insight into the relation between the exchange and Ising models for a two-dimensional lattice, an upper limit to the effective exchange integral, and a treatment of spin waves in rhombic lattices.

I. INTRODUCTION

THE quantum-mechanical theory of ferromagnetism[1] is beset by so many difficulties and uncertainties that especial importance attaches to those few quantitative relationships between measurable quantities which it is capable of predicting with reasonable rigor. One such relationship, which is generally regarded as being valid whenever the basic assumptions of the Heitler-London-Heisenberg model are applicable, is Bloch's $T^{\frac{3}{2}}$ law of variation of saturation moment with temperature near the absolute zero, based on the theory of spin waves.[2] According to this model the decrease of saturation moment with increasing temperature is determined by the "stiffness" of the exchange coupling which tends to align the spins of all the atoms parallel. This same stiffness, in competition with anisotropy forces, determines the thickness and specific surface energy of the boundary region, known as the Bloch wall, which separates adjacent domains having different directions of magnetization.[3] If the anisotropy constants are known, one can, according to this model, deduce the exchange stiffness and hence the temperature variation of magnetization from a knowledge of the Bloch wall energy, or vice versa. When this is done, the relation between these, in principle, measurable quantities [Eq. (5) below] turns out to involve only the saturation magnetization, and to be independent of such details of the model as the number of nearest neighbors. This suggests that the validity of this relation is more general than that of the Heitler-London-Heisenberg model from which it was derived. This surmise acquires added plausibility from the success of some attempts to develop the theory of spin waves on a more or less phenomenological basis.[4] The principal purposes of the present paper are to verify this surmise, to give a more soundly based phenomenological theory of spin waves, and to show that with the aid of this theory one can deduce quite simply all of the formulas governing a broad class of properties of a ferromagnetic substance in the region of low temperatures.

Since only rather simple reasoning is required for the exposition of the present approach to spin wave theory, and for the derivation of practical results from it, we shall present these topics first, in Secs. IIA and IIB, respectively. The applications include calculations of the effect of anisotropy and magnetic forces on spin waves and the $T^{\frac{3}{2}}$ law, and it will be shown that the results of Holstein and Primakoff[5] on the field dependence of intrinsic magnetization can be derived easily by the present method. Appendix A gives a brief derivation of the principal equations of the theory for the special case in which the atomic model is assumed, and evaluates the coefficient in the $T^{\frac{3}{2}}$ law for a simple rhombic lattice. Section III is devoted to an analysis of the justification of the theory of spin waves and especially of the form of it presented in Sec. II, which enables all of the properties of spin waves to be derived from the Bloch wall coefficient, A, defined by Eq. (3) below. This analysis, though incomplete, seems to us to indicate strongly that the methods of Sec. II are justified, and that their justification is not contingent upon the choice of any particular approximate model for the ferromagnetic electrons. A corollary of this conclusion is that the criticisms which Wohlfarth[6] has

[1] For a brief critical review of this field see, for example, J. H. Van Vleck, Revs. Modern Phys. 17, 27 (1945).
[2] F. Bloch, Z. Physik 61, 206 (1930); 74, 295 (1932); C. Møller, Z. Physik 82, 559 (1933); W. Opechowski, Physica 4, 715 (1937).
[3] F. Bloch, Z. Physik 74, 295 (1932); L. Landau and E. Lifshitz, Physik. Z. Sowjetunion 8, 153 (1935); E. Lifshitz, J. Phys. (U.S.S.R.) 8, 337 (1944); L. Néel, Cahiers phys. 25, 1 (1944). For a summary see C. Kittel, Revs. Modern Phys. 21, 541 (1949).
[4] G. Heller and H. A. Kramers, Proc. Roy. Acad. Amsterdam 37, 378 (1934); E. Lifshitz, J. Phys. (U.S.S.R.) 8, 337 (1944); W. Döring, Z. Physik 124, 501 (1947). In Appendix A of the present paper we give a simple derivation of the phenomenological theory from the atomic model.
[5] T. Holstein and H. Primakoff, Phys. Rev. 58, 1098 (1940).
[6] E. P. Wohlfarth, Proc. Leeds Phil. Soc. 5, 213 (1949). E. C. Stoner, Report of the Grenoble Conference (1950).

recently leveled against the theory of spin waves and the $T^{\frac{3}{2}}$ law are not justified.

A brief recapitulation of the results yielded by the atomic model for the temperature variation of magnetization[3] and for the Bloch wall[3] will serve to clarify our first objectives and to introduce some basic equations and definitions. If $M(T)$ is the saturation magnetization at temperature T, the $T^{\frac{3}{2}}$ law can be written as[3]

$$M(T)/M(0)=1-(T/\Theta)^{\frac{3}{2}}+O(T^2), \tag{1}$$

where for any crystal structure of high symmetry[6a]

$$\theta^*=2.21Z(R_n^2/\Omega_0)^{2/3}S_0^{5/3}(J/k), \tag{2}$$

Z being the number of nearest neighbors of any given atom, R_n their distance, Ω_0 the atomic volume, S_0 the spin quantum number of an individual atom, k Boltzmann's constant, and J the interatomic exchange integral, defined so that the effective interaction energy of two nearest neighbor atoms is a constant minus $2J\mathbf{S}_{01}\cdot\mathbf{S}_{02}$. The temperature dependence given by Eq. (1) constitutes a significant prediction even if J is regarded as an adjustable parameter; however, as we have pointed out above, the same model which leads to Eq. (1) also leads to a relation between J and the specific surface energy of the Bloch wall. This surface energy, and the thickness of the transition region as well, can be computed by a simple variational calculation based on the assumption that the energy per unit volume at any point in the transition region is a sum of two terms: a term arising from anisotropy and magnetostrictive effects, which depends on the local orientation of the magnetization vector, and a term

$$A|\nabla\mathbf{M}|^2/M^2 \tag{3}$$

proportional to the square of the rate at which the direction of the magnetization vector $\mathbf{M}$ is changing with position.[6b] The atomic model on which Eq. (2) is based gives for the coefficient A in Eq. (3)

$$A=ZS_0^2R_n^2J/6\Omega_0. \tag{4}$$

Since the other quantities entering into the surface energy of the Bloch wall are measurable, elimination of J between Eqs. (2) and (4) amounts to a prediction of a definite relationship between this surface energy and the variation of saturation magnetization with temperature, both measurable quantities.[7,8] It is noteworthy that the relation obtained from Eqs. (2) and (4), *viz.*,

$$A=0.0754(S_0/\Omega_0)^{\frac{1}{3}}k\theta^*, \tag{5}$$

involves only the magnetization per unit volume, and is independent of the atomic arrangement. We shall attempt to show in this paper that Eq. (5) is always valid, regardless of whether the atomic model used by Heisenberg and Bloch is a good approximation.

II. FIELD THEORY OF SPIN WAVES

A. Basic Equations

We shall begin by showing how the properties of spin waves of long wavelength can be derived formally by treating the ferromagnetic material as a continuous medium in which the densities of the three components of spin are regarded as amplitudes of a vector field which is quantized in the way demanded by the known commutation relations for spin components. Our approach will be merely a more sophisticated version of that used by Lifshitz[4] who, following a suggestion of Landau, interpreted the energy (3) as implying the existence of a restoring torque tending to straighten out any distortion in the spin alignment and who used this torque to construct a quasi-classical time-dependent wave equation for the spin. This approach differs from that of Heller and Kramers[4] and that of Döring[4] in that it is not based explicitly on a model in which each electron is attached to a particular atom; and it differs from that of Bloch[2] and of Møller[2] both in this respect and in that the problem is formulated in terms of densities of spin moment, rather than in terms of probability amplitudes for the different states of spin.

Consider the vector operator defined by

$$\mathbf{s}^{(r)}=\sum_i \boldsymbol{\sigma}^{(i)}\delta(\mathbf{r}-\mathbf{r}_i), \tag{6}$$

where $\sigma_x^{(i)}$, $\sigma_y^{(i)}$, $\sigma_z^{(i)}$ are the Pauli matrices for the ith electron, $\mathbf{r}_i$ is its position vector, δ is the Dirac delta-function, and the summation is over all the electrons of a ferromagnetic crystal. The operator (6) represents the density of spin moment per unit volume at the point $\mathbf{r}$, in units of $\hbar/2$. Its Fourier components are the operators

$$\mathbf{s}^{(k)}=\sum_i \exp(i\mathbf{k}\cdot\mathbf{r}_i)\boldsymbol{\sigma}^{(i)}. \tag{7}$$

[6a] It is shown in Appendix A that for a simple rhombic lattice J has merely to be replaced by the geometric mean of the J's going with the three rectangular directions.

[6b] As none of the references we have cited explains why Eq. (3) should be the most general allowable form for this term in a cubic crystal, a word of explanation is in order here. Since we are interested only in non-uniformities in spin direction which change very gradually with position, we wish an expression which is of the lowest order in the derivatives of $\mathbf{M}$ which the symmetry of the problem permits; this requires that the expression be quadratic in the derivatives, but as there are three such quantities which have the symmetry required for an isotropic medium (*viz.* $|\nabla\mathbf{M}|^2$, $(\nabla\cdot\mathbf{M})^2$, and $|\nabla\times\mathbf{M}|^2$), and four which have the symmetry required for a cubic crystal, one might think that any linear combination of these would be a possible form for the required energy expression. The reason this is not so is that the energy expression in question is intended to represent only the energy increase which would result from the given variation of $\mathbf{M}$ if there were no magnetic terms in the hamiltonian, the latter being taken into account by magnetic, anisotropy, and magnetostrictive terms in the macroscopic calculation (see Kittel, reference 3). When magnetic terms are omitted from the hamiltonian, the energy is invariant with respect to spin rotations, so the required expression must have the form $\sum_{\alpha\beta\gamma\delta}C_{\alpha\beta}(\partial M_\alpha/\partial x_\gamma)(\partial M_\alpha/\partial x_\delta)$, with $C_{\alpha\beta}$ a tensor with the symmetry of the crystal. For cubic crystals Eq. (3) is, therefore, the most general allowable form, while for hexagonal and tetragonal classes two coefficients, A_{11} and $A_\perp$, would be required.

[7] Careful measurements of M at low temperatures have been made for several ferromagnetic elements and alloys by M. Fallot, Ann. physique 6, 305 (1936).

[8] A rough measurement of the surface energy of Bloch wall in 3.85 percent SiFe has been obtained by Williams, Bozorth, and Shockley, Phys. Rev. 75, 155 (1949); there is hope that more accurate measurements may be possible in the future.

From the commutation relations

$$\sigma_x^{(l)}\sigma_y^{(l)}-\sigma_y^{(l)}\sigma_x^{(l)}=2i\delta_{ll}\sigma_z^{(l)},$$

etc., we find easily

$$s_x^{(r)}s_y^{(r')}-s_y^{(r')}s_x^{(r)}=2is_z^{(r)}\delta(\mathbf{r}-\mathbf{r}') \tag{8}$$

$$s_x^{(k)}s_y^{(k')}-s_y^{(k')}s_x^{(k)}=2is_z^{(k+k')}, \tag{9}$$

with corresponding equations resulting from cyclic permutation of x, y, z. If k and k' are small and if the specimen has an almost uniform spontaneous magnetization in the z-direction, the right of Eq. (9) will have very nearly the eigenvalue zero if $\mathbf{k}+\mathbf{k}'\neq 0$, and the eigenvalue $4iS$ if $\mathbf{k}+\mathbf{k}'=0$, where S is the total spin quantum number for the ferromagnetic ground state of the specimen, which we suppose to have very nearly the same energy and magnetic moment as the state in question. Since the hermitian adjoint of $\mathbf{s}^{(k)}$ is $\mathbf{s}^{(k)+}=\mathbf{s}^{(-k)}$, we can rewrite Eq. (9) for this case as

$$s_x^{(k)+}s_y^{(k)}-s_y^{(k)}s_x^{(k)+}\approx 4iS\delta_{kk'}. \tag{10}$$

We now make the assumption that, since the mean energy of any slightly non-uniform distribution of spin density is given by the volume integral of Eq. (3), this integral in operator form can be used as a hamiltonian to find the stationary states associated with the spin fluctuations. The legitimacy of this assumption will be discussed in Sec. III below; it is obviously applicable only to spin disturbances of long wavelength. For the present case, where $\mathbf{M}$ is always oriented very nearly in the z-direction, this hamiltonian for a specimen of volume Ω takes the form

$$H'=(A\Omega^2/4S^2)\int|\nabla\mathbf{s}^{(r)}|^2d\tau=(A\Omega/4S^2)\textstyle\sum_k k^2\mathbf{s}^{(k)+}\cdot\mathbf{s}^{(k)}$$

$$\approx(A\Omega/4S^2)\textstyle\sum_k k^2(s_x^{(k)+}s_x^{(k)}+s_y^{(k)+}s_y^{(k)}) \tag{11}$$

if higher order terms in $s_x^{(k)}$ and $s_y^{(k)}$ are neglected. The general term of the summation in Eq. (11) can be thrown into harmonic oscillator form by expressing it in terms of the hermitian operators defined by

$$\begin{aligned}
Q_+^{(k)}&=(8S)^{-\frac{1}{2}}(s_x^{(k)}+s_x^{(k)+}),\\
P_+^{(k)}&=(8S)^{-\frac{1}{2}}(s_y^{(k)}+s_y^{(k)+}),\\
Q_-^{(k)}&=i(8S)^{-\frac{1}{2}}(s_y^{(k)}-s_y^{(k)+}),\\
P_-^{(k)}&=i(8S)^{-\frac{1}{2}}(s_x^{(k)}-s_x^{(k)+}).
\end{aligned} \tag{12}$$

It is easily verified that the first two and the last two lines of Eq. (12) each constitute a canonically conjugate pair. The hamiltonian (11) reduces to

$$H'=(2A\Omega/S)\sum_{\text{half }k}\tfrac{1}{2}(P_+^{(k)2}+Q_+^{(k)2}+P_-^{(k)2}+Q_-^{(k)2})k^2, \tag{13}$$

where the summation is to be extended over only half of k-space, since the contributions of $\mathbf{k}$ and $-\mathbf{k}$ to Eq. (11) are both included in the kth term of Eq. (13).

The hamiltonian (11) or (13) yields both the equations of motion of the spin system in time, and the eigenvalues of the energy. The latter are of course sums of expressions of the form $(n_\pm^{(k)}+\frac{1}{2})(2A\Omega/S)k^2$, where $n_\pm^{(k)}=0,\ 1,\ 2,\ \cdots$. Since the ground state, whose energy we shall take to be E_0, is the state for which all $n_\pm^{(k)}=0$, the levels are

$$E(n_\pm^{(k)2}s)=E_0+\sum_{\text{half }k}(n_+^{(k)}+n_-^{(k)})(2A\Omega/S)k^2. \tag{14}$$

Thus, the energy of a spin wave of wave vector $\mathbf{k}$ is $(2A\Omega/S)k^2$; this relation between A and the energy of the spin wave is the same as that yielded by the atomic-model theories of reference 2; and when the usual statistical treatment is employed to calculate the number of spin waves excited at temperature T, it gives a value for the θ^* of Eq. (1) agreeing with Eq. (5).

The time derivative of the spin density at the point $\mathbf{r}$ can be obtained from the integral expression for the hamiltonian in Eq. (11): using the usual square bracket abbreviation for the commutator of two operators and the summation convention for repeated suffixes, we have

$$\begin{aligned}
-i\hbar\dot{s}_\alpha^{(r)}&=[H',\,s_\alpha^{(r)}]\\
&=(A\Omega^2/4S^2)\int\left[\frac{\partial s_\beta^{(r')}}{\partial x_\gamma'}\frac{\partial s_\beta^{(r')}}{\partial x_\gamma'},\,s_\alpha^{(r)}\right]d\tau'\\
&=(A\Omega^2/4S^2)\int\left\{\frac{\partial s_\beta^{(r')}}{\partial x_\gamma'}\frac{\partial}{\partial x_\gamma'}[s_\beta^{(r')},\,s_\alpha^{(r)}]\right.\\
&\qquad\left.+\frac{\partial}{\partial x_\gamma'}[s_\beta^{(r')},\,s_\alpha^{(r)}]\frac{\partial s_\beta^{(r')}}{\partial x_\gamma'}\right\}d\tau'\\
&=2i(A\Omega^2/4S^2)\epsilon_{\alpha\beta\mu}(\nabla^2 s_\beta^{(r)}s_\mu^{(r)}+s_\mu^{(r)}\nabla^2 s_\beta^{(r)})
\end{aligned} \tag{15}$$

by Eq. (8), where $\epsilon_{\alpha\beta\mu}=1$ if $\alpha\beta\mu$ is an even permutation of xyz, -1 if an odd permutation, and 0 otherwise. If we set $\mathbf{M}=-(e\hbar/2mc)\mathbf{s}^{(r)}$ in Eq. (15) and ignore the noncommutativity of the different components, we get the equation of motion derived phenomenologically by Landau and Lifshitz[3] and by Döring:[4]

$$d\mathbf{M}/dt=-2(e/mc)(A/M^2)\mathbf{M}\times\nabla^2\mathbf{M}. \tag{16}$$

Note that this is the same as Eq. (A4) of Appendix A. As can be seen from this or from the classical approximation to the motion of one of the oscillators of Eq. (13), a spin wave of large amplitude is a disturbance in which the direction of $\mathbf{M}$ at each point of space moves in time around a narrow cone, the amplitude of the motion being a sinusoidal function of position. From this physical picture of the motion it is obvious that the first two terms of Eq. (1) will give a good approximation to the saturation moment as long as the temperature is low enough so that the only disturbances of the spin system which are appreciably excited are ones of sufficiently long wavelength for Eq. (3) to apply to them, i.e., of a wavelength much greater than the lattice constant.

B. Effect of Magnetic Fields, Anisotropy, etc., on Spin Waves

So far we have considered only the energy levels of an assembly of electrons uninfluenced by any purely magnetic forces. In actual materials there will be a spin-orbit interaction giving rise to anisotropy effects, a long-range magnetic interaction of the spins which will increase the energy of states for which the magnetization has a divergence, and, of course, a magnetic interaction of the electrons with any external field which may be applied. The last-named interaction is modified by the spin-orbit interaction in such a manner as to give an effective g-factor differing slightly from 2; higher order effects of this sort will for simplicity be neglected in the present treatment, though they might be treated by methods similar to those used here. To this approximation, at least, the magnetic effects which we have named can all be taken into account by adding appropriate terms to the hamiltonian (11) or (13). If one is not interested in zero-point energy, the effect of these additional terms on the energy levels can be calculated even more simply by merely adding appropriate terms to the phenomenological equation of motion (16) and calculating the frequencies of the normal modes classically. Such calculations amount to a simplified version of the theory of Holstein and Primakoff,[5] with the advantage of not being based on any particular atomic model. In this section we shall carry these calculations far enough to show that anisotropy and spin-spin interactions do not modify the $T^{\frac{3}{2}}$ law (1) appreciably, and shall give expressions which need only to be integrated by the methods of Sec. IV of reference 5 in order to give the formulas of Holstein and Primakoff for the dependence of intrinsic magnetization on field.

Our starting point is Eq. (16) which gives the contribution of the spatial variation of the magnetization $\mathbf{M}$ to the time derivative $d\mathbf{M}/dt$; we must add to this the contributions of the various magnetic interactions. A magnetic field $\mathbf{H}$, whether externally imposed or due to the spins themselves, contributes a term $-(e/mc)\mathbf{M}\times\mathbf{H}$ to $d\mathbf{M}/dt$. The effect of anisotropy forces on $d\mathbf{M}/dt$ is similar to the effect of a field, and can be written $-(e/mc)\mathbf{M}\times\mathbf{H}_{ett}$ when $\mathbf{M}$ deviates only slightly from a direction of easy magnetization. For example, for a cubic crystal with the (001) direction an easy direction of magnetization the anisotropy energy per unit volume is given, for small values of the angle θ between $\mathbf{M}$ and (001), by $f_K\cong K\theta^2$, where K is the first-order anisotropy constant. Comparison with the expression $-\mathbf{H}\cdot\mathbf{M}$ for the magnetic energy gives, therefore, for this case

$$H_{ett}=2K/M. \tag{17}$$

Gathering together the terms enumerated, we have as the equation of motion for $\mathbf{M}$,

$$d\mathbf{M}/dt=-(e/mc)[2(A/M^2)\mathbf{M}\times\nabla^2\mathbf{M}+\mathbf{M}\times(\mathbf{H}_{ext}+\mathbf{H}_{ett}+\mathbf{H}_s)], \tag{18}$$

where $\mathbf{H}_{ext}$ is the externally applied field and $\mathbf{H}_s$ is the field due to the spins themselves. The only complicating feature in the problem of determining the normal frequencies is the fact that $\mathbf{H}_s$ depends on the distribution of $\mathbf{M}$. Explicitly, it is determined by

$$\nabla\cdot\mathbf{H}_s=-4\pi\nabla\cdot\mathbf{M},\quad \nabla\times\mathbf{H}_s=0. \tag{19}$$

If we try to get a solution of the form

$$\mathbf{M}=\mathbf{M}_s+\Delta\mathbf{M}_0\exp[i(\omega t+\mathbf{k}\cdot\mathbf{r})] \tag{20}$$

$$\mathbf{H}_s=\mathbf{H}_0\exp[i(\omega t+\mathbf{k}\cdot\mathbf{r})], \tag{21}$$

we find from Eq. (19)

$$\mathbf{H}_0=-4\pi\mathbf{k}\cdot\Delta\mathbf{M}_0\mathbf{k}/k^2.$$

Inserting this into Eq. (18), taking $\mathbf{M}_s$ in the z-direction, and neglecting second-order terms, we get the pair of equations

$$i\omega\Delta M_{0x}=-\xi(k_xk_y/k^2)\Delta M_{0x}-[\eta k^2+\zeta+\xi(k_y^2/k^2)]\Delta M_{0y} \tag{22}$$

$$i\omega\Delta M_{0y}=[\eta k^2+\zeta+\xi(k_x^2/k^2)]\Delta M_{0x}+\xi(k_xk_y/k^2)\Delta M_{0y},$$

where $\xi=4\pi M_s(e/mc)$, $\eta=2(A/M_s)(e/mc)$, $\zeta=(H_{ext}+H_{ett})(e/mc)$. These give a secular equation for ω, whose solution is

$$\omega^2=\eta^2k^4+(2\eta\zeta+\xi\eta\sin^2\theta_k)k^2+\zeta^2+\xi\zeta\sin^2\theta_k, \tag{23}$$

where θ_k is the angle between $\mathbf{k}$ and the z-direction, i.e., $\mathbf{M}_s$.

The first term on the right of Eq. (23) represents the square of the frequency of a spin wave in the absence of magnetic interactions and coincides with the value used in the preceding section. For large k the difference between this and the correct frequency is given by

$$\hbar\omega-\hbar\eta k^2\sim\hbar[\zeta+(\xi/2)\sin^2\theta_k]=2(H_{ext}+H_{ett})\beta+4\pi M_s\beta\sin^2\theta_k, \tag{24}$$

where β is the Bohr magneton, $e\hbar/2mc$. As $k\to0$,

$$\hbar\omega\to\hbar[\zeta^2+\zeta\zeta\sin^2\theta_k]^{\frac{1}{2}}=[(H_{ext}+H_{ett})\times(H_{ext}+H_{ett}+4\pi M_s\sin^2\theta_k)]^{\frac{1}{2}}\beta, \tag{25}$$

a quantity which is always less than Eq. (24). Equation (25) is related to the expression $(BH)^{\frac{1}{2}}$, which occurs in the theory of ferromagnetic resonance. From Eqs. (24) and (25) one can infer the behavior shown schematically in Fig. 1 for $\hbar\omega$ as a function of k. It is easily verified that the difference $(\hbar\omega-\hbar\eta k^2)$ is always less than the right of Eq. (24), so if this quantity is $\ll kT$ over the range of temperatures normally used in comparing the $T^{\frac{3}{2}}$ law with experiment, the conventional treatment which assumes $\omega=\eta k^2$ can legitimately be used for the calculation of θ^* in Eq. (1). If $(H_{ext}+H_{ett})\ll4\pi M_s$, the condition is $T\gg4\pi M_s/k=1.7°$ if $M_s=2\times10^3$ gauss; it is thus fairly well satisfied for the common ferromagnetic substances over the experimentally significant part of the low temperature range. However, for paramagnetic salts (if such exist) with high anisotropy

energy and low Curie points the anisotropy corrections could be very important and could change the character of the temperature dependence of the saturation magnetization.

The complete expression for the magnetization M at any low temperature T can be deduced as a function of H_{ext} by evaluating the integral

$$\int_0^\infty \frac{k^2 dk}{\exp(\hbar\omega/kT)-1}, \tag{26}$$

which is proportional to $M(0)-M(T)$. Since ω is given by Eq. (23), approximations must be used to evaluate the integral; as this problem has been fully discussed by Holstein and Primakoff in Sec. IV of their paper,[5] we shall give merely the correspondence between our notation and theirs, which enables the treatment we have just given to be substituted for the first three sections of their paper. They express $\hbar\omega$ as $(A_k^2-|B_k|^2)^{\frac{1}{2}}$, where, as comparison of their expressions with Eq. (23) shows, we must take

$$A_k=(4A/M_s)\beta k^2+2(H_{ext}+H_{eff})\beta+4\pi M_s\beta\sin^2\theta_k \tag{27}$$

$$|B_k|=4\pi M_s\beta\sin^2\theta_k. \tag{28}$$

Holstein and Primakoff[5] have pointed out that even at the absolute zero the magnetization is slightly dependent on the field, and that, strictly speaking, this variation should be added to that of $M(T)-M(0)$ to get the total variation of $M(T)$ with H_{ext}. This variation of $M(0)$ with H_{ext}, which arises from the field dependence of the zero-point energy of the spin waves, is negligible for most practical purposes; however, it is interesting to examine how it comes about physically. Consider a spin wave whose wave vector $\mathbf{k}$ is in the x-direction, $\mathbf{M}_s$ being, as always, in the z-direction. From Eq. (22) we find for the ratio of axes of the elliptical cone which the spin vector describes

$$\Delta M_{0z}/\Delta M_{0y}=i[(\eta k^2+\zeta)/(\eta k^2+\zeta+\xi)]^{\frac{1}{2}}. \tag{29}$$

A straightforward calculation of the magnetic, anisotropy, and exchange energy associated with this spin wave gives

$$\text{total energy}=[\Omega/4(e/mc)M_s][(\eta k^2+\zeta+\xi)|\Delta M_{0x}|^2+(\eta k^2+\zeta)|\Delta M_{0y}|^2], \tag{30}$$

where Ω is the volume of the specimen. Setting this equal to $\hbar\omega/2$ and using Eq. (29), we can calculate the zero-point amplitudes ΔM_{0x} and ΔM_{0y}. In particular, we find

$$|\Delta M_{0x}|^2|\Delta M_{0y}|^2=(4\beta M_s/\Omega)^2. \tag{31}$$

Thus the geometric mean of $|\Delta M_{0x}|^2$ and $|\Delta M_{0y}|^2$ is always the same as in the simple theory which neglects magnetic effects. Their algebraic mean, which determines the magnetization reversal associated with the spin wave, is always greater than the geometric mean, by an amount which increases as their ratio departs increasingly from unity. If $(H_{ext}+H_{eff})\ll 4\pi M_s$, the absolute value of the right of Eq. (29) will be $\ll 1$ for spin waves of small k, so that these spin waves will give a greater magnetization reversal than the simple theory predicts, and in particular, a nonvanishing zero-point reversal.

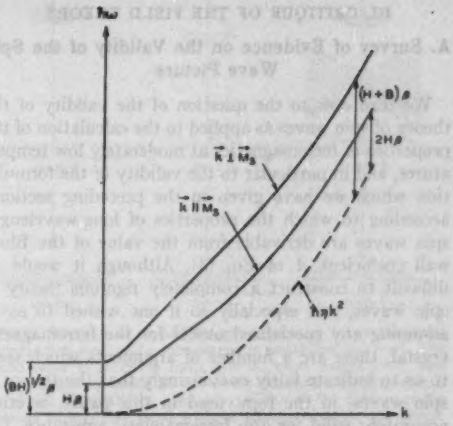

FIG. 1. Schematic variation of the frequency ω of a spin wave with its wave vector $\mathbf{k}$, in the presence of external and anisotropy fields, for $\mathbf{k}\|\mathbf{M}_s(\theta=0)$ and $\mathbf{k}\perp\mathbf{M}_s(\theta=\pi/2)$. The dashed line is the parabola given by the simple theory, ignoring magnetic and anisotropy terms. Distances above it are expressed in terms of $H=H_{ext}+H_{eff}$ and $B=H+4\pi M_s$. When H becomes $\ll 4\pi M_s$, the $\theta=0$ curve approaches the dashed parabola, while for small k the curve for $\theta=\pi/2$ approaches a straight line passing through the origin.

It is interesting to note that for a two-dimensional lattice the integral corresponding to Eq. (26), which has k instead of k^2 in the numerator, diverges if ω is taken proportional to k^2, as in the simple theory, but converges if ω is modified by an anisotropy field according to Eq. (23). The divergence given by the simple theory signifies that in the absence of anisotropy a two-dimensional lattice cannot be ferromagnetic;[5a] the convergence in the presence of anisotropy suggests that in layer lattices with exchange interaction the anisotropy energy may be able to induce a type of ferromagnetic behavior.

[5a] This was first pointed out by F. Bloch, Z. Physik 61, 206 (1930). The transition in thin films between three dimensions and two dimensions has recently been studied theoretically by M. J. Klein and R. S. Smith, Phys. Rev. 81, 378 (1951). However, L. Onsager, Phys. Rev. 65, 117 (1944), finds that if one uses the Ising model interaction $\Sigma S_i{}^z S_j{}^z$, two-dimensional lattices are ferromagnetic. The different types of behavior can be understood physically in terms of the energy required to reach a state of zero magnetic moment, starting from a saturated ground state. For a plane array N atoms on a side the energy required on the Ising model is $\approx NJ$, while on the correct exchange model it is $\approx J$. The latter result is readily demonstrated: the exchange energy between two spins making an angle φ with each other is $\approx J\varphi^2$, where we wish φ to be of the order of $1/N$ for a state of zero net moment. The number of pairs of spins involved is of the order of N^2, so that the energy is $\approx J(1/N)^2N^2=J$.

III. CRITIQUE OF THE FIELD THEORY

A. Survey of Evidence on the Validity of the Spin Wave Picture

We turn now to the question of the validity of the theory of spin waves as applied to the calculation of the properties of ferromagnetics at moderately low temperatures, and in particular to the validity of the formulation which we have given in the preceding sections, according to which the properties of long-wavelength spin waves are derivable from the value of the Bloch wall coefficient A of Eq. (3). Although it would be difficult to construct a completely rigorous theory of spin waves, and especially so if one wished to avoid assuming any specialized model for the ferromagnetic crystal, there are a number of arguments which seem to us to indicate fairly convincingly that the theory of spin waves, in the form used in this paper, is fairly accurately valid for any ferromagnetic substance, i.e., that equations such as Eqs. (1), (5), etc., are correct over an experimentally significant range of temperatures, and that this validity is not dependent on the choice of any particular theoretical model. Since Wohlfarth[6] and Stoner[6] have recently argued the contrary, we shall undertake to summarize the evidence from the literature and to add some new arguments.

Evidence from the past literature consists of a number of indications that the theory of spin waves is valid for the atomic model. These include:

(i) Bethe's[9] rigorous calculation of the energy levels of a linear chain of one-electron atoms, based on the hamiltonian $-J\Sigma\mathbf{S}_i\cdot\mathbf{S}_j$. This shows that the distribution of states in energy for this model is at low energies asymptotically the same as that given by Bloch's[3] theory of spin waves, and does not deviate significantly from the latter until energies are reached for which the mean number of reversed spins is a perceptible fraction of the total.

(ii) Opechowski's[2] calculation of the partition function for a three-dimensional array of atoms, with the hamiltonian $-J\Sigma\mathbf{S}_i\cdot\mathbf{S}_j$. This calculation, though not rigorous in the mathematical sense, is significant in that it uses an approach totally different from that of the spin wave theory, yet arrives at an identical result; moreover, by evaluating the T^2 term in Eq. (1), it indicates that the $T^{\frac{3}{2}}$ law is a good approximation until several percent of the spins have been reversed. It is interesting to note that the statistical treatment of Kramers,[10] on which Opechowski based his work, assumes at the outset the physically obvious fact that the crystal is homogeneous; i.e., that the logarithm of the partititon function is asymptotically proportional to the number N of atoms in the crystal. This fact can be seen, in an intuitive way, to be the reason that the criterion for validity of Bloch's theory should be the smallness of the mean fraction r/N of the spins which are reversed, rather than the smallness of the ratio r^3/N, whose exponential $\exp(r^3/N)$ gives the factor by which Bloch's theory overestimates the number of states with r reversed spins.

(iii) The analysis of Holstein and Primakoff,[5] who have made a rough estimate of the errors involved in Bloch's spin wave treatment and have concluded that they are probably small in the range of temperatures where the proportion of reversed spins is not over one or two percent.

From this evidence one might conclude merely that the theory of spin waves and the $T^{\frac{3}{2}}$ law are valid for the atomic model, but that they might fail for metals, where the occurrence of nonintegral magneton numbers shows the atomic model in its simple form to be inapplicable. However, it will be shown in a forthcoming paper by one of us[11] that spin waves also have a place in the so-called "itinerant electron" model of a ferromagnetic metal, and that, at least as far as the calculations have been carried, the whole theory of Sec. IIA seems to be as valid for this as for the atomic model.

Forgetting specific models for the moment, one can argue quite generally that for any ferromagnetic there must exist many low lying energy states which differ from the ground state principally in having the direction of the magnetization vector $\mathbf{M}$ fluctuate from point to point; moreover, if by linear combinations of these we form a state in which $\mathbf{M}$ approximates to a classical vector field of varying direction, the change of $\mathbf{M}$ with time must be given by Eq. (16). This can be seen from the fact that application of a magnetic field $-2(A/M^2)\nabla^2\mathbf{M}$ would make the given distribution of $\mathbf{M}$ an equilibrium distribution; the time change of $\mathbf{M}$ in the absence of any such field will therefore be essentially the same as that which would be produced by the reverse field, and the latter is known from ferromagnetic resonance experiments to be a gyroscopic response to the type (16). It therefore seems fairly certain that the $\mathbf{k}$th Fourier component of the temperature fluctuations in $\mathbf{M}$ will have the amplitude given by the equipartition principle whenever this amplitude is large enough for this component of the motion to be treated classically. This seems to justify the spin wave theory for the calculation of the temperature variation of magnetization, as far as the contributions of very small wave vectors $\mathbf{k}$ are concerned. If we can justify the theory for values of $\mathbf{k}$ for which the quantum energy is of the order of kT, therefore, it will probably be safe to accept the theory completely.

The following two sections will be devoted for the most part to the problem just mentioned, or more specifically, to the problem of the existence of excited states of the crystal which have the properties of spin waves with single-quantum excitation, and the energies of these states. This problem is much simpler for a ferromagnetic insulator than for a metal, for reasons which are illustrated in Fig. 2. Here the energies of the various stationary states are depicted for various values of the quantum numbers commonly used to classify the states. These quantum numbers are S, the total spin, S_z, the z-component of spin, and $\mathbf{k}$, the total wave vector, defined by the condition that $\exp(-i\mathbf{k}\cdot\mathbf{t})$ be the eigenvalue of the operation of translating the whole

[9] H. A. Bethe, Z. Physik **71**, 205 (1931); *Handbuch der Physik* XXIV 2, p. 604. Some, for our purposes, minor corrections have been given by L. Hulthén, Arkiv Mat. Astron. Fysik **26A**, No. 11 (1938).

[10] H. A. Kramers, Communs. Kamerlingh Onnes Lab. Univ. Leiden, Suppl. No. 83 (1936).

[11] C. Herring, *Energy of a Bloch Wall on the Band Picture, II. Perturbation Approach* (to be published).

wave function by a lattice vector $\mathbf{t}$. In general there will be an infinite number of eigenfunctions associated with each set of values of these quantum numbers. As is shown graphically in Fig. 2, the corresponding energy values have a continuous distribution if we are dealing with a metal; but for the case of a ferromagnetic insulator the lower lying states are discrete, at least for the ground-state value of S and the next smaller value.[12] This difference between insulators and metals makes the case of an insulator much easier to discuss. We shall, therefore, attack insulators first, in the section to follow, where without assuming any specific model it will be shown that the energy of a spin wave of wave vector $\mathbf{k}$ is asymptotically $(2A\Omega/S)k^2$ when k is small, provided the Slater picture of Fig. 2 is qualitatively correct and provided two further physical assumptions, both almost certainly correct, are fulfilled. By showing the kind of physical assumptions which one must make to establish this result, this proof will clarify the problem of justifying the field theory for the case of a ferromagnetic metal, which we shall discuss in Sec. IIIC.

B. Relation of the Wall and Spin Wave Problems for an Insulator

Referring to Fig. 2, let us consider a ferromagnetic insulator whose ground state has energy E_0 and quantum numbers S, $k=0$, and let Ψ_0 be that one of the degenerate set of ground-state wave functions which has $S_z=S$. For an insulator we may define a spin wave state in general to be any eigenstate Ψ_k of spin $(S-1)$ and wave vector $\mathbf{k}\neq 0$; we shall be concerned almost exclusively with spin wave states of the lowest band, defined as those whose energies join on continuously to E_0 as $\mathbf{k}$ is decreased to zero.

Let us assume the spin wave states and their energies to be known, and calculate the coefficient A in Eq. (3) by a perturbation method. If we assume a small torque $\sigma_y R \sin kx$ to act on each electron, the hamiltonian will contain a term which by Eq. (7) may be written

$$(R/2i)(s_y^{(k)}-s_y^{(-k)}). \tag{32}$$

The perturbation of the energy of Ψ_0 by this operator can be calculated and compared with what we would expect phenomenologically from Eq. (3). For the perturbed state we may set

$$M_y=M_y^0 \sin kx. \tag{33}$$

The change in energy density, relative to the unperturbed state, consists of a positive term of the form (3)

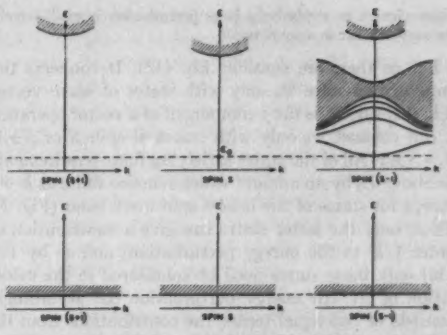

FIG. 2. Portions of typical energy spectra for a ferromagnetic insulator (top row) and a ferromagnetic metal (bottom row). The ground state is taken to have spin S, wave vector $k=0$, and energy E_0. For an insulator the lowest excited states with spin S correspond essentially to excitation of one of the ferromagnetic electrons to a higher band without change of spin; the lowest states for spin $(S+1)$ correspond to excitation of an electron of minority spin to a higher band, with reversal of spin. For spin $<S$, on the other hand, there are spin wave states whose energies get almost as low as E_0, and, at somewhat higher energies, a continuum corresponding to reversal of spins of electrons in the ferromagnetic band. The form shown for these levels is essentially that given by Slater (reference 12). For a metal with partially filled bands of both spins, on the other hand, there is an energy continuum whose bottom for $k\neq 0$ or for spin $\neq S$ is only infinitesimally above E_0; a metal with only completely filled bands of minority spin would differ from the case shown in having no low-lying states of spin $(S+1)$.

and a negative term proportional to the amount of yielding to the applied force; if Ω is the volume of the crystal the change in energy is therefore, to the second order in R,

$$\Delta E=(\Omega A M_y^{0\,2}k^2/2M^2)-(\Omega R M_y^0/2).$$

The value of M_y^0 must be so chosen as to make this a minimum; this gives

$$M_y^0=RM^2/2k^2A, \tag{34}$$

and

$$\Delta E=-\Omega R^2M^2/8k^2A, \tag{35}$$

or

$$A=-\Omega R^2M^2/8k^2\Delta E. \tag{36}$$

Thus, A can be calculated from the second-order energy perturbation by Eq. (36) or from the first-order perturbation of $\mathbf{M}$ by Eq. (34). If the perturbations are calculated by applying the Rayleigh-Schrödinger method with the perturbation operator (32), this method of calculating A involves an assumption which we shall label (a) to facilitate reference to it later:

(a) It is assumed that the value of A associated with very small perturbations—i.e., those for which $M_y^0<$the zero-point fluctuation in the corresponding Fourier component of M_y—is the same as that going with the larger perturbations to which Eq. (3) is intended to apply. It seems physically obvious that this will be the case here, because the energy depends only on local conditions,

[12] These qualitative facts relating to the existence and spectrum of spin waves for an insulator have been elegantly demonstrated by J. C. Slater, Phys. Rev. 52, 198 (1937). Slater's picture is based on a solution of the quantum-mechanical problem which is only approximate, but which is sufficiently good to leave no doubt that the qualitative features of the spectrum would be unchanged by any further refinements, provided that the ground state of the insulator can be at least roughly described as having a filled band of majority spin electrons.

whose change in a relatively large perturbation is qualitatively the same as that in a small one.[13]

Let us therefore consider Eq. (32). It connects the unperturbed state Ψ_0 only with states of wave vector $\pm\mathbf{k}$, and since it is the y component of a vector operator, it can connect Ψ_0 only with states of spin S or $S\pm1$, $S_z=S\pm1$. All of the states satisfying these requirements lie above E_0 by an amount which remains finite as $k\to0$, except for states of the lowest spin wave band (Fig. 2). Thus, only the latter states can give a contribution of order $1/k^2$ to the energy perturbation; and so by Eq. (36) only these states need be considered in the calculation of A. The energy perturbation ΔE accordingly consists of two equal terms, the contributions from the spin wave states Ψ_k and Ψ_{-k} of the lowest band. Explicitly,

$$\Delta E=-R^2|[\Psi_k, s_y^{(k)}\Psi_0]|^2/2(E_k-E_0). \quad (37)$$

Now, it is not hard to see that, as $k\to0$, the numerator of Eq. (37) must approach a limit independent of the detailed nature of the wave functions. A simple way of proving this is to calculate the energy of the state $s_y^{(k)}\Psi_0$. For small k this state is everywhere very similar to Ψ_0 as far as local properties of the wave function are concerned, and its energy is easily shown to differ from E_0 by an amount of order k^2, being, as is shown in Appendix B,

$$(s_y^{(k)}\Psi_0, Hs_y^{(k)}\Psi_0)/(s_y^{(k)}\Psi_0, s_y^{(k)}\Psi_0) = E_0+(N/2S)k^2 \quad (38)$$

rydberg units if k is in a_H^{-1}, where N is the total number of electrons in the specimen. Since $s_y^{(k)}\Psi_0$ has wave vector $\mathbf{k}$, it must be a linear combination of Ψ_k and states of the higher spin wave bands. Since the latter have energies which remain above E_0 by a finite amount as $k\to0$, their coefficients must be $0(k)$, so we must have

$$|(\Psi_k, s_y^{(k)}\Psi_0)|^2=(s_y^{(k)}\Psi_0, s_y^{(k)}\Psi_0)+0(k^2). \quad (39)$$

In Appendix B it is shown that the first term on the right of Eq. (39) has asymptotically the value $2S$ when the specimen is very large and k very small.

Combining this value of Eq. (39) with Eqs. (37) and (36) we get for the value of the coefficient A in Eq. (3)

$$A=\frac{S}{2\Omega}\lim_{k\to0}\left(\frac{E_k-E_0}{k^2}\right) \quad (40)$$

in agreement with Eq. (14). This relation should be rigorously valid for any ferromagnetic insulator. Besides (a), we have used two further assumptions in its derivation:

(b) It has been assumed that the only states with which $s_y^{(k)}$ connects Ψ_0 are the spin wave state Ψ_k of the lowest band and other states whose energies remain above E_0 by a finite amount as $k\to0$.

(c) Appendix B has made use of the assumption that when the system is in the state Ψ_0, there is no long-range correlation between the values of the x- and y-components of the spins of electrons found in elements of volume which are a moderately large distance apart.

The former of these, especially, is not obviously true for a metal, since, as Fig. 2 shows, there is a continuum of states with which $s_y^{(k)}$ might conceivably connect Ψ_0. However, we shall cite evidence in the next section that something very similar to this assumption is probably true for metals.

We have thus shown that for an insulator the correctness of the energies predicted by the field theory of Sec. IIA for states of single-quantum excitation is equivalent to the correctness of assumptions (a), (b), and (c). This complements the classical argument, given at the end of the preceding section, to the effect that the theory should be correct for motions with many-quantum excitation.

C. Spin Waves in a Metal

As a background for a discussion of spin waves in a metal it will be helpful to recall some of the properties which the itinerant electron model predicts for the energy spectrum of a metal. In the familiar form of the theory using this model the various energy levels must be classified merely according to the z-component of spin, since the determinantal wave functions which the theory uses are in general not eigenfunctions of $\mathbf{S}^2$. When overlapping bands are present, the minimum of the total energy occurs in general for a state corresponding to partially filled bands of both spins; this is of course the way in which nonintegral magneton numbers are explained by this model. This fact implies that there will in general be low-lying excited states of the metal with both higher and lower values of S_z than the ground state. It is commonly assumed that for a more exact model the same property would be possessed by the total spin S. If this is the case, a decrease of magnetization with temperature can result only from there being more states per unit energy in the low energy range for values of S smaller than the ground state value than for values the same amount larger. The usual form of the itinerant electron model does in fact predict an asymmetry of this sort in the distributions for different values of S_z, and this asymmetry has been shown by Stoner[14] to lead to a temperature variation of magnetization of the form

$$M(T)/M(0)\sim1-CT^2. \quad (41)$$

[13] The correctness of this assumption can be confirmed for a special case in the Slater-Fock approximation of determinantal wave functions, since calculations with and without this assumption agree. These will be reported in two papers to be published by C. Herring.

[14] E. C. Stoner, Proc. Roy. Soc. (London) **A165**, 372 (1938). Stoner's derivation assumes a parabolic band form but is easily generalized to bands of arbitrary form, no specializing assumption being necessary except that the exchange terms in the energy be approximated in such way as to yield an electronic specific heat linear in T at low temperatures. However, whereas C in Eq. (41) is always positive if the band form is parabolic, it may be of either sign with more general band forms.

When in the ground state one of the two directions of spin has only completely filled or completely empty bands of electrons, there is a minimum energy below which excited states of higher or lower spin do not exist, the lowest such states being ones of lower spin; for this case (41) is replaced by an exponential approach to saturation.

The success of the itinerant electron model in accounting for such phenomena as electronic specific heat suggests that the true energy states of a ferromagnetic metal correspond to a considerable degree with those given by the picture just described. However, it is easy to show that the correspondence is incomplete in one important respect: there exist low-lying states of the metal which are orthogonal to all the low-lying states of the usual itinerant electron model; and, as far as we have been able to deduce their properties, these states are of the nature of spin waves. To show that these states exist, consider the state Ψ_w of the metal which is derived from the ground state Ψ_0 by applying a sinusoidal perturbing torque of amplitude R and long wavelength $2\pi/k$ to the spin system, i.e., by adding a term of the form (32) to the hamiltonian. The derivative $\partial\Psi_w/\partial R$ will be a linear combination of those states of the metal with which the perturbation operator connects Ψ_0, and in order that the energy of Ψ_w contain a term of order R^2/k^2 as $k\rightarrow 0$ [see Eq. (35)], at least some of these states must have energies which are infinitesimal of order k^2. Now, if the stationary states of the metal are assumed to be of the determinantal form occurring in the itinerant electron theory, the only states with which the perturbation operator (32) will connect Ψ_0 will be states with an electron removed from some state $\mathbf{k}_s$ and placed in a state $(\mathbf{k}_s+\mathbf{k})$ of opposite spin. When k is small, these states all have energies which lie above that of the ground state by amounts of the order of the exchange energy J of an electron; none of the energies is infinitesimal. Thus, the assumption that all the low-lying excited levels are the ones given by the usual itinerant electron theory leads to a contradiction with the existence of a term of the form (3) in the energy. It will be shown later by one of us[11] that when Ψ_w is approximated by a determinant, $\partial\Psi_w/\partial R$ is, in fact, independent of all the low-lying excited states which appear in the usual itinerant electron theory and has a mean energy E_k which is related to A by Eq. (40).

One is thus led to surmise that the low-lying stationary states of a ferromagnetic metal are of two types: first, states which may be described as having "no spin waves excited" and which have a distribution in energy and in S which is qualitatively similar to the distribution in energy and S_z which the itinerant electron model predicts; second, states derivable from these by excitation of spin waves. Each state of the former type may, we surmise, be the ancestor of many successive generations of the second type, of successively lower values of S. These progency will cause a marked asymmetry in the densities of states for spins higher and lower than that of the ground state, and will lead to the $T^{\frac{1}{2}}$ law (1); however, they will contribute only a $T^{\frac{1}{2}}$ term to the specific heat,[15] which as $T\rightarrow 0$ will be swamped by the T term contributed by the parent states. If, as this picture suggests, the $T^{\frac{3}{2}}$ effect of Eq. (41) and the $T^{\frac{1}{2}}$ effect of Eq. (1) are simultaneously present, it will provide a natural explanation for the apparent mild contradiction between the experiments of Fallot[4] and the theoretical finding of Opechowski[3] that on the atomic model the coefficient of the small T^2 term in Eq. (1) should have a positive sign.

Although this hypothesis is still very much in the realm of speculation, the evidence already discussed in support of it can be reinforced by a few additional fragments of reasoning. To begin with, we may inquire what meaning can be given to the conception of a "state with no spin waves excited." The reasoning of the preceding section and of Appendix B suggests that the states to which this designation can most conveniently be applied are those states with $S_z=S$ which satisfy assumption (c), i.e., which have no long-range correlation between the x- and y-components of the spins of electrons in different parts of the crystal, if stationary states with this property exist. It is shown in Appendix B that any operator of the form $[s_x^{(k)}+is_y^{(k)}]$, k small, takes any state of the type just mentioned into a state whose normalization integral is very small. Since this operator is essentially the destruction operator for a spin wave of wave vector $\mathbf{k}$ in the field theory, this suggests describing the states in question as having "no spin waves excited," at least as far as long wavelength spin waves are concerned. Moreover, any linear combination of a small number of such states will have approximately the same property. Finally, it is physically plausible that when the hamiltonian operates on a wave function without long-range spin correlations, the result will nearly always be a wave function with the same property. It is, therefore, reasonable to expect that stationary states will exist which possess, or almost possess, this property.

A second point concerns the interpretation of the result, quoted above, that when the eigenfunction Ψ_w in a sinusoidal perturbing field is approximated by a determinant of one-electron functions, the mean energy of $\partial\Psi_w/\partial R$ is given by Eq. (40). Now for an insulator $\partial\Psi_w/\partial R$ is an eigenfunction with energy E_k, plus terms of order k as $k\rightarrow 0$; for a metal, on the other hand, we have to consider the possibility that $\partial\Psi_w/\partial R$ may be a linear combination of a number of low energy eigenfunctions with appreciably different energies. One might at first think that mere knowledge of the mean energy of $\partial\Psi_w/\partial R$ would give almost no information on the energies of the latter states, since some might lie above and some below the mean. However, it is shown in

[15] See, for example, N. F. Mott and H. Jones, *Theory of the Properties of Metals and Alloys* (Oxford University Press, 1936), p. 237.

Appendix C by a comparison of this mean energy with the perturbed energy of Ψ_w and an application of the Schwarz inequality one can deduce the relation

$$\bar{E}-E_0\leq(2\Omega/S)Ak^2+0(k^4), \tag{42}$$

where $\bar{E}$ is the mean energy of $\partial\Psi_w/\partial R$, E_0 is the ground state energy, and k is the wave vector of the perturbation (32). The equality, i.e., Eq. (40), can hold only if the expansion coefficients c_i and energies E_i of the eigenfunctions contained in $\partial\Psi_w/\partial R$ satisfy the condition

$$c_i(E_i-E_0)=c_i\delta E+0(k), \tag{43}$$

where δE is independent of i. For this case the energies E_i of these states for which c_i is of order k^{-2} or larger must lie in a very narrow range centered at the point $(E_0+\delta E)$. Thus, if the equality which has been proved to hold in Eq. (42) in the determinantal approximation holds true in general, $\partial\Psi_w/\partial R$ will be very nearly an eigenfunction of a single energy, which may be called a spin wave. Moreover, it is shown in Appendix C that in this case $\partial\Psi_w/\partial R$ will differ only infinitesimally from a multiple of $(P_-^{(k)}+iQ_-^{(k)})\Psi_0$, where the operator in parentheses is just the creation operator for the "minus" type of spin wave in the theory of Sec. IIA.

D. Miscellaneous Comments

It is worth pointing out that there are more familiar problems which involve an approximation similar to that involved in the substitution of the H' of Eq. (11), a quadratic expression in the spin densities, for the true hamiltonian H. This substitution is *not* analogous to the substitution of $-2\sum J_{ij}\mathbf{S}_i\cdot\mathbf{S}_j$ for the true hamiltonian in an exchange degeneracy problem: in the latter case a certain subspace of Hilbert space, known at the outset, is taken into itself by the approximate hamiltonian, whose matrix in this subspace coincides with that of the true hamiltonian; in our case no such subspace is known. This leads to the paradox that, although the eigenfunction of Eq. (11) having a $n_+^{(k)}=1$, other n's$=0$, is proportional to $(P_+^{(k)}+iQ_+^{(k)})\Psi_0$, where Ψ_0 is the ground-state wave function, nevertheless, as can be seen from the analysis of Sec. IIIB, the energy of the state $(P_+^{(k)}+iQ_+^{(k)})\Psi_0$ as calculated with the true hamiltonian is in general significantly higher than the correct energy as given by Eq. (14).

The use of Eq. (11) is more nearly analogous to the use of the adiabatic approximation to calculate the low-lying vibrational levels of a molecule, a procedure which leads to a paradox of the same form as that just mentioned. If R is the internuclear distance in a diatomic molecule, p_R the conjugate momentum, μ the reduced mass, and ω the angular frequency of the vibration in R, the reader can easily verify that the wave function obtained by operating on the ground state eigenfunction with $p_R+i\mu\omega(R-R_0)$ has a mean energy, computed with the true hamiltonian for electrons and nuclei, which differs from that of the first excited state by an amount of the same order as the energy of excitation itself. Another example, which resembles our magnetic problem more closely, is the problem of computing the quantized energies of the low-lying acoustical modes of vibration of a crystal whose unit cell contains atoms which do not occupy symmetry positions. It is well known that the energies of these acoustical vibrational levels can be computed from a knowledge of the elastic constants of the crystal; i.e., of the minimum energy consistent with a given long-wavelength variation of the mean displacement of the atoms in a unit cell. In general, however, any elastic distortion will change the relative positions of the atoms in a unit cell,[18] and the eigenstates of a phenomenological hamiltonian constructed in the way we have been discussing will not manifest this change; they will therefore have the wrong energy when the energy is computed with the correct hamiltonian. Since the relative displacements are of the order of the amplitude, a, of the wave times its wave vector, k, the energy discrepancy per unit volume will be of order a^2k^2, which is of the same order as the vibrational energy itself. In spite of this the phenomenological hamiltonian gives the correct energies.

Another point worth noting is that Eq. (38), which was derived primarily as a tool for the proof of Eq. (40), gives as a by-product an upper limit to E_k, and correspondingly an upper limit to A. In atomic units

$$A<N/4\Omega. \tag{44}$$

If this is applied to a case in which the Heitler-London-Heisenberg model is valid and in which it is legitimate to treat the ferromagnetic electrons as a system independent of the other electrons, so that $N/\Omega=2S_0/\Omega_0$, we have from Eq. (4)

$$J<3/ZS_0R_a^2. \tag{45}$$

Although this limit is some tens of times larger than the J's usually assumed for ferromagnetic substances, it is interesting that a relation of this kind should exist, since the definition of J would lead one to expect merely an upper limit going as R_a^{-1} and, of course, independent of Z.

We wish to thank Professor J. M. Luttinger for some illuminating discussions of field theory.

APPENDIX A. SEMICLASSICAL THEORY OF SPIN WAVES ON THE ATOMIC MODEL, WITH APPLICATION TO RHOMBIC LATTICES

We give first a semiclassical derivation of spin-wave theory on the atomic model. The derivation is rather simpler and more concise than previous derivations in the literature.

The hamiltonian of the system is

$$H'=-2J\Sigma_{i>j}\mathbf{S}_i\cdot\mathbf{S}_j, \tag{A1}$$

where $\mathbf{S}_i$ is the spin operator in units of $\hbar$ for the ith atom. Each atom has $2S_0$ resultant electron spins. The quantum equation of

[18] See, for example, M. Born and M. Goeppert-Mayer, *Handbuch der Physik* XXIV 2, p. 630.

motion for $\mathbf{S}_m$ is

$$\begin{aligned} i\hbar d\mathbf{S}_m/dt &= [\mathbf{S}_m, H'] \\ &= 2J[(\Sigma \mathbf{S}_i\cdot\mathbf{S}_j)\mathbf{S}_m - \mathbf{S}_m(\Sigma \mathbf{S}_i\cdot\mathbf{S}_j)] \\ &= 2J\Sigma_i[(\mathbf{S}_m\cdot\mathbf{S}_i)\mathbf{S}_m - \mathbf{S}_m(\mathbf{S}_m\cdot\mathbf{S}_i)] \\ &= -2J\Sigma_i \mathbf{S}_i\times[\mathbf{S}_m\times\mathbf{S}_m], \end{aligned}$$

which becomes, using the commutation relation $\mathbf{S}\times\mathbf{S}=i\mathbf{S}$,

$$\hbar d\mathbf{S}_m/dt = 2J\mathbf{S}_m\times\Sigma\mathbf{S}_i. \tag{A2}$$

For a simple cubic lattice with lattice constant a we have by series expansion

$$\Sigma_i \mathbf{S}_i = 6\mathbf{S}_m + a^2\nabla^2\mathbf{S} + \cdots, \tag{A3}$$

where the S's are now considered as classical vectors, and not as quantum operators. For small distortions we neglect higher order terms in the series expansion, and thus we have the equation of motion

$$\hbar d\mathbf{S}/dt = 2Ja^2[\mathbf{S}\times\nabla^2\mathbf{S}]$$

for the spin considered as a classical quantity. One can easily verify, by replacing (A3) by an expression involving $\frac{1}{2}\Sigma R_\mu R_\nu \partial^2\mathbf{S}_m/\partial x_\mu\partial x_\nu$, that for any lattice of cubic symmetry with Z nearest neighbors to each lattice site,

$$\hbar d\mathbf{S}/dt = (ZR_n^2J/3)\mathbf{S}\times\nabla^2\mathbf{S}, \tag{A4}$$

where R_n is the separation of nearest neighbors. Let

$$\mathbf{S} = \mathbf{S}_0 + \boldsymbol{\epsilon} \tag{A5}$$

where $\mathbf{S}_0$ is the unperturbed spin vector, and $\boldsymbol{\epsilon}$ represents a spin wave of small amplitude. With this substitution Eq. (A4) reduces to

$$d^2\epsilon_x/dt^2 = -(ZR_n^2JS_0/3\hbar)^2\nabla^4\epsilon_x, \tag{A6}$$

where we have supposed that $\epsilon/S_0 \ll 1$, thereby determining the range of validity of the theory. Equation (A6) is essentially a wave equation, and it has solutions of the form

$$\epsilon_x = \epsilon_0 \exp[i(\omega t + \mathbf{k}\cdot\mathbf{r})],$$

where

$$\hbar\omega = (ZR_n^2JS_0/3)k^2. \tag{A7}$$

This is the fundamental relation between frequency and wave number of a spin wave. The wave is quantized in the usual way, setting $E = n\hbar\omega$, where n is readily shown to be the number of reversed spins in the system.

We go on to consider spin wave theory for a simple rhombic lattice with exchange integrals J_a, J_b, J_c connecting neighbors along the three mutually perpendicular axes a, b, c. The equation of motion becomes

$$\hbar d\mathbf{S}/dt = 2\mathbf{S}\times\left(a^2J_a\frac{\partial^2\mathbf{S}}{\partial x^2} + b^2J_b\frac{\partial^2\mathbf{S}}{\partial y^2} + c^2J_c\frac{\partial^2\mathbf{S}}{\partial z^2}\right), \tag{A8}$$

which leads to the relation

$$\hbar\omega = 2S_0(a^2J_ak_x^2 + b^2J_bk_y^2 + c^2J_ck_z^2). \tag{A9}$$

The reversed magnetization is proportional to

$$\int dk_x dk_y dk_z/[\exp(\hbar\omega/kT) - 1];$$

on substituting

$$\begin{aligned} x^2 &= 2S_0a^2J_ak_x^2/kT; \quad z^2 = 2S_0c^2J_ck_z^2/kT; \\ y^2 &= 2S_0b^2J_bk_y^2/kT; \quad r^2 = x^2+y^2+z^2; \end{aligned}$$

the integral becomes

$$\frac{N(kT/2S_0)^{\frac{3}{2}}}{J_a^{\frac{1}{2}}J_b^{\frac{1}{2}}J_c^{\frac{1}{2}}}\int \frac{4\pi r^2 dr}{\exp(r^2)-1},$$

where $N = 1/abc$ is the number of atoms per unit volume. This expression goes over into the usual expression for a simple cubic crystal on letting $a=b=c$, $J_a=J_b=J_c$. For the rhombic case we have

$$M_s = M_0[1 - 0.117(kT/2S_0)^{\frac{3}{2}}/J_a^{\frac{1}{2}}J_b^{\frac{1}{2}}J_c^{\frac{1}{2}}]. \tag{A10}$$

APPENDIX B. SOME PROPERTIES OF STATES OF THE FORM $s_y^{(k)}\Psi_0$, ETC.

Let Ψ_0 be a state with total spin S and z-component of spin $S_z = S$, and consider the state $s_y^{(k)}\Psi_0$, where $s_y^{(k)}$ is the kth Fourier component of the y-component of spin density, as defined by Eq. (7). The normalization integral of this state is the mean value, in the state Ψ_0, of the operator

$$s_y^{(k)+}s_y^{(k)} = N + \Sigma_{i\neq j}\sigma_y^{(i)}\sigma_y^{(j)}\cos[\mathbf{k}\cdot(\mathbf{r}_j - \mathbf{r}_i)], \tag{B1}$$

where N is the total number of electrons present. The mean value of the second term of (B1) in the state Ψ_0 is

$$\begin{aligned} &(\Psi_0, \Sigma_{i\neq j}\sigma_y^{(i)}\sigma_y^{(j)}\cos[\mathbf{k}\cdot(\mathbf{r}_j-\mathbf{r}_i)]\Psi_0) \\ &\quad = \int\int \Delta P(\mathbf{r}_1,\mathbf{r}_2)\cos[\mathbf{k}\cdot(\mathbf{r}_1-\mathbf{r}_2)]d\tau_1 d\tau_2, \end{aligned} \tag{B2}$$

where $\Delta P(\mathbf{r}_1,\mathbf{r}_2)d\tau_1 d\tau_2$ is the probability that, when the system is in the state Ψ_0, an electron will be found in $d\tau_1$ at $\mathbf{r}_1$, another in $d\tau_2$ at $\mathbf{r}_2$, these two having parallel y-components of spin, minus the corresponding probability for antiparallel y-components. Now, since Ψ_0 is an eigenfunction of S_z, the mean value of the y-component of spin of an electron found at any given point of space vanishes; if we may assume the physical nature of the problem to require that the spin distributions in $d\tau_1$ and $d\tau_2$ approach statistical independence as $|\mathbf{r}_1-\mathbf{r}_2|$ becomes large, we must have

$$\Delta P(\mathbf{r}_1,\mathbf{r}_2)\to 0 \quad \text{as} \quad |\mathbf{r}_1-\mathbf{r}_2|\to\infty.$$

This requirement, though undoubtedly fulfilled by the ground state of an insulator, is, as we shall see below, not necessarily fulfilled by other states, e.g., by spin wave states. Actually, it is to be expected that ΔP will differ significantly from zero only when $|\mathbf{r}_1-\mathbf{r}_2|$ is less than a few lattice spacings. Since we are interested only in infinitesimal values of k, we may therefore set $\cos[\mathbf{k}\cdot(\mathbf{r}_1-\mathbf{r}_2)]=1$ in Eq. (B2):

$$\begin{aligned} (\text{B2}) &= \int\int \Delta P(\mathbf{r}_1,\mathbf{r}_2)d\tau_2 + O(k^2) \\ &= (\Psi_0, \Sigma_{i\neq j}\sigma_y^{(i)}\sigma_y^{(j)}\Psi_0) + O(k^2). \end{aligned} \tag{B3}$$

The scalar product in Eq. (B3) is easily expressed in terms of the spin quantum numbers. For

$$\begin{aligned} \mathbf{S}^2 &= (3N/4) + (\tfrac{1}{4})\Sigma_{i\neq j}\sigma_z^{(i)}\sigma_z^{(j)} + (\tfrac{1}{4})\Sigma_{i\neq j}[\sigma_x^{(i)}\sigma_x^{(j)} + \sigma_y^{(i)}\sigma_y^{(j)}]S_z^2 = \\ &\quad (N/4) + (\tfrac{1}{2})\Sigma_{i\neq j}\sigma_z^{(i)}\sigma_z^{(j)}. \end{aligned}$$

Combining, we have

$$2(\mathbf{S}^2 - S_z^2) - N = \tfrac{1}{2}\Sigma_{i\neq j}(\sigma_x^{(i)}\sigma_x^{(j)} + \sigma_y^{(i)}\sigma_y^{(j)}). \tag{B4}$$

Now, in any eigenstate of S_z the means of the two terms on the right of Eq. (B4) are the same, so for the state Ψ_0 for which $\mathbf{S}^2$ is $S(S+1)$ and S_z is S,

$$(\Psi_0, \Sigma_{i\neq j}\sigma_y^{(i)}\sigma_y^{(j)}\Psi_0) = 2S - N. \tag{B5}$$

Combining (B5), (B3), (B2), and (B1) we have, therefore,

$$(s_y^{(k)}\Psi_0,\ s_y^{(k)}\Psi_0) = 2S + \delta, \tag{B6}$$

where δ is $O(k^2)$ as $k\to 0$ and $O(1)$ as N and the size of the crystal become infinite at fixed k.

Next consider the mean energy $\hat{E}_k$ of $s_y^{(k)}\Psi_0$, given by

$$\begin{aligned} \hat{E}_k(s_y^{(k)}\Psi_0,\ s_y^{(k)}\Psi_0) &= (s_y^{(k)}\Psi_0,\ Hs_y^{(k)}\Psi_0) \\ &= E_0(s_y^{(k)}\Psi_0,\ s_y^{(k)}\Psi_0) + (\Psi_0,\ s_y^{(k)+}[Hs_y^{(k)} - s_y^{(k)}H]\Psi_0). \end{aligned} \tag{B7}$$

Only the kinetic energy operator contributes to the commutator; in atomic units we have

$$\begin{aligned} s_y^{(k)+}[Hs_y^{(k)} - s_y^{(k)}H] &= k^2 s_y^{(k)+}s_y^{(k)} \\ &\quad - 2i\mathbf{k}\cdot\Sigma_{i,j}\sigma_y^{(i)}\sigma_y^{(j)}\exp[i\mathbf{k}\cdot(\mathbf{r}_j-\mathbf{r}_i)]\nabla_j. \end{aligned} \tag{B8}$$

It is clear at this point that the $\hat{E}$ given by Eq. (B7) will be $E_0 + O(k^2)$ if Ψ_0 has any symmetry property which requires $\hat{E}_k$ and $\hat{E}_{-k}$ to be the same. To evaluate the coefficient of k^2 explicitly for the case where Ψ_0 is the ground state of an insulator we may take this symmetry property to be invariance under Wigner's

TABLE I. Group-theoretical restrictions on the lengths of components of $s^{(k)}\Psi_0$.

Subspace Wave function	$(S-1)$	S	$(S+1)$
$(s_x^{(k)}+is_y^{(k)})\Psi_0$	0	0	L_+
$s_z^{(k)}\Psi_0$	0	L_0	$L_+/(2S+2)^{\frac{1}{2}}$
$(s_x^{(k)}-is_y^{(k)})\Psi_0$	L_-	$L_0(2/S)^{\frac{1}{2}}$	$L_+/[(S+1)(2S+1)]^{\frac{1}{2}}$

time-reversal operation,[17] and shall accordingly replace the second term on the right of Eq. (B8), which we may call G, by the average of G, the time-reversed operator, and the adjoints of these, the latter averaging being permissible since the mean value of G must be real. The result is

$$G\to\mathbf{k}\cdot\Sigma_{i,j}\sigma_y^{(i)}\sigma_y^{(j)}(\sin[\mathbf{k}\cdot(\mathbf{r}_j-\mathbf{r}_i)]\nabla_j-\nabla_j\sin[\mathbf{k}\cdot(\mathbf{r}_j-\mathbf{r}_i)])$$
$$=-k^2\Sigma_{i\neq j}\sigma_y^{(i)}\sigma_y^{(j)}\cos[\mathbf{k}\cdot(\mathbf{r}_j-\mathbf{r}_i)]. \quad \text{(B9)}$$

Combining with Eqs. (B8) and (B7) and the previous evaluation of Eq. (B2), we have, finally,

$$\bar{E}_k=E_0+(N/2S)k^2 \quad \text{(B10)}$$

to within an error which is $O(k^4)$ as $k\to 0$, and $O(N^{-1})$ as $N\to\infty$.

A slight extension of the argument leading to Eq. (B6) enables us to calculate the orders of magnitude of the portions of $s^{(k)}\Psi_0$ which have spins $(S-1)$, S, and $(S+1)$. Remembering that Ψ_0 has $S_z=S$, we can use the group-theoretical relations between the different matrix elements of a vector operator[18] to express the lengths of the projections of the various $s_\mu^{(k)}\Psi_0$ ($\mu=x, y, z$) onto the subspace of spin S' in terms of a single constant dependent on S', as shown in Table I. The entries in the table are the values of the square root of the normalization integral of the projection of the wave function indicated at the left of each row onto the subspace of the spin indicated in each column. Without further assumptions regarding the nature of the state Ψ_0 we can say nothing about the values of the constants L_+, L_0, L_-. However, if Ψ_0 has the property of having no long-range correlations between x- and y-components of spin density we can evaluate them by the method used for Eq. (B6). We have

$$(s_x^{(k)}+is_y^{(k)})^+(s_x^{(k)}+is_y^{(k)})=2N-4S_z$$
$$+\Sigma_{i\neq j}(\sigma_x^{(i)}\sigma_x^{(j)}+\sigma_y^{(i)}\sigma_y^{(j)})\cos[\mathbf{k}\cdot(\mathbf{r}_j-\mathbf{r}_i)]$$
$$-\Sigma_{i\neq j}(\sigma_x^{(i)}\sigma_y^{(j)}-\sigma_y^{(i)}\sigma_x^{(j)})\sin[\mathbf{k}\cdot(\mathbf{r}_j-\mathbf{r}_i)]. \quad \text{(B11)}$$

The square of the quantity L_+ of Table I is the expectation value of (B11). If Ψ_0 has the property just mentioned and has in addition any symmetry property which requires this to be the same for $\mathbf{k}$ and $-\mathbf{k}$, this expectation value is given to within an error of order Nk^2 by setting the cosine equal to unity and the sine to zero in (B11); using (B4) this gives

$$L_+^2=O(Nk^2). \quad \text{(B12)}$$

A similar argument using the operator $s_x^{(k)}+s_x^{(k)}$ gives a value for $L_0^2+L_+^2/(2S+2)$; neglecting the second of these terms, we find

$$L_0^2=O(Nk^2). \quad \text{(B13)}$$

The operator $(s_x^{(k)}-is_y^{(k)})^+(s_x^{(k)}-is_y^{(k)})$ differs from the right of (B11) only in having a plus sign for the term $4S_z$; its mean value gives $[L_-^2+(2L_0^2/S)+L_+^2/(S+1)(2S+1)]$, and since the last two of these terms are negligible compared with the first, we have

$$L_-^2=8S+O(Nk^2). \quad \text{(B14)}$$

[17] E. Wigner, Göttingen Nachrichten (1932), p. 546.

[18] See for example E. Wigner, *Gruppentheorie und ihre Anwendung auf die Quantenmechanik der Atomspektren* (Friedrich Vieweg und Sohn, Braunschweig, 1931), p. 264.

It is now very easy to show that the lack of long-range correlations between x- and y-components of spin density, which we have assumed in deriving the preceding equations, especially Eq. (B12), cannot be valid for states with spin waves excited. For suppose Ψ_0 to be a state with no spin waves excited, so that Eqs. (B12), (B13), and (B14) apply to it. Then

$$(s_x^{(k)}-is_y^{(k)})\Psi_0/L_-=\Psi_1+O(k), \quad \text{(B15)}$$

where Ψ_1 is a state of spin $(S-1)$, which, for the case where Ψ_0 is the ground state of an insulator, differs only by $O(k)$ from the normalized eigenfunction of the lowest spin-wave band. Taking the scalar product of (B15) with Ψ_1 and using the properties of adjoint operators,

$$([s_x^{(-k)}+is_y^{(-k)}]\Psi_1,\Psi_0)=L_-[1+O(k)]=O(N^{\frac{1}{2}}),$$

whence it is obvious that the length of $[s_x^{(-k)}+is_y^{(-k)}]\Psi_1$ is $O(N^{\frac{1}{2}})$, rather than $O(N^{\frac{1}{2}}k)$ as it would be if Eq. (B12) applied to it.

APPENDIX C. MEAN ENERGY OF $\partial\Psi_w/\partial R$

Let $\Psi_w(R)$ be the ground-state eigenfunction of the sum of the crystal hamiltonian and the perturbation (32). Its energy will be of the form $(E_0+\Delta E)$, where E_0 is the energy of the unperturbed ground-state eigenfunction Ψ_0 and

$$\Delta E=-R^2\Sigma_i|\Delta_{i0}|^2/(E_i-E_0), \quad \text{(C1)}$$

where Δ_{i0} is the matrix element of the perturbation connecting the eigenfunctions Ψ_0 and Ψ_i. Defining c_i as the coefficient of $R\Psi_i$ in Ψ_w, i.e.,

$$c_i=-\Delta_{i0}/(E_i-E_0), \quad \text{(C2)}$$

we can rewrite Eq. (C1) as

$$\Delta E=R^2\Sigma_i c_i\Delta_{i0}^*. \quad \text{(C3)}$$

The mean value $\bar{E}$ of the crystal hamiltonian in the state $\partial\Psi_w/\partial R$ is given by

$$\bar{E}-E_0=-(\Sigma_i c_i\Delta_{i0}^*)/\Sigma_i|c_i|^2. \quad \text{(C4)}$$

Applying the Schwarz inequality to Eq. (C4) and noting that the left side is >0, we have

$$\bar{E}-E_0\leq[(\Sigma_i|\Delta_{i0}|^2)/\Sigma_i|c_i|^2]^{\frac{1}{2}}. \quad \text{(C5)}$$

Likewise, applying the Schwarz inequality to Eq. (C3) and using Eq. (36) of the text,

$$A\geq\Omega M^2/8k^2[(\Sigma_i|\Delta_{i0}|^2)(\Sigma_i|c_i|^2)]^{\frac{1}{2}}. \quad \text{(C6)}$$

The equality holds in Eqs. (C5) and (C6) if and only if $\Delta_{i0}\propto c_i$, i.e., if E_i is the same for all states for which $\Delta_{i0}\neq 0$. Now, if Ψ_0 satisfies the postulate (c) of Sec. IIB, regarding the absence of long-range correlations between x- and y-components of spin, we have from Eq. (B6) of Appendix B

$$\Sigma_i|\Delta_{i0}|^2=\text{mean square of (32)}/R^2=S+O(k^2). \quad \text{(C7)}$$

Combining Eqs. (C5), (C6), and (C7) gives, therefore, with $M=2S/\Omega$,

$$\bar{E}-E_0\leq(2\Omega/S)Ak^2+O(k^4). \quad \text{(C8)}$$

If the $O(k^4)$ in Eq. (C8) is to be merely that due to the $O(k^2)$ in Eq. (C7), the multidimensional vectors c and Δ must be parallel, as mentioned above. However, if $(\bar{E}-E_0)$ departs from the first term on the right of (C8) by this plus an additional amount of order k^4, these two vectors may make a small angle of order k with each other, so that we have merely

$$\Delta_{i0}=-c_i(E_i-E_0)=-c_i\delta E+O(k), \quad \text{(C9)}$$

where δE is some constant independent of i, but dependent on k and of order k^2, so that $c_i\delta E$ is $O(k^{-1})$.

Letters to the Editor

PUBLICATION of brief reports of important discoveries in physics may be secured by addressing them to this department. The closing date for this department is five weeks prior to the date of issue. No proof will be sent to the authors. The Board of Editors does not hold itself responsible for the opinions expressed by the correspondents. Communications should not exceed 600 words in length.

Products of the High Energy Helium Ion and Deuteron Bombardment of Tungsten

S. E. TURNER AND L. O. MORGAN
Department of Chemistry, University of Texas, Austin, Texas
January 2, 1951

AN investigation has been carried out on the radiation characteristics of radioactive species obtained by processing used exit strips from the 60" cyclotron of the University of California at Berkeley. During the period of service of these strips the cyclotron had been operated to produce 44-Mev helium ions and 22-Mev deuterons. It was determined that these samples received long and intense bombardments, but quantitative data are not available.

Tantalum, rhenium, and osmium fractions were separated from the tungsten by a variety of chemical methods, including precipitation of tantalum as the pentoxide, distillation of osmium tetroxide, distillation or solvent extraction of rhenium compounds, and ion exchange purification of rhenium fractions. Activity was observed in all fractions, attributable in most cases to previously reported nuclear species. The total activity of the tantalum fraction was identified as Ta^{182}, formed by $W(d, \alpha)$ and $W(n, p)$ reactions, with the reported[1] radiation characteristics. Os^{185} was the only active species[1] observed in the osmium fraction. The half-life, over a 600-day decay period, was found to be 97 days. Analysis of aluminum absorption curves indicated the presence of electrons having ranges of 14 mg/cm² (*ca* 0.1 Mev), 35–40 mg/cm² (0.17–0.19 Mev), and *ca* 280 mg/cm² (0.7 Mev).

The total decay curve of the rhenium fraction was resolved into two components, with apparent half-lives of 50±3 days and 155±5 days. The radiation characteristics of the shorter-lived material agreed well with previously reported data[1] for Re^{184}. After decay of the 50-day activity, resolution of aluminum absorption curves indicated the presence of electrons having visual ranges of *ca* 15 mg/cm² (0.1 Mev), 77–80 mg/cm² (0.29–0.30 Mev), and 300 mg/cm² (0.76 Mev). A graphical representation of the aluminum absorption data, with the low energy component eliminated, is given in Fig. 1. Lead absorption curves contained components with half-thicknesses of 224 mg/cm² (0.074 or 0.138 Mev) and 10.3 g/cm² (1.07 Mev).

Wilkinson and Hicks[2] have reported a long-lived component in the rhenium fraction from processed exit strips. Their data indicated a half-life of *ca* 240 days and somewhat different radiation characteristics: 0.16-Mev e^-, 1.0-Mev gamma- and x-radiation. They assigned the activity to Re^{183}. Stover[3] found a rhenium daughter of Os^{183} with a half-life of *ca* 120 days. No other characteristics were reported. It is probable that the material investigated by Wilkinson and Hicks and that studied in this laboratory were mixtures of Re^{183} and a longer-lived isotope of rhenium, possibly Re^{186}. The latter could have been formed by the $W(\alpha, p)$ reaction. In support of this contention, there is a marked increase in apparent half-life with increase in lead absorber thickness (see data for sample Re-III, Table I), which can be explained only on the basis of multiple activities. The data are entirely compatible with the assumption of an isotopic mixture comprising *ca* 90 percent of 120–140-day activity and *ca* 10 percent of 250–300-day activity. The mixture studied by Wilkinson and Hicks would have been, of necessity, predominantly the longer-lived isotope,

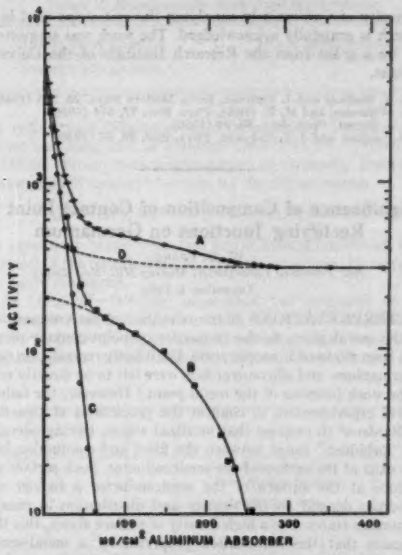

FIG. 1. Aluminum absorption curve for the long-lived component of the rhenium fraction. Curve (A) represents the unresolved data; (B) the 300-mg/cm² component; and (C) the 77–80-mg/cm² component. Curve (D) represents background of gamma- and x-radiation.

thus accounting for the difference in radiation characteristics. The existence of Re^{186}, with a half-life of several months, has also been suggested by Lindner and Coleman[4] as a product of multiple neutron capture by Re^{187}.

The proposed isotopic characterizations considered in this discussion are summarized in Table II.

The cooperation of J. G. Hamilton, T. M. Putnam, G. B. Rossi, and their associates in the Crocker Radiation Laboratory of the

TABLE I. Rhenium decay data.

Sample	Added absorber Be(g/cm²)	Pb(mg/cm²)	Long-lived component (days)	Short-lived component (days)	Period of observation (days)
Re-I	···	···	159	···	150
Re-II-V*	···	···	130	47	650
Re-III	2	···	157	53	700
	2	250	155	49	700
	2	700	175	48	700
	2	2000	175	48	700
	2	3500	175	48	700

* Derived from the composite decay curve of the indicated samples, which had undergone a variety of purification procedures. These samples were all from the same tungsten sample.

TABLE II. Rhenium isotopes.

Isotope	Radiations: Particles (Mev)	γ-rays (Mev)	Half-life period (days)	Produced by (possible reactions)
Re^{183}	0.1; 0.30; 0.76	1.07	120–140	$W(d, n)$ $W(\alpha, p)$ $W(d, 2n)$ $W(\alpha, p2n)$ $W(d, 3n)$ $W(\alpha, p3n)$
Re^{186}	0.1; 0.2; 0.7	1.00	50±3	$W(d, n)$ $W(\alpha, pn)$ $W(d, 2n)$ $W(\alpha, p2n)$ $W(\alpha, p3n)$
Re^{187}	0.16	1.0	250–300	$W(\alpha, p)$

University of California in supplying the exit strips used in this research is gratefully acknowledged. The work was supported in part by a grant from the Research Institute of the University of Texas.

[1] G. T. Seaborg and I. Perlman, Revs. Modern Phys. 20, 585 (1948).
[2] G. Wilkinson and H. G. Hicks, Phys. Rev. 77, 314 (1950).
[3] B. J. Stover, Phys. Rev. 80, 99 (1950).
[4] M. Lindner and J. S. Coleman, Phys. Rev. 78, 67 (1950).

Significance of Composition of Contact Point in Rectifying Junctions on Germanium

W. G. Pfann
Bell Telephone Laboratories, Murray Hill, New Jersey
December 4, 1950

INTERPRETATIONS of the relevance of the composition of the metal point to the properties of point-contact rectifiers have been modified in recent years. Until fairly recently, properties of germanium- and silicon-rectifiers were felt to be directly related to the work function of the metal point.[1] However, the failure of several experimenters to confirm the predictions of this theory led Bardeen[2] to propose that localized states, having energies in the "forbidden" range between the filled and conduction bands, may exist at the surface of the semiconductor. Such surface states produce at the surface of the semiconductor a barrier whose properties depend on the density and distribution in energy of the surface states. For a high density of surface states, this theory indicates that the rectification properties of a metal-semiconductor junction will be independent of the metal.

However, experiments with *n*- and *p*-germanium transistors indicate that the composition of the contact point *can* influence the properties of rectifying junctions. While such results are not inconsistent with Bardeen's theory, they do indicate that surface states can be considerably modified in particular junctions. Briefly, the significant feature of the metal point is its content of donors and acceptors. By means of an electrical treatment known as forming, it appears that donors or acceptors from the point can be introduced to or into the germanium, thereby affecting the space-charge region and the electrical properties of the junction. Two illustrations of the role of point composition in determining the properties of metal-germanium junctions are given below.

(1) It is observed that a pressure contact made with any metallic point to *p*-germanium usually results in but poor rectification. This has been ascribed to the existence of surface states which are such that the potential barrier they produce is of negligible height.[3] For many common contact materials, electrical forming of such a junction does not markedly improve the rectification. However, for a point which contains donors, such as

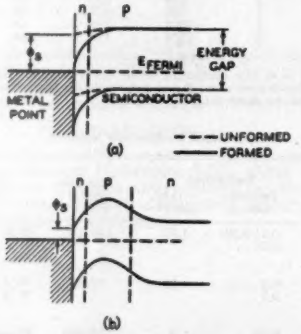

FIG. 1. Energy level diagrams showing rectifying barriers at contacts containing donors: (a) *p*-germanium; (b) *n*-germanium.

TABLE I. Forward and reverse currents at 1 volt of rectifying junctions on *n*-germanium as functions of antimony concentration in the metallic electrode.

Row	Wgt. % Sb	I_F (ma)	I_R (ma)
A	None	35	0.035
B	0.0001	33	0.026
C	0.001	37	0.10
D	0.01	3.1	2.4

phosphor bronze, it is found that forming increases the forward conductivity of the rectifying junction, thereby improving it as a rectifier and as an emitter of electrons in the *p*-germanium transistor.[4] The changes which are observed on forming with a phosphor bronze point can be interpreted as the result of the introduction of donors from the point to the germanium, with a resultant lowering of ϕ_s, the effective work function for electrons leaving the metal, as shown in Fig. 1a.

(2) In a recent letter Shockley[5] discusses theories of α, the current-multiplying factor in the transistor. According to one of these, the *pn*-hook theory, the space-charge region about the collector junction of an *n*-germanium transistor is as shown qualitatively in Fig. 1b. Results of experiments with contact-point alloys are consistent with Shockley's model and appear to indicate that the *n*-zone can be produced by electrical forming if donors are present in the point-electrode.[6] *n*-germanium transistors were prepared having as collectors a series of alloys graded with respect to donor (Sb) concentration. After forming the collectors (using the same emitter composition in all transistors), it was found that α increased with antimony concentration and that the forward and reverse current of the collector junctions were as shown in Table I.

Mean values are given for groups of 4 or 5 junctions. The data may be interpreted as follows:

The values of rows A and B represent fairly good rectifying junctions in *n*-germanium; ϕ_s is high and the reverse current of electrons is small. Since ϕ_s is high, a *p*-type inversion layer exists and a large hole current is present in the forward direction. Row C: the forward current is still large, but the reverse current has increased. The increase in antimony concentration has caused some lowering of ϕ_s, possibly only at small patches in the contact interface. Row D: sufficient antimony is present to produce an *n*-type inversion layer, as in Fig. 1b, which completely encloses the metal point. ϕ_s is here quite low and as a result the reverse current of electrons is large and the forward current of holes is small.

While the examples given here pertain to donors in the point electrode, it appears that corresponding effects can be caused by acceptors.

The writer is indebted to Mr. R. J. Kircher for contributions to the experimental data on point compositions.

[1] H. C. Torrey and C. A. Whitmer, *Crystal Rectifiers* (McGraw-Hill Book Company, Inc., New York, 1948), Chapter IV.
[2] J. Bardeen, Phys. Rev. 71, 717 (1947).
[3] J. Bardeen and W. G. Pfann, Phys. Rev. 77, 401 (1950).
[4] W. G. Pfann and J. H. Scaff, Phys. Rev. 76, 459 (1949).
[5] W. Shockley, Phys. Rev. 77, 294 (1950).
[6] We discuss here only the *n*-zone. Experimental results which indicate the existence of a chemical *p*-zone have been described by L. B. Valdes, to be published in Proc. Inst. Radio Engrs.

Microwave Study of Ge, Si, and S Masses*

S. Geschwind and R. Gunther-Mohr
Columbia University, New York, New York
December 11, 1950

THE relative masses of the stable Ge isotopes of even mass number and the mass difference ratios $(S^{33}-S^{32})/(S^{34}-S^{32})$ and $(Si^{30}-Si^{29})/(Si^{30}-Si^{28})$ have been determined from the isotopic shift in the pure rotational absorption spectrum of GeH_3Cl^{36}, $O^{16}C^{12}S$, and SiH_3Cl^{35}, respectively.

TABLE I. Experimentally determined masses of the even Ge isotopes compared with masses calculated from semi-theoretical mass formula, assuming exact agreement for Ge^{70} and Ge^{74}.

Nucleus	Experimentally determined masses	Masses calculated from Bohr-Wheeler formula
Ge^{70}	69.94952	69.94952
Ge^{72}	71.94848	71.94816
Ge^{74}	73.94862	73.94862
Ge^{76}	75.94994	75.95077

Assuming the Ge^{70} and Ge^{74} masses to be correctly given by the Bohr-Wheeler formula, the Ge^{72} and Ge^{76} masses were calculated in a manner analogous to that used in determining the relative masses of Se from the OCSe spectrum.[1]

The experimentally determined masses and the values given by the semi-empirical mass formula[2] are listed in Table I. The error in mass determination due to a combination of experimental error and uncertainty due to zero-point vibration, is 0.4 mMU. These results, plotted in Fig. 1, indicate essential agreement with the semi-empirical mass formula although the Ge^{76} mass is 0.8 mMU less than predicted and must be regarded as a real deviation. It would appear that the curvature of the mass defect vs mass number curve is slightly smaller than predicted, similar to the findings[1] for Se.

Of particular interest is the mass of Ge^{72}, which has 40 neutrons. According to the assignment of energy levels in the nuclear shell model by Mayer,[3] and Haxel, Jensen, and Suess,[4] 40 neutrons should complete a $p_{1/2}$ subshell, so that a small break might be expected in the mass defect curve at Ge^{72}. As pointed out elsewhere,[1] this break should be unaffected by errors in the assumed Ge^{70} and Ge^{74} masses or by uncertainties due to zero-point vibrations. That no such break occurs is interpreted to mean that the $p_{1/2}$ and $g_{9/2}$ levels lie within 0.3 mMU, for any larger separation would give an unambiguous break in the mass defect curve.

From the absolute frequencies of the $J=1\rightarrow2$ transition in $O^{16}C^{12}S$, corresponding to S^{32}, S^{33}, and S^{34}, which were measured to an accuracy of 5 kc or better, and from the absolute frequencies of the $J=1\rightarrow2$ transition in SiH_3Cl^{28} for the three stable isotopes of Si, which were measured to an accuracy of 15 kc, the mass difference ratios $(S^{32}-S^{33})/(S^{34}-S^{33})$ and $(Si^{30}-Si^{29})/(Si^{30}-Si^{28})$ were calculated, neglecting zero-point vibrations, and were found to be

$$(S^{32}-S^{33})/(S^{34}-S^{33})=0.500714\pm0.00003;$$
$$(Si^{30}-Si^{29})/(Si^{30}-Si^{28})=0.49941\pm0.00005.$$

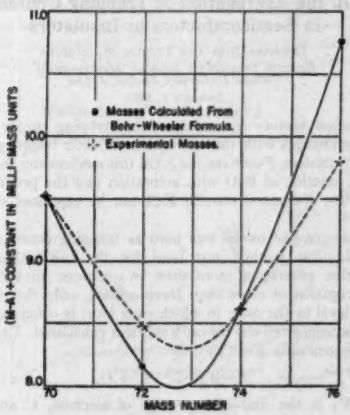

FIG. 1. Variation of masses of even Ge isotopes as a function of mass number.

TABLE II. Experimentally determined sulfur masses.

$S^{32}=31.98199\pm0.00021$	$S^{36}=34.98046\pm0.00035$
$S^{33}=32.98187\pm0.00025$	$S^{34}=35.97954\pm0.0006$
$S^{34}=33.97890\pm0.0003$	

The sulfur mass differences were measured by Davisson[5] using nuclear reactions, and he obtained $(S^{32}-S^{33})/(S^{34}-S^{33})=0.50060\pm0.00008$. From mass spectrometer experiments, Duckworth, Preston, and Woodcock[6,7] obtain for the silicon masses

$$(Si^{30}-Si^{29})/(Si^{30}-Si^{28})=0.499341\pm0.00006.$$

The agreement between the two sets of results justifies an earlier estimate[1] of the outside limit of the error introduced by neglecting zero-point vibrations.

The $O^{16}C^{12}S^{32}-O^{16}C^{12}S^{34}$ separation was measured by Low and Townes;[8] and Koski, Wentink, and Cohen[9] measured the $O^{16}C^{12}S^{33}-O^{16}C^{12}S^{34}$ separation. Combining these results with ours, the sulfur masses were determined using S^{32} and S^{34} as

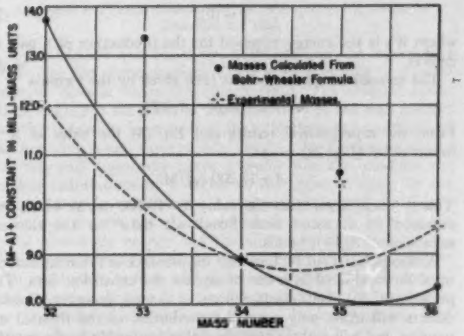

FIG. 2. Variation of sulfur masses as a function of mass number. The masses given by the Bohr-Wheeler formula have been adjusted so that the predicted S^{34} mass coincides with the experimental value.

reference masses and taking[10] $S^{32}=31.98199$, and $S^{34}=33.97890$, using the $(S^{34}-S^{33})$ difference measured by Davisson.[5] The sulfur masses, listed in Table II and plotted in Fig. 2, give for the odd-even mass differences in S^{33} and S^{35}, 2.0 ± 0.3 and 1.7 ± 0.3 mMU, respectively, compared with $\delta=0.036/A^{3/4}=2.6$ and 2.4 mMU, respectively, given by the Fermi formula.

The error stated is a combination of experimental error and the margin of error to be allowed in fitting a curve to the experimental points. In this low mass number region the semi-empirical mass formula deviates from the experimental mass by as much as 3 mMU, and so for a comparison with the experimental masses it has been adjusted to the S^{34} mass. The measured frequencies and other details will appear in a forthcoming publication.

The authors wish to express their indebtedness to Professor Townes for suggesting this problem and for his continual aid and interest.

* Work supported jointly by the Signal Corps and ONR.

[1] Geschwind, Minden, and Townes, Phys. Rev. 78, 174 (1950).
[2] The semi-empirical formula used throughout was of the Bohr-Wheeler type, but with constants given by E. Fermi, *Nuclear Physics* (University of Chicago Press, Chicago, 1950), p. 8. We are indebted to Dr. N. Metropolis of the Los Alamos Scientific Laboratory for furnishing us with a table of atomic masses calculated from the semi-empirical formula.
[3] M. Y. Mayer, Phys. Rev. 75, 1969 (1949).
[4] Haxel, Jensen, and Suess, Phys. Rev. 75, 1766 (1949).
[5] P. W. Davisson, Phys. Rev. 75, 757 (1949).
[6] Duckworth, Preston, and Woodcock, Phys. Rev. 79, 188 (1950).
[7] H. E. Duckworth and R. S. Preston, Phys. Rev. 79, 402 (1950).
[8] W. Low and C. H. Townes, Phys. Rev. 75, 529 (1949).
[9] Koski, Wentink, and Cohen, Phys. Rev. 81, 296 (1950).
[10] A. S. Penfold, Phys. Rev. 80, 116 (1950).

Lattice Defects in Silver Bromide

H. KANZAKI
Second Faculty of Engineering, University of Tokyo, Chiba, Japan
December 18, 1950

AN anomalous specific heat of AgBr was first predicted by Mott and Gurney.[1] The writer has measured the specific heat of AgBr (polycrystalline) from room temperature to its melting point (420°C). The heating velocity used was about 2°C per minute. A large increase in the specific heat was observed above 250°C, accompanying the production of lattice defects. The specific heat-temperature curve is shown in Fig. 1. The total energy required for the production of defects below 420°C was found to be 620 cal/M.

Generally, the number of defects in ionic crystals is thought to vary with the temperature according to the formula

$$n = n_0 \exp(-A/kT). \tag{1}$$

When all of the defects are dissociated,[2]

$$A = \tfrac{1}{2}W_0; \tag{2}$$

and when all defects are associated to defect pairs,

$$A = W_0, \tag{3}$$

where W_0 is the energy required for the production of a pair of defects.

The anomalous specific heat is then given by the formula

$$\Delta C \propto T^{-2} \exp(-A/kT). \tag{4}$$

From the experimental results and Eq. (4) the value of A is found to be[3] (Fig. 2a)

$$A = 17{,}200 \text{ cal/M}.$$

This is much larger than the value $A = 10{,}500$ cal/M which was obtained by Lawson[4] from Strelkow's data[5] on the thermal expansion of AgBr crystals.

As was pointed out by Lawson,[4] the presence of Schottky defects must be considered in order to explain the expansion data. The presence of Frenkel defects cannot be denied, however. Frenkel defects will make only a small contribution to the thermal expansion, but will make a considerable contribution to the specific heat. It is possible that the presence of both types of defects will lead to different activation energies for the specific heat and the thermal expansion.

The writer has examined Strelkow's data carefully and has found that in the temperature range above 300°C the value of A was 15,400 cal/M, and below 300°C it was 8500 cal/M (Fig. 2b).

Lawson has estimated that 4 percent defect sites should be present at 690°K. Using the value $A = 15{,}400$ cal/M, the total energy required to produce these defects is 1230 cal/M from Eq. (2), and 615 cal/M from Eq. (3). This energy is expected to be smaller than the value 620 cal/M obtained from the specific heat, if the presence of both defect types is considered.

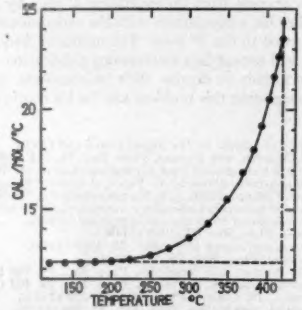

FIG. 1. Specific heat-temperature curve for AgBr.

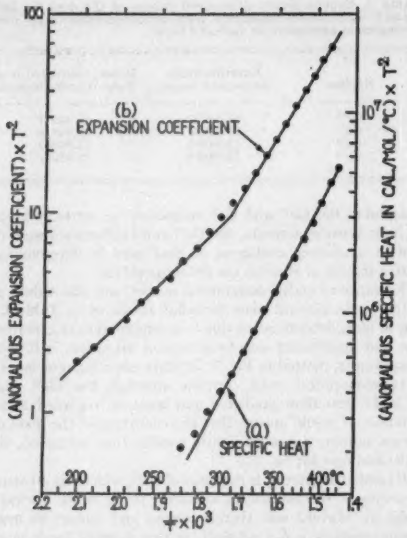

FIG. 2. (a) Anomalous specific curve in AgBr. (b) Anomalous expansion coefficient in AgBr (after Strelkow).

In consideration of the different experimental conditions, it seems certain that we must choose Eq. (3), rather than Eq. (2), for this temperature range of higher activation energy.

I am indebted to Professor R. Kubo for helpful suggestions and discussions.

[1] N. F. Mott and R. W. Gurney, *Electronic Processes in Ionic Crystals* (Clarendon Press, Oxford, 1940), p. 48.
[2] Reference 1, pages 41 and 47.
[3] The activation energy for ionic conduction between 100°C and 300°C was 17,800 cal/M. The value given by Koch and Wagner is 18,200 cal/M (reference 1, p. 46).
[4] A. W. Lawson, Phys. Rev. **78**, 185 (1950).
[5] P. G. Strelkow, Physik. Z. Sowjetunion **12**, 77 (1937).

On the Aggregation of Trapping Centers in Semiconductors or Insulators

TADATOSI HIBI AND TETSUO MATSUMURA
Research Institute for Scientific Measurements, Tôhoku University, Sendai, Japan
January 2, 1951

IN semiconductors or insulators, the trapping energy of electrons changes with the aggregation of their trapping centers (impurity centers, F-centers, etc.). On this mechanism, the change of work function of BaO with activation and the production of A-, C-, D-, E-centers, etc., in KCl can be explained quantitatively.[1-3]

A hydrogen-like model was used as trapping center, and the Heitler-London method was used for the calculation of the aggregation process of more than two centers. In the case of the aggregation of more than three centers, only the energy of highest level in the case, in which each level is occupied in turn by an electron from the lowest level, was calculated. The highest energy is generally given by

$$E = W_0 + \Sigma^{n-1}(C - J),$$

where W_0 is the first-order energy of electron, C and J are coulomb and exchange energies between the fixed center and any one of other centers, respectively.

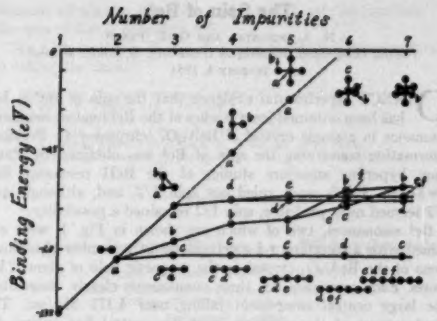

FIG. 1. Change in the trapping energy of an electron in BaO by the aggregation of impurities. The connected groups show the assumed types of aggregations of impurities.

As an example of semiconductors, BaO was chosen; and the trapping energy of an electron in each isolated impurity center was taken to be 1.32 ev. Assuming that the centers aggregate at intervals of two atomic distances where their wave functions do not overlap one another, the change in activation energy with aggregation of centers was calculated. The results obtained are shown in Fig. 1, and the experimental results of the work function distributed from 1.63 ev to 1.00 ev can be explained. It seems,

TABLE I. Absorption centers in KCl.

	F(ev)	A(ev)	E(ev)	R_1(ev)	D(ev)	R_2(ev)	C(ev)
Calculation	2.19	2.07	1.95	1.83	1.71	1.59	1.47
Mollnar (room temp.)	2.19			1.85		1.68	1.50
Petroff (−170°C)	2.19	2.07	1.93		1.70		1.52
Petroff (+20°C)	2.19			1.84		1.68	1.50
Scott and Bupp (room temp.)	2.19			1.85		1.68	1.50
Ottmer (room temp.)	2.19						1.50

however, that the aggregations shown by the dotted lines do not take place only with the thermal activation.

Figure 2 shows the results of similar calculations on the color centers in KCl which resulted from the consideration of the aggregation of F-centers. In Table I these results are compared with experimental results. It is evident that they are in good agreement quantitatively with these experimental results. The experimental result that the centers are produced in the order of

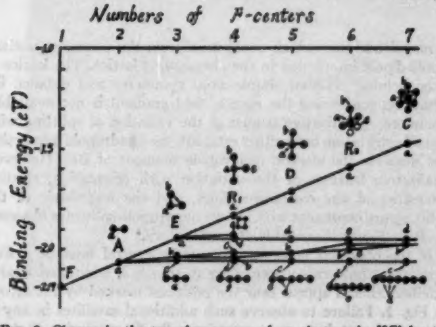

FIG. 2. Change in the trapping energy of an electron in KCl by the aggregation of F-centers. The connected groups show the assumed types of aggregations of F-centers.

A-, C-, D-, and E-centers, that the R-center is not observed at low temperatures, that the centers are destroyed by irradiation with light, etc., are explained qualitatively from the mechaniam of aggregation of centers. Also, Scott[3] and Bupp, increasing the temperature without irradiation of light, observed the change of color centers in KCl. On this theory their experimental result can be explained quantitatively as the production of R_1-, D-, R_2-, and C-centers at 300°C, 355°C, 395°C, and 455°C, respectively.

Using the results observed by Ottmer on F-center of alkali halides of many kinds, the wavelengths of absorption by color centers in alkali halides which are as yet unobserved, can be foreseen from this theory.

[1] F. Seitz, Revs. Modern Phys. 18, 384 (1946).
[2] S. Petroff, Z. Physik 127, 443 (1950).
[3] A. B. Scott and L. P. Bupp, Phys. Rev. 79, 341 (1950).

The Determination of the Energy of a Ferromagnetic Domain Boundary

HARVEY KAPLAN
Department of Physics, University of California, Berkeley, California
December 27, 1950

WILLIAMS and Shockley[1] have discussed an experiment for the determination of the surface energy of a ferromagnetic domain boundary (Bloch wall). The original calculations neglected the effect of the anisotropy of the wall energy; but this omission is remedied in a forthcoming publication[2] (dealing with actual experimental results), in which it is shown that the wall anisotropy plays a major role and modifies the previous calculations by a factor of the order of three. In the present letter we consider two further corrections to the theory of the experiment: the effect of including the K_2 term in the crystal anisotropy energy and the effect of deformation of the wall in going around the single crystal rectangle. It was thought to be worthwhile to look into these corrections, since the experiment may well develop into an important method of measuring the magnitude of the exchange integral in ferromagnetic substances. The notation is that of reference 1.

The wall energy density is computed in the usual manner[2] as

$$\sigma_w = 2(A)^{\frac{1}{2}} \int_{\theta_1}^{\theta_2} [g(\theta)]^{\frac{1}{2}} d\theta$$

Including the K_2 correction,

$$g(\theta) = K_1 \sin^2\theta \{1 + [(K_2 \sin^2 2\lambda / 4K_1) - (\tfrac{1}{2}\cos 4\lambda + \tfrac{1}{2})] \sin^2\theta - K_2 \sin^2 2\lambda \sin^4\theta / 4K_1\},$$

where θ is the angle the magnetization in the wall makes with the magnetization in the domain on the left, and λ is the angle the wall makes with the y axis.[1] On integration the wall energy is found to be

$$\sigma_w = 2(AK_1)^{\frac{1}{2}}[1 + \lambda^2 \ln(2/\lambda) + K_2\lambda^2/4K_1]$$

In the evaluation λ has been assumed to be small.

The total energy of the crystal is

$$E = 2\int_0^{y'} [-2I_s H x + \sigma_w (1 + x'^2)^{\frac{1}{2}}] dy.$$

Following reference 1, H is assumed proportional to y. Since λ is small, the approximation $\lambda = x'$ is made. The euler equation for the problem is then obtained. This equation is integrated once,

TABLE I. Calculations on wall displacement.

λ_{max} (radians)	W (cm)	J_I (amp)	J_{II} (amp)
0.3	6.22×10^{-4}	0.316	0.330
0.2	4.29	0.256	0.266
0.1	2.23	0.166	0.171
0.05	1.13	0.102	0.105
0.02	0.45	0.051	0.052
0.01	0.23	0.029	0.030

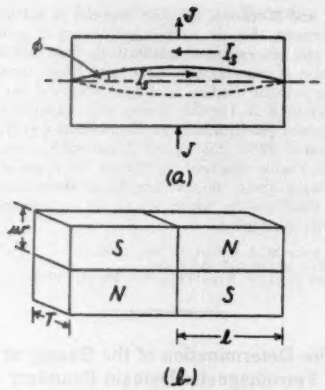

FIG. 1. (a) Top view of one leg of rectangle. (b) Approximate pole distribution due to gradual bending of wall.

using the boundary condition $x'=0$ when $y=\pm T/2$. The result is

$$\tfrac{1}{2}a[\tfrac{1}{4}T^2-y^2]=(K_2x'/2K_1)+2x'\ln(2/x'),$$

where

$$a=4\phi JI_s/10TL(K_1A)^{\frac{1}{2}}.$$

The form of the result is convenient for estimating the effect of the K_2 term.

It did not prove to be feasible to integrate again analytically. A numerical integration was carried out to determine the wall displacement, W. In this work the crystal dimensions given in reference 1 were used. The results given in Table I were obtained, taking $K_1=4.2\times10^5$ ergs/cm^3, and $K_2=1.5\times10^5$ ergs/cm^3 for iron. Here, J_I is the current without the K_2 correction, while J_{II} includes the K_2 term. The shape of the wall is effectively unchanged by the K_2 correction. Each value of W corresponds to a value of λ_{max}. The validity of the assumption of small λ is doubtful for $\lambda_{max}=0.3$. For the representative value $\lambda_{max}=0.1$, the K_2 correction is only about 2 or 3 percent.

In the preceding work the assumption was made that, although the current is applied at only one cross section of the crystal, the deformation caused in the wall is the same all around the crystal. This assumption is now justified by showing that a wall only locally deformed would give rise to a magnetostatic contribution to the crystal energy much larger than the excess energy of the wall due to its deformation. Looking at the leg to which the current is applied from the top, and assuming the wall to bend gradually back to its normal position, we see the situation shown in Fig. 1(a).

The discontinuity in the normal component of the saturation magnetization as a result of the curving wall results in a pole distribution which can be approximated by the arrangement of Fig. 1(b), where the pole density in each region is approximately $I\sim I_s\bar{\lambda}T/l$. Here, $\bar{\lambda}$ is the average angle the wall makes with the y axis. Considering the right-hand half only, the magnetostatic energy density can be approximated by the expression for the surface energy density of a series of coplanar strips, $\sigma_{ms}=0.85I^2w$. Hence, the total magnetostatic energy is

$$W_{ms}\sim(I_s\bar{\lambda}T/l)^2w\cdot w\cdot l.$$

The deformation wall energy is $\delta W_{wall}\sim\sigma_w lT\lambda^2$. Therefore, using as rough estimates $T\sim w\sim0.1$ cm, $\sigma_w\sim1$ erg/cm^2, $l\sim1$ cm, we obtain $\delta W_{wall}/W_{ms}\approx10^{-3}$. Hence, the wall can be assumed to be uniformly deformed around the crystal circumference to within about 3 percent.

I wish to thank Professor Charles Kittel for suggesting this work and for many helpful discussions.

[1] H. J. Williams and W. Shockley, Phys. Rev. **75**, 178 (1949).
[2] Williams, Shockley, and Kittel, to be published.
[3] L. Néel, Cahiers phys. **25**, 1 (1944).

The Spin of Be^9

N. A. SCHUSTER AND G. E. PAKE*
Physics Department, Washington University, St. Louis, Missouri
January 4, 1951

DIRECT experimental evidence that the spin of Be^9 is 3/2 has been obtained from studies of the Be^9 nuclear magnetic resonance in a single crystal of $BeAl_2O_4$ (chrysoberyl). Previous information concerning the spin of Be^9 was obtained by Paul[1] from hyperfine structure studies of the BeII resonance line $\lambda=3130$A. Paul's work ruled out spin 5/2, and, although spin 3/2 seemed most probable, spin 1/2 remained a possibility.

Be^9 resonances, two of which are shown in Fig. 1, were obtained with a recording r-f spectrometer at a number of orientations of the $BeAl_2O_4$ crystal in the magnetic field of about 7300 gauss. Each resonance has three components clearly discernible, the large central component falling near 4.377 Mc/sec. The displacement of the satellites from the central line varies, depending upon crystal orientation in the magnetic field, from essentially zero to 240 kc/sec for the crystal orientations thus far investigated.

Since the electric quadrupole interaction of a nucleus of spin $I>1/2$ with the gradient of an electric field breaks the nuclear resonance into $2I$ components,[2] the observed resonances offer reasonably unambiguous evidence for spin 3/2 if a quadrupole interaction is responsible for their structure.

Although it might be suggested that the splitting could originate with nuclear magnetic dipole-dipole interactions, which are known to produce resolvable splittings of resonances in certain crystals,[3] the observed Be^9 splitting exceeds by nearly two orders

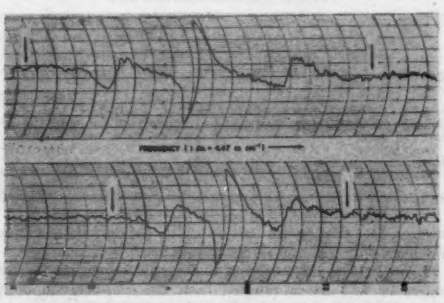

FIG. 1. Absorption curve derivatives of Be^9 magnetic resonances in a single crystal of $BeAl_2O_4$ for two crystal orientations in the magnetic field. The three quadrupole components of each resonance verify that the spin of Be^9 is 3/2. Vertical arrows mark the approximate positions at which additional components should occur if the patterns are quadrupole splittings corresponding to spin 5/2.

of magnitude that which could arise from the strongest nuclear dipole-dipole interaction in the chrysoberyl lattice. The lattice is orthorhombic[4] without simple axial symmetry and detailed information concerning the electric field gradient is not available. Therefore, quantitative studies of the variation of splitting with crystal orientation can neither establish the quadrupole interaction nor measure the electric quadrupole moment of Be^9. However, qualitative features of the variation with orientation, relative intensities of the component lines, and the magnitude of the splitting are consistent with known quadrupole splittings observed by Pound[5] and observed in this laboratory.[6]

If the observed lines were the three central lines of a five-component pattern corresponding to spin 5/2, additional weaker satellites should appear near the positions marked by the arrows in Fig. 1. Failure to observe such additional satellites in any of the experimental resonances confirms Paul's conclusion that the spin of Be^9 is not 5/2. The mere existence of an electric quadrupole

moment eliminates spin 1/2, and it seems safe to conclude that the spin of Be[9] is definitely 3/2.

We wish to thank W. G. Zinn and R. H. Sands for assistance in taking the data.

[*] Assisted by the joint program of the ONR and AEC.
[1] W. Paul, Z. Physik 117, 774 (1941).
[2] R. V. Pound, Phys. Rev. 79, 685 (1950).
[3] G. E. Pake, J. Chem. Phys. 16, 327 (1948).
[4] W. L. Bragg and G. B. Brown, Z. Krist. 63, 122 (1926).
[5] N. A. Schuster and G. E. Pake, Phys. Rev. 81, 157 (1951).

Magnetic Domain Patterns on Nickel Crystals

MIKIO YAMAMOTO AND TAKAO IWATA
Research Institute for Iron, Steel, and other Metals, Tôhoku University, Sendai, Japan
December 18, 1950

WE have succeeded in observing the magnetic powder patterns on single crystals of pure nickel whose ferromagnetic anisotropy constant $K<0$. These patterns are as simple and interpretable as those obtained by Williams and his collaborators on crystals of an iron-silicon alloy containing 4 percent silicon[1] ($K>0$) and of a nickel-cobalt alloy containing 60 percent cobalt[2] ($K<0$). The surfaces of our crystals were polished parallel to the $(\bar{1}10)$ planes very carefully, and were annealed in vacuum and polished electrolytically. The powder patterns formed with magnetite colloid were observed under the microscope with the usual light field with vertical illumination.

Two of the typical patterns and their interpretations are shown in Figs. 1 and 2. In Fig. 1 the 180° and 109° walls form the parallelogram net, and short 71° walls are also in evidence at the corners of the parallelograms. This pattern is similar to that observed on a cobalt-nickel crystal by Walker and Bozorth.[2] In addition, the tree pattern of which the trunk is the 180° wall, corresponding to the tree pattern of the first kind on the (100) planes of silicon-iron crystals,[1] is seen. In this tree pattern the angles between the branches and the trunk are about 35° and 55° on both sides of the trunk, as is expected theoretically. Moreover, as the inclination of the surface to the $(\bar{1}10)$ plane becomes larger, the branches do not become thicker but radiate smaller secondary, ternary, and other branches.

Figure 2 shows the 71° walls and the tree pattern of the second kind of which the trunk is the 71° wall. The surface of the crystal coincides with the $(\bar{1}10)$ plane at the middle of the upper part of the figure, and on the lower and left-hand parts it is inclined to the crystal plane. When this inclination is slight, the 71° wall becomes the trunk and radiates branches perpendicularly on both sides. As the inclination increases, however, branches of another type, making an angle of about 35° with the trunk, are radiated symmetrically; and thus the magnetostatic energy is greatly reduced. It is to be added that there have been observed also branches perpendicular to the trunk of the 109° wall, belonging to a third kind of tree pattern which is to be expected theoretically.

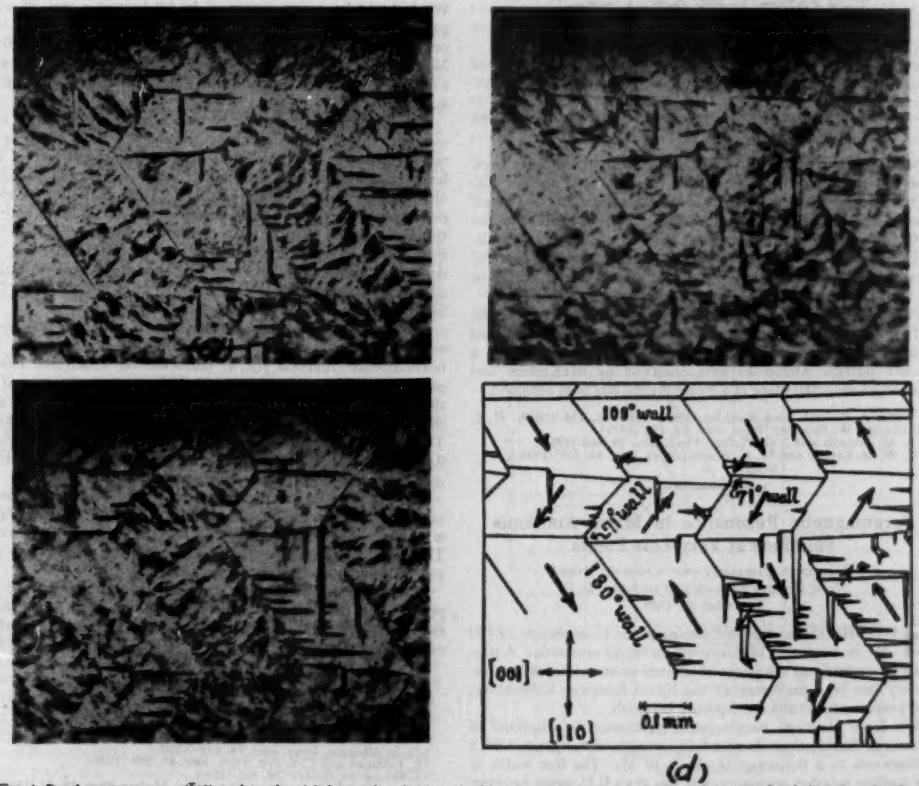

FIG. 1. Powder patterns on a $(\bar{1}10)$ surface of a nickel crystal as demagnetized by alternating magnetic field parallel to the [110] direction, showing the effect of applying a weak magnetic field normal to the surface: (a) normal field directed outward from the surface, (b) normal field zero, (c) normal field directed into the surface, (d) diagram of directions of magnetization in the domains and crystal axes.

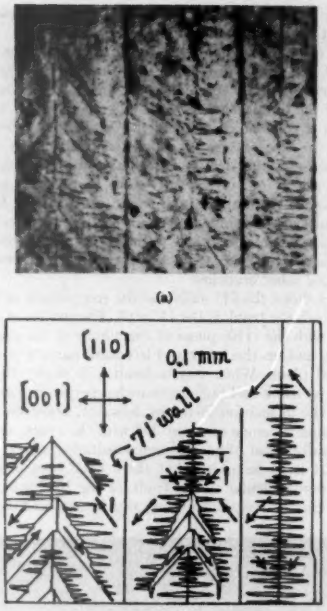

FIG. 2. Powder pattern on a (1̄10) surface of a nickel crystal as demagnetized by alternating field parallel to the [001] direction.

Although the domain patterns shown in the figures have been observed on nearly the same portion of the crystal surface, the pattern of Fig. 1 is characteristic of the state demagnetized by an alternating magnetic field parallel to the [110] direction in the (1̄10) plane, while we always observe the pattern of Fig. 2 immediately after the electrolytic polishing; and the domain pattern, obtained after demagnetization by an alternating field parallel to the [001] direction in the (1̄10) plane, is similar to the latter.

Finally, it should be noted that, even when the strain in the surface of the crystal is large, we never observe a maze pattern such as is reported for iron and silicon-iron crystals, although a dot-like pattern similar to that observed by McKeehan and Elmore[3] on the (100) plane of a nickel crystal has been obtained.

[1] Williams, Bozorth, and Shockley, Phys. Rev. 75, 155 (1949). H. J. Williams and W. Shockley, Phys. Rev. 75, 178 (1949).
[2] R. M. Bozorth and J. G. Walker, Phys. Rev. 79, 888 (1950).
[3] L. W. McKeehan and W. C. Elmore, Phys. Rev. 46, 529 (1934).

Paramagnetic Resonance in Metal Ammonia Solutions at Very Low Fields

MARTIN A. GARSTENS AND ALDEN H. RYAN
Naval Research Laboratory, Washington, D. C.
December 29, 1950

HUTCHISON has reported paramagnetic resonance at 23,700 Mc in a solution of potassium in liquid ammonia.[1] A program of research on resonance of sodium in ammonia at low frequency has been underway at the Naval Research Laboratory, and preliminary results are reported herewith.

We have observed paramagnetic resonance in solutions of sodium in liquid ammonia at a field strength of 6.7 gauss, which corresponds to a frequency of about 19 Mc. The line width of the sodium solution resonance was less than 0.25 gauss between the points of maximum slope on the absorption line. The observations were made at dry ice temperatures and at atmospheric pressure. About 10 cc of solution was used, the concentration for sodium varying from 0.1 to 0.5 M per liter of ammonia.

For all of the concentrations used the signal was much weaker than that observed in diphenyl picryl hydrazyl $(C_6H_5)_2N-NC_6H_2(NO_2)_3$ at these same low fields (i.e., as much as fifty times smaller in signal to noise). The signal strength appears to depend very sharply on the concentration of the solution. The exact relationship between concentration and signal strength is being investigated further.

The resonance in Na was also observed at 9230 Mc which correspond to a field of about 3300 gauss.

Similar observations have been made at these low fields on solutions of potassium in ammonia, with results which agree with the observations of Hutchison.[1]

[1] C. A. Hutchison and R. C. Pastor, Phys. Rev. 81, 282 (1951) and private communication.

Heat Production in Potassium

DAVID E. ALBURGER
Brookhaven National Laboratory, Upton, Long Island, New York*
January 2, 1951

RECENT determinations of the decay constants, gamma-ray and beta-ray energies, and the shape of the beta-ray spectrum of K^{40} now permit a more precise evaluation of the rate of heat production in potassium. Experiments of Sawyer and Wiedenbeck[1] have shown that 28.3±1.0 beta-rays and 3.6±0.3 gamma-rays are emitted per gram K per sec. The gamma-ray occurs in the *K*-capture branch and has an energy of 1.47±0.01 Mev, an average value taken from the measurements of Bell and Cassidy,[2] of Pringle, Standil, and Roulston,[3] and of Hofstadter and McIntyre.[4]

The predominant heat energy occurs in the beta-branch and estimates thus depend strongly on the characteristics of the beta-ray spectrum. A calculation of the mean beta-ray energy of K^{40} has been made based on the work of Bell, Weaver, and Cassidy,[5] of Alburger,[6] and of Feldman and Wu.[7] Their values for the end-point energy have a weighted mean of 1.34±0.02 Mev, and all three groups find that the shape of the spectrum agrees with the third forbidden correction factor above 500 to 700 kev. Since the deviations below 500 kev are attributed to source thickness effects, it is assumed here that the spectrum has the third forbidden shape over the entire range of energies.

The idealized momentum plot for a third forbidden type beta-emitter with end point at 1.34 Mev was constructed using the nonrelativistic function $f(Z, \eta)$ corrected for relativistic effects according to the table of Feister.[8] This was then converted to the energy distributions $N(W)WdW$ and $N(W)dW$ *versus* W and the areas under these curves were measured with a planimeter. The ratio of areas gives a mean energy for K^{40} beta-rays of 0.605±0.010 Mev, somewhat higher than the older value, 0.49 ±0.06 Mev, listed by Marinelli, Brinckerhoff, and Hine.[9]

The total heat production using the revised beta- and gamma-ray energy values and Sawyer and Wiedenbeck's emission rates is readily computed to be $(27\pm1)\times10^{-6}$ cal per gram K per year. This may be compared with $(22\pm3)\times10^{-6}$ cal per gram K per year calculated by Gráf[10] from earlier data.

The author is indebted to Dr. Francis Birch of Harvard for pointing out the desirability of a re-evaluation of the mean beta-ray energy and to Mrs. Dale Meyer who carried out the detailed calculations.

* Under contract with AEC.
[1] G. A. Sawyer and M. L. Wiedenbeck, Phys. Rev. 79, 490 (1950).
[2] P. R. Bell and J. M. Cassidy, Phys. Rev. 79, 173 (1950).
[3] Pringle, Standil, and Roulston, Phys. Rev. 77, 841 (1950).
[4] R. Hofstadter and J. A. McIntyre, Phys. Rev. 80, 631 (1950).
[5] Bell, Weaver, and Cassidy, Phys. Rev. 77, 399 (1950).
[6] D. E. Alburger, Phys. Rev. 78, 629 (1950).
[7] L. Feldman and C. S. Wu, Phys. Rev. 81, 298 (1950).
[8] I. Feister, Phys. Rev. 78, 375 (1950).
[9] Marinelli, Brinckerhoff, and Hine, Revs. Modern Phys. 19, 25 (1947).
[10] T. Gráf, Phys. Rev. 74, 831 (1948).

Periodic Deviations in the Schottky Effect for Polished Tantalum*

G. B. Finn, W. B. LaBerge,† and E. A. Coomes
University of Notre Dame, Notre Dame, Indiana
January 5, 1951

IT has been pointed out[1] that irregularities on an emitter surface may limit the accuracy with which certain observed emission phenomena can be checked against fundamental theory. This might become a serious consideration with respect to Schottky deviations, where an accurate determination of the absolute value of the electric field is necessary for a comparison of experimental data with theoretical computations. To examine this limitation, Schottky data were taken on polished tantalum wire[2] by the method previously described,[3] and the deviations for this case were compared with data previously obtained for unpolished wire.[3] A comparison of results is given in Fig. 1, in which the

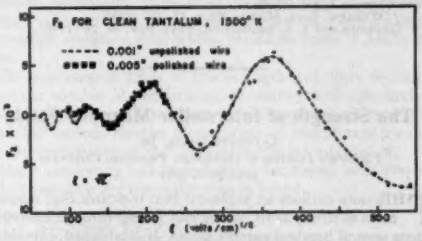

FIG. 1. Periodic deviations in the Schottky effect for a polished tantalum wire.

squares represent the data for polished wire, while the dots are the results on unpolished tantalum. The temperature for both cases was maintained at 1500±10°K. It may be noted that the squares locate positions of maxima and minima which are identical with those fixed by the dots, and that the amplitudes for the two cases are in good agreement with each other within the range of fields studied.

Under microscopic examination irregularities of the order of a quarter-wire diameter were found on the unpolished wire, but such irregularities were not observed on the polished wire. On the evidence of these data it does not appear that errors introduced by imperfections of the unpolished wire are of importance in periodic deviation experiments, at least for fields below 5×10^6 v/cm.

* This research was sponsored by the U. S. Navy Bureau of Ships.
† Now at U. S. Naval Ordnance Test Station, Inyokern, California.
[1] J. A. Becker, Revs. Modern Phys. 7, 95 (1935).
[2] The 5-mil tantalum wire was polished through the courtesy of Mr. H. W. Weinhart of Bell Telephone Laboratories.
[3] Munick, LaBerge, and Coomes, Phys. Rev. 80, 887 (1950).

The Latitude Effect of Cosmic-Ray Neutrons*

W. P. Staker,† M. Pavalow, and S. A. Korff
New York University, University Heights, New York, New York
January 2, 1951

CONTINUING our study[1] of the neutrons produced by the cosmic radiation, a set of balloon flights to study neutrons at high elevations was carried out from Churchill, Manitoba, geomagnetic latitude approx. 69°N during August, 1950. The techniques used were similar to those used in previous flights and already described.[2] The counting rates of neutron counters, filled with enriched and with depleted BF_3, were obtained up to altitudes of 62,000 ft. Figure 1 shows the neutron counting rate derived from the data, plotted on the same scale as data obtained further south and previously reported. The maximum neutron counting rate is 2.1±0.2 times that obtained at 55°N geomagnetic latitude, and the area under the curve is also double the value at 55°. The maximum occurred at an altitude of 55,800 ft, as compared with 53,600 ft at 55° and 51,700 ft at 30°. The altitude of the maximum is below that of the maximum in the total intensity of the soft component. The slope of the neutron curve, near the maximum where the statistical accuracy is the greatest, is somewhat steeper than the corresponding part at more southern latitudes.

It will be noted that the increase in neutron intensity with latitude is greater than that observed in the total intensity of the radiation by the well-known experiments of Bowen, Millikan, and Neher,[3] and by Carmichael and Dymond.[4] They obtain an increase of only about 10 percent in this 55° to 69° latitude interval. This situation is similar to that further south, where in the interval between 30.4 and 54.7°N latitude the neutron intensity also increases faster than does the total intensity.

The small change in the total intensity between 55° and 69° has been used to support the view that the primary spectrum of incoming radiation had a sharp cutoff at about 2 Bev, presumably owing to the sun's magnetic field. The neutron measurements suggest that this explanation is not correct and that the sun's field is considerably less than is sometimes assumed. The surface field of 50 gauss required to account for the 2-Bev cutoff is in our view too large, and is probably closer to 5 gauss. This view is also supported by the observations of Pomerantz.[5] The small latitude dependence in the total intensity is not surprising, since the total intensity measurements measure the flux, $\phi(E)$, multiplied by the energy, E, carried by each particle, $\int E\phi(E)dE$, and the contribution by the many low-energy particles near the poles is not great.

The number of neutrons, $N(E)$, at any latitude will be determined by the number of primaries, $P(E)$, a function of the energy, multiplied by the probability, $R(E)$, that each primary shall, through secondary processes, produce a neutron. Thus, we may say: $N(E)=P(E)R(E)$. The ratio of the number of neutrons at various latitudes is determined in these experiments. The ratio of the number of primaries, if determined by the familiar -1.8-power spectrum, allows the ratio of the probabilities of primaries of two different energies to produce neutrons to be evaluated.

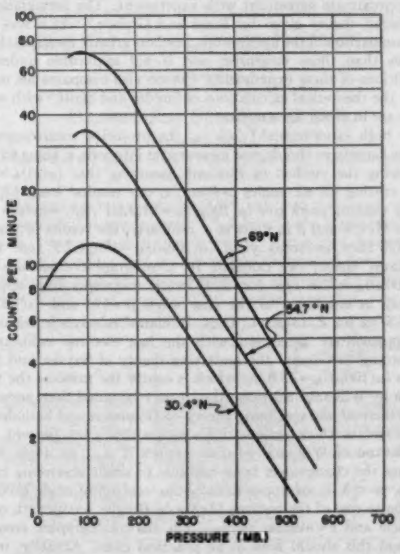

FIG. 1. Neutron counting rate as a function of altitude at various latitudes

We find that if the probability of producing neutrons is proportional to the energy of the primary, the -1.8 spectrum predicts more neutrons than are observed. Even if we assume that the probability increases more slowly than a first power of the energy, there are still too few neutrons. It appears that the primary spectrum is probably not properly represented by the -1.8 power in the energy interval between 2 Bev and 300 Mev, but the exponent is likely a number closer to unity.

The experiments will be reported in fuller detail at a later date.

The authors wish to acknowledge with thanks the assistance of several persons and agencies whose cooperation has made this work possible. They wish to thank Dr. Thomas McGavack of New York Medical College Metropolitan Hospital Research Unit at Welfare Island, who allowed tests to be made in their pressure-chamber. Also, Mr. G. W. Rowley of the Defense Research Board of Canada and Dr. K. C. Fisher, Superintendent of the Defense Research Northern Laboratory at Churchill, kindly assisted in this work, as did Dr. M. Pomerantz of the Bartol Research Foundation and M. J. Swetnick, H. Neuberg, and S. Levesque of the New York University Cosmic-Ray Group.

* This work was assisted by the joint program of the AEC and ONR.

† Now at Argonne National Laboratory, Chicago, Illinois.

[1] W. P. Staker, Phys. Rev. **80**, 52 (1950); W. O. Davis, Phys. Rev. **80**, 150 (1950).
[2] Pavalow, Davis, and Staker, Rev. Sci. Instr. **21**, 259 (1950).
[3] Bowen, Millikan, and Neher, Phys. Rev. **53**, 855 (1938).
[4] H. Carmichael and E. G. Dymond, Proc. Roy. Soc. (London) **117A**, 321 (1939).
[5] M. A. Pomerantz, Phys. Rev. **77**, 830; **78**, 325 (1950).

Multiple Scattering of Fast Particles in Photographic Emulsions

L. Voyvodic and E. Pickup
Physics Division, National Research Council, Ottawa, Canada
December 8, 1950

In recent experiments[1,2] the small angle scattering of fast particles in photographic emulsions has been measured fairly accurately. The main purpose of this note is to point out that the detailed multiple scattering theory of Williams[3] gives results in approximate agreement with experiment. The formulation of Williams' theory given by Rossi and Greisen,[4] which was used for comparison in the above work, predicts greater mean scattering angles than those measured, and is not applicable under the conditions of these experiments. Corson also compares his results with the theoretical calculations of Snyder and Scott,[5] with which they are in closer agreement.

In both experiments[1,2] $\langle\alpha(q)\rangle_{Av}$, the projected mean-angle between successive chords, was measured at intervals, q, along a track, following the method of Fowler.[6] Assuming that $\langle\alpha(q)\rangle_{Av}\propto(q)^{\frac{1}{2}}$, and cutting off all angles $>4\langle\alpha(q)\rangle_{Av}$ our results[1] from Li(p,γ) γ-ray electron pairs give $\langle\alpha(100\mu)\rangle_{Av}=21.3\pm1°/p\beta$, where p is in units Mev/c and β in units of c. Similarly, the results of Corson[2] on 115-Mev electrons yield $\langle\alpha(100\mu)\rangle_{Av}=19.6\pm2.5°/p\beta$. From Williams' theory[3] we calculate for photographic emulsions that $\langle\alpha(100\mu)\rangle_{Av}=22.8°/p\beta$ for $Z/137\beta\ll1$ (corresponding approximately in emulsions to the case when $\beta\sim1$),[7] and $\langle\alpha(100\mu)\rangle_{Av}=25.8/p\beta$ for $Z/137\beta\gg1$. Thus, Williams' relativistic relation is in approximate agreement with the fast electron calibrations. According to Corson[2] the scattering theory of Snyder and Scott gives $\langle\alpha(100\mu)\rangle_{Av}=23.0/p\beta$ which is nearly the same as the value given by Williams' relation. Also, it may be noted that, according to Williams,[3] the scattering theory of Goudsmit and Saunderson[9] gives results which agree with his own within a few percent.

The use of Williams' relation applies if α_{min}, an angle which defines the change-over from multiple to single scattering conditions, is $<\lambda/b$, an upper limit to the scattering angle given by the finite size of the nucleus ($2\pi\lambda=$ de Broglie wavelength of the particle and $b=$ nuclear radius). For the photographic emulsion method this should hold in all practical cases. Actually, in the detailed statistical treatment,[3] the variation of $\langle\alpha(q)\rangle_{Av}$ with q is more rapid than $(q)^{\frac{1}{2}}$, and the cutoff for the scattering distribution is not exactly $4\langle\alpha(q)\rangle_{Av}$ but depends slightly on q, so that, in practice, the results should be analyzed explicitly for each q used in the experiments. In our experiment,[1] where $q<100\mu$, the value of $\langle\alpha(100\mu)\rangle_{Av}$, as deduced by assuming $\langle\alpha(q)\rangle_{Av}\propto(q)^{\frac{1}{2}}$, should be increased by a few percent, bringing the results into closer agreement with Williams' relation. On the other hand, when $q>100\mu$, i.e., measuring particles with $p\beta>100$ Mev, $\langle\alpha(100\mu)\rangle_{Av}$ will be less than that deduced by assuming $\langle\alpha(q)\rangle_{Av}\propto(q)^{\frac{1}{2}}$. A more detailed analysis of our scattering results will be published when they are completed.

[1] L. Voyvodic and E. Pickup, Phys. Rev. **81**, 471 (1951).
[2] D. R. Corson, Phys. Rev. **80**, 303 (1950).
[3] E. J. Williams, Proc. Roy. Soc. (London) **169**, 531 (1939); Phys. Rev. **58**, 292 (1940).
[4] B. Rossi and K. Greisen, Revs. Modern Phys. **13**, 241 (1941).
[5] H. Snyder and W. Scott, Phys. Rev. **76**, 220 (1949).
[6] P. H. Fowler, Phil. Mag. **41**, 169 (1950).
[7] It is probably better to use the refinement of Williams' theory given by Molière, who considers all values of $Z/137\beta$. Y. Goldschmidt-Clermont, Nuovo Cimento **7**, 331 (1950).
[8] E. J. Williams, Revs. Modern Phys. **17**, 217 (1945).
[9] S. Goudsmit and J. L. Saunderson, Phys. Rev. **57**, 24 (1940).

The Strength of Interstellar Magnetic Fields

Leverett Davis, Jr.
California Institute of Technology, Pasadena, California
January 2, 1951

THIS note outlines an argument that indicates that magnetic fields as strong as 10^{-4} gauss may extend through interstellar regions several hundred parsecs across. If established, this should be significant both in astrophysics and in the study of cosmic rays.

The experimental basis for the argument is the discovery by Hiltner[1] and by Hall[2] that if the light of a star is greatly weakened by its passage through interstellar dust, it is usually partially plane polarized to a small extent. The spatial anisotropy responsible must be fairly uniform, in at least one region, over a distance of some 200 parsecs, since the planes of polarization for different stars are found to be nearly parallel[3] for low galactic latitude and galactic longitudes between 80° and 120° (or perhaps even 170°) and since the mean distance to the obscuring matter, where the polarization presumably occurs, is at least 300 parsecs. The key assumption of the argument is that this anisotropy is due to an interstellar magnetic field. A survey of other possible anisotropies seems to reveal no plausible basis for the observed polarization, while a magnetic field is required both by Spitzer and Tukey[4] and by Davis and Greenstein[5] for their theories of the origin of the polarization. In the theory of Spitzer and Tukey the field in this region is mainly normal to the plane of the galaxy; in that of Davis and Greenstein it is mainly parallel to the plane of the galaxy, perhaps along the spiral arms or perhaps making random whirls in this plane. Regardless of the exact mechanism, if a magnetic field is involved, it must have some uniformity corresponding to the observed nearly parallel alignment of the planes of polarization for different stars.

A lower limit to the strength of the field can be deduced from the requirement that the field be strong enough to maintain its large scale anisotropy in the presence of the motions of the interstellar material. This section of the argument is based on the concepts of magneto-hydrodynamics introduced by Alfvén[6] and used by Fermi[7] and Schlüter and Biermann.[8] Because of its high conductivity the interstellar medium is coupled to the magnetic field, no relative motion being permitted normal to the field. When the field is weak, the situation is dominated by the material which, as it moves, drags the lines of force with it, forming a very crooked pattern in which the directions of the field would change greatly in distances of the order of 10 parsecs. This is the situation contemplated by Fermi; but if the field is strong, it dominates the situation and any motion of the matter will be similar to that of a bead moving on a vibrating string, the lines of force not being sharply bent by the moving matter. The observed approximate

parallelism of the planes of polarization requires the latter situation. If the bending of the lines of force in a vibration is to be less than 0.2 radians, then it follows from Alfvén's formulas[9] that the connection between the magnetic field and the maximum transverse velocity of the material, v_t, is

$$B > 5v_t(4\pi\rho)^{\frac{1}{2}} \text{ gauss}, \quad (1)$$

where ρ is the density of the interstellar medium. Now v_t is $2^{\frac{1}{2}}$ times the root mean square transverse velocity and is 2 times the root mean square component along the line of sight, which may be taken to be 7½ km/sec on the basis of Adams' measurements[10] of the velocities of discrete clouds of atoms producing the multiple interstellar absorption lines. Thus, take as typical $v_t = 1.5\times10^6$ cm/sec and $\rho \geq 10^{-23}$ g/cm³ for the clouds of matter producing the lines and those producing the polarization. Then Eq. (1) gives $B \geq 10^{-4}$ gauss. Some additional support for such a large value of the magnetic field is given by the fact that in order to explain the observed interstellar polarization Spitzer and Tukey require slightly stronger fields in their detailed theory, while Davis and Greenstein require a field whose minimum value is nearly this large.

The existence of fields of this strength and their dominance over the motion of the interstellar matter indicates that the concept of isotropic turbulence may not apply to the interstellar gas.[8] The various theories of the origin of cosmic rays may also require modification if such field strengths are established.

Many interesting and most helpful discussions with Professor J. L. Greenstein are gratefully acknowledged.

[1] W. A. Hiltner, Science 109, 165 (1949).
[2] J. S. Hall, Science 109, 166 (1949).
[3] J. S. Hall and A. H. Mikesell, Pub. U. S. Naval Obs. 17, Part 1 (1950). see Figs. 4 to 7.
[4] L. Spitzer and J. W. Tukey, Science 109, 461 (1949); Astrophys. J., to be published.
[5] L. Davis and J. L. Greenstein, Phys. Rev. 75, 1605 (1949).
[6] H. Alfvén, *Cosmical Electrodynamics* (Oxford University Press, 1950).
[7] E. Fermi, Phys. Rev. 75, 1169 (1949).
[8] A. Schlüter and L. Biermann, Z. Naturforsch. 5a, 237 (1950).
[9] Reference 6, p. 80.
[10] W. S. Adams, Astrophys. J. 97, 105 (1943).

Scintillation Pulse Sizes of Solid Noncrystalline-Type Phosphors

M. G. Schorr and E. C. Farmer
Physics and Electronics Section, Tracerlab, Inc., Boston, Massachusetts
January 2, 1951

SINCE the initial report[1] on the solid noncrystalline-type phosphor, a more careful investigation of the relative pulse sizes from these scintillation materials under different types of radiation has been made. The solid phosphors are prepared by method (2) as given in reference 1. For some applications where large light pulses are not required, the plastic phosphor offers several advantages.

Measurements have been made using a Jordan-Bell type amplifier with a 0.2-μsec rise time. Data were taken utilizing three different photo-multiplier tubes: RCA 5819, 1P21, and 1P28 at fixed tube voltages and at room temperature. All samples studied were 5 mm thick. Integral bias curves were obtained and then analyzed to give average pulse sizes. Here the average pulse height results are proportional to the area under the integral bias curves divided by the extrapolated counting rates. Table I summarizes some representative values obtained in this fashion using several of each of the different type photo-tubes and different samples of plastic phosphor. The stilbene used in the experiments was purified and grown in our laboratories. Also included are values for a typical liquid phosphor. The results of other authors are included for comparison.

Although Kallmann's value represents integrated output current, it is included here because it should also be proportional to average pulse size. Of particular interest from the table is the relative improvement of the plastic phosphor on using the ultraviolet sensitive photo-multiplier tubes. A rough analysis of these

TABLE I. Ratios of pulse heights of several phosphors.

Tube type	Stilbene/1 percent terphenyl in plastic β's and γ's	Po-α's	Anthracene/1 percent terphenyl in xylol β's and γ's	Anthracene/stilbene β's and γ's
RCA 5819	6.0	3.5	7.3	1.8
Harrison[a]			2.9	
Hofstadter[b]				1.67
RCA 1P21	3.5		2.5	1.3
Harrison[a]			2.0	
Montgomery[c]			3.3[e]	
RCA 1P28	3.4		2.3	1.2
Harrison[a]			1.5	
Kallmann[d]			2.2	

[a] See reference 2.
[b] R. Hofstadter, Nucleonics, p. 69 (May, 1950).
[c] C. G. Montgomery and D. D. Montgomery, Phys. Rev. 80, 737 (1950).
[d] H. Kallmann and M. Furst, Phys. Rev. 79, 857 (1950).
[e] This value for both cosmic particles and gamma-rays.

data based on the average spectral responses of the three different type photo-multiplier tubes yields an emission maximum of about 3700A for the plastic phosphor, which is in good agreement with the emission spectra of terphenyl liquids as reported by Harrison.[3] However, work is in progress to obtain more accurate emission data. Further, it is estimated that for the light geometry employed that each Sr-90 beta-particle results in the emission of about 6 photo-electrons at the photo-cathode of the RCA 5819 tube as compared with 63 for anthracene. One could expect to improve these figures by a factor of two with better optical coupling. Also, our investigations indicate that the pulse size increases with increase in degree of polymerization.

Since one possible application of the plastic phosphor would lie in the use of very large samples, the light pulses from a long rod (3 cm diam×20 cm) has been studied under irradiation from a beta-source. Preliminary results give total light transmitted through 20 cm of material about ¼ that of the light generated near the photo-tube end of the rod with a corresponding loss in counting efficiency.

Information on both the "long rod" experiments and studies on the effect of polymerization will be reported at a later date.

[1] M. G. Schorr and F. L. Torney, Phys. Rev. 80, 474 (1950).
[2] F. G. Harrison and G. T. Reynolds, Phys. Rev. 79, 732 (1950).

Gamma-Ray Spectrum of K^{40}†

Myron L. Good
Department of Physics, Duke University, Durham, North Carolina
December 4, 1950

THE gamma-ray spectrum of K^{40} has been measured using a scintillation spectrometer. The crystal was a one-inch cube of NaI-Tl mounted as shown in Fig. 1. A modified Jordan and Bell pulse amplifier and an electronic differential pulse height discriminator were employed. Amplifier gain and discriminator window width were monitored by a pulse generator, the pulse

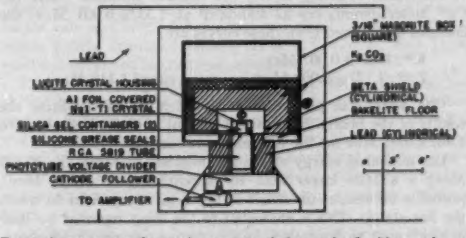

FIG. 1. Arrangement of crystal, sources, and photo-tube. In this experiment the entire cross-hatched region was filled with K_2CO_3.

voltage measurement being made by a standard cell potentiometer which also served to monitor the photo-tube supply voltage.

The source of K^{40} was 25 lb of normal potassium carbonate in a box surrounding the crystal housing (Fig. 1). The beta-shield was 1.5-mm brass in this experiment. For comparison spectra, Co^{60} and Zn^{65} were used. They were placed at position *I* (Fig. 1) to minimize scattering effects.

Photo-tube gain was monitored during the data run by means of a standard source of gamma-radiation placed at position *II*. Gain shifts of one or two percent were encountered and corrected.

The differential pulse height distributions of Zn^{65}, Co^{60}, and K^{40} were recorded, corrections being made for amplifier linearity and window width variations. The K^{40} background was subtracted from the comparison spectra. For the K^{40} itself, background was negligible. The data (Fig. 2) show photo-electron lines well resolved from the Compton distributions. The annihilation quanta of the (≈3 percent abundant) positrons[1] of Zn^{65} yield a prominent photo-electron line (P_2). The Compton edge is lost in the counts arising from backscattered radiation. The photo-electron line

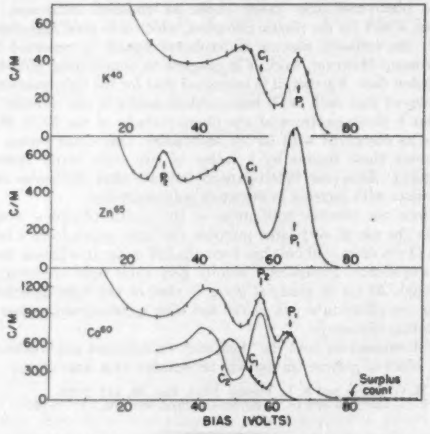

FIG. 2. Pulse height distributions from gamma-rays on NaI-Tl. The photo-electron lines are marked by *P*, the calculated Compton maxima by *C*. The area of the rectangle on the Co^{60} curve is equal to the surplus count at 79 v. The various energy scales are not the same. The Co^{60} curve was resolved into two components by making use of the known energy ratio of the two gamma-rays and by using the Zn^{65} line shape for the shape of the photo-electron line of the lower gamma-ray of Co^{60}. The sums of the counting rates for the points on the two component curves equal the counting rates for the experimental points of the upper curve. This procedure only moved the upper photo-electron line by ≈1 percent.

centers were located using Gaussian plots, which they fit very well. Surplus counts revealed no high energy gammas in K^{40} or in Zn^{65}. The surplus count obtained with Co^{60} is undoubtedly due to coincident counting of the two cascade gammas. Using the Co^{60} upper gamma-ray as standard[2] at 1.332±0.001 Mev, the energies determined from these curves are:

K^{40}: 1.459±0.007 Mev
Zn^{65}: 1.127±0.009 Mev (accepted value[3] 1.118 Mev).

This work was performed independently and confirms the results of the nearly identical experiment of Bell.[4] Bell obtained 1.462±0.01 Mev for the K^{40} gamma-ray energy.

The measured energy of the annihilation quantum line (0.520 Mev) is a little larger than the accepted value (0.511 Mev), probably because of the shape of the large background on which the line stands. This is analogous to the effect reported by Bell[4] in which m_0c^2, as determined by subtracting pair-peak from photo-peak energies, is consistently too low.

The error given for K^{40} is smaller than that for Zn^{65} because in the case of K^{40}, the comparisons to the standard source were made without turning the tube off, and hence are more consistent. About two-thirds of the errors arise from tube gain shifts.

The author wishes to express his indebtedness to Drs. Walter M. Nielsen and Henry W. Newson for their cooperation in this work.

† This work was supported in part by joint contract with ONR and AEC.

[1] W. M. Good and W. C. Peacock, Phys. Rev. 69, 680 (1946).
[2] Lind, Brown, and DuMond, Phys. Rev. 76, 591A, 1838 (1949).
[3] Jensen, Laslett, and Pratt, Phys. Rev. 76, 430L (1949).
[4] Bell and Cassidy, Phys. Rev. 79, 173L (1950).
[5] Bell, Science 112, 7 (1950).

The Fast Neutron Disintegration of C^{12} and B^{10}

J. L. PERKIN
Wheatstone Physics Laboratory, King's College, London, England
January 8, 1951

BORON-LOADED nuclear research emulsions were exposed to neutrons with energies extending up to 24 Mev. The neutrons were produced from a lithium target bombarded by 7-Mev deuterons from the Cavendish Laboratory cyclotron.

Calculations similar to those described by Green and Gibson[1] were carried out to identify the 700 disintegration stars observed in the emulsion with the following results: (a) 485 stars caused by the $C^{12}(n, n)3\alpha$ reaction, (b) 100 stars caused by the $B^{10}(n, H^3)2\alpha$ reaction, (c) 35 stars which could have been caused by either reaction, (d) 80 stars which did not satisfy either of the calculations.

The disintegration of the compound nuclei C^{13} and B^{11} formed in these reactions may proceed through a number of possible intermediate stages. If the experimental values for the energies of the emitted particles are used, the excited states of the nuclei involved in these various possible modes of disintegration can be calculated for each star. Comparison of the results with the values of the excited states found in previous experiments[2] shows that most, if not all, of the disintegrations proceeded via an intermediate stage involving the Be^8 nucleus.

A histogram of the values of the excited states of Be^8 for the $B^{10}(n, H^3)2\alpha$ reaction is shown in Fig. 1(a). Although statistically weak, the histogram does indicate levels at points previously reported.

The results for the reaction $C^{12}(n, n)3\alpha$ are complicated by the fact that the identities of the two α-particles associated with the disintegration of the intermediate nucleus Be^8 are not known. If all possible values for the energy of the excited state of Be^8 are plotted (i.e., three per star), the significant values appear as peaks on a continuous background at points known from other

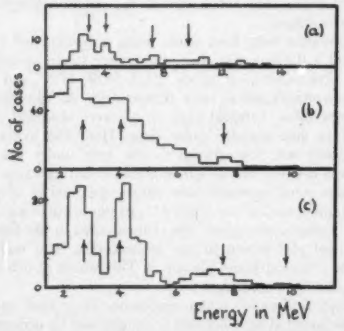

FIG. 1. Excited states of the intermediate nucleus Be^8: (a) from the reaction $B^{10}(n, H^3)2\alpha$, (b) from the reaction $C^{12}(n, n)3\alpha$ (all possible values), (c) from the reaction $C^{12}(n, n)3\alpha$ (unique values). The arrows refer to the values of the excited states previously known.

experiments [Fig. 1(b)]. The evaluation of the maximum (or minimum) angle between the α-particles from the Be^8 nucleus, for any given excited state and at any incident neutron energy, enabled the excited state of the Be^8 nucleus involved in 269 of the stars to be fixed uniquely. A histogram of these values is shown in Fig. 1(c).

The positions and widths of the excited states found agree, in general, with those observed by Green and Gibson,[3] using the reaction $Li^7(d, n)Be^8$, and by Richards.[4] No ground state was indicated although it is possible that stars of this type escaped observation owing to the very small angle between the α-particles emitted from this state.

The excited level at 5 Mev previously observed was not taken into account, as there seems to be good evidence for believing that a γ-ray is emitted from this level and that disintegration into two α-particles is forbidden. Some of the stars in group (d) can be accounted for in this way. However, the calculations performed on stars due to the $B^{10}(n, H^3)2\alpha$ reaction, where the direction of the incident neutron can be calculated instead of being assumed, show that most of the stars in group (d) originated from scattered neutrons.

No deviation from isotropy within the rather large limits of statistical error was found for the angular distribution of α-particles from the intermediate Be^8 nucleus in the center-of-mass coordinates of that nucleus for either reaction. A deviation from isotropy was indicated, however, in the angular distribution of the triton emitted in the first state of the reaction $B^{10}(n, H^3)2\alpha$.

From these results the percentage probability of a particular excited state (y) of Be^8 being formed in a nuclear event can be deduced. Figure 2 shows graphs of this percentage probability against incident neutron energy for the excited state found in the two reactions. The curves were drawn using the relation

$$\text{percentage probability} = (P_y/\Sigma_y P_y)\times 100,$$

where P_y is the total probability of an excited state, y being formed independently of the competition of other excited states. It was found that the experimental points could be best fitted if it were assumed that

$$P_y \propto x_y \exp(-Kx_y),$$

where x_y is the excess incident neutron energy above the threshold for the formation of an excited state y, and K is a constant.

Using only one value of K for each reaction, a fit was obtained for the variation of the percentage probability of the formation of all the excited states. Now the total probability, P_y, can be considered as a product of two factors, one being the internal probability of formation and the other being the penetrability factor. The latter is initially the dominant factor leading to a sharp rise from the threshold energy to the top of the potential barrier.

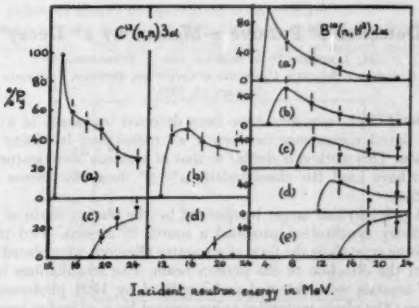

FIG. 2. The percentage probability (percent P_y) for the formation of the excited states of the intermediate nucleus Be^8 in the reactions $C^{12}(n, n)3\alpha$ and $B^{10}(n, H^3)2\alpha$. The excited states of Be^8 are given by (a) =2.65, (b) =4.0, (c) =7.25, (d) =9.8, (e) =13.5 Mev. The curves were calculated using the relation $P_y = x_y \exp(-Kx_y)$, where K=0.1 for the $C^{12}(n, n)3\alpha$ reaction and K=0.3 for the $B^{10}(n, H^3)2\alpha$ reaction.

Support for this view is forthcoming from the positions of the maxima in the two curves for P_y corresponding to the values for K obtained for the two reactions. It is found that they correspond to the excess incident neutron energy required to allow the triton and α-particle to escape over the top of the potential barriers of the compound nuclei C^{13} and B^{11}, respectively.

My thanks are due Dr. Burcham for permission to use the Cavendish Laboratory cyclotron, and to the Department of Scientific and Industrial Research for financial assistance.

[3] L. L. Green and W. M. Gibson, Proc. Phys. Soc. (London) **62**, 296 (1949).
[3] L. L. Green and W. M. Gibson, Proc. Phys. Soc. (London) **63**, 407 (1949).
[3] W. F. Hornyak and T. Lauritsen, Revs. Modern Phys. **20**, 191 (1948).
[4] H. T. Richards, Phys. Rev. **59**, 796 (1941).

Fission in Am^{243}

G. C. HANNA, B. G. HARVEY, N. MOSS, AND P. R. TUNNICLIFFE*
Atomic Energy Project, National Research Council of Canada, Chalk River, Ontario, Canada
January 8, 1951

SLOW neutron irradiation of Am^{241} produces a nuclide with a large slow neutron fission cross section. Chemical separation in ion-exchange resin columns shows that the fission is due to an americium isotope. The growth of fission rate with pile irradiation shows that Am^{242} g sec (the long-lived ground state) is responsible. Values for its fission and capture cross sections have been obtained.

Americium samples for fission measurements were prepared by ion-exchange separation of the americium from the irradiated Am^{241}. Sources were prepared (in most cases) by evaporation of the purified americium onto smooth platinum disks from a tantalum or wolfram filament at 2000°C. The Am^{241} in each source was estimated by α-counting in a low geometry proportional counter.[1] The fission rate in a neutron beam $\frac{1}{2}$ in. in diameter was measured using the fission chamber recently described.[2] The neutron beam intensity (about 4.5×10^5 neutrons/cm²/sec) was monitored with a Pu^{239} source mounted in a separate shallow chamber in the same beam. In earlier experiments[3] we have measured the total cross section, σ_1, of Am^{241}, and the partial cross section, $f\sigma_1$, for Cm^{242} production. (In fact, the samples used in that investigation also appear here as Nos. 3 to 7 inclusive.) Values of the Am^{241} destruction parameter, $\sigma_1 f'(\sigma)d\sigma = at$, were calculated with the aid of the pile operating log.

If $g\sigma_1$ is the partial cross section for the formation from Am^{241} of Am^{242} g sec and if the latter has a total cross section of $\sigma_2 = n\sigma_1$, then it can be shown that after irradiation (Am^{242} g sec)/(Am^{241}) $= [g/(n-1)]\{1-\exp[-(n-1)at]\}$. The specific fission rate (fission counts per 10^6 α-dpm of Am^{241} in a neutron beam of standard intensity) will then be of the form $N = N_1 + N_2 \times\{1-\exp[-(n-1)at]\}$. N_1 is the fission rate of Am^{241}, and N_2 is the "saturation" fission rate of Am^{242} g sec.

The fission cross section of Am^{241} was determined separately as 3.0 barns, giving N_1=28.8 cpm in the standard neutron beam. Other subsidiary experiments gave fission cross sections of about 20 barns and 5 barns (as an upper limit) for Pu^{239} and Cm^{243}. These latter figures were required (along with the spontaneous fission rate of Cm^{243}[3] for making very small corrections to the rather lightly irradiated sources (Nos. 4, 5, and 6), since these were not subjected to chemical separation.

Figure 1 shows the experimental values of $(N-N_1)$ and the theoretical curves for n=8, 9, and 10. The value n=9 gives the best fit, but the "scatter" in the results is greater than our estimated error. This may arise partly from variations in the neutron energy spectrum between different pile irradiation-positions, particularly if a strong resonance were involved, since several widely separated irradiation-positions were used and at widely differing times.

Taking[3] n=9 and σ_1=887 barns, we obtain for σ_2, the total Am^{242} g sec cross section, 8000 barns. This does not involve a

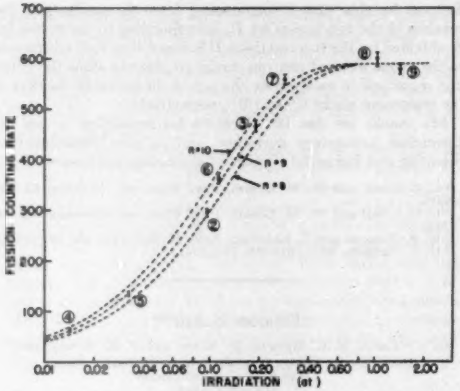

FIG. 1. The relation between Am^{242} fission rate (corrected for the presence of Am^{241}) and irradiation. The fission rate is expressed in counts/min per 10^4 α-$d\beta m$ of the accompanying Am^{241} in a flux of 4.5×10^5 neutrons/cm²/sec. The abscissas are in units of $\sigma t=\sigma_1 \int(n\sigma)dt$, which measures the destruction of Am^{241}.

knowledge of g, that is, of the actual amount of Am^{242} g sec present. However, the deduction of the fission cross section (σ_{1f}) does involve g. On comparison of the saturation fission rate of Am^{242} g sec with that of the Pu^{239} monitor, we obtain $\sigma_{1f}=500/g$. Recently O'Kelley and co-workers[4] gave a value of 0.2 for the I.T. branching ratio of Am^{242m}; this is clearly a lower limit for g, but probably a fairly close one.[3] With $g=0.2$, $\sigma_{1f}=2500$ barns; and hence the capture cross section is 5500 barns.

The shape of the curve (Fig. 1) in the very heavy irradiation region shows that any contribution from fission in Am^{243} is negligible. Taking $g=0.2$, we obtain an upper limit of about 25 barns for the fission cross section of Am^{243}.

It is a pleasure to acknowledge our debt to Mr. Philip B. Aitken for the design of equipment used in the handling of large α-activities.

* Now at Atomic Energy Research Establishment, Harwell, England.
[1] Hanna, Harvey, and Moss, Phys. Rev. 78, 617 (1950).
[2] Hanna, Harvey, Moss, and Tunnicliffe, to be published.
[3] Hanna, Harvey, and Moss, to be published.
[4] O'Kelley, Barton, Crane, and Perlman, Phys. Rev. 80, 293 (1950).

Note on Soft Gamma-Component of Cosmic Rays*

F. G. REST, L. REIFFEL, AND C. A. STONE
Armour Research Foundation of Illinois Institute of Technology, Chicago, Illinois
December 4, 1950

THE soft gamma-component of cosmic rays has been studied at 30,000 feet using the G-M counter geometry illustrated in Fig. 1. This arrangement minimizes the effects of dead space between tubes and the intrinsic inefficiency of the tubes for ionizing particles. Copper tubes with 0.031-inch walls were used to absorb Compton electrons with energies greater than 2 Mev. $A-B$ (A without B) counts, therefore, correspond to gamma-rays of energy less than 4 Mev. This nominal high energy cutoff is not sharp, owing to the distribution of Compton electrons and the geometry of the detector.

TABLE I. Counting rates at 30,000 feet.

Radiation	Counting rate	Omnidirectional flux
$A-B$ (soft gamma)	78 ±2 cpm	3.4 photons cm^{-2} sec^{-1}
AB (ionizing)	718 ±6 cpm	0.45 particles cm^{-2} sec^{-1}
A (both)	797 ±6 cpm	3.9 rays cm^{-2} sec^{-1}

$A-B$, AB, and A counts were observed simultaneously with circuits of 1 μsec resolution. The data thus obtained, corrected for aircraft contamination, are given in Table I.

The omnidirectional $A-B$ flux was calculated assuming a mean counter efficiency of 1 percent for photons.[1] There is good agreement between this observed photon flux and that calculated from the area under the gamma-ray portion of the cosmic-ray pulse distribution curve obtained with a scintillation counter and a differential analyzer.[2] (For a 10-percent mean crystal efficiency the scintillation data yields 3.8 photons cm^{-2} sec^{-1}.)

The calculation of the omnidirectional AB flux is based on a measured mean counter efficiency of 97 percent and a cosine squared variation with zenith angle.[3] The value obtained here compares closely with an interpolated value of 0.48 particle cm^{-2} sec^{-1} at 30,000 feet, using the estimates given by Montgomery.[4]

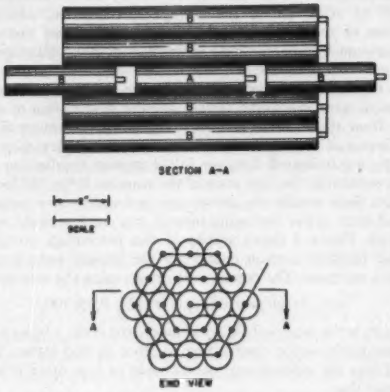

FIG. 1. Detector for soft gamma-radiation.

These investigations are being carried further, and data regarding altitude and directional intensity variations will be presented in a future publication.

* This work has been performed as one aspect of a project carried on under contract with the United States Department of the Air Force.
[1] H. Bradt, *et al.*, Helv. Phys. Acta 19, 77 (1946).
[2] Reiffel, Stone, and Rest, to be published.
[3] Biehl, Neher, and Roesch, Phys. Rev. 76, 914 (1949).
[4] D. J. X. Montgomery, *Cosmic Ray Ray Physics* (Princeton University Press, Princeton, 1949), p. 131.

Detection of Positive π-Mesons by π^+ Decay*

M. JAKOBSON,** A. SCHULZ, AND J. STEINBERGER†
Radiation Laboratory, University of California, Berkeley, California
January 12, 1951

POSITIVE π-mesons have been detected by means of a delayed coincidence between a π^+ meson and its decay μ^+ meson. This method is similar to that of previous investigators[1-3] who have used the characteristic $\mu^+-\beta^+$ decay for meson detection.

A polyethylene target bombarded by the photon beam of the Berkeley synchrotron provided a source of mesons. Two transtilbene crystals in the form of a counter telescope were placed 90° from the direction of the photon beam. The scintillations from the crystals were detected and amplified by 1P21 photo-multipliers. The photo-multiplier pulses, caused by a π^+ meson passing through one crystal and stopping in the second, open a gate of width 0.08 μsec which is then delayed 0.025 μsec. If the μ^+ meson pulse arising from the decay of the stopped π^+ meson appears during the time the gate is open, the meson is counted

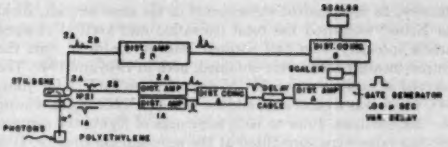

FIG. 1. Block diagram of electronics.

(Fig. 1). The amplifiers and coincidence circuits are of a distributed type.[4] The gate generator is a non-symmetrical cathode coupled multivibrator using miniature tubes.

In order to determine the detection efficiency, the meson counting rate was measured as a function of pulse height for (1) the π^+ meson pulse in the first crystal, (2) the π^+ meson pulse in the second crystal, (3) the μ^+ meson pulse in the second crystal. Curves for the π^+ meson pulses are of the same type as those of Steinberger.[3] A plateau was obtained for the μ^+ meson pulse (Fig. 2) by varying the gain of the amplifier providing the signals for the $\pi-\mu$-coincidence circuit. This plateau shows that all μ^+ mesons, which stop in the crystal during the time the gate is open, are counted.

With delayed coincidence detection, the accidental background is proportional to the length of gate used. Since the ratio of the π^+/μ^+ mean lives is of the order of 0.01, the accidental background is reduced by going to the faster decay scheme. With the present apparatus, the background is reduced only by a factor of 10 from that of reference 3. This is due to the larger ratio of pulse width to half-life and the difficulty of discrimination with narrower pulse widths. To lower the background further, a triple delayed coincidence involving $\pi^+-\mu^+-\beta^+$ decay has been used. This requires that the $\mu^+-\beta^+$ decay as well as the $\pi^+-\mu^+$ decay must take place in the second crystal. The background and counting efficiency are both lower when the $\pi^+-\mu^+-\beta^+$ detection scheme is used, but the ratio of counting efficiency to background is increased.

As an application of this method, the π^+ meson mean life[5-7] was measured by varying the gate delay. The delay was increased and decreased in cycles to minimize the effect of beam fluctuations and detection sensitivity changes. In order to obtain the accidental delayed coincidences, the gate is delayed for a time long compared to a π^+ mean life. The finite length of the gate does not need to be taken into account, since this does not affect the slope of the curve. Calculations show that the effect of the decay of the μ^+ mesons into positrons can be neglected. This is owing to the fact that only a small fraction of the positrons occur at each delay; in addition, only about 30 percent or less of these positrons lose sufficient energy in the crystal to be counted.

Eight lengths of RG 63/U cable were used to provide the variable delay. The delay of each cable was measured, using a synchroscope, by photographing the reflections of pulses sent down the cable. Cable delays were measured to 2 percent.

The 5641 meson counts, with a background of 398 at each of the seven points (Fig. 3), give for the mean life

$$\tau_m = 2.54 \pm 0.11 \times 10^{-6} \text{ sec.} \quad \text{(Standard deviation.)}$$

The corresponding half-life is $\tau_{\frac{1}{2}} = 1.76 \pm 0.08 \times 10^{-6}$ sec. This value agrees with that of reference 5 but lies outside the standard deviations of previous measurements.[6,7]

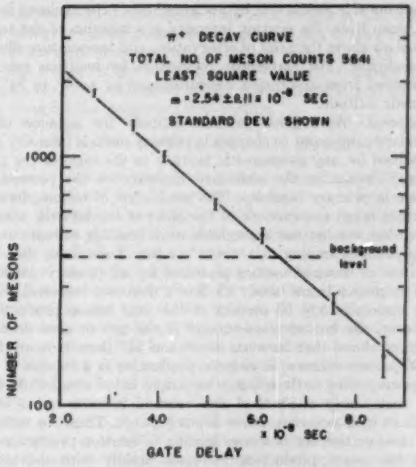

FIG. 3. The number of π^+ mesons at each gate delay plotted against the gate delay.

We wish to thank Professor E. McMillan and Professor O. Chamberlain for their encouragement and advice. Thanks also are due to Dr. Leininger for kindly providing the crystals and to the synchrotron crew for aid in carrying out the bombardments.

* This work was performed under the auspices of the AEC.
** Whiting Fellow, University of California.
† Now at Columbia University, New York, New York.

[1] F. Rasetti, Phys. Rev. 60, 198 (1941).
[2] Alvarez, Longacre, Ogren, and Thomas, Phys. Rev. 77, 732 (1950).
[3] J. Steinberger and A. S. Bishop, Phys. Rev. 78, 494 (1950).
[4] C. Wiegand, Rev. Sci. Instr. 21, 12, 975 (1950).
[5] Chamberlain, Mozley, Steinberger, and Wiegand, Phys. Rev. 79, 394 (1950).
[6] Kraushaar, Thomas, and Henri, Phys. Rev. 78, 486 (1950).
[7] E. A. Martinelli and W. K. H. Panofsky, Phys. Rev. 77, 465 (1950).

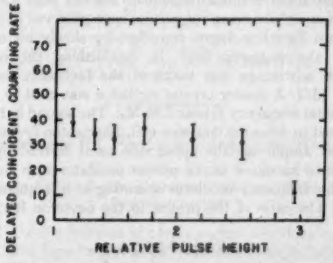

FIG. 2. Pulse 2B plateau. Plot of delayed coincidence counting rate against the relative height of a pulse required to make a delayed coincidence. Obtained by counting the number of delayed coincidences for different gain settings of amplifier 2B.

The Neutrons from the Nucleonic Component as an Indicator of Changes in Primary Intensities*

J. A. SIMPSON, JR.
Institute for Nuclear Studies, University of Chicago, Chicago, Illinois
December 18, 1950

TWO important factors in the selection of a suitable secondary component for low altitude observation of the changes and fluctuations of the primary cosmic-ray intensity are (a) uniqueness of interpretation of the observed intensity changes and (b) response of the secondary component to changes in the primary intensity. In this note the meson component and the neutrons from the nucleonic component will be compared briefly with respect to these factors.

Interpretation.—It has been shown that, owing to the short mean lives of the π and μ mesons, the temperature expansion and contraction of the atmosphere, especially in the 50 to 150-mb region,[1] where the meson production is large, has a pronounced

effect on the meson intensity observed at greater atmospheric depths; hence, it is difficult to distinguish between changes of secondary intensity caused by the atmosphere and changes caused by primary intensity.

Along with meson production, the primary radiations also generate a nucleonic component composed of high energy nucleons which, in turn, produce stars throughout the atmosphere of intermediate and low energies. These stars emit neutrons with energies up to the order of 10 to 30 Mev which are readily detected. It can be shown that almost the entire yield of atmospheric neutrons arises from star production by nucleons.[2] Since the nucleons have long mean lives, the neutron intensity is a function of the total mass of air above the point of observation, and temperature effects are negligible. The barometric coefficients for neutrons can be determined from absorption measurements[3] at $\lambda=0°$ to 54° N magnetic latitude.

Response.—At a given pressure altitude the response of a secondary component to changes in primary particle intensity can be defined for any geomagnetic latitude as the ratio of the percentage change in the secondary intensity to the percentage change in primary intensity. The production of mesons, having sufficient range to penetrate of the order of one-half the atmosphere, does not become appreciable until reaching proton cut-off energies corresponding to $\sim\lambda=45°$ or less. Even then, the contribution of charged mesons produced by all primary particles with momenta below about 15 Bev/c does not represent more than approximately 50 percent of the total meson production. However, the latitude dependence[3] of the fast or slow neutron intensity shows that between $\lambda=0°$ and 54° there is more than a 400 percent increase in neutron production in a column of atmosphere, owing to the primary radiations below about 15 Bev/c, and that nearly one-half of this fourfold increase comes from particles with momenta below about 8 Bev/c. Thus, the ratio of the cross section for processes leading to neutron production to that for meson production increases rapidly with decreasing primary particle energy. This was discussed by Simpson[3] and, more recently, by Forbush, Stinchcomb, and Schein.[4] Hence, the nucleonic component appears most suitable for measurement of changes in low energy primary particle intensity.

The slow neutron intensity is generally measured isotropically by detectors sensitive only to the disintegration of B^{10}. This discrimination against unrelated charged particle events and the lifetime of slowed neutrons increases the statistical accuracy of neutron measurements.

As an example, the measurement of the neutron intensity changes at 30,000-feet pressure altitude[5] (312 g cm^{-2} air) can be compared with concurrent measurements of charged particle intensity. In independent experiments in the same aircraft, Biehl and Neher[6] measured the total ionization and vertical charged particle intensity with and without lead at the same time the neutron measurements were obtained, both in 1948 and 1949. The observed intensities at $\lambda=56°$ N are given in Table I for June, 1948, which was a quiet day, and for October, 1949 flights during solar disturbances. Prior to both sequences of flights the neutron counting rates were normalized at the geomagnetic equator. It is seen that the response of the neutron component for singly charged primary particles of momenta <2 Bev/c is at least an order of magnitude greater than the response of the meson component. Owing to atmospheric absorption, this neutron intensity increase could not have been observed at sea level.

Adams and Braddick[7] have recently described a sharp increase of neutron intensity at sea level following a solar flare.[4] It is evident from their results that the primary particles producing the increase must have had higher energies than those associated with the measurements in October, 1949. They observed a response for the neutron component at least a factor of 40 greater than for the corresponding μ-meson increase of intensity measured by Elliot.[8]

TABLE I. Data for $\lambda=56°$ N geomagnetic latitude and 30,000-feet pressure altitude comparing concurrent measurements of the neutron and charged particle intensities. Neutron intensities were normalized at the geomagnetic equator in 1948 and 1949.

Observation	Neutron intensity[a,b] (counts per minute)	Total ionization[c] (ions cm^{-3} sec^{-1} (atmos of air)$^{-1}$)	Vertical charged particle intensity without lead[c]
Flight June, 1948 (quiet day intensity)	660	106	775
Flight October 27, 1949 (disturbed day intensity)	850	106	775
Percent change between 1948 and 1949	+30	0	0
Percent of shift of "knee" between October 27 and 31, 1949	~+3	0	0

[a] Reference 3.
[b] Reference 5.
[c] Reference 6.

* Assisted by the joint program of the ONR and AEC.

[1] A. Duperier, Proc. Phys. Soc. (London) **A62**, 684 (1949), and references therein.
[2] J. A. Simpson, Jr., Proceedings of the Echo Lake Conference on Cosmic Rays, 1949.
[3] J. A. Simpson, Jr., Phys. Rev. **73**, 1389 (1948).
[4] Forbush, Stinchcomb, and Schein, Phys. Rev. **79**, 501 (1950).
[5] J. A. Simpson, Jr., Phys. Rev. **81**, 639 (1951).
[6] A. T. Biehl and H. V. Neher, Phys. Rev. **78**, 172 (1950).
[7] N. Adams and H. J. Braddick, Phil. Mag. **41**, 501–503 (1950).
[8] H. Elliot and D. W. N. Dolbear, Proc. Phys. Soc. (London) **A63**, 137 (1950).

Magnetic Moment of the Deuteron

B. SMALLER, E. YASAITIS, AND H. L. ANDERSON*
Argonne National Laboratory, Chicago, Illinois
January 8, 1951

A PRECISION measurement of the ratio of the magnetic moment of the proton to that of the deuteron has been carried out using the magnetic resonance method. The apparatus was that used by Anderson[1] in the measurement of the magnetic moment of He^3, with a number of improvements. Gas samples were used so that the magnetic shielding correction could be calculated in a reliable way.

The measurements were made using mixtures of H_2 and D_2 in a small volume (0.6 cm^3) at high pressure (100 atmos) in a region where the magnetic field inhomogeneity was less than 3×10^{-6}. Two r-f coils having rectangular cross sections were used. These were oriented at right angles to each other and to the magnetic field. The proton coil nested snugly inside the deuteron coil. The space exterior to the coils was filled with Teflon plastic, thereby confining the gas to the region inside the coils. The possible fractional difference in the central value of the magnetic field for the two substances in this arrangement was less than 2×10^{-7}.

The proton and deuteron resonances were observed at the same time on two Esterline-Angus recorders by slowly increasing or decreasing the magnetic field. In establishing the resonance frequencies, advantage was taken of the fact that their ratio is close to 13/2. A master crystal oscillator was used to generate a fundamental frequency f_0 near 2.36 Mc. The second harmonic of this was used to drive the deuteron coil. The proton frequency was obtained by amplifying the upper side band derived by mixing the thirteenth harmonic of the master oscillator with the output of a variable frequency oscillator operating at a frequency f near 0.068 Mc. The ratio of the proton to the deuteron frequency is given by

$$R=\tfrac{1}{2}(13+f/f_0).$$

The relative error in the determination of R by this method is only 1/450 of the relative error in the determination of either f or f_0.

The frequency at which the magnetic field was modulated was 25 cycles, large enough to affect the shape of the otherwise sharp deuteron signal by frequency modulation effects.[3] A study of these effects showed that our line shapes could be correctly described by applying the analysis of Karplus[3] to our arrangement. We were able to show that by operating with dispersion unbalance of the r-f bridge, use of the center of symmetry of the resonance pattern in making the frequency comparisons was justified. The strength of the r-f signal was kept well below the saturation level, and the amplitude of the magnetic field modulation was 0.024 gauss, small enough so that the line widths were not excessively broadened.

Results of seven independent measurements are given in Table I. The stated uncertainty is about twice the usual probable error.

TABLE I. Measured values of μ_H/μ_D.

Run	Pressure H_2	lb/in.² D_2	μ_H/μ_D	
47	300	700	3.25719876	
49	300	500	3.25719803	
56	520	880	3.25719818	
57	300	500	3.25720074	
58	320	880	3.25720064	
59	660	740	3.25719854	Coils rotated 90°
60	660	740	3.25719825	Coils rotated 90°
			Mean 3.25719902 ±0.00000060	

In an earlier measurement with H_2O-D_2O mixtures, we obtained $\mu_H/\mu_D=3.25719986\pm0.00000045$.

The corrections for magnetic shielding calculated for H_2 and D_2 using Ramsey's formula[4] and new values for the rotational magnetic field[5,6] are very nearly the same. However, a difference in the magnetic shielding constant σ arises from changes in the amplitude of the molecular vibration.[7] For the first term in Ramsey's formula, Newell[8] has calculated that the contribution to σ is greater for D_2 by $(1.1\pm0.2)\times10^{-7}$. He points out that this change could be canceled by the effect of the molecular vibration in the second term. Accordingly, we give for the ratio of the magnetic moments

$$\mu_p/\mu_d=3.2571990\pm0.0000010.$$

This result is in agreement with, but ten times more accurate than that obtained by Levinthal.[9] It lies outside the experimental error of the result of Lindström.[10]

This result is comparable in accuracy with the new measurements by Prodell and Kusch[11] of the hyperfine structure in hydrogen and deuterium. Taken together these measurements provide a critical test of the theory of the structure of the deuteron.[12]

* Institute for Nuclear Studies, University of Chicago, Chicago, Illinois.
[1] H. L. Anderson, Phys. Rev. **76**, 1460 (1949).
[2] We are indebted to Dr. R. V. Pound for pointing this out to us.
[3] R. Karplus, Phys. Rev. **73**, 1027 (1948).
[4] N. F. Ramsey, Phys. Rev. **78**, 699 (1950).
[5] Kolsky, Phipps, Ramsey, and Silsbee, Phys. Rev. **79**, 883 (1950).
[6] Kolsky, Phipps, Ramsey, and Silsbee, Phys. Rev. **80**, 483 (1950).
[7] G. F. Newell, Phys. Rev. **80**, 476 (1950).
[8] G. F. Newell, private communication.
[9] E. C. Levinthal, Phys. Rev. **78**, 204 (1950).
[10] G. Lindström, Phys. Rev. **78**, 817 (1950).
[11] A. G. Prodell and P. Kusch, Phys. Rev. **79**, 1009 (1950).
[12] F. Low, Phys. Rev. **79**, 361 (1950).

A Model for Photo-Nuclear Reactions

LUIS MARQUEZ
Institute for Nuclear Studies, University of Chicago, Chicago, Illinois
December 7, 1950

MANY of the features of photo-nuclear reactions induced by gamma-rays from 6 to 100 Mev can be explained by using a model which assumes the gamma-ray to be absorbed by a single nucleon in a process similar to the photoelectric effect[1] and the photo-disintegration of the deuteron.[2]

In this process the cross section for the photo-nuclear absorption for one nucleon is

$$\sigma(W)=(8\pi^3e^2\nu_0/c)|z_{0E}|^2,$$

where

$$z_{0E}=\int U_0[(A-Z)/A]\phi_E d\tau\cong\tfrac{1}{2}\int U_0\phi_E d\tau$$

for a proton, and

$$z_{0E}=\int U_0(-Z/A)z\phi_E d\tau\cong-\tfrac{1}{2}\int U_0\phi_E d\tau$$

for a neutron. All symbols have their usual meanings, and $A\cong2Z$. The energy of the outgoing nucleon, aside from a small correction for momentum conservation, is $E_N=W-\epsilon_N$, where ϵ_N is the binding energy of the nucleon, and $W=h\nu$ is the energy of the gamma-ray. The total cross section is $\sigma_T=A\sigma(W)$; and the sum rule gives for the integrated cross section

$$\int_0^\infty\sigma_T d\nu=\pi^2e^2\hbar A/2Mc=0.015A \text{ Mev-barn},$$

as given by Levinger and Bethe.[3] The cross section, $\sigma(W)$, as a function of W will depend on the wave functions, which are not known. However, from analogy with similar processes[3-6] one would expect a rise at the threshold, ϵ_N, a maximum at about $2\epsilon_N$, and then a tail-off. This explains why the cross section for photo-emission of one nucleon is larger than two, and so on.

The fate of the nucleon which absorbed the gamma-ray will be determined by the size of the nucleus. In light elements, the nucleon will probably escape without being very much disturbed, and $\sigma(\gamma,p)/\sigma(\gamma,n)\cong1$. In medium and heavy nuclei, the nucleon will collide with other nucleons and form a compound nucleus; protons will be affected by the potential barrier. In the compound nucleus the emission of neutrons is more probable than the emission of protons, and (γ,n) will be favored over (γ,p). If there is enough energy available, several nucleons can be emitted. All this is in agreement with the presence of high energy protons in gamma-ray bombardment,[5] and with the (γ,p) and (γ,n) yields.[6,7]

Even in the medium and heavy elements, the nucleon that absorbs the gamma-ray near the surface can escape. Therefore, in bombardments of medium nuclei with monoenergetic gamma-rays, one expects that the ratio $\sigma(\gamma,p)/\sigma(\gamma,n)$ is proportional to $A^{-\frac{1}{3}}$ as long as $E_N>B$, where B is the potential barrier; and this is in rough agreement with Wäffler's results.[8]

Empirically, $\sigma(W)$ can be found in the light elements from the energy distribution of nucleons from gamma-ray bombardments if the gamma-ray spectrum is known; and it is always possible to find $\sigma(W)$ if the cross sections for $\sigma(\gamma,p)$, $\sigma(\gamma,n)$, $\sigma(\gamma,pn)$, $\sigma(\gamma,2n)$, etc., are all known as functions of W: their addition will give $\sigma(W)$. A crucial test of the model is the energy distribution of protons from light elements irradiated with high energy monochromatic gamma-rays.

[1] W. Heitler, *Quantum Theory of Radiation* (Oxford University Press, London, 1936), second edition, pp. 119, 127.
[2] H. Bethe and R. Peierls, Proc. Roy. Soc. (London) **A149**, 176 (1935).
[3] J. S. Levinger and H. A. Bethe, Phys. Rev. **78**, 115 (1950).
[4] M. Verde, Helv. Phys. Acta **23**, 453 (1950).
[5] B. C. Diven and G. M. Almy, Phys. Rev. **80**, 407 (1950).
[6] A. K. Mann and J. Halpern, Phys. Rev. **81**, 318 (1950). M. L. Perlman and G. Friedlander, Phys. Rev. **74**, 442 (1948). M. L. Perlman and G. Friedlander, Phys. Rev. **75**, 988 (1949).
[7] H. Wäffler and O. Hirzel, Helv. Phys. Acta **21**, 200 (1948).
[8] O. Hirzel and H. Wäffler, Helv. Phys. Acta **20**, 373 (1947).

On the Branching Ratio of the π^+ Meson*

FRANCES M. SMITH
Radiation Laboratory, University of California, Berkeley, California
January 8, 1951

EARLY experiments on π^+ mesons, using photographic emulsions as detectors, have seemed to show[1] that some of the π^+ mesons, upon stopping in matter, do not decay into μ^+ mesons.

These studies were concerned with mesons of fairly low energy so that the emulsion would be the only stopping material. Ilford

C_2 and C_3 emulsions were used in order to facilitate the identification of the mesons. In many cases the processed emulsions showed an apparent non-uniformity in sensitivity, and since the μ-meson track is rather tenuous in the region of the terminus of the π-track, there is a chance of missing the decay. For a more intensive study of the decay scheme, a much more sensitive emulsion is required. Ilford G_5 and Eastman NTB_3 emulsions were chosen for the present study.

The apparatus used in this study consisted of a brass chamber for holding the plates and the target. The target was 0.036-inch carbon. This assembly was mounted on a probe and inserted into the vacuum chamber of the 184-inch cyclotron. The circulating beam of 345-Mev protons irradiated the target. Mesons emitted in the backward direction entered a channel cut into the brass holder. This channel was of such dimensions that π^+ mesons from the target, with energies between 6 and 8 Mev only, will enter the emulsion after a turn of 180°. No μ-mesons from decay of the π stopping in the target can get into the plate chamber. μ-mesons from decay in flight of the π-mesons could get into the emulsion only if they were emitted in a narrow cone in the forward or backward direction. These would not be confusable with π-mesons from the target as their ranges in the emulsion would be too great or too small to have the correct energy.

The plates were studied using a high power microscope. Only those mesons which stopped in the emulsion at a distance greater than 10 microns from either surface of the undeveloped emulsion were counted.

Meson scattering from the channel walls gave a background fairly uniformly distributed, with respect to range, in the emulsion.

The analysis of the results consisted of a calculation of the number of background μ-mesons expected to fall in the main distribution. This number was subtracted from the number of mesons showing no decay found in the main distribution.

A preliminary estimate of the percentage of π-mesons from the target which do not decay into μ-mesons is, $R=0.3\pm0.4$ percent. This indicates that the branching ratio of the π^+ mesons is less than 1 percent and probably zero. A more complete account of this work will be published at a later date.

I wish to thank Dr. L. W. Alvarez for his many helpful suggestions in this study. I wish also to thank J. Vale and the cyclotron crew for their help in the use of the cyclotron and J. Willat for microscope work.

* This work was performed under the auspices of the AEC.

[1] Burfening, Gardner, and Lattes, Phys. Rev. 75, 382 (1949).

Neutron Capture Cross Sections and Level Density

H. Hurwitz, Jr.
Knolls Atomic Power Laboratory, Schenectady, New York
and
H. A. Bethe*
Cornell University, Ithaca, New York
January 11, 1951

It is known experimentally that neutron capture cross sections as well as nuclear binding energies exhibit fluctuations from isotope to isotope, which are related to whether the neutron and proton numbers are odd, even, or magic. It is difficult to understand the relation between the fluctuations in these two quantities if one assumes that level densities depend primarily on excitation energies measured from the ground state. The fluctuations can be correlated qualitatively, however, by the hypothesis that the significant quantity in determining level densities is the excitation energy measured not from the ground state but from a characteristic level which depends in a smooth way on the number of neutrons and protons in the nucleus.[1] This would imply that those factors which make the ground state low for even-even nuclei or nuclei with a magic number of neutrons or protons do not have an appreciable influence on the level densities at excitations corresponding to that of the compound nucleus in a capture process. In terms of the supermultiplet theory, the hypothesis is equivalent to saying that the odd, even, or magic property of N and Z has a strong influence on the supermultiplets of high symmetry but has comparatively little influence on the distribution of multiplets of low symmetry which correspond to high excitation. The same situation would be expected from the shell model since nuclei with almost completed shells and high binding energy should have fewer low lying states than nuclei with partially filled shells and relatively lower binding energy. Experiments of Kinsey, at Chalk River, on capture gamma-ray spectra indicate the correctness of this picture by showing few low lying levels for magic and near magic nuclei.[2] (These experiments give information on level densities in an excitation range lower than that at which the compound nucleus is initially formed in a capture process.)

This hypothesis implies that the neutron capture cross section is determined primarily by the binding energy of the target nucleus rather than that of the final nucleus. If the target nucleus has high binding energy, the initial system of free neutron plus target nucleus will have low energy so that the compound nucleus will be formed with low energy as compared to the smoothly varying characteristic energy. The level density will therefore be small, and hence, the capture cross section will tend to be small. One would therefore conclude that the number of neutron resonances and the average capture cross section would be large for odd-odd nuclei, intermediate for odd-even and even-odd nuclei, and small for even-even nuclei.[3] Nuclei with magic numbers of either protons or neutrons should have particularly few resonances for low energy incident neutrons and hence, small capture cross sections.

If the alternative assumption were made that the level density depends primarily on excitation measured from the ground state, it would follow that the capture cross sections should be largest where the total energy released in the capture process is largest. Thus, even Z-odd N nuclei would be expected to have higher level densities and average capture cross sections than do odd Z-even N nuclei, and odd Z-even N nuclei would be expected to have roughly the same capture cross sections as do even-even nuclei. Actually, it appears that even Z-odd N nuclei do not have larger capture cross sections than do odd Z-even N nuclei, and that even Z-even N nuclei have smaller cross sections than do odd Z-even N nuclei.

Since the neutron width, Γ_n, is roughly proportional to the level spacing, the capture cross section, when averaged over a neutron spectrum which is broad compared with the level spacing, will not depend strongly on the level spacing if the neutron width is small compared with the gamma-width.[4] Therefore, the above conclusions on average capture cross sections apply particularly to incident neutron energies in the range of a few kilovolts and above, where the ratio Γ_n/Γ_γ is not small.

* Consultant, Knolls Atomic Power Laboratory.

[1] The characteristic energy might be given by an expression similar to the Weizsäcker semi-empirical formula for the nuclear binding energy as a function of N and Z without the odd-even term. E. Feenberg, Revs. Modern Phys. 19, 239 (1947).

[2] B. B. Kinsey, report to the Brookhaven Conference on Neutron Physics, November 1950, unpublished.

[3] These conclusions have been reached independently on the basis of experimental evidence by Harris, Muehlhause, and Thomas, Phys. Rev. 79, 11 (1950).

[4] Feshbach, Peaslee, and Weisskopf, Phys. Rev. 71, 145 (1947), Eq. (28).

An Investigation of the Existence of a Sodium Lithium Molecule*

B. B. Phillips,† H. M. Froslie,‡ and R. H. McFarland
Kansas State College, Manhattan, Kansas
January 8, 1951

The vapors of the alkali metals have been examined extensively for absorption spectra. It has been established from their band absorption that these metals form diatomic molecules in both pure metals and in combinations of two dissimilar metals.

Walter and Barratt[1] examined and identified the absorption spectra of Li_2, Na_2, K_2, Rb_2, Cs_2, LiK, LiRb, LiCs, NaK, NaRb, NaCs, KRb, RbCs, and KCs.

The identification of a NaLi molecule is complicated by the existence of Na_2 and Li_2 band systems in the regions of the visible, near infrared and ultraviolet. Since the probability of molecular formation is a function of the product of the concentration of the atoms involved, it seemed possible that one component of a sodium-lithium mixture might be held at a low vapor pressure and the other at a high vapor pressure to increase the probability of observing the NaLi molecule.

In our experiment the lithium metal was placed in an absorption cell constructed of nickel and having water-cooled quartz windows. A nickel side tube was connected to the absorption cell to contain the sodium. Heating units were arranged around the absorption cell and side tube to control the temperature of the sodium and lithium metals independently.

The lithium metal was maintained at 850°C. A series of absorption spectrograms was then taken with the sodium at temperatures of 435, 460, 485, and 510°C, respectively. A similar procedure was used for maintaining constant high sodium with increasing lithium vapor pressures.

The results of this experiment confirm the previous work of Walter and Barratt. No bands attributable to a NaLi molecule were observed in the region 3000 to 8000A. No explanation is available, particularly as it is the only member not observed of the complete set of binary molecular systems obtainable with the alkali metals.

* Contribution No. 10, Department of Physics, Kansas State College, Manhattan, Kansas.
† Now at Airport Station, Weather Bureau, Memphis, Tennessee.
‡ Now at South Dakota State College, Brookings, South Dakota.
[1] J. M. Walter and S. Barratt, Proc. Roy. Soc. (London) A119, 257 (1928).

Photo-Production of Neutral Mesons in Nuclear Electric Fields and the Mean Life of the Neutral Meson*

H. PRIMAKOFF†
Laboratory for Nuclear Science and Engineering, Massachusetts Institute of Technology, Cambridge, Massachusetts
January 2, 1951

IT has now been well established experimentally that neutral π-mesons (π^0) decay into two photons.[1] Theoretically, this two-photon type of decay implies zero π^0 spin;[2] in addition, the decay has been interpreted as proceeding through the mechanism of the creation and subsequent radiative recombination of a virtual proton anti-proton pair.[3] Whatever the actual mechanism of the (two-photon) decay, its mere existence implies an effective interaction between the π^0 wave field, φ, and the electromagnetic wave field, **E**, **H**, representable in the form:

$$\text{Interaction Energy Density} = \eta(\hbar/\mu c)(\hbar c)^{-1}\varphi \mathbf{E}\cdot\mathbf{H}. \quad (1)$$

Here φ has been assumed pseudoscalar, the factors $\hbar/\mu c$ and $(\hbar c)^{-1}$ are introduced for dimensional reasons (μ = rest mass of π^0), and η is a dimensionless constant determined by the decay mechanism.[4]

One can obtain η immediately (by a first-order perturbation calculation) in terms of the mean life, τ, of a neutral π-meson at rest, *viz.*:[5]

$$\tau^{-1} = \pi^2\eta^2\mu c^2/2\hbar. \quad (2)$$

The effective interaction of Eq. (1) can now be used for a calculation of the probability of the inverse process: π^0 production in photon-photon collisions, or, for the calculation of the probability of the more interesting process: π^0 production in the collision of a photon with an external, approximately static electric field; e.g., the Coulomb field of a (slowly recoiling) nucleus. The total cross section σ for this last process is, from a first-order perturbation treatment of Eq. (1), proportional to η^2; i.e., to τ^{-1}; one obtains[6]

$$\sigma \approx 32\pi^2\frac{\hbar/\mu c}{c\tau}Z^2\left(\frac{e^2}{\hbar c}\right)\left(\frac{\hbar}{\mu c}\right)^2\frac{4}{3}\left(\frac{\hbar\kappa}{\mu c}\right)^2, \quad \text{for} \quad \hbar\kappa \ll \hbar k \approx \mu c \quad (3)$$

$$\sigma \approx 32\pi^2\frac{\hbar/\mu c}{c\tau}Z^2\left(\frac{e^2}{\hbar c}\right)\left(\frac{\hbar}{\mu c}\right)^2, \quad \text{for} \quad R(k-\kappa) \approx \frac{(2Z)^{\frac{1}{3}}}{2}\frac{\mu c}{\hbar k} \ll 1. \quad (4)$$

In Eqs. (3) and (4), $\hbar k$, $\hbar\kappa = \hbar k[1-(\mu c/\hbar k)^2]^{\frac{1}{2}}$ are, respectively, the momenta of the incident photon and produced neutral π-meson; the angular distribution of the mesons is strongly collimated about the direction of the incident photon if $\hbar k \gg \mu c$. In deducing Eq. (3), it has been supposed that the nuclear protons remain approximately at rest during time intervals of the order of several periods of the incident electromagnetic wave [since $v_{\text{proton}} \approx \frac{1}{2}c$ and $(ck)^{-1} \leqq \hbar/\mu c^2$], and that the probability of finding any pair of protons a distance r apart is proportional to $\exp(-r/R)$, where $R \approx \hbar(2Z)^{\frac{1}{3}}/\mu c$ is the nuclear radius. It is seen from Eqs. (3) and (4) that the electric fields of the Z protons contribute "coherently" to the π^0 production, once the photon energy exceeds $\frac{1}{2}(2Z)^{\frac{1}{3}}\mu c^2$.

Thus, if τ is less than, say, 10^{-17} sec, Eq. (4) indicates that a Z^2 term should be observable in the total cross section for production of neutral π-mesons in photon-nucleus collisions. Since no such term has so far been experimentally detected,[7] one can set a very rough lower limit on τ: $\tau > 5\times10^{-18}$ sec. An approximate upper limit of 5×10^{-14} sec seems to be indicated by cosmic-ray data.[8]

* Assisted by the joint program of the ONR and AEC.
† On leave from Washington University, St. Louis, Missouri.
[1] Steinberger, Panofsky, and Steller, Phys. Rev. 78, 802 (1950); Panofsky, Aamodt, Hadley, and Phillips, Phys. Rev. 80, 94 (1950).
[2] C. N. Yang, Phys. Rev. 77, 243 (1950); D. C. Peaslee, Helv. Phys. Acta 23, 845 (1950); we exclude the possibility of the π^0 spin being >1.
[3] J. Steinberger, Phys. Rev. 76, 1180 (1949), and other references quoted there.
[4] Marshak, Tamor, and Wightman, Phys. Rev. 80, 765, 766 (1950); K. Brueckner, Phys. Rev. 79, 641, 187 (1950).
[5] The mechanism of π^0 decay via interaction with virtual proton anti-proton pairs gives, if for example γ_5 coupling is used between the meson and nucleon wave fields, $\tau^{-1} = (\mu c^2/16\pi^2\hbar)(\mu c^2/Mc^2)^2(e^2/\hbar c)$ (reference 3), so that in this case, $\eta = (\mu/8\pi^2 M)(e^2/\hbar c)^{\frac{1}{2}}(e^2/\hbar c)$.
[6] Another possible process predicted from Eq. (1) involves the one-photon decay of a π^0 in an external (nuclear) electric field. If τ' is the mean life of this decay, one obtains (with N as the number of nuclei per unit volume, and using Eq. (4))

$$\tau/\tau' = \tau c N\sigma 2k^2\left[\kappa^2 + (\mu c\kappa/\hbar)^2\right]^{-\frac{1}{2}} \approx 64\pi^2 Z^2(e^2/\hbar c)(\hbar/\mu c)^2 N \ll 1.$$

[7] Observations of Steinberger, Panofsky, and Steller quoted by R. F. Mozley, Phys. Rev. 80, 493 (1950).
[8] Carlson, Hooper, and King, Phil. Mag. 41, 701 (1950).